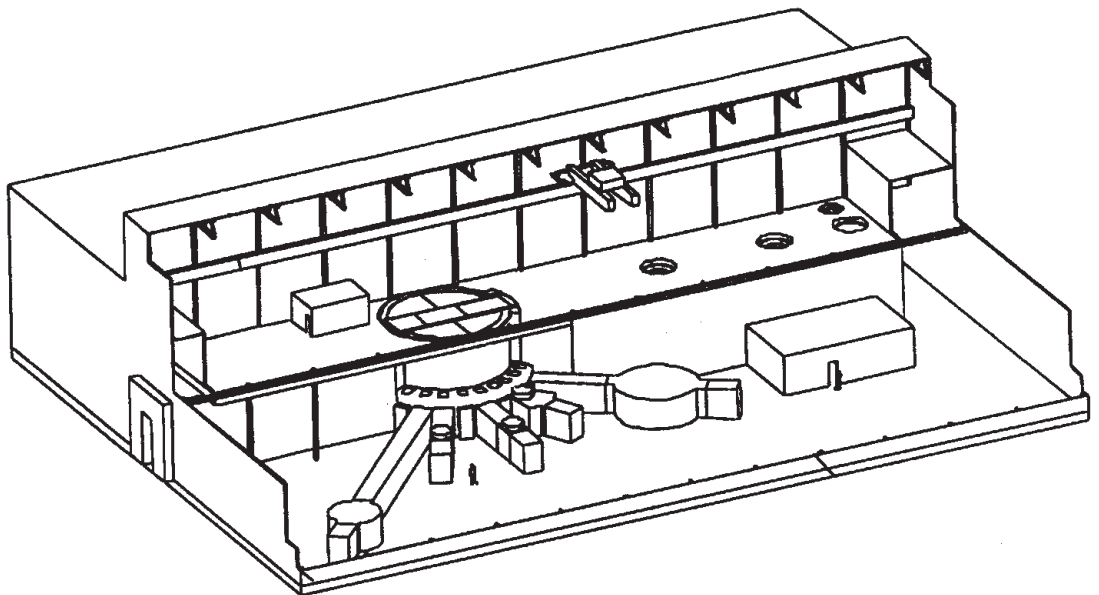


SATIF-3  
SHIELDING ASPECTS  
OF ACCELERATORS,  
TARGETS  
AND  
IRRADIATION  
FACILITIES



*Proceedings of the Third Specialists Meeting on*

***Shielding Aspects  
of Accelerators, Targets  
and Irradiation Facilities***

Tohoku University  
Sendai, Japan  
12-13 May 1997

*jointly organised by*

OECD/Nuclear Energy Agency

Shielding Working Group of the Reactor Physics Committee

Radiation Safety Information Computational Centre

Tohoku University

## ORGANISATION FOR ECONOMIC CO-OPERATION AND DEVELOPMENT

Pursuant to Article 1 of the Convention signed in Paris on 14th December 1960, and which came into force on 30th September 1961, the Organisation for Economic Co-operation and Development (OECD) shall promote policies designed:

- to achieve the highest sustainable economic growth and employment and a rising standard of living in Member countries, while maintaining financial stability, and thus to contribute to the development of the world economy;
- to contribute to sound economic expansion in Member as well as non-member countries in the process of economic development; and
- to contribute to the expansion of world trade on a multilateral, non-discriminatory basis in accordance with international obligations.

The original Member countries of the OECD are Austria, Belgium, Canada, Denmark, France, Germany, Greece, Iceland, Ireland, Italy, Luxembourg, the Netherlands, Norway, Portugal, Spain, Sweden, Switzerland, Turkey, the United Kingdom and the United States. The following countries became Members subsequently through accession at the dates indicated hereafter: Japan (28th April 1964), Finland (28th January 1969), Australia (7th June 1971), New Zealand (29th May 1973), Mexico (18th May 1994), the Czech Republic (21st December 1995), Hungary (7th May 1996), Poland (22nd November 1996) and the Republic of Korea (12th December 1996). The Commission of the European Communities takes part in the work of the OECD (Article 13 of the OECD Convention).

### NUCLEAR ENERGY AGENCY

*The OECD Nuclear Energy Agency (NEA) was established on 1st February 1958 under the name of the OEEC European Nuclear Energy Agency. It received its present designation on 20th April 1972, when Japan became its first non-European full Member. NEA membership today consists of all OECD Member countries, except New Zealand and Poland. The Commission of the European Communities takes part in the work of the Agency.*

*The primary objective of the NEA is to promote co-operation among the governments of its participating countries in furthering the development of nuclear power as a safe, environmentally acceptable and economic energy source.*

*This is achieved by:*

- *encouraging harmonization of national regulatory policies and practices, with particular reference to the safety of nuclear installations, protection of man against ionising radiation and preservation of the environment, radioactive waste management, and nuclear third party liability and insurance;*
- *assessing the contribution of nuclear power to the overall energy supply by keeping under review the technical and economic aspects of nuclear power growth and forecasting demand and supply for the different phases of the nuclear fuel cycle;*
- *developing exchanges of scientific and technical information particularly through participation in common services;*
- *setting up international research and development programmes and joint undertakings.*

*In these and related tasks, the NEA works in close collaboration with the International Atomic Energy Agency in Vienna, with which it has concluded a Co-operation Agreement, as well as with other international organisations in the nuclear field.*

© OECD 1998

Permission to reproduce a portion of this work for non-commercial purposes or classroom use should be obtained through the Centre français d'exploitation du droit de copie (CFC), 20, rue des Grands-Augustins, 75006 Paris, France, Tel. (33-1) 44 07 47 70, Fax (33-1) 46 34 67 19, for every country except the United States. In the United States permission should be obtained through the Copyright Clearance Center, Customer Service, (508)750-8400, 222 Rosewood Drive, Danvers, MA 01923 USA, or CCC Online: <http://www.copyright.com/>. All other applications for permission to reproduce or translate all or part of this book should be made to OECD Publications, 2, rue André-Pascal, 75775 Paris Cedex 16, France.

NUCLEAR SCIENCE COMMITTEE

*Proceedings of the Third Specialists Meeting on*

**SHIELDING ASPECTS  
OF ACCELERATORS, TARGETS  
AND IRRADIATION FACILITIES**

Tohoku University  
Sendai, Japan  
12-13 May 1997

*jointly organised by*

OECD/NEA

Shielding Working Group of the Reactor Physics Committee of Japan  
Radiation Safety Information Computational Centre  
Tohoku University

NUCLEAR ENERGY AGENCY  
ORGANISATION FOR ECONOMIC CO-OPERATION AND DEVELOPMENT



## FOREWORD

Accelerators play an increasingly important role in technological, energy and medical applications. As accelerators become more widely used and as their power increases, challenging new problems arise that require attention from the point of view of the characterisation of radiation environments and radiological safety.

The Nuclear Science Committee of the OECD Nuclear Energy Agency has sponsored a series of meetings on *Shielding Aspects of Accelerators and Irradiation Facilities (SATIF)* which are held every 18 months. SATIF-1 was held on 28-29 April 1994 in Arlington, Texas; SATIF-2 on 12-13 October 1995 at CERN in Geneva, Switzerland; and SATIF-3 was held on 12-13 May 1997 at Tohoku University in Sendai, Japan.

A specific task force was set up to co-ordinate the group's activities. Objectives included:

- identifying needs and carrying out experiments to improve the knowledge of thin and thick target neutron yields, neutron penetration, streaming, skyshine, etc.;
- making proposals, having discussions and executing shielding experiments in order to improve shield modelling;
- exchanging information on the present status of computer codes and nuclear data files in use;
- selecting shielding benchmark experiments in order to establish international collaboration in the area of method validation;
- investigating high-energy dosimetry aspects including anthropomorphic computing models.

The task force meetings are now held in conjunction with seminars on *Simulating Accelerator Radiation Environments (SARE)*, which concentrate on presenting new developments and experience in simulating radiation environments and on exchanging information. Holding the meetings simultaneously has improved synergy between the different aspects and research communities. The forthcoming meetings will be held along with a topical meeting on *Accelerator Applications (AccApp'98)*. The fourth SARE meeting will be held on 13-15 September 1998 in Knoxville, TN, USA, and the fourth SATIF meeting will immediately follow on 17-18 September 1998 at the same location.

The current proceedings provide a summary of the discussions, decisions and conclusions together with the text of the presentations made at the third SATIF meeting.

We would like to express our gratitude to the organising committee, in particular to those having taken care of the local arrangements for the shaping of the technical programme and for chairing the different sessions. Special thanks go to Amanda McWhorter and Frédérique Joyeux for their dedication in editing these proceedings and their efforts to improve the layout of the text.

This text is published on the responsibility of the Secretary-General of the OECD. The views expressed do not necessarily correspond to those of the national authorities concerned.



## TABLE OF CONTENTS

<b>Executive Summary</b> .....		9
<b>Session I: Source Term and Related Data – Electron Accelerator</b> .....		19
<b>Chairs: A. Ferrari and H. Hirayama</b>		
<i>Gas Bremsstrahlung and Narrow Beam Dosimetry</i> .....		
		21
<i>M. Pelliccioni</i>		
Some Preliminary Results About Narrow Beam Dosimetry.....		
		23
<i>M. Pisharody, P.K. Job, S. Magill, J. Proudfoot, R. Stanek</i>		
Measurement of Gas Bremsstrahlung from the Insertion Device Beam Lines of the Advanced Photon Source.....		
		33
<i>Photoneutron and Photopion – DDX and Spectrum</i> .....		
		41
<i>T. Fukahori, Japanese Nuclear Data Committee</i>		
Status of Nuclear Data Evaluation for JENDL Photonuclear Data File.....		
		43
<i>C.Y. Fu, T.A. Gabriel, R.A. Lillie</i>		
PICA95: An Intranuclear-Cascade Code for 25 MeV to 3.5 GeV Photon-Induced Nuclear Reactions.....		
		49
<i>A. Fassò, A. Ferrari, P.R. Sala</i>		
Total Giant Resonance Photonuclear Cross-Sections for Light Nuclei: A Database for the FLUKA Monte Carlo Transport Code.....		
		61
<b>Session II: Source Term and Related Data – Proton and Ion Accelerator</b> .....		75
<b>Chairs: L.A. Charlton and K. Shin</b>		
<i>Thin Target Yield Measurements and Compilation</i> .....		
		77
<i>P. Nagel, P. Vaz</i>		
Summary of Compiled Experimental Data from Intermediate Energy Neutron and Proton Interactions with Different Nuclides (EXFOR Database) .....		
		79
<i>Thick Target Yield Measurements and Compilation</i> .....		
		81
<i>K. Shin, S. Ono, K. Ishibashi, S. Meigo, H. Takada, N. Sasa, H. Nakashima, S. Tanaka, N. Nakao, T. Kurosawa, T. Nakamura, Y. Uwamino</i>		
Thick Target Yield Measurements in TIARA, KEK and HIMAC .....		
		83

<i>Spallation Neutron Source Facility</i> .....	95
<i>D. Filges, P. Cloth, R.-D. Neef, H. Schaal</i>	
Radiation Physics of High Power Spallation Targets: State of the Art Simulation Methods and Experiments, The “European Spallation Source” (ESS) .....	97
<i>T.A. Gabriel, J.N. Barnes, L.A. Charlton, J. DiStefano, K. Farrell, J. Haines, J.O. Johnson, L.K. Mansur, S.J. Pawel, M. Siman-Tov, R. Taleyarkhan, M.W. Wendel, T.J. McManamy, M.J. Rennich, A. Williams</i>	
Overview of the National Spallation Neutron Source with Emphasis on the Target Station.....	115
<i>M. Furusaka, H. Ikeda</i>	
Overview of the Spallation Neutron Source Project in JHF.....	141
<b>Session III: Shielding</b> .....	147
<b>Chairs: N. Mokhov and K. Hayashi</b>	
<i>Shielding Benchmark Problem – Review of Analysis</i> .....	149
<i>Y. Nakane, Y. Sakamoto, K. Hayashi, T. Nakamura</i>	
Intercomparison of Neutron Transmission Benchmark Analyses for Iron and Concrete Shields in Low, Intermediate and High Energy Proton Accelerator Facilities .....	151
<i>Attenuation Length – Definition and Intercomparison</i> .....	183
<i>H. Hirayama, Attenuation Length Sub-Working Group (Japan)</i>	
Intercomparison of the Medium-Energy Neutron Attenuation in Iron and Concrete.....	185
<i>Shielding Experiments and Compilation</i> .....	197
<i>Y. Sakamoto, H. Nakashima, Y. Uwamino, N. Nakao, H. Handa, T. Nakamura T. Shibata, TIARA Experimental Group, ISIS Experimental Group</i>	
Bulk Shielding Experiments at TIARA and ISIS .....	199
<b>Session IV: Miscellaneous Topics – Part I</b> .....	207
<b>Chairs: L. Waters and Y. Uwamino</b>	
<i>Neutron Facility for Shielding Experiment and Detector Calibration</i> .....	209
<i>T. Nakamura, M. Takada, N. Nakao, M. Baba, T. Iwasaki, H. Nakashima, Sh. Tanaka, S. Meigo, Y. Sakamoto, Y. Nakane, Su. Tanaka, Y. Uwamino, N. Nakanishi</i>	
Neutron Facility for Shielding and Cross-Section Experiments in Japan .....	211
<i>C. Birattari, T. Rancati, A. Ferrari, M. Höfert, T. Otto, M. Silari</i>	
Recent Results at the CERN-EC High Energy Reference Field Facility.....	219

<b><i>Dosimetry and Instrumentation</i></b> .....	235
<i>V. Mares, A. Sannikov, H. Schraube</i>	
The Response Functions of a <sup>3</sup> He Bonner Spectrometer and Their Experimental Verification in High Energy Neutron Fields .....	237
<i>A.G. Alexeev, S. Kharlampiev, T. Kosako</i>	
Re-Calculation of Energy Response of Tissue Equivalent Proportional Counter for Neutron Above 20 MeV .....	249
<b>Miscellaneous Topics – Part II</b> .....	263
<b>Chairs: F. Clapier and Y. Sakamoto</b>	
<b><i>Activation</i></b> .....	265
<i>N. Pauwels, F. Clapier, P. Gara, J. Proust, T. Nakamura, E. Kim</i>	
Test of Activation Detectors (Bi and Al) as Neutron Spectrometer in the Range 6 to 140 MeV .....	267
<i>V.I. Ivanov, N.M. Sobolevsky, V.G. Semenov</i>	
Computer Version of the Handbook on Radionuclide Production Cross-Sections at Intermediate Energies (the NUCLEX Code) .....	277
<b><i>Dose Conversion Coefficient and Anthropomorphic Phantom</i></b> .....	287
<i>M. Pelliccioni</i>	
Conversion Coefficients for High-Energy Radiation .....	289
<i>S. Iwai, T. Uehara, O. Sato, N. Yoshizawa, S. Furihata, S. Takagi, S. Tanaka, Y. Sakamoto</i>	
Overview of Fluence to Dose Equivalent Conversion Coefficients for High-Energy Radiations – Calculational Methods and Results of Effective Dose Equivalent and Effective Dose Per Unit Particle Fluence .....	299
<b>Session V: Present Status of Computer Codes and Cross-Section and Shielding Data Libraries</b> .....	333
<b>Chairs: B. Kirk and P. Vaz</b>	
<i>B. Kirk, E. Sartori, P. Vaz</i>	
Progress Report on the Collection of Computer Codes and Data Sets for Accelerator Shielding Analysis .....	335
<b>List of Participants</b> .....	359



## EXECUTIVE SUMMARY

The main objectives of the SATIF meetings are:

- to promote the exchange of information among scientists in this particular field;
- to identify areas where international co-operation can be fruitful;
- to carry on a programme of work in order to achieve progress in specific priority areas.

The first SATIF meeting (SATIF-1) took place on 29-30 April 1994 in Arlington, Texas (USA), and the second meeting (SATIF-2) was held from 12-13 October 1995 at CERN (European Laboratory for Particles Physics) in Geneva, Switzerland.

In the meantime, the seventh meeting of the NEA Nuclear Science Committee, held on 29-30 May 1996, approved the setting up of a specific Task Force on Shielding Aspects of Accelerators, Targets and Irradiation Facilities. As a consequence, the SATIF specialists meetings became regular meetings of this Task Force.

The third Specialists Meeting on Shielding Aspects of Accelerators Targets and Irradiation Facilities (SATIF-3) took place from 12-13 May 1997 in Sendai, Japan. It was jointly organised by:

- the OECD Nuclear Energy Agency;
- the Shielding Working Group of the Reactor Physics Committee of Japan;
- the Radiation Safety Information Computational Center of the USA;
- Tohoku University.

About fifty specialists attended the meeting, including physicists, engineers and technicians from laboratories, institutes, universities and industries in France (IN2P3), Germany (DESY, KFA Jülich, University of Munich), Italy (INFN, ENEA, LNGS), Sweden (University of Uppsala), Japan (JAERI, KEK, RIKEN, INS, Universities of Tokyo and Kyoto, Mitsubishi, Hitachi), USA (ANL, CEBAF, Fermilab, LANL, RSICC and SLAC) and the Russian Federation (IHEP) as well as representatives from international organisations (OECD/NEA and CERN).

The meeting was organised in six sessions on the following topics:

- **Session 1** – Source Term and Related Data – Electron Accelerator
  - *Subsession 1-1* Gas Bremsstrahlung and Narrow Beam Dosimetry
  - *Subsession 1-2* Photoneutron and Photopion – DDX and Spectrum

- **Session 2** – Source Term and Related Data – Proton and Ion Accelerator
  - *Subsession 2-1* Thin Target Yield Measurements and Compilation
  - *Subsession 2-2* Thick Target Yield Measurements and Compilation
  - *Subsession 2-3* Spallation Neutron Source Facility
- **Session 3** – Shielding
  - *Subsession 3-1* Shielding Benchmark Problem – Review of Analysis
  - *Subsession 3-2* Attenuation Length – Definition and Intercomparison
  - *Subsession 3-3* Shielding Experiments and Compilation
- **Session 4** – Miscellaneous Topics
  - *Subsession 4-1* Neutron Facility for Shielding Experiments and Detector Calibration
  - *Subsession 4-2* Dosimetry and Instrumentation
  - *Subsession 4-3* Activation
  - *Subsession 4-4* Dose Conversion Coefficients and Anthropomorphic Phantom
- **Session 5** – Present Status of Computer Codes and Cross Section and Shielding Data Libraries
  - *Subsession 5-1* Current Status of Computer Codes and Data Sets for Accelerator Shielding Analysis
  - *Subsession 5-2* A Standard for Shielding Calculations
- **Session 6** – Discussions and Future Actions

About 24 papers were presented at the meeting. An extensive discussion took place during Session 6, with the following objectives:

- to review the progress achieved since the SATIF-2 meeting held on 12-13 October 1995 at CERN;
- to monitor the status of the agreed actions (on experiments, basic data, codes and methods) undertaken since then;
- to identify and initiate new co-operative actions;
- to improve common understanding of problems that have technical and safety significance.

It was generally recognised that substantial developments took place during this period and that significant progress has been achieved. However, in order to achieve further progress participants felt that substantial efforts should be developed and actions undertaken in several areas, including:

- basic data (new measurements, compilation of existing neutron, proton, light ion and pion cross-section data in the intermediate energy range above a few dozens of MeV, forward bremsstrahlung yields from thick targets at energies above 100 MeV, photoproduction data namely photonuclear cross-sections and photonuclear yields and angular distributions for all common elements at all energies, photopion yields and angular distributions at energies above 200 MeV, isotope production data, etc.).
- nuclear models and computer codes in the intermediate energy range (code validation, intercomparison of codes, comparison between experimental data and predictions from existing computer codes implementing nuclear models);
- shielding experiments (measurements of forward and lateral attenuation of iron and concrete for proton and ion accelerators up to a few tens of GeV and as deep as possible i.e. at least 5-6 meters, measurement of forward and lateral attenuation at electron accelerators);
- new or better measurements of many activation detector excitation functions (in particular C-11 production by neutrons and pions in the energy range above 100 MeV and Bi production);
- benchmark data (development of new benchmark exercises, further compilation of existing benchmark data sets, etc.);
- anthropomorphic computational models (compilation of existing models, phantom geometries and material compositions, dosimetric studies, etc.).

In the next section, a detailed list of the actions decided at the SATIF-3 Meeting is provided. Taking each of the presentations at SATIF-3, actions to be undertaken or continued and which concern the corresponding subject and/or related topics are listed as specific items; the names of those designated at the SATIF-3 Meeting to perform the monitoring and follow up of the work are indicated. The listed actions reflect and incorporate the assessment, made by the SATIF-3 participants, of the status of the actions undertaken since the SATIF-2 Meeting.

As can be seen in the relevant items, two important topics proposed by Japan which will be followed-up at the SATIF-4 Meeting concern shielding benchmark calculations and attenuation length calculations.

These areas will greatly benefit from the definition of new experiments and by undertaking new international intercomparison exercises.

The high quality of the SATIF-3 Meeting and its excellent organisation would not have been possible without the work of the Local Organising Committee and its Chairman Prof. T. Nakamura, and the continuous help of Dr. N. Yoshizawa.

Acknowledgements are also due to the members of the Scientific Committee of SATIF-3 (F. Clavier, A. Fassò, A. Ferrari, T. Gabriel, H. Hirayama, N. Ipe, B. Kirk, N. Mokhov, T. Nakamura, E. Sartori and L. Waters) for their contribution in shaping the technical programme.

## New or continued actions decided at SATIF-3

### *Gas bremsstrahlung and narrow beam dosimetry*

- **Narrow beam dosimetry – Organ and effective doses estimated between 1 MeV and 1 GeV** (*M. Pelliccioni*)
  - include more organs in the computations;
  - include more energies in the calculations;
  - extend energy range of the computations;
  - determine how adequately average doses over organs describe narrow beam effects;
  - co-ordinate effort to push official bodies (e.g. ICRP) to include narrow beams issues;
  - define a new quantity and agree on how to score it.
- **Gas bremsstrahlung measurements performed at APS** (*P.K. Job*)
  - compare with calculation.

### *Photoneutron and photopion data*

- **Nuclear data evaluation for the JENDL Photonuclear Data File** (*T. Fukahori*)
  - make data available;
  - address question of how to handle targets for which data are not available.
- **Need for experimental data to build confidence in predicting spectra and angular distributions** (*N. Ipe, A. Fassò, S. Ban and P. Degtyarenko are involved in the different aspects*):
  - SLAC/KEK collaboration has finalised a proposal;
  - CEBAF is building detectors.
- **Giant dipole resonance photonuclear cross-sections** (*A. Fassò*)
  - check energy regions near threshold;
  - redo calculations with new version of PEANUT/FLUKA;
  - complete data with parametrisation for missing nuclei;
  - extend to heavier nuclei – **requesting support from NEA.**

- **PICA95 code** (*C.Y. Fu*)
  - make code available;
  - make gamma and pion cross-section data available;
  - comparison PICA95 and CEM95;
  - photopion yields and angular distributions are needed for  $E > 200$  MeV;
  - more generally, there is a lack of available data for double differential cross-sections of pion emission.

*Thin target (measurements and compilations)*

- **EXFOR database** (*P. Vaz*)
  - make access to data more user-friendly;
  - include database from LBL.

*Thick target (measurements, compilations and needs)*

- **Thick target yield measurements at TIARA, KEK, HIMAC** (*K. Shin*)  
(*Several measurements have been carried out*)
  - benchmark new version of QMD Model with measured data;
  - continue experiments at HIMAC;
  - need data for Deuterons and He-3.
- **Spallation sources** (*D. Filges, L. Charlton, H. Ikeda*)
  - data urgently needed for materials damage, gas production (H, He) for structural materials and lifetime limitations;
  - verification of cross-sections and nuclear models used for mercury;
  - residual nuclei distributions for residual radioactivity, afterheat and transmutation atom generation in target and structure materials, including recoiling nuclei in radiation damage;
  - verification of calculated integral and differential neutron flux density and secondary particle distribution from an engineered target-moderator-reflector system;
  - planned experiments – material irradiation at SINQ, LAMPF, Jülich;

- multiplicity, energy deposition, charged particle production on thin and thick targets at Cosy-Jülich;
- mercury target neutron performance and stress investigations at the AGS (BNL).

*Data needed for RAD damage by photons (magnets)*

***Shielding (experiments, facilities, benchmarks and intercomparisons)***

- **Shielding benchmark – Neutron transmission for iron and concrete for low, intermediate and high energy proton machines** (*Y. Nakane and K. Hayashi*)
  - Perform new benchmark experiments:
    - 1) 43 MeV and 68 MeV through iron and concrete shields (TIARA, JAERI);
    - 2) 230 MeV protons through concrete shields (Loma Linda);
    - 3) 500 MeV protons through iron beam stop and concrete shields (KEK);
    - 4) 1.5 -24 GeV protons through concrete shields (AGS, BNL);
    - 5) 12 GeV protons through concrete shields (PS-CERN, KEK);
    - 6) 24 GeV protons through iron beam dump (PS-CERN).

*The following questions need further discussion:*

- Add FLUKA results to Problem 1 in summary?
- Add 200 MeV benchmark problem?
- Add  $E > 400$  MeV results to intercomparisons to find asymptotic value of  $\lambda(E)$ ?
- Study total and low energy neutron dose equivalent/attenuation in iron separately?
- Study  $\lambda_D(E)$  for incident protons?
- Add results of analytical (especially asymptotic) considerations to the intercomparisons?

*Collaboration between code users and code developers is recommended before results are released.*

- **Attenuation lengths** (*H. Hirayama*)
  - comparisons between codes;
  - comparison of iron cross-sections;
  - detailed comparison of neutron spectrum;

- comparison at higher energies;
- comparison for neutrons produced by high energy protons.

*Need definition of attenuation length.*

- **Shielding experiments at TIARA and ISIS – Dose equivalent rates behind concrete for target irradiated by 0.05-10 GeV proton beams** (*Y. Sakamoto*)
  - need deeper bulk shielding experiments at intermediate and high energy (neutrons) to verify shielding codes for accelerator facility design.

*Plans exist to perform experiments at  $E > 1 \text{ GeV}$  at KEK and AGS, BNL.*

- **Neutron facility for shielding experiment and detector calibration** (*T. Nakamura*)
  - calibration and response measurements of various neutron detectors;
  - neutron scattering cross-section measurements;
  - charged particle production cross-section measurements;
  - neutron spectral and dose distribution in several media;
  - thin and thick target neutron yields by heavy ions.
- **CERN-CEC high energy reference field facility** (*M. Silari*)
  - beam time available in 1998-1999 – participants encouraged to make use of this opportunity;
  - shielding configuration of radiation dump.

### *Miscellaneous*

- **Response functions of Bonner spectrometer in high energy neutron fields** (*V. Mares*)
  - perform simulations with MCNPX (LAHET-MCNP code merger) as soon as it will be released;
  - add another high energy channel.
- **Energy response of tissue equivalent proportional counter for neutrons of  $E > 20 \text{ MeV}$**  (*E. Gelfand*)
  - make instrument response functions and instrument design details available.
- **Test of activation detectors as neutron spectrometer (6-140 MeV)** (*F. Clapier*)
  - continue experimental work.

- **Computer version of Handbook on Radionuclide Production Cross-Section at Intermediate Energies** (*N. Sobolevski*)
  - make computer version available (limited subset).

### *Conversion coefficients*

- **Conversion coefficients for high energy radiation** (*M. Pelliccioni*)
  - include photonuclear reactions;
  - provide results for pion calculations;
  - liaison ICRP-ICRU;
  - propose new operational quantity since ambient dose equivalent is not appropriate for high energies;
- **Conversion coefficients for high energy particles** (*S. Iwai*)
  - compile report including conversion coefficients for various anthropomorphic computational models and radiation types at high energies;
  - appoint working group (*L. Waters, S. Iwai, M. Pelliccioni, V. Mares*) which will submit a proposal to ICRP.

### *Computer codes and data sets for shielding analysis*

- **Current status of computer codes and data sets for accelerator shielding analysis** (*B. Kirk, E. Sartori, P. Vaz*)
  - NEA/RSICC take a proactive role in exchanging information on new codes, etc., with SATIF participants;
  - continue work at RSICC and NEA/DB on the SINBAD database to include additional shielding benchmark experimental data sets;

*Participants to inform NEA/RSICC on availability of codes and data.*

### *Anthropomorphic data*

- **Collection of anthropomorphic data for dosimetry studies** (*E. Sartori, V. Mares*)
  - co-operate with R. Loesch, developer of the database being implemented at DOE;
  - get information on the code MRIPP.

- **GSF anthropomorphic computational models** (*V. Mares*)
  - make anthropomorphic computational models (often erroneously called “phantoms”) available.

*Mares will contact authors.*

### **Looking into the future...**

The technological applications of accelerators, targets and irradiation facilities cover a wide range of domains, from basic research to accelerator based transmutation, material science or medicine.

The analysis and solution of shielding problems related to the development and operation of accelerators, targets and irradiation facilities involves the understanding of the physics of the interactions of different particles (neutrons, protons, electrons, photons, pions, light and heavy ions) in an energy range spanning over several orders of magnitude.

The community of participants in the SATIF meetings includes physicists, engineers and technicians coming from different fields of science and technology. Given the increasing number of facilities in operation, under construction, being commissioned or being planned, their diversity (proton accelerators, electron accelerators, spallation sources, radioactive nuclear beams, etc.) and the increasing complexity of the associated shielding problems, this community feels that an effective follow-through process will be necessary in order to make sure substantial progress is achieved, ensuring that a sound technical basis is established for proper licensing and operation of these facilities.

In this context, it was requested that the NEA strengthen its role of co-ordinating the collection and dissemination of experimental or evaluated data, computer programs, benchmark data sets and exercises. It was felt that an effective follow-up of the recommendations performed and actions undertaken in the different areas and fields concerned, could only benefit from the NEA role of providing secretariat and organisational support and assistance to the members of the Task Force and to their activities. In this framework, a specific follow-through process co-ordinated by the NEA has been established to regularly monitor the progress achieved and to collect and make available newly released relevant information (data sets , computer codes, etc.).

Finally, it was decided to hold the next SATIF meeting (SATIF-4) at Knoxville, Tennessee, USA, on 17-18 September 1998, before the ANS Topical Meeting on Accelerator Applications (AccApp '98) which will take place in Gatlinburg, Tennessee, USA, from 20-23 September 1998, and to assign the local organisation responsibility to the Oak Ridge National Laboratory (ORNL).



# **SESSION I**

## **Source Term and Related Data – Electron Accelerator**

*Chairs: A. Ferrari and H. Hirayama*



# *Gas Bremsstrahlung and Narrow Beam Dosimetry*



## **SOME PRELIMINARY RESULTS ABOUT NARROW BEAM DOSIMETRY**

**Maurizio Pelliccioni**

Istituto Nazionale di Fisica Nucleare, Italy

### **Abstract**

Organ doses and effective doses have been estimated by Monte Carlo simulations with the FLUKA code in the case of an anthropomorphic phantom exposed to narrow beams of various kinds of radiation. The energy range from 1 MeV to 1 GeV has been investigated. Though the work is still in progress, some preliminary results are presented.

## Introduction

Data for protection against ionising radiation from external sources are usually expressed in terms of conversion coefficients from measured quantities to radiation protection quantities calculated in various irradiation geometries. All the geometries are related to a broad unidirectional beam, or plane parallel beam, virtually of infinite extent, irradiating an anthropomorphic phantom. When an assessment of partial exposures of human body is required, the broad-beam data are inadequate. In particular, when applied to narrow beams, they lead to errors in the estimates of the body quantities, the degree depending on the irradiation geometry and on the kind and energy of particles. The exposures to gas bremsstrahlung and synchrotron radiation beams are typical circumstances in which data adequate for narrow beam dosimetry are required.

At the SATIF-2 meeting a group of experts, including the author of this paper, was charged with the problem of narrow beam dosimetry. Some preliminary calculations have been performed and the results are presented here.

Calculations have been carried out by Monte Carlo simulations with the most recent version of the FLUKA code [1] for narrow beams of various kinds of monoenergetic particles normally incident on some selected organs of an hermaphrodite phantom. The mathematical model of the phantom has already been described in previous papers [2,3]. Photons, electrons, protons and neutrons have been considered as primary particles. The energy range investigated was 1 MeV to 1 GeV.

## Calculations

Calculations have been performed prevalently with monoenergetic photons as primary particles. A  $0.2 \times 0.2$  cm<sup>2</sup> square beam has been considered impinging somewhere on a fixed organ (target organ) of the phantom. The organs selected as targets were: brain, breast, lung, oesophagus, ovaries, pancreas, stomach, testes, thyroid.

The energy per primary particle deposited in the 68 regions of the hermaphrodite phantom, representing the various organs and tissues of the human body, has been determined to be a result of the simulations. The organ doses have been estimated as arithmetic mean of the doses received by the single constituent regions. The effective dose has been evaluated according to the definition given in ICRP Publication 60 [4], as modified in ICRP Publication 69 [5].

The statistical uncertainties were estimated by making calculations in several batches and computing the standard deviation of the mean. The total number of histories was large enough to keep the standard deviation on the effective doses below few per cent.

The calculated results are presented in Tables 1-4 for photon energy of 1 MeV, 10 MeV, 100 MeV and 1 GeV, respectively. In each table the following data are given: target organ; dose to the target organ followed by the standard deviation (in brackets); other organs significantly irradiated, i.e. other organs whose equivalent doses, when multiplied for the pertinent weighting tissue factors, have resulted at least as large as 1% of the weighted target dose ( $w_{\text{TARG}} \times H_{\text{TARG}}$ ); effective dose, followed by the standard deviation (in brackets); per cent contribution of organs different from the target one in the calculation of the effective dose (E).

It was found that in general when the target is one among ovaries, testes, thyroid (except at 100 MeV), male lung (except at 1 MeV) or oesophagus (at 1 GeV), only the dose received by the target organ is important for purposes of effective dose assessment. In these cases, the differences between effective dose and weighted target organ dose are negligible, usually under few per cent.

When the beam is incident on the oesophagus (except at 1 GeV), on the stomach (at 1 and 10 MeV), on the thyroid (at 100 MeV), or on the male lung (at 1 MeV), the contribution to the effective dose of the doses to organs different from the target one is still less than 10%.

Conversely, in the case of a beam directed toward brain, breast, pancreas or stomach (at energies from 100 MeV), some organs in addition to the target one give an appreciable contribution to the effective dose. In particular, when the stomach is the target organ, there is a contribution (15-17% on the whole) from the kidney, the muscle (at 100 MeV) and especially the spleen. In the case of the breast, the difference between effective dose and weighted organ dose can be as large as 82.9%, mainly because of the equivalent dose in the lung. For the brain, about 70% of the effective dose is due to red bone marrow and bone surface and, limited to 1 MeV, to the skin. Finally, when the beam impinges on the pancreas, there is a large contribution to the effective dose (about 60% on the whole) from the equivalent doses in the red bone marrow and sometimes in the liver.

A graphical presentation of the calculated results is given in Figures 1 and 2, in which the doses to the target organs and the effective doses are plotted as a function of photon energy respectively. In both figures the name of the concerned target organ is reported close to the data. From these figures, it is made clear that both organ doses and effective doses increase with photon energy. The greatest values always occur when the ovaries are the target. The effective dose per primary photon in the case of a whole body irradiation is also included in Figure 2. Its values have been derived from the conversion coefficients fluence to effective dose for AP irradiation, according to previous calculations [3,6].

It is evident from Figure 2 that the irradiation of a single organ by a narrow beam generally gives rise to a value of the effective dose per primary photon greater than in the case of a parallel beam covering the phantom homogeneously. This is also generally true when the organ irradiated is one of minor weight in the calculation of the effective dose, such as the brain or pancreas, because of the dose received by other more important organs, usually red bone marrow. Thus the data obtained from whole body exposure never seem to provide a conservative estimate of the effective dose for a narrow beam irradiation, at least for the geometries investigated here.

It is also of some interest to note that the organ doses and the effective dose slightly depend on the beam size. As an example, in Table 5, for the irradiation of the breast, the effective dose is shown as a function of the photon energy at a number of beam sizes ranging from 0.04 cm<sup>2</sup> (pencil beam) to 49 cm<sup>2</sup> (about the size of the breast).

Some preliminary calculations have been also performed for other kinds of primary particles: electrons, protons and neutrons. The energy range investigated was again 1 MeV-1 GeV. In these cases only two target organs were considered, the breast and testes. The calculated results are summarised in Figures 3 and 4 in terms of effective dose.

It can be seen that the effective dose always rises with the increasing energy in the case of electrons, it decreases for protons above 100 MeV, and it is relatively flat for neutrons. For the irradiation of testes, only the organ dose to the target is important to estimate the effective dose,

as well as for photons. Conversely, in the case of the breast, various organs give contribution to the effective dose, especially the lung in the energy range 0.1 – 1 GeV. On the basis of the available conversion coefficients for broad beam incidence [7,8,9], the effective dose per primary particle related to a whole body irradiation can be also calculated. It would give an underestimate of the values shown in Figures 3 and 4, for all radiation type and incident energy on the human body considered here.

## **Conclusions**

The preliminary results presented above enable to estimate the organ doses and the effective dose for some conditions of exposure of the human body to narrow beams, in the energy range 1 MeV to 1 GeV. The present information can be considered supplementary to existing data concerning conversion coefficients from fluence to limiting quantities, calculated for a phantom exposed to broad beams. At the moment, no simple rules of thumb valid in all circumstances can be suggested. The conversion coefficients for broad beam irradiation, however, never seem to allow a conservative estimate of the effective dose for the case of a body exposure to a narrow beam.

## REFERENCES

- [1] A. Fassò, A. Ferrari, J. Ranft and P.R. Sala, “An Update about FLUKA”, Proceedings of the Second Workshop on Simulating Accelerator Radiation Environments, CERN 8-11 Oct. 1995 (1997), pp. 158-170.
- [2] M. Pelliccioni and M. Pillon, “Comparison between Anthropomorphic Mathematical Phantoms Using MCNP and FLUKA Codes”, *Radiat. Prot. Dos.*, 67 (1996), pp. 253-256.
- [3] A. Ferrari, M. Pelliccioni and M. Pillon, “Fluence to Effective Dose and Effective Dose Equivalent Conversion Coefficients for Photons from 50 keV to 10 GeV”, *Radiat. Prot. Dos.*, 67 (1996), pp. 245-251.
- [4] International Commission on Radiological Protection, 1990, Recommendations of the International Commission on Radiological Protection, ICRP Publication 60, Annals of ICRP, (1991), p. 21 (1-3).
- [5] International Commission on Radiological Protection, Age-Dependent Doses to Members of the Public from Intake of Radionuclides: Part 3 Ingestion Dose Coefficients, ICRP Publication 69, Annals of ICRP, (1995), p. 25 (1).
- [6] A. Ferrari, M. Pelliccioni and M. Pillon, “High-Energy Electron and Photon Dosimetry”, Health Physics of Radiation Generating Machines, Proceedings of the 30th Midyear Topical Meeting of the Health Physics Society, S. José, California (USA), 5-8 January (1997), pp. 151-181.
- [7] A. Ferrari, M. Pelliccioni and M. Pillon, “Fluence to Effective Dose and Effective Dose Equivalent Conversion Coefficients for Electrons from 5 MeV to 10 GeV”, *Radiat. Prot. Dos.*, p. 62 (9), (1997) pp. 97-104.
- [8] A. Ferrari, M. Pelliccioni and M. Pillon, “Fluence to Effective Dose and Effective Dose Equivalent Conversion Coefficients for Protons from 5 MeV to 10 TeV”, *Radiat. Prot. Dos.* (in press).
- [9] A. Ferrari, M. Pelliccioni and M. Pillon, “Fluence to Effective Dose Conversion Coefficients for Neutrons up to 10 TeV”, *Radiat. Prot. Dos.* (in press).

**Figure 1. Target organ doses as a function of photon energy**

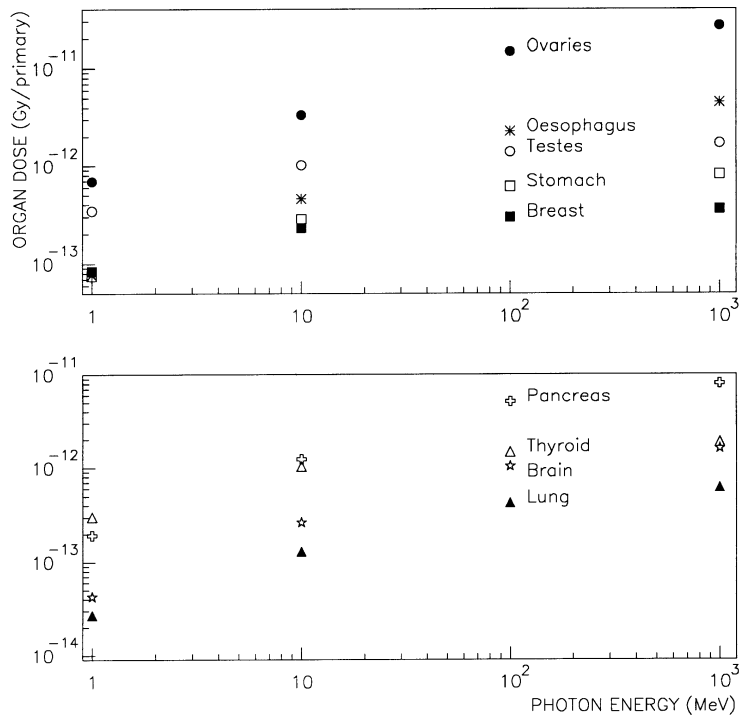


**Figure 2. Effective dose as a function of photon energy for various target organs**

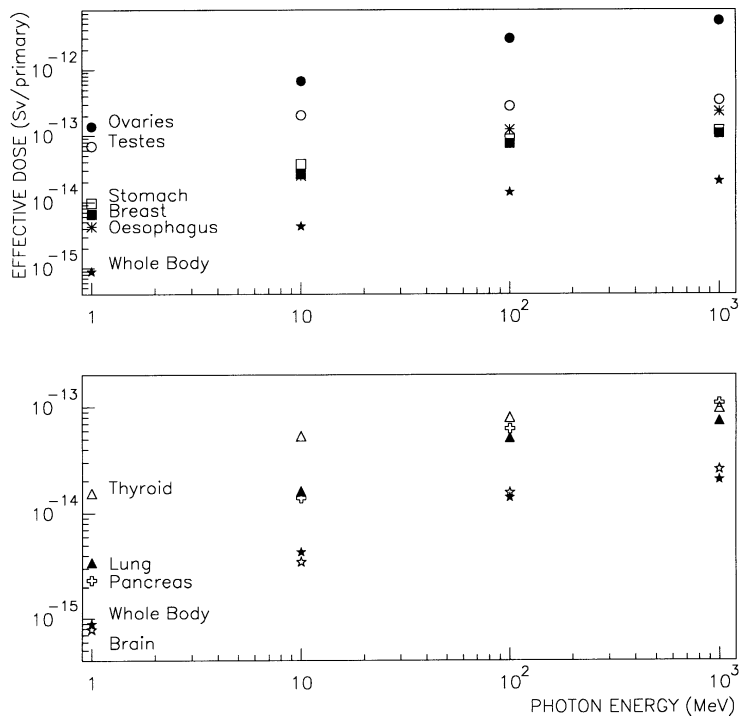


**Figure 3. Effective dose as a function of particle energy for various primary beam impinging on the breast**

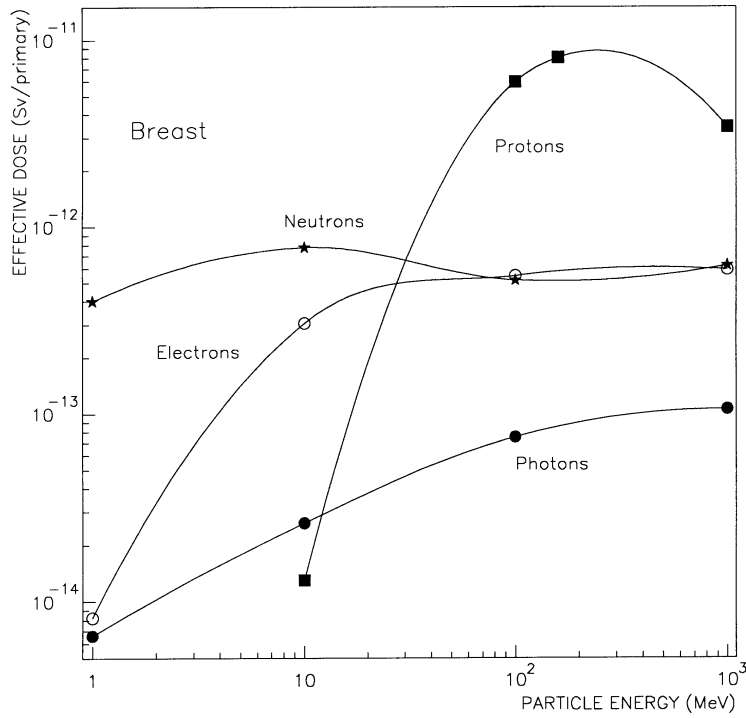


**Figure 4. Effective dose as a function of particle energy for various primary beam impinging on the testes**

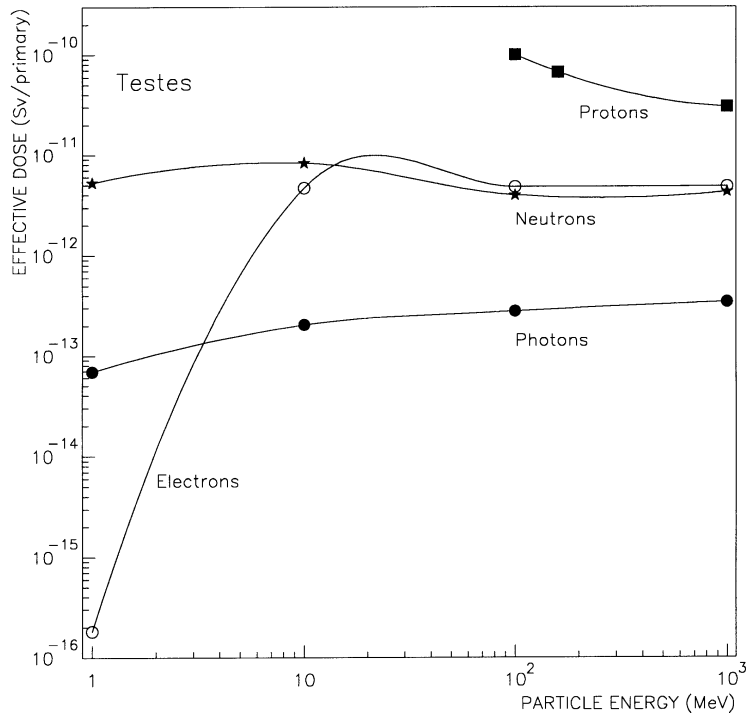


**Table 1. A summary of the irradiation of the phantom by a photon narrow beam of energy 1 MeV**

TARGET ORGAN	DOSE TO THE TARGET ORGAN (Gy/primary)	OTHER ORGANS IRRADIATED (Gy/primary)	EFFECTIVE DOSE (Sv/primary)	$\frac{E - w_{TARG} H_{TARG}}{E}$
Testes	$3.45 \cdot 10^{-13}$ (0.27%)		$6.91 \cdot 10^{-14}$ (0.27%)	0.17%
Stomach	$7.52 \cdot 10^{-14}$ (0.33%)	Spleen $8.66 \cdot 10^{-14}$	$9.58 \cdot 10^{-15}$ (0.31%)	5.85%
Thyroid	$3.04 \cdot 10^{-13}$ (0.56%)		$1.54 \cdot 10^{-14}$ (0.55%)	1.11%
Lung (male)	$2.69 \cdot 10^{-14}$ (0.27%)	Stomach $1.15 \cdot 10^{-15}$ Spleen $1.02 \cdot 10^{-15}$	$3.43 \cdot 10^{-15}$ (0.27%)	6.04%
Breast	$8.41 \cdot 10^{-14}$ (0.27%)	Lung $1.41 \cdot 10^{-14}$	$6.59 \cdot 10^{-15}$ (0.2%)	36.2%
Oesophagus	$7.73 \cdot 10^{-14}$ (0.61%)	Lung $1.93 \cdot 10^{-15}$	$4.26 \cdot 10^{-15}$ (0.58%)	9.31%
Brain	$4.26 \cdot 10^{-14}$ (0.06%)	R.Bo.Ma. $4.45 \cdot 10^{-15}$ Bone S. $3.43 \cdot 10^{-15}$ Skin $1.15 \cdot 10^{-15}$	$7.91 \cdot 10^{-16}$ (6.90%)	73.1%
Pancreas	$1.94 \cdot 10^{-13}$ (0.33%)	Liver $6.99 \cdot 10^{-15}$ R.Bo.Ma. $5.99 \cdot 10^{-15}$	$2.33 \cdot 10^{-15}$ (2.33%)	58.8%
Ovaries	$6.89 \cdot 10^{-13}$ (0.30%)		$1.38 \cdot 10^{-13}$ (0.30%)	0.31%

**Table 2. A summary of the irradiation of the phantom by a photon narrow beam of energy 10 MeV**

TARGET ORGAN	DOSE TO THE TARGET ORGAN (Gy/primary)	OTHER ORGANS IRRADIATED (Gy/primary)	EFFECTIVE DOSE (Sv/primary)	$\frac{E - w_{TARG} H_{TARG}}{E}$
Testes	$1.02 \cdot 10^{-12}$ (0.73%)		$2.04 \cdot 10^{-13}$ (0.73%)	0.09%
Stomach	$2.84 \cdot 10^{-13}$ (0.34%)	Spleen $6.11 \cdot 10^{-13}$	$3.73 \cdot 10^{-14}$ (0.31%)	8.59%
Thyroid	$1.04 \cdot 10^{-12}$ (0.51%)	R.Bo.Ma. $1.10 \cdot 10^{-14}$	$5.33 \cdot 10^{-14}$ (0.61%)	2.74%
Lung (male)	$1.30 \cdot 10^{-13}$ (0.60%)	Stomach $4.04 \cdot 10^{-15}$	$1.62 \cdot 10^{-14}$ (0.59%)	3.45%
Breast	$2.31 \cdot 10^{-13}$ (0.47%)	Lung $1.21 \cdot 10^{-13}$	$2.62 \cdot 10^{-14}$ (0.30%)	56.0%
Oesophagus	$4.60 \cdot 10^{-13}$ (0.27%)	Lung $8.52 \cdot 10^{-15}$ R.Bo.Ma. $4.17 \cdot 10^{-15}$	$2.46 \cdot 10^{-14}$ (0.30%)	6.62%
Brain	$2.66 \cdot 10^{-13}$ (0.12%)	R.Bo.Ma. $1.69 \cdot 10^{-14}$ Bone S. $1.41 \cdot 10^{-14}$	$3.47 \cdot 10^{-15}$ (10.7%)	61.7%
Pancreas	$1.24 \cdot 10^{-12}$ (0.30%)	R.Bo.Ma. $4.91 \cdot 10^{-14}$	$1.39 \cdot 10^{-14}$ (3.33%)	55.3%
Ovaries	$3.37 \cdot 10^{-12}$ (0.12%)		$6.76 \cdot 10^{-13}$ (0.13%)	0.30%

**Table 3. A summary of the irradiation of the phantom  
by a photon narrow beam of energy 100 MeV**

TARGET ORGAN	DOSE TO THE TARGET ORGAN (Gy/primary)	OTHER ORGANS IRRADIATED (Gy/primary)	EFFECTIVE DOSE (Sv/primary)	$\frac{E - w_{TARG} H_{TARG}}{E}$
Testes	$1.39 \cdot 10^{-12}$ (0.21%)		$2.79 \cdot 10^{-13}$ (0.21%)	0.19%
Stomach	$6.12 \cdot 10^{-13}$ (0.59%)	Spleen $2.63 \cdot 10^{-12}$ Kidney $2.24 \cdot 10^{-14}$ Muscle $2.06 \cdot 10^{-14}$	$8.70 \cdot 10^{-14}$ (0.50%)	15.5%
Thyroid	$1.47 \cdot 10^{-12}$ (0.33%)	Bone S. $1.26 \cdot 10^{-13}$ R.Bo.Ma. $4.76 \cdot 10^{-14}$ Skin $2.49 \cdot 10^{-14}$	$7.98 \cdot 10^{-14}$ (1.59%)	7.95%
Lung	$4.26 \cdot 10^{-13}$ (0.48%)		$5.15 \cdot 10^{-14}$ (0.48%)	0.82%
Breast	$2.99 \cdot 10^{-13}$ (0.72%)	Lung $5.00 \cdot 10^{-13}$	$7.52 \cdot 10^{-14}$ (0.37%)	80.1%
Oesophagus	$2.27 \cdot 10^{-12}$ (0.99%)	R.Bo.Ma. $3.71 \cdot 10^{-14}$ Lung $3.12 \cdot 10^{-14}$	$1.22 \cdot 10^{-13}$ (1.15%)	7.01%
Brain	$1.03 \cdot 10^{-12}$ (0.29%)	R.Bo.Ma. $8.21 \cdot 10^{-14}$ Bone S $6.19 \cdot 10^{-14}$	$1.56 \cdot 10^{-14}$ (18.2%)	66.8%
Pancreas	$5.08 \cdot 10^{-12}$ (0.40%)	R.Bo.Ma. $2.77 \cdot 10^{-13}$	$6.23 \cdot 10^{-14}$ (6.85%)	59.2%
Ovaries	$1.48 \cdot 10^{-11}$ (0.47%)		$2.97 \cdot 10^{-12}$ (0.47%)	0.30%

**Table 4. A summary of the irradiation of the phantom  
by a photon narrow beam of energy 1 GeV**

TARGET ORGAN	DOSE TO THE TARGET ORGAN (Gy/primary)	OTHER ORGANS IRRADIATED (Gy/primary)	EFFECTIVE DOSE (Sv/primary)	$\frac{E - w_{TARG} H_{TARG}}{E}$
Testes	$1.72 \cdot 10^{-12}$ (0.75%)		$3.44 \cdot 10^{-13}$ (0.75%)	0.18%
Stomach	$8.17 \cdot 10^{-13}$ (0.37%)	Spleen $4.02 \cdot 10^{-12}$	$1.18 \cdot 10^{-13}$ (0.31%)	17.2%
Thyroid	$1.87 \cdot 10^{-12}$ (0.75%)	Bone S. $2.36 \cdot 10^{-13}$ R.Bo.Ma. $2.21 \cdot 10^{-14}$	$9.74 \cdot 10^{-14}$ (1.02%)	3.83%
Lung (male)	$6.16 \cdot 10^{-13}$ (0.32%)		$7.42 \cdot 10^{-14}$ (0.32%)	0.27%
Breast	$3.60 \cdot 10^{-13}$ (0.62%)	Lung $7.28 \cdot 10^{-13}$	$1.06 \cdot 10^{-13}$ (0.59%)	82.9%
Oesophagus	$4.51 \cdot 10^{-12}$ (0.37%)		$2.29 \cdot 10^{-13}$ (0.39%)	1.68%
Brain	$1.59 \cdot 10^{-12}$ (0.20%)	R.Bo.Ma. $1.44 \cdot 10^{-13}$ Bone S. $1.03 \cdot 10^{-13}$	$2.57 \cdot 10^{-14}$ (14.2%)	69.1%
Pancreas	$7.95 \cdot 10^{-12}$ (0.42%)	R.Bo.Ma. $5.36 \cdot 10^{-13}$	$1.08 \cdot 10^{-13}$ (8.94%)	63.1%
Ovaries	$2.71 \cdot 10^{-11}$ (0.44%)		$5.44 \cdot 10^{-12}$ (0.44%)	0.24%

**Table 5. Effective dose (Sv/primary photon) at a number of photon energies and beam sizes in the case of the irradiation of the breast**

Photon Energy (MeV)	Beam size (cm <sup>2</sup> )				
	0.04	1.0	4.0	16.0	49.0
1	$7.2 \cdot 10^{-15}$	$7.2 \cdot 10^{-15}$	$7.1 \cdot 10^{-15}$	$6.9 \cdot 10^{-15}$	$6.1 \cdot 10^{-15}$
10	$3.1 \cdot 10^{-14}$	$3.1 \cdot 10^{-14}$	$3.0 \cdot 10^{-14}$	$2.8 \cdot 10^{-14}$	$2.4 \cdot 10^{-14}$
100	$9.2 \cdot 10^{-14}$	$9.2 \cdot 10^{-14}$	$9.0 \cdot 10^{-14}$	$8.7 \cdot 10^{-14}$	$7.6 \cdot 10^{-14}$
1000	$1.3 \cdot 10^{-13}$	$1.3 \cdot 10^{-13}$	$1.3 \cdot 10^{-13}$	$1.2 \cdot 10^{-13}$	$1.1 \cdot 10^{-13}$

# MEASUREMENT OF GAS BREMSSTRAHLUNG FROM THE INSERTION DEVICE BEAM LINES OF THE ADVANCED PHOTON SOURCE

**M. Pisharody<sup>1</sup>, P.K. Job<sup>1</sup>  
S. Magill<sup>2</sup>, J. Proudfoot<sup>2</sup>, R. Stanek<sup>2</sup>**

<sup>1</sup>Experimental Facilities Division

<sup>2</sup>High-Energy Physics Division

Argonne National Laboratories

9700 S. Cass Ave., Argonne IL 60439, USA

## Abstract

Bremsstrahlung is produced in the Advanced Photon Source (APS) storage ring when the beam particle interacts with the storage ring components or with the residual gas molecules in the storage ring vacuum. The interaction of the particles with the gas molecules occurs continually during storage ring operation. Gas bremsstrahlung is important at the insertion device straight sections of the synchrotron radiation sources, because the contribution from each interaction adds up to produce a narrow monodirectional beam that travels down the beam lines. At the Advanced Photon Source (APS), with long storage ring beam straight paths (15.38 metres), gas bremsstrahlung in the insertion device beam lines can be significant. This paper presents the results of the bremsstrahlung measurement in the insertion device beam lines of the APS. The bremsstrahlung spectrum and the total energy radiated in a beam line is measured by a hermetic lead glass calorimeter. The calorimeter consists of 25 lead glass blocks, each 6 cm×6 cm×35 cm in size. Twenty-five phototubes connected to the lead glass blocks collected the signal. The bremsstrahlung spectrum and the total energy radiated were measured as a function of beam current (20-100 mA) at 7.0 GeV particle energy for both electrons and positrons. The vacuum in the entire straight section was continuously monitored by six ion gauges during the data collection. The calibration procedure of the calorimeter and the residual gas analysis of the vacuum are also presented. The measured bremsstrahlung spectrum was fitted to a function that shows an approximate 1/E behaviour. The gas bremsstrahlung rate from the APS undulator beam line straight path of 15.38 m is measured as  $60.0 \pm 2.0$  GeV/sec/nT/mA. Significant bremsstrahlung contribution from sources other than the residual gas molecules has been observed. The maximum bremsstrahlung energy measured during these experiments in a beam line is  $369.0 \pm 22.0$  GeV/sec/nT/mA.

## Introduction

High energy electron storage rings generate energetic bremsstrahlung photons through radiative interaction of the electrons (or positrons) with the residual gas molecules inside the storage ring [1,2]. The resulting radiation exits at an average emittance angle of  $(m_0c^2/E)$  radian with respect to the electron beam path, where  $m_0c^2$  is the rest mass of the electron and  $E$  its kinetic energy. Thus, at straight sections of the storage rings, moving electrons will produce a narrow and intense monodirectional photon beam. At synchrotron radiation facilities, where beam lines are channelled out of the storage ring, a continuous gas bremsstrahlung spectrum, with a maximum energy of the electron beam, will be present.

There are a number of compelling reasons that a measurement of the bremsstrahlung characteristics be conducted at the synchrotron radiation sources. Although the number of residual gas molecules present in the storage ring at typical nTorr vacuum is low, because of the long straight paths of the in the storage ring significant quantity of bremsstrahlung will be produced. This may pose a radiation hazard. It is then imperative that personnel be shielded from dose rates due to this radiation [3]. There are a few measurements available for gas bremsstrahlung, especially for the higher electron beam energies [4,5]. The quantitative estimates of gas bremsstrahlung from storage rings as evaluated by Monte Carlo codes also have several uncertainties [6,7]. They are in general calculated for air at atmospheric pressure, the results of which are then extrapolated to typical storage ring vacuum values (of the order of  $10^{-9}$  Torr). Realistically, the actual pressure profile can vary inside the narrow vacuum chamber. Also, the actual chemical composition of the residual gas inside the storage ring is generally different from that of air.

The 7 GeV stored electron beam energy and the long (5 m) insertion device (ID) straight sections with long straight paths, approximately 5 m on either side of the IDs, provide us with a unique opportunity to carry out the gas bremsstrahlung measurements at the Advanced Photon Source (APS) [8]. The first optical enclosures (FE) of the ID beam lines are suitable to perform such measurements. The ID is kept fully open to minimise the synchrotron radiation background. The bremsstrahlung beam emerges as a narrow cone along the beam line into the FOE with a characteristic opening angle of  $146 \mu\text{rad}$ , making it a few millimetres in diameter downstream of the ID in the FOE. Such a narrow intense bremsstrahlung beam can only be measured accurately using a high energy electromagnetic calorimeter that possess good resolution and a fast time response. Lead glass has the desired properties and a segmented array of this material with the right dimensions will practically contain the entire bulk of electromagnetic shower generated by the incident bremsstrahlung beam. Such a calorimeter has enabled us to accurately measure the bremsstrahlung energy spectrum and rate at APS. This paper presents the results of those measurements.

## Experimental set-up

The experimental set-up consists of a  $5 \times 5$  array of lead glass detectors with photomultiplier readouts and an associated data acquisition system. Figure 1 gives the schematic view of the experimental set-up. The lead glass, having a depth of approximately 15 radiation lengths, contains 97% of the bremsstrahlung shower longitudinally. The Moliere Radius of the lead glass is 3 cm. Therefore the  $5 \times 5$  array, as seen from Figure 1, will completely contain the shower transversally. Figure 2 gives the schematic of the data acquisition system. The signals from the individual phototubes are read out into the ADCs. The signal from the central tube with an appropriate threshold is used as the trigger. The digitised data from the ADC is stored into a memory unit for the subsequent slow read out by the computer.

Figure 1. Schematic of the lead glass calorimeter

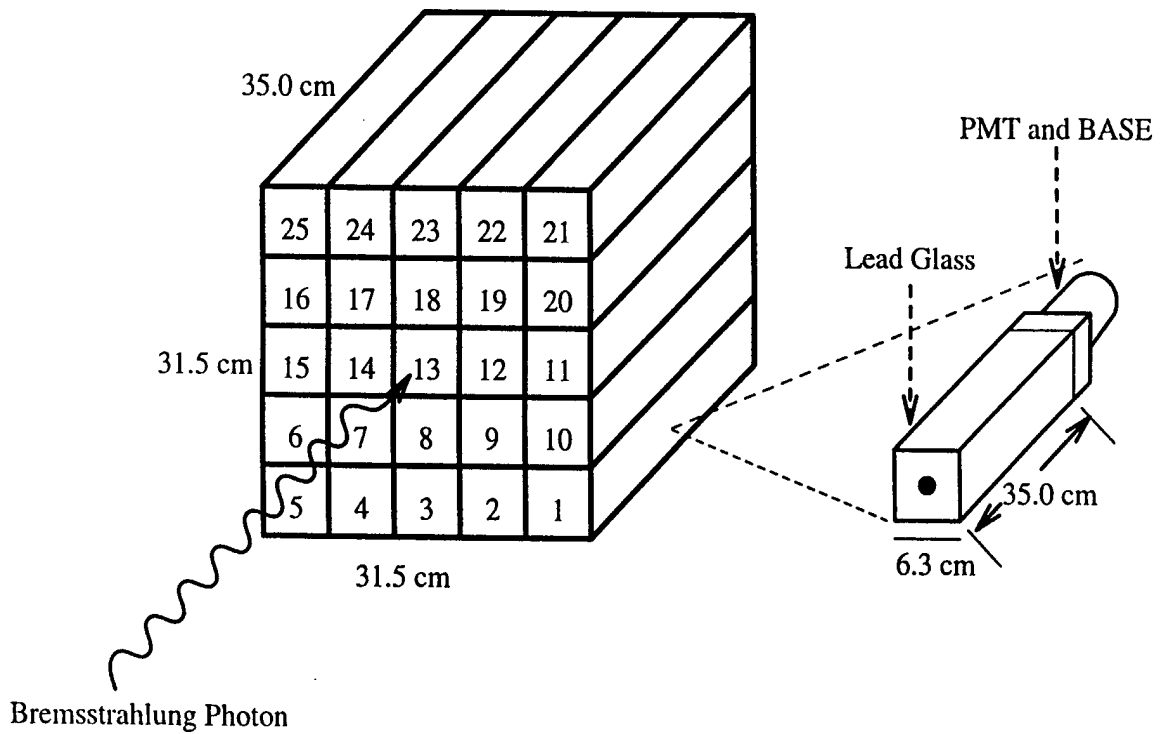
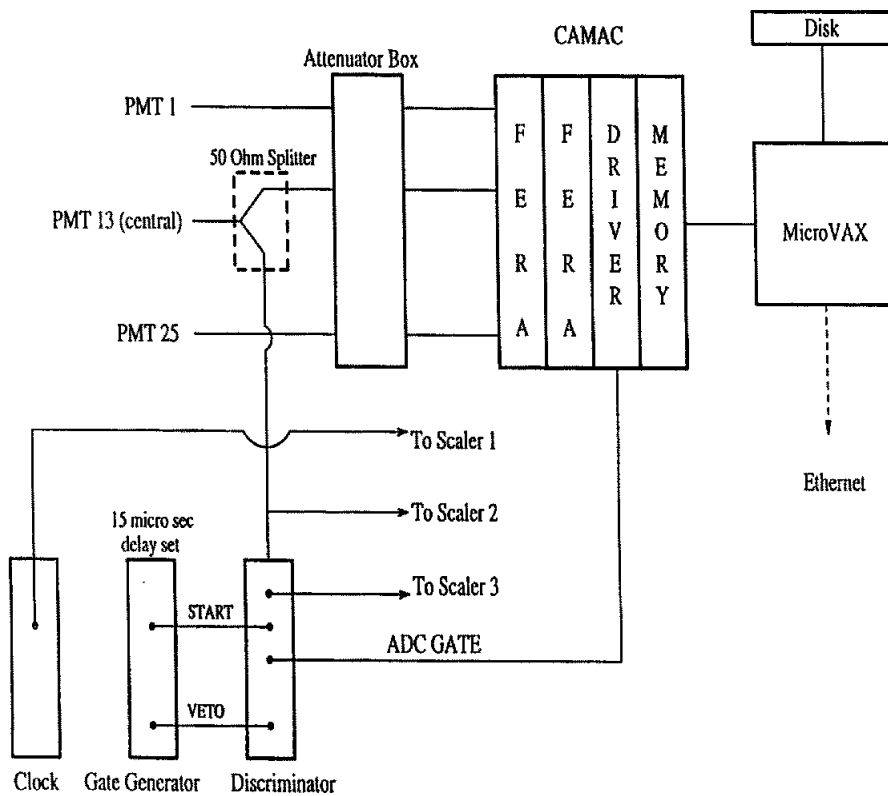
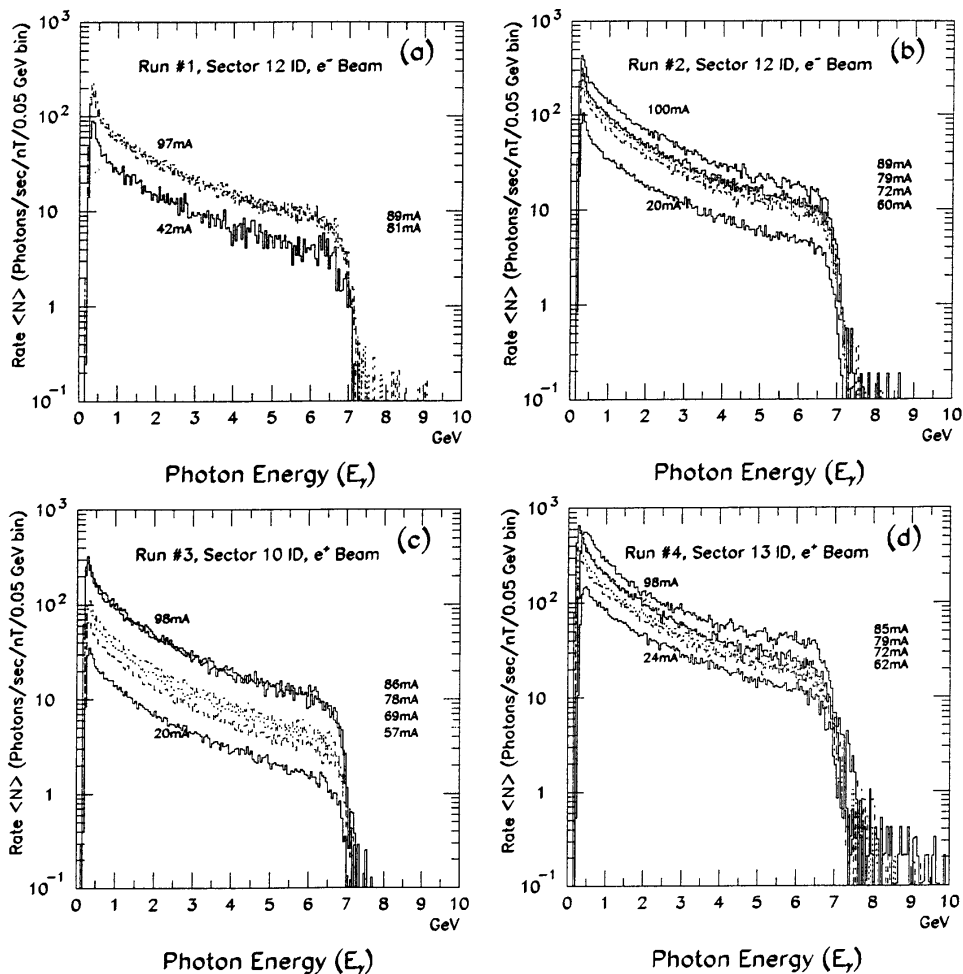


Figure 2. Schematic of the data acquisition system



The measurement of the gas bremsstrahlung spectrum and intensity were conducted as a function of storage ring parameters, such as beam current and vacuum. Figure 3 gives the measured bremsstrahlung spectrum at the four different experimental runs. Total integrated gas bremsstrahlung energy radiated in the normalised units of GeV/sec/nT/mA was then evaluated, and the resulting maximum dose equivalent was estimated using existing conversion factors [9]. The experiment was repeated at various ID beam lines as different experimental runs with both electrons and positrons in the storage ring.

**Figure 3. Measured bremsstrahlung spectra as a function of beam current for different experimental runs**



## Analysis of results

Table 1 gives the corrected bremsstrahlung energy results, normalised to vacuum and storage ring beam current. The results are corrected for the dead-time losses (a maximum of 3.5% for the largest beam current), longitudinal leakage ( $4.31 \pm 0.1\%$ ), and threshold cut-off effects ( $2.8 \pm 0.1\%$ ). The normalised bremsstrahlung energy, as given in Table 1, shows consistent values within each individual run, but they often vary from run to run and sector to sector. The results from Table 1 are also shown plotted in Figures 4 and 5. Both figures show the bremsstrahlung energy, normalised to the beam current, as a function of the storage ring vacuum for different experimental runs.

**Table 1. Summary of measured bremsstrahlung energy rates**

Run # beam line and beam type	Beam current $I_b$ (mA)	Observed energy (dead-time corrected) $E_{uncorr}$ (GeV/sec/nT)	Energy correction (leak & thrsh.) $\Delta E$ (GeV/sec/nT)	Corrected brems. energy <sup>†</sup> $E_{corr}=E_{uncorr}+\Delta E$ (GeV/sec/nT)	Normalised corrected brems. energy $E_{corr}/I_b$ (GeV/sec/nT/mA)
	41.90	3 592	277	3 869	92.0±2.0
<b>1, 12 ID</b>	80.86	7 335	567	7 902	98.0±2.0
$e^-$	88.61	7 784	601	8 385	95.0±2.0
	96.70	8 155	630	8 785	91.0±2.0
	59.68	8 326	643	8 969	150.0±4.0
	64.71	9 080	701	9 781	151.0±4.0
<b>2, 12 ID</b>	71.82	10 225	790	11 015	153.0±4.0
$e^-$	78.64	10 642	822	11 464	146.0±4.0
	87.77	11 085	856	11 941	136.0±4.0
	54.81	2 945	227	3 172	58.0±2.0
	56.92	3 036	234	3 270	57.0±2.0
<b>3, 10 ID</b>	61.65	3 312	256	3 568	58.0±2.0
$e^+$	69.34	4 047	313	4 360	63.0±2.0
	78.25	4 894	378	5 272	67.0±2.0
	62.35	15 392	1 189	16 581	266.0±22.0
	72.37	17 381	1 342	18 723	259.0±22.0
<b>4, 13 ID</b>	77.48	22 829	1 763	24 592	317.0±22.0
$e^+$	85.32	22 571	1 743	24 314	285.0±22.0
	90.15	30 921	2 388	33 309	369.0±22.0

<sup>†</sup> The statistical error on this corrected bremsstrahlung energy is ±0.45%.

**Figure 4. Normalised bremsstrahlung energy rate as a function of the storage ring vacuum**

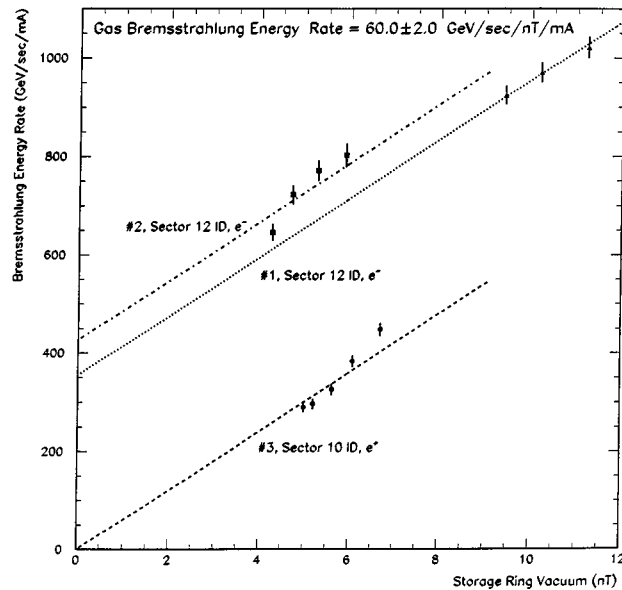


**Figure 5. Normalised bremsstrahlung energy rates as a function of the storage ring vacuum**

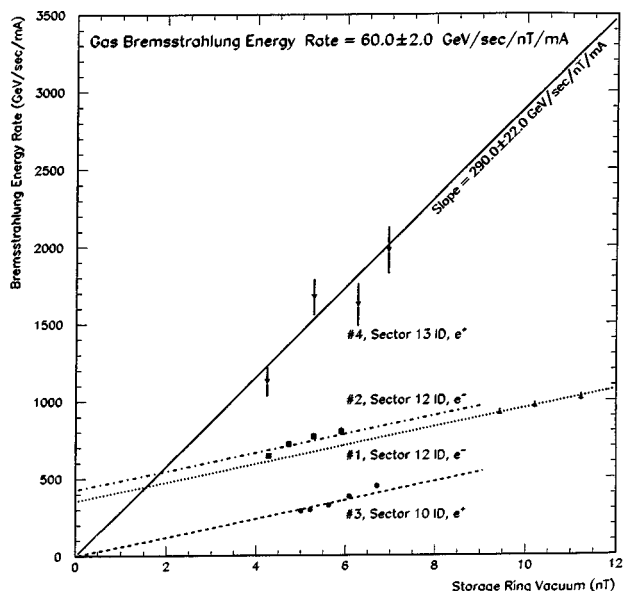


Figure 4 represents data from run Nos. (12-ID beam line), 2 (12-ID beam line) and 3 (10-ID beam line), showing straight line fits of the form  $y=mx+c$ ,  $m$  being the slope and  $c$  being the y-intercept. The errors shown are the measure of the deviation of each data point from the mean value as obtained from a least square fit. The slope of these fitted straight lines gives the gas bremsstrahlung energy rate from the storage ring straight path of 15.38 m, normalised to both the vacuum and beam current. The y-intercepts of these straight lines give the bremsstrahlung energy rates from the storage ring straight path of 15.38 m, when the vacuum of the storage ring is zero nTorr. This is the contribution to the total bremsstrahlung energy rate by non-gas particle interactions in the storage ring straight path, which differ from sector to sector. The analysis shows that there is a significant bremsstrahlung contribution from sources other than the residual gas molecules in the beam straight path of the storage ring. The gas bremsstrahlung energy rate is calculated as  $60.0 \pm 2.0$  GeV/sec/nT/mA from Figure 4. This value is consistent for the data from run Nos. 1 and 2, both conducted at 12-ID beam line, and also from the data from run No. 3 conducted at 10 ID beam line. However, as shown in Figure 5, the data from run No. 4 obtained from 13-ID beam line show a corresponding gas bremsstrahlung energy rate that is approximately a factor of four higher than those obtained from the other three data sets. This observation is consistent with a vacuum leak detected in this sector during the data collection. The presence of vacuum leaks in a sector can cause a change in the effective  $Z$  of the residual gas in the straight path, giving rise to three to four times higher  $Z^2$  values than what is expected under normal operating conditions. This correspondingly enhances the gas bremsstrahlung production rate from the sector. It is also observed that, in the beam current range for which the measurements were conducted, the bremsstrahlung energy rate for a given vacuum is proportional to the current. As is evident from Chapter 5, gas bremsstrahlung energy rate did not show any difference between the electron and positron runs. Thus the variations in the normalised bremsstrahlung energy rate seen in Table 1 can be attributed to the differences in the non-gas bremsstrahlung contribution from sector to sector, and to the enhanced gas bremsstrahlung production rate due to the presence of vacuum leaks.

The measured bremsstrahlung rates are converted into the dose equivalent rates by using the available fluence to dose conversion factors [9]. The fluence spectra is calculated using the cross-sectional area corresponds to the average bremsstrahlung beam size at the detector, calculated

from the emission angle at the source point. Table 2 gives the normalised dose equivalent rates corresponding to the bremsstrahlung energy radiated from the 15.38 m of particle beam straight path. Only one typical value per run is given. Table 2 shows that the gas bremsstrahlung dose equivalent rate measured at beam line is  $4.2 \times 10^{-4}$  Sv/hr/nT/mA, corresponding to an energy rate of  $67.0 \pm 2.0$  GeV/sec/nT/mA and the maximum bremsstrahlung dose equivalent rate measured at a beam line is  $2.18 \times 10^{-3}$  Sv/hr/nT/mA.

**Table 2. Normalised maximum dose equivalent values corresponding to measured bremsstrahlung energy rates**

Run # beam line and beam type	Beam current $I_b$ (mA)	Estimated vacuum $P$ (nT)	Normalised corrected brems. energy $E_\gamma$ (GeV/sec/nT/mA)	Maximum dose equivalent $D_{eq}$ (Sv/hr/nT/mA)
<b>1, 12 ID, <math>e^-</math></b>	80.86	9.43	98.0 $\pm$ 2.0	5.74 $\times 10^{-4}$
<b>2, 12 ID, <math>e^-</math></b>	78.64	5.28	146.0 $\pm$ 4.0	9.13 $\times 10^{-4}$
<b>3, 10 ID, <math>e^+</math></b>	78.25	6.69	67.0 $\pm$ 2.0	4.20 $\times 10^{-4}$
<b>4, 13 ID, <math>e^+</math></b>	90.15	8.49	369.0 $\pm$ 22.0	2.18 $\times 10^{-4}$

## Conclusions

The lead glass calorimeter, by virtue of its sensitivity and fast response, is found to be a very effective detector for the accurate measurement of bremsstrahlung from electron storage rings. This calorimeter can be calibrated using the maximum energy of the observed bremsstrahlung spectrum, which is equal to the energy of the particle beam in the storage ring. The gas bremsstrahlung rate from the APS undulator beam line straight path of 15.38 m is measured as  $60.0 \pm 2.0$  GeV/sec/nT/mA. This corresponds to a maximum dose equivalent rate of approximately  $4.2 \times 10^{-4}$  Sv/hr/nT/mA. The analysis shows that there is a significant bremsstrahlung contribution from sources other than the residual gas molecules in the beam straight path of the storage ring. The maximum bremsstrahlung energy rate measured in a sector over the course of this experiment is  $369.0 \pm 22.0$  GeV/sec/nT/mA, which corresponds to a maximum dose equivalent value of approximately  $2.18 \times 10^{-3}$  Sv/hr/nT/mA. In the beam current range for which the measurements were conducted, the bremsstrahlung energy rate for a given storage ring vacuum is found to be proportional to the current. We did not observe any difference in the measured gas bremsstrahlung energy rate between the positron and electron runs.

## Acknowledgements

Work supported in part by the US Department of Energy, Contract No. W-31-109-ENG-38.

## REFERENCES

- [1] H.A. Bethe and W. Heitler, *Proc. Roy. Soc.*, A146, 84 (1934).
- [2] W. Heitler, “Quantum Theory of Radiation”, Oxford University Press, London (1944).
- [3] H.J. Moe, “Advanced Photon Source – Radiological Design Considerations”, APS-LS-141 (1991).
- [4] A. Rindi, “Gas Bremsstrahlung from Electron Storage Rings”, *Health. Phys.*, 42, 187 (1982).
- [5] A. Esposito and M. Pelliccioni, “Gas Bremsstrahlung Production in the ADONE Electron Storage Ring”, LNF 86-23, INFN Report (1986).
- [6] G. Tromba and A. Rindi, “Gas Bremsstrahlung, a Monte Carlo Evaluation”, *Nucl. Instr. Meth.*, A292, 700 (1990).
- [7] A. Ferrari *et al.*, “Estimation of Fluence Rate and Dose Rate Due to Gas Bremsstrahlung”, *Nucl. Instr. Meth.*, B83, 518 (1993).
- [8] M. Pisharody *et al.*, “Gas Bremsstrahlung in the Insertion Device Beam Lines at APS”, ANL-APS-LS-260 (1997).
- [9] D.W.O. Rogers, “Fluence to Dose Conversion Factors”, *Health. Phys.*, 46, 891 (1984).

# *Photoneutron and Photopion – DDX and Spectrum*



**STATUS OF NUCLEAR DATA EVALUATION  
FOR JENDL PHOTONUCLEAR DATA FILE**

**Tokio Fukahori**

**Japanese Nuclear Data Committee (Photonuclear Data Evaluation WG)**

Nuclear Data Centre, Department of Reactor Engineering

Japan Atomic Energy Research Institute

Tokai-mura, Naka-gun, Ibaraki-ken, 319-11 Japan

E-mail: fukahori@cracker.tokai.jaeri.go.jp

**Abstract**

For  $\gamma$ -ray induced reaction data up to 140 MeV, the JENDL Photonuclear Data File is provided for applications such as electron accelerator shielding and radiation therapy. The file will include the photonuclear reaction data for 29 elements (50 isotopes) from  $^2\text{H}$  to  $^{238}\text{U}$ . The photon absorption cross-section is evaluated with the giant dipole resonance model and quasi-deuteron model, and the decaying processes are estimated with the statistical model with preequilibrium correction by using MCPHOTO and ALICE-F codes. The evaluation work is now in a final stage. The present status of the Photonuclear Data File is reviewed in this paper.

## Introduction

Nuclear data in the energy range up to a few GeV are necessary to many applications, including accelerators used in physics research, radiation therapy, medical isotope production and transmutation of radioactive waste. The JAERI Nuclear Data Centre has started evaluation work in co-operation with the Japanese Nuclear Data Committee (JNDC) to produce files related to high energy, which are JENDL High Energy File, JENDL PKA/KERMA File and JENDL Photonuclear Data File.

For  $\gamma$ -ray induced reaction data up to 140 MeV ( $\pi$ -threshold), the JENDL Photonuclear Data File is provided for applications such as neutron shielding and estimation of radioactive isotopes produced in electron accelerators and radiation therapy. The photon absorption cross-section is evaluated with the giant dipole resonance model and quasi-deuteron model, and the decaying processes are estimated with the statistical model with preequilibrium correction by using MCPHOTO [1] and ALICE-F [2] codes. The isotopes shown in Table 1 are planned to be included in the file. The evaluation work is now in a final stage. In this paper, the present status of the JENDL Photonuclear Data File and preliminary results for several nuclides are reported.

**Table 1. The nuclei to be included in the JENDL Photonuclear Data File**

29 elements, 50 isotopes

H-2, C-12, N-14, O-16, Na-23, Mg-24, 25, 26\*, Al-27, Si-28\*, 28\*, 30\*, Ca-40\*, 48, Ti-46, 48, V-51\*, Cr-52, Mn-55, Fe-54\*, 56\*, Co-59, Ni-58\*, 60\*, 61\*, 62\*, 64\*, Cu-63, 65, Zn-64\*, Zr-90, Nb-93\*, Mo-92, 94\*, 96\*, 98\*, 100, Cs-133\*, Gd-160\*, Ta-181\*, W-182\*, 184, 186\*, Au-197, Pb-206, 207, 208, Bi-209\*, U-235\*, 238\*

\*Compilation has been finished and the tasks are now in the review stage.

## Recommended format of the file

The major applications of intermediate energy nuclear data need isotope production cross-section and double differential light particle spectra, fundamentally. Though it is necessary to include individual product nuclides for isotope production cross-sections, it seems that composite particle spectra, which are not identified the emitted reaction and summed up the same particle from all the reaction channels, might be enough to use for each application. It is no meaning to separate the origin of the emitted processes in this energy region in consideration of format.

The physical qualities which are necessary for the files are roughly classified into cross-section (MF=3) and double differential particle emission spectra (MF=6) in ENDF-6 format. For the cross-section, total adsorption, photoneutron and isotope and particle production cross-sections should be included. The evaluation information, comments and covariance data are also included in MF=1 and MF=33, possibly. The format structure of the file is summarised in Table 2.

## Evaluation method

Evaluation for JENDL Photonuclear Data File is performed through a combination of experimental data and theoretical calculation, because of lack of experimental data. In this section, outline of evaluation method is reviewed.

**Table 2. Physical quantities and (MF,MT) numbers in ENDF-6 format recommended for JENDL Photonuclear Data File**

MF	MT	Quantities
1	451	Descriptive data and dictionary
3	3	Total photoabsorption cross-section
3	5	Total isotope production cross-section
3	18	Fission cross-section
3	201	Neutron production cross-section
3	203	Proton production cross-section
3	204	Deuteron production cross-section
3	205	Triton production cross-section
3	206	<sup>3</sup> H production cross-section
3	207	Production cross-section
6	5	Branching ratios of isotope production cross-section
6	201, 203-207	Normalised double-differential cross-section for light particles
33	3	Covariance of total photoabsorption cross-section

### *Experimental data collection*

Some of the experimental data for photonuclear reactions are available as ATLAS of photoneutron cross-section and EXFOR. JNDC has also compiled the Photonuclear Reaction Data Index [3] in a CINDA-like format.

### *Photoabsorption and photoneutron cross-section*

Data fitting with the least squares procedure and theoretical calculations are combined to evaluate photoabsorption and photoneutron cross-sections. The fitting function for photoabsorption cross-section  $\sigma_{abs}(E)$  is described as:

$$\sigma_{abs}(E) = \sigma_{abs}^{GDR}(E) + \sigma_{abs}^{QDM}(E)$$

where the notations of ‘‘GDR’’ and ‘‘QDM’’ are Giant Dipole Resonance Model and Quasi-Deuteron Mode, respectively. In the GDR region, multiple Lorentz resonance curves are used as follows:

$$\sigma_{abs}^{GDR}(E) = \sum_{i=1}^n \frac{\sigma_{abs}^i}{1 + \left[ \frac{(E^2 - E_i^2)^2}{E^2 \Gamma_i^2} \right]}$$

For QDM, a new formalism by Chadwick *et al.* [4] was adopted as:

$$\sigma_{abs}^{ZDM}(E) = \frac{L}{A} NZ \sigma_d(E) f(E)$$

where  $L$  is the Levinger Parameter,  $\sigma_d(E)$  photodisintegration cross-section of free deuteron,  $f(E)$  Pauli-blocking function. If experimental data for photoabsorption cross-section are not available and those of photoneutron cross-section exist, branching ratio of photoneutron cross-section  $R(\gamma, nx)(E)$  was assumed to be:

$$\sigma_{(\gamma, nx)}(E) = R_{(\gamma, nx)}(E) \sigma_{abs}(E)$$

In cases where no experimental data was available, some systematics and parameter compilation of GDR were used.

### ***Other quantities***

For every energy spectra, angular distributions and double differential cross-sections for emitted light particles and isotope production cross-sections, the codes MCPHOTO [4] and ALICE-F [2] were used with results of photoabsorption cross-sections calculated by GDR and QDM. For rather flat angular distribution, modified Kalback's systematics by Chadwick was used in the following formula:

$$\frac{d^2\sigma}{dEd\Omega} = \frac{1}{4\pi} \frac{2a}{e^a - e^{-a}} e^{a \cos\theta} \frac{d\sigma}{dE}$$

$$a = a_{Kalbach} \sqrt{E_\gamma / 2m}$$

### **Sample results of the file**

The sample results of JENDL Photonuclear Data File are shown in Figures 1-6. These are preliminary results and all the evaluated results will be checked in the reviewing stage.

### **Summary**

The present status and outline of evaluation method have been reviewed. Photoabsorption cross-sections are evaluated using data fitting by Lorentz resonance curves, systematics for GDR and ZDM cross-sections by Chadwick *et al.* Other types of cross-sections are evaluated using theoretical calculations by MCPHOTO and ALICE-F. The evaluation is now in final stage. After review work, the JENDL Photonuclear Data File will hopefully be released in 1997.

## **REFERENCES**

- [1] N. Kishida and H. Kadotani, private communication.
- [2] T. Fukahori, "ALICE-F Calculation of Nuclear Data up to 1 GeV", Proc. Specialists Meeting on High Energy Nuclear Data, Tokai, Ibaraki, 3-4 Oct. 1991, JAERI-M 92-039, p. 114 (1992).
- [3] T. Asami and T. Nakagawa, JAERI-M 93-195 (1993).
- [4] M.B. Chadwick *et al.*, *Phys. Rev.*, C44, 814 (1991).

Figure 1.  $(\gamma, xn)$  cross-section for  $^{51}\text{V}$

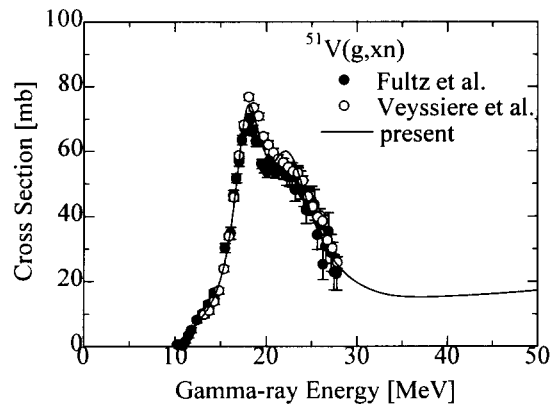


Figure 2.  $(\gamma, xn)$  cross-section for  $^{181}\text{Ta}$

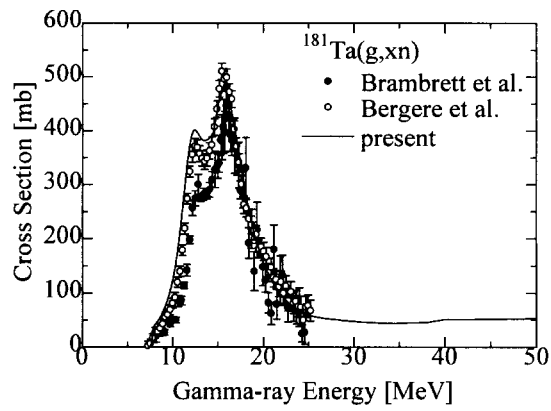


Figure 3.  $(\gamma, 1n)$  cross-section for  $^{51}\text{V}$

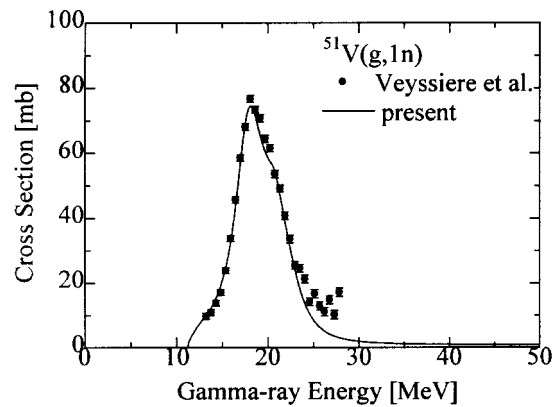


Figure 4.  $(\gamma,2n)$  cross-section for  $^{51}\text{V}$

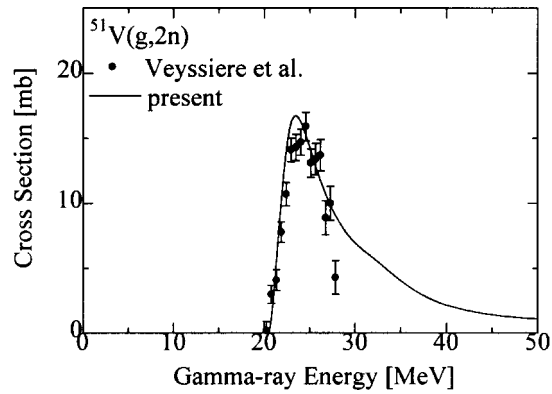


Figure 5. Photofission cross-section for  $^{235}\text{U}$

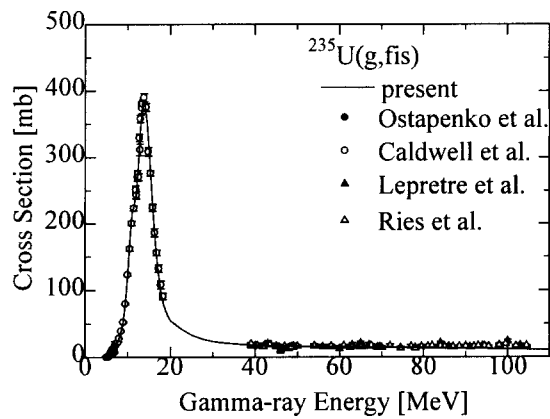
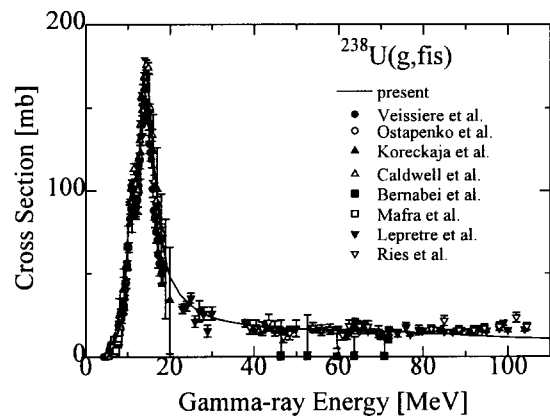


Figure 6. Photofission cross-section for  $^{238}\text{U}$



**PICA95: AN INTRANUCLEAR-CASCADE CODE FOR  
25 MEV TO 3.5 GEV PHOTON-INDUCED NUCLEAR REACTIONS**

**C.Y. Fu, T.A. Gabriel and R.A. Lillie**

Oak Ridge National Laboratory, Oak Ridge, TN 37831

**Abstract**

PICA95, an intranuclear-cascade code for calculating photon-induced nuclear reactions for incident photon energies up to 3.5 GeV, is an extension of the original PICA code package that works for incident photon energies up to 400 MeV. The original code includes the quasi-deuteron break-up and single) pion production channels. The extension to an incident photon energy of 3.5 GeV requires the addition of multiple-pion production channels capable of emitting up to five pions. Relativistic phase-space relations are used to conserve both energy and momentum in multi-body break-ups. Fermi motion of the struck nucleon is included in the phase-space calculations as well as secondary nuclear collisions of the produced particles. Calculated doubly differential cross-sections for the productions of protons, neutrons,  $\pi^+$ ,  $\pi^0$  and  $\pi^-$  for incident photon energies of 500 MeV, 1 GeV and 2 GeV are compared with predications by other codes. Due to the sparsity of experimental data, more experiments are needed in order to refine the gamma nuclear collision model.

## Introduction

The code package PICA [1,2], on which the present extension is based, contains three separate modules – PIC, MECCAN and EVAP. The photon energy range in which the calculations are applicable is between approximately 25 and 400 MeV. All target nuclei with mass numbers greater than or equal to 4 are possible. The program PIC can accommodate incident mono-energetic photons as well as thin-target bremsstrahlung spectra, thin-target bremsstrahlung difference spectra and thick-target bremsstrahlung spectra. For the last type of spectra the user must furnish the photon spectral data. PIC writes a history tape containing data on the properties of the particles (protons, neutrons,  $\pi^+$ ,  $\pi^0$  or  $\pi^-$ ) escaping from the nucleus. The data consist of the types of escaping particles and their energies and angles of emission. MECCAN utilises the data of the PIC history tape to calculate cross-sections such as the non-elastic cross-section or the doubly differential cross-section for each of the outgoing particles with energy-angle correlated distributions. EVAP then carries the nuclear reaction through the additional phase of evaporation. It calculates the energy spectra of particles (protons, neutrons, deuterons, tritons,  $^3\text{He}$  and alpha particles) “boiled off” from the excited nucleus after the cascade has stopped. Evaporation particle multiplicities and residual nuclei (radio-chemical) production cross-sections can also be obtained.

PIC includes the quasi-deuteron break-up (photo-deuteron absorption) and single-pion production channels. At an incident photon energy of about 400 MeV, double-pion productions become possible. The present extension of PIC to an incident photon energy of 3.5 GeV requires the addition of multiple-pion production channels capable of emitting up to five pions. The total number of reaction channels increases from 5 in PICA to 41 in PICA95. Cross-sections for the major channels are taken from the recently evaluated data used in the EG code [3]. Cross-sections for the reaction channels without experimental data are assumed to have the same shape as those with experimental data and with the same number of outgoing pions but can be scaled by an input factor (see details in the sections *Multi-pion channels* and *Comparisons with other calculations*). Relativistic phase-space relations are used to conserve energy and momentum in multi-body break-ups. Fermi motion of the target nucleon is included in the phase-space calculations as well as secondary nuclear collisions of the produced particles.

The upper incident photon energy in PICA95 is limited by the secondary particle cascade part of PIC. Intranuclear cascades of the secondary particles (protons, neutrons,  $\pi^+$ ,  $\pi^0$  or  $\pi^-$ ), produced by the primary photon interaction with nucleons, are based on the MECC code of Bertini [4]. In MECC, the upper energy limit for pions is 2.5 GeV and that for nucleons is 3.5 GeV. In PICA95, secondary pions of energies greater than 2.5 GeV is set to 2.5 GeV before MECC subroutines are called to continue the intranuclear cascades. This procedure causes a truncation in the pion production spectra for incident photon energies between 2.7 GeV and 3.5 GeV but the loss in the total energy of pion production for an incident photon energy of 3.5 GeV is less than 2%.

The new code package PICA95 changes only PIC. MECCAN and EAP still work the same way as described in [2]. Calculated doubly differential cross-sections for the productions of protons, neutrons,  $\pi^+$ ,  $\pi^0$  and  $\pi^-$  for incident photon energies of 500 MeV and 1 GeV are compared with predictions using CEM95 [5,6] and by Degtyarenko [7] using DINREG [8,9]. For the incident photon energy of 2 GeV, comparisons are only made with DINREG. CEM95 is an intranuclear cascade code similar to PICA95 but is limited to incident photon energies below 1 GeV, above which the triple-pion contributions, not included in CEM95, become significant. Differences in the predicted particle production, spectra between PICA95 and CEM95 may be due to differences in the input cross-sections, nucleon densities, nuclear level densities, and pion potentials; DIINREG is not an intranuclear cascade code but is based on entirely different concepts such as a thermodynamic

quark source in the excited nucleus, the rules of high-energy hadron production and some empirical parameters derived from electron-induced reactions. DINREG has been used up to 10 GeV but a detailed documentation of this code is not yet available.

## Multi-pion channels

The reaction channels included in PICA95 are listed in Table 1. The first five channels are used in PICA while all 41 channels are included in PICA95. Cross-sections for the channels used in PICA95 and the method used for conserving energy and momentum are described in this section.

The cross-sections for reaction numbers 2, 4, 6, 12, 20 and 30 were taken from the EG code [3] that considered the most recent experimental data for these cross-sections. These cross-sections and that of reaction 1 are shown in Figure 1. The cross-sections of reactions 3 and 5 are set to be the same as 2 and 4, respectively, assuming charge symmetry. All double-pion cross-sections are assumed to have the same cross-section shape as channel number 6 but may be scaled by an input factor. The same approach is used for scaling all other triple-pion cross-sections to channel number 12, four-pion cross-sections to channel number 20, and five-pion cross-sections to channel number 30. The values of the scaling factors used in the present calculations are given in the following section.

In Table 1, the cross-sections tabulated in the EG code are marked. These are reaction numbers 2-6, 12, 13, 20, 30, 33. However, not all of these cross-sections are tabulated in PICA95. In PICA95, the cross-sections of reactions 3 and 5 have been set to 2 and 4, respectively, as described above, assuming charge symmetry. The cross-section of reaction number 13 has been set equal to that of 12 because these two cross-sections are rather close. For the same reason, the cross section of reaction 33 has been set equal to that of 30. Therefore, only cross-sections for reaction numbers 1, 2, 4, 6, 12, 20 and 30 are tabulated in PICA95 as shown in Figure 1. As discussed above, scale factors can be used to alter these cross-sections. In fact, most of the cross-sections are weakly known and need to be refined.

The decision to use scale factors for unknown cross-sections is based on an observation of the assumptions used in the CEM95 and EG codes. CEM95 includes channel numbers 8 and 10, the double- $\pi^0$  productions, while EG ignores them. These two extreme assumptions tend to make a factor of two difference in  $\pi^0$  production spectra near an incident photon energy of 1.25 GeV where the double-pion production cross-section (see Figure 1) is the largest. It is therefore better to keep the multi- $\pi^0$  channels open until new experimental data are available to help make a good decision on the scaling factors. It is easier to set a cross-section to a different value than to add a new reaction channel into the code.

In ICA, only two-particle relativistic kinematics with Fermi motion of the struck nucleon are needed. But multi-particle relativistic kinematics with Fermi motion are also required in PICA95. The latter requirement is met by combining standard relativistic phase-space relations with the two-body kinematics with the Fermi motion already in PICA.

Many other reaction channels, containing outgoing particles like deltas, rhos, etas, omegas, etc., are open for an incident photon energy of 3.5 GeV. In particular, delta and rho channels are open below 500 MeV. These channels are not included in PICA95. Even though these missing reaction channels have small cross-sections [3], most of them, including the delta and rho channels, produce protons, neutrons or pions. Thus their absence tends to lead to underprediction of the present PICA95 results by up to 30%.

## Comparisons with other calculations

The PICA95 results presented in this section were obtained using scale factors for the cross-sections that are unity except for multiple- $\pi^0$  cross-sections that have scale factors inversely proportional to the number of  $\pi^0$ 's produced. To demonstrate this, consider the following example. The scale factors for reaction numbers 8 and 10, the double- $\pi^0$  channels, are 1/2 and the scale factors for reaction numbers 32 and 38, the five- $\pi^0$  channels, are 1/5. These scale factors represent an intermediate choice between the assumptions made in the CEM95 and EG codes.

Calculated double differential cross-sections for Cu for the production of protons, neutrons,  $\pi^+$  and  $\pi^0$  for incident photon energies of 500 MeV and 1 GeV are compared with predictions using CEM95 by authors of this report and using DINREG by Degtyarenko in Figures 2-5. For the incident photon energy of 2 GeV, the comparisons shown in Figures 6 and 7 are only with DINREG. The energy spectra for  $\pi^-$  are omitted in this report because they are very similar to those for  $\pi^+$ . Each figure compares the energy spectra in two angular groups – the forward angles (0 to 90 degrees laboratory) and the backward angles energies greater than 25 MeV. For energies below 25 MeV the spectral comparisons are listed in tables as discussed below. All symbols in Figures 2-7 represent histograms that are shown only for one set of spectra. The spectra for the backward angles have been scaled in the figures by a factor of 0.1 for clarity.

The total reaction cross-sections and particle multiplicities are given in Tables 2 and 3. The product of a particle multiplicity and the total reaction cross-section gives the energy-integrated cross-section for the production of that particle. Table 2 corresponds to the forward-angle data above 25 MeV shown in the figures. Table 3 is for total multiplicities including the backward angles and all energies. PICA95 yields the smallest reaction cross-sections and the largest multiplicities. For protons and neutrons, the multiplicities from DINREG are between PICA95 and CEM95. For pions, PICA95 is closer to CEM95 than to DINREG.

The large multiplicities predicted by PICA95 could be partly due to the lack of a pre-equilibrium reaction model that would bridge the gap between the existing intranuclear cascade and evaporation models. In addition, the EVAP code does not include the subtraction of recoil energy from the excitation energy. Inclusion of both in PICA95 would lead to smaller multiplicities.

Figures 2-7 show that the spectral shapes for protons and neutrons in the three calculations are similar, but those for pions are only similar between PICA95 and CEM95. The minima in the pion spectra near 150 MeV, seen in CEM95, are not in DINREG. These minima can be well-explained by the large pion resonance [4] at 150 MeV that scatters or absorbs pions produced near the resonance. The 2 GeV comparisons between CEM95 and DINREG, the proton and neutron spectra are in good agreement in magnitude and in shape, and the pion spectra are in good agreement in shape except at 150 MeV.

## Conclusions

Proton, neutron,  $\pi^+$ ,  $\pi^0$  and  $\pi^-$  spectra produced by high-energy photons on Cu calculated by PICA95 are compared with results predicted by CEM95 at 500 MeV and 1 GeV, and with results predicted by DINREG at 500 MeV, 1 GeV and 2 GeV. Predicted reaction cross-sections by the three codes agree within 50%, but multiplicities differ by a factor of 2 for nucleons and by a factor of 4 for

pions. Shapes of the nucleon spectra are in good agreement for all cases shown, but shapes of the pion spectra by DINREG do not show the large dips near 150 MeV seen in the PICA95 and CEM95 results, particularly for the 500 MeV comparisons.

The comparisons shown in this report represent the status of the predictive capabilities of photonuclear codes available for photon energies in the low-GeV range. Improvements in theory and/or adjustments in input cross-sections and parameters may be required when new experimental data become available. Until then, codes compared in this report are being applied to aid in the design of high-energy detectors, in the interpretation of data acquired in such detectors, and in the assessment of radiation doses in and around proposed accelerators.

An addition of pre-equilibrium reaction model in PICA95 to link the existing intranuclear cascade and evaporation models is in progress.

### *Acknowledgements*

The authors acknowledge help from Stephan Mashnik of Dubna, Russia, for making CEM95 operational at Oak Ridge National Laboratory; P. Corvisiero of Genova, Italy for sending the EG code and Pavel Degtyarenko of CEBAF for sending his calculated results for Cu. This work was sponsored by Office of Energy Research, Division of Nuclear Research, US Department of Energy, under contract DE-AC05-84OR21400 with Lockheed Martin Energy Systems, Inc.

## REFERENCES

- [1] T.A. Gabriel and R.G. Alsmiller Jr., “Photonuclear Disintegration at High Energies (350 MeV)”, *Phys. Rev.*, 181, 1035 (1969) and ORNL-TM-2481, February (1969).
- [2] T.A. Gabriel, M.P. Guthrie and O.W. Hermann, “Instructions for the Operation of the Program Package PICA, An Intranuclear-Cascade Calculation for High-Energy (20 to 400 MeV) Photon-Induced Nuclear Reactions”, ORNL-4687, September (1971).
- [3] P. Corvisiero *et al.*, *Nuc. Inst. Med.*, A346, 433-440 (1994).
- [4] Hugo W. Bertini, “Intranuclear Cascade Calculation of the Secondary Nucleon Spectra from Nucleon-Induced Interactions in the Energy Ranyg Range 340 to 2900 MeV and Comparisons with Experiment”, *Phys. Rev.*, 188, 1711-1730 (1969).
- [5] T. Gabriel, G. Maino, S.G. Mashnik, “Analysis of Intermediate Energy Photonuclear Reactions”, XII International Seminar on High Energy Physics Problems – Relativistic Nuclear Physics and Quantum Chromodynamics, E2-94-424, Dubna, Russia, 12-17 September (1994).
- [6] Stephan G. Mashnik, “User Manual for the Code CEM95”, Bogoliubov Laboratory of Theoretical Physics, Joint Institute for Nuclear Research, Dubna, Russia (1995).
- [7] P.V. Degtyarenko and G. Stapleton, “Radiation for High Energy Electron Accelerators – Past and Future”, a presentation at the second workshop on Simulation Accelerator Radiation Environment (SARE2), CERN, Geneva, Switzerland, 9-11 October (1995).
- [8] M.V. Kossov, “Monte Carlo Generator for Nuclear Gragmentation Induced by Pion Capture”, MC93 International Conference on Monte Carlo Simulation in High Energy and Nuclear Physics, Tallahassee, Florida, USA, p. 190, 22-26 February (1993).
- [9] P.V. Degtyarenko *et al.*, *Phys. Rev.*, C50, 541 (1994).

**Table 1. Reaction channels used in PICA95**

Reaction number	Struck particle	Exit particles
1 *	(n,p)	n p
2 *	p	n pi+
3	n	p pi-
4 *	p	p pi0
5 *	n	n pi0
6 *	p	p pi+ pi-
7	p	n pi+ pi0
8	p	p pi0 pi0
9	n	n pi+ pi-
10	n	p pi- pi0
11	n	n pi0 pi0
12 *	p	p pi+ pi- pi0
13 *	p	n pi+ pi+ pi-
14	p	n pi+ pi0 pi0
15	p	p pi0 pi0 pi0
16	n	n pi+ pi- pi0
17	n	p pi+ pi- pi-
18	n	p pi- pi0 pi0
19	n	n pi0 pi0 pi0
20 *	p	p pi+ pi+ pi- pi-
21	p	p pi+ pi- pi0 pi0
22	p	p pi0 pi0 pi0 pi0
23	p	n pi+ pi+ pi- pi0
24	p	n pi+ pi0 pi0 pi0
25	n	n pi+ pi+ pi- pi-
26	n	n pi+ pi- pi0 pi0
27	n	n pi0 pi0 pi0 pi0
28	n	p pi+ pi- pi- pi0
29	n	p pi- pi0 pi0 pi0
30 *	p	p pi+ pi+ pi- pi- pi0
31	p	p pi+ pi- pi0 pi0 pi0
32	p	p pi0 pi0 pi0 pi0 pi0
33 *	p	n pi+ pi+ pi+ pi- pi-
34	p	n pi+ pi+ pi- pi0 pi0
35	p	n pi+ pi0 pi0 pi0 pi0
36	n	n pi+ pi+ pi- pi- pi0
37	n	n pi+ pi- pi0 pi0 pi0
38	n	n pi0 pi0 pi0 pi0 pi0
39	n	p pi+ pi+ pi- pi- pi-
40	n	p pi+ pi- pi- pi0 pi0
41	n	p pi- pi0 pi0 pi0 pi0

\* Cross-section known to some extent [1,3]

**Table 2. Comparisons of total reaction cross-sections and multiplicities (>25 MeV, forward angles) for Cu**

Energy (MeV)	Total XS (mb)	Multiplicity (>25 MeV, <90 deg)					
		p	n	pi+	pi0	pi-	
500	PICA95	10.18	1.35	1.53	.181	.220	.219
	CEM95	11.21	.790	.960	.109	.125	.127
	DINREG	15.14	.823	1.30	.050	.100	.042
1000	PICA95	8.33	1.97	2.22	.436	.496	.480
	CEM95	9.18	1.07	1.30	.191	.262	.238
	DINREG	9.95	1.51	2.09	.093	.142	.085
2000	PICA95	5.73	3.12	3.59	.900	1.01	.960
	DINREG	7.70	2.51	3.25	.253	.340	.254

**Table 3. Comparisons of total reaction cross-sections and multiplicities (all energy, all angle) for Cu**

Energy (MeV)	Total XS (mb)	Multiplicity (all energy angle)					
		p	n	pi+	pi0	pi-	
500	PICA95	10.18	4.88	7.16	.309	.385	.376
	CEM95	11.21	2.33	4.20	.175	.201	.209
	DINREG	15.14	2.45	4.87	.074	.153	.064
1000	PICA95	8.33	6.71	9.18	.683	.784	.752
	CEM95	9.18	2.88	4.61	.283	.392	.339
	DINREG	9.95	4.13	7.00	.120	.194	.119
2000	PICA95	5.73	10.47	13.73	1.310	1.516	1.427
	DINREG	7.70	6.85	10.38	.305	.425	.302

**Figure 1. Cross-sections of photon-induced reactions tabulated in PICA95; the reaction number shown corresponds to that listed in Table 1**

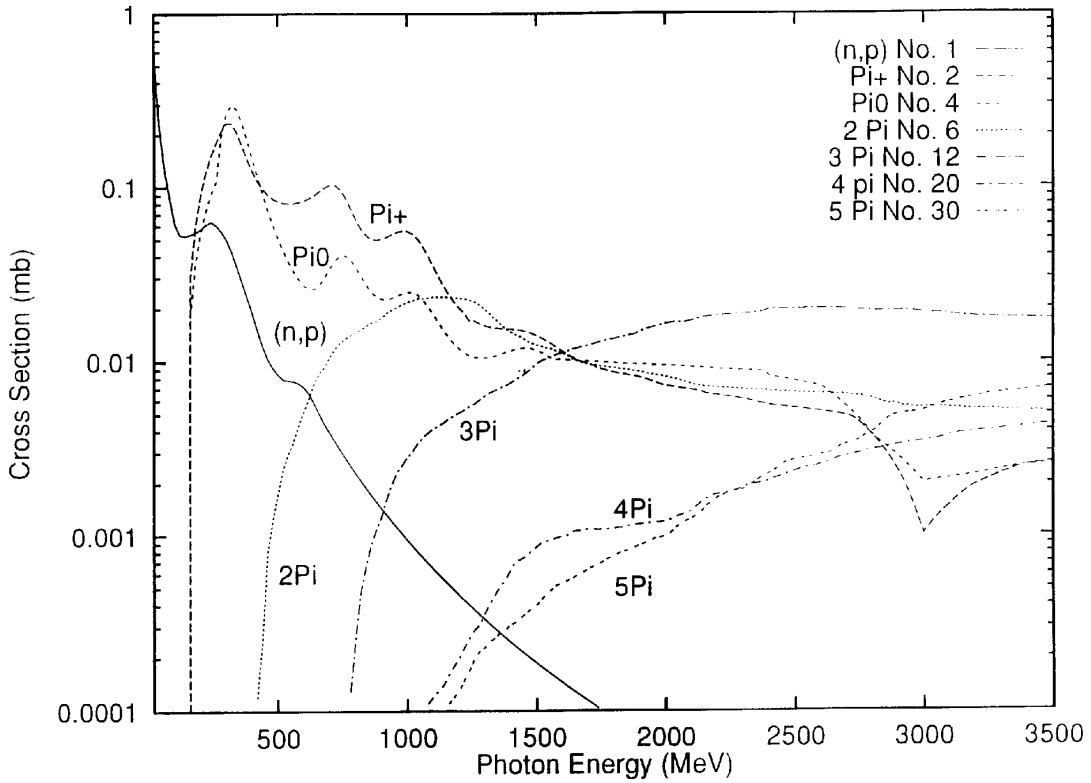


**Figure 2. Proton and neutron spectra from 500 MeV photon on Cu**

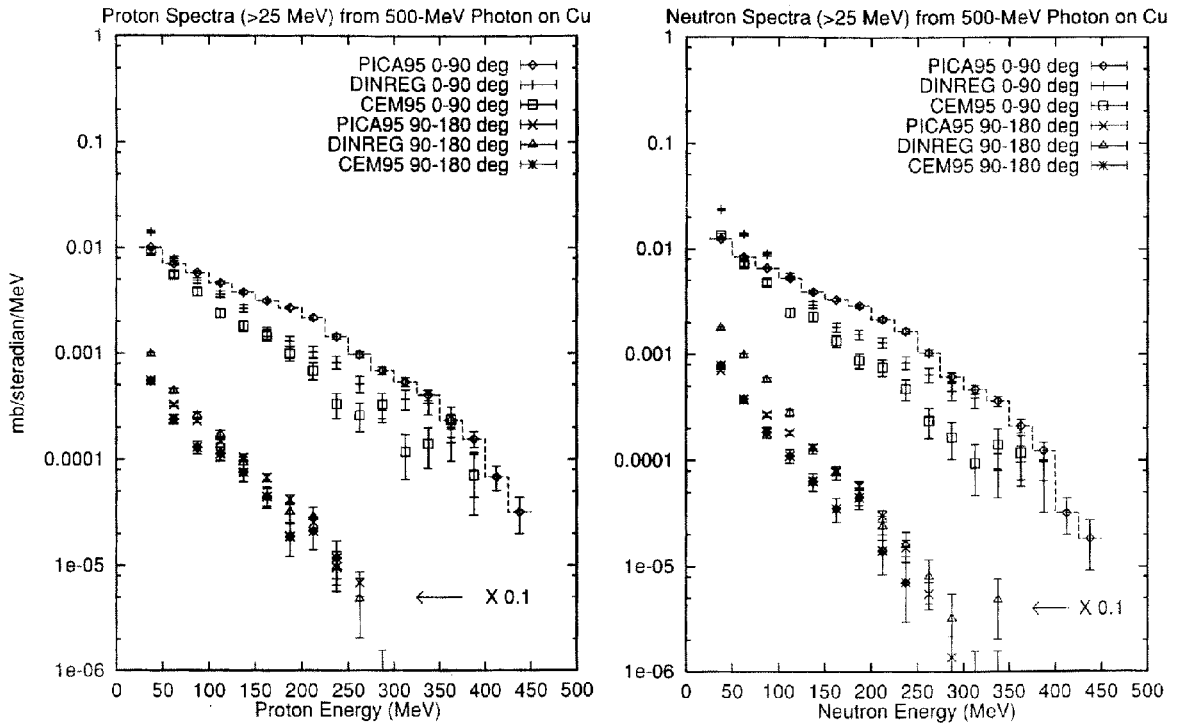


**Figure 3.  $\pi^+$  and  $\pi^0$  spectra from 500 MeV photon on Cu**

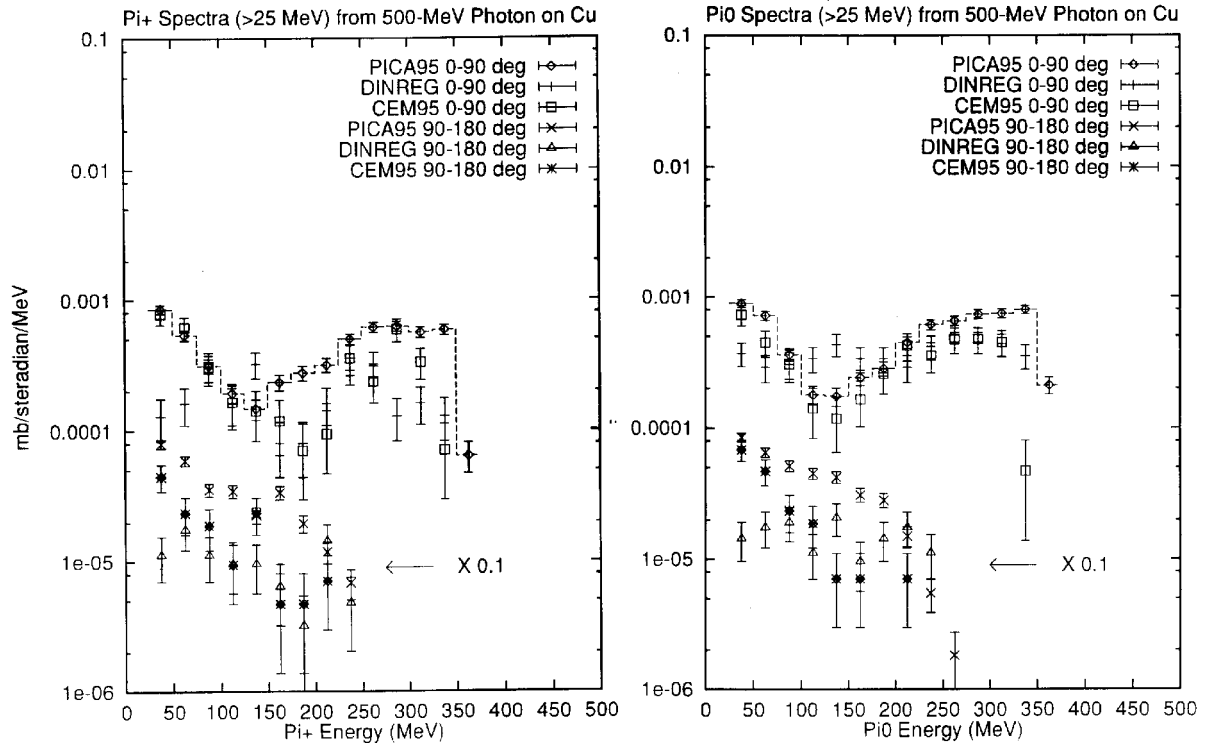


**Figure 4. Proton and neutron spectra from 1 GeV photon on Cu**

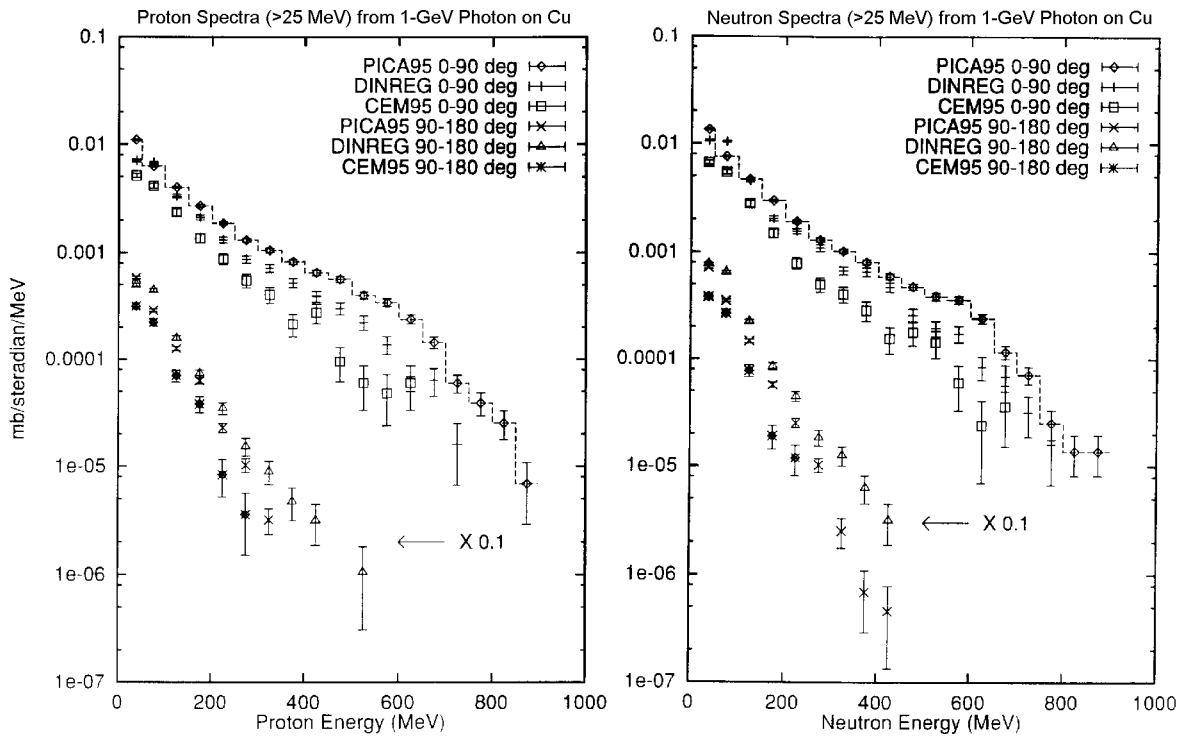


Figure 5.  $\pi^+$  and  $\pi^0$  spectra from 1 GeV photon on Cu

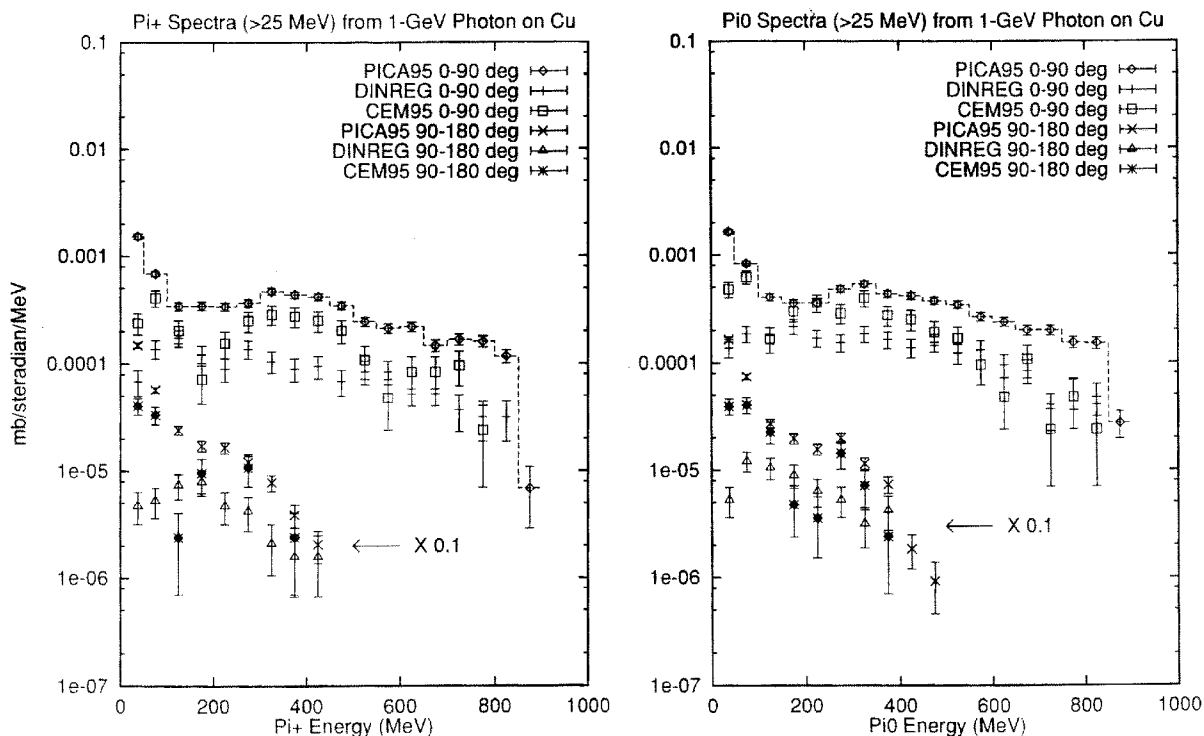


Figure 6. Proton and neutron spectra from 2 GeV photon on Cu

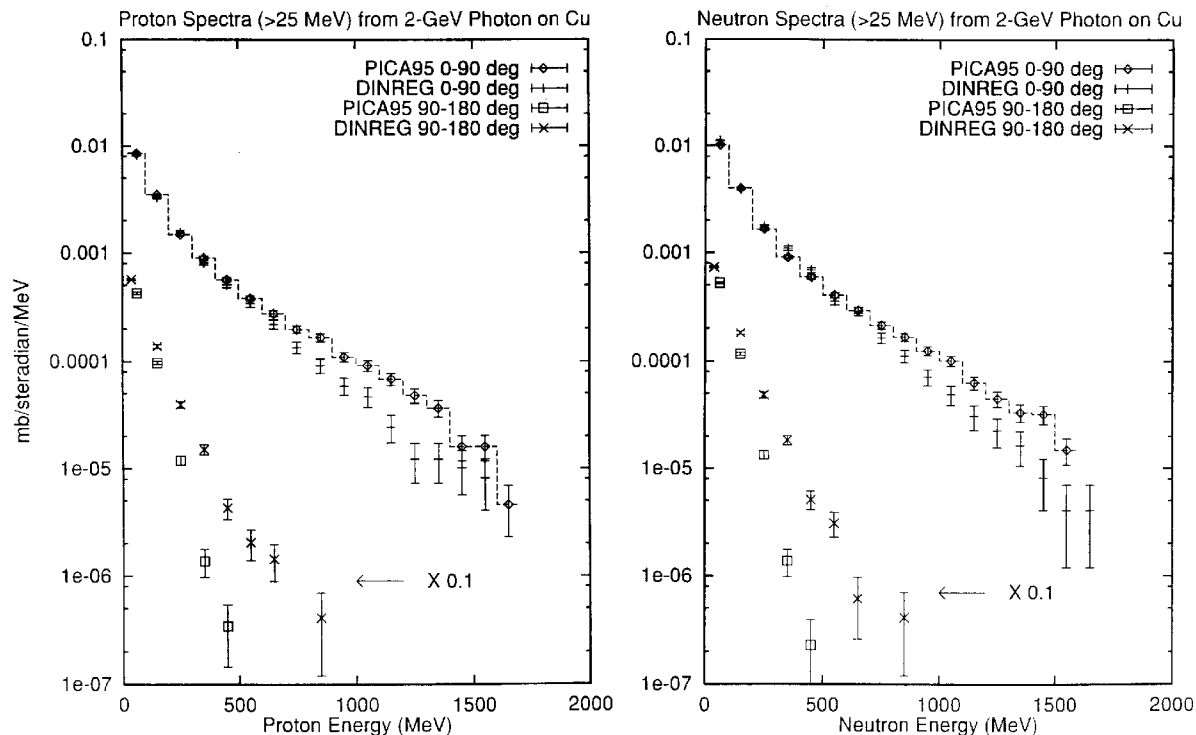
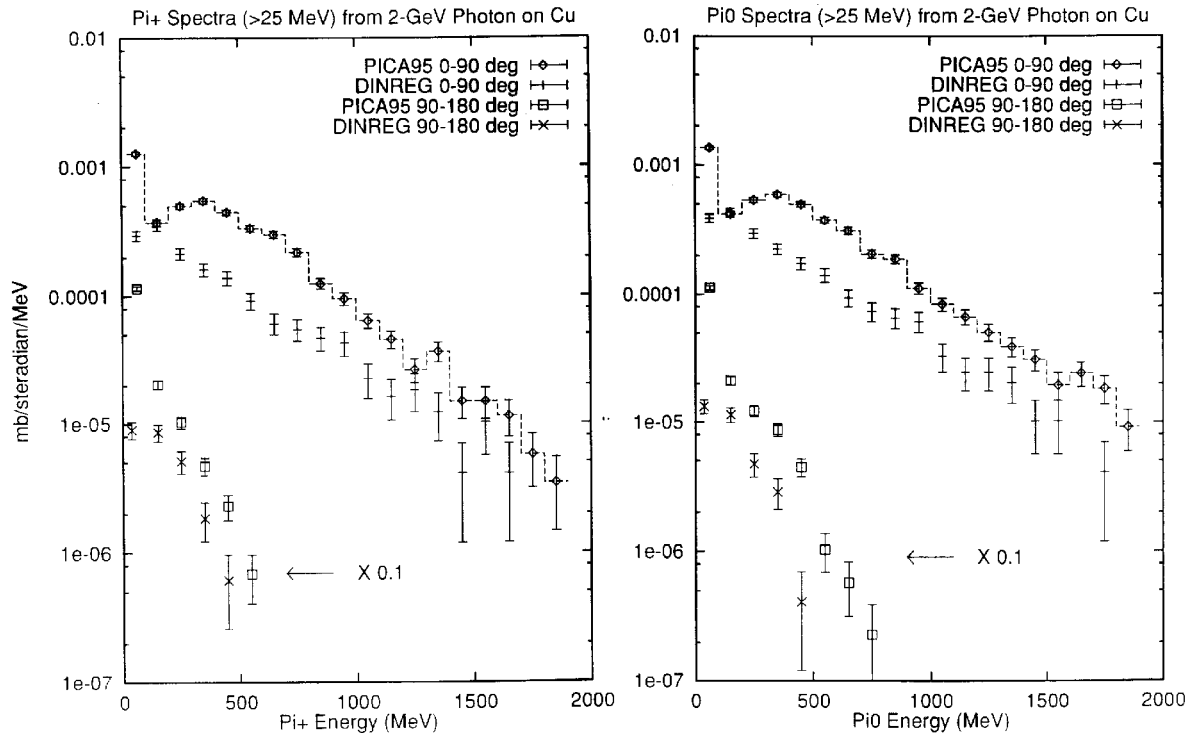


Figure 7.  $\pi^+$  and  $\pi^0$  spectra from 2 GeV photon on Cu



**TOTAL GIANT RESONANCE PHOTONUCLEAR CROSS-SECTIONS  
FOR LIGHT NUCLEI: A DATABASE FOR THE FLUKA  
MONTE CARLO TRANSPORT CODE**

**A. Fassò**

SLAC, Radiation Physics Department, ms 48, P.O. Box 4349, Stanford CA 94309, USA

**A. Ferrari, P.R. Sala**

INFN, Sezione di Milano, Via Celoria 16, I-20133 Milano, Italy

**Abstract**

The use of Monte Carlo programs to design electron accelerator shielding is limited by the lack of suitable photonuclear total cross-section data in the energy region below 30 MeV. This is especially important for light nuclei, in which the total and the ( $\gamma$ ,n) cross-sections differ considerably from each other and cannot be easily parameterised. An attempt has been made to compile a database as complete as possible for nuclei with  $Z \leq 29$ , using all available information. The data will be included in the FLUKA data library, extending the code capability to simulate photonuclear reactions at any energy and in as many nuclei as possible.

## Introduction

Up to recent times, Monte Carlo programs have played a very different role in the shielding design of electron and proton machines. While existing transport codes can be applied to study all aspects of proton accelerator shielding, only a more limited range of problems connected with electron machines (target calculations, thin shields, gas bremsstrahlung, synchrotron radiation) has been handled by Monte Carlo so far, at least in a single stage. This is because traditional electron-photon transport codes do not simulate photonuclear reactions, which are the source of the dominant radiation component behind thick shields. Bulk shielding assessment is thus mainly based on empirical source terms and attenuation lengths, sometimes inserted into computer programs [1]. However, such programs and analytical formulae are generally applicable only to very simplified geometries and to a maximum of two or three target and shielding materials.

More complex situations are either treated in a simplified, conservative way, or require the coupling of two Monte Carlo codes. An electron-photon transport code is first needed to score energy and possibly position dependent photon fluence in a region of space; then the fluence so obtained is folded with experimental photoneutron cross-sections to produce a source for a neutron transport code [2,3,4]. This technique, however, in addition to being rather cumbersome, lacks the spatial, angular and energy resolution of a full Monte Carlo simulation, since a lot of information is lost in the process of converting a scored photon fluence into a neutron source.

A transport code capable of simulating not only the electromagnetic interactions of photons and electrons, but also photonuclear reactions, would find interesting applications not only in shielding but also in dosimetry. The unwanted dose to the patient due to photoneutrons produced both in the structure of medical accelerators and in the tissue of the body, which has been investigated by several authors using the multistage technique described above [5,6,7], could be assessed with better accuracy. In addition, such a code could help to predict induced activity in structural components of electron accelerators and background neutron radiation in physics experiments [8].

## Monte Carlo

### *Existing and past implementations of photonuclear reactions*

Photonuclear interactions have actually already been implemented in a more or less comprehensive manner in a few Monte Carlo transport codes. The first was probably PICA, written by Gabriel and originally based on the Levinger quasi-deuteron model coupled with the Bertini intranuclear cascade-evaporation model [9]. The present version also includes single pion production and, according to the author [10], has been extended to the energy region below 30 MeV using the photoneutron cross-sections reported in the first edition of the so-called "Berman's Atlas" [11]. It is not clear from [10] if the code can handle any nucleus, including those not reported by Berman, and if photonuclear reactions other than ( $\gamma,n$ ) are implemented below 30 MeV.

Barashenkov [12] described a similar code based on his intranuclear cascade model, covering the energy range 50 MeV-1.3 GeV and nuclei with  $A \geq 27$ . However, that code doesn't seem to have been used outside the USSR.

Other implementations of photonuclear reactions (limited to photoneutron reactions) have been reported by Alsmiller and Moral [13,14] and by Hansen *et al.* [15]. The cross-sections used were those reported in Berman's Atlas. Morioka and Kadotani [16] have announced a version of the SANDYL code including photonuclear processes. None of these codes seems to be in use at present.

A more recent program is DINREG by Degtyarenko [17], based on a high energy multifragmentation model of M. Kossov. The author claims in [17] that this code has been empirically extended to apply to the "region of lower nuclear excitations", but gives neither further detail about the actual lower limit, nor information about the cross-sections used.

The implementation of photoneutron production in MCNP4A has been recently announced [18], but it is limited to just four nuclides having a very low photoneutron threshold energy, and the cross-section is calculated analytically in an approximate manner.

## **FLUKA**

The work presented here is connected with the attempt to extend the capability of the FLUKA code to simulate in detail photonuclear reactions at any energy and in any nuclide. The photonuclear module of FLUKA, which was already presented at the Eighth International Conference on Radiation Shielding in Arlington [19], has been successfully benchmarked for photon energies larger than 30 MeV. The cross-sections used by the code are calculated and analytically in the quasi-deuteron energy range, and are tabulated from published experimental data for energies around the  $\Delta$  resonance and above. The interaction is simulated via the PEANUT intranuclear cascade-preequilibrium evaporation code [20] below about 700 MeV, and according to the Vector Meson Dominance model above.

FLUKA can also handle in principle photonuclear reactions in the energy region of the Giant Dipole Resonance (GDR), although not quite with the same accuracy as those in the quasi-deuteron region. Several physical models have been developed to describe the collective nuclear excitation which is typical of photon energies between about 8 and 30 MeV, but to our knowledge none of them has been successful enough to suggest a practical application, and in any case no Monte Carlo event generator has yet been reported. However, while there is no simple way to predict the excitation function, the nuclear de-excitation is very similar to that of a typical compound nucleus. Therefore, the interaction cross-section must be read from tables or parameterised, but the energy dissipation in the nucleus can be treated by the PEANUT pre-equilibrium-evaporation module.

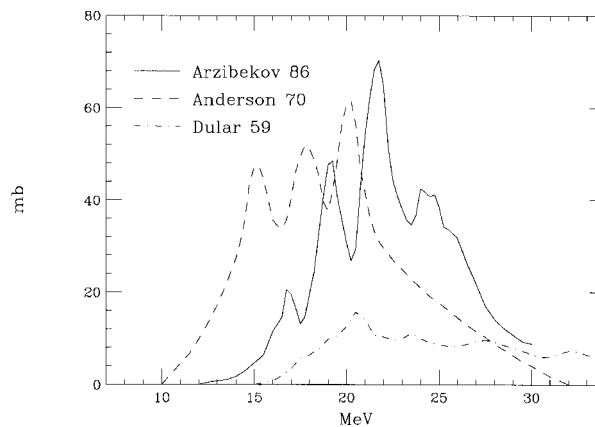
In the first version presented in Arlington, all cross-sections were parameterised according to a formula proposed by Dietrich and Berman [21], and that was sufficient to reproduce fairly accurately the experimental thick target data by Barber and George [22]. However, that formula does not apply to light nuclei and refers in any case to photoneutron reactions, while the probability of interaction is described by the total photoabsorption cross-section. For heavy nuclei the values of the two cross-sections are sufficiently close to justify such an approximation, but in low- $Z$  nuclei the emission of charged particles can be very important, and in some cases the total cross-section can be much larger than the photoneutron one.

Many elements contained in the concrete used for shielding, and all the important constituents of tissue have a low atomic number; therefore the capability of FLUKA to simulate most cases of practical interest would be greatly diminished unless total photoabsorption cross-sections for light nuclei be made available in one way or another.

## Available data

As a first step it was found necessary to search the literature for any published experimental cross-sections; total if possible, but also  $(\gamma,n)$ ,  $(\gamma,p)$ , etc., with the hope of being able to reconstruct the total cross-section as a sum of the partial ones. However, this is not an easy task, since published data on photonuclear reactions are sparse, often inconsistent, incomplete and affected by large errors (especially those found in the older literature). As an example, Figure 1 reports the total photoabsorption cross-section of  $^{32}\text{S}$  as given by three different authors [23,24,25]. Discrepancies of the same order are not uncommon among data published before 1970. Old measurements are also often badly documented; for instance it is not always clear whether the reported data refer to  $(\gamma,1n) + (\gamma,2n)$  (cross-section for photoneutron interaction with emission of any number of neutrons), or to  $(\gamma,1n) + 2(\gamma,2n)$  (neutron yield cross-section). Inconsistent notation has been used (and is still being used) by different authors:  $\sigma(\gamma,n)$ ,  $\sigma(\gamma,Tn)$ ,  $\sigma(\gamma,Sn)$ ,  $\sigma(\gamma,sn)$ ,  $\sigma(\gamma,xn)$ ,  $\sigma(\gamma,n_i)$  are given non-uniform and often overlapping meanings. No data is ever reported in numerical form, but always as graphical plots (often of very poor quality).

**Figure 1.  $\sigma_{\text{tot}}$  of  $^{32}\text{S}$  as reported in [23,24,25]**



## Reviews and bibliographies

Several published reviews have been of great help over the course of preparing the present database. The first of these is the new edition of the well known “Berman’s Atlas” [21]. The data reported in the Atlas have the great advantage of being available on request in numerical form and are all of good quality, the authors having excluded any measurements not performed with monoenergetic photon beams. Indeed, old data obtained by unfolding measurements made with bremsstrahlung radiation present often large errors and spurious fluctuations in the excitation curve. However, modern statistical techniques presently allow to limit unwanted correlation, and many photoneutron cross-sections not reported in the Atlas have been found equally interesting, in particular those measured by the Melbourne and by the Moscow groups. Useful compilations of earlier measurements can be found in a report by Lund University [45] (up to 1972) and in the Abstract Sheets of the National Bureau of Standards (up to 1982) [46]. A more recent compilation, also containing some evaluations, is that of Blokhin and Nasyrova [47], based on the EXFOR data library. We were made aware of the existence of this document only recently, and thus it has not been used for the present work.

There are also useful bibliographical reviews such as those of the IAEA [48] and of JAERI [49], but much of the interesting data cited in these reviews were published in local journals or internal reports that are difficult to find.

So far, no attempt seems to have been made to publish a comprehensive collection of evaluated data, such as the celebrated BNL-325 for the neutron cross-sections.

### *Total cross-sections*

Total photoabsorption cross-sections have been measured with good accuracy only for a limited number of nuclei, either of natural isotopic composition or single nuclides; the main sources for the present compilation have been the papers of Ahrens *et al.* [26,27], Bezić *et al.* [28,29] and McNeill [30]. Some examples are shown in Figures 2, 3, and 4.

**Figure 2. Total photoabsorption cross-section of  $^9\text{Be}$  ([26] completed at the lowest energies with data of [31-34])**

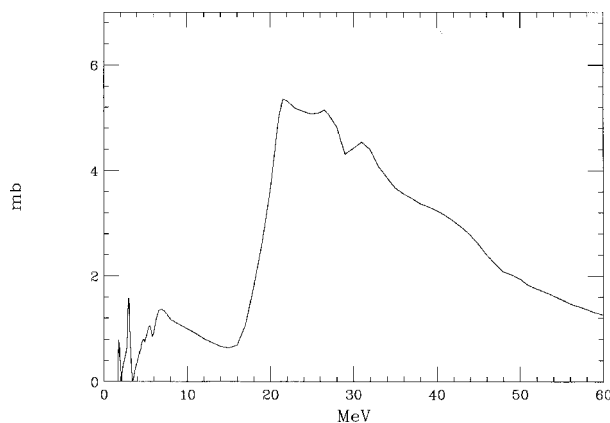


**Figure 3. Total photoabsorption cross-section of  $^{15}\text{N}$ , from McNeill *et al.* [30]**

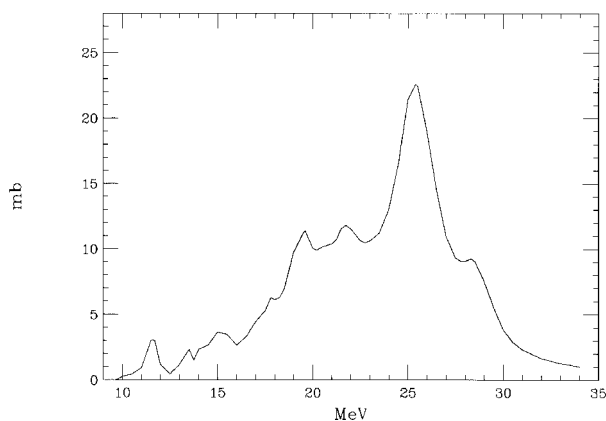
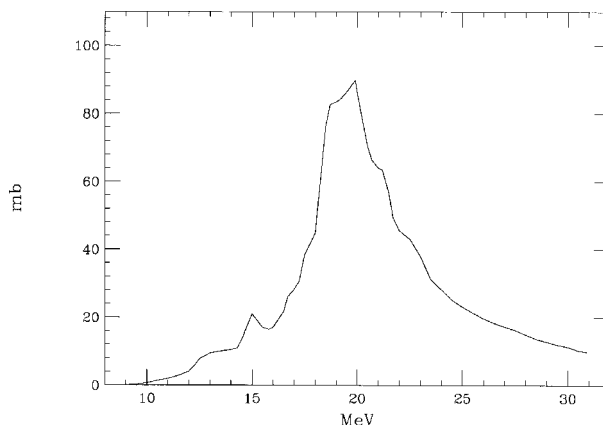


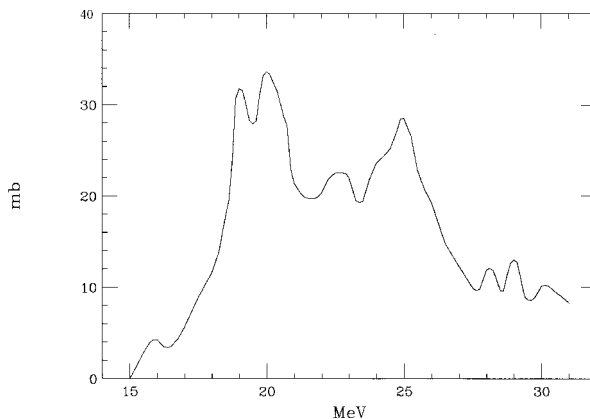
**Figure 4. Total photoabsorption cross-section of  $^{nat}\text{C}$ , from [28]**



### *Summing partial cross-sections*

Other useful data, not measured directly, but reconstructed as sums of experimental partial cross-sections, have been found in [25,35-39]. An example is shown in Figure 5.

**Figure 5. Total photoabsorption cross-section of  $^{24}\text{Mg}$ , evaluated by Irgashev *et al.* [35] summing published partial cross-sections**



In particular, a very accurate evaluation of total cross-sections of  $^{12}\text{C}$ ,  $^{14}\text{N}$  and  $^{16}\text{O}$  has been published by Fuller [40]. As an example, Figure 6 displays the total cross-section of  $^{16}\text{O}$  measured by Ahrens *et al.* [26] and corrected by Fuller especially at the lowest energies.

On the other hand, it has not been possible so far, except in the single case of  $^4\text{He}$  (see Figures 7 and 8), to collect sufficient data to perform the same kind of reconstruction on further nuclides. There are several reasons why summing partial cross-sections has turned out to be more difficult than expected. In very light nuclei several channels are available for emission of charged particles without accompanying neutron:  $(\gamma, \text{P})$ ,  $(\gamma, \alpha)$ ,  $(\gamma, \text{d})$ ,  $(\gamma, \text{t})$ , etc., and it is difficult to find reliable information about all of them for the same nuclide. In addition, the instruments used to detect charged particles have a detection threshold which is difficult to account for. Finally, detection usually takes place at only one or two fixed angles but the angular distribution is generally not uniform.

**Figure 6. Total photoabsorption cross-section of  $^{16}\text{O}$ , measured by Ahrens *et al.* [26], and modified by Fuller [40]**

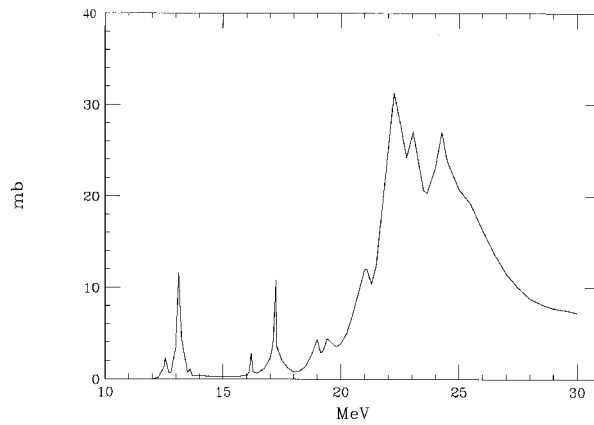


**Figure 7.  $\sigma_{\gamma p}$  of  $^4\text{He}$  from different authors [41-44] and adopted curve**

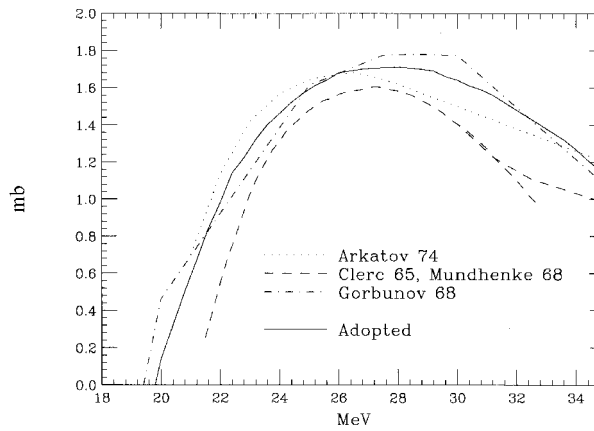
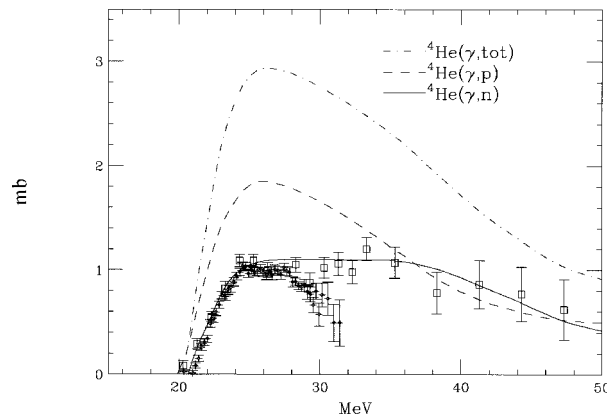


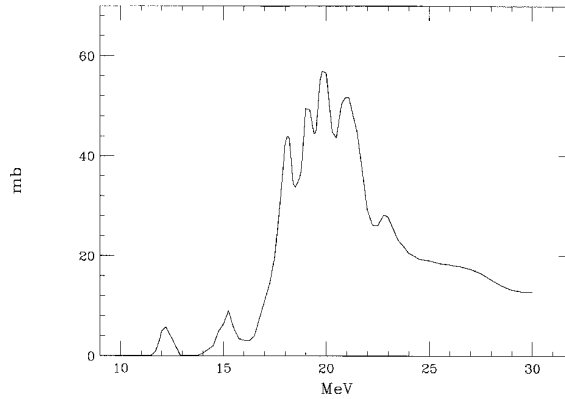
**Figure 8.  $\sigma_{\text{tot}}$  of  $^4\text{He}$  obtained by summing  $\sigma_{\gamma n}$  and  $\sigma_{\gamma p}$**



### Sum of difference of isotopes

While in several cases the cross-section of a natural mixture of nuclides has been obtained by summing those of the various components, the reverse has also occurred; Figure 9 shows the cross-section of  $^{28}\text{Si}$  derived by subtraction of that of  $^{29}\text{Si}$  and  $^{30}\text{Si}$ , measured by McNeill *et al.* [30] from that of natural silicium, measured by Bezić *et al.* [28].

**Figure 9. Total photoabsorption cross-section of  $^{28}\text{Si}$ , obtained by subtraction of  $^{29}\text{Si}$  and  $^{30}\text{Si}$  from  $^{\text{nat}}\text{Si}$**

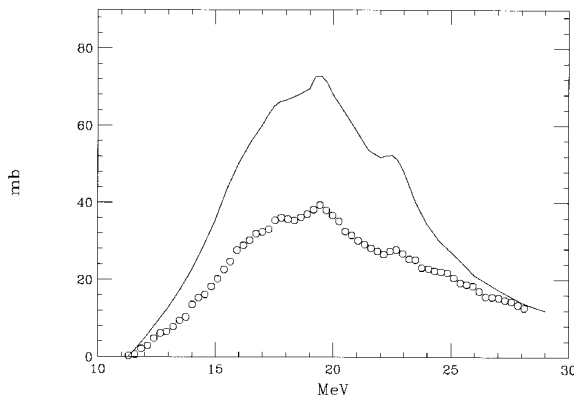


### Renormalising $\gamma,n$ data with PEANUT

In order to evaluate the total cross-section of nuclei for which only  $\gamma,n$  cross-sections are available, the PEANUT code was run standalone providing the relative frequency of inelastic events with and without emission of neutrons. The total cross-section was obtained by multiplying the photoneutron cross-sections by the ratio  $\frac{N}{N_n}$ , where  $N$  is the total number of simulated events, and  $N_n$  is the number of events in which at least one neutron was emitted. A similar scheme was used to correct  $\gamma,Tn$  cross-sections (neutron yields). An example is given in Figure 10, where the experimental  $\gamma,n$  data by Veysi ere *et al.* [50] (as reported in Berman's Atlas) are presented together with the calculated total cross-section.

**Figure 10. Total photoabsorption cross-section of  $^{45}\text{Sc}$ , obtained by correcting experimental photoneutron cross-sections with PEANUT calculated factors**

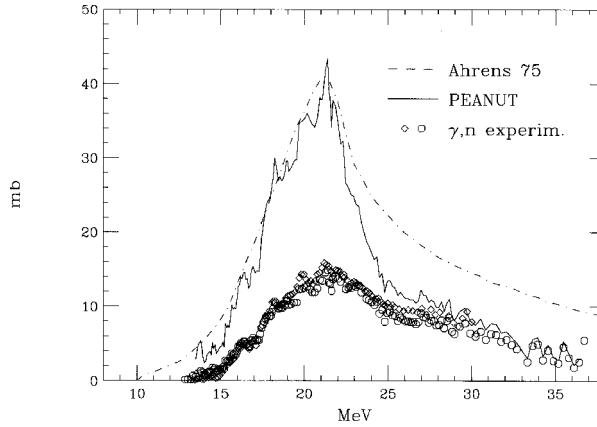
*symbols = experimental points, solid curve = evaluated total cross-section*



To give an idea of the accuracy which can be attained with this method, the total cross-section calculated with PEANUT from photoneutron data from Saclay and Livermore, reported by Dietrich and Berman [21], is compared in Figure 11 with that measured by Ahrens *et al.* [26].

**Figure 11. Total photoabsorption cross-section of  $^{27}\text{Al}$ , obtained by correcting experimental photoneutron cross-sections with PEANUT**

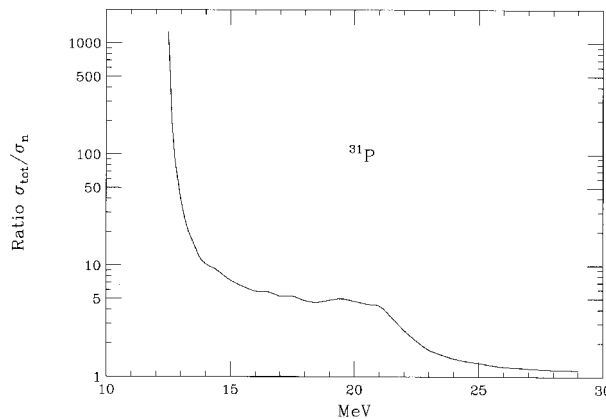
*symbols = experimental points, solid curve =  $\sigma_{tot}$  calculated by PEANUT, dashed curve = measured by Ahrens *et al.* [26]*



As can be seen, the agreement is not equally good over the whole energy range, but deviations of that order can be acceptable in those cases where no direct measurement is available. As already shown, discrepancies of the same order occur frequently among the oldest experimental data.

More comparisons of this kind will be made in the near future to identify possible systematic differences. It must also be stressed that this technique can be applied successfully only when the ratio  $\sigma(\gamma,tot)/\sigma(\gamma,n)$  is not too large. For neutron-poor nuclei such as  $^{54}\text{Fe}$  and  $^{58}\text{Ni}$ , and also close to neutron emission threshold in nuclei with low threshold for charged particle emission, that ratio can become very large and even small uncertainties can be amplified into unphysical cross-section values (see Figure 12).

**Figure 12. Ratio total/photoneutron cross-section calculated by PEANUT for  $^{31}\text{P}$**



## Available and missing nuclides

At present, the status of the FLUKA photonuclear cross-section database is the following:

Measured total cross-section:	$^3\text{H}$ , $^3\text{He}$ , $^7\text{Li}$ , $^{\text{nat}}\text{Li}$ , $^9\text{Be}$ , $^{12}\text{C}$ , $^{13}\text{C}$ , $^{14}\text{N}$ , $^{15}\text{N}$ , $^{16}\text{O}$ , $^{17}\text{O}$ , $^{18}\text{O}$ , $^{19}\text{F}$ , $^{23}\text{Na}$ , $^{24}\text{Mg}$ , $^{25}\text{Mg}$ , $^{26}\text{Mg}$ , $^{27}\text{Al}$ , $^{29}\text{Si}$ , $^{30}\text{Si}$ , $^{\text{nat}}\text{Si}$ , $^{32}\text{S}$ , $^{\text{nat}}\text{Ca}$
Published evaluation:	$^{34}\text{S}$
$\gamma, n + \gamma, p$ :	$^4\text{He}$
Sum of components:	$^{\text{nat}}\text{He}$ , $^{\text{nat}}\text{B}$ , $^{\text{nat}}\text{C}$ , $^{\text{nat}}\text{N}$ , $^{\text{nat}}\text{O}$ , $^{\text{nat}}\text{Mg}$
Difference:	$^6\text{Li}$ , $^{28}\text{Si}$ , $^{35}\text{Cl}$
Measured $\gamma, n$ renormalised by PEANUT:	$^{10}\text{B}$ , $^{11}\text{B}$ , $^{\text{nat}}\text{Cl}$ , $^{40}\text{Ar}$ , $^{\text{nat}}\text{K}$ , $^{42}\text{Ca}$ , $^{45}\text{Sc}$ , $^{48}\text{Ti}$ , $^{50}\text{Ti}$ , $^{51}\text{V}$ , $^{\text{nat}}\text{Cr}$ , $^{55}\text{Mn}$ , $^{\text{nat}}\text{Fe}$ , $^{59}\text{Co}$ , $^{60}\text{Ni}$ , $^{\text{nat}}\text{Cu}$ , $^{63}\text{Cu}$ , $^{65}\text{Cu}$
Theoretical $\gamma, n$ renormalised by PEANUT:	$^{37}\text{Cl}$
$\gamma, n$ available, but not renormalisable:	$^{\text{nat}}\text{Ne}$ , $^{31}\text{P}$ , $^{46}\text{Ti}$ , $^{58}\text{Ni}$ , $^{54}\text{Fe}$
Nothing available:	$^{20}\text{Ne}$ , $^{21}\text{Ne}$ , $^{22}\text{Ne}$ , $^{\text{nat}}\text{S}$ , $^{33}\text{S}$ , $^{36}\text{S}$ , $^{36}\text{Ar}$ , $^{38}\text{Ar}$ , $^{36}\text{K}$ , $^{38}\text{K}$ , $^{40}\text{K}$ , $^{43}\text{Ca}$ , $^{44}\text{Ca}$ , $^{46}\text{Ca}$ , $^{48}\text{Ca}$ , $^{\text{nat}}\text{Ti}$ , $^{50}\text{V}$ , $^{\text{nat}}\text{V}$ , $^{50}\text{Cr}$ , $^{52}\text{Cr}$ , $^{53}\text{Cr}$ , $^{54}\text{Cr}$ , $^{56}\text{Fe}$ , $^{57}\text{Fe}$ , $^{58}\text{Fe}$ , $^{\text{nat}}\text{Ni}$ , $^{61}\text{Ni}$ , $^{62}\text{Ni}$ , $^{64}\text{Ni}$

As can be seen, there are reasonable data for 47 nuclei, but there are still about 30 for which no data whatsoever has yet been found. Many of them are of relatively low importance in most practical shielding and dosimetry problems, and for others the data about natural composition are normally sufficient. A few however, like nickel and titanium, are important structural materials. The goal of this work was to set up a database as complete as possible, but it is feasible to envisage in a first stage a situation similar to that of neutrons, for which calculations are possible only if the material of interest is available in the cross-section library.

As an alternative, there is however some hope that a total cross-section excitation curve can be “guessed” even for those nuclides for which no data have been found. At any given photon energy, the total cross-section can be represented as a simple function of the quantity  $NZ/A$ , as shown in Figure 13.

The slope varies with energy, and between 22 and 30 MeV the function is not a simple power law but reaches a constant value at about  $NZ/A = 5$  (Figure 14).

There is more data scattering at the two ends of the 9-35 MeV energy range, but that affects only the tails of the excitation curve and should not be important for most applications.

**Figure 13. Total photoabsorption cross-section at 17 MeV vs. NZ/A**

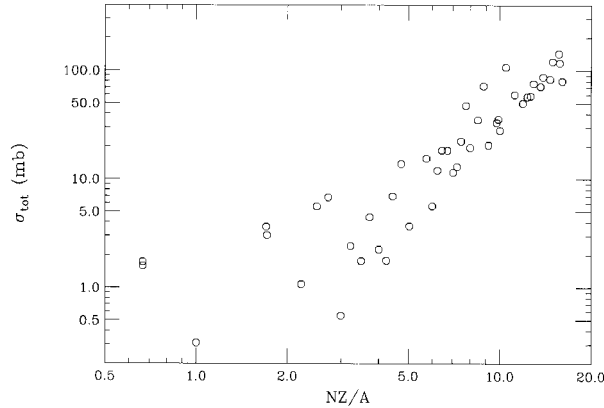
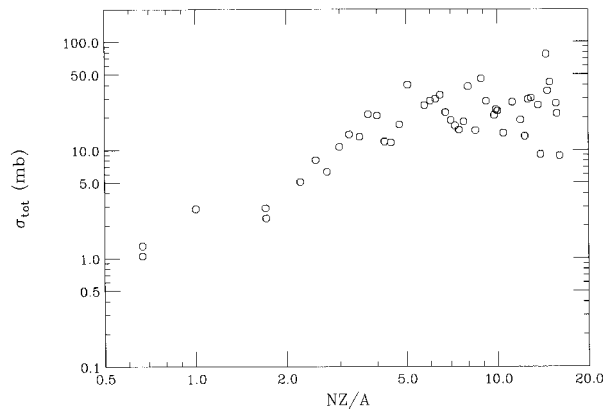


**Figure 14. Total photoabsorption cross-section at 25 MeV vs. NZ/A**

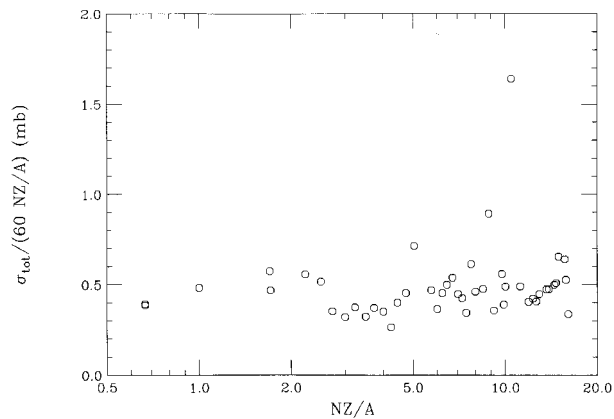


### Future work

The present status of the database allows it to be implemented immediately in FLUKA. However, it is still possible to add a few refinements. The shape of the excitation curves can be improved near threshold using detailed information about thresholds for each partial channel and about Coulomb barriers. The Thomas-Reiche-Kuhn (TRK) sum rule can be used to spot anomalies either in the experimental data or in the renormalisation; an example is shown in Figure 15, where an abnormally high value for  $^{42}\text{Ca}$  was identified. That cross-section, obtained by renormalising photoneutron data of [51] using PEANUT, will be further renormalised so as to bring down the integral of the excitation curve over the interval 0 to 35 MeV to a value equal to one-half of  $60 NZ/A$ . (The TRK rule predicts twice that value but only if the integral is calculated up to the photopion threshold.)

It would also be interesting to extend the comparison of data from different sources; for the time being this has been done only in a few cases in order to obtain as soon as possible the most complete library. In general, for example, preference has been given to measurements reported by Dietrich and Berman (when available) because a better consistency among data could be expected, but a good evaluation should take all the existing experiments into account.

**Figure 15. Integral  $f\sigma_{\text{tot}}(E)dE$  divided by 60 NZ/A, vs. NZ/A; the anomalous value at NA/A = 10.5 is that of  $^{42}\text{Ca}$**



The compilation work will continue also for heavier nuclei, but with less emphasis on total versus photonuclear cross-sections.

Finally, this attempt will hopefully encourage other groups and possibly some professional nuclear data evaluators to join our effort to create a photonuclear cross-section library in numerical form.

## REFERENCES

- [1] W.R. Nelson, T.M. Jenkins, "The SHIELD11 Computer Program", SLAC Radiation Physics Note RP-97-1 (1997).
- [2] A. Fassò, M. Pelliccioni, "Evaluation of Radiation Skyshine from the Main Rings of the DAΦNE Project", Frascati Internal Report LNF-92/111 (IR) (1992).
- [3] H. Nakashima *et al.*, "Accelerator Shielding Benchmark Experiment Analyses", Proc. SATIF-2, Geneva, 12-13 October 1995, OECD/NEA, Paris (1996), p. 115.
- [4] J.C. Liu, W.R. Nelson, K.R. Kase, X.S. Mao, *Rad. Prot. Dosim.*, 70, 49 (1997).
- [5] S. Agosteo, A. Foglio Para, F. Gerardi, M. Silari, A. Torresini, G. Tosi, *Phys. Med. Biol.*, 38, 1509 (1993).
- [6] C. Manfredotti, U. Nastasi, W. Ornato, A. Zanini, *Rad. Prot. Dosim.*, 44, 457 (1992).
- [7] X.S. Mao, K.R. Kase, J.C. Liu, W.R. Nelson, J.H. Kleck, S. Johansen, *Health Phys.*, 72, 524 (1997).

- [8] A. Fassò, S. Rokni, V. Vylet, “Radiation Studies for a High Energy Free Electron Laser”, Presented as SARE-3, KEK, 5-9 May (1997).
- [9] T.A. Gabriel *et al.*, “PICA, An Intranuclear Cascade Calculation for High Energy Photon-Induced Nuclear Reactions”, ORNL-4687 (1971).
- [10] P.K. Job, T.A. Gabriel, “The Photoneutron Yield Predictions by PICA and Comparison with the Measurements”, Proc. SATIF-2, Geneva, 12-13 October 1995, p. 93.
- [11] B.L. Berman, “Atlas of Photoneutron Cross-Sections Obtained with Monoenergetic Photons”, UCRL 78482 (1976).
- [12] V.S. Barashenkov *et al.*, *Nucl. Phys.*, A231, 462 (1974).
- [13] R.G. Alsmiller, Jr., H.S. Moran, *Nucl. Instr. Meth.*, 48, 109 (1967).
- [14] R.G. Alsmiller, Jr., H.S. Moran, *Nucl. Instr. Meth.*, 51, 339 (1967).
- [15] E.C. Hansen, C.S. Bartoletti, P.B. Daitch, *J. Appl. Phys.*, 46, 1109 (1975).
- [16] S. Morioka, H. Kadotani, “A Monte Carlo Simulation of Electron-Photon Cascades Including Photonuclear Processes”, presented at Int. Conf. on Nuclear Data for Science and Technology, Mito (Japan), 30 May-3 June 1988, Century Research Centre Corporation Rep. CRC-ET0188.4 (1988).
- [17] P. Degtyarenko, “Applications of the Photonuclear Fragmentation Model to Radiation Protection Problems”, Proc. SATIF-2, Geneva, 12-13 October 1995, p. 67.
- [18] F.X. Gallmeier, “Photoneutron Production in MCNP4A”, Proc. 1996 ANS Topical Meeting, No. Falmouth, Mass., 21-25 April 1996, p. 780.
- [19] A. Fassò, A. Ferrari, P.R. Sala, “Designing Electron Accelerator Shielding with FLUKA”, Proc. Eighth Int. Conf. on Radiation Shielding, Arlington (Texas) 24-28 April 1994, p. 643.
- [20] A. Fassò, A. Ferrari, J. Ranft, P.R. Sala, “FLUKA: Performances and Applications in the Intermediate Energy Range”, Proc. SATIF-1, Arlington (Texas), 28-29 April 1994, p. 287.
- [21] S.D. Dietrich, B.L. Berman, *At. Data Nucl.*, Data Tables 38, 199 (1988).
- [22] W.C. Barber, W.D. George, *Phys. Rev.*, 116, 1551 (1959).
- [23] J. Dular *et al.*, *Nucl. Phys.*, 14, 131 (1959).
- [24] D.W. Anderson *et al.*, *Nucl. Phys.*, A156, 74 (1970).
- [25] U.R. Arizibekov *et al.*, *Sov. J. Nucl. Phys.*, 44, 727 (1986).
- [26] J. Ahrens *et al.*, *Nucl. Phys.*, A251, 479 (1975).
- [27] J. Ahrens *et al.*, “Total Absorption Cross-Sections, Particularly Above 30 MeV”, Proc. Int. Conf. on Photonuclear Reactions and Applications, Asilomar (California), Vol. 1, 1974, p. 23.

- [28] N. Bezić *et al.*, *Nucl. Phys.*, A117, 124 (1968).
- [29] N. Bezić *et al.*, *Nucl. Phys.*, A128, 426 (1969).
- [30] K.G. McNeill *et al.*, *Phys. Rev.*, C47, 1108 (1989).
- [31] J.H. Gibbons *et al.*, *Phys. Rev.*, 114, 1919 (1959).
- [32] W. John and J.M. Prosser, *Phys. Rev.*, 127, 231 (1962).
- [33] B.L. Berman *et al.*, *Phys. Rev.*, 163, 958 (1967).
- [34] R.J. Hughes *et al.*, *Nucl. Phys.*, A238, 189 (1975).
- [35] K.M. Irgashev *et al.*, *Nucl. Phys.*, A483, 109 (1988).
- [36] B.S. Ishkanov *et al.*, *Sov. J. Nucl. Phys.*, 33, 303 (1981).
- [37] B.S. Ishkanov *et al.*, *Phys. At. Nucl.*, 60, 319 (1997).
- [38] Y.I. Assafiri, M.N. Thompson, *Nucl. Phys.*, A460, 455 (1986).
- [39] D. Ehhalt *et al.*, *Z. Phys.*, 197, 210 (1965).
- [40] E.G. Fuller, *Phys. Rep.*, 127, 185 (1985).
- [41] Yu.M. Arkatov *et al.*, *Sov. J. Nucl. Phys.*, 19, 598 (1974).
- [42] H.G. Clerc *et al.*, *Phys. Lett.*, 18, 316 (1965).
- [43] R. Mundhenke *et al.*, *Z. Phys.*, 216, 232 (1968).
- [44] A.N. Gorbunov, M. Spiridonov, *Sov. Phys.*, JETP 6, 16 (1958).
- [45] B. Bülow, B. Forkman, “Photonuclear Cross-Sections”, LUNP 7208 (1972).
- [46] E.G. Fuller, H. Gerstenberg, “Photonuclear Data – Abstract Sheets, 1955-1982”, NBSIR 83-2742.
- [47] A.I. Blokhin, S.M. Nasyrova, “Plots of the Experimental and Evaluated Photoneutron Cross-Sections”, IAEA INDC(CCP)-337 (1991).
- [48] V.A. Varlamov, M.E. Stepanov, V.V. Sapuneko, “Photonuclear Data Index 1986-1990”, IAEA INDC(CCP)-348 (1992).
- [49] T. Asami, T. Nakagawa, “Bibliographic Index to Photonuclear Reaction Data (1955-1992)”, JAERI-M 93-195 (1993).
- [50] A. Veysière *et al.*, *Nucl. Phys.*, A227, 513 (1974).
- [51] Y.I. Assafiri *et al.*, *Nucl. Phys.*, A357, 429 (1981).

# **SESSION II**

## **Source Term and Related Data – Proton and Ion Accelerator**

*Chairs: L.A. Charlton and K. Shin*



***Thin Target Yield  
Measurements and Compilation***



**SUMMARY OF COMPILED EXPERIMENTAL DATA FROM INTERMEDIATE  
ENERGY NEUTRON AND PROTON INTERACTIONS WITH DIFFERENT NUCLIDES  
(EXFOR DATABASE)**

**Pierre Nagel and Pedro Vaz**

OECD/NEA Data Bank

12 Boulevard des Iles, 92130 Issy-les-Moulineaux, France

**Abstract**

Shielding of modern high-intensity accelerators in the intermediate energy range requires double differential cross-sections for neutrons, pions, light and heavy ions for energies between 20 MeV and 5 GeV. The need to develop efforts to compile, in a computer readable form, basic atomic and nuclear data in this energy range, emerged at the Second Specialists Meeting on Shielding Aspects of Accelerators, Targets and Irradiation Facilities (SATIF-2) held at CERN<sup>1</sup> – Geneva (Switzerland) on 12-13 October 1995. At the same time, participants recognised that the existing data are scarce and is mostly scattered among internal reports and journal articles. The availability of these data should also contribute to improve the modelling and the accuracy of computer codes making predictions in the intermediate energy range.

The EXFOR (Exchange Format) database is a comprehensive compilation of world-wide experimental neutron reaction data, including, besides the numerical data, bibliographic information as well as information on the measurement methods and data uncertainty analysis. Up to 1996, EXFOR data included a complete compilation of experimental neutron induced reaction data, a selected compilation of charged particle induced reaction data and a selected compilation of photon induced reaction data. From 1997 onwards, a selected compilation of intermediate energy data (neutron, proton, low mass nuclides) has been included into the EXFOR database. This work has been conducted in the framework of the NEA Nuclear Science Committee (NSC) projects and activities, namely on Intermediate Energy Nuclear Data and on Partitioning and Transmutation of Nuclear Waste. In this paper these activities are briefly reviewed and a simplified graphic description is performed of the (non-elastic and elastic) proton and neutron cross-section data sets in the intermediate energy range, which have been included into the EXFOR database. Information on available data files can be found at the NEA web site at <http://www.nea.fr/html/dbdata/dbexfor.html>.

---

<sup>1</sup> CERN is the European Laboratory for Particle Physics in Geneva (Switzerland)



***Thick Target Yield  
Measurements and Compilation***



## THICK TARGET YIELD MEASUREMENTS IN TIARA, KEK AND HIMAC

**K. Shin, S. Ono**

Department of Nuclear Engineering  
Kyoto University

**K. Ishibashi**

Department of Nuclear Engineering  
Kyusyu University

**S. Meigo, H. Takada, N. Sasa, H. Nakashima, S. Tanaka**

Japan Atomic Energy Research Institute

**N. Nakao**

High Energy Accelerator  
Research Organisation, KEK

**T. Kurosawa, T. Nakamura**

Cyclotron Radiation Isotope Centre  
Tohoku University

**Y. Uwamino**

The Institute for Physical  
and Chemical Research

### Abstract

Measurements of double differential thick target neutron yields performed in Japan with different ions, energies and targets are reviewed. At the synchrotron at KEK, 0.5 and 1.5 GeV protons were injected into a 20 cm thick lead target, and emitted neutrons were measured by a multi-detector system at 5 angles. The data were compared with NMTC/JAERI and the in-medium nucleon-nucleon cross-section improved the discrepancy between the measured and calculated data. The lower energy proton (68 MeV), alpha particle (100 MeV), C(220 MeV), Ar(460 MeV) ions were used at TIARA facility of JAERI, Takasaki, where neutron and gamma-ray yields were measured for C, Fe, Zr and Au targets at 7 angles. The measured data for proton were used to benchmark the NMTC-ISOBAR and NMTC-3STEP codes to show better agreement with the former model. The QMD+SDM model was applied to analyse the data of all ions and some discrepancies were pointed out. At HIMAC the measurements of double differential neutron yields were made by higher energy ions: alpha particles, C and Ne ions of 100, 180 and 400 MeV/u injected to C, Al, Cu, Pb thick targets. The data were obtained at 6 angles.

## Measurements of spallation neutrons from a thick lead target bombarded with 0.5 and 1.5 GeV protons at KEK [1]

### *Experimental procedure*

The experiment was carried out at the  $\pi$  2 beam line of the National Laboratory for High Energy Physics (KEK) in a series of double differential neutron production cross-section measurements [2]. An illustration of the experimental arrangement is shown in Figure 1. The incident proton was supplied as the secondary particle generated by an internal target which was placed in the accelerator ring of the 12 GeV proton synchrotron. The intensity of the incident particle was so weak ( $<10^5$  particles/pulse) that incident protons were counted one by one with beam scintillators. The size of the incident beam was 2.0 cm in the perpendicular plane and 1.6 cm in the horizontal one in FWHM, respectively. The protons were identified from pions produced at the internal target by the TOF method with a pair scintillators (Pilot U) which were located at a separation distance of 20 m.

The lead target was a rectangular parallelepiped  $15 \times 15 \times 20$  cm<sup>3</sup>. It was thick enough to stop 0.5 GeV protons completely, while it caused the energy loss of 0.26 GeV on average for 1.5 GeV protons. The proton beam was dumped in a carbon block pile with an area of  $0.5 \times 0.5$  m<sup>2</sup> and a thickness of 1 m which was surrounded by sufficiently thick iron blocks. The dump was located 8.5 m down from the lead target.

NE213 scintillators having a size of 12.7 cm in diameter and 12.7 cm in thickness were used as neutron detectors. They were placed at 30°, 60°, 90°, 120° and 150° angles with respect to the beam axis and at a common distance of 1 m from the target. At the 15° angle, the distance was 1.5 m so that better energy resolution was achieved. In order to isolate reactions induced by the charged particles produced in the lead target, NE102A scintillators of  $17 \times 17 \times 1$  cm<sup>3</sup> were used as veto counters.

In the analysis of the measured data, the distance between the centres of the target and the detector was used as a flight path length. This caused a standard deviation of the distance less than 6%, as estimated by a Monte Carlo calculation. The detection efficiencies were calculated by the SCINFUL code [3] below 80 MeV. Above this energy, the calculated efficiency by the CECIL code [4] was adjusted such that it was smoothly connected to the SCINFUL result at 80 MeV.

Since the target was thicker than the mean free path for the neutrons with the energy below 200 MeV, most neutrons reacted with the target more than once before they left the target. The scattered neutrons may cause delay in the flight time. The unfolding analysis was employed by the FORIST code [5] with a response matrix calculated by SCINFUL. The neutron spectrum below 3 MeV was determined by the unfolding technique. The lower limit of the measured energy range was 1.6 MeV.

### *Calculation*

The calculation was carried out with codes NMTC/JAERI [6] and MCNP-4A [7]. NMTC/JAERI calculated the nuclear reactions and particle transport above 20 MeV. MCNP-4A calculated the neutron transport below 15 MeV using a cross-section library FSXLIB-J3R2 processed from the nuclear data file JENDL-3.2 [8]. Additional calculations were also performed by substituting the in-medium nucleon-nucleon cross-section parameterised similarly to those by Cugnon [9].

## ***Results of KEK Experiment***

The experimental spectra are shown in Figures 2 and 3 in comparison with calculations. It can be observed that the results calculated with free space nucleon-nucleon cross-sections are in good agreement with the experimental ones in the lower energy range below 20 MeV at all angles for both incident energies. The calculated results are about 50% or more lower than the experimental data between 20 and 80 MeV. On the other hand, the results calculated with the in-medium cross-sections show much better agreement with the experimental ones in this energy range and also overall measured spectra in the angular range smaller than 60 for both incident energies. The underestimation for the backward neutron emission still remained, because the pre-equilibrium process or the refraction and reflection process was not included yet in this analysis.

## **Measurements of thick target neutron yields for lower energy ions at TIARA**

### ***Experimental method***

The experiment was performed at the AVF cyclotron TIARA of JAERI, Takasaki. Accelerated ion beams of 68 MeV protons, 100 MeV alphas, 220 MeV.

$^{12}\text{C}^{5+}$  and 460 MeV  $^{40}\text{Ar}^{13+}$  from the cyclotron, which were chopped to pulses, hit the thick targets. The experimental arrangement is shown in Figure 4. Combinations of the incident ions and targets for which measurements were made are shown in Table 1. The targets were 3 cm in diameter and their thickness was varied depending on the incident ion; typical thickness adopted for heavy ions was 3.2, 1.3, 1.8 and 2.0 mm for C, Fe, Zr and Au targets, respectively. They are thicker than the ion range. The contribution of the background neutrons caused by the room scattering was measured at every angle using an iron shadow block of  $20 \times 20 \times 80 \text{ cm}^3$ .

The secondary neutrons emitted at angles of  $0^\circ$ ,  $15^\circ$ ,  $30^\circ$ ,  $45^\circ$ ,  $60^\circ$ ,  $90^\circ$  and  $120^\circ$  to the beam direction were measured by the TOF method, using a 12.7 cm in diameter by 12.7 cm in thickness BC501A scintillator. The flight path length was 5 m at the forward angles ( $45^\circ$ ) and 2.5 m at the other angles. The time resolution determined from the gamma-ray flush peak was 2-3 ns, which was mostly determined by the beam pulse width. The detector efficiency for neutrons was estimated by the SCINFUL code with modified deuteron light output [10] and the angular distribution of H(n,n) reaction cross-section [11].

The secondary gamma rays were measured simultaneously with the neutrons by the same detector, using a pulse shape discriminator which had a wide dynamic range over 500:1. The pulse height was calibrated by standard gamma ray sources and an Am-Be source. The obtained pulse height spectra were unfolded to gamma-ray energy fluences by the FERDO-U code [12] with response functions calculated by the EGS4 code [13].

The number of particles incident on the target was measured by the current integrator connected to the target, which was surrounded by a -500 V suppressor grid to repel secondary electrons emitted from the target. Three additional neutron monitors were located in the counting room to check the fluctuation in the beam current. It was found the relative error in the current monitor was within 2%.

## ***Calculation method***

Calculations of the inclusive differential neutron production cross-sections were made by the QMD code [14] and the statistical decay model (SDM) calculation by Weisskopf-Ewing model. The connection between the two models was made at 100 fm/c. In the calculation the maximum impact parameter was defined as  $1.4(A_t^{1/3} + A_p^{1/3})(\text{fm})$  by the mass numbers of incident and the target nuclei. Since the experiments were carried out with the thick target, calculations of the differential neutron production cross-sections were made at several energy points, decreasing the ion energy from the incident beam one. The data were integrated with the ion range to obtain thick target yields, where the interpolation and extrapolation of the data were made. The attenuation of incident ions in the targets were corrected for p and alphas because of relatively longer range for these ions than others.

For protons, calculations by the revised NMTC/JAERI [14] were also used. The modification in the intra-nuclear cascade calculation with pre-equilibrium process (NMTC-3STEP), or inclusion of nuclear medium effects in terms of the reflection and refraction with the in-medium nucleon-nucleon cross-sections (NMTC-ISOBAR).

## ***Results of TIARA Experiment***

An example of the neutron spectra of the 68 MeV proton incidence are showed in Figure 5 for the Au target. The NMTC-3STEP tends to give overestimation of the neutron spectrum at the forward angles, but good agreements at the backward angles. A similar trend is seen for other targets. The NMTC-ISOBAR gave satisfactory agreement with the experiment at all angles.

The QMD+SDM calculation gave an underestimation to measured neutron spectra for the 100 MeV alpha incidence, especially at forward angles. This underestimation is improved for the Au target. The comparison of the QMD calculation with present experimental data is demonstrated in Figures 6 and 7 for the 220 MeV C and 460 MeV Ar ions incident on the C target, respectively. The overestimation of the yields by the QMD+SDM calculation is seen for 220 MeV C on the C target at all angles. When the target becomes heavier, the agreement becomes better at forward angles as shown in Figure 8, while the neutron fluences at large angles are still overestimated. Also for 460 MeV Ar cases as shown in Figure 6 as an example, a similar trend is seen for the QMD+SDM calculation, but in a slightly larger magnitude than for the C ion cases. One reason for these discrepancies may be in the initial state of nuclei, which was automatically set by the QMD code, having some sort of excited energies.

An example of the gamma-ray spectra is shown in Figure 9 for the 68 MeV protons incidence on the C target. The gamma-ray angular distribution in the figure is isotropic. The strong discrete gamma rays from the first and second excited levels of C are clearly seen. The same thing is pointed out for gamma rays of 100 MeV alpha particles on the C target. These discrete gamma rays become obscure when the incident beam becomes heavier, as illustrated in Figure 10 for Ar ions on the C target, where the spectrum is completely changed to continuous one. Considering the possibility of the gain shift, the gamma-ray yields are almost isotropic.

## Measurements of secondary neutrons at HIMAC

### *Experimental procedure*

The measurements of secondary neutrons from high energy heavy ions are being made at the HIMAC accelerator at the National Institute of Radiological Science. The combination of incident ions and targets are listed in Table 2. The target was a 10 cm by 10 cm square shape; the thickness stopped the incident ions completely.

The experimental set-up is shown in Figure 11. The NE213 scintillator of 12.7 cm diameter by 12.7 cm thickness are used as E counters and NE102A plastic scintillators (12.7 cm by 12.7 cm and 0.5 cm thickness) for  $\Delta E$  counters. A thin NE102A plastic scintillator (3 cm diameter by 0.05 cm thickness) is set near the end of the beamline. The output pulses of this counter are used as the start signals of the TOF measurement and also to count the absolute number of the beam particle incident on the target. For discriminating between neutrons and charged particles, the output pulses of the  $\Delta E$  counter placed in front of the E counter is used.

The contribution of the background neutrons caused by the room scattering is measured at  $90^\circ$  with a rectangular iron shadow block of  $15 \times 15 \times 60 \text{ cm}^3$  located between the target and the detector. The detector efficiency is estimated by the Cecil code.

### *Results of HIMAC experiment*

Typical results of double differential neutron yields are shown in Figures 12 and 13 for the 180 MeV/u C ions hitting the C and Pb targets. These spectra are smaller than calculated ones by the HIC code [15] except for at  $90^\circ$ . It was known that the HIC gave higher estimated values at forward angles from the comparison with Cecil's measurements [16] with 337 MeV/u Ne ions. However, it may be also pointed out that the data obtained at HIMAC have softer spectra as compared to Cecil's thick target measurements by 710 MeV alpha particles [17]. The experiment is still going on and new data will become available in the near future.

## Conclusions

Three experiments on thick target neutron yields made by different groups in Japan are reviewed here. The lead experiment at KEK with the 0.5 and 1.5 GeV proton shows the NMTC with in-medium cross-section gives acceptable estimation of the neutron spectra. Similar experiments for different materials are going on in France under international co-operation arrangements.

The TIARA experiments led to modifications of the NMTC to ISOBAR model resulting in very good agreement with the measured data. The QMD+SDM gave discrepancies from the measured data in a different manner, depending on the incident ion and the target. A revised version of the QMD has recently been developed and the measured data will be used for benchmarking the new code.

The reported data of the HIMAC experiment are not the final ones. Since the experiment is still ongoing, we can expect new data in the near future. The thick target yields in several tens of MeV per nucleon energy region are desired to fill the gap between the TIARA experiment and the HIMAC experiment.

## REFERENCES

- [1] Meigo *et al.*, “Measurements of Spallation Neutrons from a Thick Lead Target Bombarded with 0.5 and 1.5 GeV Protons”, Proceedings ICANS-XII, 11-14 October 1995, PSI, Switzerland, pp. 442-453.
- [2] Ishibashi *et al.*, “Measurement of Neutron-Production Double-Differential Cross-Sections for Incident Protons of 0.8, 1.5 and 3 GeV”, Proc. Int. Conf. Nucl. Data for Sci. and Technol., Gatlinburg (1994).
- [3] K. Dickens, “SCINFUL: A Monte Carlo Based Computer Program to Determine a Scintillator Full Energy Response to Neutron Detector for En between 0.1 and 80 MeV”, ORNL-6436 (1988).
- [4] A. Cecil *et al.*, *Nucl. Instr. Methods*, 161, 439 (1979).
- [5] H. Johnson and B.W. Wehring, “The FORIST Unfolding Code”, ORNL/RSIC-40 (1976).
- [6] Nakahara and T. Tsutsui, “A Code System for High Energy Nuclear Reactions and Nucleon-Nucleon Transport Code,” JAERI-M82-198 (1982).
- [7] F. Briesmeister, *ed.*, “MCNP: A General Monte Carlo N-Particle Transport Code Version 4A”, LA-12625 (1993).
- [8] Shibata *et al.*, Japanese Evaluated Nuclear Data Library, Version-3-JENDL-3, JAERI-1317 (1990).
- [9] Cugnon *et al.*, *Nucl. Phys.*, A352, 505 (1981).
- [10] Meigo, private communication.
- [11] A. Arndt *et al.*, *Phys. Rev.*, D35, 128 (1987).
- [12] Shin *et al.*, *Nucl. Technol.*, 53, 78 (1981).
- [13] R. Nelson *et al.*, SLAC-265 (1985).
- [14] Takada, *J. Nucl. Sci. Technol.*, 33, 275 (1996).
- [15] A. Cecil *et al.*, *Phys. Rev.*, C24, 2013 (1981).
- [16] A. Cecil *et al.*, *Phys. Rev.*, C21, 2471 (1980).

**Table 1. Combinations of used ion and target in TIARA experiment**

Incident Ion	Energy (MeV)	Targets
p	68	Be, C, Al, Cu, Nb, Au, Pb
He	100	C, Zr, Au
C	220	C, Fe, Zr
Ar	460	C, Fe, Zr

**Table 2. Combinations of used ion and target in HIMAC experiment**

Incident Ion	Energy (MeV/u)	Targets
He	100, 180, 400	C, Al, Cu, Pb
C	100, 180, 400	C, Al, Cu, Pb
Ne	100, 180, 400	C, Al, Cu, Pb

**Figure 1. Experimental arrangement of thick target yields at KEK**

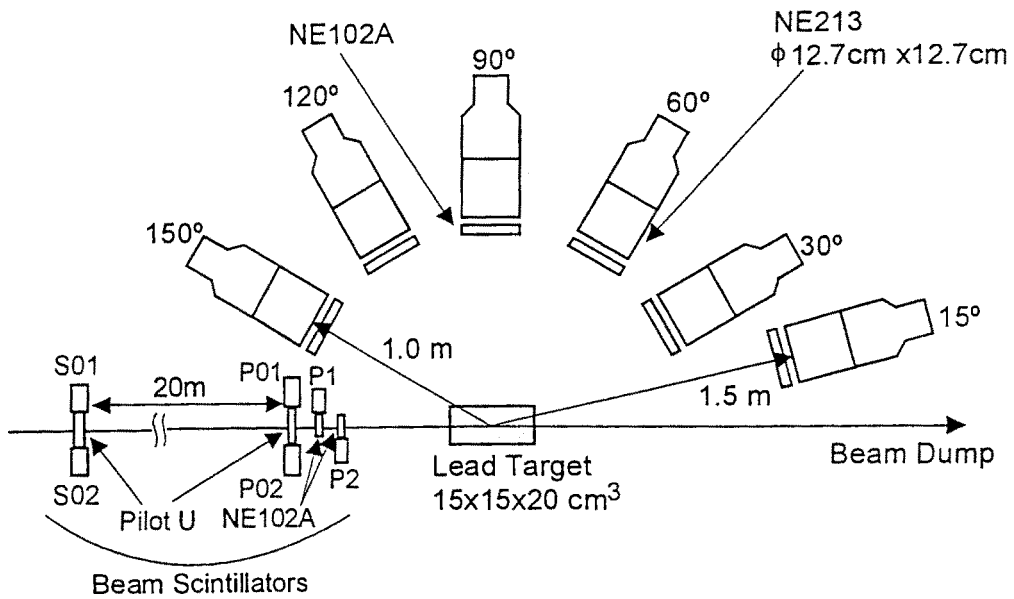


**Figure 2. Differential neutron yields from Pb target bombarded by 0.5 GeV protons**

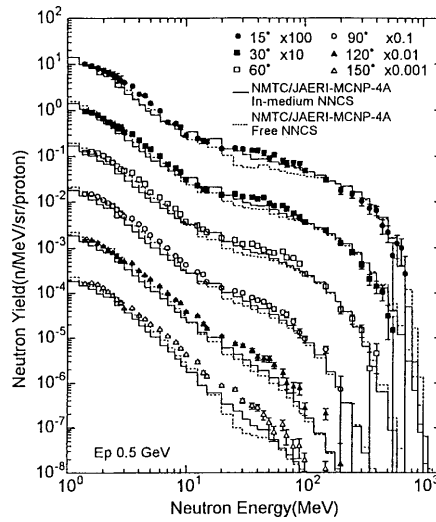


**Figure 3. Differential neutron yields from Pb target bombarded by 1.5 GeV protons**

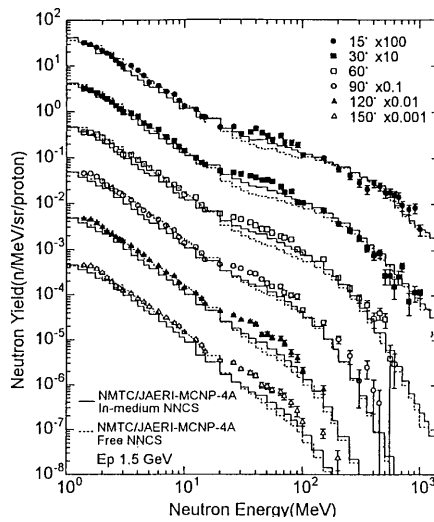


**Figure 4. Experimental arrangement at TIARA AVF cyclotron**

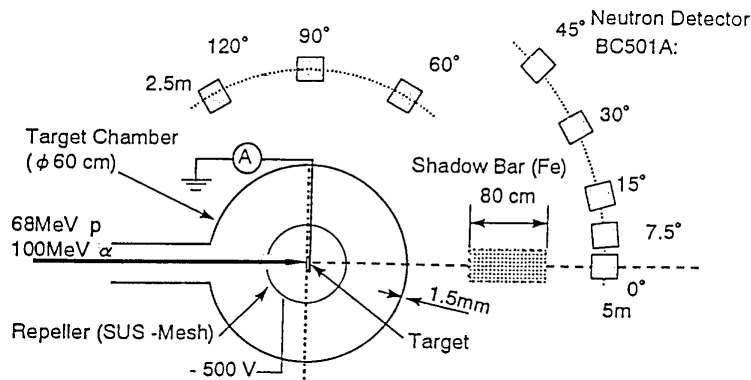


**Figure 5. Neutron spectra from Au target bombarded by 68 MeV protons**

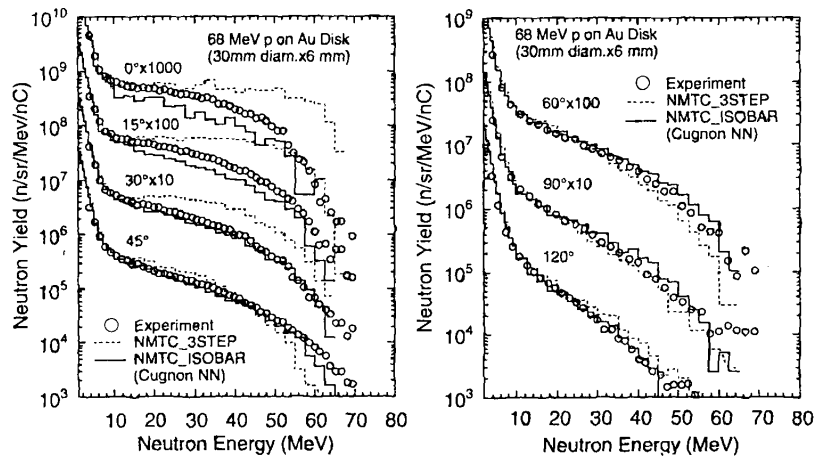


**Figure 6. Neutron spectra from C target bombarded by 220 MeV C ions**

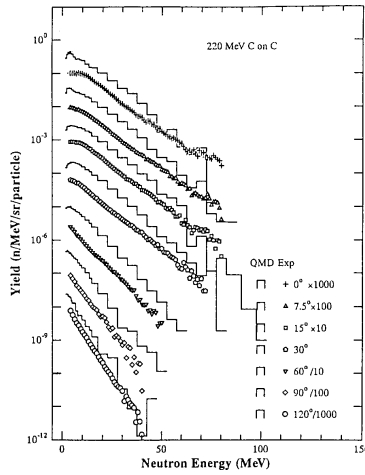


**Figure 7. Neutron spectra from C target bombarded by 460 MeV Ar ions**

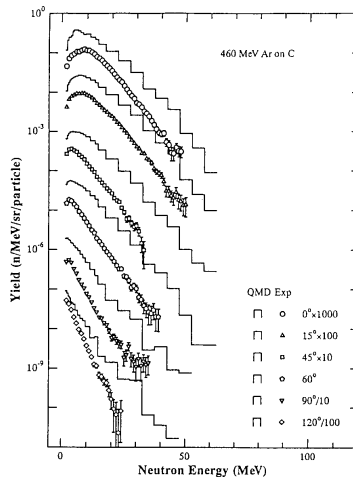


Figure 8. Neutron spectra from Zr target bombarded by 220 MeV C ions

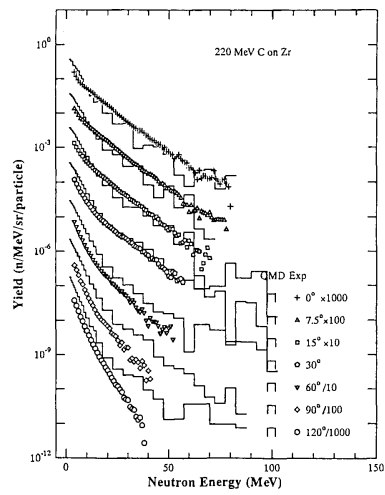


Figure 9. Gamma ray spectra from C target of the 68 MeV proton incidence

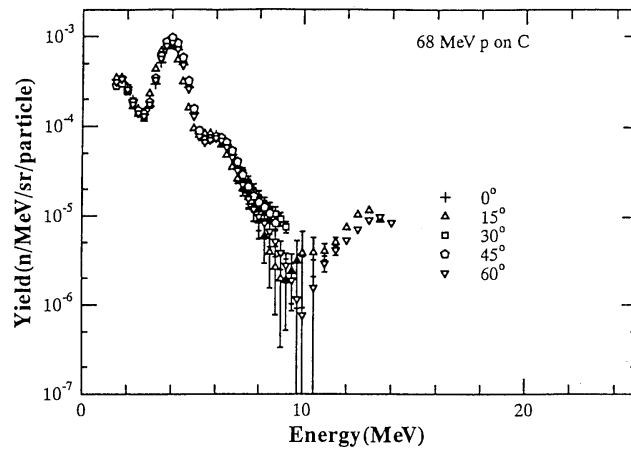
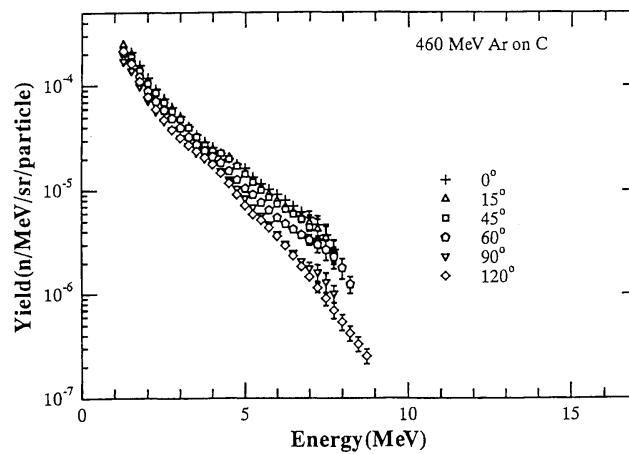
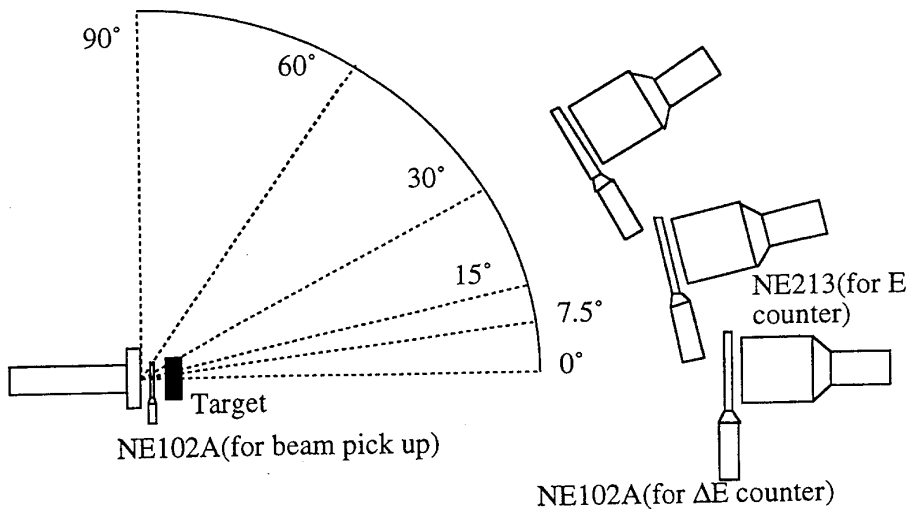


Figure 10. Gamma ray spectra from C target of the 460 MeV Ar incidence



**Figure 11. Experimental set-up of measurements at HIMAC**



**Figure 12. Differential neutron yields for 180 MeV/u C ion on C target**  
*Calculation was made by HIC*

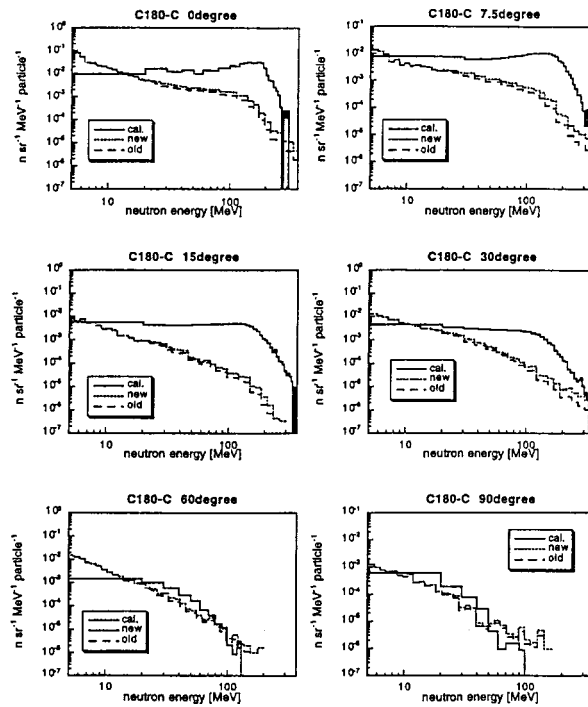
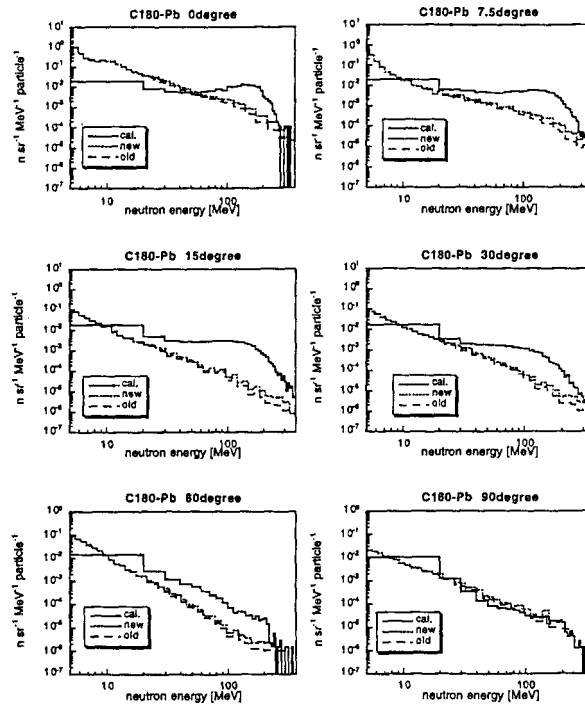


**Figure 13. Differential neutron yields for 180 MeV/u C ion on Pb target**  
*Calculation was made by HIC*



# *Spallation Neutron Source Facility*



**RADIATION PHYSICS OF HIGH POWER SPALLATION TARGETS:  
STATE OF THE ART SIMULATION METHODS AND EXPERIMENTS,  
THE “EUROPEAN SPALLATION SOURCE” (ESS)**

**D. Filges, P. Cloth, R.-D. Neef, H. Schaal**

Forschungszentrum Jülich GmbH

Institut für Kernphysik

D-52425 Jülich, Germany

**Abstract**

Particle transport and nuclear interactions of planned high power spallation targets with GeV proton beams can be simulated using widely developed Monte Carlo transport methods. This includes available high energy radiation transport codes and systems for low energy, earlier developed for reactor physics and fusion technology. Monte Carlo simulation codes and applied methods are discussed. The capabilities of the world-wide existing state-of-the-art computer code systems are demonstrated. Results of computational studies for the “European Spallation Source” (ESS) mercury high power target station are given. The needs for spallation related data and planned experiments are shown.

## Introduction

Today's advanced accelerator technology opens new interesting applications as spallation neutron sources, accelerator transmutation of nuclear waste (ATW), accelerator production of tritium (APT), and electronuclear breeding and energy amplifying (ADTT). During the last decade several spallation neutron sources [8] started operation. The experience of these facilities encouraged the scientific community to start new projects to develop next generation neutron sources to increase the usable neutron fluxes by at least one order of magnitude. It seems possible for the "European Spallation Neutron Source" [1] (ESS) project based on a proton accelerator of 5 MW beam power to reach a maximum pulsed peak thermal neutron flux of about  $2 \cdot 10^{17} \text{ n} \cdot \text{cm}^{-2} \cdot \text{s}^{-1}$ .

The other next generation spallation neutron source projects are based on 1 MW proton beam power and are studied in: ANL [2], BNL [3], KEK [4], LANL [5], ORNL [6,54], and PSI [7]. The first 1 MW neutron spallation source – SINQ [7] – started operation in December 1996. All target systems for ADTT, APT and spallation neutron sources involve the same physical processes and similar technical problems.

As the planned use in each of the above cases requires high intensity particle beams which cause sophisticated demands on material and geometry choices, one has to optimise the systems very carefully. Therefore detailed particle production and transport models and computer code systems have been developed. These models and codes were extensively tested, used, and validated in connection with the existing pulsed and continuous neutron spallation sources for condensed matter studies and with detector and hadron calorimeter development at meson factories and high energy accelerators.

## Requirements of calculation methods

To develop high power spallation targets the calculational methods have to be applied to demonstrate feasibility, to optimise the design configuration and to support the engineering layout. The requirements of the calculational methods in spallation technology are the predictions for the following interesting questions, which have to be answered for all high current accelerators and their target stations:

- neutron, gamma and charged particle production and fluxes;
- energy deposition and heating;
- radioactivity and after heat;
- materials damage by radiation;
- high energy source shielding.

Particle fluxes and power density optimisation is mainly influenced by the possibilities of cooling target, windows and containment. Temperature gradients have to be kept in certain limits to avoid failure by stress. Radiation damage is produced by different mechanisms as displacements per atom (dpa), gas production, and nuclide transmutation, which worsen the mechanical properties and limit the lifetime of the target and structure materials. Activation leads to global hazard rating of the target station. Cooling circuits with their radiolysis and corrosion problems of light and heavy

water have to be studied, especially, because radioactivity is transported through pumps, valves and heat exchangers outside the target containment with its activity barriers. Shielding of spallation facilities is different compared to nuclear reactor systems and fusion devices; due to the high energy neutron component this influences the safety and environment. Finally the uncertainties of the simulations should be assessed based on comparisons of the results of calculations with benchmark experiments and with existing spallation facilities. The development, construction, and operating experience is published in great detail in the ICANS I-XIII-proceedings [8] over the last twenty years.

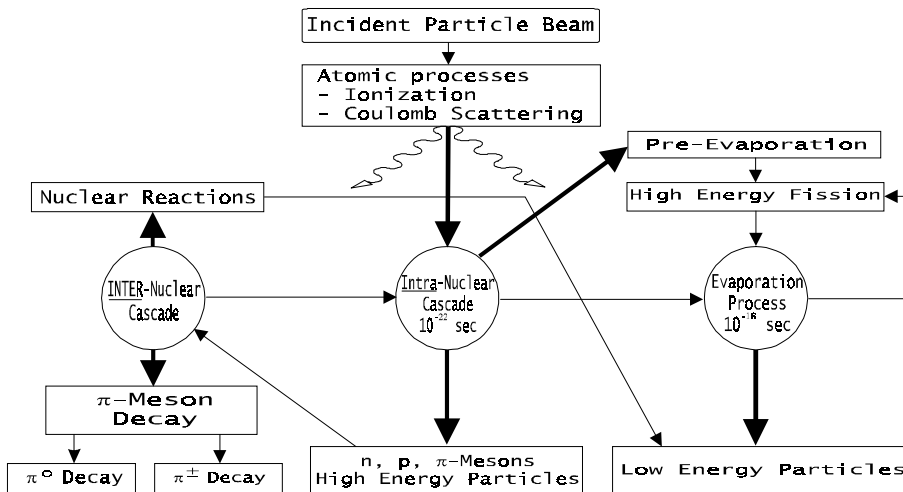
The above listed problems call for general calculational methods in terms of output, materials, geometry, beam parameters, etc. This leads to large Monte Carlo particle transport computer code systems.

### Models and computational methods

The characteristics of the main problem in thick target particle transport is the creation of particle showers of very different particle types like n, p,  $\pi^\pm$ ,  $\pi^0$ ,  $e^\pm$ ,  $\mu^\pm$ ,  $\gamma$ 's, etc. of high multiplicity in a large energy range from several GeV down to thermal and even subthermal energies of the neutrons. The state-of-the-art simulation codes are able to transport different particle types through complex three-dimensional geometries of realistic material composition.

There are basically four categories of particle interactions which must be taken into account when high energy beams bombard thick targets: atomic processes, high energy non-elastic and elastic collisions, pion and muon decay, and the effects of low energy ( $\leq 20$  MeV) neutron interactions. For the proton beam energy range of spallation source applications, the secondary particles produced in a single so called spallation collision proceed to undergo subsequent collisions, generating a multiplicity of particles inside the target material. This process is generally referred to as a "hadronic cascade", since it is the hadrons – neutrons, protons, and charged pions – which are effective in the "radiation transport" through the target system. The scheme of performance of the phenomenology involved is given in Figure 1 and has been studied previously in a number of different applications [8].

**Figure 1. Logical scheme of the interaction mechanisms produced by high energy proton bombardment of thick targets**



### *Physics models and codes for thick target simulations*

There are different methods in generating non-elastic events in hadron-nucleus collisions. The most popular generators are: 1) sampling from single particle inclusive cross-sections, mainly used above several GeV; 2) sampling from phase space, mainly used for sampling of well defined exclusive channels; 3) sampling from exclusive cross-sections, using elastic and non-elastic nucleon-nucleon and pion-nucleon cross-sections to find types and sites of the collisions inside the nucleus. Double differential cross-sections are used to find the final states of collision. As an example the Bertini INC model [9] may be mentioned in combination with evaporation and high energy fission.

There are essentially several hadronic transport computer codes with multipurpose use for thick target systems. Table 1 gives a list of the existing codes.

**Table 1. Multipurpose transport codes for hadronic shower simulations**

<b>Code name</b>	<b>Model</b>	<b>Further code development at</b>
HETC [10] { LAHET [11] NMTC [12]	Intranuclear cascade	ORNL LANL JAERI FZ-Jülich
DUBNA [13]	Intranuclear cascade	Dubna
FLUKA [14]	Dual Parton (high energy) Intranuclear cascade	CERN
ISABEL [15]	(In addition nucleus-nucleus interaction)	Weizmann/LANL

The codes for hadronic shower simulations (see Table 1) as discussed above are not applicable to low-energy ( $\leq 20$  MeV) nuclear collisions. Charged particles produced  $\leq 20$  MeV in spallation collisions have short ranges and predominately come to rest before having further nuclear collisions, so usually only the low-energy neutrons and photons produced need to be further transported. The inapplicability of the hadronic shower models to low-energy neutron and photon collisions is not a problem because there are large databases of experimental nuclear cross-sections available for low-energy neutrons and photons for a wide range of target nuclei. This results from extensive fission reactor and fusion research, so it is not necessary to resort to a theoretical collision model at lower energies. Furthermore, for low-energy neutrons and photons, numerous transport computer codes have been developed (see Table 2).

**Table 2. Low energy neutron-gamma transport codes**

<b>Code name</b>	<b>Model</b>	<b>Reference</b>
MORSE	3-D Monte Carlo	Ref. 16
MCNP	3-D Monte Carlo	Ref. 17
ANISN/ONETRAN	1-D $S_N$ -deterministic	Refs. 18, 19
DOT/TWOTRAN	2-D $S_N$ -deterministic	Refs. 20, 21
TRIDENT	3-D $S_N$ -deterministic	Ref. 21

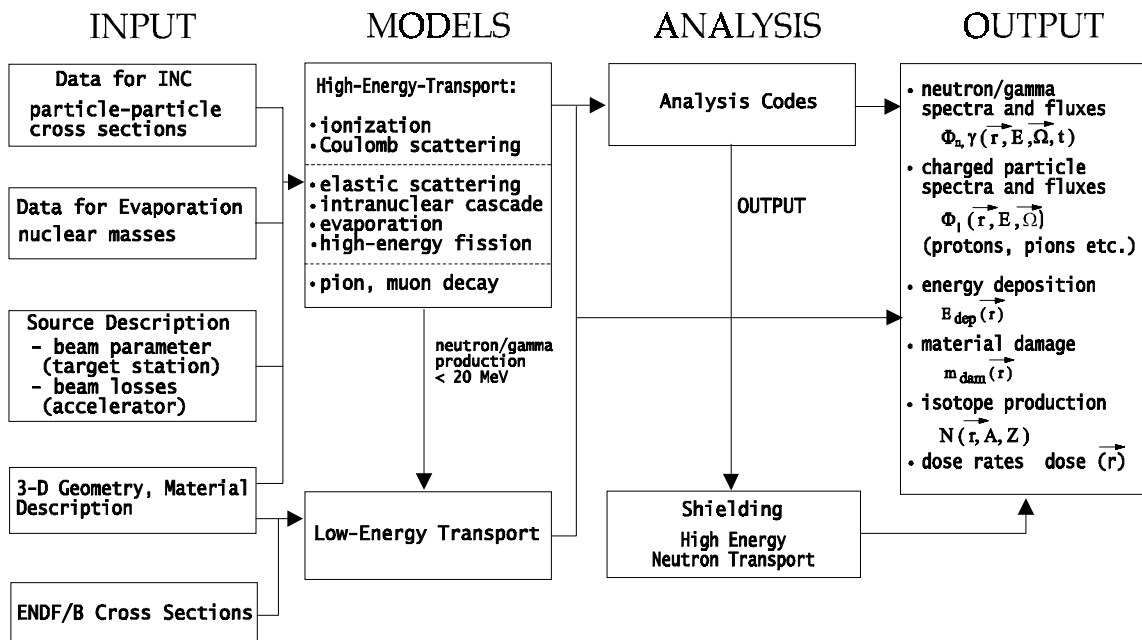
The shower codes provide a complete description (energy, angle, and spatial distributions) of the low-energy neutrons produced in spallation collisions, which allows them to be coupled with any of the available low-energy transport codes. For cross-section, evaluation and calculation codes such as ALICE [22], GNASH [23], and NJOY [24], are necessary.

To avoid the calculations with many stand alone codes in different energy ranges, several general purpose code systems were generated, which combine the necessary codes in a standardised input-output via a common file. Available and well documented code systems are summarised in Table 3. Hadronic showers contain neutral and charged pions, which decay into high energy photons, electrons and positrons, and induce electro-magnetic showers in target systems. The simulation of these showers is treated with electron-gamma shower codes. The most common code for these calculations is EGS [25], which is part of most of the code systems given in Table 3. Photons produced by de-excitation and by decay of residual nuclei may be treated by electro-magnetic shower codes or by standard n, $\gamma$ -transport codes shown in Table 2. A general scheme depicting the logic of the calculations is given in Figure 2.

**Table 3. Code systems for spallation target simulations**

Code name	Laboratory	Reference
CALOR	ORNL	Ref. 26
HERMES	FZ-Juelich	Ref. 27
LCS	LANL	Ref. 11
PSI-HETC/OSR	PSI	Ref. 28
TIERCE	CEA, Bruyeres-le-Chatel	Ref. 29
FLUKA-94	CERN/University Milano	Ref. 30
SHIELD	INR	Ref. 13, 31
SITHA	DUBNA	Ref. 32

**Figure 2. Logic scheme of thick target calculations**



## *Special purpose simulations*

### *High energy neutron source shielding*

Most probably the energy of the source protons which hit the spallation target will be at least between 1 and 2 GeV. Therefore, neutrons of such high energies will be produced. Neutrons of energies above 100 MeV are deep penetrating particles and determine the shielding thickness.

The calculation of neutron transport can be done in two ways. Either with Monte Carlo codes or with deterministic codes. The Monte Carlo codes have the advantage of good three-dimensional geometrical treatment but the disadvantage of being very time consuming to get good statistics. The deterministic codes have the advantage of being very fast running but the disadvantage that only simple geometries are possible.

The two methods can be coupled, in using the advantages of both and gain calculation time; in the target area, where geometry is complicated and important and where protons still produce spallation neutrons, Monte Carlo methods are the choice for simulation calculations. As soon as the neutrons have to be transported through thick homogenous walls discrete ordinates codes can be used. Details of applications are given in [33].

While these codes have the advantage of containing state-of-the-art physics treatments and cross-section data, they require considerable set-up and computer time. It is not practical to run these large transport codes for detailed calculations to address all of the numerous radiation safety questions and engineering type design problems associated with target station and accelerator shielding.

Based on the exponential attenuation relation for the shield attenuation of high-energy radiation there exist codes using approximate semi-empirical physics treatments, e.g. CASL [33,34], and providing sufficient accuracy for many practical problems.

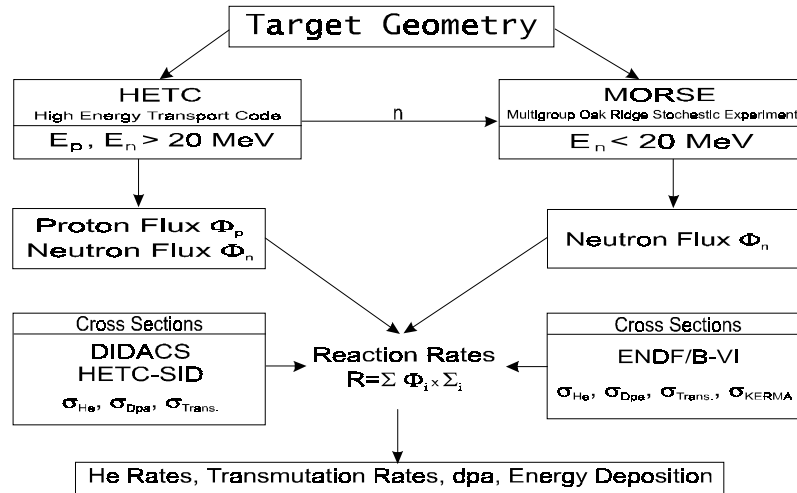
### *Materials damage by radiation*

For high power spallation targets an essential point is the estimation of lifetime of heavy irradiated components. Material failure has safety and economic aspects. Accelerated protons as well as produced secondary particles cause materials damages by mainly three different mechanisms as helium embrittlement, displacements, and transmutation. Therefore, first of all, beam windows, target containment, inner target structure and thick solid target materials damages have to be studied. In the past, most research work has been performed in fusion and reactor technology for particle energies below 20 MeV. This knowledge is very valuable but even more important is damage induced by particles of energies above 20 MeV. Until now no correct description of the experimental data on Helium production and recoil energy distributions at these higher energies has yet been achieved. On the other side the results of calculations with different models do not agree. As an example helium production is either overestimated [35] or underestimated [35].

### *Radioactivity and after heat*

For spallation neutron sources it is important to know the amount of radioactivity caused by beam losses in the accelerator and the beamlines, because this knowledge allows to decide where hands on maintenance is possible and where remote-handling systems have to be foreseen, and the amount of radioactivity produced in the target, because this makes it possible to decide how to handle and deposit the burnt targets.

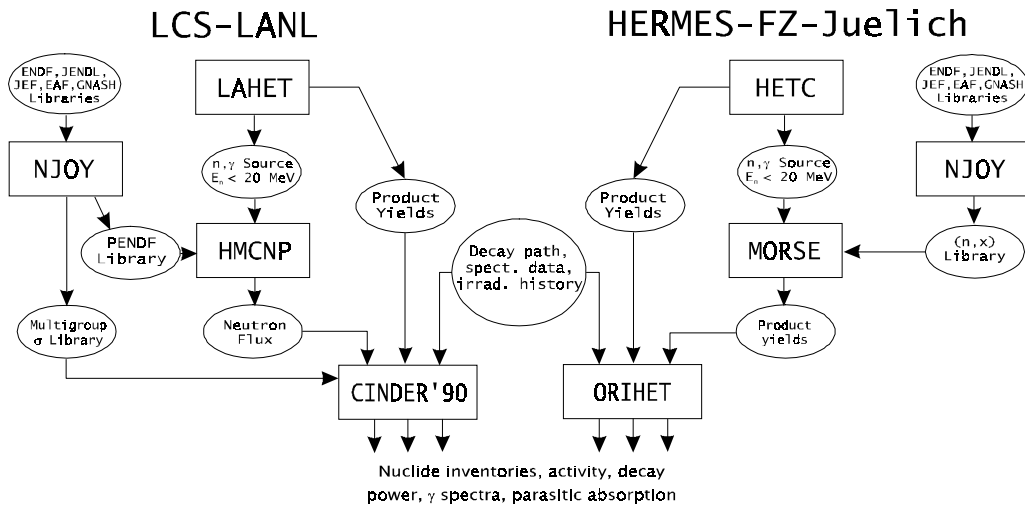
**Figure 3. HERMES method to calculate radiation damage of materials**



The procedure to calculate radioactivity and after heat consists of the following steps: the Monte Carlo code that treats the interaction of incident ion and bombarded nucleus using intranuclear cascade-evaporation model generates as an important result the distribution of the residual nuclei. This distribution can be interpreted as the production rate of spallation induced radioactive nuclides. The Monte Carlo code that treats the neutrons in the energy range below 20 MeV generates the neutron flux that can be collapsed with those neutron capture cross-sections that lead to other nuclides than the original target nuclei. Those reaction rates are the production rates caused by low energy neutrons. All the reaction rates described before are input for a nuclide generation and depletion code that solves the decay equation for decay chains using half life, decay mode, gamma energies, and other relevant data of the nuclides in ground and metastable states.

In Figure 4 the calculation procedure used in the frame of HERMES and LCS is shown. In the case of the LANL code systems, the corresponding codes are LAHET to HETC, MNCP to MORSE and CINDER [36] to ORIHET [37].

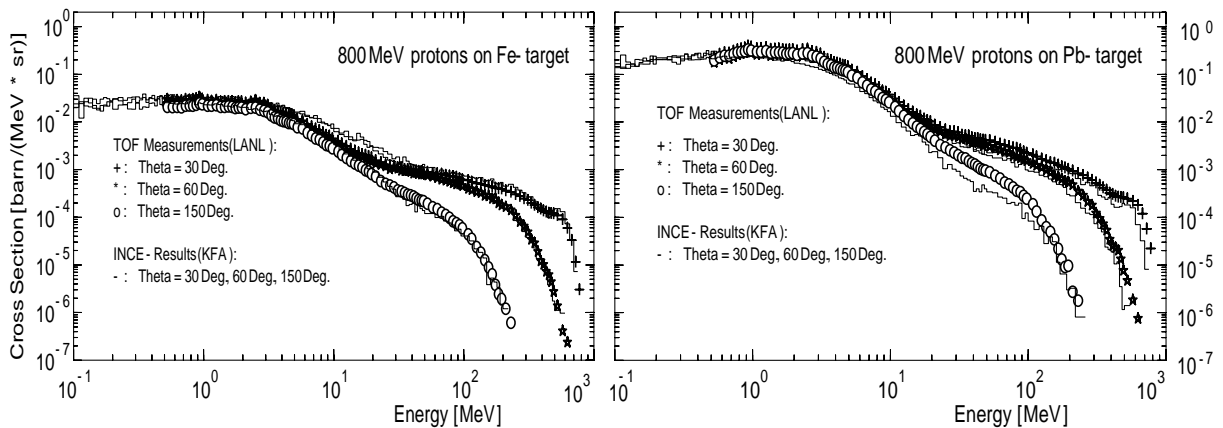
**Figure 4. Simulation procedures to calculate radioactivity and after heat with code systems LCS and HERMES (see Table 3)**



## Model validation

Manifold experiments have been performed to proof and validate the physical models of secondary particle production and transport of particles through matter and their Monte Carlo simulations. Two kinds of experiments have to be distinguished – so called “thin” – and “thick” target experiments. Cross-section measurements of double differential particle production and excitation functions are necessary to validate the basic nuclear model assumptions. Details and results of these experiments are given in Ref. [39]. As an example for double differential cross-section measurements Figure 5 shows the comparison of the iron and lead target neutron production induced by 800 MeV protons and Monte Carlo simulation.

**Figure 5: Measured double differential neutron production cross-section of iron and lead and Monte Carlo calculations**



The most extensive measurements are undertaken at LANL [40] but only below 800 MeV incident proton energy. Results of measurements for higher energies were recently published and others are planned [41,42,43]. Michel *et al.* [44] had published a large amount of measured excitation functions of residual nuclei, which are useful to validate residual nuclei production and they are important for isotope production and transmutation.

A key factor in the design of each spallation target system is the neutron production in thick target systems to benchmark the code systems given in Table 3 above. In the past, many thick target experiments were performed in connection with the development of spallation neutron sources for neutron scattering applications [8]. These experiments included the measurements of quantities with both integral and differential natures. The most important of these was the accurate determination of the total neutron yield [45,46]. Recently new preliminary results were published showing excellent agreement for n/p-ratios of lead and lithium targets, except for thorium-Li-fluorid targets with the LCS system calculations [47]. Results of the comparison of experiments and calculations of n/p yield are given in Table 4. A good review about results and uncertainties between different experimental groups are summarised in Ref. [55].

**Table 4. Measured neutron/proton-ratios compared to LCS-system simulations**

Target	Energy [MeV]	n/p measured	n/p calculated	Ratio meas./calc.
Lead	800	22.5±1.1	22.2	1.01
Th-Li-F	800	11.1±0.6	12.6	0.88
Lithium	400	4.4±0.3	4.4	1.00

Further experiments at higher incident proton energies on “thin” and “thick” targets are planned to be performed at SATURNE [43,48] and at CERN [49]. Also high energy calorimeter detector resolution measurements are very suitable for the validation of Monte Carlo simulation code systems, because one may check correlation and conservation laws for the shower propagation in thick targets [50,51].

### Examples of model applications for the ESS mercury target station

Simulation codes have been used for the design of various neutron spallation sources (IPNS, LANSCE, ISIS, KEK, PSI) and extensively tested during the operation of these facilities. This experience – over a period of 20 years [8] – is relevant and applicable to the next generation of spallation neutron sources such as ESS [1,53] and NSNS [6,54].

To show the performance of next generation spallation sources some examples of simulated complex target systems of ESS are presented. A schematic representation of the ESS mercury target is depicted in Figure 6.

#### *Energy deposition*

Using the defined elliptical beam cross-section ( $6 \times 20 \text{ cm}^2$ , 5 MW proton beam power at  $E_p=1334 \text{ GeV}$ ), calculations for the temperature distribution in the window and the target volume were carried out. The axial distribution of the power density in the central cylinder of 1 cm radius was obtained from Monte Carlo calculations and is shown in Figure 7, together with a fitted curve.

**Figure 6. Schematic representation of the ESS liquid-mercury metal target system [1]**

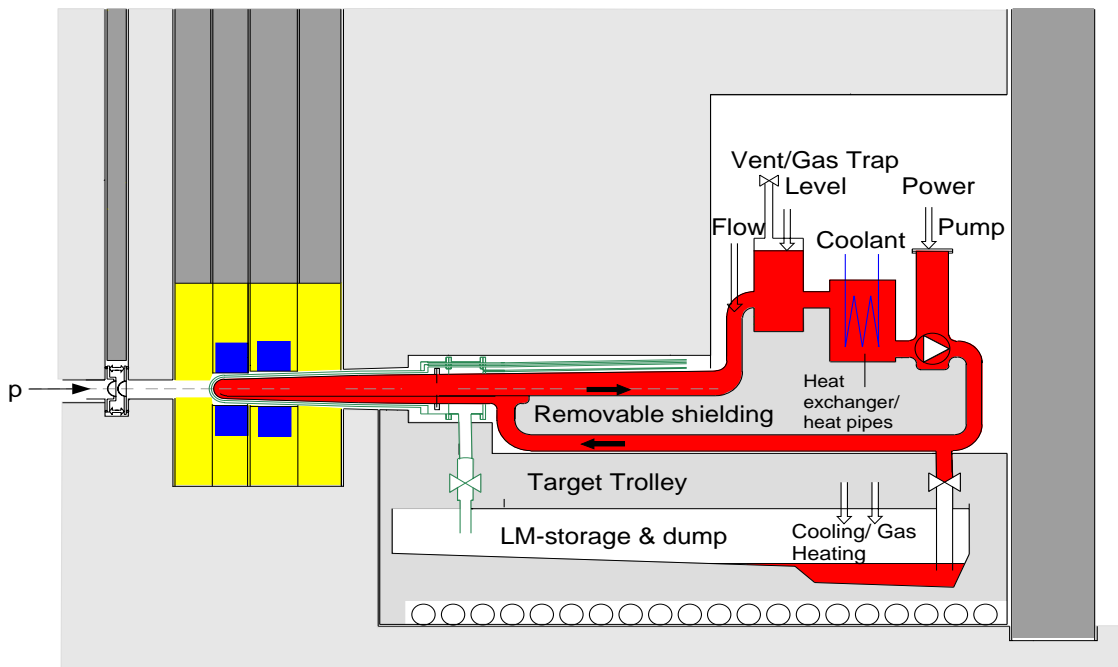
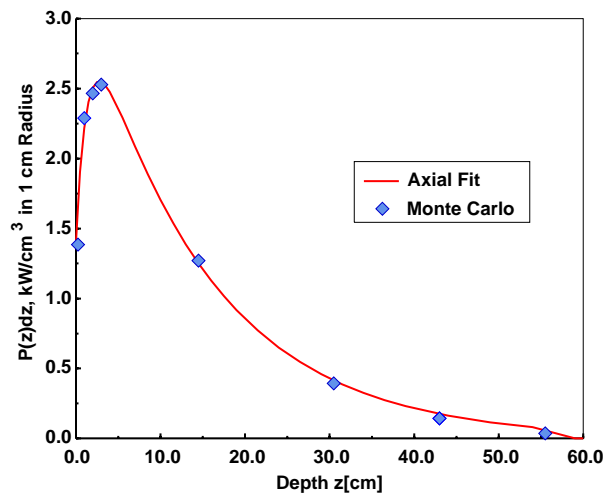


**Figure 7. Power density in the central cylinder of 1 cm radius of the mercury target for beam of 5 MW as obtained from Monte Carlo calculations**



These calculations give a total deposited power of 2372 kW i.e. 47% of the total beam power. The rest of the beam energy is taken by escaping particles or by binding energy.

For the power deposition in the window, Monte Carlo results yield a peak power density of 1.4 kW/cm<sup>3</sup> in steel, corresponding to a value of 2.27 kW/(mA/cm<sup>2</sup>) at 79 μA/cm<sup>2</sup> and a density of 7.8 g/cm<sup>3</sup>.

### *Materials damage and lifetime*

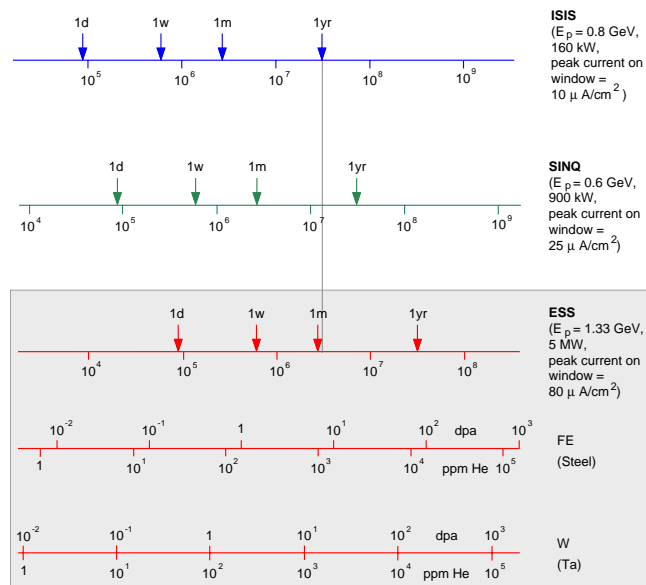
Reliable lifetime estimates are not yet possible at present. Only a lower limit based on information from a spent ISIS target and four beam windows irradiated in LAMPF can be given. The ISIS target operated for several years with varying beam power and duty times which add up to an equivalent full power service of about one year. If scaled by the peak current density (80 μA/cm<sup>2</sup> at ESS vs. 10 μA/cm<sup>2</sup> at ISIS) this corresponds to about six weeks for ESS. A comparison is shown in Figure 8. Allowing for the fact that higher stress levels and thermal cycles may affect the lifetime, this implies an upper limit of six weeks for a tantalum target at ESS. Although this is relatively short, it is the same order of magnitude as the core lifetime in a modern high flux reactor such as at the ILL.

The doses, which steel windows survived at LAMPF, are significantly higher and these windows were routinely removed from the beam without visible damage or failure. Optimistically one may, therefore, expect that the life time of a target shell will be at least two to three times longer than that of a tantalum target.

### *Moderator neutron fluxes*

The ESS is a short pulsed neutron source with a proton pulse length of 1 μs and a repetition rate of 50 Hz. The goal is to reach the highest possible peak neutron flux densities for an incident proton beam of 1.334 GeV and an average current of 3.75 mA or 2.34 10<sup>16</sup> protons per second. For pulsed measurements a short decay time of the neutron pulse is also essential. Therefore the influence of the reflector materials and coolants on pulse height and decay time has to be studied.

**Figure 8. Displacement and helium production in Fe and W, respectively (bottom lines), as a function of service time for targets exposed to the proton beams of ISIS, SINQ and ESS (top lines). For comparison a rectangular beam profile with a diameter of 7 cm has been assumed in all cases, giving dpa and helium numbers averaged over the beam cross-sections [1].**



The neutron performance of the target station is influenced by reflector size, reflector material and moderator position which all have to be optimised. The influence of iron shielding around the target-moderator-reflector-system was also studied. The Be reflector of  $60 \times 60 \times 100 \text{ cm}^3$  gives the maximum peak neutron flux density of  $1.6 \cdot 10^{17}$  neutrons per  $\text{cm}^2$  per second, whereas the Pb reflector of  $150 \times 150 \times 150 \text{ cm}^3$  gives maximum peak neutron flux density of  $2.1 \cdot 10^{17}$  neutrons per  $\text{cm}^2$  per second, about 30% higher compared to Be reflector. Also the long term decay constant  $\tau = 165 \mu\text{s}$  for a Pb reflected system is half the value of a Be reflected system. The conclusion of the reflector size study is that the optimum reflector size is about 100-150 cm in all dimensions. Cuts through the 3-D target geometry for Monte Carlo simulations are given in Figure 9. Time dependent thermal neutron flux densities for Pb and Be reflected targets are shown in Figure 10.

**Figure 9. Cuts through the 3-D target geometry for Monte Carlo simulations (outside the reflector vacuum boundary conditions are assumed; reflector size  $60 \times 60 \times 80 \text{ cm}^3$ ), upstream moderator midpoint position 11 cm, downstream moderator midpoint position 37 cm**

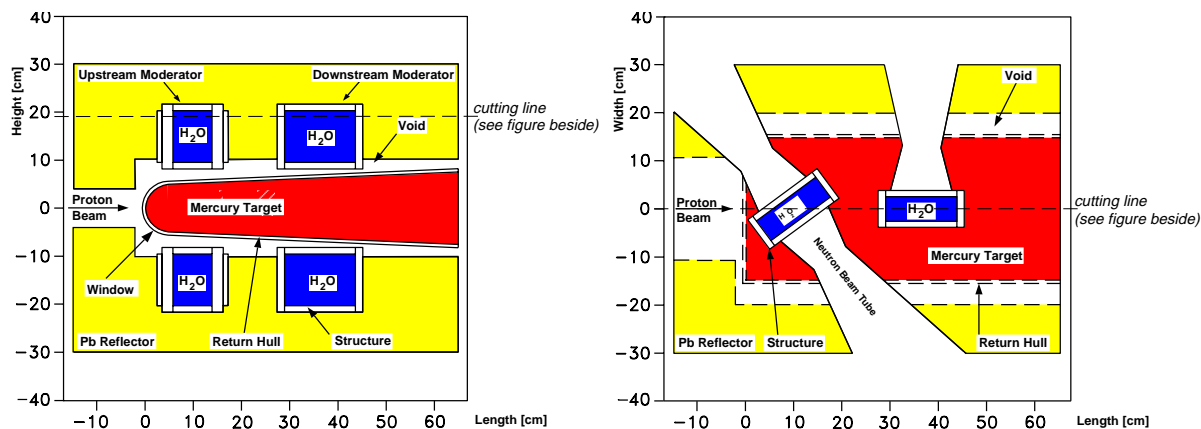
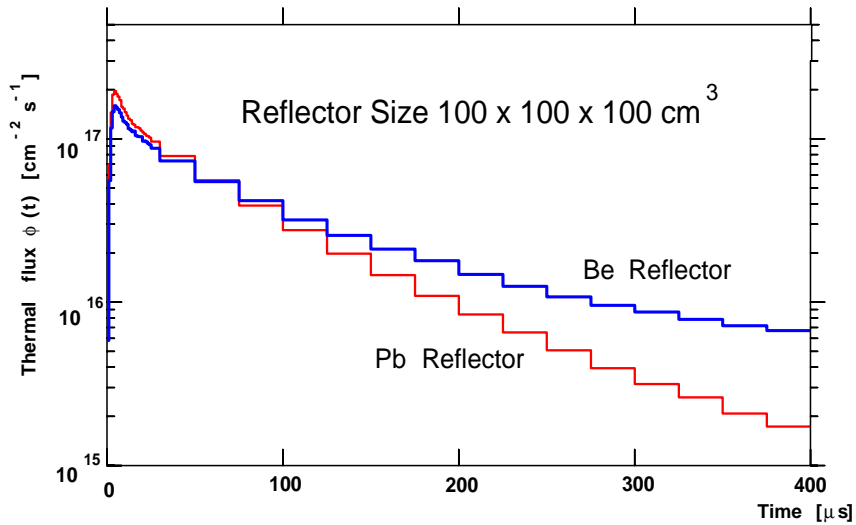


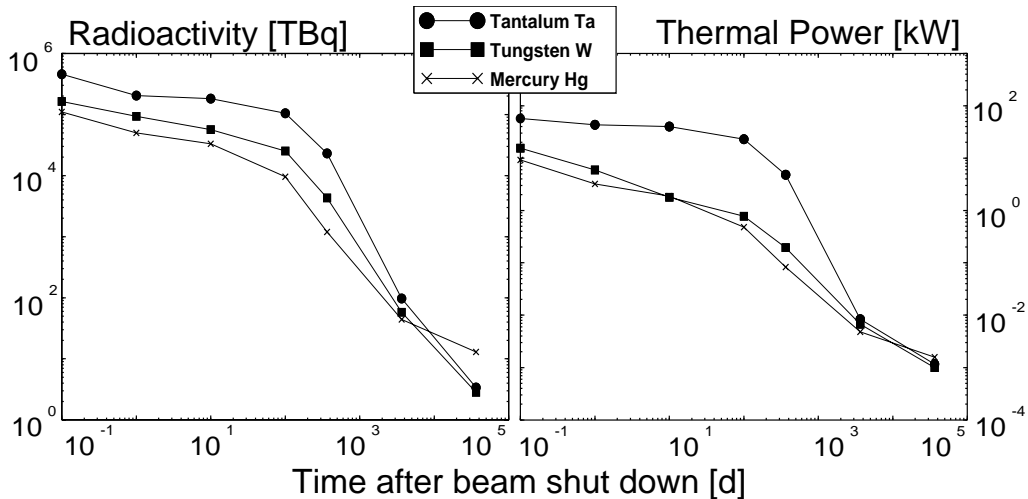
**Figure 10. Comparison of time dependent thermal neutron flux density for Pb and Be reflected targets**



**Radioactivity and after heat**

As an example, decay chain calculations in Figure 11 show the time behaviour of the radioactivity compared for different target materials W, Ta, Hg of the proposed “European Spallation Source (ESS)” with incident proton energy of 1.33 GeV and 5 MW beam power.

**Figure 11. Time behaviour of radioactivity in Tbq in Ta-, W-, and Hg-targets after one year of full power operation [38]**

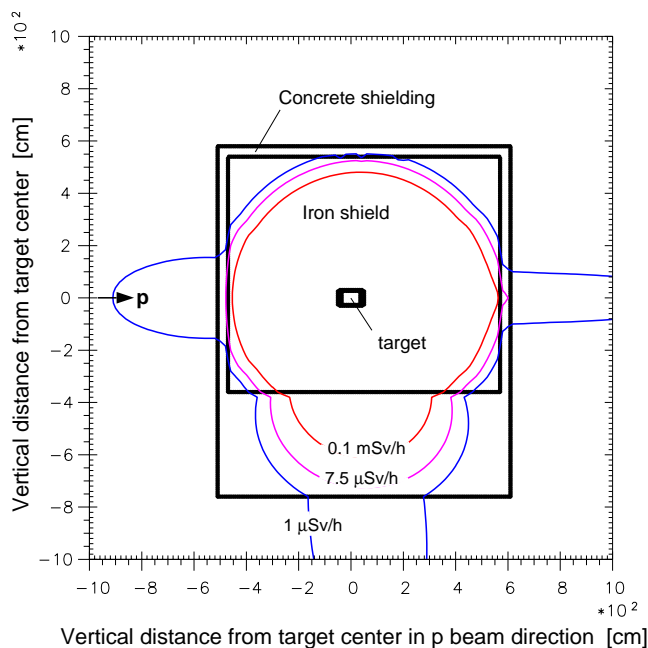


**Shielding**

The shielding layout for the ESS target station was based on semi-empirical physics treatment by the CASL-code [34]. As an example, Figure 12 shows the dose rates in vertical cross-section through target shield along the proton beam. The radius of the target area is 50 cm, the radius of the

iron shield 520 cm. The thickness of the iron shield perpendicular to the proton beam should be 480 cm. Below the target the iron thickness can be reduced if a large concrete base is built. From Figure 12 it can be seen that the desired dose rate value of 7.5  $\mu\text{Sv/h}$  lies inside the shielding.

**Figure 12. Iso-dose rates in vertical cross-section through target shielding along proton beam**



Isodose rates in vertical cross section through target shield  
(proton beam : 3.748 mA, 1.334 GeV)

### Overall performance parameter of the ESS target

In Table 5 important performance parameters of the ESS mercury target system are given.

**Table 5. The performance of the ESS mercury target<sup>1)</sup> systems [1]**

$n/p$ <sup>2)</sup>	$\bar{\Phi}$ [ $\text{n}\cdot\text{cm}^{-2}\cdot\text{s}^{-1}$ ]	$\hat{\Phi}$ [ $\text{n}\cdot\text{cm}^{-2}\cdot\text{s}^{-1}$ ]	Energy <sup>3)</sup> Deposition [kW]	After Heat <sup>4)</sup> [kW]	Radioactivity <sup>4)</sup> [TBq]
40.0	$6.2 \times 10^{14}$	$1.9 \times 10^{17}$	2800	9.2	$1.1 \times 10^5$

1) Pb reflected with 15 vol % D<sub>2</sub>O coolant;

2) neutron yield in the whole system;

3) only in mercury for 5 MW beam power;

4) after beam shut off and 1 year operation.

### Needs for spallation related data and planned experiments

The ability to predict, on a theoretical or computational basis, all aspects of radiation physics is crucial not only to the performance optimisation of the whole system, but also by advising engineers in their decisions with respect to the effect on the source characteristics. While the standard of computational models for neutronics and nucleonics calculations is generally quite high, there are still some areas where more research is urgently needed. These include:

- verification of cross-sections and nuclear models used for mercury;
- verification of calculated integral and differential neutron flux density and secondary particle distribution from an “engineered” target-moderator-reflector system;
- residual nuclei distributions for induced radioactivity, afterheat and transmutation atom generation in target and structural materials;
- correlation effects by gas production (H and He) and by recoiling nuclei in radiation damage;
- efficiency of shielding (materials combinations) against different types of radiation;
- development of scattering kernels for cold sources.

The following experiments are under way and planned by various international collaborations:

- NESSI Collaboration at COSY-Jülich (Neutron Scintillator Silicon Detector):
  - neutron and charged particle multiplicities upto 2.5 GeV incident proton energies;
  - energy deposition in target and structure materials.
- AGS-collaboration at BNL-Brookhaven:
  - mercury spallation target station mock-up experiments up to 24 GeV incident proton energy;
  - neutron leakage reactions rates distributions, energy deposition, pressure waves, spallation products.
- RECOIL-collaboration at COSY-Jülich:
  - measurement of fragment emission from proton induced reactions with nuclei relevant to radiation damage in ESS structure and target materials.

## Summary

The spallation neutron source projects [8] made many data available for extensive evaluations of the theoretical models and codes. Therefore the simulation code systems for high power spallation neutron sources are highly developed to assess all important physical and technical parameters. In the low energy regime ( $\leq 20$  MeV) particle production and transport could be based on nuclear and fusion reactor experience. Still cross-sections libraries must be completed. In the high energy range a need exists for excitation functions, gas production, and damage cross-section measurements. Also the systematic of double differential production cross-sections of neutrons, protons and pions in the energy range up to several GeV is incomplete.

## REFERENCES

- [1] The European Spallation Source Study, Volume III, ESS-96-53-M, ISBN-090-237-6-659, Nov. 1996.
- [2] J.M. Carpenter, Proc. ICANS-XIII, PSI-Proceedings 95-02 (1995), pp. 777-797 or ANL Report ANL-95/13 (1995).
- [3] Y.Y. Lee *et al.*, Proc. ICANS-XIII, PSI-Proc. 95-02 (1995), pp. 802-807 or H. Ludewig *et al.*, Proc. ICANS-XIII, PSI-Proceedings 95-02 (1995), pp. 808-813.
- [4] M. Furusaka *et al.*, Proc. ICANS-XIII, PSI-Proceedings 95-02 (1995), pp. 836-842.
- [5] N. Bultmann *et al.*, Report LA-UR-95-4300 (1995) or R. Pynn and D. Weinacht, Proc. ICANS-XIII, PSI-Proceedings 95-02 (1995), pp. 798-801.
- [6] B. Appleton, Proc. ICANS-XIII PSI-Proceedings 95-02 (1995), pp. 814-818.
- [7] G.S. Bauer, IAEA, Vienna, TECDOC-836 (1995), pp. 97-114.
- [8] Information on ICANS is available on World Wide Web under the following URL address: <http://www.pns.anl.gov/icans/icansdescript.html>.
- [9] H. Bertini, Report ORNL-TM-1996 (1967).
- [10] T.W. Armstrong and K.C. Chandler, *Nucl. Sci. Eng.* 49 (1972), p. 110.
- [11] R.E. Prael and H. Lichtenstein, Report LA-UR-89-3014 (1989).
- [12] Y. Nakahara and T. Tsutsui, Report JAERI-M82-198 (1982).
- [13] V.S. Barashenkov *et al.*, *Atomnaya Energiya*, 32 (1972), p. 217.
- [14] P.A. Aarnio *et al.*, Report CERN TIS-RP 168 (1986).
- [15] Y. Yariv and Z. Fraenkel, *Phys. Rev.*, C20 (1979), p. 2227.
- [16] M.B. Emmett, Report ORNL-4972 (1975).
- [17] W.L. Thompson *et al.*, Report LANL-7396-M (1979).
- [18] W.W. Engle, Report ORNL-K-1693 (1967).
- [19] T.R. Hill, Report LA-5990-MS (1975).

- [20] W.A. Rhoades *et al.*, Report ORNL-TM-6529 (1979).
- [21] R.E. Alcouffe *et al.*, Report LA-10049-11 (1990) or T.J. Seed *et al.*, Report LA-6735-11 (1977).
- [22] M. Blann and H.K. Vonach, *Phys. Rev.*, C28 (1983) p. 1475.
- [23] P.G. Young *et al.*, Report LA-12343-MS (1992).
- [24] R.E. MacFarlane *et al.*, Report LA-9303-M (1982).
- [25] W.R. Nelson *et al.*, Report SLAC-265 (1985).
- [26] T.A. Gabriel *et al.*, Report ORNL/TM-11060 (1989).
- [27] P. Cloth *et al.*, Report JUEL-2203 (1988).
- [28] F. Atchison, Report NEA NSC/DOC/(95) 2 (1995).
- [29] O. Bersillon, Second ADTT Conf., (1996).
- [30] A. Fassò *et al.*, Proc. Specialists Meeting, Issy-Les-Moulineaux (France) (1994), p. 271.
- [31] A.V. Dementyev *et al.*, Proc. Specialists Meeting, Issy-Les-Moulineaux (France) (1994), p. 237.
- [32] A.V. Daniel *et al.*, Proc. Specialists Meeting, Issy-Les-Moulineaux (France) (1994), p. 301.
- [33] D. Filges *et al.*, Proceedings of a Specialist Meeting, Arlington, Texas (USA), Report OECD/GG-9501-1 DCX,(1994), pp. 53-270.
- [34] B. Wolfertz, Report Jül-3197 (1996).
- [35] A.Y. Konabeyev, *J. Nuc. Mat.*, 195 (1992), pp. 286-300.
- [36] W.B. Wilson *et al.*, Report LA-UR-93-3080 (1993).
- [37] F. Atchison and H. Schaal, private communication (1996).
- [38] D. Filges *et al.*, Proc. ICANS-XIII, PSI-Proceedings 95-02 (1995), pp. 537-546.
- [39] P. Cloth *et al.*, Proc. Specialists Meeting, Issy-Les-Moulineaux (France) (1994), pp. 219-236.
- [40] M.M. Meier *et al.*, *Nucl. Sci. Eng.*, 104 (1990), p. 289 or *Nucl. Sci. Eng.*, 110 (1992) p. 289
- [41] T. Nakamoto *et al.*, ICANS-XII, RAL-Proceedings Report 94-025 (1993), pp. T-80-T-89.
- [42] S. Meigo *et al.*, 95- ICANS-XIII, PSI Proceedings-20 (1995), pp. 442-448.
- [43] S. Leray, Proc. of a Specialists Meeting, Issy-Les-Moulineaux (France) (1994), pp. 379-385 or Second Int. Conf. on ADTT, 3-7 June 1996, Kalmar, Sweden.

- [44] R. Michel *et al.*, NIM B103 (1995), pp. 183-222.
- [45] J.S. Fraser *et al.*, *Canadian of Phys.*, 49 (1971), p. 2061.
- [46] R.G. Vassil'kov, V.S. Yurevich, ICAN-XI, KEK Report 90-25 (1991), pp. 340-353.
- [47] G. Morgan *et al.*, AIP Conf. Proc. 346 (1995), pp. 663-672.
- [48] J. Fréhaut, AIP Conf. Proc. 346 (1995), pp. 673-681.
- [49] D. Hilscher *et al.*, Int. Workshop on Nuclear Methods for Transmutation, Dubna, Russia, 29-31 May (1996).
- [50] B. Anders *et al.*, NIM A277 (1989), pp.56-67.
- [51] F. Barreiro *et al.*, NIM A292 (1990) pp. 259-278.
- [52] F. Atchison, Proc. Specialists Meeting, Issy-Les-Moulineaux (France) (1994), pp. 349-361.
- [53] H. Lengeler, Proc. ICANS-XIII, PSI-Proceedings 95-02 (1995), pp. 819-830.
- [54] B. Appleton, NSNS-Workshop, 31 Oct.-1 Nov. 1996, Oak Ridge, USA.
- [55] M.S. Zucker *et al.*, ADTT-Cof., Kalmar 1996, Sweden.



## **OVERVIEW OF THE NATIONAL SPALLATION NEUTRON SOURCE WITH EMPHASIS ON THE TARGET STATION**

**Tony A. Gabriel, John N. Barnes, Lowell A. Charlton, James DiStefano,  
Ken Farrell, John Haines, Jeffrey O. Johnson, Louis K. Mansur,  
Steve J. Pawel, Moshe Siman-Toy, Rusi Taleyarkhan, Mark W. Wendel**  
Oak Ridge National Laboratory\*, P.O. Box 2008, Oak Ridge, Tennessee 37831, USA

**Thomas J. McManamy, Mark J. Rennich, Al Williams**  
Engineering, Lockheed Martin Energy Systems, Inc.  
P.O. Box 2009, Oak Ridge, Tennessee 37830, USA

### **Abstract**

The technologies that are being utilised to design and build a state-of-the-art neutron spallation source, the National Spallation Neutron Source (NSNS), are discussed. Emphasis is given to the technology issues that present the greatest scientific challenges. The present facility configuration, ongoing analysis and the planned hardware research and development programme are also described.

---

\* Managed by Lockheed Martin Energy Research Corporation for the US Department of Energy under Contract No. DE-AC05-96OR22464.

## Introduction

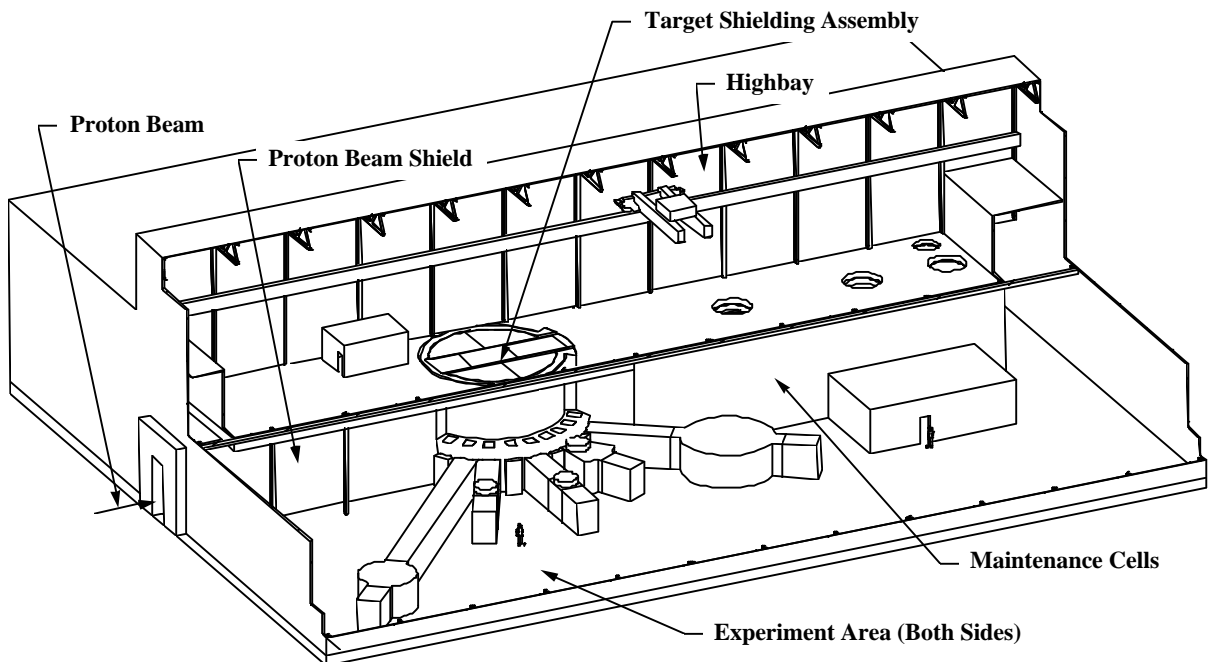
In many areas of physics, such as materials, biology and nuclear engineering, it is extremely valuable to have a very intense source of neutrons so that the structure and function of materials can be studied. One facility proposed for this purpose is the National Spallation Neutron Source (NSNS). This facility will consist of two parts: 1) a high-energy ( $\sim 1$  GeV) and high powered ( $\sim 1$  MW) proton accelerator (60 Hertz,  $< 1.0 \mu\text{s}/\text{pulse}$ ), and 2) a target station which converts the protons through nuclear interactions to low-energy ( $\lesssim 2$  eV) neutrons and delivers them to the neutron scattering instruments.

This paper deals with the second part, i.e. the design and development of the NSNS target station and the scientifically challenging issues. Many scientific and technical disciplines are required to produce a successful target station. These include engineering, remote handling, neutronics, materials, thermal hydraulics, and instrumentation. Some of these areas will be discussed below.

## Target station configuration and maintenance

The target and experimental systems for the NSNS are located in a single building. As shown in Figure 1, the target is positioned within an iron and concrete shielding monolith approximately 12 m in diameter. The proton beam enters the mercury target horizontally and the produced neutrons after moderation are used by the scattering instruments. These neutrons exit through 18 neutron beam tubes projecting from the sides. The majority of the 62 m $\times$ 83 m building is reserved for the scattering instruments located on the neutron beamlines, however, remote handling hot cells projecting from the back of the shielding are provided for handling the activated target, moderator and reflector components. This region also contains utilities used for the target. Another cell for utility systems is located beneath the main floor level.

Figure 1. Cutaway view of target facility



The target facility can be segregated into four areas for discussion:

- target assembly including the moderators and reflectors;
- neutron beam tube systems;
- remote handling systems;
- target system controls.

## ***Target***

### *Liquid target material*

The reference design for the NSNS incorporates mercury as its target material. A heavy liquid metal target was selected over a water-cooled solid target because (1) increased power handling capability is possible with a liquid target; (2) the liquid target material lasts the entire lifetime of the facility; and (3) the radiation damage lifetime of a liquid target system, including its solid material container, should be considerably longer. The first advantage is due to the large power loads that can be convected away from the beam-target interaction region with a flowing liquid target. The second advantage results from avoiding the radiation damage that would occur in a solid target material, which eventually leads to embrittlement and fracture of the material. Liquid target vessels will still need to be replaced periodically due to radiation damage to its container structure, but the liquid target material can be reused. The third advantage – longer irradiation lifetime – results from two effects. First, the target structural material used to enclose the liquid target can be selected based on its structural properties and resistance to radiation damage, independent of its neutron production capability, and second, with a liquid target, there is no solid material in the highest neutron flux regions. Therefore the peak displacement damage rate in the window of a liquid target is greatly reduced compared to the peak value in a solid target.

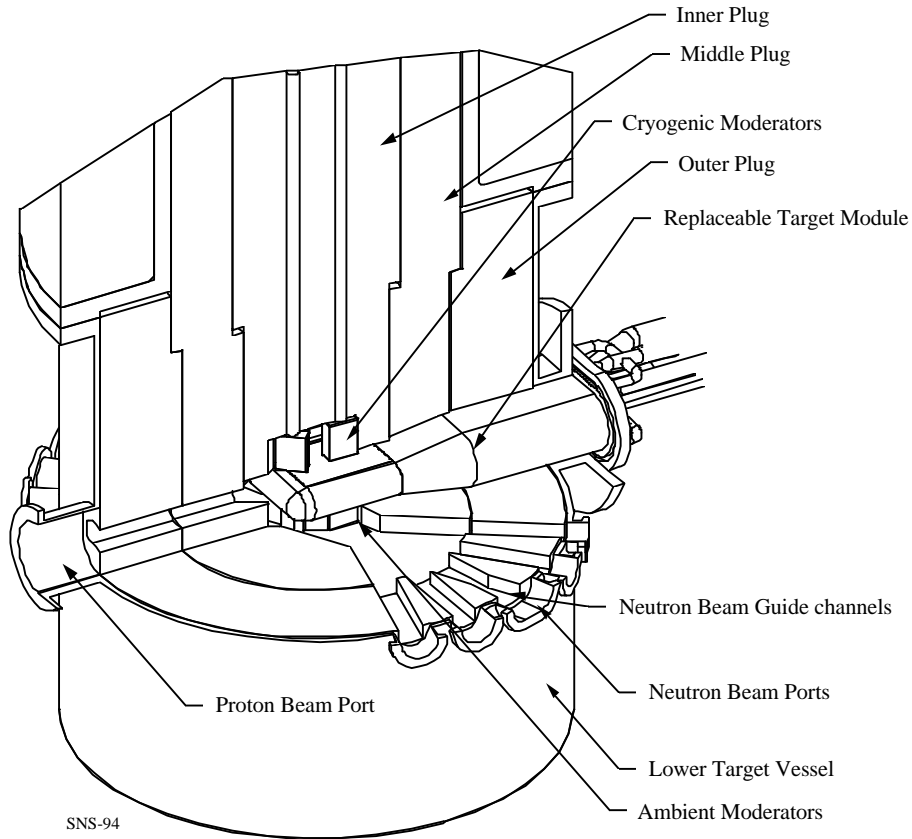
Mercury was also selected as the reference liquid target material because it (1) is a liquid at room temperature; (2) has good heat transport properties; and (3) has high atomic number and mass density resulting in high neutron yield and source brightness. One significant result from recent neutronic analysis studies has been that the neutron flux from a short-pulse (~1  $\mu$ s) neutron source is substantially greater for a mercury target than for either water-cooled tungsten or tantalum targets especially at power levels greater than 1 MW (see the section entitled *Neutronics*).

### *Mercury target design concept*

The mercury target design configuration, shown in Figure 2, has a width of 400 mm, a height of 100 mm, and a length of 650 mm. The mercury is contained within a structure made from 316-type stainless steel. Mercury enters from the back side (side outermost from the proton beam window) of the target, flows along the two side walls to the front surface (proton beam window), and returns through a 224 mm×80 mm rectangular passage in the middle of the target. Also being considered is the opposite flow, i.e. in through the 224 mm×80 mm passage and out the two side walls. The target window, i.e. portion of the target structure in the direct path of the proton beam is cooled by mercury which flows through the passage formed between two walls of a duplex structure. In this way, the window cooling and transport of heat deposited in the bulk mercury are achieved with separate

flow streams. This approach is judged to be more reliable and efficient (minimal pressure drop and pumping power) than using the bulk mercury to cool the window. Also, the duplex structure used for the window has significant structural advantages that help to sustain other loads. Beside serving as flow guides, the baffle plates used to separate the inlet and outlet flow streams are also important for maintaining the structural stability of the target.

**Figure 2. NSNS mercury target**



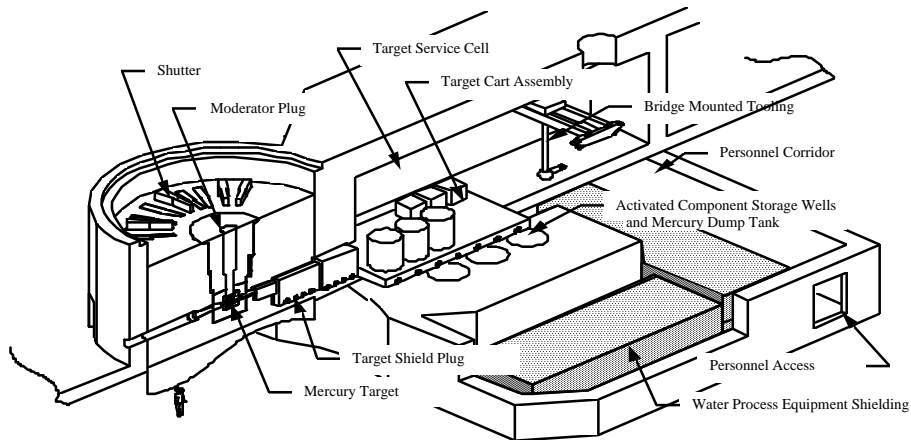
A shroud (safety container) is provided around the mercury target to guide the mercury to a dump tank in the event of a failure of the target container structure. The shroud is a water-cooled duplex structure made from austenitic, 316-type, stainless steel.

***Target station***

***Configuration***

The overall configuration for the liquid target system is shown in Figure 3. The mercury target and the water cooled shroud, which are subject to intense interactions with the proton beam, must be replaced on a regular basis. For this reason, all major liquid target system components, except the dump tank, are located on a mobile cart, which is retracted into the target hot cell for maintenance activities. The mercury contained in the target system is drained to the dump tank prior to retracting the target assembly.

**Figure 3. Target system configuration**



The heat deposited in the mercury target is transported away in the flowing mercury loop to a primary heat exchanger that is located on the target cart assembly, outside the target region shielding. The primary heat exchanger is a shell and tube type with mercury flowing in the tube side and the secondary coolant, i.e. demineralised water, flowing in the shell side. The tubes in this heat exchanger are a special, double-walled type which reduces the probability of a mercury leak into the intermediate loop. In addition to this primary heat exchanger, the mercury flow loop also includes piping, valves, fittings, pumps, expansion tanks, and mercury processing equipment. The secondary (water) loop transports the heat to a secondary heat exchanger located in the floor below the target hot cell. The tertiary flow stream utilises process water.

A water-cooled shroud is provided around the mercury target to guide the mercury to a dump tank in the event of a failure of the target vessel. This shroud is formed from a duplex structure similar to the mercury target vessel and is also made from stainless steel.

The 86-tonne target shield plug, shown in Figure 3, is designed to shield the equipment located in the target hot cell from the high energy, forward-scattered neutrons produced in the mercury target. The shield plug, which is removed as part of the target assembly during maintenance operations, is constructed from water-cooled, bulk iron encased in a stainless steel liner.

The cart assembly supports all of the mercury flow loop equipment, and provides the means for transporting the target assembly into the target hot cell.

The mercury dump tank is located below all other components in the mercury system thus ensuring that most of the mercury can be drained to the dump tank even in a passive situation (failure of the electric power system). A gas purge system is also utilised under normal circumstances to provide more complete removal of the mercury from the target systems to the dump tank. The capacity of the dump tank is greater than 1 m<sup>3</sup>, which is slightly larger than the mercury inventory in the remainder of the system. The tank is passively cooled by natural convection to remove the nuclear afterheat in the mercury.

#### *Ambient temperature moderators*

Figure 2 shows the two light-water moderators planned for the NSNS. They are located in wing geometry below the mercury target and water-cooled shroud. The moderator vessel is made from aluminium alloy-6061. The upstream moderator has a thickness of 50 mm, relative to the proton

beam, and is decoupled and poisoned to give high temporal resolution of the neutron flux. The second moderator is 100 mm thick and is coupled to produce higher neutron intensity but with less temporal resolution. Both moderators are approximately 120 mm wide and 150 mm high.

The overall heat load in the ambient moderators is estimated to be 4 kW (2 kW per moderator) based on calculations carried out for the NSNS design and on extrapolations from ISIS and ESS data. This heat load results in an overall temperature rise of less than 1°C for a nominal flow rate of 2 L/s.

### *Cryogenic moderators*

In addition to the two ambient temperature moderators located beneath the target, two cryogenic moderators, cooled with supercritical hydrogen, are located above the target as shown in Figure 2. This configuration improves the cooling and warming characteristics of the moderators. Mechanically circulated supercritical hydrogen gas at a pressure of 1.5 MPa was chosen for the moderators because it improves the cooling operation, eliminates boiling and adds flexibility in operation. The hydrogen is maintained at supercritical pressures in all parts of the loop during normal operation.

### *Reflector systems*

As identified in Figure 2, the reflector system consists of three plug assemblies, namely the inner reflector, middle plug, and the outer reflector. The inner plug consists of a stainless steel case packed with beryllium rods and cooled with heavy water and holds all four moderators. Neutron decouplers made from boral are mounted on the inner surface of the case. The heavy water flow loop includes appropriate equipment, such as piping, valves, an expansion tank, connectors, pumps, ion exchangers, and instrumentation. The system is designed with connectors to allow disconnection and removal of the reflector assembly vertically into a shielded cask for transport to the target assembly hot cell.

A middle plug holds the majority of the beryllium reflector and is similar in construction to the inner plug. The outer plug consists of nickel shielding with water cooling within a steel case and is contained within a 2 m diameter safety vessel.

### *Neutron beam transport systems*

The neutron beam tube systems provide the paths for moderated neutrons to travel through the bulk shielding to the scattering instruments. The configuration assumed at present consists of 18 beamlines looking at the four moderators as shown in Figures 1 and 2. Each moderator face which is viewed illuminates three beamlines, one normal to the face and two at plus or minus 13.75 degrees. The upper and lower forward moderators have two faces viewed and the two rear moderators each have one face viewed for a total of six viewed faces. This arrangement allows a 70 degree arc for the proton beam entrance region and a similar 70 degree arc for the remote maintenance systems at the rear of the target.

A neutron beam shutter concept similar to the ISIS vertical shutter design is planned. The shutters are in the form of stepped rectangular slabs. In the open position a hole in the shutter aligns with the neutron beam flight path and cross-section. The shutter is lowered approximately 500 mm to close. This puts approximately 2 m of heavy shielding (W or Ta) in the neutron flight path. The drive for the shutters will be located at the top. Each shutter will be made from several sections to reduce the height above the top of the bulk shielding required for removal and the size of the

shielded flask required for transport. All shutters will be the same, except for the difference in beam elevation required between beamlines viewing the upper or lower moderators. The weight of one shutter assembly is approximately 25 tonnes.

The neutron beamlines require shielding outside of the bulk target shield. This shield is both for personnel protection and also to reduce the background noise in instruments. It is assumed that standard modules will be developed to allow sections to be added or removed, depending on the requirements and locations of the scattering instruments.

### *Remote handling systems*

Optimisation of both the operating availability and predictability, while protecting personnel, is the primary goal of the maintenance systems for NSNS. Several techniques proven in successful facilities throughout the world are applied to assist the operators in meeting the operating goals. These include designing equipment from the earliest stages to reduce the need for remote handling. Operating equipment are packaged in modular assemblies designed to be replaced with on-site spares. This enables operations to continue while time-consuming repairs are performed in off-line facilities.

The As Low As Reasonably Achievable (ALARA) principle is used as guidance for all personnel and contamination control operations in NSNS. Thus, activated and contaminated equipment are shielded for transport around the facility and to the permanent storage site. Areas of potential contamination are isolated by seals and valves. Repair and replacement of active components are accomplished in the hot cell adjoining the target shielding stack as identified in Figure 3.

A target service cell is located behind the target assembly for the purpose of maintaining the highly activated target components. It measures 10 meters wide by 17.8 meters long by 8 meters high. All work is performed via remote handling techniques behind concrete shielding walls. Conventional remote handling tools such as telerobotic manipulators, CCTV and special lighting are used to assist with the replacement of target components. Modular packaging of the components is used to reduce downtime.

A general maintenance cell is located behind the target service cell primarily to maintain the moderator/reflector plug, proton beam window, neutron guide tubes and shutters. Generally all operations will be remote; however, personnel may enter the cell following extensive cleanup. The cell measures 10 meters wide, 10.9 meters long and 9.5 meters high.

The enclosed, unshielded high-bay above the target system and maintenance cells will provide the primary means of handling components in the target system. It measures 12 meters wide, 20 meters high and extends 55 meters. A 50 tonne bridge crane provides access to all of the maintenance cells, storage wells and the transportation bay. The access bay is normally accessible to personnel, consequently all activated components will be shielded and contained during operations and during component transfers between the hot cells. In addition, utility and instrument connections to the vertical access plugs (i.e. shielding, moderators, reflectors and proton beam window) are routed in shielded trenches in the floor of the bay.

## **Neutronics**

The neutronic behaviour of the target system can be obtained by using Monte Carlo techniques to track the progress of various subatomic particles as they proceed through the target. For the work presented here the codes HETC95 [1] and MCNP [2] were used. The codes were coupled in order

to provide the proper source for the low-energy MCNP calculations. Various parameters were calculated to measure the neutronic performance of the target design. The two parameters which were most often tracked in the study reported below were the neutron current (J) passing into the neutron beam channels which lead to the experimental area and the time width (W) of the beam channel neutron pulse.

For this first study, a proton energy of 1.7 GeV, a power of 1 MW, a repetition rate of 60 Hz and a proton pulse width of .5  $\mu$ s was assumed. The target assembly is shown in Figure 4. The beryllium reflector surrounds the neutron-producing mercury target, the moderators, which slow the produced neutrons to useful energies (the top cryogenic moderators are filled with liquid hydrogen and the bottom ambient moderators with water), and the neutron beam channels which guide the neutrons to the experimental area. In Figure 4, the beryllium has dimensions 0.9 m $\times$ 0.9 m $\times$ 1.008 m with the square plane perpendicular to the proton beam direction. The largest dimension of the proton beam channel is 120 mm by 320 mm. In Figure 5 the target assembly is shown as viewed from the bottom with the reflector material removed. The target, neutron beam channels and the bottom ambient moderators feeding the neutron beam channels can be seen. Two cryogenic moderators are located on the top of the target in analogous positions. The mercury target in Figure 5 is 640 mm long with a half cylinder of radius 50 mm on the end where the proton beam enters (to the right in the figure). Downstream from the half cylinder is a section with rectangular cross-section width of 300 mm and a height varying from 100 mm upstream to 150 mm at the extreme downstream end. Various moderator parameters are shown in Table 1.

**Figure 4 Target assembly enclosed in the beryllium reflector**

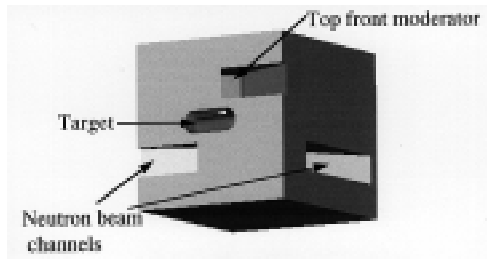
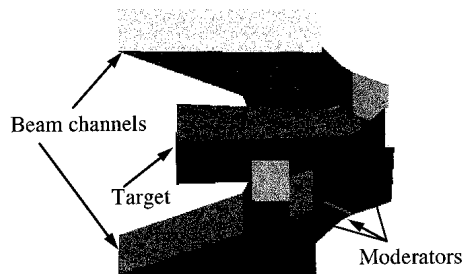


**Figure 5. Target, moderators, and the neutron beam channels as viewed from the bottom**



In the sections to follow a comparison between Hg target performance and that of W and Ta is given. Also, results showing the effect on moderator performance of poisoning (inserting a thin layer of gadolinium into the moderator centre parallel to the exit face(s)), and decoupling (surrounding the moderator and reflector with cadmium on all sides except those through which the neutrons exit) will also be presented along with a comparison of the calculated neutron spectrum with an analytic form which will facilitate optimisation of the target.

**Table 1. Moderator parameters (unless stated otherwise in text)**

Moderator	Dimensions (mm)	Decoupler Thickness (mm)	Poison Thickness (mm)
Top Upstream (Faces 1 & 2)	120×150×50	1. Cd	0.05 Gd
Top Downstream (Faces 3 & 4)	120×150×50	1. Cd	0.05 Gd
Bottom Upstream (Face 5)	120×150×50	1. Cd	0.05 Gd
Bottom Downstream (Face 6)	120×150×100	1. Cd	0.05 Gd

The size of the moderator face from which the neutrons enter the beam channel is given by the first two dimensions in the second column.

### *Mercury target*

The preferred target for NSNS is mercury. This choice is motivated by anticipated advantages in many areas. The neutronic superiority of Hg over two other commonly considered targets is shown in Table 2. This increase in neutronic performance will be slight at 1 MW but substantial at 5 MW due to the increase in the H<sub>2</sub>O cooling needed for the solid target at 5 MW. The hydrogen in the water thermalises some of the neutrons within the W or Ta target area. Since both W and Ta have large capture cross-sections these thermalised neutrons are captured and therefore lost. Calculations of the neutron flux for a 5 MW target station are shown in order to facilitate a comparison with a different study done for ESS. The results of this study are also shown. As may be seen, Hg gives a larger neutron flux than either Ta or W. This is true for both cryogenic (liquid H<sub>2</sub>) and ambient (H<sub>2</sub>O) moderators. Comparison of the neutron spectrum and pulse showed virtually identical characteristics except for the additional neutrons given by the Hg target.

**Table 2 Comparison of thermal neutron fluxes at the moderator faces for Hg, W and Ta Targets at 5 MW**

Cryogenic				
NSNS			ESS	
<i>Target</i>	$\phi_{th}$	<i>R</i>	$\phi_{th}$	<i>R</i>
Hg	$2.94 \times 10^{14}$	1.35	$3.91 \times 10^{14}$	1.23
W	$2.54 \times 10^{14}$	1.17	$3.53 \times 10^{14}$	1.10
Ta	$2.17 \times 10^{14}$	1.00	$3.19 \times 10^{14}$	1.00

Ambient				
NSNS			ESS	
<i>Target</i>	$\phi_{th}$	<i>R</i>	$\phi_{th}$	<i>R</i>
Hg	$3.35 \times 10^{14}$	1.35	$2.29 \times 10^{14}$	1.51
W	$2.91 \times 10^{14}$	1.17	$1.67 \times 10^{14}$	1.10
Ta	$2.48 \times 10^{14}$	1.00	$1.52 \times 10^{14}$	1.00

Units:  $\phi_{th}(\text{n}\cdot\text{cm}^{-2}\cdot\text{s}^{-1})$

ESS results from D. Filges, R.D. Neef, and H. Schaal "Nucl. Studies of Different Target Systems for ESS," ICANS-XIII.

NSNS "effective" fluxes were converted from  $2\pi$  steradian current calculations. The differing distances from the target to the moderator were also corrected for.

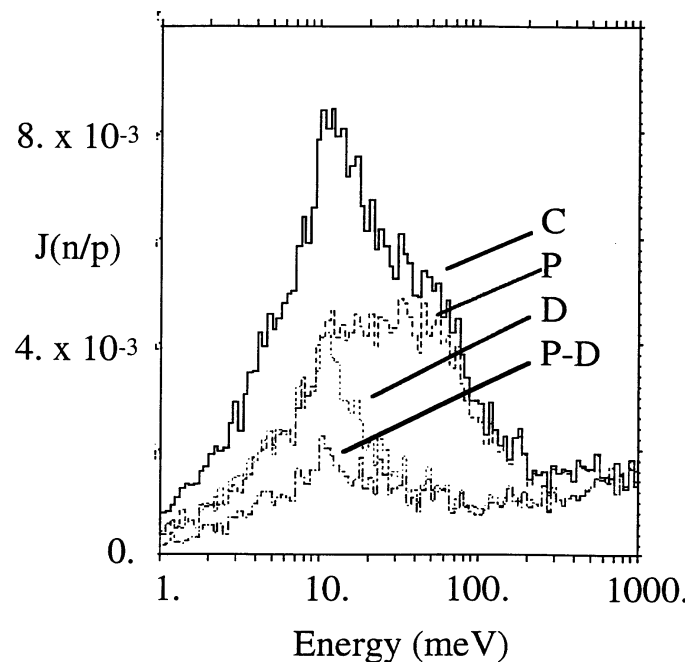
R is the ratio of the flux from the given target to that from a tantalum target.

### *Moderator enhancement*

It is desirable to maximise the neutron current ( $J$ ) emerging from the moderator and to minimise the time width ( $W$ ) of the neutron pulse. The results discussed in this section concern the use of moderator poisoning and moderator decoupling to reduce the time width of the neutron pulse. These methods successfully reduce the width but they also reduce the neutron current. Thus a trade-off is required between the neutron current and the width of the pulse. The best trade-off is determined by the target output requirements.

In order to better understand the width reduction produced by each method, the energy distribution produced will be shown first. In Figure 6, the number of neutrons per incident proton leaving a moderator face is shown versus the energy in MeV. The face used is one of the two on the front top cryogenic moderator (the two faces yield virtually identical results). Both poisoning and decoupling reduce the neutron current and using both reduces it further than using either separately. Poisoning (accomplished by gadolinium with a cut-off energy of  $\sim 1\text{-}2$  eV) changes the neutron spectrum only for energies  $\lesssim 1\text{-}2$  eV. Neutron capture in Gd above this energy is small. It may also be seen that decoupling modifies the neutron spectrum only for energies below the cadmium cut-off energy of  $\sim 4\text{-}6$  eV.

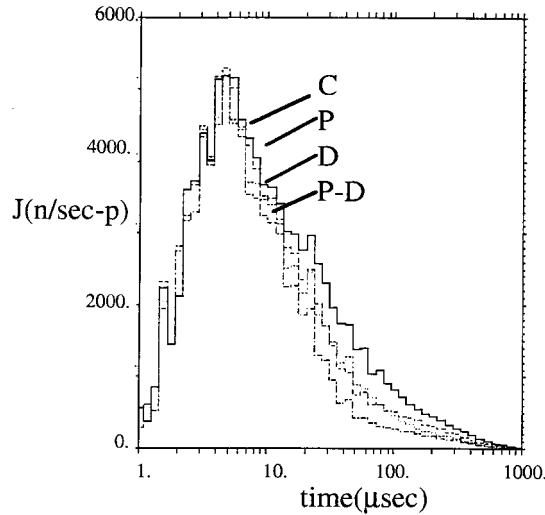
**Figure 6. Neutron energy distribution from the face of the front cryogenic moderator**  
*C = coupled, P = poisoned, D = decoupled, P-D = poisoned and decoupled*



These same effects can be seen for the ambient moderators except they are much less pronounced. This is because the peak in the energy distribution is located at a much higher energy relative to the cut-off energies of both cadmium and gadolinium which means that a much smaller proportion of the neutrons that eventually moderate to the peak energy are affected by the poisoning and the decoupling. This produces a smaller effect. The threshold for decoupling occurs at the cut-off energy for cadmium and the threshold for poisoning occurs at the cut-off energy for gadolinium. These thresholds are, however, much farther above the peak in the coupled energy distribution for the cryogenic moderator than for the ambient moderator.

The change in the shape of the neutron pulse for the cryogenic moderator due to poisoning and decoupling can be seen in Figure 7. The decoupling and poisoning preferentially affect the low energy particles which take longer to reach the moderator face. At small times all pulses are approximately the same. Only at large times do the poisoning and decoupling reduce the current and thus produce a smaller time pulse width as desired. The changes produced when an ambient moderator is considered are again smaller than for the cryogenic case. This is due to the same reasons discussed above. Time pulse distributions have also been calculated for various energy ranges, for example, 10 to 20 meV.

**Figure 7. Thermal neutron pulse from the face of the front cryogenic moderator**



The total currents from the moderator faces together with the pulse widths are shown in Table 3.

**Table 3. Maximum ( $J_{mx}$ ) and average ( $J_{av}$ ) currents and pulse widths ( $W$ ) for the front cryogenic (Faces 1 and 2) and the front ambient (Faces 3 and 4) moderators (Note that  $2\pi$  current is given instead of  $4\pi$  flux which can make the values appear a factor of  $\sim 4$  smaller)**

Neutron Currents and Pulse Widths						
Face	Coupled			Decoupled and Poisoned		
	$J_{av}$ ( $n \cdot cm^{-2} \cdot s^{-1}$ )	$J_{mx}$ ( $n \cdot cm^{-2} \cdot s^{-1}$ )	$W$ ( $\mu s$ )	$J_{av}$ ( $n \cdot cm^{-2} \cdot s^{-1}$ )	$J_{mx}$ ( $n \cdot cm^{-2} \cdot s^{-1}$ )	$W$ ( $\mu s$ )
1	$6.73 \times 10^{12}$	$9.53 \times 10^{14}$	38	$1.90 \times 10^{12}$	$8.17 \times 10^{14}$	15
2	$6.66 \times 10^{12}$	$9.20 \times 10^{14}$	38	$1.73 \times 10^{12}$	$7.83 \times 10^{14}$	14
3	$7.06 \times 10^{12}$	$1.74 \times 10^{15}$	30	$3.28 \times 10^{12}$	$1.60 \times 10^{15}$	17
4	$7.87 \times 10^{12}$	$1.91 \times 10^{15}$	26	$3.97 \times 10^{12}$	$1.80 \times 10^{15}$	17

**Analytic expression for the neutron current**

An analytic expression is given in [3] for the neutron current from a moderator face (this expression was originally from [4]). This analytic expression equates the neutron current ( $J$ ) to a product of two factors. One of these factors depends on the moderator parameters and the other

on the source of neutrons to the moderator. This offers the possibility of decoupling the performance of the moderator from that of the source thereby allowing an approximate separate optimisation. The expression is:

$$J(E) = S M(E)$$

with  $M(E)$  depending on moderator parameters and  $S$  depending on the source. Specifically:

$$M(E) = \left[ \left( I_{th} / I_{epi} \right) \left( E / E_T \right)^2 \exp(-E / E_T) + \Delta(E) E^\alpha \right], \quad S = I_{epi} = J(E)|_{1eV}, \quad (1)$$

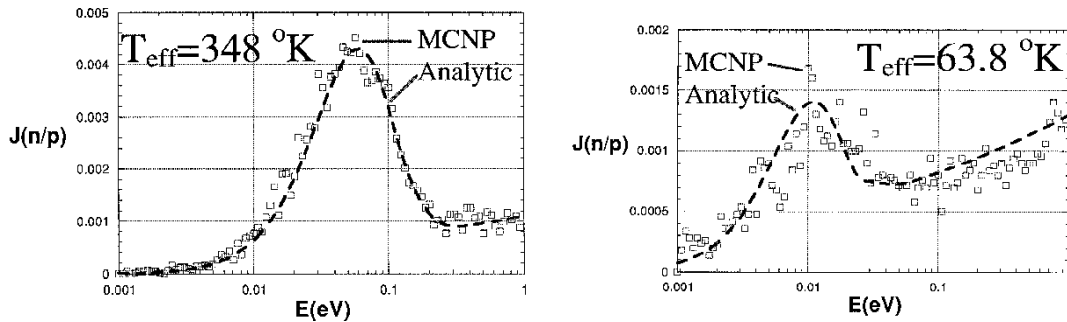
$$\Delta(E) = \left[ 1. + (5E_T / E)^\beta \right]^{-1}$$

where:  $\alpha = -2$ ,  $\beta = 7$ ,  $E_T = kT_{eff}$ .

- $E$  – the neutron energy
- $I_{th}$  – the total thermal neutron beam current
- $T_{eff}$  – an effective temperature somewhat greater than the physical temperature of the moderator

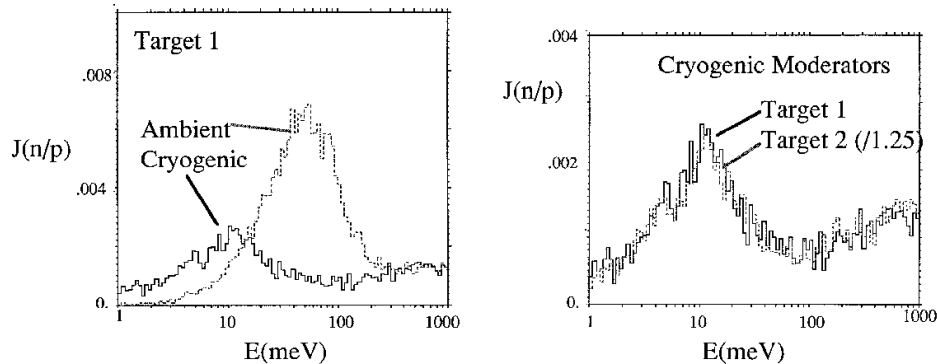
A comparison (Figure 8) between this expression and the neutronic current given by the Monte Carlo calculations shows excellent agreement for the ambient moderator face and reasonable agreement for the cryogenic moderator face.

**Figure 8. Comparison of spectra from a Monte Carlo calculation using MCNP and the analytic expression. This comparison is for a H<sub>2</sub>O moderator (top) and a liquid H<sub>2</sub> moderator (bottom)**



The success of the analytic separation into a moderator factor and a source factor is shown in Figure 9. At the top the spectrum from the ambient moderator is compared to that from the cryogenic moderator. These two moderators are placed symmetrically with respect to the Hg target in the target assembly model as indicated in Figure 5. The differences in the neutron current should be due only to the moderators themselves. The analytic expression implies that the currents from each moderator should thus be the same at 1 eV, as is true from the figure. At the bottom of the figure the moderators are identical but are placed at different distances above the Hg target. Thus the differences in the neutron current should be due to the source of neutrons to the moderators. The analytic expression would then predict that the neutron spectra from the two targets should differ by a constant (the constant being the neutron current at 1 eV). The plot at the bottom of the figure compares the spectrum from Target 1 to the spectrum from Target 2 scaled by 1.25. As predicted by the analytic expression they are (within statistics) the same. Thus the analytic treatment should provide a method of approximately optimising the moderators separately from the rest of the target station.

**Figure 9. Spectra showing the success of the analytic model. The spectra at the top are identical at 1 eV as predicted by the model. The spectra at the bottom are identical except for an overall normalisation. This is also predicted by the model.**



## Summary and conclusions for the neutronics

A Hg target is neutronically better than W or Ta, especially at the higher (>1 MW) power levels where the solid targets need more cooling water.

When a target, moderator and reflector are selected together with the geometry, the order of magnitude of the neutron current and the pulse width are determined. The results in this paper found methods which changed these neutronic properties by, at most, a factor of ~5. Thus, if a change in moderator performance of >10 is required methods other than those discussed here are needed.

It was also found that using a combination of decoupling and poisoning produced different results for an ambient moderator than for a cryogenic moderator. For an ambient moderator the pulse width could be reduced by a factor of ~2 which also resulted in a reduction in the neutron current of ~2. For a cryogenic moderator, the pulse width and current reduction was ~3.

An analytic expression was shown which should allow a better optimisation process. It should be emphasised that the target used in this study was a “first try” in a design study for NSNS and does not represent a final configuration. It is anticipated that most of the results found, however, will have a very general applicability and, for the most part, the “lessons” learned will apply in finding the best target configuration. The absolute latest neutronic results can be found in a paper by L.A. Charlton which is published in these proceedings.

## Target research

### *Mercury target performance evaluations*

The mercury target and its enclosing structure must be designed to sustain the time-averaged power loads as well as the nearly instantaneous power deposition during single pulses. Table 4 defines These time-averaged and single pulse loads. Since about 60% of the proton beam power is deposited in the target, the thermal-hydraulic system for the target is designed to remove a time-averaged power of approximately 0.6 MW corresponding to a proton beam power of 1 MW. Since the pulse frequency is 60 Hz, the amount of energy deposited in the target during a single pulse is about 10 KJ.

**Table 4. Power loads on the NSNS mercury target**

<b>Parameter</b>	<b>Value</b>
Energy of protons (GeV)	1
Pulse duration ( $\mu\text{s}$ )	0.5
Pulse frequency (Hz)	60
Percent of beam power deposited in mercury target (%)	~60
<b>Time-averaged loads</b>	
Beam current (mA)	1
Total proton beam power (MW)	1
Peak current density on target ( $\text{A}/\text{m}^2$ )	0.1
Peak beam power flux on target ( $\text{MW}/\text{m}^2$ )	
Peak volumetric heating rate in mercury ( $\text{MW}/\text{m}^3$ )	640
Peak volumetric heating rate in window ( $\text{MW}/\text{m}^3$ )	336
<b>Loads during a single pulse</b>	
Energy per pulse (kJ)	~10
Peak energy density in mercury ( $\text{MJ}/\text{m}^3$ )	10.7
Peak energy density in window ( $\text{MJ}/\text{m}^3$ )	5.6

### Handling of the time-averaged power

The power deposited in the target must be transported away without excessive mercury or stainless steel vessel temperatures or stresses. This is achieved using two separate mercury flow streams; one to transport the heat deposited in the mercury contained in regions interior to the vessel, and one to cool the stainless steel vessel structure. Three-dimensional computational fluid dynamics (CFD) simulations of the target main flow and the cooling jacket were performed using the general purpose CFD code CFDS-FLOW3D [5].

In the main mercury target flow stream, mercury enters the target through the two side channels at  $80^\circ\text{C}$  with a flow rate of 146 kg/s. The resulting bulk (volume averaged) temperature rise in the mercury is  $30^\circ\text{C}$ . As shown in Figure 10, the power deposited in the bulk mercury is effectively transported from the target with reasonable flow rates, pressure drop, and pumping power. The maximum temperature in the bulk mercury is less than  $160^\circ\text{C}$ . Temperatures in the re-circulation zone located near the flow baffles are less than  $150^\circ\text{C}$  because the heating rate for the specified parabolic profile is relatively low in this region.

As illustrated in Figure 11, a mercury flow rate of 14 kg/s in the cooling jacket provides adequate cooling for the stainless steel vessel. The inlet temperature is  $80^\circ\text{C}$ , and the temperature rise through the coolant passages formed by the two walls of the duplex structure is estimated to be less than  $30^\circ\text{C}$  (varies with passage location). The maximum stainless steel temperature on the target vessel wall is less than  $170^\circ\text{C}$  assuming good thermal contact or wetting of the mercury on the stainless steel wall. This temperature is judged to be acceptable from the materials compatibility viewpoint and is well below limits associated with excessive loss of strength or other mechanical properties.

Figure 10. Flow and temperature distributions in a preliminary mercury target design concept for a 1 MW proton beam (entire target cross-section shown)

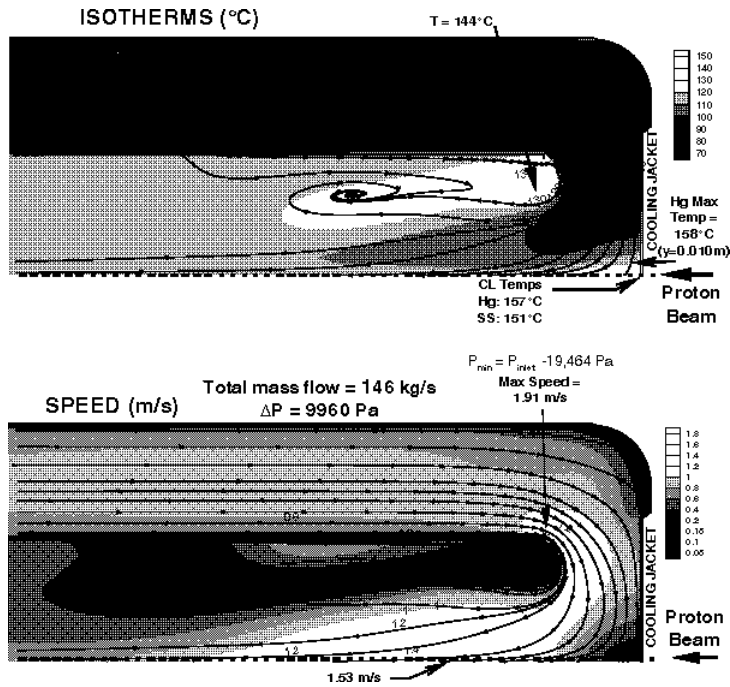
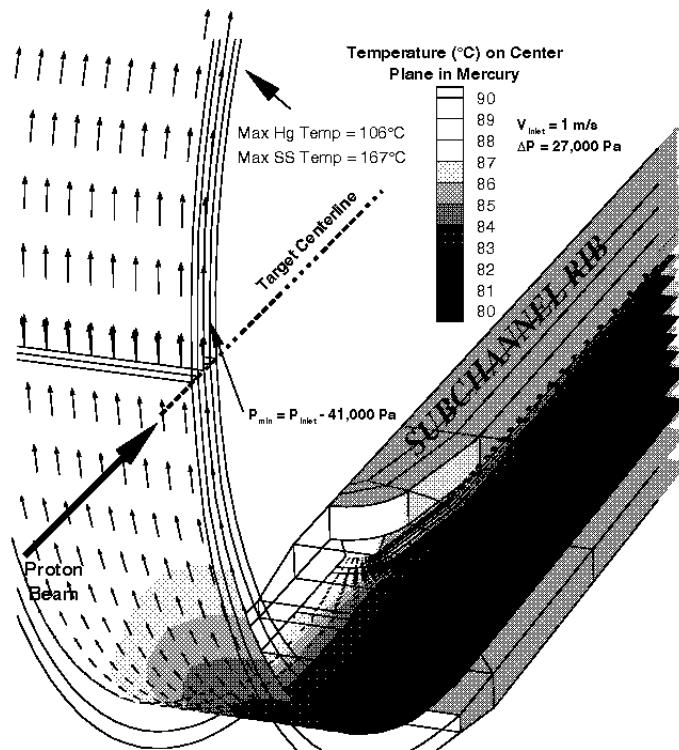


Fig. 11 Temperature and velocity profiles in the central channel of the target vessel cooling jacket for a 1 MW proton beam



## *Evaluation of the thermal-shock loads*

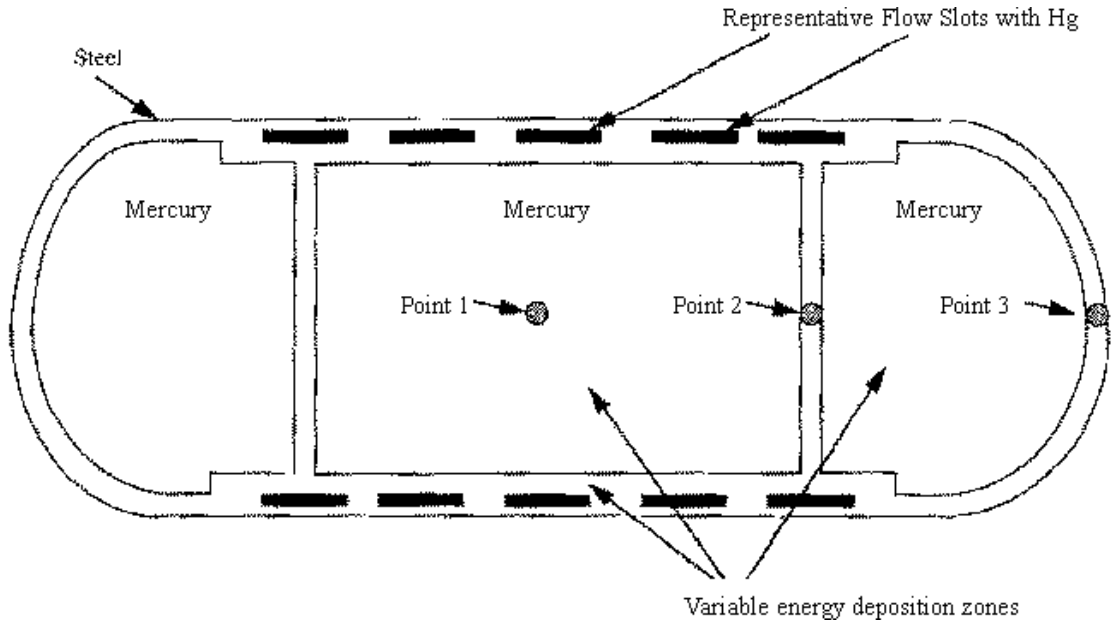
The interaction of the energetic proton beam with the mercury target leads to very high heating rates in the target. Although the resulting temperature rise is relatively small (a few °C), the rate of temperature rise is enormous ( $\sim 10^7$  °C/s) during the very brief beam pulse ( $\sim 1$   $\mu$ s). The resulting compression of the mercury will lead to the production of large amplitude pressure waves in the mercury that interacts with the walls of the mercury container, and the bulk flow field. Concerns exist in two main areas, viz., (1) impact of the effects of the combination of thermal shock on the wall due to its direct heating from the proton beam and the loads transferred from the mercury compression waves, and (2) impact of the compression-cum-rarefaction wave-induced effects such as fluid surging and potential cavitation. This has led to the conclusion that tests and analyses are required before using a liquid target (mercury) in the intense thermal load environment expected for a pulsed spallation neutron source.

The capability to understand and predict the propagation of the pressure pulses in the target (either liquid or solid) is considered to be critical for designing and constructing such a device. The CTH code [6] system developed at Sandia National Laboratory is being used to model this situation. CTH is a three-dimensional, shock-physics code, sometimes loosely referred to as a hydrocode. ORNL has developed significant expertise and related technology in use of this modelling framework to simulate explosive processes (such as molten metal-water vapour explosions) in enclosed fluid-structure systems. This technology is being used for characterising the current thermal-shock process in a coupled manner, simultaneously accounting for localised compression pulse generation due to rapid heat deposition, transport of the compression wave through the mercury, interaction of this wave with the surrounding structure, feedback to the mercury from these structures, and multi-dimensional reflection patterns including rarefaction-induced material fracture (or possible cavitation phenomena in fluids).

Whereas, a full-scale three-dimensional model for the NSNS target is under development, modelling efforts so far have examined the effects of rapid heat deposition at various target cross-sections as well as in idealised axi-symmetric geometries. These efforts have taken into account axially-and-radially varying transient heat deposition profiles in mercury and steel. A sample cross-section of the NSNS target where assessments are ongoing is shown in Figure 12 along with indications of radial variations in transient energy deposition at this particular target cross-section. Energy deposition occurs over 0.58  $\mu$ s. Resulting transient pressures in the mercury and principal stresses in the target structure are shown in Figure 13 for selected locations. It should be noted that the negative pressures in mercury shown in Figure 13 for Point 1 in Figure 12 at a time of about 50  $\mu$ s after the pulse imply that the mercury can support a rarefaction process. This result is an artefact of assuming a solid-like equation-of-state for mercury (Mie-Gruniesen form) and the presumption that liquid mercury will not cavitate. Onset of cavitation (either gaseous or vaporous) should produce significant reductions in system oscillations. However, it is recognised that related issues such as jetting and void generation-cum-collapse will need to be addressed. Developing a more realistic equation-of-state model for mercury in the regime expected in the SNS target is required to improve our understanding and predictive capability.

The minimum principle stress shown in Figure 13 for the stainless steel container at the baffle (Point 2 in Figure 12) and external shell region (Point 3 in Figure 12) near the location with peak heating shows several characteristic time scales. For Point 3, due to the significant impedance mismatches one notices short period ( $\sim 1$   $\mu$ s) variations in stresses which are associated with the characteristic time scale for transfer of pressure waves through the thickness of the stainless steel

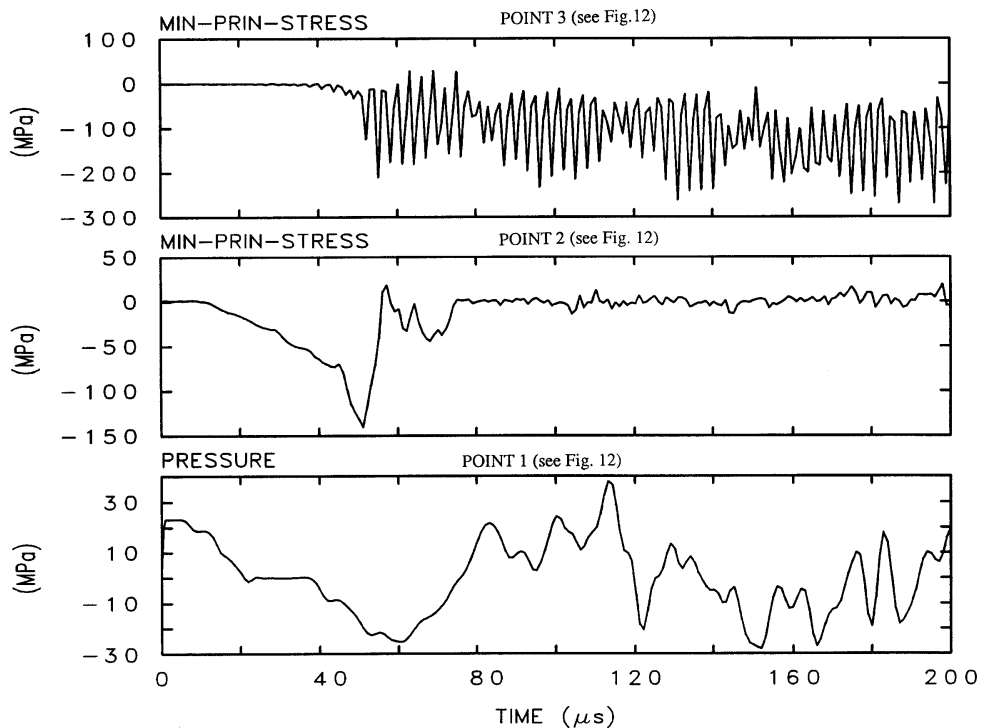
**Figure 12. CTH model schematic of NSNS target cross-section**



Notes (for 1-MW NSNS with 0.58 mic.sec. pulse):

- 1) Radial energy variation (=0.83 MJ/g/s at centre to 0.01 MJ/g/s at edges)
- 2) Mie-Gruniesen Equation-of-State (no cavitation)
- 3) Perfect contact of mercury with steel
- 4) Points 1, 2 and 3 are locations where pressure and stress variations are displayed in Figure 13.

**Figure 13. Variation of mercury pressure and stresses versus time at various locations (see Figure 12) in NSNS target (1-MW case)**



structure and result in a “ringing” type effect. The longer time scale variations (tens of microseconds) for Point 2 (superimposed with small oscillations) are due to the transport of pressure waves from the mercury to the baffle wall and transport through the steel. The resulting peak tensile stress in the stainless steel structure is found to be about -130 MPa. The (absolute) level of this stress is considerably below the yield stress of SS-316 steel. The acceptability of this stress level is not clear from a fatigue viewpoint, although existing data indicate that, with appropriate design modifications and optimisation resulting loads should be manageable. It is recognised that this stress must be examined in combination with other stresses and the dynamic (short duration) and cyclic (more than  $10^8$  cycles per month) nature of this stress must be appropriately considered along with the effects of irradiation.

### ***Critical issue and R&D plans for the mercury target***

Based mainly on the experience in operating mercury loops at the Institute of Physics in Riga, Latvia and the Centre for MHD Studies at Ben-Gurion University in Beer-Shiva, Israel, it has been concluded that the technology for all mercury flow circuit components, excluding:

- the target itself;
- spallation product related processing issues;
- specialised remote handling equipment;

already exists and is well understood and characterised. This means that the R&D programme does not need to focus on liquid metal circuit components such as pumps, heat exchangers, valves, seals, and piping. R&D plans for the first item listed above, i.e. the target itself, have been formulated and are discussed below, whereas the design and analysis of the target are not mature enough to determine whether and what types of technology development are required for the other two items. Further design and analysis of the liquid metal target system is therefore needed to define flow circuit processing and remote handling equipment requirements and thereby identify any development needs.

The three main elements of the Mercury Target R&D programme are:

- thermal shock tests and analyses;
- thermal-hydraulic tests and analyses;
- erosion/corrosion tests and analyses.

Because of the challenges posed by the intense, pulsed thermal energy deposition (~10 kJ deposited during each ~1  $\mu$ s pulse), the key feasibility issue that will be addressed in early R&D efforts is thermal shock. Simple pressure pulse tests and use of small-scale capsules of mercury in particle accelerator targets are planned for the near-term to improve our understanding of this phenomenon, and to benchmark and further develop our predictive models. Thereafter, effects on bulk fluid motion (e.g. surging), the impact and influence of engineered mitigative measures (e.g. possible use of helium bubble injection, etc.) and the effects of transient cavitation-cum-gas dissolution will need to be characterised for arriving at a qualified methodology for design applications.

Thermal-mechanical analysis and testing of the mercury target is also planned. The major issue associated with the thermal-mechanical performance of the mercury target is removal of the time-averaged power loading without excessive (1) temperatures in structural components or the mercury itself, (2) thermal stresses in the target structure, and (3) pressure drops in the flow circuit. The Thermal Hydraulic Tests and Analyses programme is divided into six elements including: (1) computational fluid dynamics (CFD) simulation of the target, (2) creation of a central mercury handling system, (3) development of diagnostics, instrumentation for mercury, (4) flow distribution tests using water as a surrogate fluid, (5) mercury thermal hydraulic parameter tests, and (6) full-scale mercury tests with steady heat sources (no pulsed heating). All thermal-hydraulic testing is scheduled to be completed prior to the completion of the final design and fabrication of the target structure.

Testing is also required to establish that the mercury target system can operate with minimal corrosion of the target and its support equipment. Past experience with liquid metals, and in particular with mercury, has demonstrated that erosion of surfaces can be a problem for certain container materials. Furthermore, mercury corrosion has been shown to be greatly enhanced in flowing systems that have temperature differences in the flow loop. Corrosion is a concern for the mercury target system because it could potentially (1) lead to failure of the target vessel, (2) cause blockage of heat exchanger, valves, or other mercury coolant loop equipment due to transfer of corroded material from one region to another, or (3) lead to excessive contamination of mercury loop equipment due to transport of radioactively contaminated species from the target region to other regions in the mercury coolant loop. Following completion of materials compatibility tests, erosion/corrosion tests will be conducted on a full-scale thermal-hydraulic loop which will be assembled for the thermal-hydraulic tests discussed above.

## **Materials technology issues for the National Spallation Neutron Source target station**

High power spallation neutron sources like the NSNS will place significant demands on materials performance. The target system will be subjected to an aggressive environment that will degrade the properties of materials. Indeed, the satisfactory performance of materials for sufficiently long time periods will determine the viability of the target station for the facility. Components at the heart of the facility include the liquid target container and return hull, beam windows, support structures, moderator containers and beam tubes, for example. A recent workshop summarised the present state of knowledge of materials for spallation sources, and began implementing materials R&D programmes for the NSNS and ESS facilities [7]. The materials R&D programme for the NSNS is oriented toward materials qualification. By this is meant informed selection of materials based on existing experimental data and analysis, testing in actual and partially simulated application environments, lifetime estimates for the NSNS environment, and iteration and optimisation of properties to improve performance. The programme is structured around technical areas expected to be key to the design, fabrication, and performance of the target station. The five overlapping areas can be termed radiation effects, compatibility, materials engineering, in-service surveillance and technical support.

Most of the present section will concentrate on radiation effects and compatibility. Materials engineering refers to the work necessary to translate knowledge gained in these areas into fabrication of components so that the necessary properties are achieved. Questions include, for example, methods of welding and joining, assembly, heat treatments, and quality assurance. An in-service surveillance programme is being developed to monitor and improve the performance of actual components. More importantly, standard specimens in a well-characterised environment that are more suitable than service components for testing and characterisation will be irradiated. Parameters to be monitored

include dose, dose rate, temperature, and target chemistry. The technical support function covers both the R&D phase of the project as well as the detailed design and construction phases. It gives a wide variety of support to the project that includes supplying materials properties data to target station engineers, and the solution of numerous applications-specific issues expected to arise.

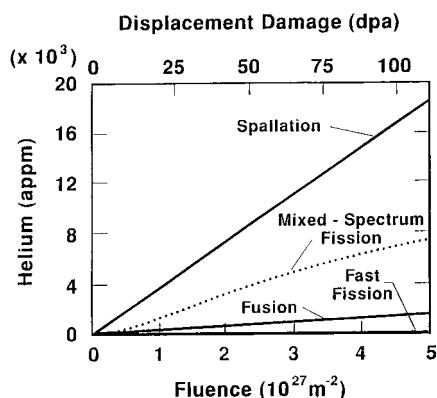
### ***Radiation effects***

Radiation effects issues are described from a somewhat general perspective here. A more complete background on this area is given in [8], and a detailed description of areas of special relevance to spallation neutron sources is contained in [7,9]. The main problems in structural materials are expected to centre around embrittlement, hardening and associated loss of ductility, and irradiation creep. Swelling at the modest temperatures currently under consideration for the NSNS, <250°C, is not likely to be a serious problem. Most experimental data on radiation effects in materials have been obtained in fission reactors. A limited amount of data from spallation neutron sources has also been accumulated. For example, some very low-dose information is available from neutron scattering targets removed from ISIS and LANSCE. Some higher dose data are available from the beam-stop experimental area of LANSCE. A new experiment is now under fabrication for irradiation in this facility to obtain moderate- and low-dose information on a number of materials intended for possible application in APT and NSNS. Supplementary information that is useful in technological investigations of radiation damage behaviour is available from ion and electron irradiation in the few-MeV range.

By contrast to the few-MeV range of neutrons in fission reactors, materials in the NSNS will be exposed to protons in the GeV range and below, and to neutrons spanning from the proton energy down to thermal energies. The common unit of measure of displacement damage is the displacement per atom, dpa. One dpa is the dose at which, on average, each atom in the material has been displaced once. Required lifetimes of the most highly irradiated components such as the target nose, target container and beam windows are expected to be in the range of tens of dpa. Transmutation rates in the spallation environment will be orders of magnitude higher than in fission reactors. The species He and H, as well as heavier transmutation products will be of concern. H production is calculated to be in the range of 1000 appm/dpa. In particular, He production is calculated to be in the range of 100 to 200 appm/dpa as compared to 0.2 to 0.5 appm/dpa in fission reactors. Figure 14 shows graphically the He production rates in several neutron spectra. Helium is an insoluble rare gas that can increase the severity of radiation effects by triggering or increasing swelling, and by causing or exacerbating grain boundary embrittlement as well as hardening the material to promote overall ductility loss. The effects of the high He production will be determined in the present R&D programme.

The NSNS is expected to operate in a pulsed mode. Most radiation effects data have been accumulated in steady conditions, albeit with interruptions for various reasons, but with no deliberate pulsing. During a pulse the instantaneous damage rate will be up to about  $10^{-2}$  dpa/s. The highest available damage rate in fission reactors is approximately  $10^{-6}$  dpa/s. In addition to the differences in microstructure caused by differences in instantaneous damage rates, the on-off cycle changes the kinetics of point defect build-up, which may result in changes in the accumulation of extended defects, such as dislocation loops. These changes in extended defect microstructure may therefore result in different mechanical properties than in steady irradiations. Some data is available from pulsed irradiations using ion accelerators [10]. In that work it was found that pulsing at different pulse intervals caused changes in the sizes of dislocation loops, which would be expected to lead to changes

**Figure 14. Helium generation as a function of neutron fluence or displacement damage in several typical particle spectra in a stainless steel containing 15% nickel. The nickel two step reaction is responsible for the high helium production rate in a mixed neutron spectrum.**

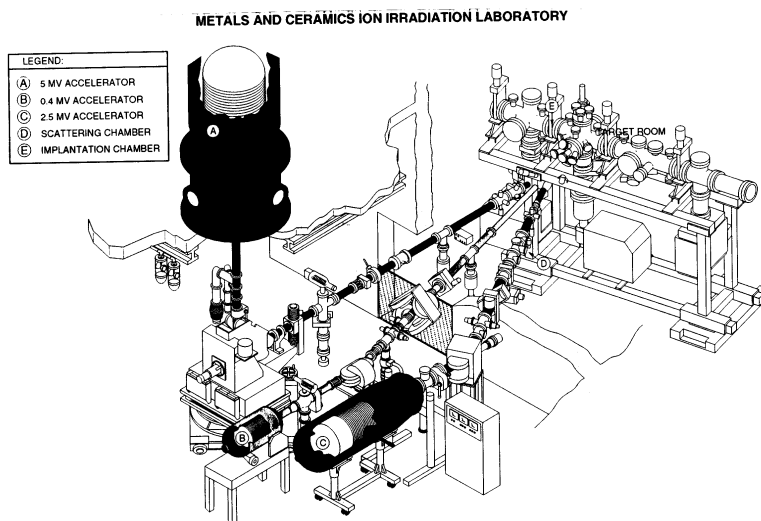


in mechanical properties in a bulk specimen. These results were consistent with theoretical predictions for the effects of pulsing. More work may be required in this area to support the NSNS. However, in the long run an in-service surveillance facility will no doubt be the best source of information on the effects of pulsing.

Also shown in Figure 14 is a special case encountered in mixed spectrum fission reactors. A few isotopes have high helium production cross-sections for thermal neutrons. For example, there is the well known  $^{10}\text{B}(n,\alpha)^7\text{Li}$  reaction, with the very high thermal reaction cross-section of nearly 4,000 barns. This reaction has been used to study the effects of simultaneous He and damage production by adding boron to various materials. Of more interest for the stainless steels of intended application in the NSNS Hg container is the two step reaction  $^{58}\text{Ni}(n,\gamma)^{59}\text{Ni}(n,\alpha)^{56}\text{Fe}$ . In a stainless steel with nickel composition of about 15%, about 68% of which is  $^{58}\text{Ni}$  in natural nickel, this reaction will produce the amount of helium as a function of dose shown by the dashed line in Figure 14. This amount of He approaches half that expected in the spallation environment at high doses. Thus, mixed spectrum fission reactor irradiations can be utilised to provide relevant information on the effects of He on stainless steels irradiated in a spallation environment.

The planned experimental portion of the radiation effects R&D programme for the NSNS consists of three parts: (1) Available spallation facilities at LANSCE and SINQ will be used for specimen irradiations. These will provide the most prototypic results, with the exception that pulsing will not be possible. In addition, the doses expected are only in the low to moderate range. (2) Special multiple beam irradiations will be carried out at the Triple Ion Facility at ORNL, Figure 15. These will make possible the investigation of the effects of simultaneous damage and gas production, by bombarding with self-ions of the material such as Fe or Ni, and simultaneously injecting He and H at typical levels for a spallation environment. Results will reveal the effects on microstructures and give some applicable information on changes in mechanical properties by means of surface hardness tests. High doses will be achieved. Pulsing effects may also be investigated with these accelerators. (3) High dose neutron irradiations will be carried out in the HFIR reactor, making use of the helium production capability shown by the dashed line in Figure 14. These reactor experiments will yield suitable specimens for true bulk mechanical testing, and give information on the effects of spallation-relevant simultaneous high dose and high helium accumulation. A combination of these three approaches will be required, since they give complementary information and none alone is adequate. The product of this work is the determination of acceptable parameter windows and estimated lifetimes for operation of the materials in the NSNS.

**Figure 15. The triple ion facility at Oak Ridge National Laboratory, where specimens can be exposed simultaneously to beams of Fe, He, and H, for example**



In parallel with the above experimental work, a programme of modelling, analysis and computations is being carried out. This work is aimed at translating the calculated particle spectra into measures of the radiation damage to be experienced by materials and components. Important measures such as displacement damage, helium and hydrogen production rates, and transmutation rates of other species both in structural materials and in the Hg target are being calculated.

Wherever possible, calculations will be compared with experiments. For example, helium contents of materials irradiated in LANSCE or SINQ will be measured and compared with predictions.

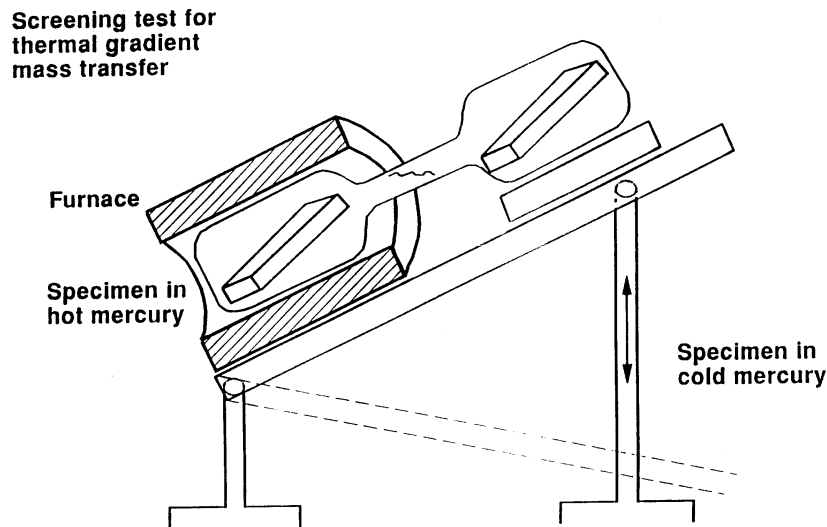
### ***Compatibility***

This effort addresses the compatibility and corrosion behaviour of materials in contact with liquid Hg, such as the container and flow baffles. The work also covers issues in associated water cooled systems. Previous experience in liquid metal systems has been evaluated for its applicability to the present system. An R&D programme for mercury compatibility with containment materials is presently in progress. An up-to-date background on this area is contained in the proceedings of a recent workshop [11]. In water systems there is already a large amount of experience. Considering this and the fact that water systems will be auxiliary systems rather than the heart of the target itself, it is considered that only a minimal level of R&D is required for water compatibility issues. The main issues in the Hg systems are considered to be temperature gradient mass transfer, liquid metal embrittlement, and wettability of materials by Hg [12]. Experimental evaluation now underway includes constant extension rate tensile tests for liquid metal embrittlement (LME) and rocker tests for temperature gradient mass transfer. Further testing is planned to include notched tensile and fatigue tests in mercury as well as small scale recirculating loop tests. This work interfaces closely with related engineering R&D on thermal hydraulics and mechanical design. In particular, it supports planned work on more prototypic large scale and high flow rate engineering test loops.

In temperature gradient mass transfer, material in higher temperature portions of a circulating system is removed and deposits in lower temperature regions. This effect can be large and may lead to narrowing and even blockage of flow paths. Important parameters include operating temperature  $T$ , the  $\Delta T$  between various parts of the system, solubility of alloy components in the liquid Hg as a function of temperature, solution and deposition rate constants, and flow rate. In austenitic stainless steels, the primary candidate material for the mercury container, Ni may dissolve preferentially from the alloy and thus be of concern for temperature gradient mass transfer. Keeping the operating temperature of the system below about 250°C, however, is expected to reduce this effect to an acceptable level. Part of the R&D effort is to determine quantitatively the  $T/\Delta T$  windows that are acceptable for this application.

The “rocker” test was devised for screening materials and  $T/\Delta T$  combinations for temperature gradient mass transfer. Figure 16 is a schematic of this apparatus. One end of a dog-bone shaped mercury-containing chamber is surrounded by a furnace. The other end is surrounded by room temperature air. Specimens of the material of interest are contained in each chamber. The configuration is rocked from end to end at intervals of minutes, alternately exposing one specimen to hot mercury and the other to cooler mercury. After testing, specimens are examined and weighed to determine mass transfer. Results of the first rocker tests are summarised in Table 5. In general, weight changes were very slight, and the addition of magnesium to the mercury did appear to promote wetting of the steel.

**Figure 16. Rocker test configuration for screening materials with respect to temperature gradient mass transfer – “ROCKER TEST”**



Liquid metal embrittlement (LME) is being investigated using constant extension rate tensile tests. Wettability can be examined as well by varying the Hg chemistry. Generally, it is expected that when Hg wets the material, liquid metal embrittlement is possible, although not inevitable. When there is no wetting it is thought that LME is not possible, although efficient heat transfer may then become a problem. Both embrittlement and wetting are being examined as a function of temperature and of chemistry by adding solutes to the mercury. Results of tests completed thus far are summarised in Table 6. No liquid metal embrittlement effects were noted, primarily measured by total elongation and reduction of area, and the addition of small amounts of gallium to mercury increased wetting of the type 316 stainless steel.

**Table 5. Results of initial rocker screening tests of type 304SS in mercury**

Average maximum temperature: 300°C Average DT: 78°C Time: 2,000 h Cycles (60s/18s): 92,000						
Capsule environment	Mg in Hg	Visual wetting		Weight change, mg/cm <sup>2</sup>		Comments
		Hot	Cold	Hot	Cold	
Air	None	No	Yes	-.14-	.12	Hg fairly bright and shiny
He	None	No	No	-.14	-.02	Hg very bright and shiny
Vac	None	Yes	Yes	-1.53	+.004	Deposit on cold leg surface
Air	100 ppm	No	Yes	-.04	-.02	Dark residue in Hg
He	100 ppm	Yes	Yes	-.92	-.03	Dark residue in Hg

**Table 6. Results of LME constant extension rate tensile tests on 316SS**

Environment	Strain rate (cm./cm.s)	Strength yield	(Mpa) Ultimate	Reduction in area (%)	Total elongation (%)	Comments
Air	9.5×10 <sup>-6</sup>	376	664	78	32	Little or no wetting
Hg <sup>a</sup>	9.6×10 <sup>-6</sup>	364	673	72	30	
Hg+1% Ga <sup>a</sup>	9.4×10 <sup>-6</sup>	393	673	80	33	
Air	4×10 <sup>-3</sup>	4.35	659	75	24	Sample wet
Hg+1% Ga <sup>a</sup>	7×10 <sup>-3</sup>	4.35	687	77	30	

<sup>a</sup> Ultrasonically agitated prior to test (to promote wetting).

Future LME tests include: • Sensitised 316SS  
 • Welded 316SS  
 • Fatigue

## Conclusions

Preliminary design and analysis indicate that a very attractive short-pulse neutron source operating at 1 MW of proton beam power can be constructed for the NSNS using liquid mercury as the target material. Research and development activities have been identified to validate design concepts and to allow future upgrades to higher power levels. Reasonable design configurations have been proposed for major component assemblies and remote handling concepts have been developed. A complete description of the NSNS project can be found in the Conceptual Design Report [13].

## REFERENCES

- [1] T.A. Gabriel *et al.*, “CALOR87: HETC87, MICAP, EGS4, and SPECT, A Code System for Analysing Detectors for Use in High Energy Physics Experiments”, Proceedings of the Workshop on Detector Simulation for the SSC, Argonne National Laboratory, 24-28 August 1987.
- [2] J.F. Briesmeister, ed., “MCNP – A General Monte Carlo Code for Neutron and Photon Transport”, Los Alamos Scientific Laboratory Report LA-7396-M, Rev. 2 (September 1986).
- [3] J.M. Carpenter and W.B. Yelon, “Neutron Sources,” *Methods of Experimental Physics*, Vol. 23A, 99 (1986).
- [4] C. J. Westcott, Chalk River Report CRRP 960 (Revised 3rd addition) (1970).
- [5] “CFX 4.1 Flow Solver User Guide”, Computational Fluid Dynamics Services, AEA Technology, Harwell Laboratory, Oxfordshire, United Kingdom, October 1995.
- [6] J.M. McGlaun and S.L. Thompson, “CTH – A Three Dimensional Shock-Wave Physics Code, “*Intl. Journal of Impact Engineering*”, Vol. 10, 251-360, 1990.
- [7] L.K. Mansur and H. Ullmaier, Proceedings of the International Workshop on Spallation Materials Technology, 23-25 April 1996, Oak Ridge, Tennessee, CONF-9604151.
- [8] L.K. Mansur, “Theory and Experimental Background on Dimensional Changes in Irradiated Alloys,” *J. Nucl. Mater.* 216 (1994) 97-123.
- [9] L.K. Mansur, “Radiation Materials Science and Technology for Spallation Neutron Sources”, presented at the Symposium on the Savannah River Accelerator Project and Complementary Spallation Neutron Sources, Columbia, SC, 14-15 May 1996.
- [10] E.H. Lee, N.H. Packan, M.B. Lewis, and L.K. Mansur, “Effects of Rapidly Pulsed Ion Bombardment on Microstructure and Phase Stability in a Ti-Modified Stainless Steel”, *Nucl. Inst. and Meth.*, B16 , 251-259, (1986).
- [11] B.R. Appleton and G.S. Bauer, Proceedings of the International Workshop on the Technology and Thermal Hydraulics of Heavy Liquid Metals (Hg, Pb, Bi, and their Eutectics), Schruns, Austria, CONF-9603171, 24-29 March 1996.
- [12] a) J.R. DiStefano and S.J. Pawel, “Compatibility of Materials with Liquid Metal Targets for SNS Applications”, in [11].  
b) J.R. DiStefano, S.J. Pawel, and J.H. DeVan, “Mercury Compatibility Issues for ORSNS”, in [7].
- [13] NSNS Conceptual Design Report, in press, Oak Ridge National Laboratory, June 1997.



## **OVERVIEW OF THE SPALLATION NEUTRON SOURCE PROJECT IN JHF**

**M. Furusaka and H. Ikeda**

Neutron Science Laboratory (KENS)

High Energy Accelerator Research Organisation (KEK)

Tsukuba-shi 305, Japan

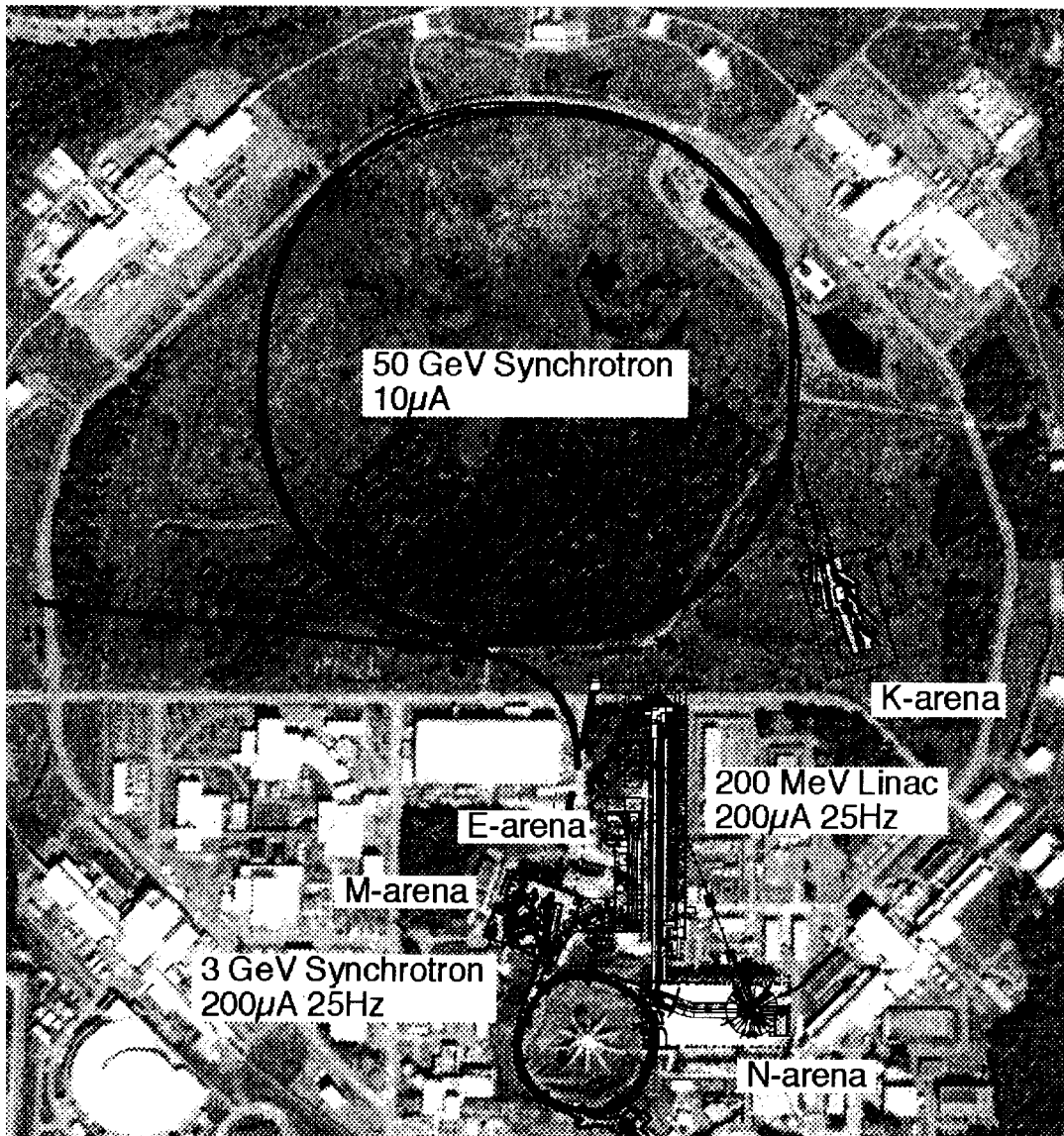
### **Abstract**

The Japan Hadron Facility Project (JHF) aims to advance the multi-disciplinary research fields, such as materials science, life science, and nuclear and particle physics, by using high intensity beams supplied by a proton accelerator complex. The pulsed spallation neutron source (SNS) facility (N-arena [1]) is one of the four facilities in the JHF project, which will become the most powerful pulsed SNS in the world when it is completed.

The Japan Hadron Facility Project (JHF) aims to advance the multi-disciplinary research fields, such as materials science, life science, and nuclear and particle physics, by using high intensity beams supplied by a proton accelerator complex. The pulsed spallation neutron source (SNS) facility (N-arena [1]) is one of the four facilities in the JHF project, which will become the most powerful pulsed SNS in the world when it is completed.

The JHF accelerator complex consists of 1) 200 MeV linac, 2) 3 GeV proton synchrotron (PS) with 200  $\mu\text{A}$  proton beams and 3) 50 GeV PS with 10  $\mu\text{A}$  protons, as shown in Figure 1. N-arena will utilise proton beam from the 3 GeV PS, which has a time-averaged beam power of 0.6 MW in about 1  $\mu\text{s}$  pulses at a repetition rate of 25 Hz. It will be upgraded to 1.2 MW or more in the future.

**Figure 1. Overall layout of the JHF project**



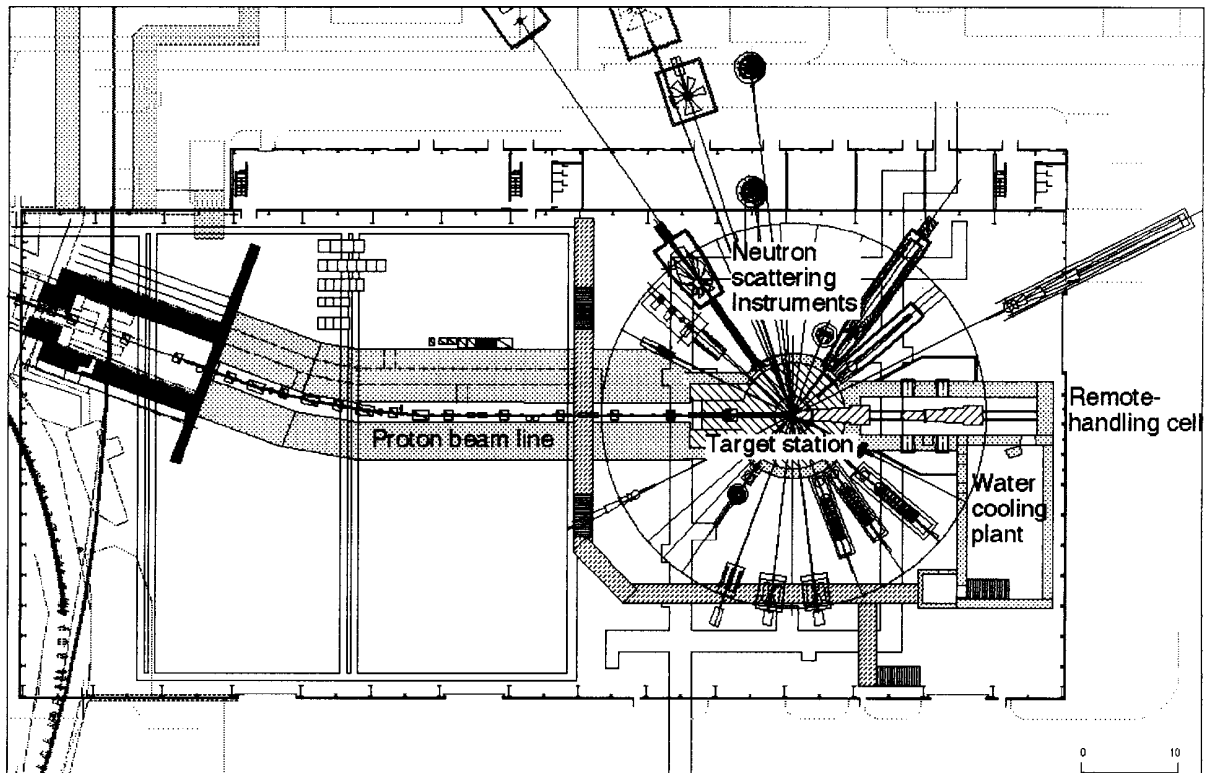
A schematic layout of N-arena is shown in Figure 2. In the N-arena, nearly thirty spectrometers will be installed, such as small-angle scattering instruments, reflectometers, diffractometers, inelastic spectrometers, polarisation instruments and so on. We re-use the existing experimental hall (East Counter Hall), which is currently used for nuclear and particle physics experiments. We have employed a horizontal proton beam-injection scheme and horizontal extraction of the neutron-generation target to the downstream direction of the proton beam for maintenance.

Two other experimental facilities are presently planned at the 3 GeV PS. The first one will utilise muons for material sciences, muon-catalysed fusion as well as particle physics, such as a  $\mu$ -e conversion experiment (M-arena). The second one will be devoted to nuclear physics research, using an ISOL-postaccelerator type radioactive beams (E-arena).

At the 50 GeV PS, various types of intermediate-energy nuclear physics are being planned which would use kaons, pions, antiprotons and primary beams, including heavy ions. Experiments of kaon rare decays and other symmetry tests, such as an experiment of neutrino oscillation using the Super-Kamiokande will be also carried out (K-arena).

We already reconstructed our laboratory (KEK) in which two institutes were established as from April 1997. The main purpose of the reconstruction was to promote the JHF project. The JHF project is a five-year project, starting from FY1998 and finish construction in FY2002. KEK has already sent a budgetary request for JHF to the Japanese government and is awaiting a decision.

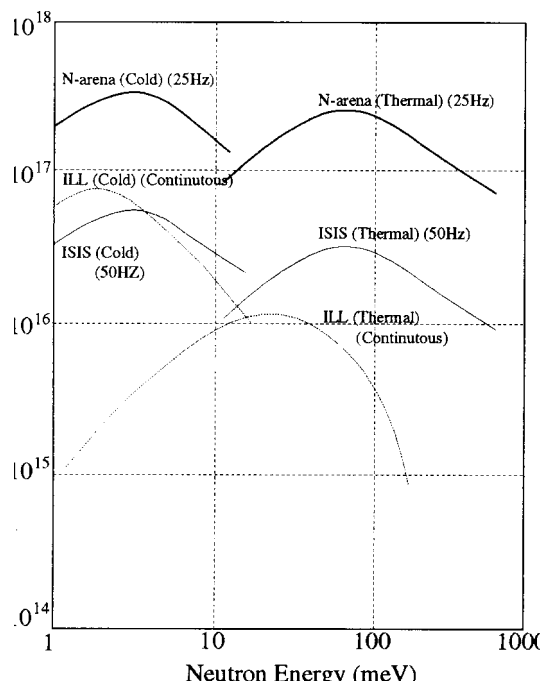
**Figure 2. Schematic layout of N-arena**



The proton beam power is only a part of the measure which characterises a SNS. More important is the overall performance of the system composed of a Target-Moderator-Reflector-Assembly (TMRA) and instruments for neutron-scattering experiments. For example, the current SNS at KEK (KENS) has a proton power of only 3 kW, compared to 160 kW at the current most powerful pulsed SNS in the world, ISIS at Rutherford Appleton Laboratory in United-Kingdom; however, the overall performances of some of the instruments at KENS are approaching 1/2-1/3 of that of ISIS in the case of the instrument viewing a cold source. In order to realise as high efficiency as possible, even at a megawatt class source, we are now performing extensive research and development tasks to optimise the TMRA system using a mock-up test facility at Hokkaido University and a neutronics calculation code system [2,3].

Instantaneous thermal and cold neutron intensity expected for N-arena is shown in Figure 3, together with those for ISIS and ILL in France, the world's most powerful research reactor. Note that an instantaneous neutron intensity per pulse is a good measure of the useful neutron flux.

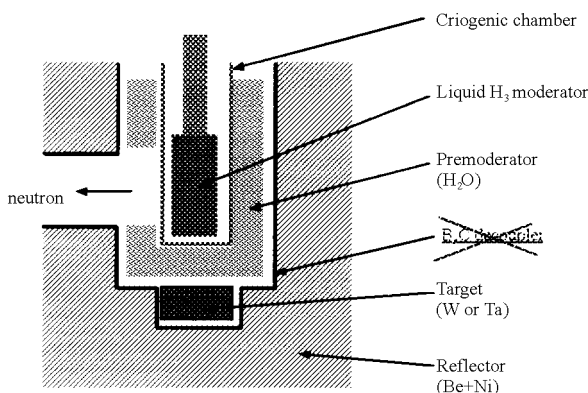
**Figure 3. Instantaneous cold and thermal neutron intensity per pulse expected for the N-arena, compared with those of ISIS and ILL**



For the target, we have two options, either a heavy-water cooled solid metal-plate target made of tungsten or tantalum or a liquid metal target system, such as mercury. For a future upgrade to over 1 MW, the use of a liquid-metal target is necessary. Thermo-hydraulic experiments for the target systems for both cases are now underway.

A sketch of the newly developed very high-performance cold moderator, namely, a coupled liquid-hydrogen moderator with a water premoderator is shown in Figure 4. Normally, such a moderator is surrounded by a decoupler made by absorbing material, such as B<sub>4</sub>C, without any premoderator. By removing the decoupler, however, the neutron flux becomes about three times as intense at the expense of a slight increase in the neutron pulse width. And furthermore, by adding

**Figure 4. Schematic layout of a coupled-liquid hydrogen moderator with a premoderator**



a water layer of a few centimetres another gain-factor of 2 in intensity is observed. This new moderator system is best for the instruments which are not affected by a neutron-pulse structure, such as small-angle scattering instruments and reflectometers. For these instruments, the size of moderator surface viewed from the sample should be small, due to the requirement of incident-beam collimation. A recent study shows that an increase in luminosity of about a few tens of a per cent could be achieved by putting a hole in middle of the liquid-hydrogen moderator (re-entrant hole) and narrowing the neutron beam-extraction hole.

Research and development of other types of moderators – such as the moderator for a high resolution spectroscopy, as well as the material choice for the reflector – is ongoing.

## REFERENCES

- [1] H. Ikeda and M. Furusaka, ed., “Proceedings of the International Workshop on Science in Neutron-Arena of JHP”, (26-27 March 1996, KEK, Tsukuba).
- [2] Y. Kiyonagi, N. Watanabe and H. Iwasa, “Premoderator Studies for a Coupled Liquid-Hydrogen Moderator in Pulsed Spallation Neutron Sources”, *Nucl. Inst. Methods*, A343 (1994) 558.
- [3] N. Watanabe, Y. Kiyonagi, M. Furusaka, “Recent Progress in Developing High-Efficiency Cryogenic Moderators”, 13th Meeting of the International Collaboration on Advanced Neutron Sources (1995, Villigen, PSI) 659.



# **SESSION III**

## **Shielding**

*Chairs: N. Mokhov and K. Hayashi*



***Shielding Benchmark  
Problem – Review of Analysis***



**INTERCOMPARISON OF NEUTRON TRANSMISSION  
BENCHMARK ANALYSES FOR IRON AND CONCRETE SHIELDS IN LOW,  
INTERMEDIATE AND HIGH ENERGY PROTON ACCELERATOR FACILITIES**

**Yoshihiro Nakane and Yukio Sakamoto**  
Japan Atomic Energy Research Institute, Japan

**Katsumi Hayashi**  
Hitachi Engineering Company, Japan

**Takashi Nakamura**  
CYRIC, Tohoku University, Japan

**Abstract**

The analyses of four neutron transmission benchmark problems for iron and concrete shields in low, intermediate and high energy proton accelerator facilities were compiled for evaluating the calculation codes and the nuclear data used in the codes. Result comparisons revealed future tasks of code and data improvements.

## **Introduction**

Accelerators are now increasing in number, beam energy and current in many fields of application such as basic science, industry, medicine and so on. In their shielding designs, nowadays, several calculation codes and nuclear data are used for source-term calculation of neutron and photon emission from the target and transport calculation in the bulk shield. Accuracy of calculation results, however, is not clearly evaluated in contrast to the nuclear reactor shielding design. Therefore, it is very important to analyse neutron transmission benchmark problems. The comparison between calculations and experiments will give us good information for modifying codes and estimating systematic errors and safety margins in the design. Furthermore, we may find what kinds of study should be done in the future in this field from these comparisons.

## **History**

The Accelerator Shielding Working Group of the Research Committee on Reactor Physics in JAERI has compiled [1,2] five kinds of experiments on thick target neutron yields by 113, 256 and 800 MeV protons, 710 MeV alphas and 150-270 MeV electrons, and shielding data of neutrons and photons generated by 52, 65 and 500 MeV protons for SATIF-1. Analyses of the experiments were carried out by the Working Group, and the results of analyses were presented [3] at SATIF-2. In the meeting, intercomparisons of benchmark analyses by each organisation using individual methods were proposed. According to the proposal, four kinds of neutron transmission benchmark problems for iron and concrete shields in low, intermediate and high energy proton accelerator facilities were prepared [4] by the Working Group for discussion at SATIF-3. The benchmark problems were widely distributed throughout the world. The WWW homepage was also prepared for the participants and the colleagues who were interested in analysing the benchmark problems.

## **Benchmark analyses**

### ***Benchmark problems***

Four neutron transmission benchmark problems have been prepared from neutron transmission experiments on iron and concrete shields for the proton energy range from 43 MeV to 24 GeV.

- No. 1 Transmission of quasi-monoenergetic neutrons generated by 43 MeV and 68 MeV protons through iron and concrete shields [5,6].
- No. 2 Neutron fluxes in and around iron beam stop irradiated by 500 MeV protons [7,8].
- No. 3 Reaction rate distributions inside thick concrete shield irradiated by 6.2 GeV protons [9].
- No. 4 Neutron and hadron fluxes inside iron beam dump irradiated by 24 GeV protons [10].

### ***Calculation methods***

Calculation methods are listed in Table 3.1 together with participants. Five, three, one and two kinds of calculations can be compared for the problem No. 1, No. 2, No. 3 and No. 4, respectively. For the problem No. 1, the results calculated with the LAHET Code System (LCS) were also submitted by P.K. Sarkar and G.P. Rao of Variable Energy Cyclotron Centre in India. The results, however, are not shown in this paper because of an author's request of withdrawal.

**Table 1. Calculation codes and participants**

Participant	Organisation	Calculation code	Benchmark problems			
			No. 1	No. 2	No. 3	No. 4
H. Nakashima Y. Nakane	JAERI (Japan)	Modified HETC-KFA2	○			
N. Nakao	KEK (Japan)	MORSE-CG	○			
K. Ueki	Ship Research Institute (Japan)	MCNP4A	○			
N. Yoshizawa	Mitsubishi Research Institute (Japan)	HETC-3STEP/MORSE-CG		○		
C.Y. Fu T.A. Gabriel	ORNL (USA)	HETC96/MORSE		○		
N. Nakao	KEK (Japan)	HETC-KFA2/MORSE-CG				○
O.E. Krivosheev N.V. Mokhov	Fermi Natl. Accelerator Laboratory (USA)	MARS13(97)	○	○	○	○
E. Nava S. Agosteo A. Ferrari P. Tabarelli M. Silari	Universita' di Milano (Italy) CESNEF, Politecnico di Milano (Italy) INFN Milano (Italy) CERN (Switzerland)	FLUKA	○			

Analyses are performed for benchmark problems marked by "○"

## Benchmark calculation

### *Problem No. 1: Transmission of quasi-monoenergetic neutrons generated by 43 MeV and 68 MeV protons through iron and concrete shields*

#### *Experiment*

Figure 1 shows the cross-sectional view of the TIARA facility with the experimental arrangement. Quasi-monoenergetic source neutrons of 40 and 65 MeV which were generated in  $^7\text{Li}$ -targets bombarded with 43- and 68-MeV protons reached the experimental room through an iron collimator embedded in the concrete wall. An iron test shield of 10 to 130 cm thickness was assembled on a movable stand with 10-cm-thick iron slabs of 120 cm×120 cm rectangular surface. A concrete test shield of 25 to 200 cm thickness was also assembled on the movable stand with 120×120×25 cm slabs. An additional iron collimator, as shown in Figure 2, was used for measurements of thinner test shields to depress the neutron leakage through the collimator wall and rotary shutter. To measure the neutron energy spectra, a 12.7 cm diameter×12.7 cm long BC501A liquid scintillation detector was placed behind the test shields. The spectra of quasi-monoenergetic source neutrons above 7 MeV, as shown the results in Figure 3, were measured by the time of flight (TOF) method with the BC501A detector. Absolute fluxes of the source neutrons in the monoenergetic peak have been calibrated for proton beam charge ( $\mu\text{C}$ ) with a proton-recoil-counter-telescope.

Figure 1. Cross-sectional view of the TIARA facility with the experimental arrangement

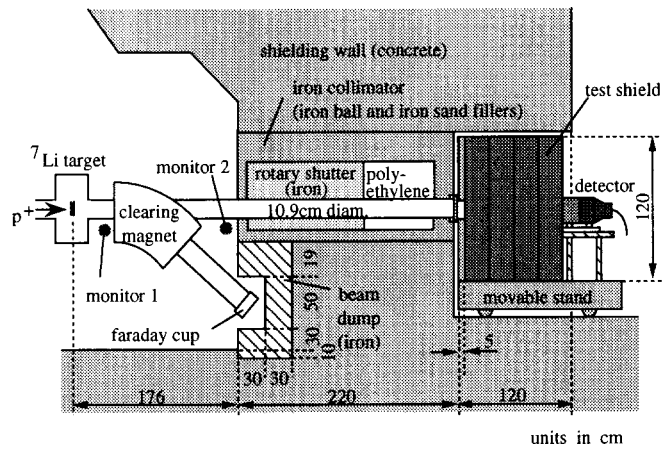


Figure 2. Top view and side view of the experimental arrangement for the shields with additional collimator

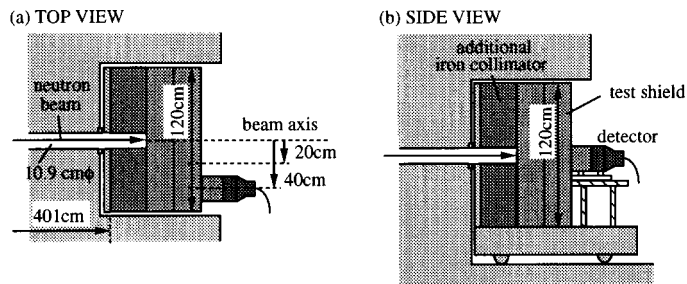
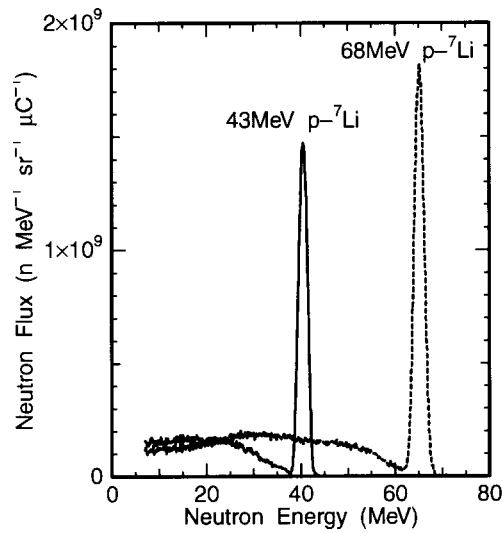


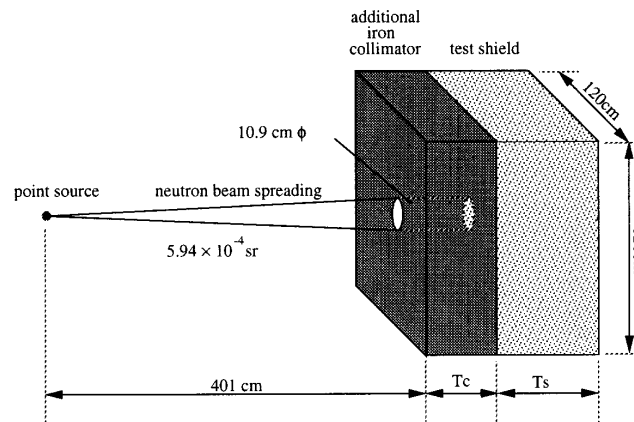
Figure 3. Source neutron spectra generated by 43- and 68-MeV protons bombarding  $^7\text{Li}$ -target



## Calculation

Five kinds of calculation codes, the MORSE-CG [11], MCNP4A [12], modified version [6] of HETC-KFA2 [13] (modified HETC) in the HERMES [14] code system, MARS13(97) [15,16] and FLUKA [17], were used for the calculation of neutron spectra behind the shields. A three-dimensional (X,Y,Z) model, as shown in Figure 4, was used in the calculations. In all calculations, measured spectra of source neutrons were used as the source spectra. Source neutrons were assumed to be emitted uniformly in a sharp cone of  $5.94 \times 10^{-4}$  steradian considering the geometry of the collimator in all calculations. Thicknesses of the test shields and the additional collimator, and peak fluxes of source neutrons per proton beam charge ( $\mu\text{C}$ ) are given in the reference [4].

**Figure 4. Calculation geometry**



In the MORSE-CG calculation, the neutron spectra behind the concrete and iron shields were calculated with using the DLC-119/HILO86 [18] and HILO86R [19] multigroup cross-section data sets, respectively. The DLC-119 library has the energy structure of 66 groups between thermal and 400-MeV energies for neutrons and of 22 groups up to 20 MeV for gamma rays using a  $P_5$  Legendre expansion. The HILO86R library is a revision of the DLC-119, in which only the cross-sections below 19.6 MeV have been exchanged with that collapsed from the JSSTD [20] data set considering self-shielding factors. In the calculation, the next event track length estimators having the same size as that of the BC501A scintillator were placed at the detector positions to estimate the flux in the detector. For the cases of concrete shields thicker than 150 cm and iron shields thicker than 100 cm, the exponential transform method was used to reduce the fractional standard deviation.

In the MCNP4A calculation, the neutron spectra on the beam axis behind the shields for the 68-MeV  $p$ -Li source neutron were calculated with using the DLC-119/HILO86 multigroup cross-section data set. In the calculation, the track length estimators were used to consider the detector shape. Both the concrete and iron shields were divided in thin cells of 2.5-cm thickness, and the energy dependent weight window bounds were assigned in each cell.

The calculations of neutron spectra in the energy range above 20 MeV with the modified HETC were made using the total and elastic scattering cross-sections obtained from the data due to Pearlstein's systematics [21]. In the calculation, the energy-dependent total and elastic scattering cross-sections are used for the extra- and intranuclear-cascade calculations, and the non-elastic scattering cross-section is obtained from the difference between the total and elastic scattering cross-sections. Track length estimators were used in the calculations.

In the MARS13 calculation, the surface flux estimator was used. A non-analogue technique (like exponential transformation and mathematical expectation estimation) was used for the thick shields.

In the FLUKA calculation, The neutron spectra behind the shields were calculated with using a 72-group library up to 20 MeV and nuclear models at higher energies. The complete self-shielded cross-sections processed from ENDF/B-VI [22] with the NJOY [23] were used for the iron, while infinitely diluted cross-sections processed from ENDF/B-VI with the NJOY were used for all other materials. To realise a more detailed geometry, concrete wall surrounding the test shields was taken into account in the geometrical model.

### Comparison and discussion

Figures 5 through 8 show the calculated and measured spectra on the beam axis. In the figures, error bars on the measurement points consist of errors of spectrum unfolding and counting statistics, and those on the calculation points consist of statistical errors in the Monte Carlo calculation. Calculated fluxes integrated in each energy region, i.e. peak and continuum regions, are summarised with the measured ones in Tables 2 through 5, and their C/E values are shown in Figures 9 and 10. MORSE-CG calculations with the DLC-119 and HILO86R libraries gave good C/E results for all shield thickness except for the iron shield of 130-cm thickness. For the thick iron shield, the results suggest that a calculation using a different variance reduction technique is required for increasing the statistics in the MORSE-CG calculation. MCNP4A calculations with the DLC-119 also gave good C/E results for the concrete shield, while those were higher than the measured ones for the thick iron shield. The fluxes calculated with the modified HETC agreed well with the measured ones for the thin shields, although the codes should be more improved for the calculation of thick shields. The MARS13 results agreed well with the measured ones for all shields except for 200-cm thick concrete and 130-cm thick iron. The FLUKA results agreed well with those measured for the concrete thickness from 25 cm to 150 cm. The FLUKA results for the iron shield thickness of 20, 40 and 100 cm also agreed well with the measured ones except for the 43-MeV  $p$ -Li neutron on the 100-cm thick shield.

**Figure 5. Transmitted neutron spectra through (1) 25-cm thick and (b) 150-cm thick concrete shields for the 43-MeV  $p$ -Li neutron source**

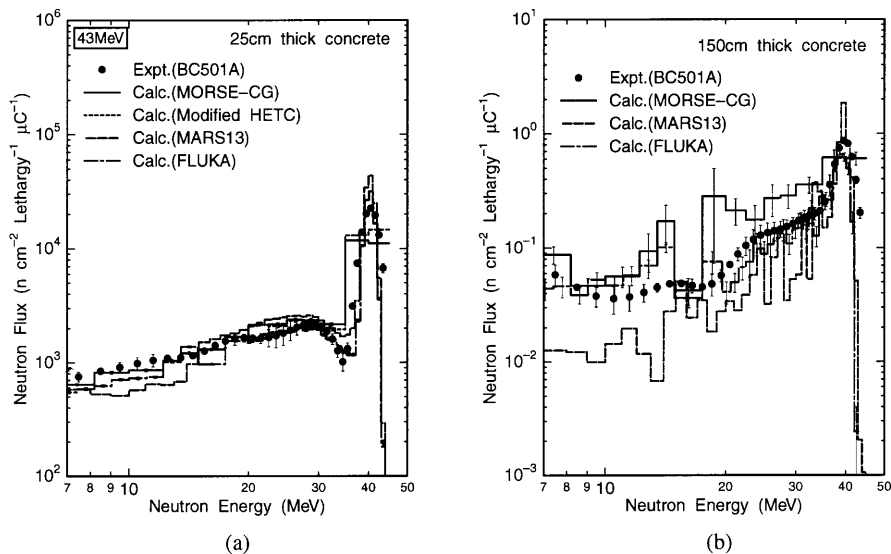


**Figure 6. Transmitted neutron spectra through (a) 25-cm thick and (b) 200-cm thick concrete shields for the 68-MeV *p*-Li neutron source**

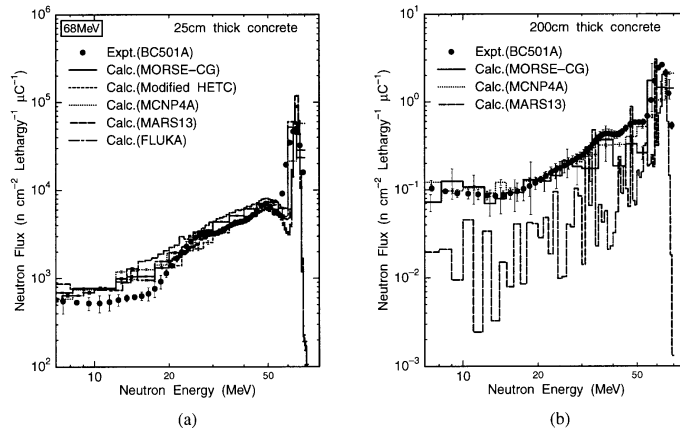


**Figure 7. Transmitted neutron spectra through (a) 20-cm thick and (b) 100-cm thick iron shields for the 43-MeV *p*-Li neutron source**

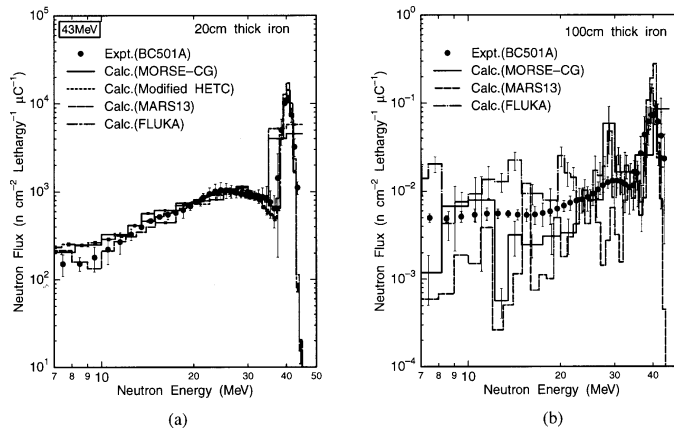


**Figure 8. Transmitted neutron spectra through (a) 20-cm thick and (b) 130-cm thick iron shields for the 68-MeV *p*-Li neutron source**

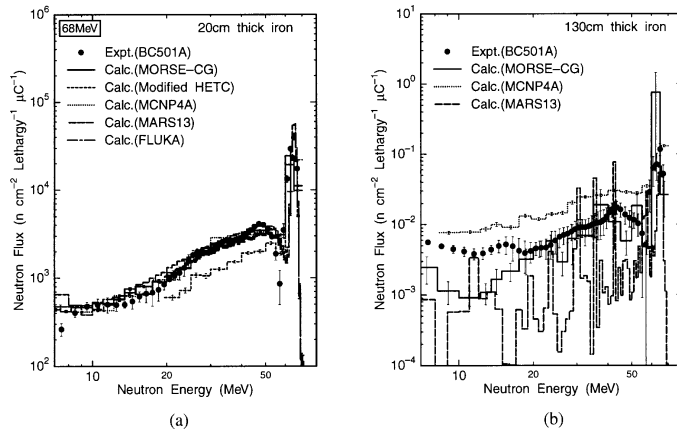


**Table 2. Calculated fluxes and C/E values behind the concrete shield for 43-MeV *p*-Li neutron**

	Thickness (cm)	Measured flux (n/cm <sup>2</sup> /μC)	Calculated flux (n/cm <sup>2</sup> /μC) and C/E value									
			MORSE-CG	C/E	MCNP4A	C/E	Mod. HETC	C/E	MARS13	C/E	FLUKA	C/E
Peak region (45-35 MeV)	25	2.69E+03*	2.89E+03	1.07			3.48E+03	1.29	3.22E+03	1.20	2.28E+03	0.85
	50	3.00E+02	3.26E+02	1.08			7.73E+02	2.57	3.97E+02	1.32	2.68E+02	0.89
	100	5.03E+00	6.01E+00	1.19			2.37E+01	4.72	5.82E+00	1.16	3.89E+00	0.77
	150	1.22E-01	1.54E-01	1.26			7.93E+00	65.18	1.18E-01	0.97	7.76E-02	0.64
Continuum region (35-10 MeV)	25	1.87E+03	2.08E+03	1.12					2.07E+03	1.11	1.74E+03	0.93
	50	1.56E+02	2.23E+02	1.42					2.00E+02	1.28	1.81E+02	1.16
	100	3.34E+00	5.67E+00	1.70					2.67E+00	0.80	3.36E+00	1.01
	150	1.10E-01	2.31E-01	2.11					6.79E-02	0.62	1.08E-01	0.99

\* Read as 2.69×10<sup>3</sup>**Table 3. Calculated fluxes and C/E values behind the concrete shield for 68-MeV *p*-Li neutron**

	Thickness (cm)	Measured flux (n/cm <sup>2</sup> /μC)	Calculated flux (n/cm <sup>2</sup> /μC) and C/E value									
			MORSE-CG	C/E	MCNP4A	C/E	Mod. HETC	C/E	MARS13	C/E	FLUKA	C/E
Peak region (70-60 MeV)	25	5.46E+03*	5.93E+03	1.09	5.99E+03	1.10	6.92E+03	1.27	6.23E+03	1.14	4.68E+03	0.86
	50	1.08E+03	1.19E+03	1.10	–	–	2.23E+03	2.06	1.42E+03	1.31	9.35E+02	0.86
	100	4.81E+01	4.79E+01	1.00	5.85E+01	1.22	1.58E+02	3.29	5.89E+01	1.22	3.29E+01	0.68
	150	2.20E+00	1.93E+00	0.88	–	–	3.27E+01	14.87	2.89E+00	1.32	1.44E+00	0.66
Continuum region (60-10 MeV)	25	5.52E+03	5.82E+03	1.05	5.90E+03	1.07			6.49E+03	1.17	4.98E+03	0.90
	50	8.40E+02	9.14E+02	1.09	–	–			1.01E+03	1.20	7.84E+02	0.93
	100	4.27E+01	5.06E+01	1.18	4.83E+01	1.13			3.48E+01	0.81	3.13E+01	0.73
	150	3.08E+00	3.81E+00	1.24	–	–			1.99E+00	0.65	2.17E+00	0.71
200	5.17E-01	4.43E-01	0.86	4.16E-01	0.81			1.93E-01	0.37	–	–	

\* Read as 5.46×10<sup>3</sup>**Table 4. Calculated fluxes and C/E values behind the iron shield for 43-MeV *p*-Li neutron**

	Thickness (cm)	Measured flux (n/cm <sup>2</sup> /μC)	Calculated flux (n/cm <sup>2</sup> /μC) and C/E value									
			MORSE-CG	C/E	MCNP4A	C/E	Mod. HETC	C/E	MARS13	C/E	FLUKA	C/E
Peak region (45-35 MeV)	10	4.21E+03*	4.05E+03	0.96			4.11E+03	0.98	4.62E+03	1.10	–	–
	20	1.02E+03	1.07E+03	1.05			1.38E+03	1.35	1.22E+03	1.19	9.91E+02	0.97
	40	5.05E+01	5.79E+01	1.15			1.27E+02	2.51	5.95E+01	1.18	5.07E+01	1.00
	70	6.80E-01	7.91E-01	1.16			6.74E+00	9.91	8.83E-01	1.30	–	–
	100	1.06E-02	1.34E-02	1.27			–	–	1.63E-02	1.54	9.19E-03	0.87
Continuum region (35-10 MeV)	10	3.54E+03	3.68E+03	1.04					3.70E+03	1.05	–	–
	20	8.22E+02	8.63E+02	1.05					8.32E+02	1.01	8.26E+02	1.01
	40	3.58E+01	4.77E+01	1.33					3.66E+01	1.02	4.56E+01	1.27
	70	5.65E-01	1.21E+00	2.13					4.04E-01	0.71	–	–
100	9.51E-03	1.24E-02	1.30					4.62E-03	0.49	1.81E-02	1.90	

\* Read as 4.21×10<sup>3</sup>

Calculated data of 70-cm thick were considered for the difference of source neutron number (3.45E9/3.15E9)

**Table 5. Calculated fluxes and C/E values behind the iron shield for 68-MeV *p*-Li neutron**

	Thickness (cm)	Measured flux (n/cm <sup>2</sup> /μC)	Calculated flux (n/cm <sup>2</sup> /μC) and C/E value									
			MORSE-CG	C/E	MCNP4A	C/E	Mod. HETC	C/E	MARS13	C/E	FLUKA	C/E
Peak region (70-60 MeV)	20	3.10E+03*	2.78E+03	0.90	2.39E+03	0.77	2.29E+03	0.74	2.88E+03	0.93	2.21E+03	0.71
	40	2.59E+02	2.77E+02	1.07	2.49E+02	0.96	3.70E+02	1.43	2.69E+02	1.04	1.73E+02	0.67
	70	6.83E+00	9.68E+00	1.42	7.72E+00	1.13	1.38E+01	2.02	6.38E+00	0.93	–	–
	100	2.27E-01	2.01E-01	0.88	2.95E-01	1.30	7.28E-01	3.20	1.96E-01	0.86	1.28E-01	0.56
	130	9.47E-03	6.21E-02	6.56	1.48E-02	1.56	–	–	3.30E-03	0.35	–	–
Continuum region (60-10 MeV)	20	3.04E+03	3.18E+03	1.05	3.20E+03	1.05			3.46E+03	1.14	2.87E+03	0.94
	40	2.62E+02	2.69E+02	1.03	2.99E+02	1.14			2.54E+02	0.97	2.27E+02	0.87
	70	7.49E+00	9.43E+00	1.26	1.12E+01	1.50			6.12E+00	0.82	–	–
	100	2.99E-01	3.51E-01	1.17	5.88E-01	1.97			1.45E-01	0.49	2.72E-01	0.91
130	1.40E-02	1.09E-02	0.78	3.21E-02	2.29			7.29E-03	0.52	–	–	

\* Read as 3.10×10<sup>3</sup>

**Figure 9. C/E values of transmitted neutron fluxes through the concrete shields in the peak and continuum energy regions for (a) 43-MeV and (b) 68-MeV *p*-Li neutron sources**

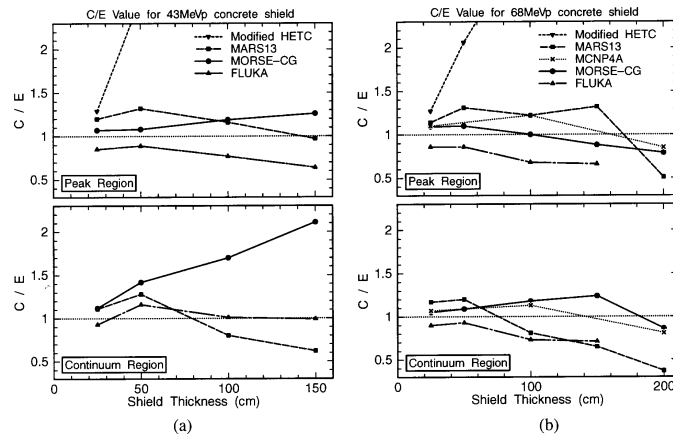
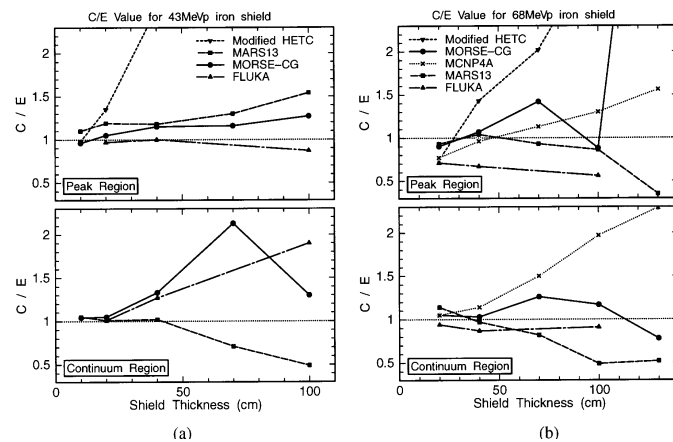


**Figure 10. C/E values of transmitted neutron fluxes through the iron shields in the peak and continuum energy regions for (a) 43-MeV and (b) 68-MeV *p*-Li neutron sources**



Transmitted spectra at the off-axis positions calculated by the MORSE-CG, modified HETC, MARS13 and FLUKA codes for the 25-cm thick concrete and the 20-cm thick iron are compared with the measured ones in Figures 11 and 12. Integrated fluxes and their C/E values are summarised in Tables 6 through 9. Calculated spectra by both the MORSE-CG and FLUKA codes gave better agreement with the measured ones than other calculations. As for the peak region in the MORSE-CG results, the difference between the experiments and calculations at the off-axis position was slightly larger than that at the position on the beam axis, while such a tendency was not so clearly found in the continuum region. The difference for the peak region indicates that the Legendre polynomial expansion up to  $P_5$  for the angular distribution of neutron scattering used in DLC119 is insufficient in this energy region where the neutron forward scattering is very strong. The fluxes of the peak region for both the 43- and 68-MeV *p*-Li neutrons by the MARS13 calculation agreed well with those measured for all concrete thickness, while those of the continuum region underestimated the measurements. For the iron shield, the fluxes of both the peak and continuum regions underestimated the measurements. The results calculated with the modified HETC for both the concrete and iron shields were considerably lower than the measured ones for the 43- and 68-MeV *p*-Li neutrons. This discrepancy is also caused by the inaccurate treatment of neutron scattering in the codes, especially at large angles.

**Figure 11. Transmitted neutron spectra at the off-axis position through 25-cm thick concrete shield for (a) 43-MeV and (b) 68-MeV  $p$ -Li neutron sources**

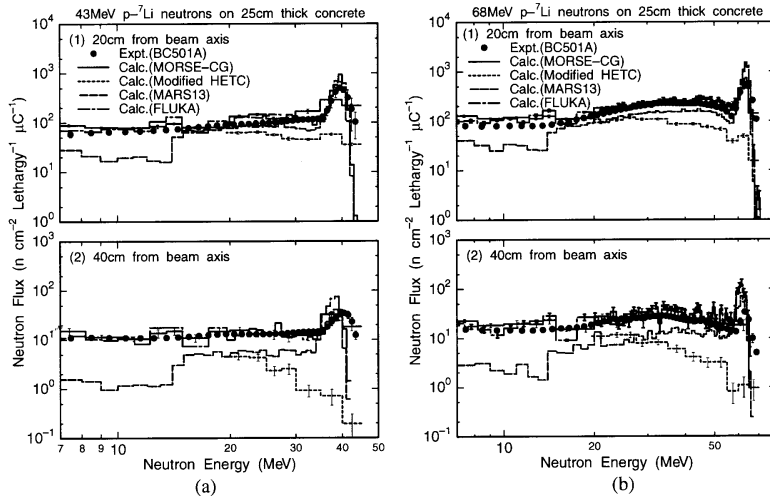


**Figure 12. Transmitted neutron spectra at the off-axis positions through 20-cm thick iron shield for (a) 43-MeV and (b) 68-MeV  $p$ -Li neutron sources**

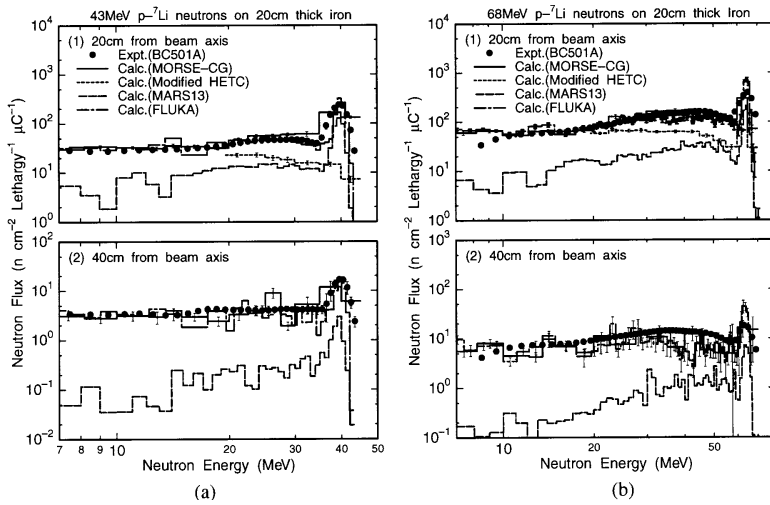


**Table 6. Calculated fluxes and C/E values at the off-axis position behind the concrete shield for 43-MeV  $p$ -Li neutron**

	Thickness (cm)	Off position (cm)	Measured flux (n/cm <sup>2</sup> /μC)	Calculated flux (n/cm <sup>2</sup> /μC) and C/E value							
				MORSE-CG	C/E	Mod. HETC	C/E	MARS13	C/E	FLUKA	C/E
Peak region (45-35 MeV)	25	20	6.52E+01*	6.41E+01	0.98	1.19E+01	0.18	6.14E+01	0.94	7.93E+01	1.22
		40	5.58E+00	6.54E+00	1.17	1.18E-01	0.02	3.79E+00	0.68	7.40E+00	1.33
	50	20	4.23E+01	5.00E+01	1.18	3.38E+01	0.80	4.72E+01	1.12	3.95E+01	0.93
		40	5.96E+00	5.79E+00	0.97	1.07E+00	0.18	5.48E+00	0.92	6.42E+00	1.08
Continuum region (35-10 MeV)	25	20	1.10E+02	1.37E+02	1.25			7.54E+01	0.69	1.33E+02	1.21
		40	1.57E+01	1.61E+01	1.03			5.34E+00	0.34	1.66E+01	1.06
	50	20	4.17E+01	5.85E+01	1.40			3.64E+01	0.87	4.91E+01	1.18
		40	8.82E+00	1.23E+01	1.39			5.62E+00	0.64	9.96E+00	1.13

\* Read as  $6.52 \times 10^1$

**Table 7. Calculated fluxes and C/E values at the off-axis position behind the concrete shield for 68-MeV *p*-Li neutron**

	Thickness (cm)	Off position (cm)	Measured flux (n/cm <sup>2</sup> μC)	Calculated flux (n/cm <sup>2</sup> μC) and C/E value							
				MORSE-CG	C/E	Mod. HETC	C/E	MARS13	C/E	FLUKA	C/E
Peak region (70-60 MeV)	25	20	5.53E+01*	4.67E+01	0.84	5.04E+00	0.09	4.70E+01	0.85	8.77E+01	1.59
		40	2.94E+00	1.53E+00	0.52	8.71E-02	0.03	3.35E+00	1.14	6.85E+00	2.33
	50	20	8.27E+00	7.27E+01	0.88	2.95E+01	0.36	6.99E+01	0.84	7.96E+01	0.96
		40	6.77E+00	5.89E+00	0.87	2.24E-01	0.03	6.72E+00	0.99	8.89E+00	1.31
Continuum region (60-10 MeV)	25	20	2.76E+02	3.10E+02	1.12			1.87E+02	0.68	3.33E+02	1.21
		40	3.58E+01	4.26E+01	1.19			1.59E+01	0.44	4.70E+01	1.31
	50	20	1.65E+02	2.26E+02	1.37			1.37E+02	0.83	1.77E+02	1.07
		40	3.14E+01	3.92E+01	1.25			2.03E+01	0.65	3.93E+01	1.25

\* Read as 5.53×10<sup>1</sup>

**Table 8. Calculated fluxes and C/E values at the off-axis positions behind the iron shield for 43-MeV *p*-Li neutron**

	Thickness (cm)	Off position (cm)	Measured flux (n/cm <sup>2</sup> μC)	Calculated flux (n/cm <sup>2</sup> μC) and C/E value							
				MORSE-CG	C/E	Mod. HETC	C/E	MARS13	C/E	FLUKA	C/E
Peak region (45-35 MeV)	0	20	8.25E+00*	3.70E+00	0.45	–	–	7.82E+00	0.95	–	–
		40	5.32E-01	2.70E-01	0.51	–	–	2.08E-01	0.39	–	–
	10	20	3.65E+01	2.99E+01	0.82	7.72E-01	0.02	1.00E+01	0.28	–	–
		40	2.53E+00	6.77E-01	0.27	–	–	2.07E-01	0.08	–	–
	20	20	3.09E+01	3.79E+01	1.23	2.82E+00	0.09	1.00E+01	0.32	2.41E+01	0.78
		40	2.17E+00	2.30E+00	1.06	–	–	2.07E-01	0.10	1.32E+00	0.61
40	20	7.73E+00	1.16E+01	1.50	4.59E+00	0.59	5.96E+00	0.77	7.18E+00	0.93	
	40	7.57E-01	1.40E+00	1.85	–	–	2.73E-01	0.36	4.55E-01	0.60	
Continuum region (35-10 MeV)	0	20	1.44E+01	5.48E+00	0.38			8.74E+00	0.61	–	–
		40	1.61E+00	5.21E-01	0.32			1.84E-01	0.11	–	–
	10	20	7.32E+01	6.17E+01	0.84			1.35E+01	0.18	–	–
		40	7.72E+00	5.58E+00	0.72			2.29E-01	0.03	–	–
	20	20	4.62E+01	5.44E+01	1.18			1.35E+01	0.29	4.89E+01	1.06
		40	4.82E+00	4.72E+00	0.98			2.29E-01	0.05	4.11E+00	0.85
40	20	8.95E+00	1.35E+01	1.51			4.39E+00	0.49	9.34E+00	1.04	
	40	1.17E+00	2.14E+00	1.83			2.10E-01	0.18	1.33E+00	1.14	

\* Read as 8.25×10<sup>0</sup>

**Table 9. Calculated fluxes and C/E values at the off-axis positions behind the iron shield for 68-MeV *p*-Li neutron**

	Thickness (cm)	Off position (cm)	Measured flux (n/cm <sup>2</sup> μC)	Calculated flux (n/cm <sup>2</sup> μC) and C/E value							
				MORSE-CG	C/E	Mod. HETC	C/E	MARS13	C/E	FLUKA	C/E
Peak region (70-60 MeV)	0	20	9.18E+00*	4.24E+00	0.46	–	–	1.11E+01	1.21	–	–
		40	5.78E-01	3.12E-01	0.54	–	–	4.12E-01	0.71	–	–
	20	20	4.33E+01	2.89E+01	0.67	7.47E+00	0.17	1.11E+01	0.26	4.13E+01	0.95
		40	1.99E+00	2.39E+00	1.20	–	–	4.12E-01	0.21	2.61E+00	1.31
	40	20	2.73E+01	2.74E+01	1.00	6.09E+00	0.22	1.29E+01	0.47	1.95E+01	0.71
40		1.92E+00	5.69E-01	0.30	–	–	6.75E-01	0.35	2.09E+00	1.09	
Continuum region (60-10 MeV)	0	20	4.74E+01	1.81E+01	0.38			3.42E+01	0.72	–	–
		40	5.70E+00	1.77E+00	0.31			1.30E+00	0.23	–	–
	20	20	1.84E+02	1.89E+02	1.03			3.42E+01	0.19	1.67E+02	0.91
		40	1.84E+01	1.35E+01	0.73			1.30E+00	0.07	1.36E+01	0.74
	40	20	5.55E+01	6.84E+01	1.23			2.83E+01	0.51	5.12E+01	0.92
40		7.46E+00	1.11E+01	1.49			1.68E+00	0.23	6.51E+00	0.87	

\* Read as 9.18×10<sup>0</sup>

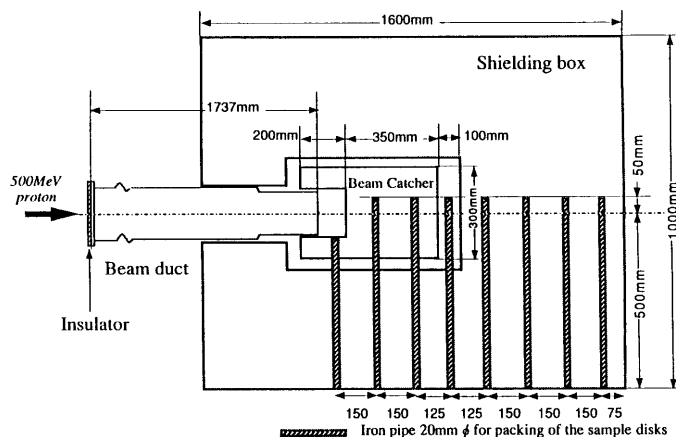
**Problem No. 2: Neutron fluxes in and around iron beam stop irradiated by 500 MeV protons**

*Experiment*

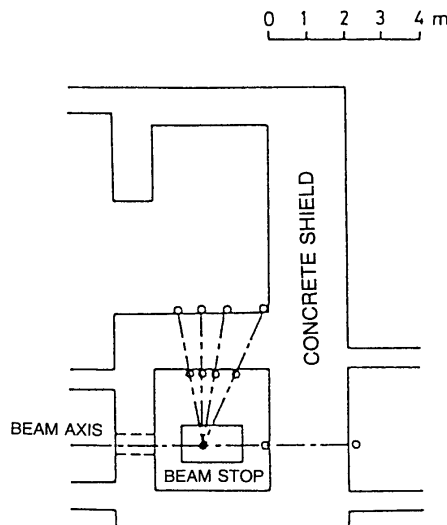
A cross-sectional plane view of a beam stop for the experiment is shown in Figure 13. The beam stop consisted of rectangular parallelepiped iron beam catcher and iron shielding box. Activation detectors of Fe, Al, Cu and Au were inserted in the beam stop to measure lateral and longitudinal distributions of saturated activities of  $^{48}\text{V}$ ,  $^{52}\text{Mn}$ ,  $^{54}\text{Mn}$  in Fe-nat,  $^{24}\text{Na}$  in  $^{27}\text{Al}$ ,  $^{58}\text{Co}$  in Cu-nat and  $^{198}\text{Au}$  in  $^{197}\text{Au}$ . The 500 MeV proton beam impinged on the beam stop perpendicularly at its centre. The beam profile was 6.0 cm (FWHM) in the horizontal and 3.0 cm (FWHM) in the vertical directions.

Figure 14 shows a plan view of a beam dump room for the experiment. Activation detectors of C and Al were set inside and outside the concrete shielding wall at 0, 65, 80, 90 and 100 degrees around the beam stop to measure distributions of saturated activities of  $^{11}\text{C}$  in  $^{12}\text{C}$ , and  $^{18}\text{F}$  and  $^{24}\text{Na}$  in  $^{27}\text{Al}$ . The beam profile was 3.0 cm (FWHM) in the horizontal and 1.5 cm (FWHM) in the vertical directions.

**Figure 13. Cross-sectional plane view of a beam stop for the experiment**



**Figure 14. Plane view of a beam dump room for the experiment**



## Calculation

Figures 15 and 16 show the geometries of the iron beam stop and the beam dump room, respectively. The beam stop was expressed with a two-dimensional (R-Z) model, while the beam dump room was expressed with a three-dimensional (X,Y,Z) model. The 500 MeV proton beam of mono-direction along the Z-axis was assumed to impinge on the origin in the figures. For the calculation of the beam stop, the beam profile was 6.0 cm (FWHM) in the horizontal and 3.0 cm (FWHM) in the vertical directions. For the calculation of the beam dump room, the beam profile was 3.0 cm (FWHM) in the horizontal and 1.5 cm (FWHM) in the vertical directions. Three calculation codes, the HETC-3STEP [24], HETC96 [25] and MARS13, were used for the beam stop calculations. The HETC-3STEP code is a modified version of HETC-KFA2 code, in which the calculation of the pre-equilibrium process is taken into account by using the exciton model. The HETC96 code is a HETC code modified for including the pre-equilibrium process. Only the HETC96 code was used for the beam dump room calculation.

**Figure 15. Calculation geometry for the beam stop**

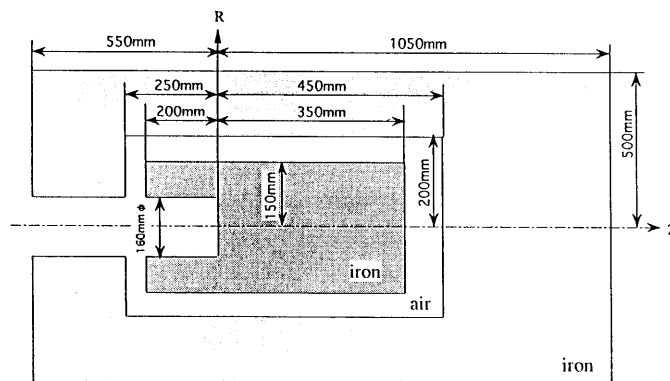
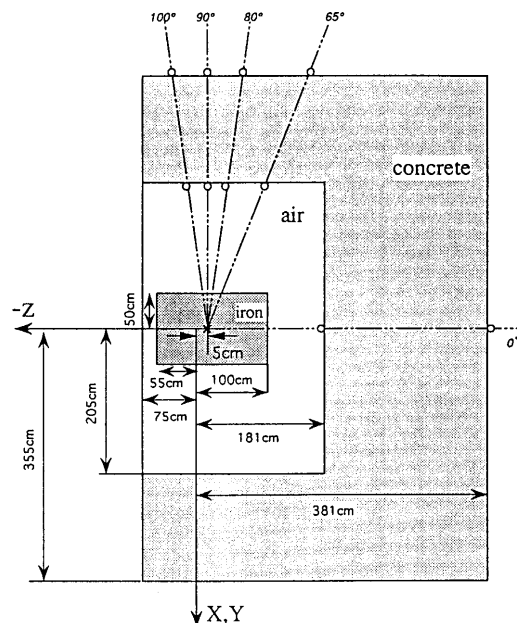


**Figure 16. Calculation geometry for the beam dump room**



The distributions of saturated activities of  $^{48}\text{V}$  and  $^{52}\text{Mn}$  in Fe,  $^{24}\text{Na}$  in  $^{27}\text{Al}$  and  $^{58}\text{Co}$  in Cu in the beam stop were calculated [3] with the HETC-3STEP code. In the beam catcher, the distribution was obtained from residual nuclei distribution calculated with the HETC-3STEP because of considering the contribution of protons to activation. Outside the beam catcher, the distribution of saturated activities was obtained from neutron fluxes and neutron reaction cross-sections. The neutron fluxes in the energy range above 19.6 MeV were calculated with the HETC-3STEP code, while those below 19.6 MeV were calculated with the MORSE-CG code using neutron group cross-section library HILO86R. Track length estimator was used to neutron flux calculations with both the HETC-3STEP and MORSE-CG codes.

The distributions of saturated activities of  $^{48}\text{V}$ ,  $^{52}\text{Mn}$  and  $^{54}\text{Mn}$  in Fe-nat,  $^{24}\text{Na}$  in  $^{27}\text{Al}$ ,  $^{58}\text{Co}$  in Cu-nat and  $^{198}\text{Au}$  in  $^{197}\text{Au}$  in the beam stop and of  $^{11}\text{C}$  in  $^{12}\text{C}$ ,  $^{18}\text{F}$  and  $^{24}\text{Na}$  in  $^{27}\text{Al}$  in the beam dump room were calculated [26] with the HETC96 code. In the calculation, neutron fluxes above 20 MeV were calculated with the HETC96 code, while those below 20 MeV were calculated with the MORSE code. In the MORSE calculation, neutron group cross-section library HILO [27] was used for  $\text{Fe}(n,x)^{54}\text{Mn}$  and  $^{27}\text{Al}(n,\alpha)^{24}\text{Na}$  reactions, while the BUGLE96 [28] library was used for  $^{197}\text{Au}(n,\gamma)^{198}\text{Au}$  reaction. For the purpose of considering the contribution of protons to activation in the beam catcher, the number of activated atoms was counted directly in the HETC96 calculation. The track length estimator was used for the calculation of the beam stop. The boundary-crossing estimator was used for the calculation of the beam dump room. Standard deviations due to the calculation statistics were generally in less than 5% for the beam stop, while those were large for some detector points.

The distribution of saturated activities for  $^{48}\text{V}$ ,  $^{52}\text{Mn}$  and  $^{54}\text{Mn}$  in Fe,  $^{24}\text{Na}$  in  $^{27}\text{Al}$  and  $^{58}\text{Co}$  in Cu in the beam stop were obtained [16] from the neutron fluxes calculated with the MARS13 code. The surface flux estimator was used in the MARS13 calculations. The contribution of protons to activation was not considered in the MARS13 calculations.

Neutron reaction cross-sections [2,4], as shown in Figures 17 through 20, were commonly used in the calculations of neutron induced activations.

**Figure 17. Neutron reaction cross-sections for  $^{nat}\text{Fe}(n,x)^{48}\text{V}$ ,  $^{nat}\text{Fe}(n,x)^{52}\text{Mn}$  and  $^{nat}\text{Fe}(n,x)^{54}\text{Mn}$  reactions**

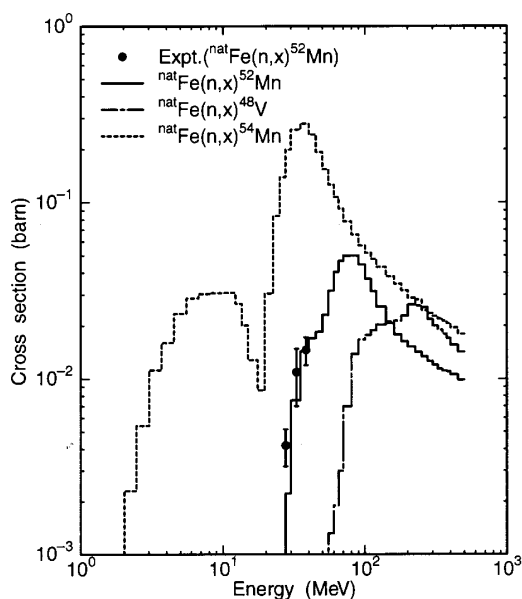


Figure 18. Neutron reaction cross-sections for  $^{27}\text{Al}(n,\alpha)^{24}\text{Na}$  and  $^{27}\text{Al}(n,x)^{18}\text{F}$  reactions

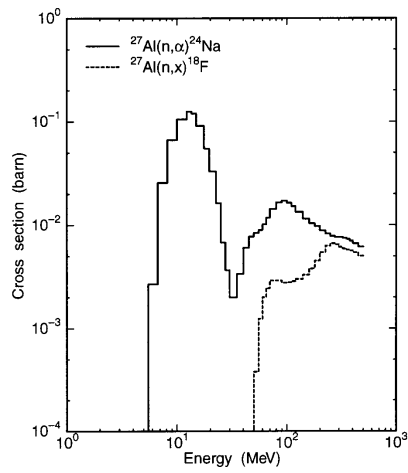


Figure 19. Neutron reaction cross-sections for  $\text{Cu}(n,x)^{58}\text{Co}$  and  $^{12}\text{C}(n,2n)^{11}\text{C}$  reactions

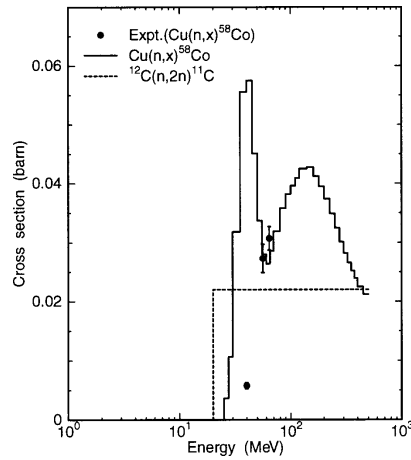
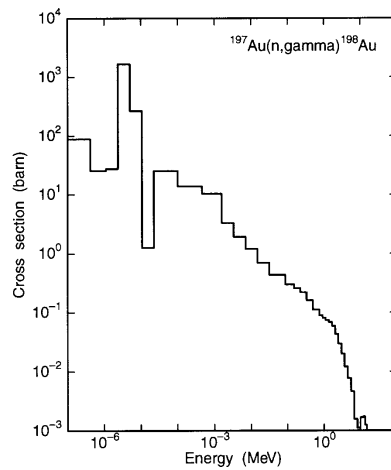


Figure 20. Neutron reaction cross-section for  $^{197}\text{Au}(n,\gamma)^{198}\text{Au}$  reaction



### Comparison and discussion

Calculated and measured distributions of saturated activities in the beam stop for  $^{48}\text{V}$ ,  $^{52}\text{Mn}$ ,  $^{54}\text{Mn}$ ,  $^{24}\text{Na}$ ,  $^{58}\text{Co}$  and  $^{198}\text{Au}$  and their C/E values except for  $^{198}\text{Au}$  are shown in Figures 21 through 31. The MARS13 calculations gave good C/E results on the whole without considering the contribution of proton reactions, while both the HETC-3STEP/MORSE-CG and HETC96/MORSE calculations overestimated the measured ones for  $\text{Fe} \rightarrow ^{48}\text{V}$  and  $\text{Fe} \rightarrow ^{52}\text{Mn}$  reactions. The separate evaluation of the proton and neutron contributions will be helpful to investigate the cause of the overestimation.

The HETC96/MORSE calculations of the beam dump room for  $^{12}\text{C}(n,2n)^{11}\text{C}$ ,  $^{27}\text{Al}(n,\text{spal.})^{18}\text{F}$  and  $^{27}\text{Al}(n,\alpha)^{24}\text{Na}$  reactions are compared with the measurements in Figures 32 through 34. Calculated values inside the concrete shield were higher than the measured ones on the whole. For  $^{12}\text{C}(n,2n)^{11}\text{C}$  and  $^{27}\text{Al}(n,\text{spal.})^{18}\text{F}$  reactions, attenuation profiles calculated for 0 degrees agreed well with the measured ones, while those for 90 and 100 degrees were lower than the measured ones.

**Figure 21. Calculated activities of  $^{48}\text{V}$  in the beam stop**

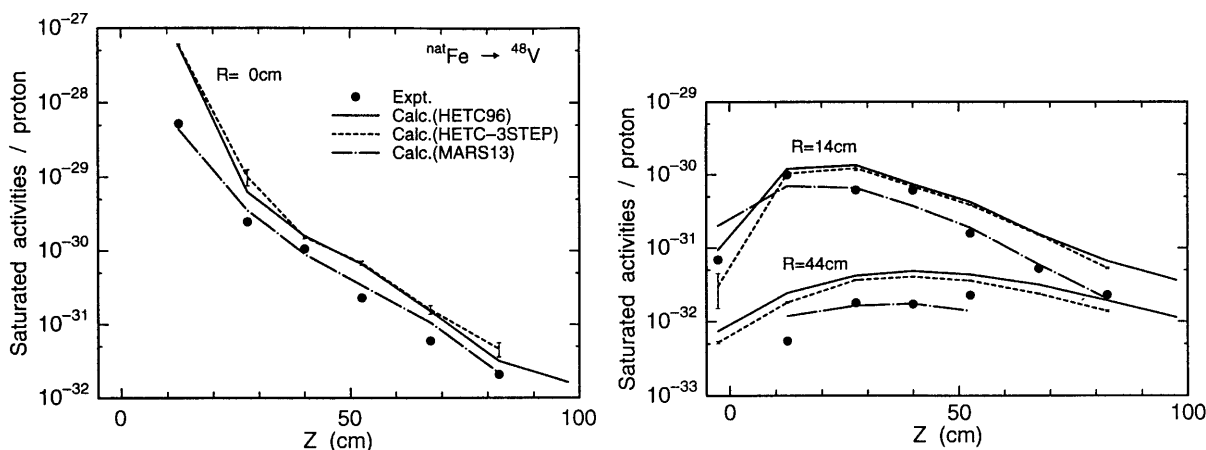


**Figure 22. C/E values of saturated activities of  $^{48}\text{V}$  in the beam stop**

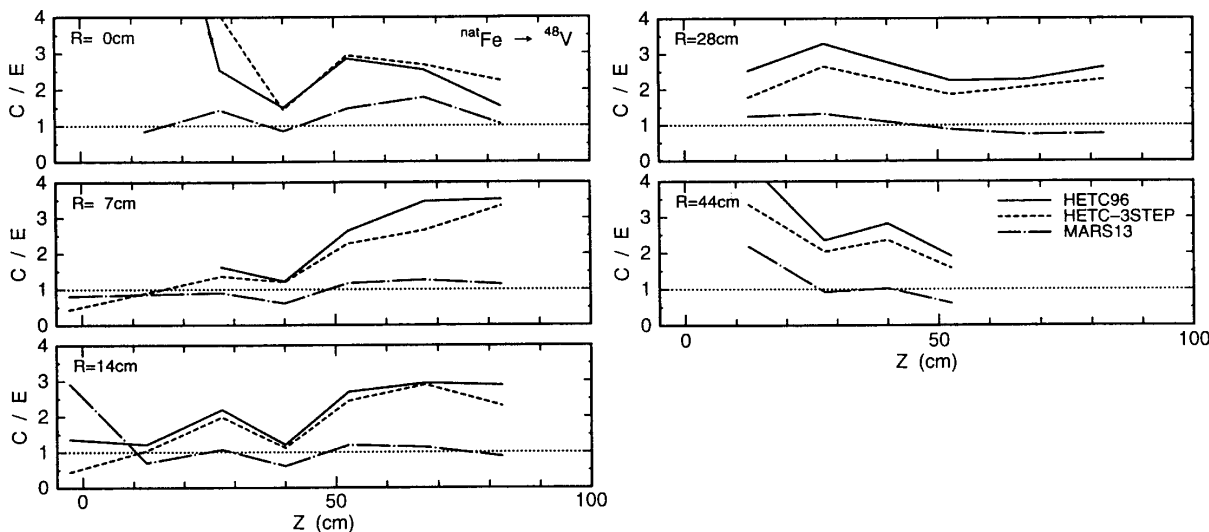


Figure 23. Calculated activities of  $^{52}\text{Mn}$  in the beam stop

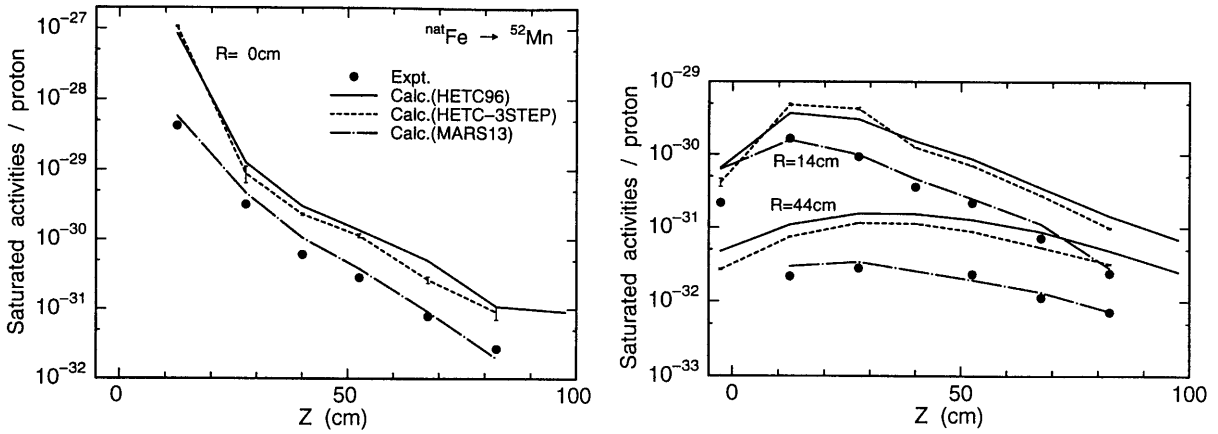


Figure 24. C/E values of saturated activities of  $^{52}\text{Mn}$  in the beam stop

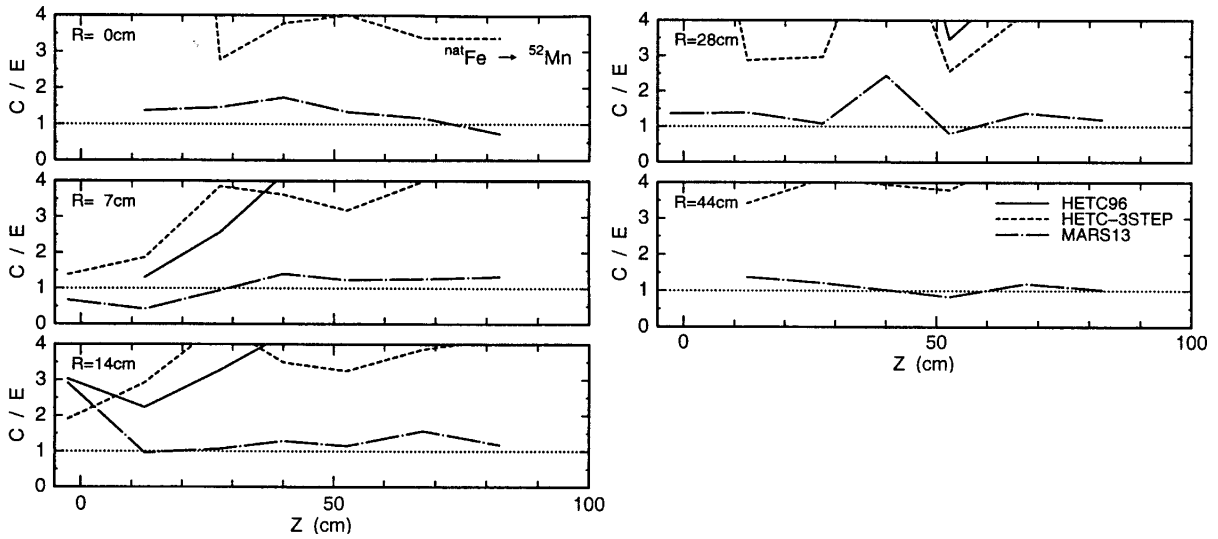


Figure 25. Calculated activities of  $^{54}\text{Mn}$  in the beam stop

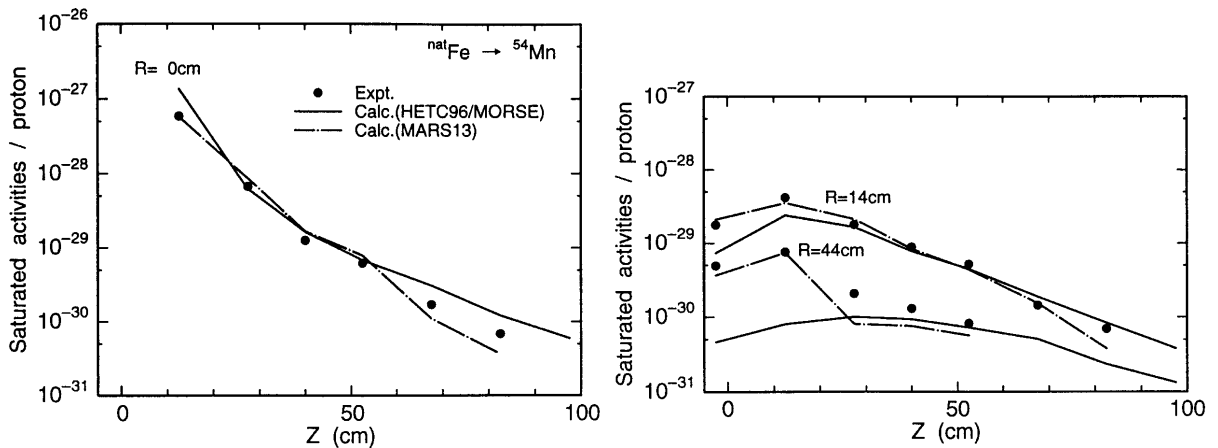


Figure 26. C/E values of saturated activities of  $^{54}\text{Mn}$  in the beam stop

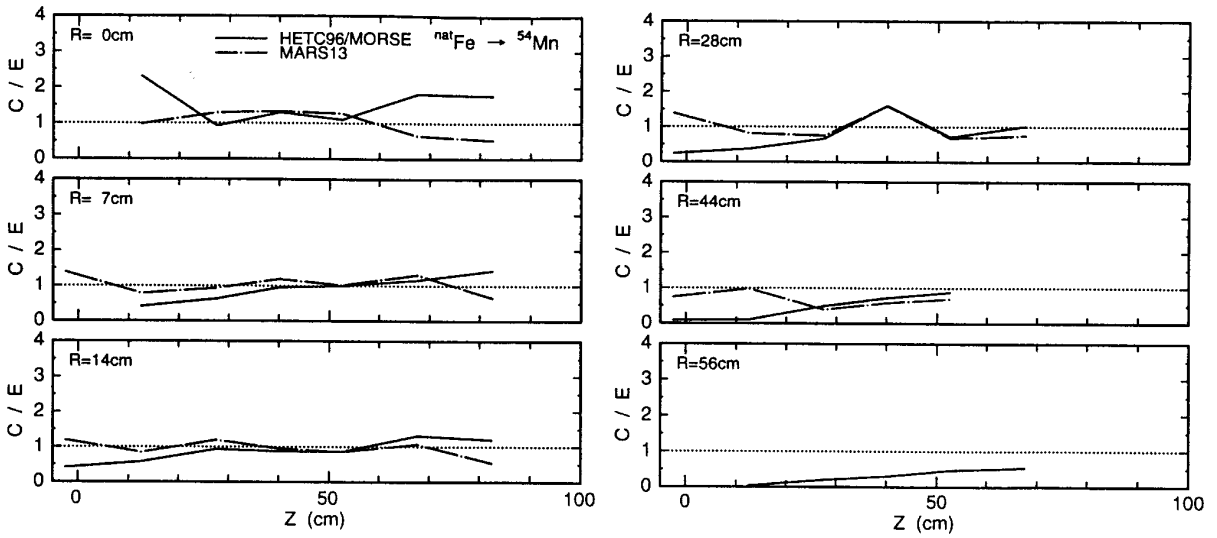


Figure 27. Calculated activities of  $^{24}\text{Na}$  in the beam stop

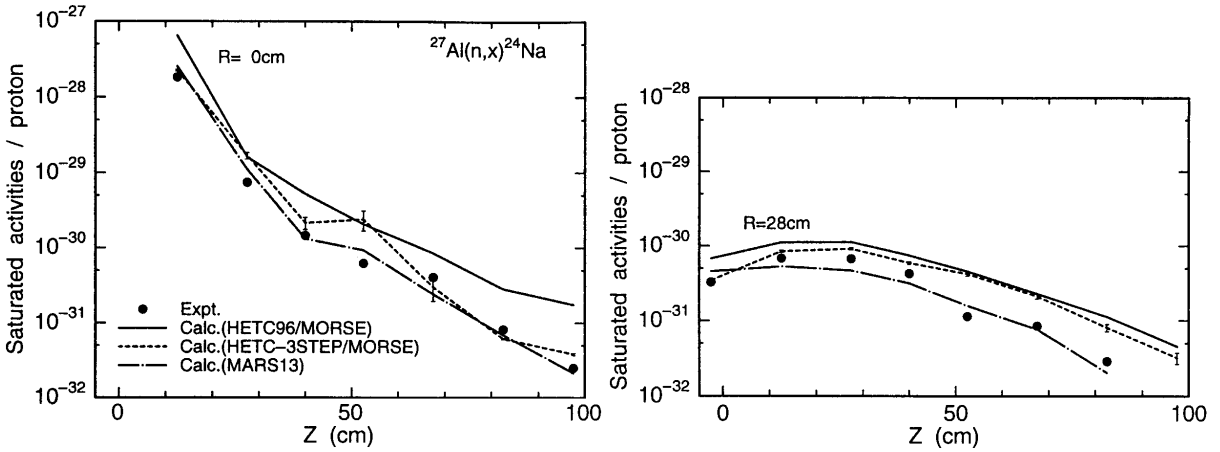


Figure 28. C/E values of saturated activities of  $^{24}\text{Na}$  in the beam stop

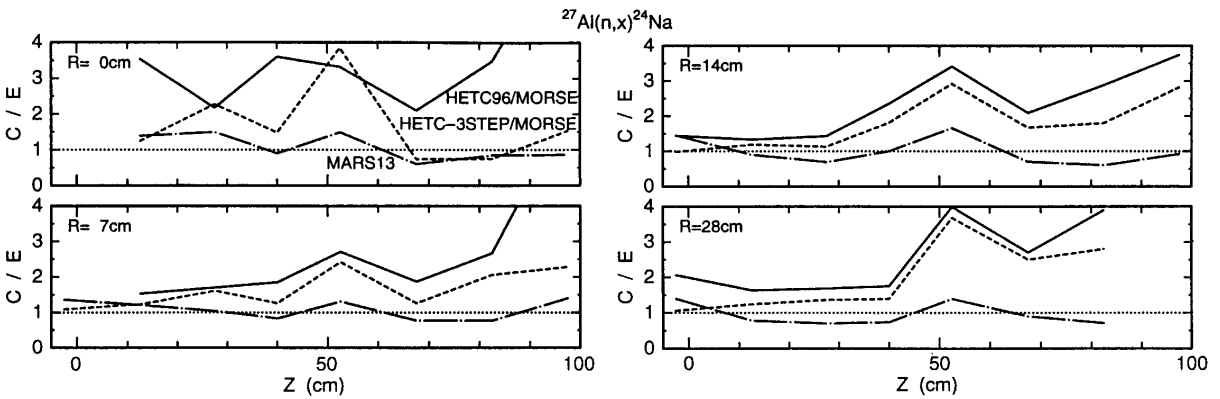


Figure 29. Calculated activities of  $^{58}\text{Co}$  in the beam stop

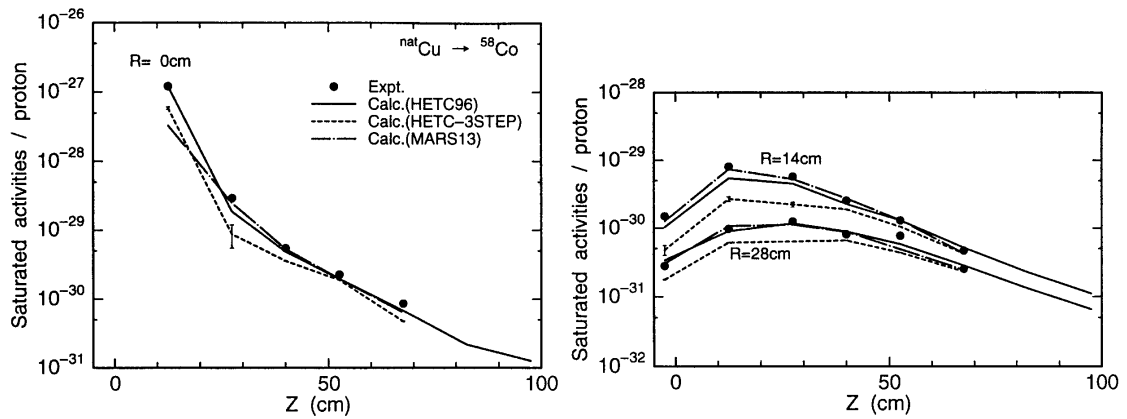


Figure 30. C/E values of saturated activities of  $^{58}\text{Co}$  in the beam stop

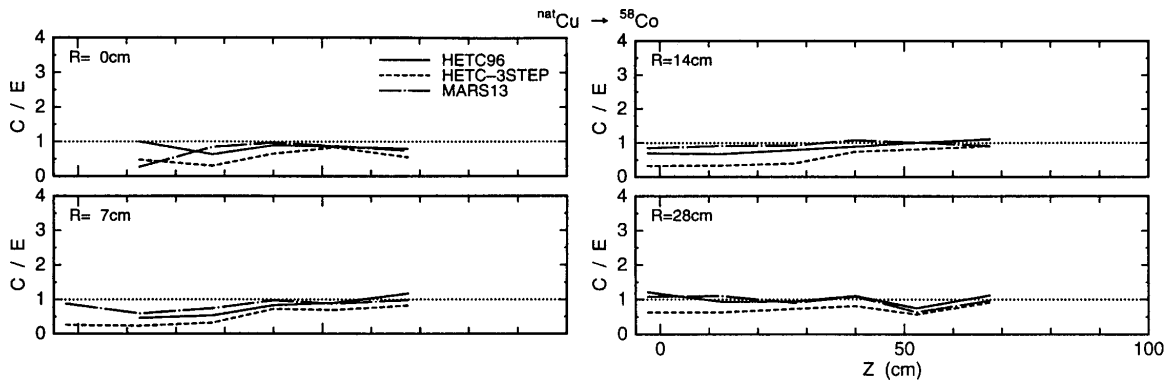


Figure 31. Calculated activities of  $^{198}\text{Au}$  in the beam stop

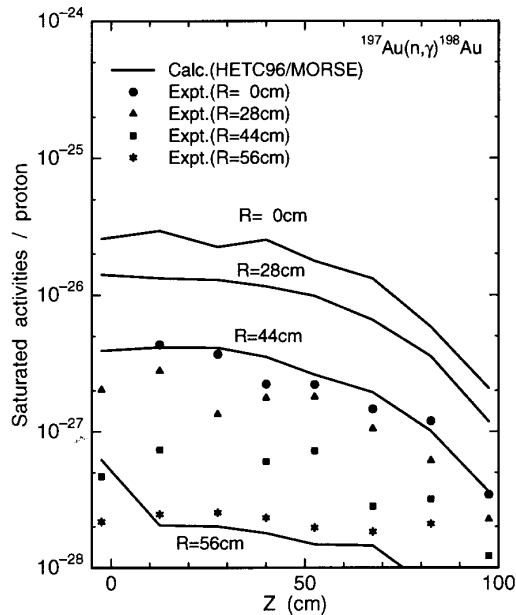


Figure 32. Calculated activities of  $^{11}\text{C}$  in the beam dump room

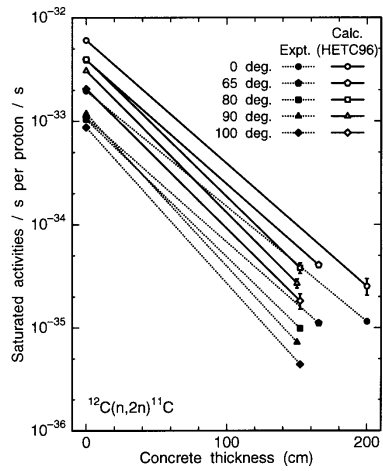


Figure 33. Calculated activities of  $^{18}\text{F}$  in the beam dump room

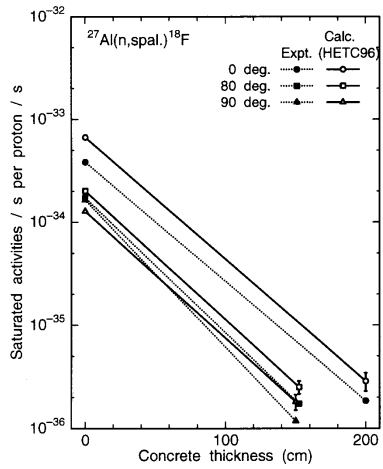
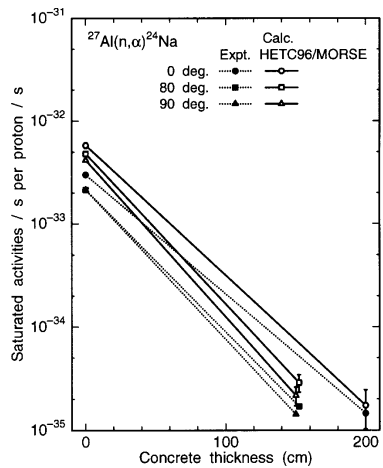


Figure 34. Calculated activities of  $^{24}\text{Na}$  in the beam dump room

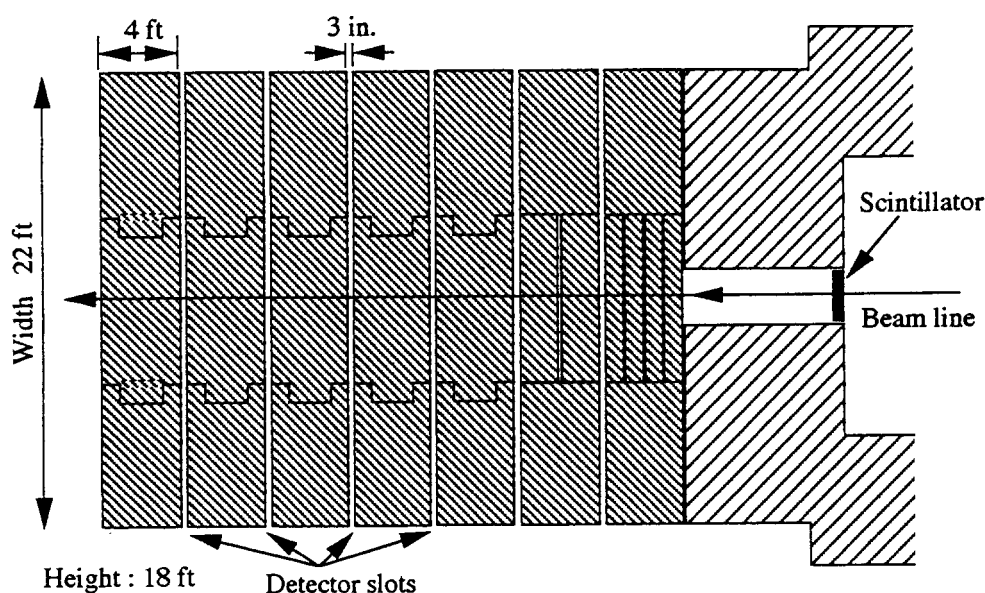


### Problem No. 3: Reaction rate distributions inside thick concrete shield irradiated by 6.2 GeV protons

#### Experiment

The experimental arrangement is shown in Figure 35. A shielding assembly consisted of seven ordinary concrete slabs of 4-ft thickness. The concrete slabs were separated by 3-inch wide gaps to allow insertion of detectors. All portions of these gaps except slots actually used for detector placement were filled with gypsum wallboard (approximately same density as concrete). Gold-foils, aluminium-discs and carbon scintillators, in the form of 4-inch diameter by thickness between 1/32 and 1 inch, were used as activation detectors. These detectors were placed at every 4-ft depth and every 1-ft from the beam axis in a lateral direction. The 6.2 GeV proton beam impinged on the surface of shielding assembly perpendicularly at its centre. The beam spot was within 2 inches in diameter. The 4.2 and 2.2 GeV proton beams were also used for the measurements of incident proton energy dependence of attenuation profiles. Relative attenuation profiles were measured.

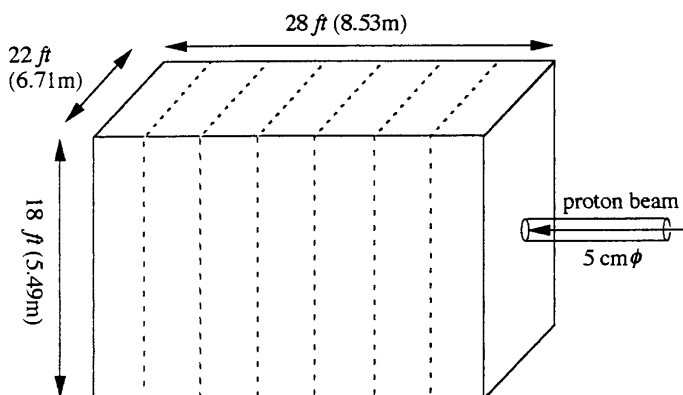
Figure 35. Plan view of shield array for the experiments



#### Calculation

The lateral-attenuation profiles for  $^{197}\text{Au}$ ,  $^{27}\text{Al}$  and  $^{12}\text{C}$  detectors were obtained from the neutron fluxes calculated with the MARS13 code. Figure 36 shows the calculation geometry. A shielding assembly consisted of seven 4-ft thick ordinary concrete slabs was described with a three-dimensional (X,Y,Z) model. A 5-cm diameter proton beam of 2.2, 4.2 and 6.2 GeV was assumed to impinge on the surface of the shielding assembly. The track length estimator was used in the MARS13 calculations. The values of cross-section for  $^{27}\text{Al}(n,\alpha)^{24}\text{Na}$  and  $^{12}\text{C}(n,2n)^{11}\text{C}$  reactions in the response calculations were 85mb in the neutron energy above 6.5 MeV and 22mb for the neutron energy above 20.4 MeV, respectively. In the calculation for  $^{197}\text{Au}(n,\gamma)^{198}\text{Au}$  reaction, the values of cross-section shown in Figure 20 were used. The contributions of protons to activation were not considered in the calculations because proton fluxes were small in comparison with neutron ones.

**Figure 36. Calculation geometry**



*Comparison and discussion*

Calculated and measured lateral attenuation profiles for  $^{12}\text{C}(n,2n)^{11}\text{C}$ ,  $^{27}\text{Al}(n,\alpha)^{24}\text{Na}$  and  $^{197}\text{Au}(n,\gamma)^{198}\text{Au}$  reactions are shown in Figures 37 through 39. Because measured data were relative values, calculated data for lateral profiles were normalised to experimental value at a depth of 4 ft on the beam axis. Calculated results agreed well with the measured ones on the whole for  $^{12}\text{C}(n,2n)^{11}\text{C}$  and  $^{27}\text{Al}(n,\alpha)^{24}\text{Na}$  reactions, while the results for  $^{197}\text{Au}(n,\gamma)^{198}\text{Au}$  reaction underestimated the measurements.

Calculated and measured attenuation profiles along the beam axis for  $^{12}\text{C}(n,2n)^{11}\text{C}$ ,  $^{27}\text{Al}(n,\alpha)^{24}\text{Na}$  and  $^{197}\text{Au}(n,\gamma)^{198}\text{Au}$  reactions are shown in Figure 40 with their C/E values. Calculated attenuation profiles on the beam axis were normalised to experimental value at a depth of 8 ft.

Calculated and measured attenuation profiles of  $^{27}\text{Al}(n,\alpha)^{24}\text{Na}$  reaction along the beam axis for incident proton energies of 2.2, 4.2 and 6.2 GeV are shown in Figure 39 with their C/E values. Attenuation profiles calculated for all proton energies were in good agreement with those measured.

**Figure 37. Lateral-attenuation profiles for carbon detector**

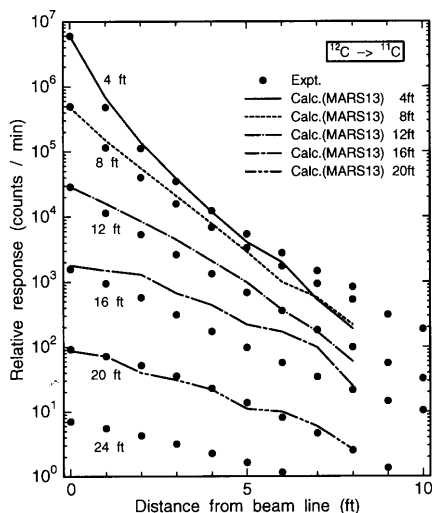


**Figure 38. Lateral-attenuation profiles for aluminium detector**

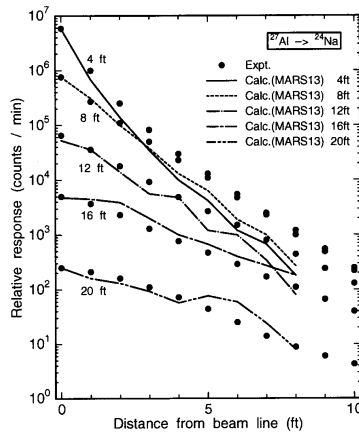


**Figure 39. Lateral-attenuation profiles for gold-foil detector**

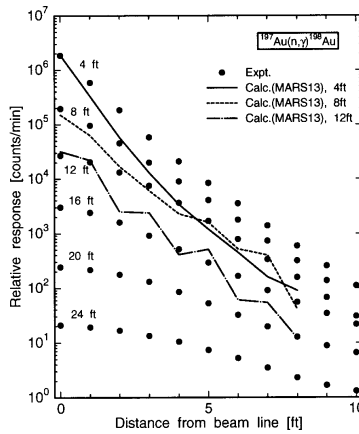


**Figure 40. Attenuation profiles along the beam axis for  $^{12}\text{C}(n,2n)^{11}\text{C}$ ,  $^{27}\text{Al}(n,\alpha)^{24}\text{Na}$  and  $^{197}\text{Au}(n,\gamma)^{198}\text{Au}$  reaction**

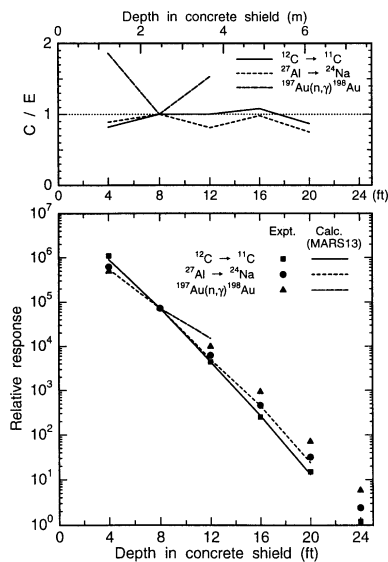
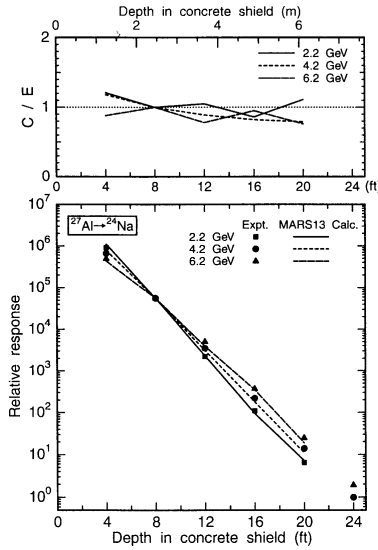


**Figure 41. Attenuation profiles of  $^{27}\text{Al}(n,\alpha)^{24}\text{Na}$  reaction along the beam axis for incident proton energies of 2.2, 4.2 and 6.2 GeV**



***Problem No. 4: Neutron and hadron fluxes inside iron beam dump irradiated by 24 GeV protons***

*Experiment*

A sketch of a beam dump used in the experiments is given in Figure 42. The beam dump consisted of 20 rectangular iron absorber slabs of 5-cm thickness, separated by 7-mm slots in which thin aluminium plates supporting the activation detectors and dosimeters were placed. The density of the iron absorber slabs was  $7.86 \pm 0.02 \text{ g/cm}^3$ . The 24 GeV proton beam impinged on the beam dump perpendicularly at its centre. Beam intensity was measured using a monitor and aluminium activation detectors placed upstream of the beam dump. The beam spot size was about 3 mm in diameter. Activation detectors,  $^{115}\text{In}$ ,  $^{32}\text{S}$  and  $^{27}\text{Al}$ , and glass dosimeter (RPL dosimeter) were used for the experiments. The activation detectors and RPL dosimeters were mounted on 0.5-mm thick and 24 cm×30 cm cross-section aluminium plates with activation detector holding holes that were accurately punched out for every detector size. A sketch of the aluminium plate for holding Al activation detectors is exemplified in Figure 43. In the figure, R and r show the exact distance from the centre of the aluminium plate and the radius of the activation detectors and RPL dosimeters, respectively. An aluminium plate was also placed in front of the first absorber slab in order to measure albedo effects (slot 0th). The measured fluxes in each slot were obtained from measured saturated activities of  $^{115\text{m}}\text{In}$  in  $^{115}\text{In}$ ,  $^{32}\text{P}$  in  $^{32}\text{S}$ ,  $^{24}\text{Na}$  and  $^{18}\text{F}$  in  $^{27}\text{Al}$  by dividing by  $n \cdot s$ ; (n: the number of atoms in the detector, s: effective cross-section (see Table 4.1 in [4]). All measured data were normalised by a condition of one proton incidence.

*Calculation*

Neutron fluxes were calculated with the MARS13 code. A three-dimensional (X,Y,Z) model, as shown in Figure 44, was used in the calculations. The 24 GeV proton beam of 3 mm in diameter was assumed to impinge on the iron beam dump (30×30×113.3 cm) at its centre. The track length estimator

Figure 42. Sketch of the dump assembly

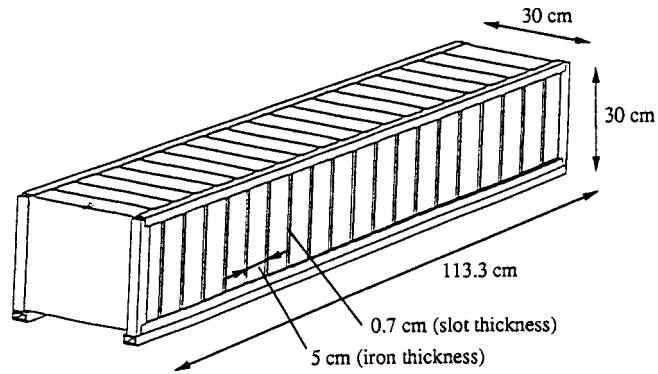


Figure 43. Sketch of an aluminium plate showing holes for Al detectors

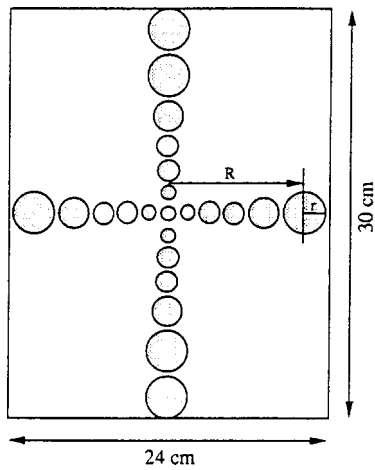
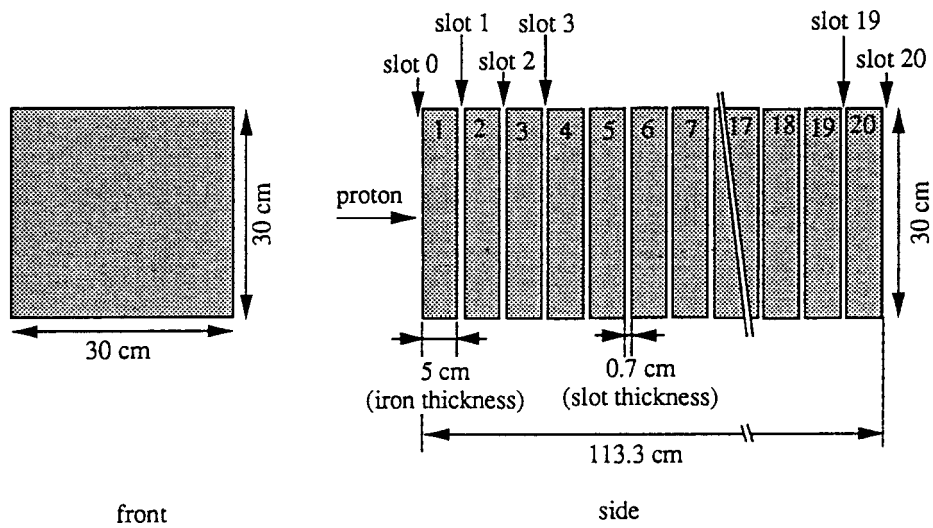


Figure 44. Geometry of iron beam dump assembly for calculation



was used in the MARS13 calculations. After the transport calculations, neutron fluxes for  $^{115}\text{In}(n,n')^{115\text{m}}\text{In}$ ,  $^{32}\text{S}(n,p)^{32}\text{P}$  and  $^{27}\text{Al}(n,\alpha)^{24}\text{Na}$  reactions were integrated in the neutron energy range from 0.8 MeV to 14.5 MeV, from 2.5 MeV to 25 MeV and from 6.5 MeV to 25 MeV, respectively. The hadron flux in the energy range above 35 MeV was also integrated for the  $^{27}\text{Al}(h,x)^{18}\text{F}$  reaction.

Neutron fluxes in the energy range above 400 MeV were also calculated [29] with the HETC-KFA2 code in the HERMES code system. In the calculation, neutron fluxes in the energy range below 400 MeV were calculated with the MORSE-CG code using the HILO86R multigroup cross-section data set. The calculation geometry was expressed with a 34-cm diameter and 100-cm long cylindrical iron. The 7-mm slots for detectors in the experiments were not considered in the calculation geometry. The 24 GeV proton pencil beam was assumed to impinge on the iron beam dump at its centre. The surface flux estimators considering detector shapes were used in the calculations. After the transport calculations, neutron fluxes for  $^{115}\text{In}(n,n')^{115\text{m}}\text{In}$ ,  $^{32}\text{S}(n,p)^{32}\text{P}$  and  $^{27}\text{Al}(n,\alpha)^{24}\text{Na}$  reactions were integrated in the neutron energy range from 0.8 MeV to 15 MeV, from 3 MeV to 25 MeV and from 6 MeV to 25 MeV, respectively. Both neutron and proton fluxes in the energy range above 35 MeV were integrated as hadron fluxes for the  $^{27}\text{Al}(h,x)^{18}\text{F}$  reaction.

### Comparison and discussion

Figures 45 through 48 show the calculated and measured results for  $^{27}\text{Al}\rightarrow^{24}\text{Na}$ ,  $^{32}\text{S}\rightarrow^{32}\text{P}$ ,  $^{115}\text{In}\rightarrow^{115\text{m}}\text{In}$  and  $^{27}\text{Al}\rightarrow^{18}\text{F}$  reactions. The calculated absorbed doses of RPL dosimeters are shown in Figure 49 with the measured ones. For comparison, results calculated with the FLUKA code in [30] are also shown in the figures.

The MARS13 calculations gave good C/E results on the whole, although calculated fluxes for some cases were higher than the measured ones. The HETC/MORSE results were higher than those measured, especially on the surface of the dump assembly.

**Figure 45. Calculated fluxes at the detector positions (a) from Slot 0 to Slot 6 and (b) from Slot 7 to Slot 20 for  $^{27}\text{Al}\rightarrow^{24}\text{Na}$  reaction with the measured ones**

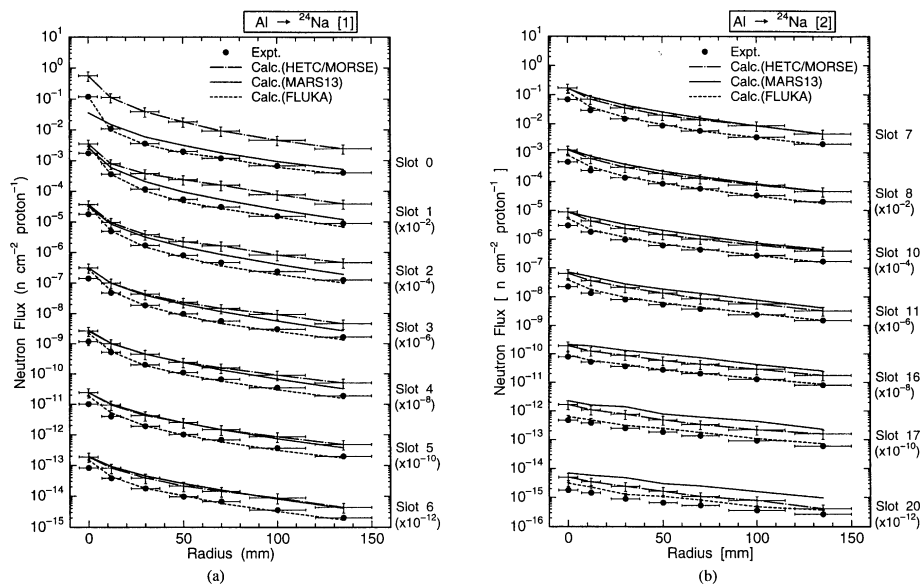


Figure 46. Calculated fluxes for  $^{32}\text{S} \rightarrow ^{32}\text{P}$  reaction with the measured ones

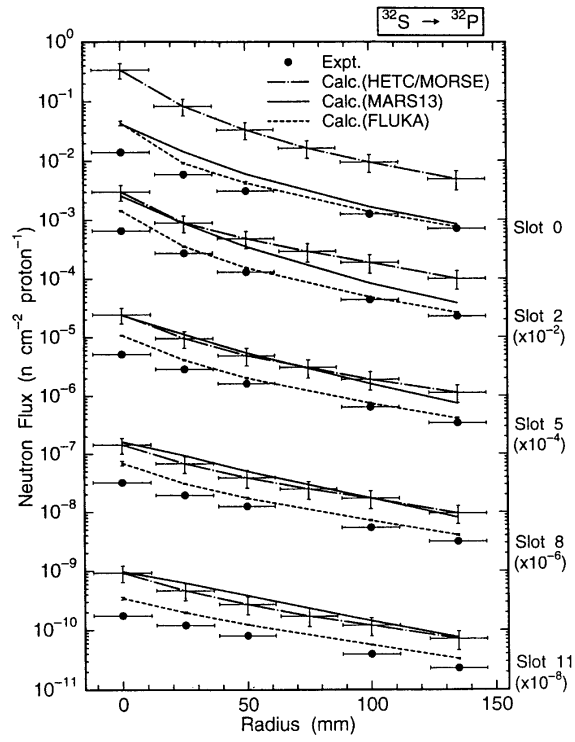


Figure 47. Calculated fluxes for  $^{115}\text{In} \rightarrow ^{115\text{m}}\text{In}$  reaction with the measured ones

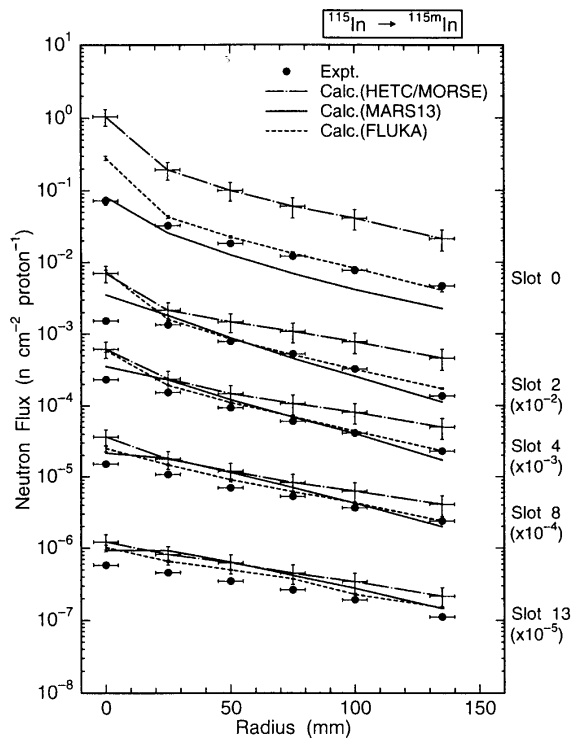


Figure 48. Calculated fluxes for  $^{27}\text{Al} \rightarrow ^{18}\text{F}$  reaction with the measured ones

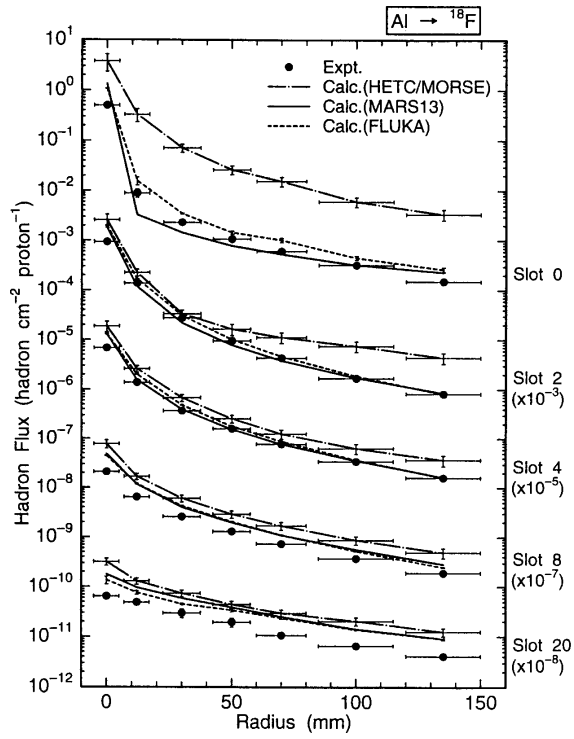
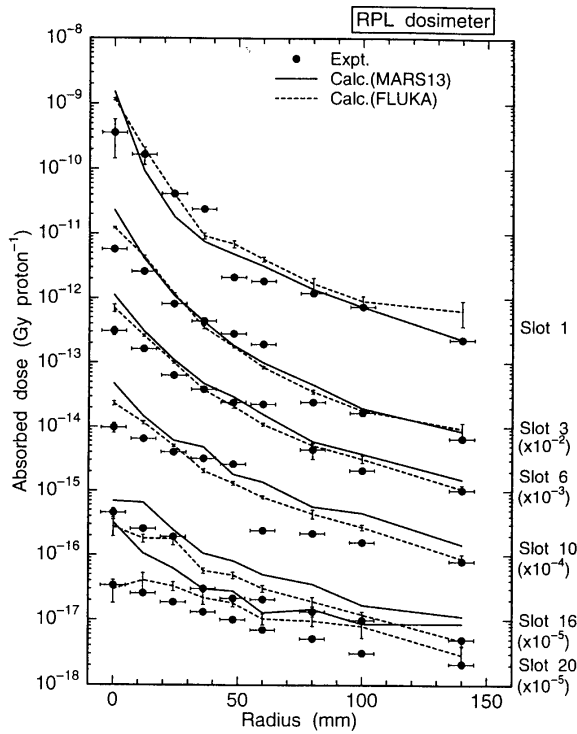


Figure 49. Calculated absorbed doses of RPL dosimeters with the measured ones



## Summary

Calculated results of neutron transmission benchmark problems for iron and concrete shields in low, intermediate and high energy proton accelerator facilities were compiled for evaluating the calculation codes and the nuclear data used in the codes. Although this is only the first version of the compilation, interim code evaluations are listed below for each benchmark problem.

- (1) *Problem No. 1 – Transmission of quasi-monoenergetic neutrons generated by 43 MeV and 68 MeV protons through iron and concrete shields.* The MCNP4A and MORSE-CG codes with DLC-119 and HILO86R multigroup libraries gave good C/E results. It is recommended to use a higher  $P_l$  expansion approximation for MORSE-CG and an energy continuous cross-section library for MCNP4A code. The MARS13 and FLUKA codes also gave good C/E results. There is yet room for improvement in HETC code.
- (2) *Problem No. 2 – Neutron fluxes in and around iron beam stop irradiated by 500 MeV protons.* The MARS13 calculations gave good C/E results for the beam stop calculations on the whole without considering the contribution of proton reactions, while the calculations for both the HETC-3STEP/MORSE-CG and HETC96/MORSE overestimated the measured ones for  $\text{Fe} \rightarrow {}^{48}\text{V}$  and  $\text{Fe} \rightarrow {}^{52}\text{Mn}$  reactions. The separate evaluation of the proton and neutron contributions will be helpful to investigate the cause of the overestimation.
- (3) *Problem No. 3 – Reaction rate distributions inside thick concrete shields irradiated by 6.2 GeV protons.* The MARS13 code gave good C/E results on the whole except for  ${}^{197}\text{Au}(n,\gamma){}^{198}\text{Au}$  reaction.
- (4) *Problem No. 4 – Neutron and hadron fluxes inside iron beam dump irradiated by 24 GeV protons.* The MARS13 code gave good C/E results. The HETC-KFA/MORSE-CG codes overestimated the measurements, especially on the surface of the dump assembly.

As a whole, the results calculated with the MARS13 code agree well with the measured ones for all problems. In the future, it is expected that FLUKA, LCS and other results will be submitted for the remaining problems.

## REFERENCES

- [1] K. Hayashi *et al.*, “Accelerator Shielding Benchmark Analysis and Future Items to be Solved”, Proceedings of First Specialists Meeting on Shielding Aspects of Accelerators, Targets and Irradiation Facilities, OECD Documents, OECD/NEA (1995).
- [2] H. Nakashima *et al.*, “Benchmark Problems for Intermediate and High Energy Accelerator Shielding”, JAERI-Data/Code 94-012 (1994).
- [3] H. Nakashima *et al.*, “Accelerator Shielding Benchmark Experiment Analyses”, Proceedings of Second Specialists Meeting on Shielding Aspects of Accelerators, Targets and Irradiation Facilities, OECD Documents, OECD/NEA (1996).
- [4] Y. Nakane *et al.*, “Neutron Transmission Benchmark Problems for Iron and Concrete Shields in Low, Intermediate and High Energy Proton Accelerator Facilities”, JAERI-Data/Code 96-029 (1996).
- [5] N. Nakao *et al.*, “Transmission Through Shields of Quasi-Monoenergetic Neutrons Generated by 43- and 68-MeV Protons - I: Concrete Shielding Experiment and Calculation for Practical Application”, *Nucl. Sci. Eng.*, 124, 228 (1996).
- [6] H. Nakashima *et al.*, “Transmission Through Shields of Quasi-Monoenergetic Neutrons Generated by 43- and 68-MeV Protons - II: Iron Shielding Experiment and Analysis for Investigating Calculation Methods and Cross Section Data”, *Nucl. Sci. Eng.*, 124, 243 (1996).
- [7] Y. Arakita, H. Hirayama, T. Inagaki and M. Miyajima, “Study of an Iron Beam Stop for 500 MeV Protons”, *Nucl. Instrum. Methods*, 164, 255-265 (1979).
- [8] S. Ban, H. Hirayama and K. Katoh, “Measurement of Secondary Neutron Fluxes Around Beam Stop for 500 MeV Protons”, *ibid.*, 184, 409-412 (1981).
- [9] A.R. Smith, “Some Experimental Shielding Studies at the 6.2-BeV Berkeley Bevatron”, Proceedings of the USAEC First Symposium on Accelerator Radiation Dosimetry and Experience, p. 365, CONF-651109 (1965).
- [10] A. Fassò *et al.*, “Measurements of Low-Energy Neutrons in an Iron Calorimeter Structure Irradiated by 24 GeV/c Protons”, CERN/TIS-RP/90-19 (1990).
- [11] G.R. Straker, P.N. Stevens, D.C. Irving and V.R. Cain, “MORSE Code – A Multigroup Neutron and Gamma Ray Monte Carlo Transport Code”, ORNL-4585 (1970).
- [12] J.F. Briesmeister, “MCNP4<sup>TM</sup> – A General Monte Carlo N-Particle Transport Code, Version 4A”, LA-12625-M (1993).

- [13] T.W. Armstrong *et al.*, *Nucl. Sci. Eng.*, 49, 82 (1972).
- [14] P. Cloth *et al.*, “HERMES: A Monte Carlo Program System for Beam-Materials Interaction Studies”, FA-IRE-E AN/12/88 (1988).
- [15] N.V. Mokhov, “The MARS Code System Users Guide, Version 13(95)”, Fermilab-FN-628 (1995).
- [16] N.V. Mokhov *et al.*, “New MARS and its Applications”, presentation at the Simulation of Accelerator Radiation Environments, SARE-3, 7-9 May 1997, KEK, Tsukuba, Japan.
- [17] P.A. Aarnio, J. Lindgren, J. Ranft, A. Fassò and G.R. Stevenson, Reports CERN/TIS-RP/168 (1986) and CERN/TIS-RP/190 (1987).
- [18] R.G. Alsmiller, J.M. Barnes and J.D. Drischler, “Neutron-Photon Multigroup Cross Sections for Neutron Energies  $\leq 400$  MeV (Revision 1)”, ORNL/TM-9801 (1986).
- [19] H. Kotegawa, Y. Nakane, A. Hasegawa and S. Tanaka, “Neutron-Photon Multigroup Cross-Sections for Neutron Energies up to 400 MeV: HILO86R – Revision of HILO86 Library”, JAERI-M 93-020 (1993).
- [20] A. Hasegawa, “Development of a Common Nuclear Group Constants Library System: JSSTD-295n-104 $\gamma$  Based on JENDL-3 Nuclear Data Library”, Nuclear Data Science and Technology, pp. 232, Springer Verlag (1991).
- [21] S. Pearlstein, “Medium Energy Nuclear Data Libraries; A Case Study, Neutron and Proton-Induced Reactions in  $^{56}\text{Fe}$ ”, *J. Astrophys.*, 346, 1049 (1989).
- [22] P.F. Rose (comp.), “ENDF-201: ENDF/B-VI Summary Documentation”, BNL-NCS-17541 (1991).
- [23] R.E. MacFarlane, “The NJOY Nuclear Data Processing System, Version 91”, LA-12740-M, (1994).
- [24] N. Yoshizawa, K. Ishibashi and H. Takada, “Development of High Energy Transport Code HETC-3STEP Applicable to the Nuclear Reaction with Incident Energies above 20 MeV”, *J. Nucl. Sci. Technol.*, 32, 601 (1995).
- [25] F.S. Alsmiller *et al.*, Oak Ridge National Laboratory, to be published (1997).
- [26] C.Y. (Peter) Fu *et al.*, “Comparisons of HETC96/MORSE(HILO) Calculations with Activation Data Taken in an Iron Beam Stop Irradiated by 500 MeV Protons at KEK”, presentation at the Simulation of Accelerator Radiation Environments, SARE-3, 7-9 May 1997, KEK, Tsukuba, Japan.
- [27] R.G. Alsmiller and J. Barish, “Neutron-Photon Multigroup Cross-Sections for Neutron Energies  $\leq 400$  MeV”, ORNL/TM-7818 (1981).

- [28] J.E. White *et al.*, “BUGLE-96: A Revised Multigroup Cross-Section Library for LWR Applications Based on ENDF/B-VI RELEASE 3”, CONF-960415-37, 10 (1996).
- [29] N. Nakao *et al.*, “Calculation of Radiation Fields Inside Iron Beam Dump Irradiated by 24 GeV/c Proton”, presentation at the Simulation of Accelerator Radiation Environments, SARE-3, 7-9 May 1997, KEK, Tsukuba, Japan.
- [30] A. Fassò *et al.*, “A Comparison of FLUKA Simulations with Measurements of Fluence and Dose in Calorimeter Structures”, *Nucl. Instrum. Methods Phys. Res.*, A332(3), 459-468 (1993).

# *Attenuation Length – Definition and Intercomparison*



## **INTERCOMPARISON OF THE MEDIUM-ENERGY NEUTRON ATTENUATION IN IRON AND CONCRETE**

**Hideo Hirayama**

KEK, High Energy Accelerator Research Organisation  
1-1 Oho, Tsukuba, Ibaraki, 305 Japan

**Attenuation Length Sub-Working Group (Japan)**

### **Abstract**

The neutron attenuation inside various materials has not been well understood until now, especially in the medium-energy region below 1 GeV. It is desired to obtain common agreements concerning the behaviour of neutrons inside various materials. This is necessary in order to agree on a definition of the attenuation length, which is very important for the shielding calculations of high energy accelerators. As one attempt to accomplish this goal, the Japanese participants of SATIF2 proposed to compare the variation in the neutron spectra and dose equivalents inside various shielding materials produced by medium-energy neutrons between the various computer codes and data; this was cited as an action suitable for SATIF. The problems to be calculated were prepared by the Attenuation Length Sub-Working Group in Japan, and sent to all participants concerning this action. The results from three groups were sent to the organiser at the end of March. This paper presents comparisons between three groups, as well as future themes which result from this intercomparison.

## **Introduction**

The neutron attenuation inside various materials has not been well understood until now, especially in the medium-energy region below 1 GeV. It is desired to obtain common agreements concerning the behaviour of neutrons inside various materials. This is necessary in order to agree on a definition of the attenuation length, which is very important for the shielding calculations of high energy accelerators. As one attempt to accomplish this goal, the Japanese participants of SATIF2 proposed to compare the variation in the neutron spectra and dose equivalents inside various shielding materials produced by medium-energy neutrons between the various computer codes and data; this was cited as an action suitable for SATIF. The problems to be calculated were prepared by the Attenuation Length Sub-Working Group in Japan, and sent to all participants concerning this action. The results from three groups were sent to the organiser at the end of March. This paper presents comparisons between three groups, as well as future themes which result from this intercomparison.

## **Problems for an intercomparison**

At the first step, the following problems were proposed to be calculated by various codes with their own databases.

### ***Source neutron energy***

Source neutrons are uniformly distributed within the following energy region:

- 40-50 MeV;
- 90-100 MeV;
- 180-200 MeV;
- 375-400 MeV.

### ***Geometry***

As for the geometry, the following two cases are proposed:

- spherical, radius of 6 m with a point isotropic source at the centre;
- planar, 6 m thick with normal-incident parallel beams.

### ***Shielding material***

As typical shielding materials, iron and concrete were selected. The densities of two materials and a composition of concrete are also presented (Table 1):

- iron (density  $7.87 \text{ g cm}^{-3}$ );
- concrete (density  $2.27 \text{ g cm}^{-3}$ ) [Type 02-a, ANL-5800, 660 (1963)].

**Table 1. Composition of concrete**

Element	Atomic number density ( $10^{24}/\text{cm}^3$ )	Weight percent
H	1.3851E-2	1.02
C	1.1542E-4	1.00
O	4.5921E-2	53.85
Mg	1.2388E-4	0.22
Al	1.7409E-3	3.44
Si	1.6621E-2	34.21
K	4.6205E-4	1.32
Ca	1.5025E-3	4.41
Fe	3.4510E-4	1.41

***Energy group and fluence to the dose-equivalent conversion factor***

The following energy group is presented as the standard; it is required that the neutron spectra are presented in this energy group, if possible.

**Table 2. Upper energy of 66 neutron energy group (MeV)**

4.00E+2	3.75E+2	3.50E+2	3.25E+2	3.00E+2	2.75E+2	2.50E+2	2.25E+2
2.00E+2	1.80E+2	1.60E+2	1.40E+2	1.20E+2	1.10E+2	1.00E+2	9.00E+1
8.00E+1	7.00E+1	6.50E+1	6.00E+1	5.50E+1	5.00E+1	4.50E+1	4.00E+1
3.50E+1	3.00E+1	2.75E+1	2.50E+1	2.25E+1	2.00E+1	1.75E+1	1.49E+1
1.35E+1	1.22E+1	1.00E+1	8.19E+0	6.70E+0	5.49E+0	4.49E+0	3.68E+0
3.01E+0	2.46E+0	2.02E+0	1.65E+0	1.35E+0	1.11E+0	9.07E-1	7.43E-1
4.98E-1	3.34E-1	2.24E-1	1.50E-1	8.65E-2	3.18E-2	1.50E-2	7.10E-3
3.35E-3	1.58E-3	4.54E-4	1.01E-4	2.26E-5	1.07E-5	5.04E-6	2.38E-6
1.12E-6	4.14E-7	0.10E-9					

In dose calculations, it is recommended to use the neutron flux-to-dose equivalent conversion factor (Table 3) in order to avoid any ambiguity due to the conversion factor used. The values given in Table 3 are the conversion factors of the neutron corresponding to the neutron energies given in Table 2.

**Table 3. Neutron flux-to-dose conversion factor [(Sv/hr)/(n/sec/cm<sup>2</sup>)]  
(ICRP51(1987)[1], 20-400 MeV Table 23, below 20 MeV Table 21)**

2.25E-6	2.20E-6	2.15E-6	2.10E-6	2.05E-6	1.99E-6	1.93E-6	1.86E-6
1.82E-6	1.79E-6	1.77E-6	1.74E-6	1.72E-6	1.70E-6	1.68E-6	1.67E-6
1.65E-6	1.64E-6	1.63E-6	1.62E-6	1.61E-6	1.60E-6	1.59E-6	1.58E-6
1.57E-6	1.56E-6	1.55E-6	1.54E-6	1.53E-6	1.52E-6	2.11E-6	1.89E-6
1.80E-6	1.68E-6	1.56E-6	1.47E-6	1.38E-6	1.36E-6	1.46E-6	1.40E-6
1.34E-6	1.29E-6	1.28E-6	1.30E-6	1.26E-6	1.22E-6	1.13E-6	1.00E-6
7.92E-7	5.79E-7	4.21E-7	2.78E-7	1.32E-7	5.72E-8	3.17E-8	2.80E-8
2.51E-8	2.25E-8	2.44E-8	2.78E-8	3.15E-8	3.40E-8	3.63E-8	3.87E-8
3.98E-8	2.88E-8						

### ***Quantities to be calculated***

The following quantities are required for calculations involving intercomparisons:

- dose equivalent at 50, 100, 150, 200, 250, 300, 350, 400, 450 and 500 cm;
- neutron spectrum in  $n/cm^2/MeV/source$  neutron at 100, 200, 300, 400 and 500 cm.

### **Summary of contributors**

The results from three groups were sent to the organiser before the end of March. Table 4 lists the participants, the name of the computer code used and the name of the data base used in the computer code.

**Table 4. Summary of contributors**

<b>Name of participants and organisation</b>	<b>Name of computer code used for calculations</b>	<b>Name of database used in the computer code</b>
Dominik Dworak (Krakow, Poland) Klaus Tesch, (DESY, Germany) Herbert Dinter, (DESY, Germany)	MORSE	HILO86
Nikolai Mokhov (FNAL)	MARS13(97)	Library data in MARS
Nagao Tadashi & Sakamoto Yukio (JAERI)	ANISN-JR	HIRO86R

### **Results and discussion**

The attenuation of the dose equivalents inside concrete is summarised in Tables 5 and 6 for planar and spherical geometry, respectively. Table 6 gives the dose equivalents multiplied by the radius (m) squared. MORSE calculations were performed for only the plane-geometry case with a cylinder of 500 cm diameter and 500 cm length.

The results agree well between three calculations, except in the case of a 40-50 MeV source. As an example, the results for a 90-100 MeV source in the plane geometry are shown in Figure 1.

The neutron attenuation lengths of concrete for both geometries are shown in Figure 2. All of the results agree fairly well with each other, and show the same tendency to increase along with an increase in the source neutron energy. Figure 2 gives also the neutron attenuation lengths by Paterson and Thomas [2]. The present results agree well with those by Paterson and Thomas at 50 and 100 MeV, but are smaller at 200 and 400 MeV. It seems that present results reach a high energy limit at a higher energy region than those by Paterson & Thomas.

**Table 5. Dose equivalents inside concrete for plane parallel neutrons (pSv per source neutron per cm<sup>2</sup>)**

Depth (cm)	45-50 MeV source			90-100 MeV source		
	MORSE HILO86	MARS	ANISN-JR HILO86R	MORSE HILO86	MARS	ANISN-JR HILO86R
25	6.48E+02			7.89E+02		
50	3.25E+02	3.11E+02	3.72E+02	5.53E+02	6.47E+02	6.09E+02
75	1.34E+02			3.41E+02		
100	5.13E+01	3.57E+01	5.83E+01	1.97E+02	2.10E+02	2.14E+02
125	1.76E+01			1.07E+02		
150	5.92E+00	3.21E+00	6.81E+00	5.83E+01	5.85E+01	6.29E+01
200	6.32E-01	2.86E-01	7.08E-01	1.56E+01	1.54E+01	1.67E+01
250	5.12E-02	1.44E-02	6.92E-02	4.04E+00	3.96E+00	4.18E+00
300	2.90E-03	1.67E-04	6.51E-03	9.73E-01	9.76E-01	1.00E+00
350		3.61E-06	6.00E-04	2.36E-01	2.73E-01	2.34E-01
400		3.35E-09	5.39E-05	7.68E-02	7.85E-02	5.34E-02
450		5.85E-12	4.75E-06	1.30E-02	1.99E-02	1.20E-02
500		4.01E-14	4.14E-07	4.71E-03	2.73E-03	2.68E-03
Depth (cm)	180-200 MeV source			375-400 MeV source		
	MORSE HILO86	MARS	ANISN-JR HILO86R	MORSE HILO86	MARS	ANISN-JR HILO86R
25	9.70E+02			1.31E+03		
50	8.08E+02	1.08E+03	8.77E+02	1.20E+03	2.26E+03	1.29E+03
75	6.02E+02			9.81E+02		
100	4.16E+02	4.72E+02	4.41E+02	7.35E+02	1.14E+03	7.80E+02
125	2.81E+02			5.33E+02		
150	1.81E+02	1.84E+02	1.93E+02	3.72E+02	5.06E+02	4.00E+02
200	7.40E+01	6.77E+01	7.74E+01	1.73E+02	2.15E+02	1.87E+02
250	2.81E+01	2.21E+01	2.93E+01	7.49E+01	8.92E+01	8.16E+01
300	1.05E+01	7.83E+00	1.07E+00	3.13E+01	3.53E+01	3.42E+01
350	3.69E+00	3.04E+00	3.77E+00	1.25E+01	1.51E+01	1.39E+01
400	1.47E+00	8.30E-01	1.30E+00	4.75E+00	5.40E+00	5.49E+00
450	3.49E-01	3.02E-01	4.42E-01	2.30E+00	2.30E+00	2.13E+00
500	9.62E-02	7.84E-02	1.48E-01	4.27E-01	1.20E+00	8.14E-01

**Table 6. Dose equivalents multiplied by the radius (m) squared inside concrete for point isotropic neutrons(pSv\*m<sup>2</sup> per source neutron)**

Radius (cm)	45-50 MeV source		90-100 MeV source	
	MARS	ANISN-JR HILO86R	MARS	ANISN-JR HILO86R
50	8.72E-03	3.30E-03	5.43E-03	5.08E-03
100	4.82E-04	6.20E-04	1.96E-03	1.86E-03
150	5.69E-05	9.00E-05	6.19E-04	5.83E-04
200	6.00E-06	1.15E-05	1.79E-04	1.60E-04
250	7.75E-07	1.30E-06	5.23E-05	4.63E-05
300	1.03E-08	1.47E-07	1.22E-05	1.22E-05
350	1.19E-09	1.54E-08	3.32E-06	3.12E-06
400	4.61E-13	1.55E-09	9.73E-07	7.80E-07
450	1.38E-15	1.53E-10	1.58E-07	1.91E-07
500	5.48E-18	1.46E-11	1.20E-08	4.60E-08
Radius (cm)	180-200 MeV Source		375-400 MeV Source	
	MARS	ANISN-JR HILO86R	MARS	ANISN-JR HILO86R
50	8.90E-03	6.86E-03	1.82E-02	9.61E-03
100	4.27E-03	3.77E-03	9.84E-03	6.54E-03
150	1.80E-03	1.75E-03	4.75E-03	3.71E-03
200	7.00E-04	7.45E-04	2.21E-03	1.90E-03
250	2.51E-04	3.00E-04	8.94E-04	9.09E-04
300	9.27E-05	1.16E-04	3.64E-04	4.14E-04
350	3.09E-05	4.36E-05	1.56E-04	1.82E-04
400	1.01E-05	1.60E-05	5.78E-05	7.73E-05
450	3.44E-06	5.77E-06	2.13E-05	3.21E-05
500	2.22E-06	2.05E-06	1.08E-05	1.31E-05

**Figure 1. Attenuation of the dose equivalent inside concrete (plane geometry)**

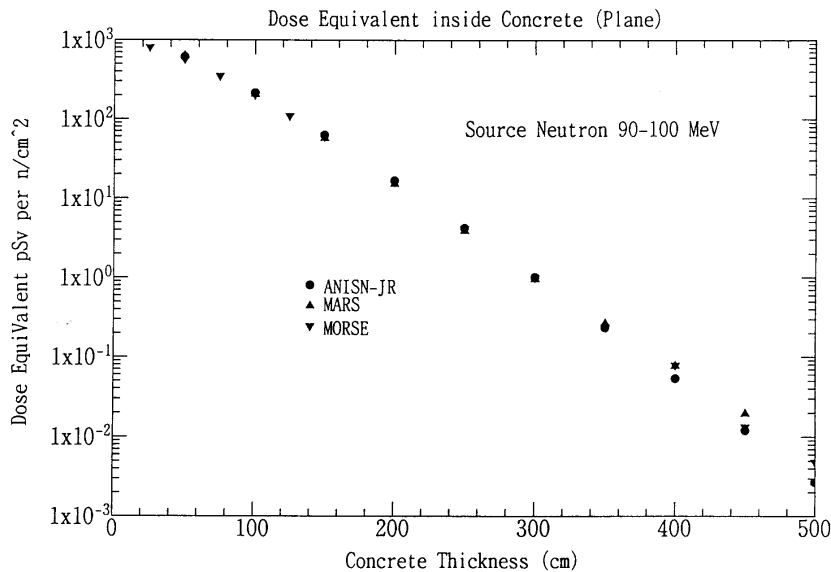
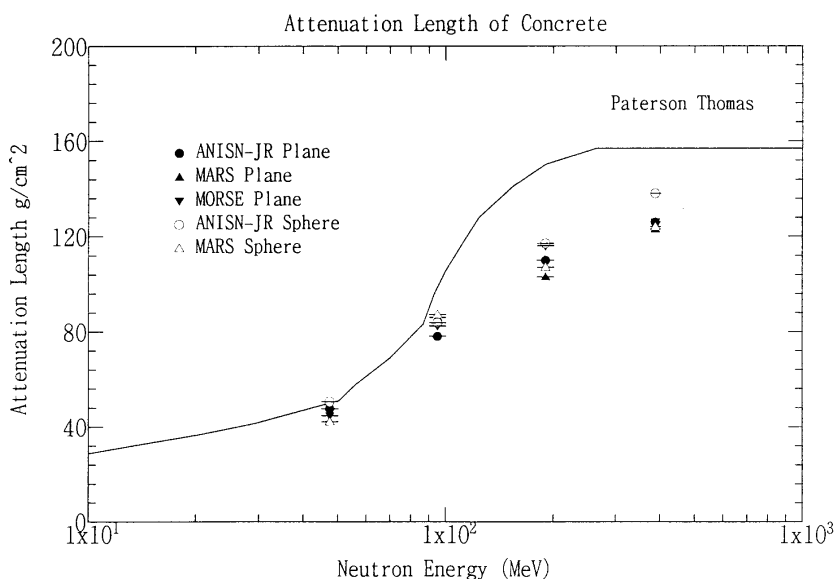


**Figure 2. Comparison of the attenuation length of concrete**



The attenuation of the dose equivalent inside iron is summarised in Tables 7 and 8 for the planar and spherical geometry, respectively. In Table 8, the dose equivalents multiplied by radius (m) squared are given. MORSE calculations were performed for only the planar geometry case with a cylinder of 400 cm diameter and 300 cm length.

**Table 7(a). Dose equivalents inside iron for plane parallel neutrons (pSv per source neutron per cm<sup>2</sup>)**

Depth (cm)	45-50 MeV Source			90-100 MeV Source		
	MORSE HILO86	MARS	ANISN-JR JILO86R	MORSE HILO86	MARS	ANISN-JR HILO86R
15	1.90E+03			2.91E+03		
30	1.24E+03			2.32E+03		
50	5.35E+02	2.64E+02	5.60E+02	1.23E+03	7.14E+02	1.20E+03
75	1.51E+02			4.21E+02		
100	3.87E+01	2.16E+01	4.35E+01	1.23E+02	7.10E+01	1.13E+02
125	7.52E+00			3.27E+01		
150	1.87E+00	2.61E+00	3.22E+00	9.20E+00	7.62E+00	8.75E+00
175	2.95E-01			2.88E+00		
200	6.37E-02	3.78E-01	2.71E-01	7.74E-01	1.20E+00	7.16E-01
225	7.39E-02			1.68E-02		
250	4.15E-03	7.90E-02	2.57E-02	1.65E-03	1.87E-01	6.55E-02
275	9.10E-04			5.61E-04		
300		1.90E-02	2.60E-03		3.34E-02	6.49E-03
350		4.35E-03	2.70E-04		7.45E-03	6.67E-04
400		1.12E-03	2.82E-05		1.91E-03	6.94E-05
450		1.57E-04	2.93E-06		3.20E-04	7.24E-06
500		1.06E-05	3.04E-07		1.86E-05	7.51E-07

**Table 7(b). Dose equivalents inside iron for plane parallel neutrons (pSv per source neutron per cm<sup>2</sup>)**

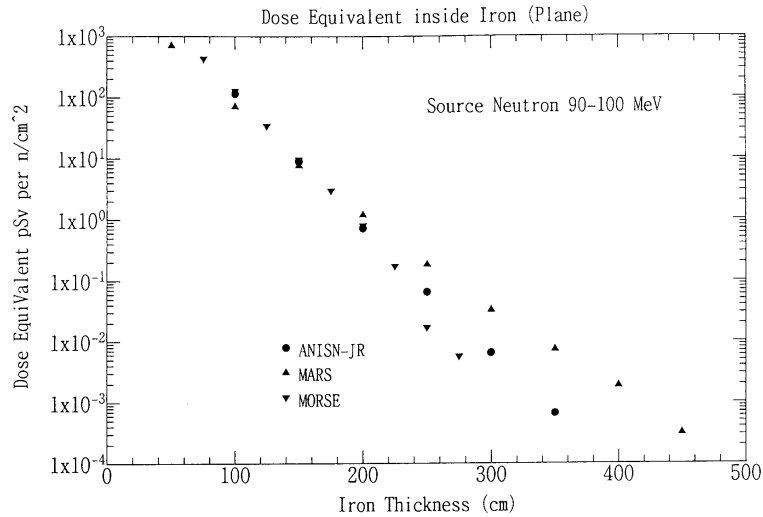
Depth (cm)	180-200 MeV Source			375-400 MeV Source		
	MORSE HILO86	MARS	ANISN-JR HILO86R	MORSE HILO86	MARS	ANISN-JR HILO86R
15	4.20E+03			6.59E+03		
30	3.84E+03			6.32E+03		
50	2.44E+03	1.53E+03	2.60E+03	4.19E+03	3.15E+03	4.35E+03
75	1.01E+03			1.84E+03		
100	3.63E+02	2.02E+02	4.34E+02	7.56E+02	4.96E+02	8.22E+02
125	1.15E+02			2.52E+02		
150	3.71E+01	2.16E+01	4.97E+01	8.66E+01	5.90E+01	1.05E+02
175	1.00E+01			2.54E+01		
200	3.88E+00	3.15E+00	4.92E+00	6.93E+00	7.23E+00	1.13E+01
225	1.17E+00			1.50E+00		
250	5.73E-01	4.86E-01	4.65E-01	3.13E-01	1.22E+00	1.15E+00
275	1.50E-01			6.83E-02		
300	7.24E-02	1.02E-01	4.41E-02		1.76E-01	1.13E-01
350		1.95E-02	4.27E-03		5.50E-02	1.12E-02
400		4.84E-03	4.25E-04		9.21E-03	1.11E-03
450		4.75E-04	4.31E-05		7.73E-04	1.12E-04
500		3.83E-05	4.43E-06		2.18E-04	1.14E-05

**Table 8. Dose equivalents multiplied by the radius (m) squared inside iron for point isotropic neutrons (pSv\*m<sup>2</sup> per source neutron)**

Radius (cm)	45-50 MeV Source		90-100 MeV Source	
	MARS	ANISN-JR HILO86R	MARS	ANISN-JR HILO86R
50	6.30E-03	1.36E-02	1.15E-02	1.98E-02
100	1.11E-03	2.14E-03	2.12E-03	3.50E-03
150	2.00E-04	2.38E-04	3.58E-04	4.22E-04
200	4.32E-05	2.65E-05	7.52E-05	4.64E-05
250	1.05E-05	3.11E-06	1.76E-05	5.30E-06
300	2.93E-06	3.74E-07	4.68E-06	6.24E-07
350	8.26E-07	4.52E-08	1.35E-06	7.52E-08
400	2.10E-07	5.39E-09	3.98E-07	8.88E-09
450	5.37E-08	6.32E-10	1.20E-07	1.04E-09
500	4.78E-09	7.33E-11	2.95E-08	1.21E-10
Radius (cm)	180-200 MeV Source		375-400 MeV Source	
	MARS	ANISN-JR HILO86R	MARS	ANISN-JR HILO86R
50	2.11E-02	3.18E-02	4.00E-02	5.11E-02
100	4.28E-03	7.08E-03	9.33E-03	1.33E-02
150	7.56E-04	1.58E-03	1.69E-03	2.05E-03
200	1.48E-04	1.15E-04	3.08E-04	2.63E-04
250	3.44E-05	1.32E-05	7.00E-05	3.14E-05
300	8.91E-06	1.52E-06	1.72E-05	3.66E-06
350	2.82E-06	1.75E-07	5.11E-06	4.21E-07
400	6.25E-07	2.03E-08	1.79E-06	4.81E-08
450	1.74E-07	2.37E-09	4.56E-07	5.55E-09
500	7.15E-08	2.73E-10	2.38E-07	6.30E-10

Large differences can be seen between the MARS results and other ones, especially deep inside iron at all source energies. As an example, the results of 90-100 MeV source for the planar geometry case are shown in Figure 3.

**Figure 3. Attenuation of the dose equivalent inside iron (Plane geometry)**



The neutron attenuation lengths of iron for both geometries are shown in Figure 4. The variation in the attenuation length for different source neutron energies was small for each calculation. On the other hand, the attenuation lengths vary greatly, depending on the calculation method or geometry. The total dose equivalents inside iron are influenced by slow neutrons below a few tenths keV. Figure 5 shows the attenuation length of the dose equivalents due to neutrons above 20- or 100 MeV neutrons, calculated by ANISN-JR. The attenuation length of the dose equivalents, not including low-energy neutrons, shows a clear dependence on the energy of the source neutrons, like that of concrete. It is, therefore, supposed that the differences between the different computer codes and data may become smaller in comparisons of these quantities.

**Figure 4. Comparison of the attenuation length of iron**

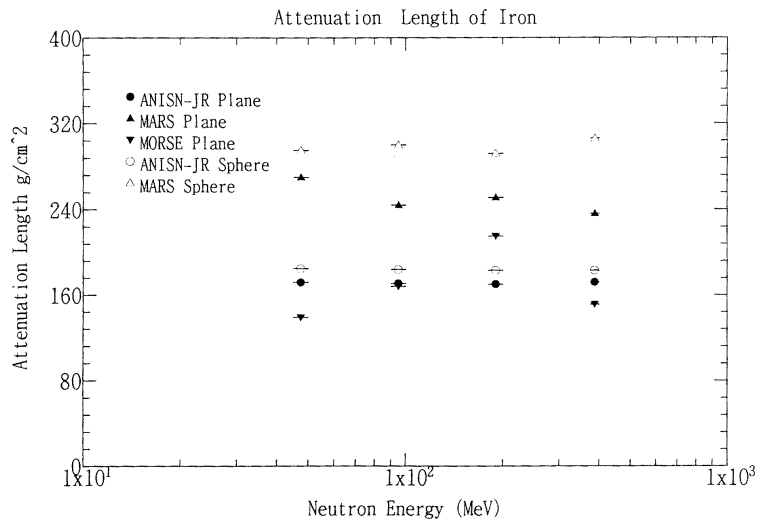
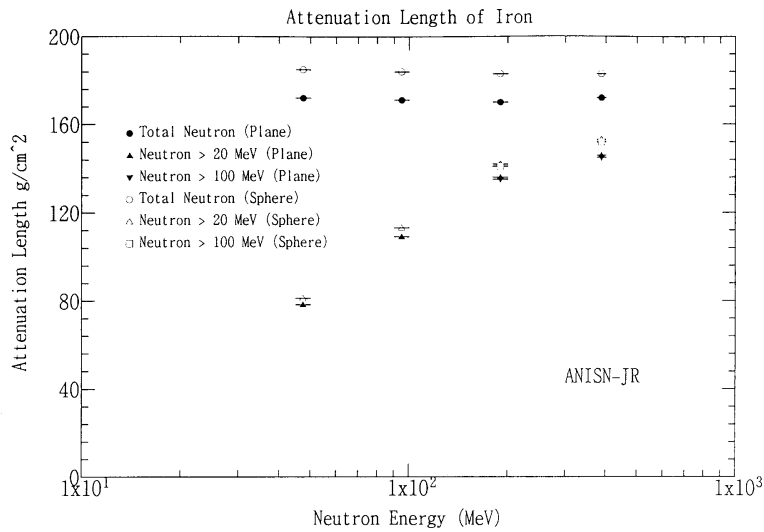


**Figure 5. Attenuation length of the dose equivalents inside iron due to neutrons above 20- or 100 MeV neutrons calculated by ANISN-JR**



### Future themes

From the comparisons mentioned above, it is necessary to perform the following intercomparisons as the next step:

- *Concrete shield*
  - neutron dose-equivalent attenuation for higher energy source neutrons in order to confirm whether the attenuation length reaches a constant value or not.
- *Iron shield*
  - compare the cross-section database used in each computer code in order to understand the reason for the large difference in the attenuation tendency;
  - the neutron dose-equivalent attenuation due to neutrons without low-energy ones to confirm the consistent tendency with the Moyer model obtained by ANISN-JR;
  - neutron dose-equivalents attenuation for higher energy source neutrons to confirm whether the attenuation length reaches a constant value or not.
- *Both shields*
  - comparisons of the neutron spectrum;
  - neutron dose equivalents attenuation due to protons incident on a target.

## **Conclusion**

This intercomparison was very useful for understanding the neutron attenuation inside shielding materials of concrete and iron, even with a comparison between three groups. Good agreements were obtained in the case of concrete. The attenuation length of concrete was understood fairly well from this intercomparison. On the other hand, the results for iron are different, especially between MARS and others which use HILO86 based data. It is necessary to check the cross-section data in the case of iron. The definition of the attenuation length for iron must also be discussed due to the large contribution of low-energy neutrons to the total dose equivalents.

It is desired to continue this type of intercomparison, including the contributions of other groups.

## **REFERENCES**

- [1] ICRP Publication 51, "Data for Use in Protection Against External Radiation", Annals of the ICRP 17 (2/3) (1987).
- [2] W. Paterson and R. H. Thomas, "Accelerator Health Physics", Academic Press, New York and London (1973).



# *Shielding Experiments and Compilation*



## BULK SHIELDING EXPERIMENTS AT TIARA AND ISIS

**Yukio Sakamoto**

**Hiroshi Nakashima**

Japan Atomic Energy Research Institute  
Tokai Establishment, Japan

**Yoshitomo Uwamino**

Institute of Physics and Chemistry  
Research, RIKEN, Japan

**Noriaki Nakao**

High Energy Accelerator Research  
Organisation, Tanashi Branch, Japan

**Hiroyuki Handa**

Hitachi Engineering, Japan

**Takashi Nakamura**

Tohoku University, Cyclotron and  
Radioisotope Centre, Japan

**Tokushi Shibata**

High Energy Accelerator  
Research Organisation, Japan

**Shun-ichi Tanaka<sup>1</sup>, Susumu Tanaka<sup>1</sup>,  
Yoshihiro Nakane<sup>1</sup>, Hiroshi Takada<sup>1</sup>,  
Shinichiro Meigo<sup>1</sup> Kazuo Shin<sup>2</sup>,  
Mamoru Baba<sup>3</sup>, Makoto Nakao<sup>3</sup>**

TIARA Experimental Group  
<sup>1</sup> JAERI

<sup>2</sup> Kyoto University

<sup>3</sup> Tohoku University

**Tooru Okubo<sup>4</sup>, Shingo Sato<sup>4</sup>, David Perry<sup>5</sup>,  
Katsumi Hayashi<sup>6</sup>, Masasato Saitou<sup>6</sup>,  
Koubun Yamada<sup>7</sup>, Teruo Abe<sup>7</sup>**

ISIS Experimental Group

<sup>4</sup> KEK

<sup>5</sup> Rutherford Appelton Lab

<sup>6</sup> Hitachi Eng.

<sup>7</sup> Business Automation

### Abstract

Benchmark shielding experiments were performed on a thick bulk shield at 90 MV, both at the TIARA cyclotron facility of the Japan Atomic Energy Research Institute and the intense spallation neutron source facility ISIS of the Rutherford Appleton Laboratory. In TIARA quasi-monoenergetic neutrons were used to measure neutron energy spectra, reaction rates and dose rates with various detectors behind iron, ordinary concrete and polyethylene with various thickness. Analyses have been made using MORSE-CG, MCNP4A and DOT3.5 codes with group cross-sections HILO86, and HETC-KFA2 code in the HERMES system. This experiment was adopted to one benchmark problem of the accelerator bulk shielding and was analysed by using various codes in SATIF group. For ISIS, reaction rates were measured by using activation detectors at the surface of the top shield. The ISIS experiment was analysed using HERMES with multi-layer techniques, ANISN, DOT3.5 and TORT with HILO86R cross-section library. The streaming neutrons are well analysed through the use of the three-dimensional discrete ordinates code TORT.

## Introduction

The costs of radiation shields in an intense high-energy accelerator facility contributes to a considerable portion of total costs, shielding design is important for the construction on facility and radiation safety. It is essential to confirm the nuclear data and model codes for shielding design in the intermediate energy region above 20 MeV. Thus, experimental studies on accelerator shielding have been planned and carried out in a 90 MV cyclotron, Takasaki Ion Accelerator for Advanced Radiation Facility (TIARA) and an intense spallation neutron source facility ISIS of the Rutherford Appleton Laboratory. In SATIF, the preliminary results of experiments and analyses were reported in [1,2]. In this report, the progress are described hereafter.

## TIARA experiment

The cross-sectional view on the beam course for neutron bulk shielding experiments is shown in Figure 1. The quasi-monoenergetic neutrons produced by p-Li reactions at 0 degrees in the Li target were transported to the shielding experimental space through the iron rotary shutter collimator inserted in the 2.2-m thick concrete shielding wall. Figure 2 gives the energy spectra of 40- and 65-MeV source neutrons obtained by the TOF measurement with the BC501A organic liquid scintillator. The absolute peak fluxes were estimated by the measurements with PRT (Proton Recoil counter Telescope).

The characteristics of bulk shielding experiments at TIARA are as follows:

- 1) quasi-monoenergetic neutron sources between 20 and 90 MeV;
- 2) low background measurements by the separation of target room and experimental space;
- 3) beam axis and off-beam axis measurements with collimated neutrons;
- 4) neutron spectrum and reaction rates for the energy range from source neutron to thermal neutron measured by various spectrometer and detectors with different neutron energy sensitivity.

Neutron energy spectra above a few MeV behind the shield were measured with organic liquid scintillator BC501A and the FERDOU unfolding code, and those between thermal energy and source neutron energy with multi-moderator counter (bonner sphere) and the SAND-2 unfolding code. Neutron reaction rates and dose rates were also measured with  $^{238}\text{U}$  and  $^{232}\text{Th}$  fission counters, rem counter, track detectors and TLDs. Measured all data for iron and concrete shields were reported in [3] and [4]. Those were also compiled to the neutron transmission benchmark problems for iron and concrete shields in low energy proton accelerator facilities [5]. An intercomparison of shielding calculation codes has been done in the one of the activities of SATIF group [6].

The neutron spectra calculated by using various codes behind iron, concrete and polyethylene were compared with measured ones [7,8,9,10]. Analyses have been made by using of MORSE-CG, MCNP4A and DOT3.5 codes with group cross-sections HILO86, and HETC-KFA2 code in the HERMES system. The measured and calculated neutron energy spectra on the beam axis transmitted through polyethylene shields of various thickness are shown in Figure 3 for 65-MeV quasi-monoenergetic source neutrons. The bonner sphere detector gives the spectra over the entire

energy range from thermal to peak energy in Figure 3(a), and the BC501A detector gives the spectra above a few MeV in Figure 3(b). The calculated spectra with MORSE code are in good agreement with the BC501A spectra above a few MeV for thinner polyethylene shield, but become larger than the BC501A spectra with the shield thickness. The neutron energy spectra measured the BC501A detector on the surface on and off the beam axis are compared with the MORSE calculation in Figure 4. As a whole, the MORSE calculation gives rather good agreement with the experiment, but the over-estimation of the calculation results becomes larger for 61.0 cm thick polyethylene for 65-MeV quasi-monoenergetic neutrons. This facts lead to a conclusion that angular distributions given by the Legendre expansion coefficients in the calculation have some problems.

## ISIS experiment

The ISIS facility consists of a 70-MeV  $H^+$  linear accelerator, an 800-MeV proton synchrotron and a target station. The beam intensity was about 180 microA at the target with 50 Hz repetition rate. A cross-sectional view along the 800-MeV proton beam axis is shown in Figure 5 for the target station. The tantalum target is placed at the centre of the helium-filled stainless-steel vessel. The moderators and reflectors for thermal and cold neutrons are placed around the target, and the spallation neutron source is shielded with 3-m thick iron and a 1-m thick ordinary concrete shield. The neutron flux distribution at the top of the target station where there is few penetrations was measured unlike the side shielding where there are many neutron beam channels and beamshutters. Neutron reaction rates were measured by the activation detectors and dosimeters placed directly on the surface of the shield top of the target station.

Neutron reaction rates were measured by indium-activation multi-moderator spectrometer,  $^{12}C(n,2n)^{11}C$  activation detector,  $^{27}Al(n,2n\alpha)^{22}Na$  activation detector and  $^{209}Bi(n,xn)$  activation detector. Fast neutron dose were measured by solid state neutron track detectors, photon and thermal-neutron dose were measured with thermoluminescence dosimeters. Figure 6 shows the fast neutron distribution along y axis measured with track detectors. The neutron strengths downstream of the proton beam are largely due to the existence of the helium duct.

Source neutron spectrum from tantalum target was calculated with HETC-KFA2 code. Transmission neutron spectra in bulk shield were also calculated by using HETC-KFA2 code with multi-layer technique. As a reference, ANISN code was used with HILO86R cross-section library. Table 1 shows the ratio of calculated value to the experimental result [11]. The ratio for HETC result varies form 0.2 to 0.3 for six decades attenuation. The ratio for ANISN result varies from 0.05 to 0.1 and smaller than that for HETC result. For the evaluation of stray neutron through the helium duct, DOT and TORT calculations were made [12]. Table 4 show C/E values  $^{209}Bi(n,10n)$ ,  $(n,7n)$  and  $(n,6n)$  reaction rates, and neutron does equivalents. Near the exit of helium duct at 4 m apart from the centre, C/E values of TORT calculation provide 1.18 - 1.53, which are improved from the C/E values: 4.83 - 5.72 of DOT calculation which overestimated the streaming neutrons through the helium duct by the approximation of helium duct to annular ling in R-Z geometry. Both the C/E values of DOT and TORT calculation indicate the tendency that as the measured position approaches the centre of the shield top, C/E values decrease to below one. The point apart from the duct, where the streaming effects were migrated, was caused by the error concerning the deep penetration through the thick iron and concrete shield. The error may be produced by the insertion of source neutron strength above 400 MeV to the top energy group of HILO86R, the ambiguity of nominal density of iron and concrete shields, and the accuracy of neutron cross-section and Legendre Expansion.

## Summary and future plan

The experimental data for bulk shielding of intermediate energy neutron above 20 MeV were obtained at TIARA and ISIS.

Neutron spectra of 40- and 65-MeV quasi-monoenergetic neutron transmitted through the iron, concrete and polyethylene shields in TIARA calculated by MORSE, DOT3.5 and MCNP with the HILO86 library are in good agreement with the measured ones on beam axis. On the off-beam axis, the MORSE results are also in good agreement with measured ones in spite of a low number of Legally expansion of scattering cross-section.

In the ISIS experiment, the neutron strength distribution was measured with various activation detectors and dosimeters. The neutron strength was large downstream along the proton beam line due to the existence of helium duct. The stray neutron strength through the duct can be evaluated by the TORT code. In the bulk shield, the ANISN result is smaller than that of HETC because of the insertion of neutron source above 400 MeV to the top energy group, the accuracy of neutron group cross-section and Legendary expansion.

More deeper bulk shielding experiments of intermediate and high energy neutron will be necessary to verify the shielding code for accelerator facility design. We have plans for concrete shielding experiments of high energy neutrons above 1 GeV in KEK and AGS of BNL.

## REFERENCES

- [1] S. Tanaka *et al.*, "Shielding Experiments and Analysis at 90 MV AVF Cyclotron Facility, TIARA", Proc. of the Specialists Meeting on Shielding Aspects of Accelerators, Targets and Irradiation Facilities, OECD Documents, 195 (1995).
- [2] Y. Uwamino *et al.*, "Study on Bulk Shielding of an 800-MeV Proton Accelerator", Proc. of the Specialists Meeting on Shielding Aspects of Accelerators, Targets and Irradiation Facilities, OECD Documents, 185 (1995).
- [3] H. Nakashima *et al.*, "Experiments on Iron Shield Transmission of Quasi-Monoenergetic Neutrons Generated by 43- and 68-MeV Protons via the Li-7(p,n) Reaction", JAERI-Data/Code 96-005 (1996).
- [4] N. Nakao *et al.*, "Experimental Data on Concrete Shield Transmission of Quasi-Monoenergetic Neutrons Generated by 43- and 68-MeV Protons via the Li-7(p,n) Reaction", JAERI-Data/Code, to be published.
- [5] Y. Nakane *et al.*, "Neutron Transmission Benchmark Problems for Iron and Concrete Shields in Low, Intermediate and High Energy Proton Accelerator Facilities", JAERI-Data/Code 96-029 (1996).

- [6] Y. Nakane *et al.*, submitted to this specialists meeting.
- [7] H. Nakashima *et al.*, "Transmission Through Shields of Quasi-Monoenergetic Neutrons Generated by 43- and 68-MeV Protons - II: Iron Shielding Experiment and Analysis for Investigating Calculational Method and Cross-Section Data", *Nucl. Sci. Eng.*, 124, 243 (1996).
- [8] H. Nakao *et al.*, "Transmission Through Shields of Quasi-Monoenergetic Neutrons Generated by 43- and 68-MeV Protons - I: Concrete Shielding Experiment and Calculation for Practical Application", *Nucl. Sci. Eng.*, 124, 228 (1996).
- [9] H. Nakao *et al.*, "Measurements and Calculations of Neutron Energy Spectra Behind Polyethylene Shields Bombarded by 40- and 65-MeV Quasi-Monoenergetic Neutron Source", *J. Nucl. Sci. Tech.*, 34, 348 (1997).
- [10] H. Nakane *et al.*, "Benchmark Calculation of the Transmission of Quasi-Monoenergetic Neutrons generated by 43 and 68 MeV Protons through Iron and Concrete Shields", submitted at SARE3.
- [11] Y. Uwamino *et al.*, "Bulk Shielding Experiment of High Energy Neutron at ISIS", Genshikaku Kenkyu, ISBN-0367-4176, 41, 89 81996 (in Japanese).
- [12] H. Handa *et al.*, "Analyses of the High Energy Neutron Shielding Experiments in ISIS", submitted at SARE3.

**Figure 1. Cross-sectional view of the neutron beam course at TIARA facility**

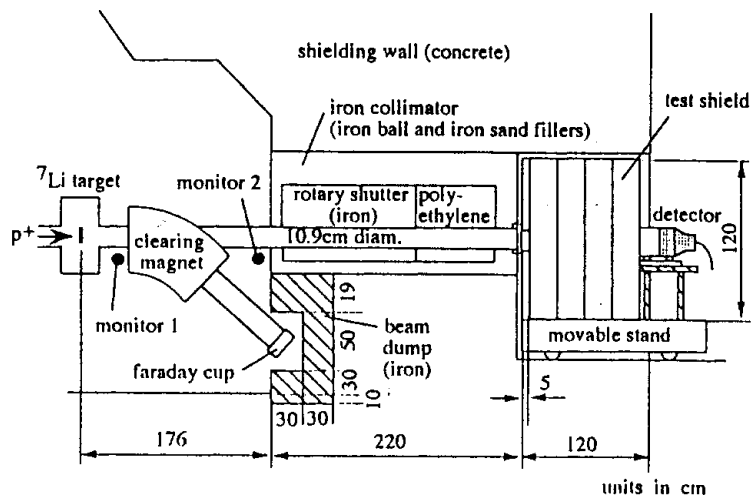


**Figure 2. Energy spectra of quasi-monoenergetic neutron sources measured with the BC501A detectors using TOF method**

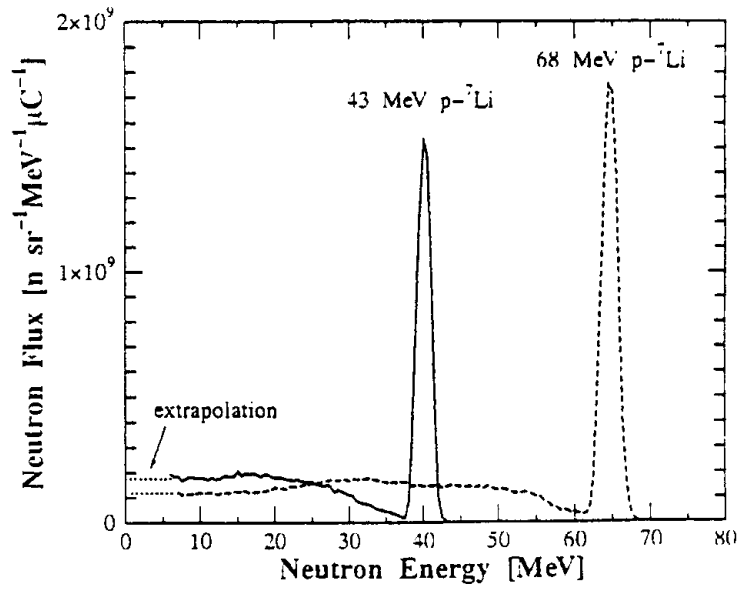


**Figure 3. Comparison of measured and calculated neutron energy spectra behind various thick shield using 65 MeV quasi-monoenergetic neutrons**

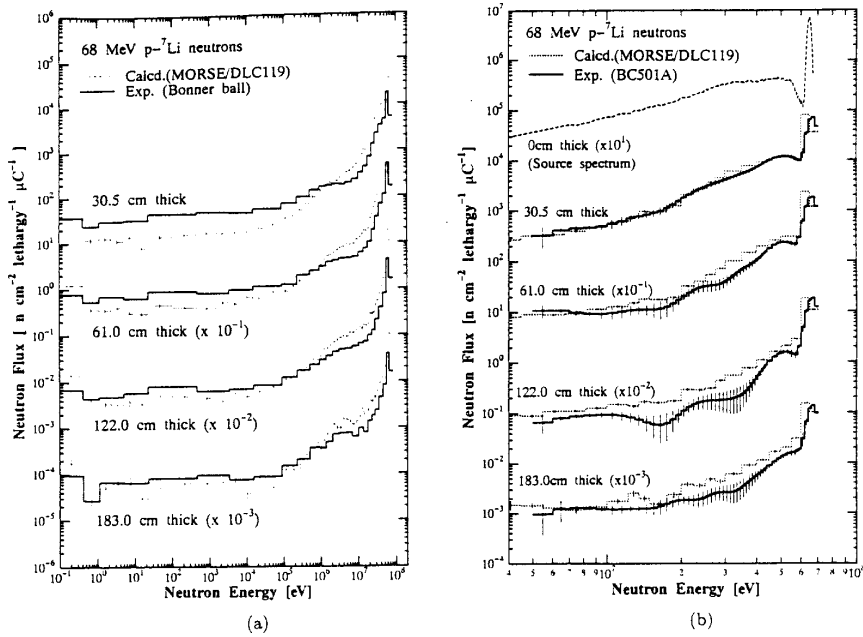


**Figure 4. Comparison of measured and calculated neutron energy spectra on the shield surface on and off the beam axis (a) 30.5-cm thick and (b) 61.0-cm thick shield using 65 MeV quasi-monenergetic neutrons**

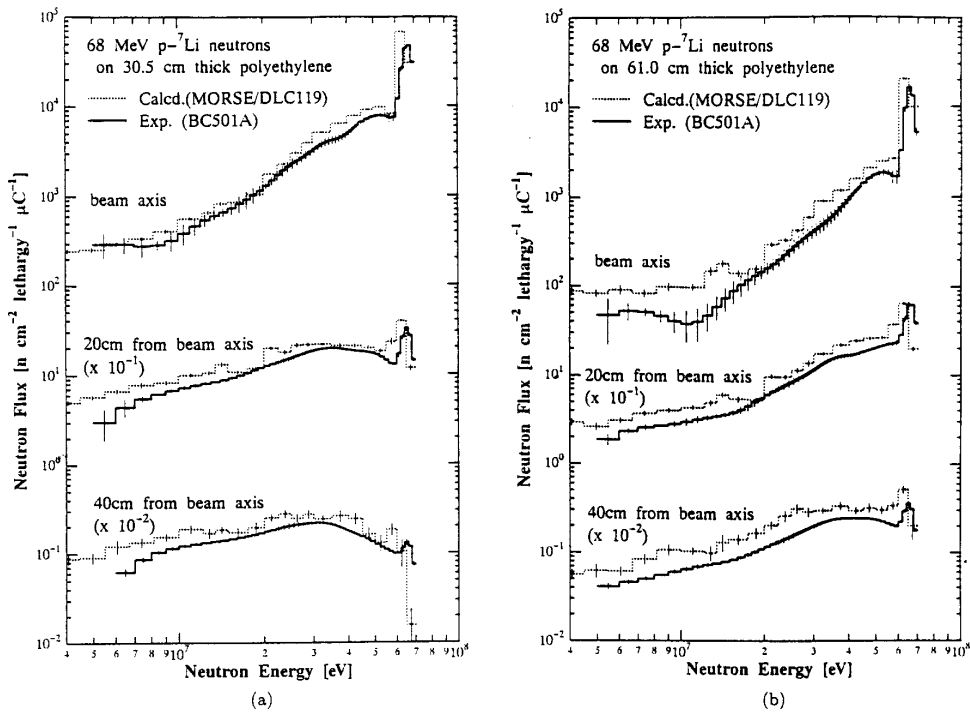


**Figure 5. Cross-sectional view along the beam axis of the ISIS target station**

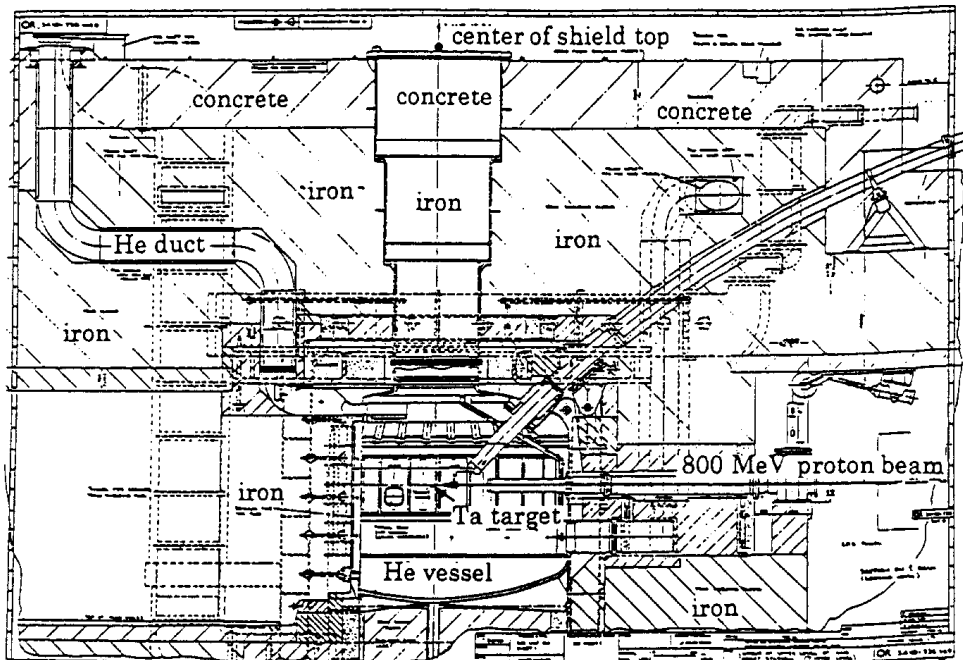


**Figure 6. Fast neutron distribution along y axis measured truck detectors (the numbers in the figure show the x values)**

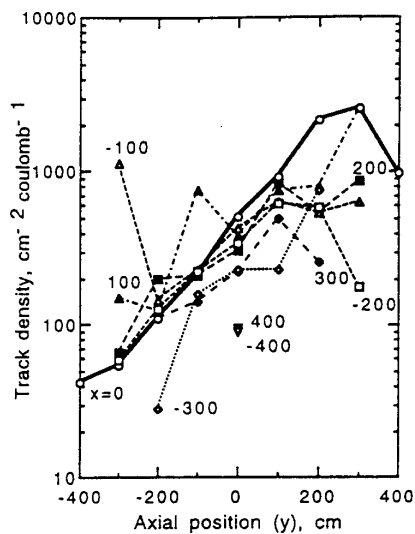


**Table 1. Ratio and calculated values to experimental results at bulk shields**

Item	Calculation ANISN	Calculation HETC	Experiment	C/E ANISN	C/E HETC
$^{209}\text{Bi}(n,10n)^{200}\text{Bi}$ <sup>1)</sup>	$8.13 \times 10^{-22}$	$2.63 \times 10^{-21}$	$1.03 \times 10^{-20}$	0.079	0.26
$^{209}\text{Bi}(n,7n)^{203}\text{Bi}$ <sup>1)</sup>	$2.87 \times 10^{-21}$	$1.07 \times 10^{-20}$	$6.25 \times 10^{-20}$	0.046	0.17
$^{209}\text{Bi}(n,6n)^{204}\text{Bi}$ <sup>1)</sup>	$3.38 \times 10^{-21}$	$1.30 \times 10^{-20}$	$6.52 \times 10^{-20}$	0.052	0.20
Dose equivalent <sup>2)</sup>	15.9	56.7	170	0.094	0.33

<sup>1)</sup> The absolute values are in reaction atom<sup>-1</sup> coulomb<sup>-1</sup>.

<sup>2)</sup> The absolute values are in  $\mu\text{Sv/h}$  at 100  $\mu\text{A}$ .

**Table 2. Comparison between calculated values and experimental ones with consideration of duct steaming effect**

Reaction	Method	Horizontal distance from the centre of shield top											
		4m <sup>3</sup>		3m		2m		1m		0m		-1m	
		Response	C/E	Response	C/E	Response	C/E	Response	C/E	Response	C/E	Response	C/E
$^{209}\text{Bi}$ <sup>1)</sup> (n,10n) $^{200}\text{Bi}$	measured	5.62E-20 <sup>a</sup>		1.45E-19		7.99E-20		3.57E-20		1.03E-20		–	
	DOT	3.22E-19	5.72	3.93E-19	2.71	8.22E-20	1.03	1.07E-20	0.30	3.69E-21	0.36	–	–
	TORT	8.60E-20	1.53	1.24E-19	0.86	5.05E-20	0.63	–	–	–	–	–	–
$^{209}\text{Bi}$ <sup>1)</sup> (n,7n) $^{203}\text{Bi}$	measured	2.28E-19		5.88E-19		4.05E-19		1.72E-19		6.25E-20		2.73E-20	
	DOT	1.10E-18	4.83	1.31E-18	2.23	3.57E-19	0.88	5.13E-20	0.30	1.52E-20	0.24	2.67E-21	0.10
	TORT	2.68E-19	1.18	4.21E-19	0.72	1.84E-19	0.45	–	–	–	–	–	–
$^{209}\text{Bi}$ <sup>1)</sup> (n,6n) $^{204}\text{Bi}$	measured	2.39E-19		6.25E-19		4.32E-19		1.84E-19		6.52E-20		3.17E-20	
	DOT	1.29E-18	5.41	1.53E-18	2.45	4.25E-19	0.98	6.27E-20	0.34	1.89E-20	0.29	3.11E-21	0.10
	TORT	3.13E-19	1.31	4.99E-19	0.80	2.19E-19	0.51	–	–	–	–	–	–
Neutron <sup>2)</sup> dose equivalent	measured									170			
	DOT									86	0.51		
	TORT									–			

<sup>1)</sup> The absolute values are in reaction atom<sup>-1</sup> coulomb<sup>-1</sup>.

<sup>2)</sup> The absolute values are in  $\mu\text{Sv/h}$  at 100  $\mu\text{A}$ .

<sup>3)</sup> The positive value means forward direction of proton beam.

<sup>a</sup> Read as  $5.62 \times 10^{-20}$ .

# **SESSION IV**

## **Miscellaneous Topics – Part I**

*Chairs: L. Waters and Y. Uwamino*



*Neutron Facility for  
Shielding Experiment  
and Detector Calibration*



## NEUTRON FACILITY FOR SHIELDING AND CROSS-SECTION EXPERIMENTS IN JAPAN

**T. Nakamura, M. Takada**  
Cyclotron and Radioisotope Centre  
Tohoku University  
Aoba, Aramaki, Sendai 980-77, Japan

**N. Nakao**  
Institute for Nuclear Study  
University of Tokyo  
Midori-cho 3-2-1, Tanashi 188, Japan

**M. Baba, T. Iwasaki**  
Department of Nuclear Engineering  
Tohoku University  
Aoba, Aramaki, Sendai 980-77, Japan

**H. Nakashima, Sh. Tanaka, S. Meigo, Y. Sakamoto, Y. Nakane**  
Tokai Establishment  
Japan Atomic Energy Research Institute  
Tokai 319-11, Japan

**Su. Tanaka**  
Takasaki Establishment  
Japan Atomic Energy Research Institute  
Watanuki, Takasaki 370-12, Japan

**Y. Uwamino, N. Nakanishi**  
Institute of Physical and Chemical Research  
Hirosawa 2-1, Wako 351-01, Japan

### Abstract

We have developed the quasi-monoenergetic neutron fields using  ${}^7\text{Li}(p,n)$  reaction at three AVF cyclotron facilities: 1) Cyclotron and Radioisotope Centre, Tohoku University (CYRIC) for 20-40 MeV protons, 2) Takasaki Research Establishment, Japan Atomic Energy Research Institute (TIARA) for 40-90 MeV protons, and 3) Institute of Physical and Chemical Research (RIKEN) for 70-210 MeV protons. Using these neutron fields, we have been performing experiments on 1) response functions and efficiencies of neutron detectors, 2) neutron-induced charged particle production cross-sections, 3) neutron penetration through shielding materials, and 4) neutron activation and spallation cross-sections.

## Introduction

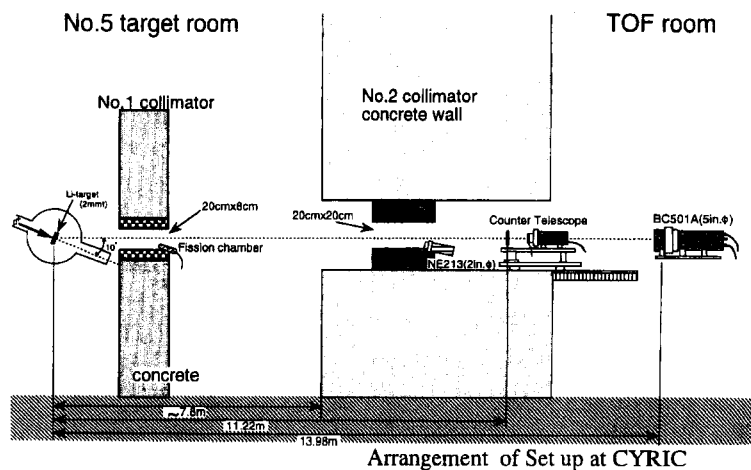
Interest to neutron reaction data is world-wide increasing from the viewpoints of intense neutron source of material study, nuclear transmutation of radioactive wastes, induced radioactivity and shielding design of high energy and intense accelerators. Nevertheless, neutron reaction data in the energy range above 20 MeV are still very poor and no evaluated data file exists at present, mainly due to the fact that a very limited number of facilities have quasi-monoenergetic neutron fields available for neutron reaction cross-section and shielding experiments above 20 MeV.

In this study, we have developed the quasi-monoenergetic neutron fields using  ${}^7\text{Li}(p,n)$  reaction at three AVF cyclotron facilities; 1) Cyclotron and Radioisotope Centre, Tohoku University (CYRIC) for 20-40 MeV protons [1], 2) Takasaki Research Establishment, Japan Atomic Energy Research Institute (TIARA) for 40-90 MeV protons, and 3) Institute of Physical and Chemical Research (RIKEN) for 70-210 MeV protons. Using these neutron fields, we have been performing experiments on 1) response functions and efficiencies of neutron detectors, 2) neutron-induced charged particle production cross-sections, 3) neutron penetration through shielding materials, and 4) neutron activation and spallation cross-sections and so on [2]. These experimental results are quite valuable data in the intermediate neutron energy region, and are partly used as benchmark experimental data for evaluation of calculational methods and intercomparison of computer codes.

## CYRIC neutron field

The CYRIC neutron field was set up in the 45 m long neutron TOF room as shown in Figure 1 [1]. The 25 and 35 MeV proton beams were transported to the scattering chamber through a beam swinger system in the target room to hit a 2 mm thick natural Li target having about 2 MeV loss of incident proton energy. The proton beam was inclined at 10 degrees to the horizontal line with a beam swinger in order to shield spurious neutrons produced from the Faraday cup. The neutrons produced at 10 degrees were extracted to the TOF room through the double collimators. The No. 1 collimator consists of concrete having 1 m thickness and 20 cm $\times$ 8 cm aperture, and the No. 2 collimator, which is situated in the 2.83 m thick concrete wall of 100 cm $\times$ 50 cm aperture, consists of 30 cm thick iron and 30 cm thick polyethylene having a 30 cm $\times$ 20 cm aperture.

Figure 1. Cross-sectional view of the CYRIC neutron calibration field



For measurement of the absolute fluence of neutrons in the high energy peak and relative spectral neutron fluence, three methods were used, including the proton recoil counter telescope (PRCT), the activation method of Li target and the TOF method using a 12.7 cm diameter by 12.7 cm long BC501A organic liquid scintillator. The PRCT consists of Si-SSD dE counter and NaI(Tl) E counter coupled with a large annular type polyethylene radiator. The absolute neutron fluence of the monoenergetic peak region is also given by the activation technique of the Li target. The monoenergetic peak neutrons are generated from the  ${}^7\text{Li}(p,n0,1){}^7\text{Be}$  reaction, the ground state plus first-excited state (0.429 MeV) of  ${}^7\text{Be}$ . The second (4.57 MeV) and higher excited states of  ${}^7\text{Be}$  decay with particle emission and do not remain as the  ${}^7\text{Be}$  nucleus. The peak neutron fluence in the forward direction can be determined by the following equations:

$$\phi(E_p) = N({}^7\text{Li})I_p \left( \frac{d\sigma}{d\Omega} \right)_{\theta=0} \quad (1)$$

$N({}^7\text{Li})$       number of  ${}^7\text{Li}$  in the target

$I_p$             number of injected protons

$\left( \frac{d\sigma}{d\Omega} \right)_{\theta=0}$       differential  ${}^7\text{Li}(p,n)$  cross-section at 0 deg for monoenergetic peak (ground + 1st ex. state)

$$N({}^7\text{Be}) = N({}^7\text{Li})I_p\sigma \quad (2)$$

$N({}^7\text{Be})$       number of  ${}^7\text{Be}$  produced in the target

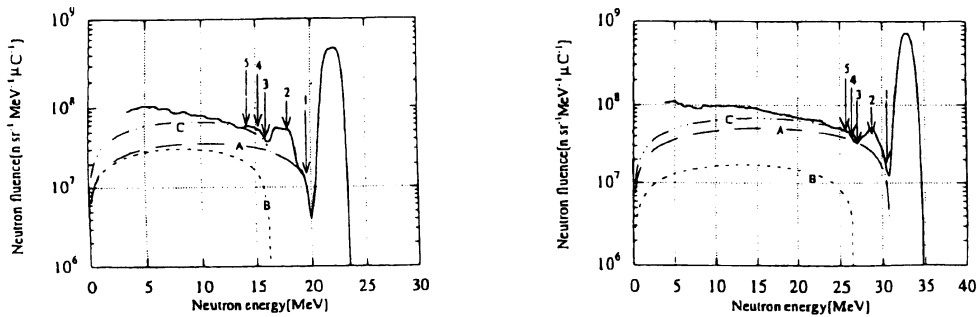
$$\sigma = \int_{4\pi} \left( \frac{d\sigma}{d\Omega} \right) d\Omega$$

$$\phi(E_p) = \frac{N({}^7\text{Be}) \left( \frac{d\sigma}{d\Omega} \right)_{\theta=0}}{\sigma} = N({}^7\text{Be})R \quad (3)$$

The amount of  ${}^7\text{Be}$  can be obtained by measuring the 0.478 MeV gamma rays from  ${}^7\text{Be}$  and accordingly, the peak neutron fluence is given from the ratio R in Eq. (3), which has already been determined by Y. Uwamino *et al.* [3].

The neutron spectra measured with TOF are shown in Figure 2. The monoenergetic peak of 22.2 and 32.9 MeV having 1.9 and 1.8 MeV FWHM was obtained by 25 and 35 MeV proton bombardment, respectively, with the low energy continuum coming from the higher excited states of  ${}^7\text{Be}$ . The 22.2 and 32.9 MeV peak neutron fluences obtained by these three methods are shown in Table 1, together with percentage errors in square brackets. The peak neutron fluences measured with the three methods agree each other within the errors, except the values at 25 MeV proton energy by the TOF method. We decided that the peak neutron fluence given by the PRT is the best value because of the lowest errors. The neutron fluence during the experiment was monitored simultaneously with the  ${}^{238}\text{U}$  fission chamber fixed closely to the target (Figure 1). The 22.2 and 32.9 MeV peak neutron fluences were  $1.2 \times 10^3$  and  $1.8 \times 10^3$  n cm<sup>-2</sup> μC<sup>-1</sup> at the collimator exit behind 8.6 m from the target.

**Figure 2. Neutron spectra at 10° for 25- and 35-MeV p-Li reactions measured with the TOF method. The A to C lines represent three-body phase-space analysis for continuum neutrons**



Neutron spectrum of the  ${}^7\text{Li}(p,n){}^7\text{Be}$  reaction at 10deg for 25MeV proton. Neutron spectrum of the  ${}^7\text{Li}(p,n){}^7\text{Be}$  reaction at 10deg for 35MeV proton.  
 A: three body phase-space from  ${}^7\text{Li}(p,n+{}^3\text{He}+{}^4\text{He})$   
 B: three body phase-space from  ${}^7\text{Li}(p,n+p+{}^4\text{He})$   
 C: A+B

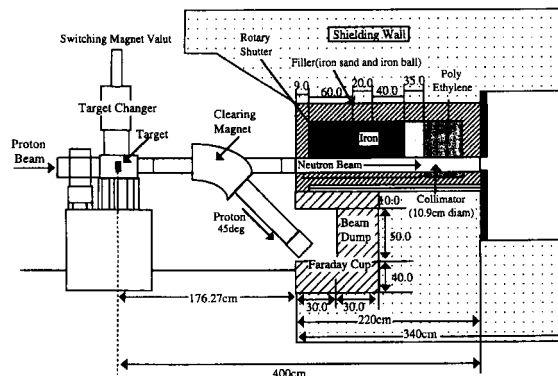
**Table 1. Characteristics of neutron fields at CYRIC (P-F unit is [n/sr/microC])**

P-energy	N-energy	FWHM (MeV)	Peak-fluence-PRT	P-F-Li	P-F-TOF
25 MeV	22.2 MeV	1.9	8.72E+08 (4.3%)	8.53E+08 (7.3%)	7.44E+08 (9.3%)
35 MeV	32.9 MeV	1.8	1.34E+09 (3.2%)	1.46E+09 (7.8%)	1.45E+09 (9.8%)

### TIARA neutron field

The TIARA neutron field has been established for the neutron shielding and cross-section experiments [4]; a cross-sectional view is shown in Figure 3. The 3.6 to 6.6 mm-thick 99.9% enriched  ${}^7\text{Li}$  targets settled in the target chamber in the cyclotron room were bombarded by the proton beams of 45 to 90 MeV at 0 degrees. The protons that penetrated the target were bent down toward the beam dump by the clearing magnet and their integrated charges were measured with the current integrator through a Faraday cup. The neutrons produced at 0 degrees were extracted through the 10.9 cm diameter collimator penetrating 220 cm thick concrete wall between the cyclotron and the experimental rooms. Inside the 340 cm thick concrete wall an empty space of 120- $\times$ 120- $\times$ 120 cm is equipped for the shielding experiment.

**Figure 3. Cross-sectional view of the TIARA neutron calibration field**

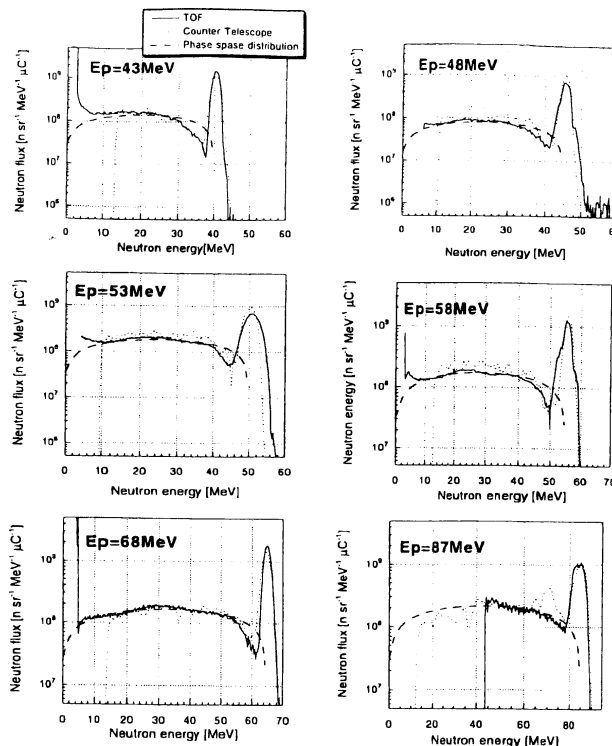


The absolute fluences of source neutrons in the monoenergetic peak per proton beam charge were determined with the same PRT as used in the CYRIC field and are listed in Table 2 with errors and peak energy spread, FWHM, for five proton energies. The neutron fluence during the experiment was monitored simultaneously with the  $^{238}\text{U}$  and  $^{232}\text{Th}$  fission chambers fixed closely to the target as seen in Figure 3. The energy spectra were measured with the PRT and the TOF method using the BC501A organic liquid scintillator and are shown in Figure 4. The TOF spectra and the PRT spectra show generally good agreement together both at peak region and at continuum region. They are also in good agreement with the calculated spectra using the phase space analysis. The peak neutron fluences have values of  $1.7 - 4.0 \times 10^4 \text{ n cm}^{-2} \mu\text{C}^{-1}$  at the collimator exit behind 4 m from the target for 45 to 90 MeV proton incidence.

**Table 2. Characteristics of neutron fields at TIARA**

Proton energy	Neutron energy	FWHM (MeV)	Peak neutron fluence [ $\text{n/cm}^2/\text{C}$ ]
43 MeV	40.0 MeV	3.0	2.24E+10
48 MeV	45.0 MeV	2.4	2.03E+10
53 MeV	51.0 MeV	5.1	2.61E+10
58 MeV	55.0 MeV	3.0	2.91E+10
63 MeV	61.0 MeV	2.6	2.39E+10
68 MeV	65.0 MeV	3.0	3.01E+10
78 MeV	75.0 MeV	3.4	3.34E+10
88 MeV	85.0 MeV	5.0	4.26E+10

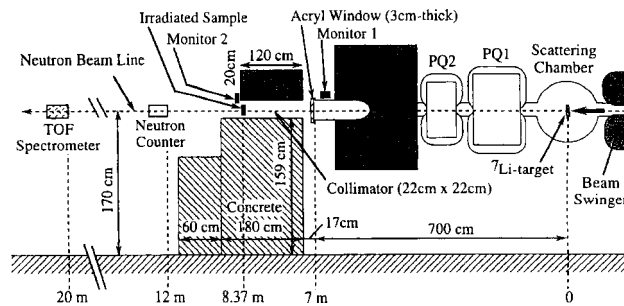
**Figure 4. Neutron spectra at  $0^\circ$  for 43-, 48-, 53, 58-, 68-, and 87- MeV p-Li reactions measured with the TOF and PRT methods, together with the phase space analysis for continuum neutrons**



## RIKEN neutron field

The RIKEN neutron field has been established at the E4 experimental room of the separate sector ring cyclotron. The proton beams having energies of 70, 80, 90, 100, 110, 120, 135, 150 and 210 MeV were injected on a 10 mm thick 99.8% enriched  $^7\text{Li}$  target in the target chamber through the beam swinger. Protons passed through the target were cleared out by the magnet and absorbed in the spectrograph coupled to the beam swinger system to measure the proton beam current. Neutrons produced at 0 degrees were extracted through the vacuum window of 3-cm thick acryl and transported through the iron-concrete collimator of 22 cm $\times$ 22 cm aperture and 120 cm length. Figure 5 gives the cross-sectional view of the RIKEN neutron field.

**Figure 5. Cross-sectional view of the RIKEN neutron calibration field**



The neutron spectra were measured with the TOF method using BC501A and the absolute neutron fluence with the Li activation method using the  $^7\text{Be}$  activity from the  $^7\text{Li}(p,n)^7\text{Be}$  reaction. Figure 6 gives the measured energy spectra and Table 3 gives the peak neutron energies, their FWHMs and the peak neutron fluences for the above eight proton energies. The neutron fluence during the experiment was monitored simultaneously with 20 $\times$ 20 mm by 0.5 mm thick NE102A plastic scintillator set at the collimator exit. The peak neutron fluences at the collimator exit behind 8.37 m from the target are about  $1.3 \times 10^4 \text{ n cm}^{-2} \mu\text{C}^{-1}$  for 70 to 210 MeV proton incidence.

**Figure 6. Neutron spectra at 0 degree for 80-, 90-, 100-, 110-, 120-, 135-, 150-, and 210-MeV p-Li reactions measured with the TOF method**

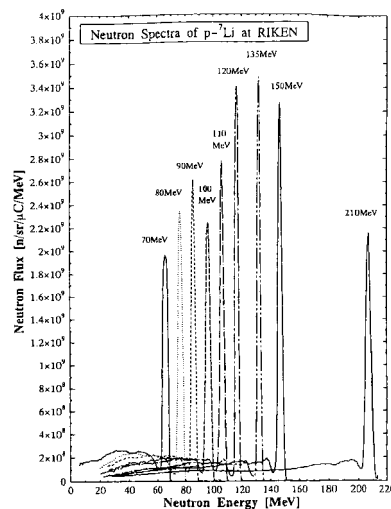


**Table 3. Characteristics of neutron fields at RIKEN**

<b>Proton energy</b>	<b>Neutron energy</b>	<b>FWHM (MeV)</b>	<b>Peak neutron fluence [n/cm<sup>2</sup>/C]</b>
80 MeV	76 MeV	4.0	1.34E+10
90 MeV	86 MeV	2.8	1.42E+10
100 MeV	97 MeV	3.2	1.65E+10
110 MeV	107 MeV	2.9	1.47E+10
120 MeV	117 MeV	2.8	1.53E+10
135 MeV	132 MeV	4.0	1.51E+10
150 MeV	147 MeV	3.0	1.89E+10

## **Conclusion**

We have developed four monoenergetic neutron fields over the wide energy range between 20 MeV and 210 MeV at three cyclotron facilities. These fields are useful for neutron detector calibration, response function measurement, neutron shielding and cross-section measurements.

## **REFERENCES**

- [1] M. Takada, T. Nakamura, M. Baba, T. Iwasaki, T. Kiyosumi, *Nucl. Instr. Methods*, A372, 253-261 (1996).
- [2] T. Nakamura, *et al.*, "Study on the Behavior and Transport of High Energy Particles Through Matter", Research Report for the Grant-in-Aid for Scientific Research from the Ministry of Education in Japan, Cyclotron and Radioisotope Center, Tohoku University (1996).
- [3] Y. Uwamino, T.K. Soewarsono, H. Sugita, Y. Uno, T. Nakamura, T. Shibata, M. Imamura, S. Shibata, *Nucl. Instr. Methods*, in press.
- [4] N. Nakao, H. Nakashima, T. Nakamura, Sh. Tanaka, Su. Tanaka, K. Shin, M. Baba, Y. Sakamoto, Y. Nakane, *Nucl. Sci. Eng.*, 124, 228-242 (1996).



## RECENT RESULTS AT THE CERN-EC HIGH ENERGY REFERENCE FIELD FACILITY

**C. Birattari, T. Rancati**

Università di Milano, Dipartimento di Fisica, Via Celoria 16, 20133 Milan, Italy

**A. Ferrari**

INFN, Sezione di Milano, Via Celoria 16, 20133 Milan, Italy

**M. Höfert, T. Otto, M. Silari**

CERN, 1211 Geneva 23, Switzerland

### Abstract

A reference facility for the intercomparison of active and passive detectors in high energy neutron fields has been available at CERN since 1993. A charged hadron beam (protons, pions) with momenta of 120 GeV/c or 205 GeV/c (positive or negative) hit a copper target, 50 cm thick and 7 cm in diameter. The secondary particles produced in the interaction are filtered by a shielding of either 80 cm of concrete or 40 cm of iron. Behind the iron shielding, the resulting neutron spectrum has a maximum of about 1 MeV, with an additional high energy component. Behind the concrete shielding, the neutron spectrum has a pronounced maximum at about 100 MeV and resembles the high energy component of the radiation field created by cosmic rays at commercial flight altitudes. A wide variety of investigations with active and passive neutron dosimeters are performed twice a year in these two calibration fields. The paper overviews recent results from the facility. Results of measurements of the radiation fields with a Tissue Equivalent Proportional Counter (TEPC) spectrometer agree well with the latest Monte Carlo calculations performed with the FLUKA code. Good agreement is also found between the Monte Carlo results and experimental data taken by a set of Bonner spheres. Recent improvements to the facility are discussed.

## Introduction

A reference radiation facility for the calibration and intercomparison of dosimetric devices in high energy stray radiation fields is available at CERN since 1993. In addition to the obvious interest for testing instrumentation and passive detectors used around high energy particle accelerators, this programme is partially supported by the European Commission, Directorate General XII, in the framework of a research programme for the assessment of radiation exposure at civil flight altitudes [1]. These reference fields are, in fact, sufficiently similar to the cosmic ray field encountered at 10-20 km altitude such that instrumentation is tested at CERN and subsequently used for in-flights measurements on aircraft.

Several measurement campaigns have taken place in the years 1993-1996, and two are planned for 1997 (in June and in July). For each run, the beam time allocation is usually from four days to one week. Several institutions from all over Europe participate (a list is given in [2]), using a number of different techniques, both active and passive, such as multisphere systems, different models of rem counters, different types of Tissue Equivalent Proportional Counters (TEPC), nuclear emulsions, track-etch detectors, superheated drop bubble detectors, albedo dosimeters, etc. [3].

The aim of the present paper is to recall briefly the experimental set-up and give the latest results of Monte Carlo (MC) calculations of the neutron spectral fluences in the reference positions, confirmed by recent measurements made by a set of Bonner spheres. Measurements of the radiation fields with a TEPC spectrometer are also compared to the Monte Carlo results. Recent improvements to the facility are illustrated.

### The CERN-EC high energy reference field facility

The facility [2] is set up at one of the secondary beams (H6) from the Super Proton Synchrotron (SPS), in the North Experimental Area on the Preveessin site of CERN. A positive or negative hadron beam with momentum of either 120 or 205 GeV/c is stopped in a copper target, 7 cm in diameter and 50 cm in length, which can be installed in two different positions in the irradiation cave shown in Figures 1 and 2. On top of these two positions, the secondary particles produced in the target are filtered by a shielding made up of either 80 cm concrete or 40 cm iron. These roof-shields produce almost uniform radiation fields (mostly neutrons) over two areas of  $2 \times 2 \text{ m}^2$ , each of them divided into 16 squares (numbered from 1 to 16) of  $50 \times 50 \text{ cm}^2$ . Each element of these "grids" represents a reference exposure location (Figures 2 and 3). Additional measurement positions are available behind the lateral-shielding of the irradiation cave (Figures 1 and 2), at the same angles with respect to the target as for the two roof positions. Shielding is either 80 cm or 160 cm concrete, and at both positions eight additional exposure locations (arranged in  $2 \times 4$  grids made up of the same  $50 \times 50 \text{ cm}^2$  elements) are provided. The nominal measurement points are at the centre of each square at 25 cm above floor, i.e. at the centre of a  $50 \times 50 \times 50 \text{ cm}^3$  volume, where the radiation field was calculated (see the following section, *Calculated energy distributions*).

The intensity of the primary beam is monitored by an air-filled precision ionisation chamber (PIC) at atmospheric pressure, placed in the beam just upstream of the target, and connected to a current-digitising circuit. One PIC-count corresponds (within 10%) to  $2.2 \times 10^4$  particles. Typical values of dose rates are 1-2 nSv per PIC-count on top of the 40 cm iron-roof and 0.3 nSv per PIC-count on top of the 80 cm concrete-roof. By adjusting the beam intensity on the target one can vary the dose equivalent rate at the reference positions, typically in the range from 25  $\mu\text{Sv/h}$  to 1 mSv/h on the iron-roof and from 5 to 600  $\mu\text{Sv/h}$  on the concrete-roof.

Figure 1. Axonometric view of the CERN-EC facility in the experimental hall EHN1 on the Prévessin site of CERN

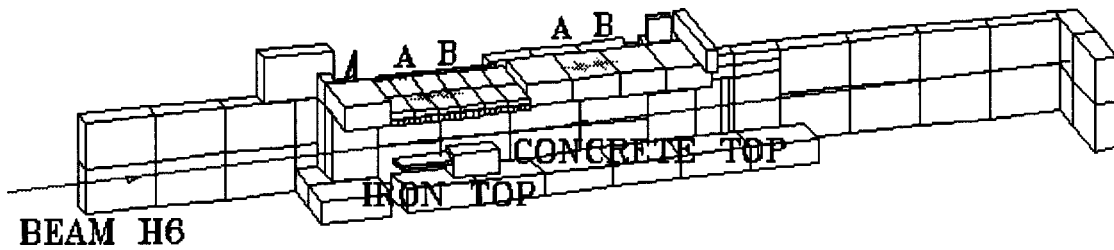


Figure 2. Plan and sectional views of the CERN-EC facility

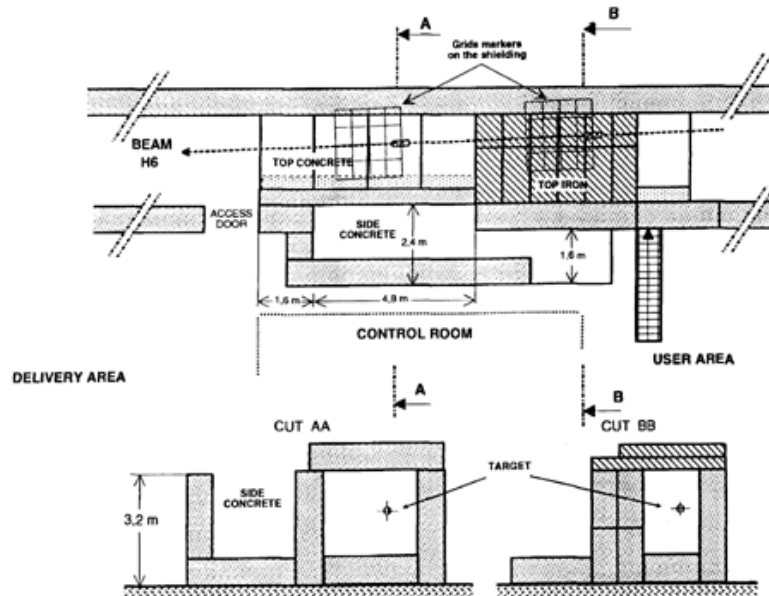


Figure 3. The reference grid with the 16 exposure locations used on the concrete and iron roof-shields. The target (in grey) and the beam direction (arrow) are shown. Each square in the grid is  $50 \times 50 \text{ cm}^2$

T 1	T 5	T 9	T 13
T 2	T 6	T 10	T 14
T 3	T 7	T 11	T 15
T 4	T 8	T 12	T 16

The beam intensity can be modified by means of three upstream collimators (C3, C5 and C6) in the H6 beam line. The influence of the collimator opening on the beam spot (size and shape) on the target was investigated [4] by taking radiographies of the beam with a  $9 \times 12 \text{ cm}^2$  Kodak X-OMAT film. While C5 affects the horizontal extension of the beam spot only slightly, C6 reduces the vertical extension strongly. C3, which is in principle used for momentum selection, also enlarges the spot horizontally, when fully open. Large variations in the beam spot may affect the radiation field at the measurement positions. For a narrow beam hitting the centre of the target, secondary particles produced on the axis of the target make at least two interactions before leaving the target and penetrating the shielding; however, if the primary interaction takes place too close to the target edge, the number of secondary interactions may change and in turn affect the energy distribution of the neutrons emerging from the shield. For a good reproducibility of the radiation field at the exposure locations, the size of the beam spot should not be changed too strongly. It was found that the best procedure is to set C6 at a sufficiently large (fixed) value and then control the beam intensity with C3 and C5. The most recent FLUKA simulations (see following section, *Calculated energy distributions*) used as input data the actual beam profile experimentally determined.

### Calculated energy distributions

Monte Carlo simulations of the neutron energy distributions at the various exposure locations were carried out in the past with the FLUKA code [2]. FLUKA has recently been improved and now includes the capability of transporting neutrons with energy below 20 MeV using a multigroup cross-section library especially developed for the code [5]. These distributions were therefore recently recalculated for all locations with the latest FLUKA version [6-11], with in addition the energy distributions for electrons, photons, muons, pions and protons.

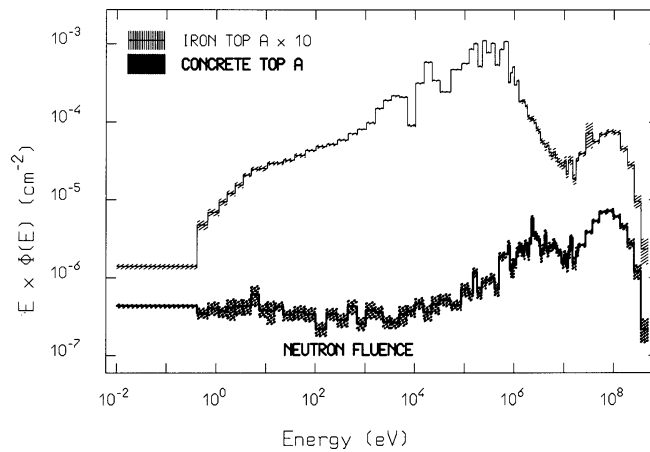
The entire experimental area (see Figures 1 and 2) was modelled using the combinatorial geometry, as previously described [12]. The concrete composition (by weight) was assumed to be 52.9% oxygen, 33.7% silicon, 4.4% calcium, 3.4% aluminium, 1.6% sodium, 1.4% iron, 1.3% potassium, 1% hydrogen, 0.2% magnesium and 0.1% carbon. Calculations were performed for the four cases, i.e. beam momentum of 120 GeV/c or 205 GeV/c an positive or negative particles. In all calculations the threshold for electrons and positrons was set between 500 keV and 5 MeV (according to the scoring region), and between 30 keV and 1 MeV for photons. For all other particles (except neutrons which are transported down to the thermal group) the threshold was set at 1 MeV. Two spherical scoring volumes (24 cm and 40 cm in diameter) were centred at each exposure location, i.e. at the centre of each  $50 \times 50 \times 50 \text{ cm}^3$  reference volume, as stated above. When this was not possible (because of overlapping with other regions) either the sphere diameter was reduced or only one sphere was considered. When two scoring regions were available the neutron fluence in the largest one was chosen because of better statistics.

The energy distributions shown in Figures 4-15 are calculated for a primary beam of positive particles (33% protons, 60% pions and 4% kaons, as determined experimentally) with 120 GeV/c momentum. The distributions are given per primary particle incident on target, for three positions indicated with letters A, C and D in Figures 4-15, representative of the various exposure locations. A fourth position (indicated with B) is meant for comparison with experimental measurements, as discussed in the next section. The positions are as follows: A) on the roof-shielding, vertically above the centre of the target, for both concrete and iron; B) on the roof-shielding, 75 cm downstream of the centre of the target; C) on the 80 cm concrete side-shielding, aligned with the centre of the target; D) on the 80 cm concrete side-shielding, 125 cm upstream of the centre of the target.

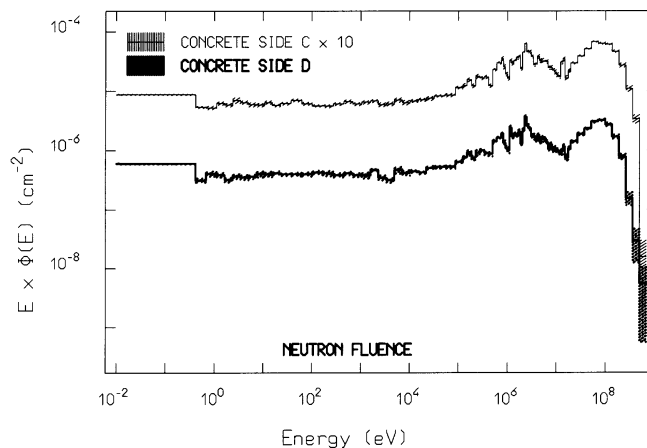
Positions A and B are indicated in Figure 1. The energy distributions do not change in shape from 120 GeV/c to 205 GeV/c, for either positive or negative particles; only the absolute fluence is larger for the higher energy.

Figure 4 compares the neutron spectral fluences in the equivalent positions on the concrete and iron roof-shields. The field on top of the iron shows a strongly pronounced component in the 0.1-1 MeV energy range with respect to concrete, while in the 10-100 MeV interval the relative spectral fluences are quite similar, with a broad peak centred at about 70 MeV. Figure 5, which gives the neutron spectra at points C and D alongside the side-shield, shows that the shape of the energy distribution does not vary within the reference field (the same is valid for the roof-shields). The fluence rate of other hadrons is much lower than that of neutrons, as can be seen from Figures 6-9. The photon fluence is almost one order of magnitude less than that of neutrons on the iron roof-shield, but almost a factor two higher than the neutron one on the concrete roof-shield, because of the contribution from (n,γ) reactions (Figures 10 and 11). The electron fluence (Figures 12 and 13) is about one order of magnitude less than that of neutrons and the muon fluence (Figures 14 and 15) almost three orders of magnitude less (which also explains the lower statistics of the spectra).

**Figure 4. Neutron spectral fluences on the concrete and iron roof-shields, location A in Figure 1**



**Figure 5. Neutron spectral fluences outside the 80 cm concrete side-shield**



**Figure 6. Proton spectral fluence on the concrete roof-shield, location A in Figure 1**

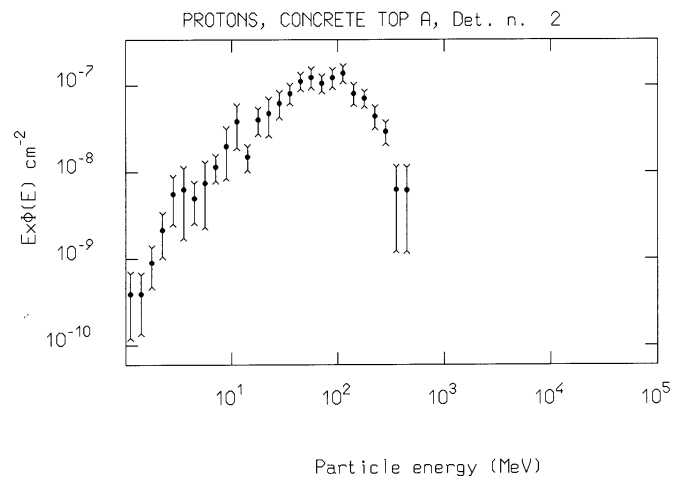


**Figure 7. Proton spectral fluence on the iron roof-shield, location A in Figure 1**

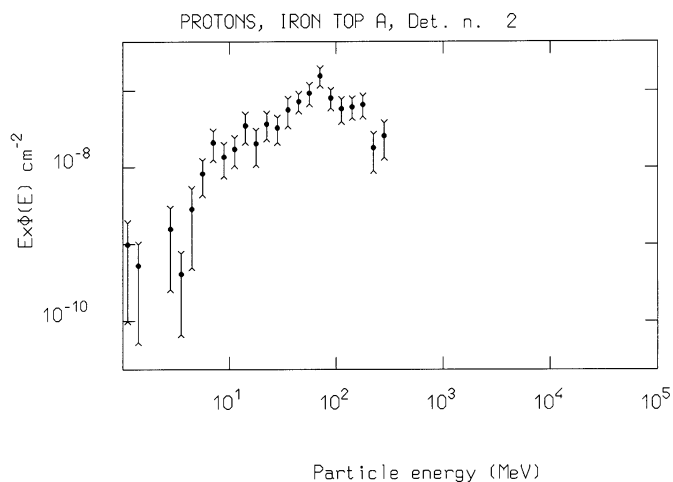


**Figure 8. Pion spectral fluence on the concrete roof-shield, location A in Figure 1**

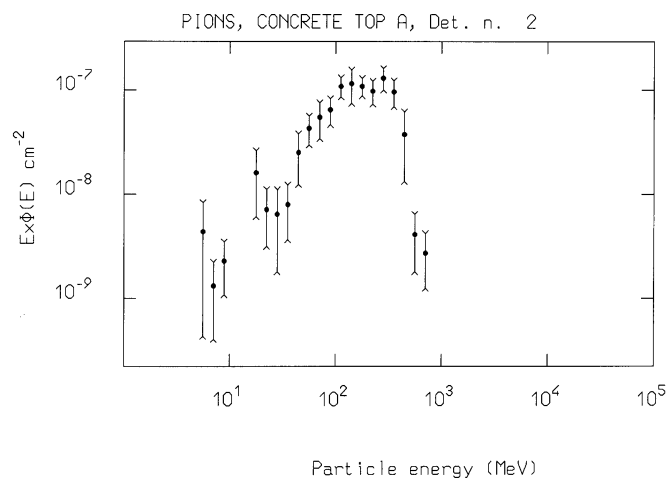


**Figure 9. Pion spectral fluence on the iron roof-shield, location A in Figure 1**

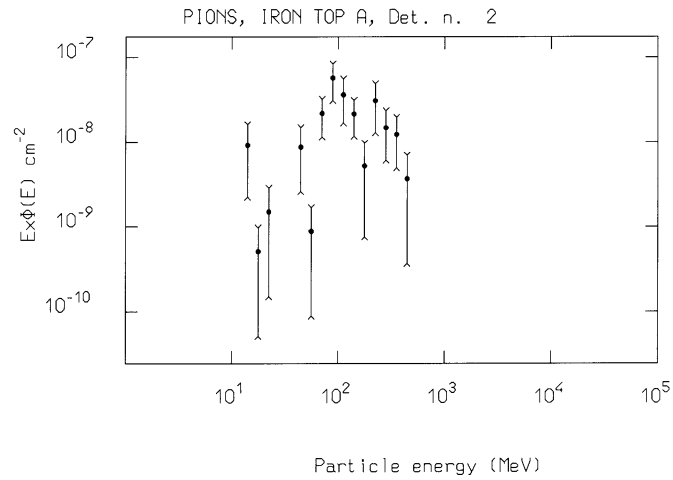


**Figure 10. Photon spectral fluence on the concrete roof-shield, location A in Figure 1**

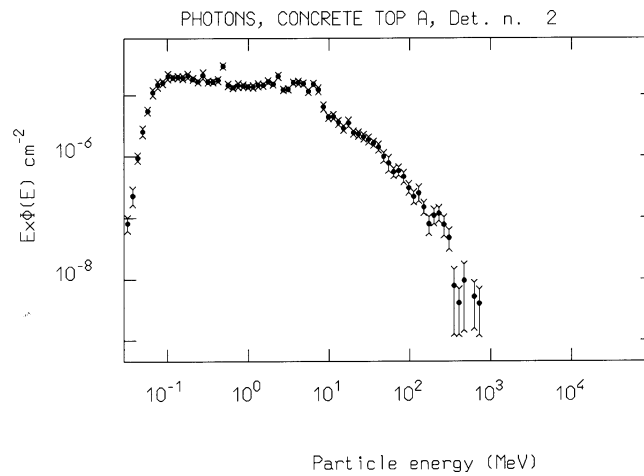


**Figure 11. Photon spectral fluence on the iron roof-shield, location A in Figure 1**

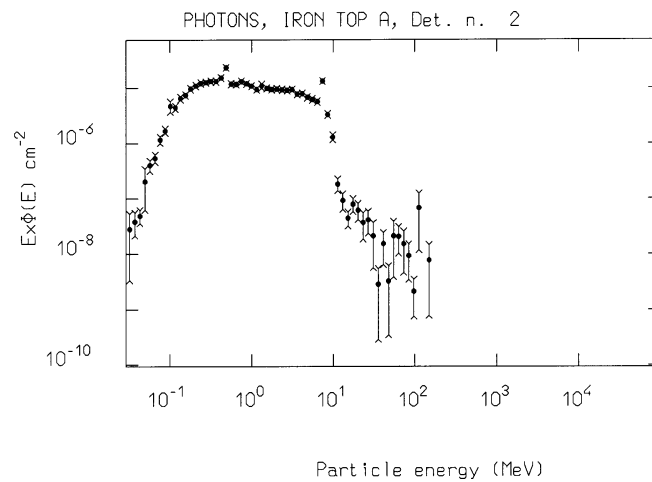


**Figure 12. Electron spectral fluence on the concrete roof-shield, location A in Figure 1**

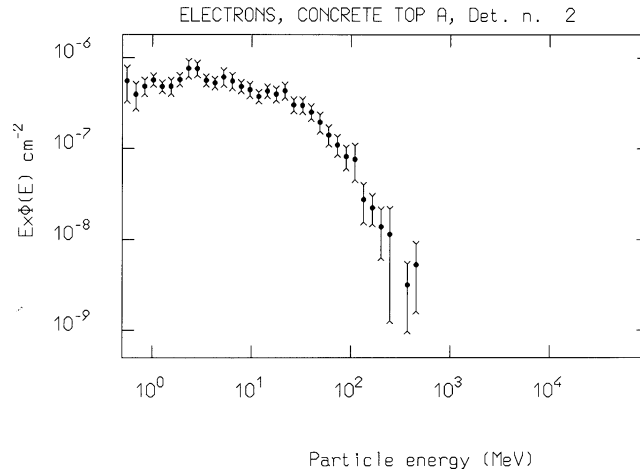


**Figure 13. Electron spectral fluence on the iron roof-shield, location A in Figure 1**

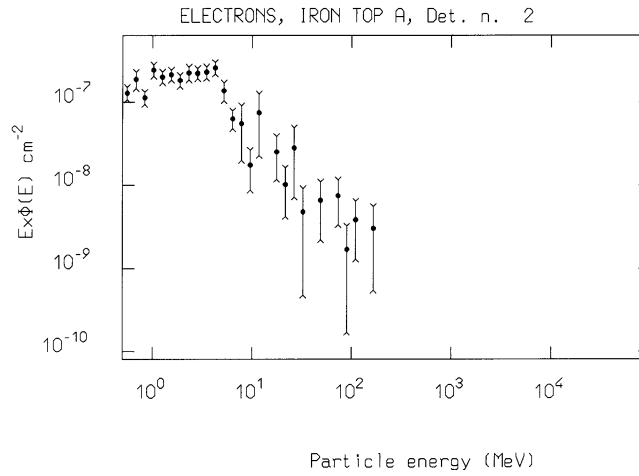


**Figure 14. Muon spectral fluence on the concrete roof-shield, location A in Figure 1**

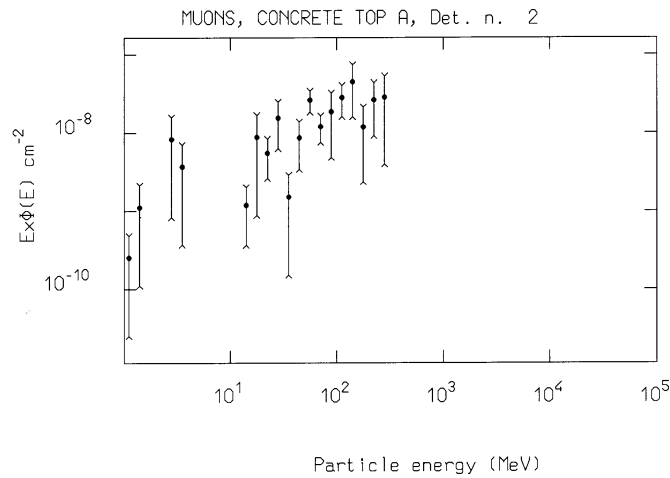
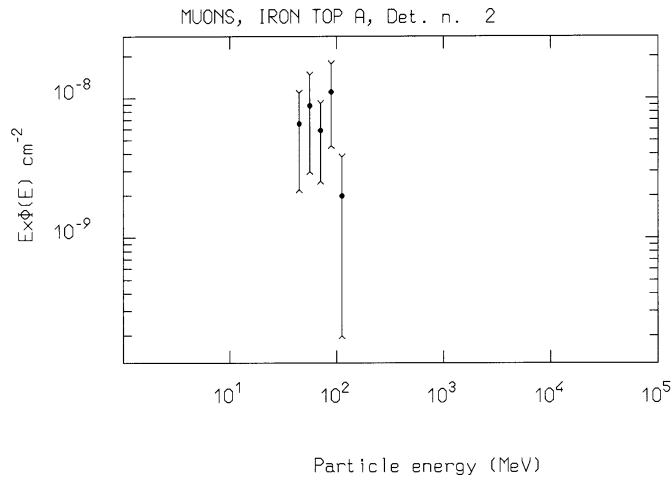


**Figure 15. Muon spectral fluence on the iron roof-shield, location A in Figure 1**



### Comparison of Bonner sphere measurements with MC calculations

The accuracy of the spectral fluences for neutrons calculated with FLUKA was checked by measurements made with a  $^3\text{He}$  proportional counter, employed bare and within a set of five polyethylene spheres (83 mm, 108 mm, 133 mm, 178 mm and 233 mm in diameter), and with the spherical version of the extended range LINUS rem counter [13-17]. The response of each detector to the neutron field at a given exposure location was evaluated using the three step procedure described in [12]. First, the response function of each detector was calculated; second, the neutron fluence at the measurement position was computed; third, the computed responses to monoenergetic neutrons were folded with the scored fluences. The response functions of the five spheres and of LINUS are shown in Figures 16 and 17. It is apparent that the improved response of LINUS above a neutron energy of about 10 MeV compensates for the decrease of the response of the other detectors.

**Figure 16. Fluence response of the five polyethylene spheres**

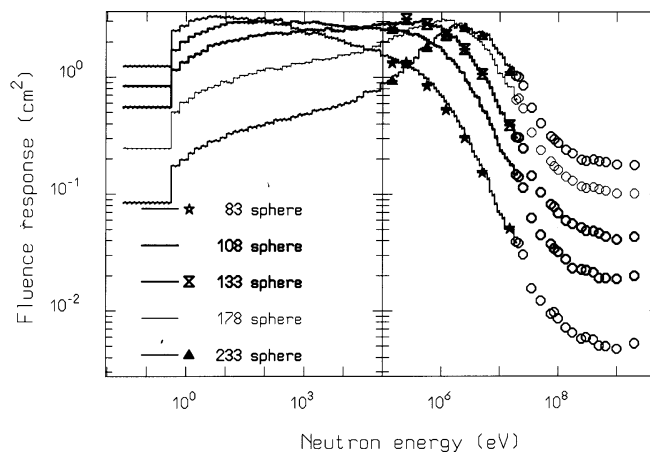
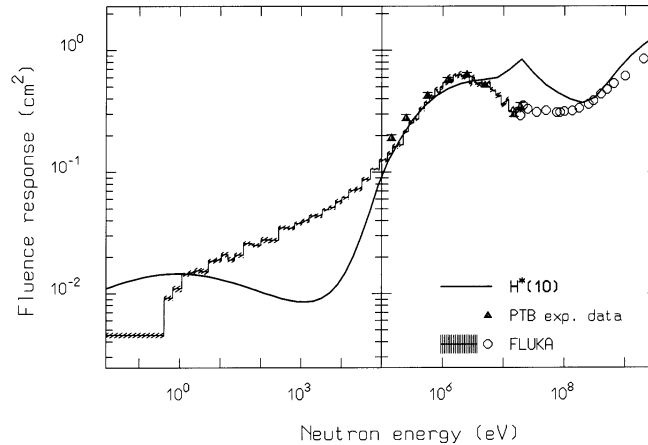


**Figure 17. Fluence response of the spherical neutron rem counter LINUS**



The expected response of each detector calculated with the above procedure is compared in Table 1 with experimental measurements made in positions A, B and D (Figure 1). Data are normalised to one PIC-count. For some locations two independent measurements were made. One should note the excellent agreement between the FLUKA predictions and the experimental results, which confirms the correctness of the spectral fluences given in the previous section. Some discrepancies are only found for the bare  $^3\text{He}$  counter, but these are explained by the fact that the response of the bare counter is strongly influenced by any object placed in the vicinity (such as other instrumentation) which has a moderating effect on the neutron field at the exposure location. This fact is reflected by the large difference in the two experimental results available for the concrete roof in position B.

**Table 1. Comparison between the FLUKA predictions and the experimental response of a bare  $^3\text{He}$  proportional counter, of the same detector within five polyethylene spheres of different diameter (83 mm, 108 mm, 133 mm, 178 mm and 233 mm), and of the spherical version of the LINUS rem counter. Statistical errors only are shown.**

	CONCRETE ROOF								CONCRETE SIDE				IRON ROOF							
	A				B				D				A				B			
	EXP.		FLUKA		EXP.		FLUKA		EXP.		FLUKA		EXP.		FLUKA		EXP.		FLUKA	
	cts/ PIC	err %	cts/ PIC	err %	cts/ PIC	err %	cts/ PIC	err %	cts/ PIC	err %	cts/ PIC	err %	cts/ PIC	err %	cts/ PIC	err %	cts/ PIC	err %	cts/ PIC	err %
S 83	-	-	-	-	0.715 0.704	0.57 0.30	0.717 0.883	3.1	0.616	0.32	0.649	2.4	12.07 11.2	0.33 0.26	12.11	1.9	12.19	0.18	13.13	1.8
S 108	-	-	-	-	0.942	0.35	0.883	3.1	-	-	-	-	17.7	0.20	19.2	1.9	-	-	-	-
S 133	0.833	0.74	0.734	2.9	0.994 1.02	0.36 0.30	0.981	3.2	0.724	0.26	0.689	2.4	22.61 19.2	0.27 0.19	21.24	1.9	24.66	0.20	23.55	1.9
S 178	-	-	-	-	0.989	0.36	1.01	3.4	-	-	-	-	16.1	0.24	16.9	1.9	-	-	-	-
S 233	0.613	0.55	0.626	3.1	0.766 0.788	0.35 0.33	0.899	3.7	0.435	0.05	0.440	2.5	9.86 9.28	0.41 0.28	9.23	2.0	10.81	0.23	10.66	2.0
Linus	0.192	0.60	0.200	3.0	0.252 0.261	0.86 0.52	0.295	3.6	0.119	0.89	0.115	2.6	2.15 2.16	0.51 0.77	1.70	2.1	2.45	0.80	2.03	2.0
Bare $^3\text{He}$	0.323	0.69	0.481	4.6	0.392 0.576	0.58 0.30	0.548	4.1	0.453	0.52	0.651	2.6	0.430	0.95	0.247	4.6	-	-	-	-

## Comparison of TEPC measurements with MC calculations

The reference instrument used to monitor the radiation field is the HANDI TEPC spectrometer [18]. For each exposure location, an absorbed dose spectrum in lineal energy  $y$  of recoiling protons and other particles is acquired. The spectrum is divided into 16 approximately equidistant channels on a logarithmic scale from  $y=50$  eV/ $\mu\text{m}$  to  $y=1.5$  MeV/ $\mu\text{m}$ . Within the approximation of the instrument,  $y$  approximates the linear energy transfer (LET)  $L$ ; the dose equivalent is evaluated from the absorbed dose by the  $Q(L)$  relationship of either ICRP21 or ICRP60, with the evaluation program of Sannikov [19]. This program sums contributions to absorbed and dose equivalent from the low LET interval  $50$  eV/ $\mu\text{m} \leq y \leq 6.12$  keV/ $\mu\text{m}$  and calls it “gamma dose” in a global manner. Contributions to the dose from recoil particles with a higher LET are called “neutron dose”. A relationship between primary beam intensity on the target and dose (or dose equivalent) rate is thus established via the PIC and the HANDI, and given in Gy/PIC-count (or Sv/PIC-count).

To compare the dose or dose equivalent experimentally determined with the results of the MC simulations, the spectral fluence calculated with FLUKA in the various locations was folded with fluence-to-dose or fluence-to-dose equivalent conversion factors to obtain the neutron absorbed dose and dose equivalent. For absorbed dose  $D^*(10)$  due to neutrons with energy up to 30 MeV, use was made of the conversion factors of Leuthold [20]. For ambient dose equivalent,  $H^*(10)$ , ICRU and ICRP have adopted the conversion factors given by Siebert and Schuhmacher [21,22] for neutron energies up to 200 MeV. Conversion factors for higher energies which can be used in these experiments have recently been calculated by Sannikov and Savitskaya [23].

Dose and dose equivalent rates evaluated by FLUKA and measured with the HANDI TEPC are compared in Tables 2-4 for three exposure locations (T2, T6 and T14) on both the concrete and the iron roof. Table 2 shows that the agreement between the calculated  $D^*(10)$  and the measured absorbed dose in a small tissue equivalent volume is satisfactory. The systematically low value measured in field T2 may be due to a slight misalignment of the beam hitting the target.

At a beam momentum of 120 GeV/c, the agreement between calculated and measured ambient dose equivalents  $H^*(10)$  is excellent for both shielding materials, as is shown in Table 3 and in Figure 18 for the whole irradiation area on the concrete roof.

Measurements for the higher beam momentum, 205 GeV/c, are given separately in Table 4, as they are converted to ambient dose equivalent with the older  $Q(L)$  relationship according to ICRP 21 [24] (the original experimental data are no longer available to allow a recalculation). Important discrepancies are found between calculations and measurements behind the iron shielding at this beam momentum [25]. This is probably due to the large contribution from neutrons in the energy range from 20 keV to 800 keV (see *Calculated energy distributions*), where TEPC detectors are known to have a low response [26,27].

The uncertainty associated to the results of the HANDI TEPC, given in Tables 2-4, is due to counting statistics and to the uncertainty in the calibration factor used in the evaluation programme. The statistical uncertainty on the FLUKA results is from 2% to 5%.

**Table 2. Comparison of absorbed dose (D) as measured by the HANDI TEPC and as calculated with the FLUKA code for a few selected irradiation positions, at 120 GeV/c beam momentum. The doses are normalised to one count of the beam monitor (PIC).**

Primary beam momentum, shielding	Field	Dose rate HANDI LET > 6 keV/μm (Gy/PIC)	Dose rate FLUKA (neutrons only) (Gy/PIC)	Ratio FLUKA/HANDI
120 GeV/c 80 cm concrete	T 2	2.42 (20) · 10 <sup>-11</sup>	3.27 · 10 <sup>-11</sup>	1.35 (8)
	T 6	3.14 (27) · 10 <sup>-11</sup>	3.76 · 10 <sup>-11</sup>	1.20 (9)
	T 14	2.69 (28) · 10 <sup>-11</sup>	3.18 · 10 <sup>-11</sup>	1.18 (10)
120 GeV/c 40 cm iron	T 2	7.48 (56) · 10 <sup>-11</sup>	9.99 · 10 <sup>-11</sup>	1.33 (7)
	T 6	10.81 (97) · 10 <sup>-11</sup>	12.65 · 10 <sup>-11</sup>	1.17(9)
	T 14	7.65 (61) · 10 <sup>-11</sup>	8.98 · 10 <sup>-11</sup>	1.17 (8)

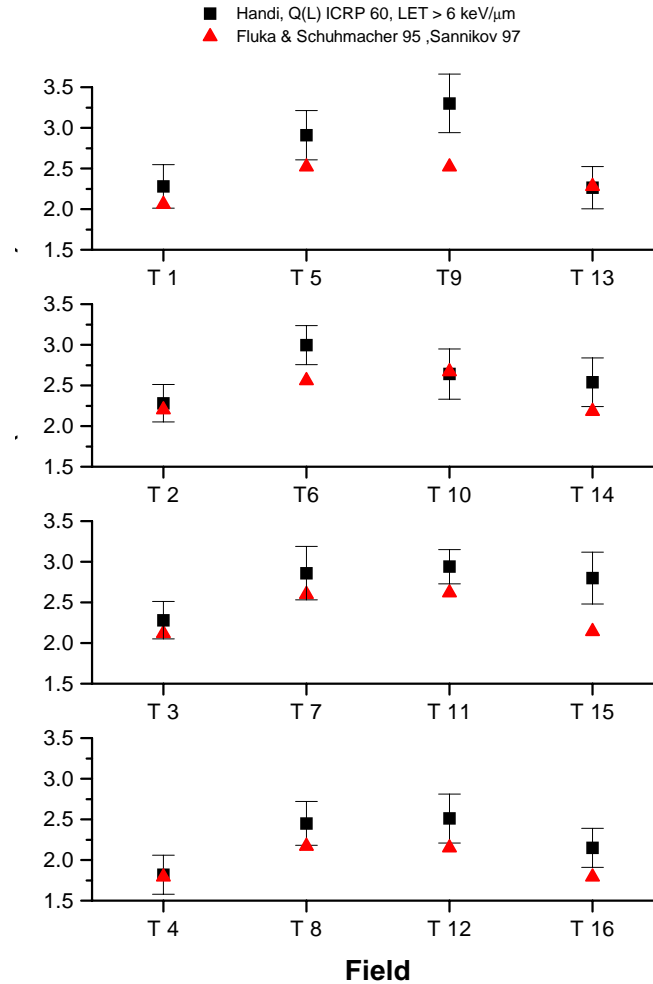
**Table 3. Comparison of dose equivalent (H\*(10) with Q(L) from ICRP 60) as evaluated from the HANDI TEPC absorbed dose spectra and from the fluence spectra calculated with the FLUKA code for a few selected irradiation positions, at 120 GeV/c beam momentum. The doses are normalised to one count of the beam monitor (PIC).**

Primary beam momentum, shielding	Field	Dose eq. rate HANDI LET > 6 keV/μm (Sv/PIC)	Dose eq. rate FLUKA (neutrons only) (Sv/PIC)	Ratio FLUKA/HANDI
120 GeV/c 80 cm concrete	T 2	2.35 (18) · 10 <sup>-10</sup>	2.20 · 10 <sup>-10</sup>	0.94 (8)
	T 6	3.01 (25) · 10 <sup>-10</sup>	2.56 · 10 <sup>-10</sup>	0.85 (10)
	T 14	2.51 (19) · 10 <sup>-10</sup>	2.18 · 10 <sup>-10</sup>	0.87 (8)
120 GeV/c 40 cm iron	T 2	1.09 (7) · 10 <sup>-9</sup>	1.18 · 10 <sup>-9</sup>	1.08 (6)
	T 6	1.49 (12) · 10 <sup>-9</sup>	1.50 · 10 <sup>-9</sup>	1.01 (8)
	T 14	1.08 (7) · 10 <sup>-9</sup>	1.04 · 10 <sup>-9</sup>	0.96 (6)

**Table 4. Comparison of dose equivalent (H\*(10) with Q(L) from ICRP 21) as evaluated from the HANDI TEPC absorbed dose spectra and from the fluence spectra calculated with the FLUKA code at 205 GeV/c beam momentum. The doses are normalised to one count of the beam monitor (PIC).**

Primary beam momentum, shielding	Field	Dose eq. rate HANDI LET > 6 keV/μm (Sv/PIC)	Dose eq. rate FLUKA (neutrons only) (Sv/PIC)	Ratio FLUKA/HANDI
205 GeV/c 80 cm concrete	T 2	3.39 · 10 <sup>-10</sup>	3.22 · 10 <sup>-10</sup>	0.95
	T 6	4.39 · 10 <sup>-10</sup>	3.95 · 10 <sup>-10</sup>	0.90
	T 14	3.75 · 10 <sup>-10</sup>	3.36 · 10 <sup>-10</sup>	0.90
205 GeV/c 40 cm iron	T 2	1.19 · 10 <sup>-9</sup>	2.17 · 10 <sup>-9</sup>	1.82
	T 6	1.64 · 10 <sup>-9</sup>	2.81 · 10 <sup>-9</sup>	1.71
	T 14	1.27 · 10 <sup>-9</sup>	1.97 · 10 <sup>-9</sup>	1.55

**Figure 18. Comparison of dose equivalent rate (in  $10^{-10}$  Sv per PIC-count) behind the concrete shield at a primary beam momentum of 120 GeV/c as measured with the HANDI TEPC (■) and as evaluated from the fluence spectra simulated with FLUKA (▲). The uncertainty on the HANDI data is dominated by counting statistics.**



The code employed to evaluate the TEPC reading obviously neglects that in the actual experimental conditions charged particles from the target penetrate the TEPC and thus contribute to the “gamma dose” in the case of muons and to both the “gamma dose” and the “neutron dose” in the case of hadrons. In addition, the contribution of muons to the low-LET fraction of the dose is a parameter of the experimental set-up which is difficult to control. A substantial muon component (which has nothing to do with that discussed in *Calculated energy distributions*) directly comes from the upstream secondary production target in the H6 beam line. These muons stream over the concrete and iron roof-shield. Their intensity depends on various factors which are not under immediate control, as the angle under which secondary particles are guided from the production target into the H6 beam line, as well as the intensity of secondary beams in neighbouring beam lines. Under the assumption that the muon dose rate stays constant, different mathematical procedures can be applied to calculate and subtract the muon contribution [28]. On the other hand, the exposure locations alongside the side-shielding are basically unaffected, while the radiation field and the dose rates are similar to those on the concrete roof-shield.

## Developments and conclusions

The results presented in the present paper shows that the CERN-EC reference field facility provides well-defined exposure locations for testing and intercomparing dosimetry instrumentation and detectors in high energy neutron fields. Some modifications were recently carried out to further improve the experimental conditions. First, the access to the zone is now through a maze, to suppress the scattered neutron component coming from the access door that might have added a contribution (not easy to estimate) to the field alongside the 160 cm concrete side-shielding (for this reason not much used until now). This maze also completely shields the control room which is always occupied by experimentalists during a run. Second, the part of the irradiation cave downstream of the concrete roof-shield is now completely covered with 80 cm concrete, to reduce to zero the already small (but again difficult to estimate) contribution from neutrons escaping from the (re-entrant) beam dump (which is approximately 10 m downstream of the second target position, the one below the concrete shield) and backscattered from the roof of the experimental hall (some 40 m above). In a limited area the shielding thickness can be reduced to 40 cm and further down to 20 cm, with the intent to create a zone to be used for the irradiation of passive dosimeters with high dose rate, i.e. considerable doses as well. The characteristics of the neutron field in this zone will be investigated in the near future.

### *Acknowledgements*

Work partially supported by the European Commission, Directorate General XII, contracts No. F13P-CT92-0026 (1992-1995) and No. F14P-CT95-0011 (1996-1999).

## REFERENCES

- [1] European Radiation Dosimetry Group, "Exposure of Air Crew to Cosmic Radiation", EURADOS Report 1996-01, eds. I.R. McAulay, D.T. Bartlett, G. Dietze, H.G. Menzel, K. Schnuer and U.J. Schrewe (1996).
- [2] M. Höfert and G.R. Stevenson, "The CERN-CEC High-Energy Reference Field Facility", Proceedings of the Eighth International Conference on Radiation Shielding, Arlington, Texas, 24-28 April 1994, American Nuclear Society, p. 635, (1994).
- [3] C. Birattari, A. Esposito, A. Fassò, A. Ferrari, J.G. Festag, M. Höfert, M. Nielsen, M. Pelliccioni, Ch. Raffnsøe, P. Schmidt and M. Silari, "Intercomparison of the Response of Dosimeters Used in High Energy Stray Radiation Fields", *Radiat. Prot. Dosim.*, 51, (1994) 87.
- [4] T. Otto and M. Silari, "The July/August 1996 Run at the CERN-CEC Reference Radiation Facility", CERN/TIS-RP/TM/96-25, (1996).
- [5] E. Cuccoli, A. Ferrari and G.C. Panini, "A Group Library from JEF 1.1 for Flux Calculations in the LHC Machine Detectors", JEF-DOC-340, (1991).

- [6] A. Fassò, A. Ferrari, J. Ranft, P.R. Sala, G.R. Stevenson and J.M. Zazula, “FLUKA92”, Proceedings of the Workshop on Simulating Accelerator Radiation Environment, Santa Fe, 11-15 January 1993, ed. A. Palounek, Los Alamos LA-12835-C, p. 134, (1994).
- [7] A. Fassò, A. Ferrari, J. Ranft and P.R. Sala, “FLUKA: Performances and Applications in the Intermediate Energy Range”, Proc. of the AEN/NEA Specialists Meeting on Shielding Aspects of Accelerators, Targets and Irradiation Facilities, Arlington, Texas (USA), 28-29 April 1994, NEA/OECD, p. 287, (1995).
- [8] A. Ferrari and P.R. Sala, “A New Model for Hadronic Interactions at Intermediate Energies for the FLUKA Code”, Proc. of the MC93 International Conference on Monte Carlo Simulation in High-Energy and Nuclear Physics, Tallahassee, 22–26 February 1993, eds. P. Dragovitsch, S.L. Linn and M. Burbank, World Scientific, Singapore, p. 277, (1994).
- [9] A. Fassò, A. Ferrari, J. Ranft and P.R. Sala, “FLUKA: Present Status and Future Development”, Proceedings of the Fourth International Conference on Calorimetry in High Energy Physics, La Biodola, Italy, 21–26 September 1993, eds. A. Menzione and A. Scribano, World Scientific, Singapore, p. 493 (1994).
- [10] A. Ferrari, P.R. Sala, G. Guaraldi and F. Padoani, “An Improved Multiple Scattering Model for Charged Particle Transport”, *Nucl. Instr. Meth.*, B71, (1992), 412
- [11] A. Fassò, A. Ferrari, J. Ranft, P.R. Sala, G.R. Stevenson and J.M. Zazula, “A Comparison of FLUKA Simulations with Measurements of Fluence and Dose in Calorimetric Structure”, *Nucl. Instr. Meth.*, A332, (1993), 459.
- [12] C. Birattari, E. De Ponti, A. Esposito, A. Ferrari, M. Magugliani, M. Pelliccioni, T. Rancati and M. Silari, “Measurements and Simulations in High Energy Neutron Fields”, Proceedings of the Second Specialists Meeting on Shielding Aspects of Accelerators, Targets and Irradiation Facilities, CERN, Geneva, 12-13 October 1995, OECD/NEA, Paris, p. 171, (1996).
- [13] C. Birattari, A. Ferrari, C. Nuccetelli, M. Pelliccioni and M. Silari, “An Extended Range Neutron Rem Counter”, *Nucl. Instr. Meth.*, A297 (1990) 250.
- [14] C. Birattari, A. Esposito, A. Ferrari, M. Pelliccioni and M. Silari, “A Neutron Survey-Meter with Sensitivity Extended up to 400 MeV”, *Radiat. Prot. Dosim.*, 44 (1992) 193.
- [15] C. Birattari, A. Esposito, A. Ferrari, M. Pelliccioni and M. Silari, “Calibration of the Neutron Rem Counter LINUS in the Energy Range from Thermal to 19 MeV”, *Nucl. Instr. Meth.*, A324 (1993) 232.
- [16] C. Birattari, E. De Ponti, A. Esposito, A. Ferrari, M. Pelliccioni and M. Silari, “LINUS: An Andersson-Braun Rem Counter with an Extended Response Function”, Proceedings of the Eighth International Conference on Radiation Shielding, Arlington (Texas), 24-28 April 1994, American Nuclear Society, p. 254, (1994).
- [17] C. Birattari, E. De Ponti, A. Esposito, A. Ferrari, M. Magugliani, M. Pelliccioni, T. Rancati and M. Silari, “Recent Developments of the LINUS Rem Counter and Characterization of High Energy Accelerator Radiation Fields”, Proc. of the Radiation Protection and Shielding Topical Meeting, No. Falmouth (Massachusetts, USA), 21-25 April 1996, American Nuclear Society, p. 129, (1996).

- [18] A. Aroua, M. Höfert and A.V. Sannikov, “On the Use of Tissue-Equivalent Proportional Counters in High-Energy Stray Radiation Fields”, *Radiat. Prot. Dosim.*, 59 (1995) 49.
- [19] A.V. Sannikov, “HAN93 Program for Evaluation of Dosimetric Values and Microdosimetric Distributions from HANDI-TEPC Measurement Data”, CERN/TIS-RP/IR/94-03 (1994).
- [20] G. Leuthold, V. Mares and H. Schraube, “Calculation of the Neutron Ambient Dose Equivalent on the Basis of the ICRP Revised Quality Factors”, *Radiat. Prot. Dosim.*, 40 (1992) 77.
- [21] B.R.L. Siebert and H. Schuhmacher, “Quality Factors, Ambient and Personal Dose Equivalent for Neutrons, Based on the New ICRU Stopping Power Data for Protons and Alpha Particles”, *Radiat. Prot. Dosim.*, 58 (1995) 177.
- [22] The International Commission on Radiological Protection, “Conversion Coefficients for Use in Radiation Protection Against External Radiation”, ICRP Publication 74, Pergamon Press, Oxford (1996).
- [23] A.V. Sannikov and E.N. Savitskaya, “Ambient Dose Equivalent Conversion Factors for High Energy Neutrons Based on the ICRP 60 Recommendations”, *Radiat. Prot. Dosim.*, 70 (1997) 383.
- [24] The International Commission on Radiological Protection, “Data for Protection Against Ionizing Radiation from External Sources”, ICRP Publication 21, Pergamon Press, Oxford (1973).
- [25] M. Höfert and T. Otto, “The CERN-EU Reference Radiation Facility and the NTA Film”, presented at the Zweites Fachgespräch über Probleme der Strahlenexposition und der Strahlenschutzmeßtechnik an Hochenergiebeschleunigern, Bundesamt für Strahlenschutz, Außenstelle Berlin, 1996, CERN/TIS-RP/97-04/CF (1997).
- [26] W.G. Alberts, E. Dietz, S. Guldbakke, H. Kluge and H. Schuhmacher, “International Intercomparison of TEPC Systems Used for Radiation Protection”, *Radiat. Prot. Dosim.*, 29 (1989) 47.
- [27] H.G. Menzel, L. Lindborg, Th. Schmitz, H. Schuhmacher and A.J. Waker, “Intercomparison of Dose Equivalent Meters Based on Microdosimetric Techniques: Detailed Analysis and Conclusion”, *Radiat. Prot. Dosim.*, 29 (1989) 55.
- [28] M. Höfert, A.V. Sannikov and G.R. Stevenson, “Muon Background Subtraction from HANDI-TEPC Measurement Data”, CERN/TIS-RP/IR/94-13 (1994).

# *Dosimetry and Instrumentation*



# **THE RESPONSE FUNCTIONS OF A $^3\text{He}$ BONNER SPECTROMETER AND THEIR EXPERIMENTAL VERIFICATION IN HIGH ENERGY NEUTRON FIELDS**

**Vladimir Mares**

Ludwig-Maximilians-University of Munich,  
Institute of Radiobiology Schillerstraße 42, D-80336 München

**Alexander Sannikov\***, **Hans Schraube**

GSF – National Research Center for Environment and Health,  
Institute of Radiation Protection Ingolstädter Landstraße 1, D-85764 Neuherberg

## **Abstract**

The neutron response functions for a Bonner Sphere Spectrometer (BSS) with  $^3\text{He}$  proportional counter were calculated employing the MCNP and LAHET Monte Carlo codes for the neutron energy range from 10 MeV to 1 GeV. The MCNP calculations were extended up to 100 MeV using the neutron cross-sections from the transport data libraries LA-100 of LANL. The effect of the different physics models implemented in the LAHET code on the response of the Bonner spectrometer are documented and the possible reasons are discussed. The MCNP and LAHET results are also compared with calculations using the Monte Carlo high energy transport code HADRON. Verification experiments were conducted at the CERN high energy calibration facility which gave some insight to the question how appropriate the physical models are which are used for the calculation of the BSS responses.

---

\* On leave from the Institute for High Energy Physics, 142284-Protvino, Russia

## Introduction

The Bonner Sphere Spectrometer (BSS) is the device commonly used in neutron spectrometry for an energy range between thermal neutrons and some hundreds of MeV. It consists of a set of polyethylene moderating spheres with a central detector for thermal neutrons. The response functions in the energy range below 20 MeV are well established by calculations and experiment. At higher energies, however, discrepancies were found between the results of different Monte Carlo codes [1].

This work was motivated by a high attention recently paid to high energy neutrons beyond 20 MeV as occurring, for example, around high energy accelerators and in altitudes of aircraft flights. This study is devoted to a more detailed study of the neutron response functions for a Bonner sphere spectrometer with  $^3\text{He}$  proportional counter applying the MCNP [2] and the LAHET [3] Monte Carlo codes for the neutron energy range from 10 MeV to 1 GeV for spheres between 2.5 and 15 inches. The data are compared with the results of the HADRON code [4]. The impact of the different responses on the neutron spectra and on dosimetric quantities will be studied through the unfolding of experimental data obtained in the CERN-CEC high energy neutron reference fields [5].

## The Bonner sphere spectrometer under study

The BSS under study included 15 spectrometry channels with the diameters: 2.5, 3, 3.5, 4, 5, 6, 7, 8, 9, 10, 11, 12 and 15 inches, and the bare spherical  $^3\text{He}$  detector. In addition, a non-homogeneous sphere of 9 inch diameter was used where the polyethylene between 3 and 4 inch diameter was replaced by a lead shell. This lead layer has no significant effect at energies below 10 MeV, while the response is increased above 10 MeV by (n,xn') nuclear processes. This 9 inch sphere with lead serves as important measuring channel for the high energy component of the neutron fields.

The spherical proportional counter was manufactured by Centronics Ltd (Type SP90), 32 mm inner diameter, filled with  $^3\text{He}$  gas of the nominal pressure of 172 kPa and of 100 kPa krypton. The helium number density was assumed at  $4.25 \cdot 10^{19} \text{ cm}^{-3}$  at 293 K, as in previous calculations [6,7], and the krypton atoms were neglected. For the calculations, the counter wall was taken to be a simple 0.5 mm thick stainless steel shell. The density of the polyethylene spheres was  $0.95 \text{ g}\cdot\text{cm}^{-3}$ .

The response characteristics of the system with the stated nominal counter gas filling had been well studied experimentally [8,9] in the range between thermal neutron energy and 15 MeV, and by calculations [6,7]. To account for differences in the actual pressure of the counter gas, a relative calibration was done using a Bonner sphere system with  $^6\text{Li}(\text{Eu})$  scintillation detector whose absolute response had been determined by the above mentioned comprehensive measurements, as well as through calculations [7]. The relative response calibration factor was derived in the field of an AmBe neutron source to be  $R_{\text{exp}}/R_{\text{calc}} = 1.025 \times (1 \pm 0.03)$ . Thus, the actual gas pressure was approximately 5% higher than the nominal one [6]. The entire system was already used to study the neutron radiation field at mountain altitudes [10,11].

The responses of the BSS were calculated as the number of absorption due to the reactions  $^3\text{He}(n,p)^3\text{H}$  ( $Q=0.765 \text{ MeV}$ ) per incident neutron fluence. The neutron fluence inside the detector volume is estimated using the path length of each neutron crossing the volume. The BSS was uniformly irradiated by a broad parallel beam of the monoenergetic neutrons starting on the surface of a disk source centred on and perpendicular to the axis of the central detector. The space between source and Bonner spheres was assumed to be vacuum.

## Computer codes

The basic code employed for the calculation of the BSS responses was the MCNP4A [2] Monte Carlo code which properly handles the new ENDF/B-VI data format up to 100 MeV. The low energy neutrons cross-sections for  $^3\text{He}$  nuclei were taken from the ENDF/B-VI [12] library and extrapolated above 20 MeV. Cross-sections for hydrogen and carbon were taken from the LA100 [13] library, which is the Evaluated Nuclear Data Library for transport calculations involving incident neutrons and protons of energies up to 100 MeV and became available in the meantime through the NEA Data Bank in France. This library is based on nuclear theory/model calculations with parametrisations obtained by matching calculations with experimental data, particularly the PSR-125/GNASH statistical/pre-equilibrium/fission theory code. The library includes neutron- and proton-induced reactions for nine targets and specifies the production cross-sections, and energy-angle correlated spectra of emitted neutrons, protons, alpha-particles, photons, and other significant charged particles. The library LA100 is written in the format ENDF/B-VI and must be processed through the NJOY 89 Nuclear Data Processing System, which is designed to handle this new format. To model the thermal neutron scattering by molecules at room temperatures, the S(alpha,beta) cross-section tables for polyethylene were used which include chemical binding and crystalline effects.

The LAHET [3] code, developed at LANL in Los Alamos, is based on the HETC high energy transport code of ORNL in Oak Ridge. This program has different options for simulation of inelastic interactions of hadrons with nuclei: Bertini and ISABEL cascade models. At the de-excitation stage of nuclear reaction, two versions of pre-equilibrium exciton model and Fermi break-up model may be used. The transport of the low energy neutrons is calculated by the code HMCNP (a modified version of MCNP).

In our previous paper [1] we observed considerable discrepancies above approximately 30 MeV between the LAHET results using the standard option including the Bertini cascade model and the Fermi break-up model on the one hand, and the MCNP and HADRON results, on the other, which brought us to the present study. Now we could employ the more recent version of LAHET code, including the new physical models like the ISABEL intranuclear cascade model and the multistage pre-equilibrium exciton model, which have become available to the public domain in the meantime.

For the comparison here we have also used the HADRON results from [1]. The high energy transport code HADRON [4] is based on the cascade-exciton model of nuclear reactions. This model includes a cascade stage, a pre-equilibrium stage and an equilibrium evaporation stage. Low energy neutrons are transported by the Monte Carlo code FANEUT.

## Comparison of response functions

The results of calculations performed by the three Monte Carlo codes (MCNP, LAHET, HADRON) are shown in Figure 1 for Bonner spheres with 3, 5, 8, 12 and 15 inch diameters as an example. The data points are plotted without error bars for clearness. On the whole, the statistical uncertainties of MCNP, LAHET and HADRON results were less than 5%. The data obtained by the MCNP using the LA-100 library [13] and HADRON [1] programs below 100 MeV agree within the limits of 15%. This is not the case for the LAHET data. The LAHET responses calculated with use of the Bertini model are considerably higher as a rule. The responses calculated by LAHET with the ISABEL model and the multistage pre-equilibrium model are lower but still overestimate the

HADRON data for spheres with diameters less than 12 inch. The more pronounced differences for small spheres in Figure 1 may be explained by the large contribution of low energy neutrons from the first interaction of neutrons with carbon nuclei. In the case of large spheres, this effect is masked by averaging the processes of neutron production and absorption over several collisions.

There are various possible reasons for such discrepancies. One of them is that the total inelastic cross-sections of hadron interactions with nuclei are calculated by the LAHET code itself in the course of the cascade model. On the contrary, MCNP and HADRON use evaluations of experimental data. This approach seems to be more preferable, especially at neutron energies below 100 MeV, where the cascade model of nuclear reactions has physical restrictions. The more important source of errors was found when we compared the calculated secondary neutron spectra from the reaction  $C(p,xn)$  at 113, 256, 597 and 800 MeV proton energy with the experimental data [14, 15]. In Figure 2 we present the comparison of double differential neutron cross-sections for the reaction  $C(p,xn)$  at 113 MeV proton energy calculated by LAHET and HADRON. At energies above some 10 MeV the Coulomb effect is negligible and hence protons instead of neutrons may be used as bombarding particles. The HADRON data are in better agreement with the experiment at low neutron energies where LAHET results in an overestimation in the both versions used. In the middle range of energy in Figure 2, the HADRON results overestimate the experimental data and the LAHET results. It can also be seen that LAHET with the BERTINI model shows some systematic underestimation in the energy range above 7 MeV for  $150^\circ$  and above 15 MeV for  $60^\circ$ . It should be emphasised that for the reaction  $(p,xn)$  and  $(n,xn)$ , respectively, the energy range below approximately 5 MeV of the created secondary neutrons is of most importance, since these neutrons are detected inside the Bonner sphere with much higher probability than neutrons beyond 10 MeV.

The Monte Carlo calculated responses in the energy range from 10 MeV to 1 GeV with roughly log-equidistant intervals in energy scale were then combined with responses from the energy range thermal to 100 MeV as published in [6,7] and jointly interpolated by a cubic spline for all spheres. The full set of the  $^3\text{He}$  BSS smoothed response functions is shown in Figure 3 from 100 keV to 1 GeV, where the data labelled with HEMA95 come from the LAHET calculations using the Bertini model and Fermi break-up above approximately 30 MeV. The response functions HEMA96 come from LAHET calculations using the ISABEL model and the multistage pre-equilibrium model above approximately 100 MeV. These LAHET responses are plotted together with the HADRON results labelled as HADRON95. The response functions for this matrix below 10 MeV were also taken from the MCNP calculations [6,7].

## Experimental procedure

The experiments were conducted over the course of the CERN-CEC collaboration at the calibration facility at the SPS-Super Proton Synchrotron at CERN, Geneva. The facility essentially consists of an 80 cm long copper target in which the 205 GeV/c proton beam is fully stopped. Two different target positions and several shielding arrangements above and on the side of the target permit different spectral conditions outside of the shielding. Because of the in-homogeneity of the fields, the spectral fluence is to be correlated exactly to the respective irradiation position which is well documented by the CERN scientists. Irradiation was performed in April 1995 at the position top iron 6, top concrete 6 (80 cm thick concrete shield), and side concrete 2 (160 cm thick concrete shield). A further description of the facility and the irradiation geometry can be found in [5].

The full set of the 15-channel BSS, as described in a previous section, *The Bonner sphere spectrometer under study*, was employed. Each sphere (channel) was irradiated separately at a distance of 25 cm between centre of the spheres and the surface of the shield. Pulse height spectra for each spectrometer channel were collected in a MCA. Spectral resolution and discrimination against any background was sufficient, and hence simple integration above the lower threshold could be applied without further corrections. The statistical uncertainty for the reading of each channel was typically better than 0.5%, the uncertainty due to the discriminator setting estimated less than 0.2%. All integral counts were normalised to the pressure and temperature corrected reading of a Precision Ion Chamber (PIC) which served as the precise reference monitor.

## Unfolded spectra

The data obtained during this experiment were used to test the impact of three response functions (HEMA95, HEMA96 and HADRON95) on the unfolding procedure. The neutron spectra were unfolded from experimental data using the BON95 code [16], which is a modified version of the BON94 [17] code based on the method of parametrisation of neutron spectra. The neutron spectrum is described by a superposition of a thermal Maxwellian peak, an  $E^{-b}$  tail of epithermal neutrons, where  $b$  is a parameter, an  $1/E$  tail of intermediate neutrons, and a Maxwellian peak of fast neutrons. For the high energy neutron component, the high energy cascade peak with the most probable energy of 100 MeV is added. The solution obtained from the parametrisation is used further as *a priori* information in the iterative procedure of the method of directional divergence described in [17].

During the unfolding work it appeared that even without any *a priori* information, e.g. without using the parametrisation solution as start estimate, the spectral shape was developed. This is not observed when the high energy channel is omitted, though the general shape is conserved in the iterative process, if this shape is used as *a priori* information. Nevertheless, for this study the BON95 code was exclusively used as described above without any further change to meet the requirements of an objective comparison of all three response functions under study, and in order to avoid the introduction of additional parameters into this comparison.

High energy neutron spectra were unfolded from the experimental data using 120-group response matrices (10 groups per order of magnitude) for neutron energies from  $10^{-9}$  to  $10^3$  MeV. The resulting neutron spectra of the CERN-CEC reference field facility are shown in Figures 4-6 in comparison with theoretical spectra calculated by the FLUKA Monte Carlo code [18]. From the comparison with the FLUKA calculations it can be concluded that there is a good agreement (within the limits of the estimated uncertainties) for spectra unfolded using the HEMA96 response matrix for both positions outside the concrete shields. The spectra unfolded using the HEMA95 and HADRON95 response matrices slightly underestimate the high energy peak. It can be explained by the higher response functions calculated for the 9"(Pb) sphere as it can be seen in Figure 3. In the case of the iron shield, there is a considerable overestimation of the measured spectrum at energies from 10 to 300 keV, and of the high energy cascade peak for all responses under study. In spite of the observed discrepancies, all the unfolded spectra are in agreement with each other within the unfolding errors.

In Table 1 the calculated integral dosimetric quantities at three positions of the CERN-CEC reference field facility are compared for all three response matrices. The dose equivalents are compared with the FLUKA calculations employing the following fluence to dose equivalent conversion factors to the unfolded spectra: below 20 MeV, data were taken from [19], based on ICRP21 quality factors and from [20] based on the ICRP60 quality factors [21] and the recent

ICRU49 [22] stopping powers. Above 20 MeV the most recent data calculated by the HADRON code [23] were used. A discussion on the impact of the various conversion factors is given in [11] which also considers the conversion factors [24] calculated before the ICRU49 data became available. A good agreement within the statistical errors can be found in Table 1 among the dosimetric quantities obtained from the different unfolded spectra. There are rather high discrepancies to the FLUKA data which can be explained by the relative high threshold set for neutrons in the transport calculations in [18]. Consequently, the neutrons were not transported down to the thermal. It should also be stressed that FLUKA data in Table 1 were obtained using the calibration factor for the precision ionisation chamber (PIC), whose uncertainty is about of 15%. Recently, for two conditions of the CERN facility improved FLUKA data [25] became available which are added as the last column of Table 1. These data are in better agreement with the experiments than the previous ones.

## Conclusions

Three neutron response functions for  $^3\text{He}$  BSS calculated by different Monte Carlo codes were compared and possible reasons of their disagreement observed above 10 MeV were discussed. The aim was to try to estimate which response matrix is the most appropriate one for the BSS with  $^3\text{He}$  proportional counter used in the high energy neutron fields. For this purpose, the experimental data at three positions of the CERN-CEC high energy reference field facility have served as the practical test for the behaviour of all response matrices under study in the unfolding procedure. The neutron spectra derived by the same unfolding method using three different response matrices are in good agreement. The only higher discrepancies were observed at the 100 MeV cascade peak where spectra unfolded with use of HEMA96 matrix were closer to the theoretical FLUKA results for positions behind the concrete shields. The differences in the derived integral dosimetric quantities were visible and may be of systematic nature though they were within the estimated error limits.

From the comparison performed in this work it is not easy to draw any conclusion as to which response matrix is more accurate and which one should be recommended for high energy neutron spectrometry. As was expected, the precise knowledge of response functions of the 9" sphere with lead is necessary for the improved estimate of high energy cascade peak at 100 MeV. Generally speaking, the use of the 15" and 18" spheres in high energy neutron fields are not sufficient when *no a priori* information is used in the unfolding procedure. This is because their responses are not sufficiently linear independent from those of the other spheres, their responses are low, and additionally, herewith, the counting statistics poor. Nevertheless, the additional use of a further high energy spectrometry channel is preferable for improvement of the experimental base in high energy neutron spectrometry.

## Acknowledgements

The authors highly acknowledge the assistance of Dr. Jaroslav Jakes and Erwin Weitzenegger during the experiments, and thank Mrs. Gertraude Schraube for her valuable help during the data preparation. This work was granted by the European Commission under contracts No. FI3P-CT92-0026 and FI4PCT95-0011.

## REFERENCES

- [1] A.V. Sannikov, V. Mares and H. Schraube, "High Energy Response Functions of Bonner Spectrometers", *Radiat. Prot. Dosim.* 70 (1997) 291.
- [2] J.F. Briesmeister (Editor), "MCNP – A General Monte Carlo N-Particle Transport Code, Version 4A", LA-12625-M, Los Alamos National Laboratory (1993).
- [3] R.E. Prael and H. Lichtenstein, "User Guide to LCS: The LAHET Code System", LANL Report LA-UR-89-3014, Los Alamos National Laboratory, (1989).
- [4] E.N. Savitskaya and A.V. Sannikov, "High Energy Neutron and Proton Kerma Factors for Different Elements", *Radiat. Prot. Dosim.* 60 (1995) 135.
- [5] M. Hoefert, D.T. Bartlett and J.C. McDonald, "The Use of Accelerator Radiation Stray Fields for the Calibration of Passive Detectors", Proc. of the American HPS 30th Midyear Meeting, San Jose, p. 503 (1997).
- [6] V. Mares, G. Schraube and H. Schraube, "Calculated Neutron Response of a Bonner Sphere Spectrometer with  $^3\text{He}$  Counter", *Nucl. Instrum. Methods*, A 307 (1991) 398.
- [7] V. Mares and H. Schraube, "Improved Response Matrices of Bonner Sphere Spectrometers with  $^6\text{LiI}$  Scintillation Detector and  $^3\text{He}$  Proportional Counter between 15 and 100 MeV. Neutron Energy", *Nucl. Instrum. Methods*, A 366 (1995) 203.
- [8] A.V. Alevra, M. Cosack, J.B. Hunt, D.J. Thomas and H. Schraube, "Experimental Determination of the Response of Four Bonner Sphere Sets to Monoenergetic Neutrons (II)", *Radiat. Prot. Dosim.*, 40, 91-102 (1992).
- [9] A.V. Alevra, J.B. Hunt, D.J. Thomas and H. Schraube, "Experimental Determination of the Response of Four Bonner Sphere Sets to Thermal Neutrons", *Radiat. Prot. Dosim.*, 54, 25-31 (1994).
- [10] H. Schraube, J. Jakes, A. Sannikov, E. Weitzenegger, S. Roesler and W. Heinrich, "The Cosmic Ray Induced Neutron Spectrum at the Summit of the Zugspitze (2963m)", *Radiat. Prot. Dosim.* 70 (1997) 405.
- [11] H. Schraube, G. Leuthold, S. Roesler and W. Heinrich, "Neutron Spectra at Flight Altitudes and their Radiological Estimation", In print: *Adv. Space Res.* (1997)
- [12] J.S. Hendricks, S.C. Frankle and J.D. Court, "ENDF/B-VI Data for MCNP", LANL Report LA-12891, Los Alamos (1994).

- [13] P.G. Young *et al.*, “Transport Data Libraries for Incident Proton and Neutron Energies to 100 MeV”, LANL Report LA-11753-MS, Los Alamos (1990).
- [14] M.M. Meier *et al.*, “Differential Neutron Production Cross-Sections and Neutron Yields from Stopping-Length Targets for 113-MeV Protons”, LANL Report LA-11518-MS Los Alamos (1989).
- [15] M.M. Meier *et al.*, “Differential Neutron Production Cross-Sections and Neutron Yields from Stopping-Length Targets for 256-MeV Protons”, LANL Report LA-11656-MS Los Alamos (1989).
- [16] A.V. Sannikov, “BON95, a Universal User-Independent Unfolding Code for Low Informative Neutron Spectrometers”, (to be published).
- [17] A.V. Sannikov, “BON94 Code for Neutron Spectra Unfolding from Bonner Spectrometer Data”, CERN internal report CERN/TIS-RP/IR/94-16 (1994).
- [18] S. Roesler and G.R. Stevenson, “July 1993 CERN-CEC Experiments: Calculations of Hadron Energy Spectra from Track-Length Distributions Using FLUKA”, CERN internal report CERN/TIS-RP/IR/93-47 (1993).
- [19] S.R. Wagner, B. Grosswendt, J.R. Harvey, A.J. Mill, H-J. Selbach and B.R.L. Siebert, “Unified Conversion Functions for the new ICRU Operational Radiation Protection Quantities”, *Radiat. Prot. Dosim.*, 12, 2 (1985) 231.
- [20] B.R.L. Siebert and H. Schuhmacher, “Quality Factors, Ambient and Personal Dose Equivalent for Neutrons Based on the New ICRU Stopping Power Data for Protons and Alpha Particles”, *Radiat. Prot. Dosim.*, 58 (1995) 177.
- [21] ICRP Publication 60 “1990 Recommendations of the ICRP”, Annals of the International Commission on Radiological Protection, Vol. 21, No. 1-3, Pergamon Press, Oxford (1991).
- [22] ICRU-Report 49 “Stopping Powers and Ranges for Protons and Alpha Particles”, International Commission on Radiation Units and Measurements, Bethesda, Maryland, USA (1993).
- [23] A.V. Sannikov and E.N. Savitskaya, “Ambient Dose Equivalent Conversion Factors for High Energy Neutrons Based on the New ICRP Recommendations”, *Radiat. Prot. Dosim.*, 70 (1997) 383.
- [24] G. Leuthold, V. Mares and H. Schraube, “Calculation of the Ambient Dose Equivalent on the Basis of the ICRP Revised Quality Factors”. *Radiat. Prot. Dosim.*, 40,2 (1992) 77.
- [25] C. Birattari, A. Ferrari, M. Höfert, T. Otto, T. Rancati and M. Silari, “Recent Results at the CERN-CEC High Energy Reference Field Facility”, to be published in: Proc. Third Specialists Meeting on Shielding Aspects of Accelerators, Targets and Irradiation Facilities, 12-13 May 1997, Sendai, Japan, OECD Nuclear Energy Agency, 1997.

**Figure 1. Fluence response of some channels of the  $^3\text{He}$  Bonner spectrometer calculated by using three different Monte Carlo codes: HADRON, MCNP and LAHET. The LAHET code is employed with cascade model Bertini and cascade model ISABEL followed by multistage pre-equilibrium model (MPM).**

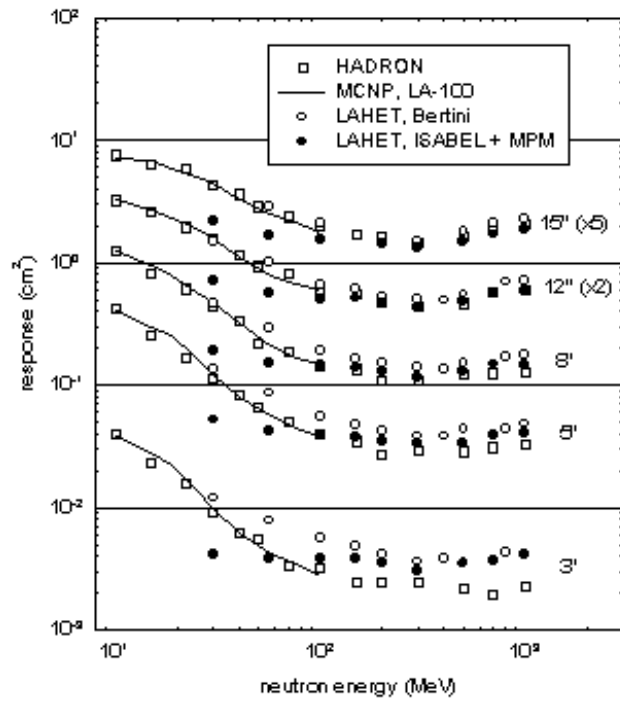


**Figure 2. Double differential cross-sections for the neutron production by  $\text{C}(p, xn)$  at four laboratory angles obtained from Monte Carlo calculations and from LANL experiments [14]**

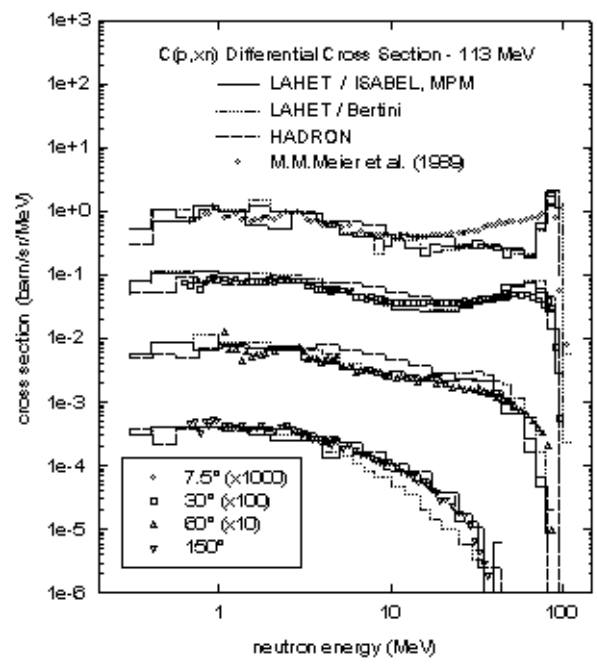


**Figure 3. Three sets of responses of the 15 channel BSS calculated with the three high energy models**

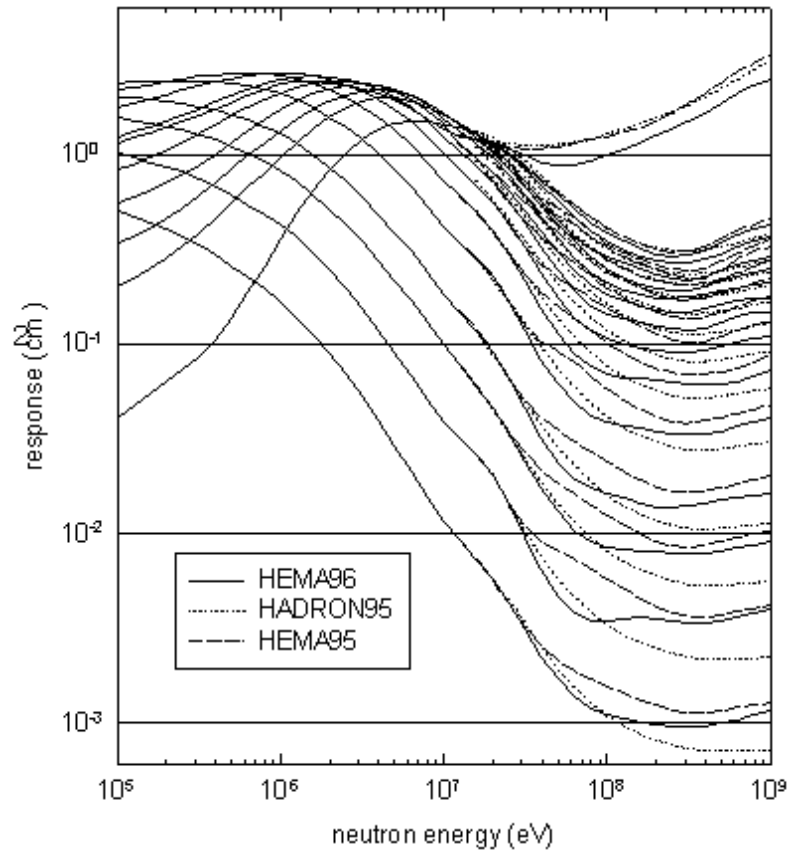


**Figure 4. Neutron energy spectra measured by the  $^3\text{He}$  BSS at the position top concrete of the CERN-CEC reference field facility in comparison with FLUKA calculations [18]**

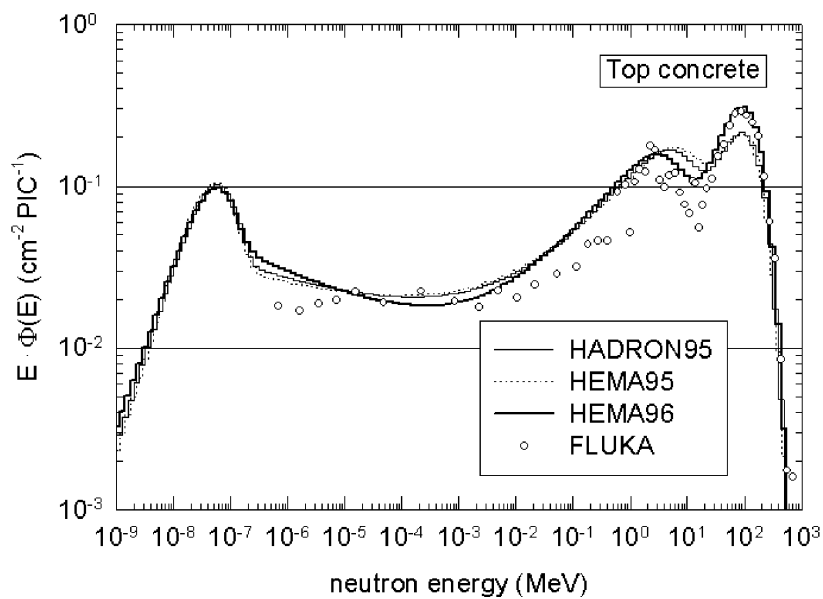


Figure 5. Neutron energy spectra measured by the  $^3\text{He}$  BSS at the position side concrete of the CERN-CEC reference field facility in comparison with FLUKA calculations [18]

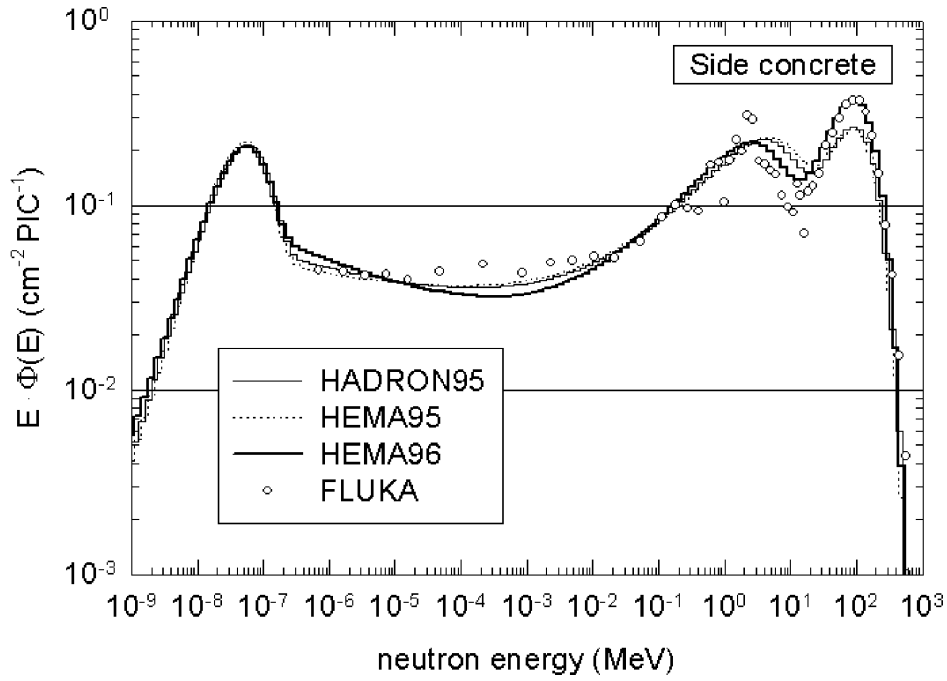
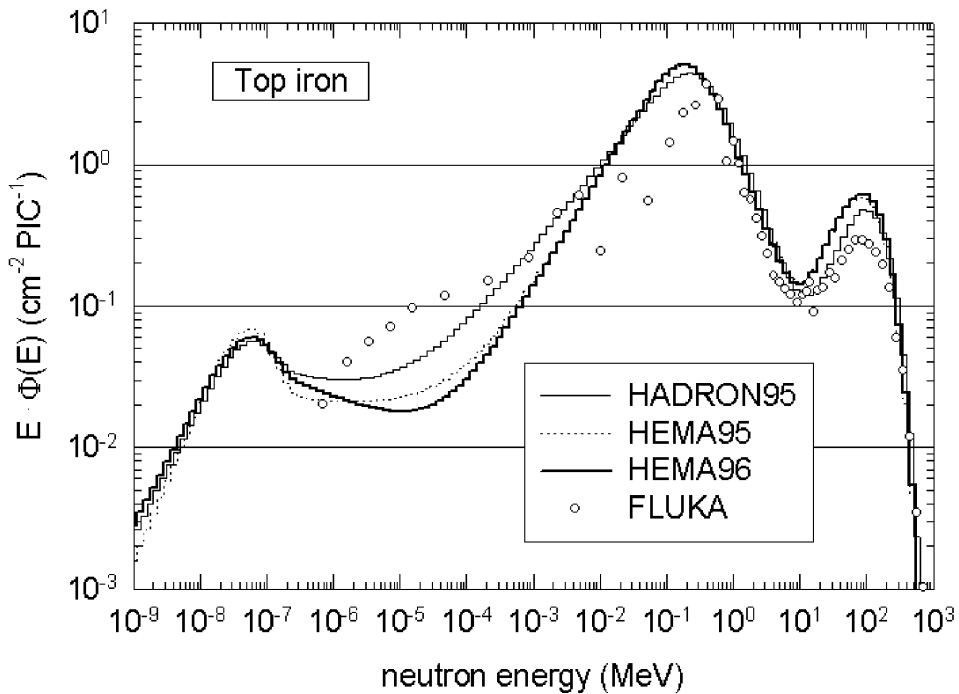


Figure 6. Neutron energy spectra measured by the  $^3\text{He}$  BSS at the position top iron of the CERN-CEC reference field facility in comparison with FLUKA calculations [18]



**Table 1. Comparison of measured integral dosimetric quantities at three positions of the CERN-CEC reference field facility using three different response matrices by unfolding with FLUKA calculation of 1993 [18] and 1997 [25]**

	<b>HADRON95</b>	<b>HEMA95</b>	<b>HEMA96</b>	<b>FLUKA [18]</b>	<b>FLUKA [25]</b>
<b>Top concrete</b>					
<b>D</b> ( $10^{-11}$ Gy/PIC)	$5.48 \pm 0.46$	$5.71 \pm 0.32$	$6.25 \pm 0.38$		
<b>H</b> ICRP-21 ( $10^{-10}$ Sv/PIC)	$4.02 \pm 0.27$	$4.15 \pm 0.20$	$4.46 \pm 0.23$	3.48	3.95
<b>H</b> ICRP-60 ( $10^{-10}$ Sv/PIC)	$4.16 \pm 0.25$	$4.28 \pm 0.18$	$4.58 \pm 0.21$		
<b>Side concrete</b>					
<b>D</b> ( $10^{-11}$ Gy/PIC)	$7.11 \pm 0.62$	$7.38 \pm 0.44$	$8.07 \pm 0.52$		
<b>H</b> ICRP-21 ( $10^{-10}$ Sv/PIC)	$5.26 \pm 0.36$	$5.41 \pm 0.26$	$5.81 \pm 0.31$	4.98	
<b>H</b> ICRP-60 ( $10^{-10}$ Sv/PIC)	$5.49 \pm 0.33$	$5.62 \pm 0.24$	$6.02 \pm 0.28$		
<b>Top iron</b>					
<b>D</b> ( $10^{-11}$ Gy/PIC)	$25.7 \pm 1.85$	$28.2 \pm 1.77$	$28.4 \pm 1.58$		
<b>H</b> ICRP-21 ( $10^{-10}$ Sv/PIC)	$25.1 \pm 0.93$	$27.3 \pm 0.94$	$27.3 \pm 0.81$	17.5	28.1
<b>H</b> ICRP-60 ( $10^{-10}$ Sv/PIC)	$30.4 \pm 0.90$	$32.8 \pm 0.93$	$32.8 \pm 0.87$		

**RE-CALCULATION OF ENERGY RESPONSE OF TISSUE EQUIVALENT  
PROPORTIONAL COUNTER FOR NEUTRON ABOVE 20 MeV**

**A.G. Alexeev, S. Kharlampiev**  
Institute for High Energy Physics,  
Radiation Research Department  
Protvino, Moscow Region, Russia 142284

**T. Kosako**  
The University of Tokyo  
Research Centre for Nuclear Science and Technology  
Tokyo 113, Japan

**Abstract**

The calculation of an energy response of the tissue equivalent proportional counter with low pressure for neutron in the energy region from 20 up to 5 GeV is performed. Dependence of TEPC neutron response and errors of measured neutron dose equivalent on a counter design and measurement methods are discussed. The comparison between calculation and measurements in radiation field at the top shielding of IHEP accelerator is presented.

## Introduction

The dosimetric method based on low pressure tissue equivalent proportional counter (TEPC) which has been put forward by H.H. Rossi [1] for microdosimetric investigation of radiation, has been widely used in radiation dosimetry [2,3]. The questions of construction, response to some types of radiation, measurement methods and application fields are presented elsewhere [1-6]. One of the application features of TEPC is that it is a major dosimetric technique for dose equivalent measurement when we deal with high energy radiation behind shielding of high energy accelerators and space ships.

High energy neutrons – those with energy above 20 MeV – are one of the important components of radiation in such cases. The calculation and experimental investigation of TEPC response for neutrons above 20 MeV has not been widely studied ([7] for example). Precise evaluations (calculated as well as experimental) of response dependence of TEPC energy is necessary for errors estimation of dose equivalent that is need for most practice (in cases of radiation safety).

In the present paper the TEPC energy response estimated by a calculation of secondary charged particles spectra by the HADRON code [8] was carried out in the neutron energy region from 20 MeV up to 5 GeV. This code based on the cascade-exiton model for hadron interonuclear cascade calculations has been resented on light nuclei. Because of an absence of standard neutron sources in the energy region of our interest, the only way to verify the TEPC's calculation was to compare doses measured by TEPC with that of other dosimetric instruments and of calculation codes in high energy radiation fields behind the top shielding of the IHEP accelerator (U-70).

## Calculation method

As was demonstrated in our previous publications [7,10,11], neutron response depends on TEPC construction and atomic composition of materials which are used in a counter design. The counter design used at IHEP is schematically presented on Figure 1. The counter body is a sphere with 10.8 cm internal diameter and is 0.2 cm thick. The body material is caprolon. The counter body is mounted in aluminium gas-non-permeable cover of 0.2 cm thick. It was filled by methane with 2.33 kPa pressure which simulated 2  $\mu\text{m}$  of soft tissue. Thin layer of aluminium (0.1  $\mu\text{m}$ ) was evaporating on the internal surface of the counter, because caprolon is not an electrical conductor material. As it was mentioned in [10], such thickness of aluminium is negligible in a calculation of TEPC energy response for neutrons above 0.3 MeV. Therefore the internal aluminium layer was not taken into account while calculations of TEPC energy response for neutrons above 20 MeV were being performed. The atomic composition of caprolon, methane and soft tissue are presented in Table 1. The measurement method, which is used in IHEP [11] allows to measure absorbed dose (D) and dose equivalent (H) of mixed radiation, neutron absorbed dose  $D_n$  and neutron dose equivalent  $H_n$ .

The TEPC response in unit of absorbed dose ( $R_D$ ,  $R_{Dn}$ ) and in units of dose equivalent ( $R_H$ ,  $R_{Hn}$ ) are then calculated as follows:

$$R_D = A \int D(y) dy \quad (1)$$

$$R_{dn} = A \int_{y>6} D(y) dy \quad (2)$$

**Figure 1. Calculational geometry**

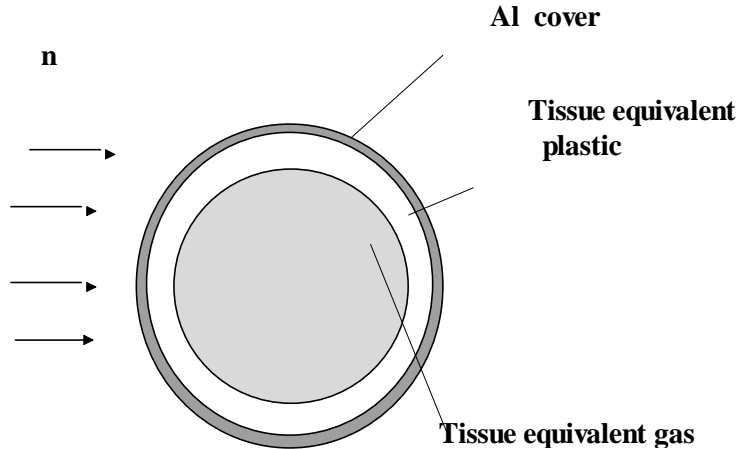


**Table 1. The atomic composition of caprolon and tissue by weight of a per cent**

	<b>H</b>	<b>C</b>	<b>N</b>	<b>O</b>
<b>Caprolon</b>	9.6	45.7	10.2	16.2
<b>Methane</b>	25.0	75.0	-	-
<b>Tissue</b>	10.1	11.1	2.6	76.2

$$R_H = A \int D(y)Q(y)dy \quad (3)$$

$$R_{hn} = A \int_{y>6} D(y)Q(y)dy \quad (4)$$

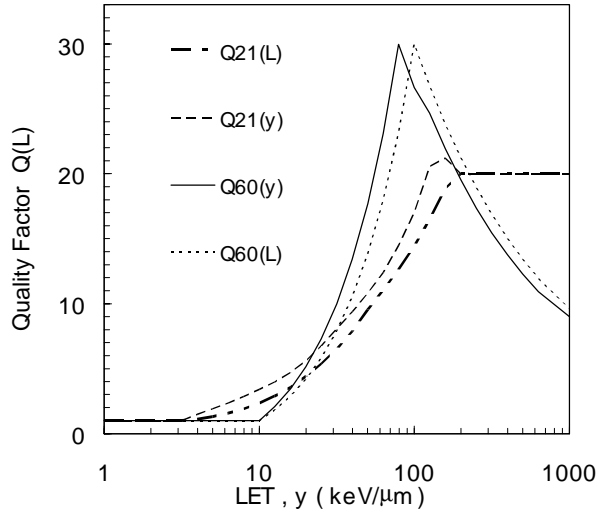
where A is conversion factor to Gy; D(y) is a distribution of energy deposition of events in one unit of linear energy (keV/μm) in sensitivity volume of counter. Q(y) is the Q-y relationship has been established s obtained for Q(L) (quality factor dependence n linear energy transfer L) relationship specified in the ICRP21 [12] and ICRU 60 [13] recommendation.

Q(Y) is used as an experimental method for dose equivalent measurement and permits to avoid the unfolding LET spectra from an experimental events spectra D(Y). The relationships Q(y) and Q(L) are presented in Figure 2. The method of D<sub>n</sub> and H<sub>n</sub> measurement is based on the fact that a contribution of a events with y>6 keV/μm into neutron dose is negligible. One the other hand the contribution of a events with y>6 keV/μm to photon or electron dose is negligible too. This method has been checked by the experiment involving the IHEP neutron reference fields described in [10].

### Calculation results

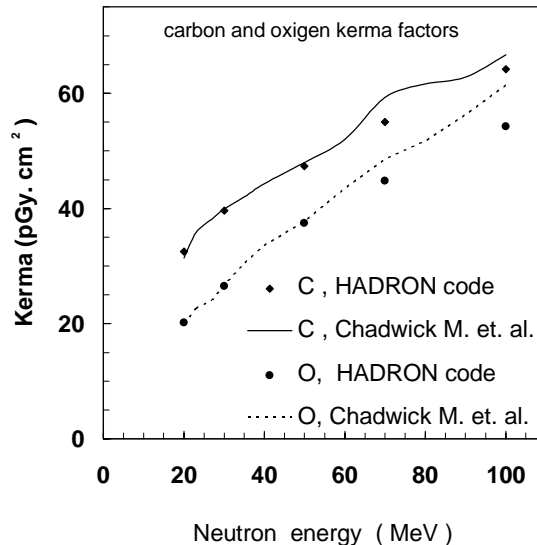
Some factors affected on neutron response of TEPC have been taken into account. These factors include the following: atomic composition of counter materials, heterogeneous of a counter, the thickness of counter body, the separate level y for γ-n discrimination.

**Figure 2. Q-L and Q-y relationship as specified in ICRP-60 and ICRP-21**



As was demonstrated in [7,10] the neutron response of TEPC depends on an atomic composition of gas filling for neutrons below 300 keV. Neutron response, in turn, depends on an atomic composition of counter body for neutrons above 300 keV. Table 1 shows that hydrogen concentration in carbon is the same for that of soft tissue. The concentration of carbon, on the other hand, is higher for caprolon. Therefore the distinction between the response of tissue equivalent counter (whose atomic composition is the same as tissue one), and response of caprolon counter depends on the variation between oxygen and carbon kerma. Figure 3 shows neutron kerma for carbon and oxygen in the energy region from 20 MeV up to 100 MeV. A comparison between the HADRON code [14] calculation and the new evaluation data [15] is presented. Maximum distinction between carbon and oxygen kerma is for 20 MeV and decreases with neutron energy increase. Good agreement exists between HADRON and the evaluation data. Thus, the effect of changing from oxygen to carbon is markedly affected for neutron response of TEPC in the energy region up to 100 MeV.

**Figure 3. Neutron carbon and oxygen kerma factor; the circles and the diamonds are the HADRON code calculation; the line is the evaluated data**



Figures 4a and 4b show the response contribution into the TEPC's response from secondary charge particles emitted in neutron interactions with gas, counter body and aluminium cover. The energy response in units of absorbed dose ( $R_D$ ) is presented in Figure 4a and the same dependence in units of dose equivalent ( $R_H$ ) is presented in Figure 4b. The contribution of particles from the neutron interactions with full gas is less than 10%. It is more or less for  $R_D$  than for  $R_H$ . It is explained by different contributions to these values from short-range recoil particle produced in neutron interactions. The aluminium cover contribution increases with energy above 1000 MeV, but its contribution to  $R_H$  remains negligible. So, for neutrons above 20 MeV the TEPC energy response depends mainly on atomic composition of the counter body.

**Figure 4a. Neutron energy response of TEPC in units of absorbed dose: total and the contributions of neutron interaction with a gas, a counter body and Al cover**

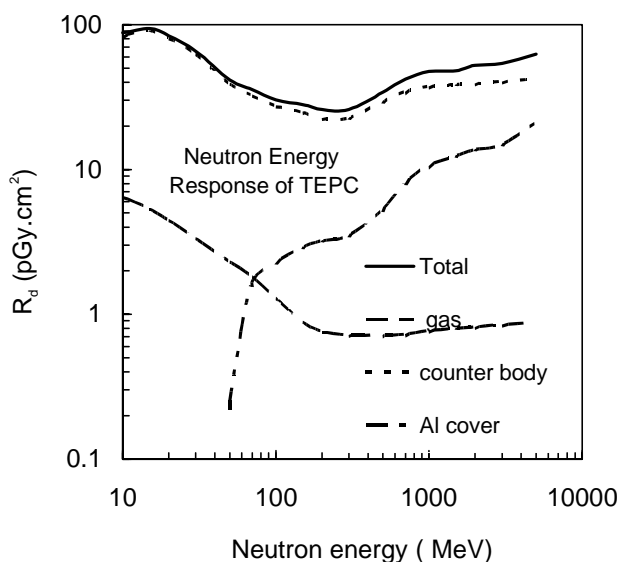
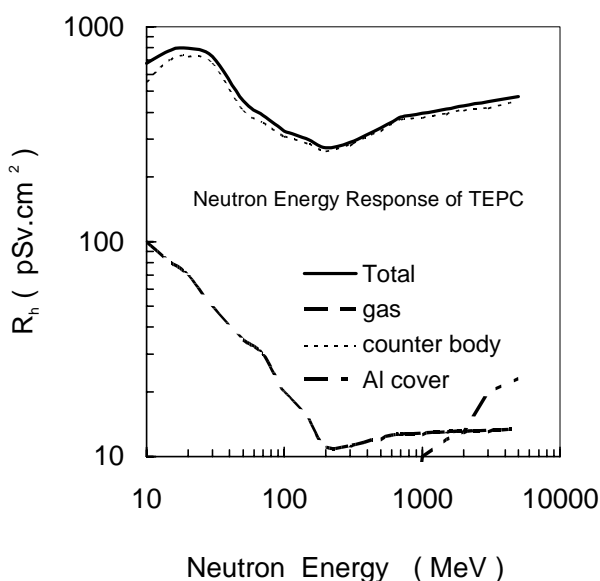
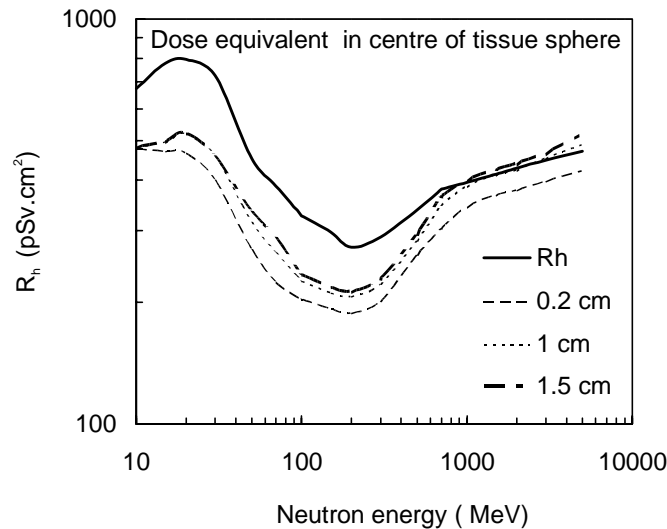


**Figure 4b. The same as in Figure 4a but in units of dose equivalent**



The TEPC method of dose equivalent measurement is based on modelling of tissue volume. The pressure of gas is dependent on a simulated value of sensitivity volume. The thickness of counter body is chosen in order to ensure the equilibrium of secondary charge particles. Equilibrium commonly exists when the range of all secondary charge particles is less than that of a thickness counter body. This condition is not met for neutrons above 20 MeV since the range of secondary protons could reach about 10 cm and more. Figure 5 shows the dose equivalent in the centre of tissue spheres of 0.2, 0.1 and 1.5 cm diameters for neutron energy from 20 MeV up to 5 GeV as well as the neutron energy response of caprolon counter with 0.2 cm thickness of body. An increase of 7 times for a diameter accompanies a change TEPC response about 20% only.

**Figure 5. Neutron dose equivalent in centre of tissue spheres with different diameters. The sphere diameter is presented in cm.  $R_h$  is the TEPC response.**



The above-mentioned higher sensitivity of caprolon counter as compared with the tissue one is explained by higher concentration of carbon in caprolon. Therefore a compromise must be reached in the choosing of a counter thickness that assures the needed response for neutrons with energy below 20 MeV.

The above-mentioned discrimination level of  $y = 6 \text{ keV}/\mu\text{m}$  is suitable for separation of neutron events from photon events in neutron energy region below 14 MeV. The contribution from high energy secondary proton events which overlap with photons events, and region of such overlap are increased with neutron energy. Figure 6 shows relative dose contribution of events (in units of linear energy) above given value of  $y$  for neutrons with energy 10, 100 and 1000 MeV in  $2 \mu\text{m}$  sensitive volume. In case of 10 MeV all absorbed dose (about 100%) is determined by events with linear energy above  $10 \text{ keV}/\mu\text{m}$ . On the other hand in the case of 100 MeV a contribution from events with  $y < 6 \text{ keV}/\mu\text{m}$  is equal to about 20%.

The ratio of TEPC response (in units absorbed dose and dose equivalent) in case  $y > 6 \text{ keV}/\mu\text{m}$  to same value for zero threshold of  $y = 0$  is present in Figure 7. Contribution of events with  $y < 6 \text{ keV}/\mu\text{m}$  into absorbed dose is increased with neutron energy and one is equal about 30% at 5 GeV. At the same time contribution of this events into dose equivalent is less 5%. So it is clear that this method of measurement of neutron dose equivalent by discrimination of events could be applied for neutrons above 14 MeV.

**Figure 6. Fraction of neutron absorbed dose due to events with linear energy above given  $y$**

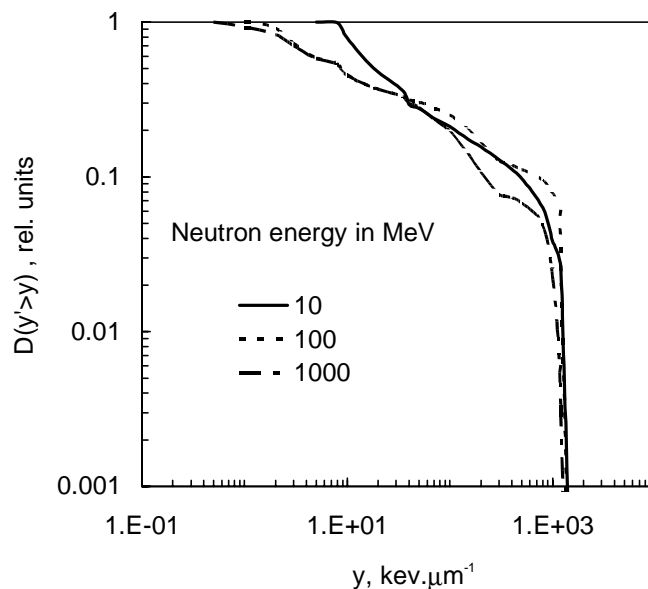


**Figure 7. Fraction of neutron absorbed dose ( $R_d$ ) and dose equivalent ( $R_h$ ) in sensitive volume of TEPC due to events with  $y < 6 \text{ keV}/\mu\text{m}$**

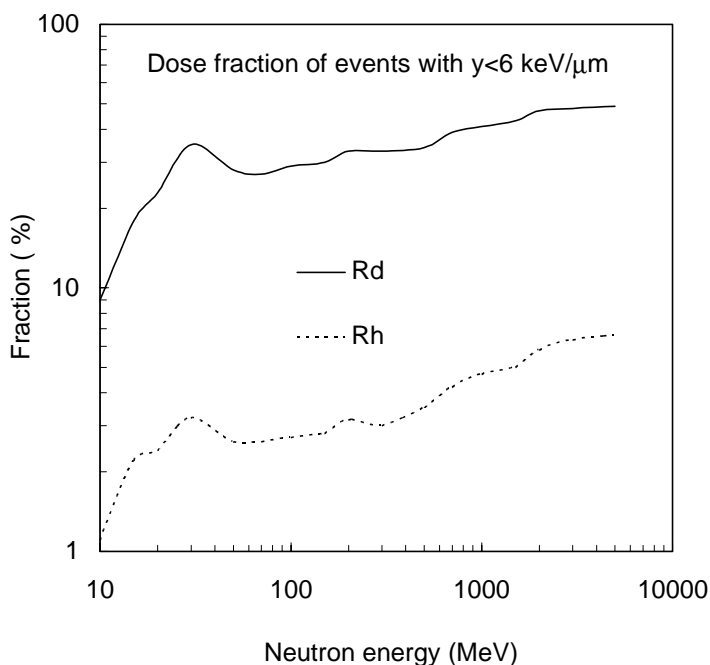
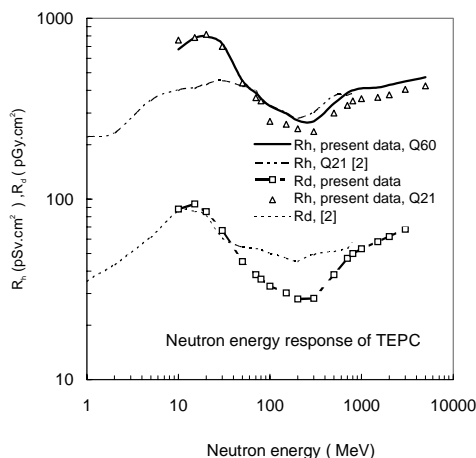


Figure 8 shows the comparison between calculation data of energy response of TEPC in units dose equivalents based on  $Q(y)$  relationship from ICRP-21 (Q21) and ICRP-60 (Q60) recommendations. The calculation data based on Q21 [7] is present too.

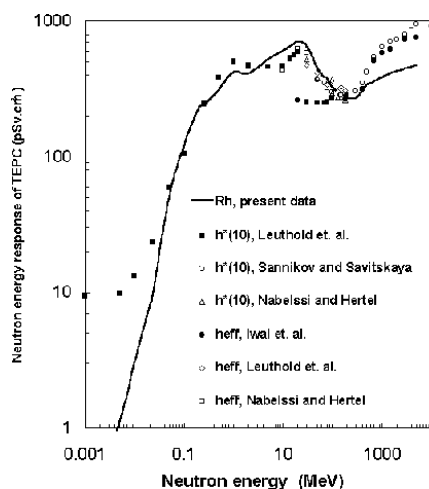
**Figure 8. Neutron energy response in units of absorbed dose and dose equivalent for  $Q(y)$  relationships specified in the ICRP-21 and ICRP-60**



Response  $R_H$  with Q60 is 10-30% higher than the one based on Q21. The distinction between present data and [7] is explained through the use of different data and codes for calculation of neutron inelastic interaction with nuclei, and so a different calculation of heavy nuclear to response exists.

The important problem is correlation of energy response of TEPC with dosimetric values which are used in radiation safety. These are ambient dose equivalent and effective dose equivalent. The comparison between neutron effective dose equivalent [16,17], ambient dose [8,17] and  $R_h$  are presented in Figure 9. The comparison shows that a measurement by TEPC provides good estimation of ambient dose value for neutron below 300 MeV. The distinction between effective dose data [16,17] appears in the energy region from 20 MeV up to 100 MeV. It could be explained in [17] by more correct calculation of contribution of heavy nuclear to dose equivalent. On the other hand the agreement between effective dose [17] and ambient dose [8] exists for neutrons above 100 MeV. Thus the TEPC measurement result is a conservative (over estimated) evaluation of dose equivalent for neutrons below 300 MeV if the distinction between data in [16] and [17] is taken into account.

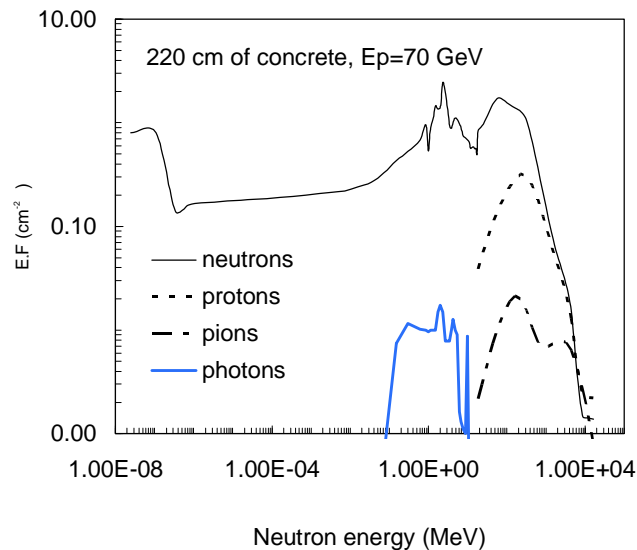
**Figure 9. Comparison of neutron response of TEPC with neutron ambient dose ( $h^*(10)$ ) and effective dose equivalent ( $h_{eff}$ )**



## Experimental verification of response

The experimental adjustment of TEPC response to high energy neutron has been carried out in measurements of dose equivalent behind top shielding in U-70 experimental hall, where high energy neutrons give a significant contribution into total dose. As a typical radiation field behind top shielding of U-70 we use the IHEP High Energy Reference Field (HEF), referring to [19] where its characteristics have been obtained by involving all available IHEP dosimetric and spectrometric instruments such as the set of measurements by TEPC, analogy component remmeter (ACR) (which include three ionisation chambers: argon fuelled, tissue-equivalent and  $^3\text{He}$  chamber in polyethylene moderator with 25.4 cm diameter), neutron multispheres spectrometer (Bonner spectrometer) together with carbon activation detector based on  $^{12}\text{C}(x, xn)^{11}\text{C}$  reaction [20]. A good agreement between HEF experimental spectrum measured by Bonner spectrometer and calculation by ROZ6H code with SADCO multigroup library of nuclear cross-sections [20] had been found in [19]. Figure 10 shows spectra of neutron, protons, photons and pions behind the side concrete shielding with 220 cm thickness arising from interaction of 70 GeV proton beam with thin iron target. As has been shown elsewhere, for example in [22], neutron spectrum behind of the side concrete shielding has a common shape (it has two peaks: in the evaporate neutron energy region and at 100 MeV).

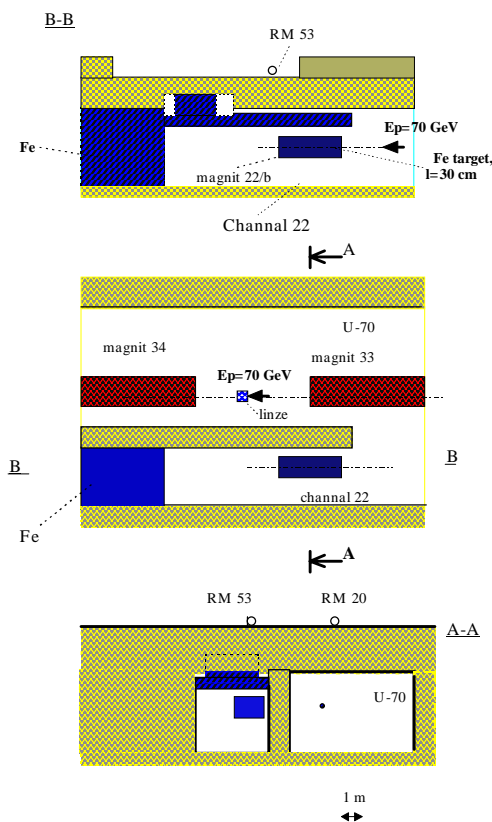
**Figure 10. Neutron, proton, pion and photon spectra behind 220 cm of concrete shielding from 70 GeV proton interacted with thin iron target. Calculation has been carried out with ROZ6H code by D. Gorbatkov.**



The shape is weakly dependent on primary proton energy and a shielding depth. The contribution of neutrons from 20 MeV up to 200 MeV to dose equivalent accounts about 66% for this spectrum.

In the present paper the measurement have been done on top shielding between seven and eight geodesical axis of U-70 in the place where the radiation monitors of 53 and 20 numbers are situated. Figure 11 shows measurement geometry. Measurements by TEPC and ACR was carried out in two points: the first is located above proton beam line of U-70 (RM 20) and the second one is above proton beam line of 22 channel (70 GeV proton energy). The measurement was carried out at 1 m height above the surface of shielding. The thickness of shielding are 220 cm concrete at the point of 20 RM location and 110 cm concrete plus 1 m iron at 53 RM point.

**Figure 11. Experimental geometry**



Average dose equivalent rate was less than 0.025 mSv/h, which allowed to neglect pick-up effect of events for TEPC. The beam loss location and operational regime of internal targets were not fixed during measurements. During measurement 22 channel was in operation.

Bonner spectrometer measurement has been carried out separately from the present one (at another regime of 22 channel and internal targets). Therefore the ratio of neutron dose equivalent for energy below 20 MeV to total neutron dose equivalent ( $H(E_n < 20 \text{ MeV})/H_n$ ) is chosen for a comparison between different experiment methods and calculation. Dose equivalents for neutrons below 20 MeV have been estimated by ACR measurement results.

The total neutron dose is result of measurement by TEPC and ACR. In the case of ACR the total neutron dose equivalent and neutron dose below 20 MeV are obtained as multiplication of  $^3\text{H}$  chamber results of measurement and the two factors which depend on a combination of readings of three chambers (Ar, tissue-equivalent and He). The ambient dose equivalent conversion factor was used for calculation  $H(E_n < 20 \text{ MeV})/H_n$  factor from neutron spectra.

Figure 12 shows the ratio of  $H(^3\text{He})/H_n$  measured by ACR in two directions (along and across proton beam line of U-70). The points of beam line above of U-70 and 22 channel are 0 and  $-4$  m co-ordinates correspondingly. The ratio remains constant along the line between measurement points of 20 RM and 53 RM in the limits of 12%.

This ratio increases with increasing of distance from beam line, because shielding thickness and consequently the contribution of scattering component raise too.

**Figure 12. Ratio of  $H(^3\text{He})/H_n$  along (1) and across (2) of beam line of U-70**

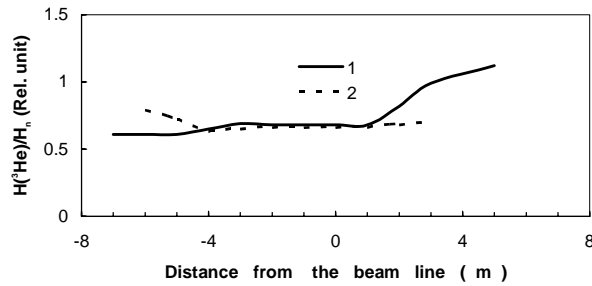
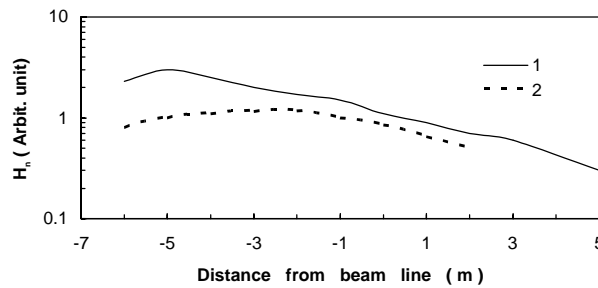


Figure 13 shows distribution of average neutron dose equivalent for the same geometry as for Figure 12. The maximum of dose rate is located above 22 channel where thickness of concrete is 1 m and additionally there are holes in shielding. The results of comparison are presented in Table 2.

**Figure 13. Neutron dose equivalent rate along (1) and across (2) of beam line of U-70**



**Table 2. Comparison of experimental and calculation data of  $H(\text{En}<20 \text{ MeV})/H_n$  ratio**

Measurement point	TEPC	ACR	ROZ6H	Bonner spectrometer	[22]
<b>RM20</b>	0.42	0.57	–	–	–
<b>RM53</b>	0.40	0.52	–	–	–
<b>Estimation</b>	–	–	0.54	0.49	0.44

The estimation of  $H(\text{En}<20 \text{ MeV})/H_n$  ratio based on experimental and calculation data varies from 0.40 to 0.54. The estimation of same factor 22] ( $H_{AB}/H_n$ ) for Anderson-Braun remmeter (which has approximately the same neutron energy response as  $^3\text{He}$  chamber in polyethylene moderator) based on experimental data for neutron spectra behind concrete shielding is equal to  $0.5\pm 0.1$ . Therefore TEPC results agree with experimental and calculated estimations. The ACR method gives a higher estimation of the  $H(\text{En}<20 \text{ MeV})/H_n$  ratio. This could be explained by the fact that ACR correction factors for evaluation of high energy neutron dose equivalent are fitted from measurement with ACR, TEPC and Bonner spectrometer at different points at top of concrete shielding of U-70.

## Conclusion

The calculation of TEPC neutron energy response has been carried out for the neutron energy range from 20 MeV up to 5 GeV. The present data agree with measurement results at top of concrete shielding of high energy proton accelerator. Measurements by TEPC allow to obtain a correct estimation of ambient dose (errors is less than 15%) for neutrons below 200 MeV.

Altering calibration methods for dosimeters, which are used in routine radiation dosimetry, is necessary because the substitution of quantities in the radiation safety field (NRB-96, ICRP-60) (for example of dose equivalent is substitute by effective dose) exists. The routine neutron radiation dosimetry (for example at IHEP) is based on detectors which do not allow to correctly measure ambient dose, effective dose for neutrons above 20 MeV. At same times ambient dose is conservative estimation of effective dose in wide neutron energy region (up to 10 GeV), TEPC can be used as a reference dosimeter for calibration of routine dosimeters in units of ambient dose for applications in high energy neutron fields.

#### *Acknowledgements*

The authors are grateful to V.N. Lebedev for support of this work, A. Sannikov and E. Savitskaya for a help in HADRON code calculation, S. Kuchinin for discussion, Yu. Bystrov and A. Abrosimov for help in measurements.

#### **REFERENCES**

- [1] H.H. Rossi, "Specification of Radiation Quality", *Radiat. Res.*, 10, pp. 522-531.
- [2] International Commission on Radiation Units and Measurements. Microdosimetry Report 36, ICRU Publications, Washington DC (1983).
- [3] J.J. Booz, A.A. Edwards and K.G. Harrison, "Proceedings of a Workshop on a Microdosimetric Counter in Radiation Protection", *Radiat. Prot. Dosim.*, 9, (3) (1984).
- [4] H.G. Menzel, H.G. Paretz and J.J. Booz, "Proceedings of Workshop on Implementation of Dose Equivalent Meters Based on Microdosimetric Techniques in Radiation Protection", *Radiat. Prot. Dosim.* (1989).
- [5] A.J. Waker, P. Pihet and H.G. Menzel, "Proceedings of a Workshop on Advance in Radiation Measurements", Application and Research Needs in Health Physics and Dosimetry (Chalk River, 1994, CEC, EUR 16177 EN), *Radiat. Prot. Dosim.*, 61(4) (1995).
- [6] A.I. Abrosimov, A.G. Alekseev, Yu.V. Bystrov, V.T. Golovachik, Sannikov, S.A. Kharlampiev "Geratebasis for die Metrologische Sincherstellung der Strahlungsüberwachung am Synchrotron Serpuchow. Kernenergie", 31 (5) 214-222 (1988).
- [7] A.I. Abrosimov, A.G. Alekseev, V.T. Golovachik, "Tissue-Equivalent Radiation Monitor for Dose Equivalent Measurement of Radiation Behind the Shielding of a Proton Accelerator Kernenergie", 34 (3) 108-111 (1991).

- [8] A.V. Sannikov and E.N. Savitskaya “Ambient Dose Equivalent Conversion Factors For High Energy Neutrons Based on the New ICRP Recommendations”, IHEP preprint 95-98, Protvino (1995).
- [9] A.I. Abrosimov, A.G. Alekseev, Yu.V. Bystrov, P.F. Maslyaev, S.A. Kharlampiev, P.N. Smirnov, “Dose Characteristics of IHEP Reference Neutron Fields”, preprint IHEP 93-43, Protvino (1993).
- [10] A.I. Abrosimov, A.G. Alekseev, A.V. Antipov, V.T. Golovachik, “Remmeter ED-02 for Dose Equivalent Measurements of Mixed Photon and Neutron Radiation”, *Kernenergie* 28(9) 390-397 (1985).
- [11] A.G. Alexeev, “Application of Low-Pressure Tissue-Equivalent Proportional Counter for IHEP Radiation Protection”, IHEP preprint 95-69, IHEP, Protvino (1995).
- [12] ICRP, Recommendation of the ICRP, Publication 21 – Oxford, Pergamon, 1987.
- [13] ICRP, Recommendations of the ICRP, Publication 60 – Oxford, Pergamon, 1990.
- [14] E.N. Savitskaya and A. Sannikov, “High Energy Neutron and Proton Kerma Factors for Different Elements”, *Rad. Prot. Dosim.*, 60 135-146 (1995).
- [15] M.B. Chadwick, P.G. Young, “Calculation and Evaluation of Cross-Sections and Kerma Factors for Neutrons to 100 MeV on  $^{16}\text{O}$  and  $^{14}\text{N}$ ”, *Nuclear Science and Engineering* 123, 1, 1-16 (1996). M.B. Chadwick, L.J. Cox. P.G. Young, A.S. Meigooni, “Calculation and Evaluation of Cross-Sections and Kerma Factors for Neutrons to 100 MeV on Carbon”, *Nuclear Science and Engineering*, 123, 1 ,17-37 (1996).
- [16] B.K. Nabelssi and N.E Hertel, “Effective Dose Equivalent and Effective Dose for Neutron from 30 to 180 MeV”, *Rad. Prot. Dos.*, (1993).
- [17] S. Iwai, T. Uehara, O. Sato, N. Yoshizawa, S. Furihata, S; Takagi, S. Tanaka, Y. Sakamoto, “Evaluation of Fluence to Dose Equivalent Conversion Coefficients for High Energy Neutrons – Calculation of Effective Dose Equivalent and Effective Dose,” private communication.
- [18] G. Leuthold, V. Mares, H Schraube, “Re-calculation of the Neutron Ambient Dose Equivalent on the Basis of the ICRP Revised Quality Factors”, *Rad. Prot. Dosim.*, 40 (2) 77-84 (1992).
- [19] A.G. Alekseev, S.A. Kharlampiev, “Dose Characteristics of IHEP Reference Neutron Fields”, *Radiat. Prot. Dosim.*, in publication (1996).
- [20] G. Britvich, V. Volkov, Yu. Kolevatov, A. Kremenetsky, V. Lebedev, V. Mayorov, Ya. Rastsvetalov, L. Trykov, A. Chumakov, “Spectra and Integral Values of Reference Neutron Fields from Radionuclide Neutron Sources”, IHEP preprint 90-48, Protvino (1990).
- [21] D.V. Gorbakov, V.P. Kryuchkov, “SADCO-2: a Modular Code System for Generating Coupled Nuclear Data Libraries to Provide High-Energy Particle Transport Calculation by Multigroup Methods”, *NIM A* 372 1, 2, 297-301 (1996).
- [22] H. Dinter, B. Rasky, K. Tesch, “Neutron Dosimetry at High Energy Accelerators”, *Nucl. Instr. Meth.*, A 376 ,104-114 (1996).



# Miscellaneous Topics – Part II

*Chairs: F. Clapier and Y. Sakamoto*



# *Activation*



**TEST OF ACTIVATION DETECTORS (BI AND AL) AS  
NEUTRON SPECTROMETER IN THE RANGE 6 TO 140 MeV**

**N. Pauwels, F. Clapier, P. Gara, J. Proust**  
Institut de Physique Nucléaire, 91406 Orsay, France

**T. Nakamura, E. Kim**  
Tohoku University, Aramaki, Aoba, Sendai, 980, Japan

**Abstract**

The energy thresholds of (n,X) reactions range from electron-volt to MeV. Unfortunately, many cross-sections are not well known above 30 MeV, the determination of neutron spectra beyond that energy being uncertain [1,2]. The work described hereafter consists of a tentative assessment of neutrons produced by 200 MeV protons impinging on a thick Al target. Al and Bi foils were activated together in order to test the practical pertinence of such a combination and verify that unfolding the experimental data leads to realistic estimates.

## Introduction

In order to assess the secondary neutrons distribution around thick targets to commission the new GANIL facility, modified by the SPIRAL [3] radioactive beam on-line separator and post accelerator, tantalum activation detectors were used to compare energy and angular relative fluxes for different projectiles through the measurement of (n,xn) reaction residues with x=2 to 12 [4]. Simultaneously the activates and dose rates resulting from materials exposed to intermediate energy neutrons were studied [5]. Given the results obtained by Tohoku University for (n,xn) cross-sections measured by the time of flight method [6] and their good agreement with ENDF/B-VI code as reported at SATIF 2, we decided to test the possibility of using Bi combined with Al as a neutron spectrometer. The expected advantage of the method is a rather simple and prompt experimental procedure as compared to other approaches. The test was performed with 200 MeV proton beam and a thick Al target. The induced radioactivity in the activation detectors was measured by high resolution gamma ray spectrometry.

## Experiment

### Activation detectors

The  $^{209}\text{Bi}$  (n,xn)  $^{209-x}\text{Bi}$  cross-sections, as available, limit the maximum neutron energy to 140 MeV (Figure 1), whereas the (n,2n) reaction threshold is at 8 MeV [6]; in practice  $^{208}\text{Bi}$  ( $T_{1/2}=3.68 \cdot 10^5$  years) cannot be measured directly, and (n,3n) reaction requires a neutron energy greater than 15 MeV. Information on lower energy neutrons can be obtained by the classical reactions producing Na isotopes in Al (Table 1).

Figure 1. Cross-section of data of  $^{209}\text{Bi}$  (n,xn) reaction compared with ENDF/B-VI

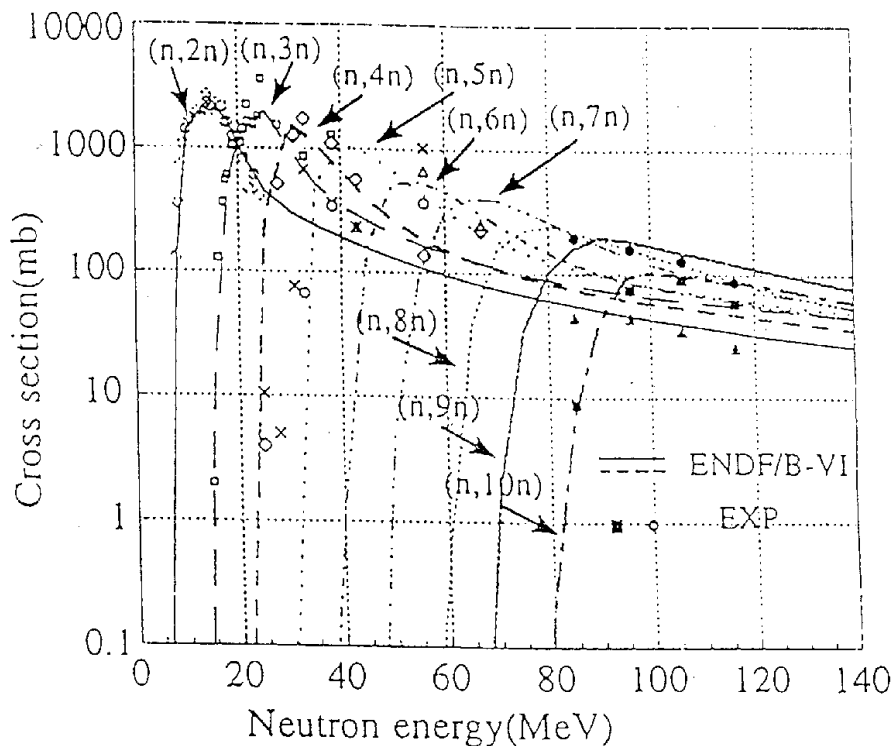


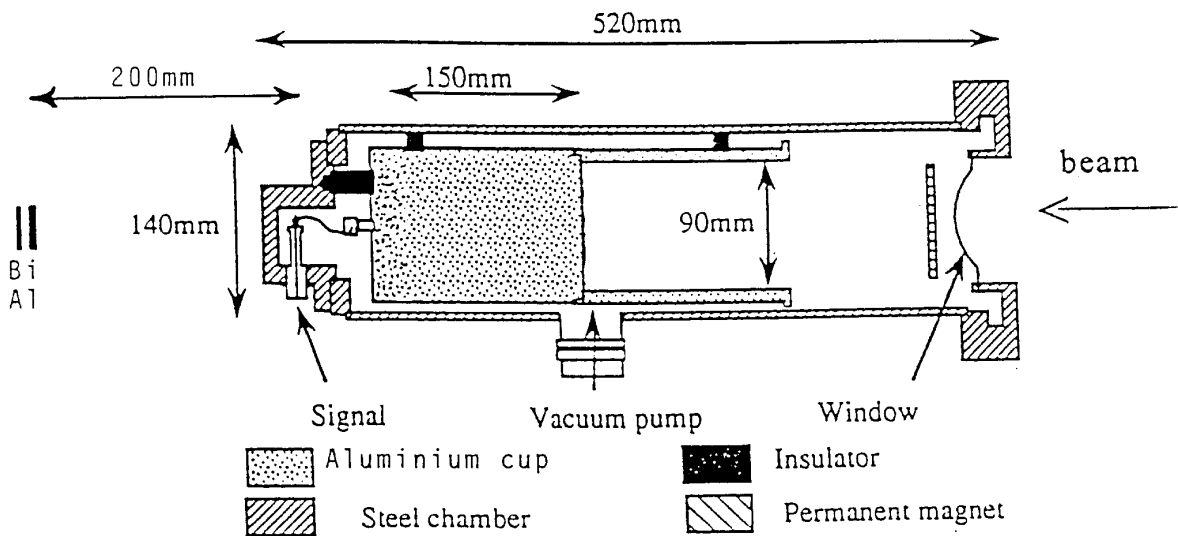
**Table 1. Nuclides information and activity results**

Detector	Reaction	Nuclide	Half life	Threshold (MeV)	Ray (keV)	Activity ( Bq )	
						Measurement	Calculation
Al	(n, $\alpha$ )	$^{24}\text{Na}$	15 h	6	1368.6	$5.53 \cdot 10^3$	$5.53 \cdot 10^3$
Al	(n,spall.)	$^{22}\text{Na}$	2.6 y	25	1274.5	1.3	0.64
Bi	(n,2n)	$^{208}\text{Bi}$	$3.8 \cdot 10^5$ y	8	*	*	*
Bi	(n,3n)	$^{207}\text{Bi}$	38 y	15	1063.6	0.16	0.14
Bi	(n,4n)	$^{206}\text{Bi}$	6.24 d	25	803	245	252
Bi	(n,5n)	$^{205}\text{Bi}$	15.31 d	30	703.3	103	101
Bi	(n,6n)	$^{204}\text{Bi}$	11.3 h	40	984	$1.87 \cdot 10^3$	$1.94 \cdot 10^3$
Bi	(n,7n)	$^{203}\text{Bi}$	11.8 h	50	820.2	$1.61 \cdot 10^3$	$1.53 \cdot 10^3$
Bi	(n,8n)	$^{202}\text{Bi}$	1.8 h	60	960.7	$6.41 \cdot 10^3$	$5.63 \cdot 10^3$
Bi	(n,9n)	$^{201}\text{Bi}$	1.85 h	70	629.1	$3.49 \cdot 10^3$	$4.38 \cdot 10^3$
Bi	(n,10n)	$^{200}\text{Bi}$	36 mn	85	1026.5	$5.81 \cdot 10^3$	$5.35 \cdot 10^3$

**Experimental set-up** (Figure 2)

The experiment took place at the Orsay Protontherapy Centre with the Synchrocyclotron formerly operated by IPN for nuclear physics. A 150 mm thick Al piece was mounted in a Faraday cup, the 200 MeV proton being completely stopped in the target [7]. The exposure was performed at 100 nA during 30 minutes, the stack of activation detectors was at a position of 20 cm after the cup and consisted in a 5 mm thick and 40 mm diameter Al sample followed by a 25 mm square and 1 mm thick Bi piece. The Bi detector analyses started 3 minutes after the end of the exposure.

**Figure 2. Experimental set-up**

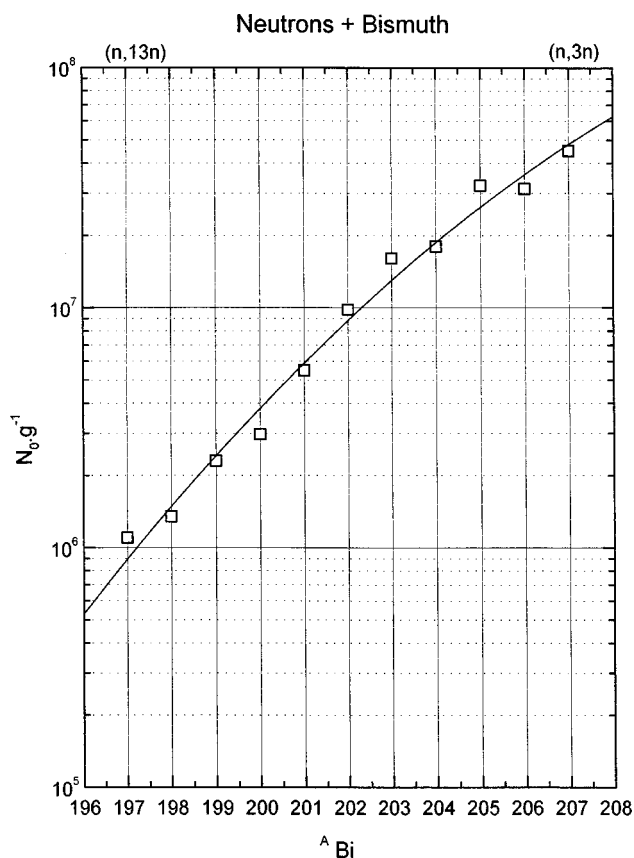


### Radioisotope productions

In Al the radioactivity of  $^{24}\text{Na}$  was measured first; then it was necessary to wait for its decay in order to detect  $^{22}\text{Na}$  with sufficient statistics.

Bi isotopes were measured at different moments because of the range of the decay constants, also  $^{205}\text{Bi}$  and  $^{207}\text{Bi}$  have a gamma line in common. The self attenuation of the gamma rays within the sample dependence with energy was investigated,  $^{198}\text{Bi}$  nuclear data sheet considered as the reference [8]. Consequently, it was possible to measure directly all Bi atoms formed in the mass range 197 to 207, by (n,3n) to (n,13n) reactions, the number of atoms per gram of  $^{208}\text{Bi}$  produced by (n,2n) reaction can be deduced with the help of a polynomial fit for all Bi isotopes measurement (Figure 3).

**Figure 3. Bismuth produced by (n,xn) reaction in atoms per unit mass at the end of the irradiation**



### Neutron and flux determination

The radioactivity induced by neutrons at a given energy is described as follows:

$$A(t) = \frac{N_a}{A} \rho e S \sigma(E) (1 - e^{-\lambda t})$$

t	– irradiation time(s)
N <sub>a</sub>	– Avogadro number
A	– mass number of the exposed matter (g)
ρ	– mass density (g·cm <sup>-3</sup> )
e	– the thickness of the sample (cm)
S	– the sample surface (cm <sup>2</sup> )
φ (E)	– the neutron flux (cm <sup>-2</sup> ·s <sup>-1</sup> )
σ(E)	– the reaction cross-section (cm <sup>2</sup> )
λ	– the isotope decay constant (s <sup>-1</sup> )

The real activation is originated by a spectrum at a given laboratory angle; the formula presented is integrated over the energy range 6 to 140 MeV. The variable φ(E) is not directly available and many experiences show that there are two compartment in the spectrum [9]. High energies are provided by direct interaction of protons with the target nuclei, the lower energies result essentially from the neutrons evaporated by the excitation energy deposited by direct interactions. The evaporation neutrons are emitted isotropically in the centre of mass frame. The others are mainly produced in forward directions because of kinematics; the overall spectrum is well described by a set of two exponential decays. We decided to represent the flux by the formula:

$$\phi(E_n) = a_1 E_n \exp(-b_1 E_n) + a_2 E_n \exp(-b_2 E_n)$$

The determination of the coefficients a<sub>1</sub>, a<sub>2</sub>, b<sub>1</sub> and b<sub>2</sub> is performed by the minimisation of chi square (χ<sup>2</sup>) for a set of ten values of induced activities:

$$\chi^2 = \left( \sum_t \frac{A_i - C_j \int_6^{140} \sigma_i(E) \phi(E) dE}{\Delta_i} \right)^2$$

The subscripts j and i label the detector type (Bi and Al) and a given radioactive species respectively, C<sub>j</sub> is equal to  $\frac{N_a}{A} \rho_j e_j S_j$ , Δ<sub>i</sub> is the error associated to radioactivity measured.

## Results

After the minimisation of χ<sup>2</sup>, for the neutron flux we obtained the following equation:

$$\phi(E_n) = 5.07 \cdot 10^{-3} E_n \exp(-0.34 E_n) + 2.84 \cdot 10^{-5} E_n \exp(-0.022 E_n)$$

The overall spectrum is presented in Figure 4, and reversibly the induced activities calculated by the latter plot are compared to the experimental data (Figure 5 and Table 1). One can see that the experimental activities are in a quite good agreement with calculated ones, this is confirmed by the χ<sup>2</sup> value which is equal to 15 (or 2.14 if divided by the number of liberty degree).

**Figure 4. Calculation of the experimental neutron flux**

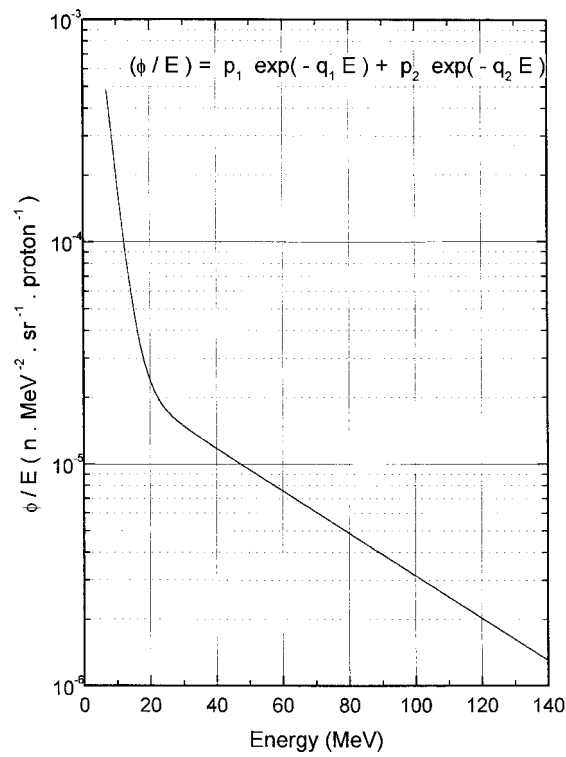
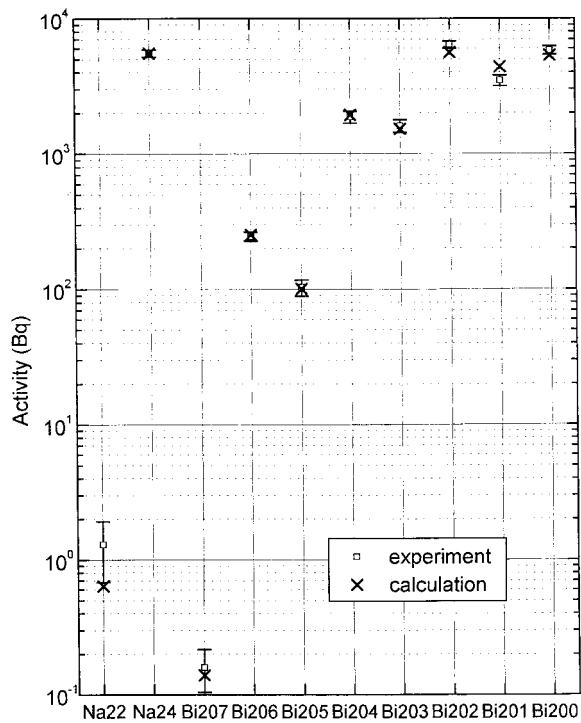
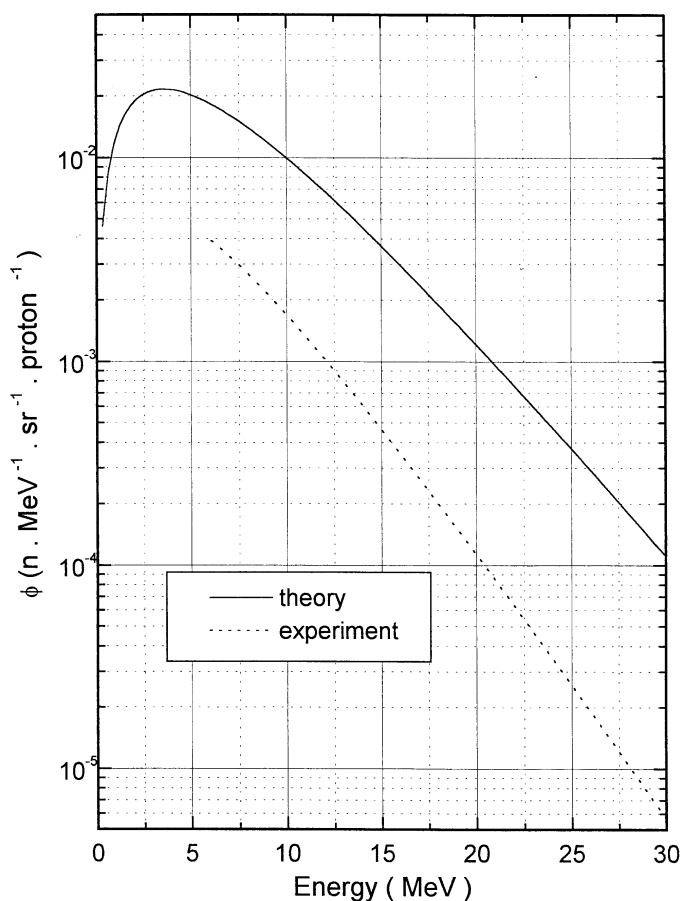


**Figure 5. Activities measured (experiment) and activities calculated with the equation found (calculation)**



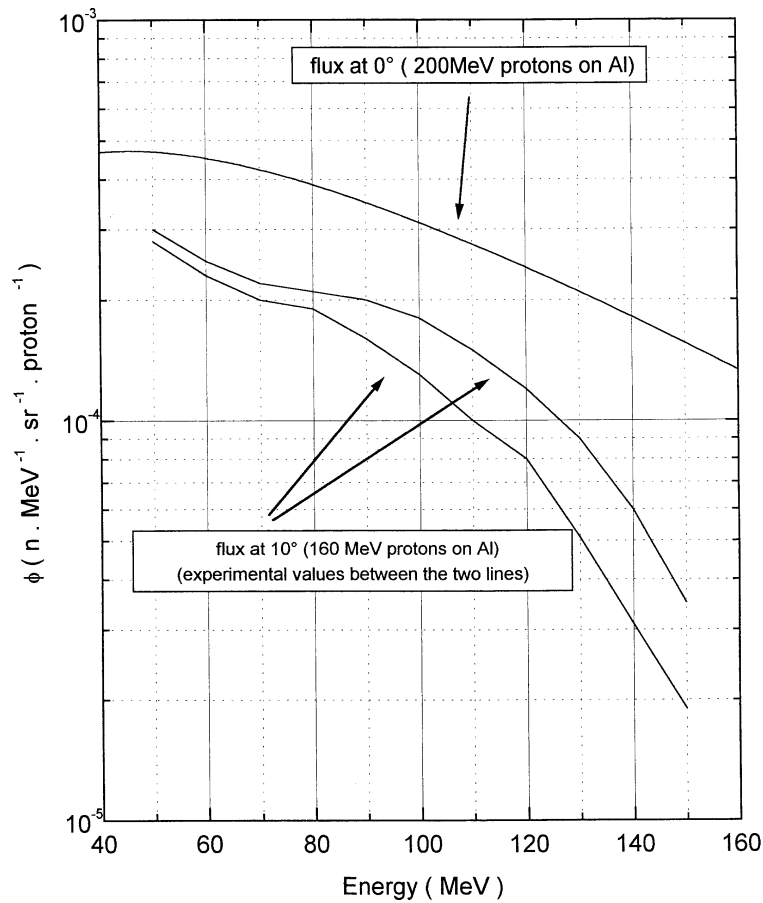
According to the reference [10], we made a theoretical calculation of the low energy distribution. When compared to the fit at low energies, the fluxes obtained from the experimental data (Figure 6), it appears that the theoretical results overestimate the flux by a factor approaching 10. Two main causes could explain the difference. The first one is that the number of available data to find the equation coefficients below 30 MeV are not numerous enough to match the prediction. We get only one nuclide with a threshold below 15 MeV and three between 15 and 30 MeV. The method could be improved by the addition of Ni with the (n,p) and (n,2n) reactions for which the energy thresholds are 1.3 MeV and 12.6 MeV respectively. The second one is that predictions do not take into consideration proton straggling, and neglect neutron interactions within the target leading to an unavoidable overestimation of the low energy fluxes. Finally, the lack of Bi excitation functions for  $x$  greater than ten is an additional experimental limitation.

**Figure 6. Low energy flux. The solid represent the experimental calculation and the dots the theoretical evaporation flux**



Previous experimental measurements of neutron spectra at  $10^\circ$  produced by 160 MeV protons bombarding an Al target [11] are compared to those obtained with the family of Bi radioactivities in this work (Figure 7). In this figure we consider only the fast neutrons (40-150 MeV) and the difference between the two spectra is not very important. Knowing that the fast neutrons are produced in a small solid angle (about  $20^\circ$ ) we can easily conclude that it is normal that our spectra is higher than the one at  $10^\circ$ . The energy difference (20%) is an other factor which lends to our determination.

**Figure 7. Fast neutron flux at 0° for 200 MeV p<sup>+</sup> on AL thick target**



## Conclusion

The results of this test using activation detectors as a fast neutron spectrometer are positive. Despite the series of remarks expressed above, the method discussed here can be considered as a reasonable tool for neutron distributions around a thick target. Some improvement for the low part of the flux has to be made. Presently the validity and limits of the method are being explored for thick targets irradiated by heavy ions ( $^{36}\text{Ar}+\text{C}$  at 95 MeV/A) with a combination of Al, Ni and Bi detectors at several angles (0°, 20°, 45°, 90°) and are about to be tested with 200 MeV deuterons bombarding Be and U targets, also at several angles.

## Acknowledgement

This work has been supported by l'Institut de Physique Nucléaire d'Orsay and the Centre de Protonthérapie d'Orsay. We wish to thank Mr. P. Roussel for his kind help.

## REFERENCES

- [1] M. Hyvönen and P. Nikkinen-Vilki, NIM 178 (1980) 451-458.
- [2] P.D. Holt, *Rad. Prot. Dosi.*, Vol. 10, N° 1-4, 251-264 (1985).
- [3] M. Lieuvin *et al.*, “Status of SPIRAL, the Radioactive Beam Project at GANIL”, Cyclotrons Conferences, Le Cap 10-1995, GANIL-S-9504.
- [4] F. Clapier, N. Pauwels and J. Proust, *Radioprotection*, Vol. 29, N° 4, 573-574 (1994).
- [5] F. Clapier, N. Pauwels, J. Proust, “Neutrons Induced Activation and Transmutation, Heavy Ions Induced Isotope Production with C, Ne, Kr at 100 MeV/A”, Second Specialists Meeting SATIF, OCDE/NEA/NSC, 12-13 October 1995, CERN, Geneva, Switzerland.
- [6] T. Nakamura, “Activation Cross-Section Measurements Using Quasi-Monoenergetic Neutrons Fields from 20 to 150 MeV”, Second Specialists Meeting SATIF, OCDE/NEA/NSC, 12-13 October 1995, CERN, Geneva, Switzerland.
- [7] C.F. Williamson, J.P. Boujot, J. Picard, “Table of Range and Stopping Power of Chemical Elements for Charged Particles of Energy 0.05 to 500 MeV”, CEA report (1966).
- [8] G. Erdtmann, W. Soyka, “The Gamma Rays of the Radionuclides”, Verlag Chemie, New-York, 1979.
- [9] T. Nakamura, NIM A240 (1985), 207-215.
- [10] T. Nakamura, Y. Uwamino, *Phys. Rev. C*, Vol. 29, 1317 (1984).
- [11] J.W. Wachter, W.R. Burrus, W.A. Gibson, *Phys. Rev.*, Vol. 161, 971 (1967).



**COMPUTER VERSION OF THE HANDBOOK ON RADIONUCLIDE PRODUCTION  
CROSS-SECTIONS AT INTERMEDIATE ENERGIES (THE NUCLEX CODE)**

**V.I. Ivanov, N.M. Sobolevsky**

Institute for Nuclear Research RAS, 117312 Moscow, Russia

**V.G. Semenov**

Research Centre of Spacecraft Radiation Safety  
of the Health Ministry of Russia, 123182 Moscow, Russia

**Abstract**

A computer version of Springer's Handbook manyvolume on radionuclides production cross-section in nuclear reactions at intermediate energies is previewed. The Handbook contains published experimental values of cross-sections (total about 80.000 experimental points). Projectiles are protons, pions, deuterons, tritons,  $^3\text{He}$  nuclei and alpha particles. Nuclei-targets cover range from Helium to transuraniums. Energy area extends from reaction thresholds up to the data measured. The main features of the NUCLEX code are presented.

## Introduction

Since 1991 Springer has issued eight subvolumes of a manyvolume Handbook on radionuclide production at intermediate energies [1]. The Handbook contains published experimental values of cross-section of radionuclides production in nuclear reactions. Projectiles are protons, pions, deuterons, tritons,  $^3\text{He}$  nuclei, and alpha particles. The energy range of the projectiles extends from a threshold of a reaction up to several GeV or even higher (up to the data measured). Nuclei-targets cover range from Helium to transuraniums.

The data on cross-sections are presented in the form of excitation functions, i.e. as dependence of formation cross-section of a given radionuclide on a projectile energy for a given nucleus-target. All excitation functions are tabulated and representative ones (more than 8-10 points) are depicted as well. Subvolumes I/13a-d deal with protons as projectiles and contain about 40.000 cross-section values. Subvolume I/13e includes about 3000 points on pion induced reactions and few antiproton data. Subvolumes I/13f-h concern deuteron, triton,  $^3\text{He}$  and alpha induced reactions (correspondingly 9.300, 230, 4.500, and 23.000 experimental values). So there is a total of about 80.000 experimental values in 10.000 excitation functions including 2.300 depicted ones. The data were extracted from more than 1.500 original publications. The Handbook claims to be the most complete compilation of its kind in existing literature.

It is a natural idea to elaborate a computer version of this Handbook. The NUCLEX code (NUCLEAR reaction EXcitation functions) is an original computer version of the manyvolume Springer's Handbook. The NUCLEX code is intended to raise up the availability of this very complete data collection for specialists in pure and applied nuclear physics. It provides the efficiency of data search and analysis. Moreover, the newest data published after printed version was issued are included in the NUCLEX database to keep the collection in a current state. The NUCLEX code runs under MS WINDOWS 3.x or higher and requires about 5 Mb on the hard disk.

In the same manner as in the Handbook, the data on radionuclide production cross-sections are presented in the form of excitation functions. Having chosen an excitation function of interest or a set of these, the user can observe and compare them on the screen in graphic form and store or print out as well. Each excitation function is provided with the list of references on a basis of which it was constructed. For the user's convenience the reference data on the isotope abundance and decay periods can be displayed.

## Sketch of the NUCLEX for WINDOWS

### *Start*

When the NUCLEX code runs from WINDOWS, the illumination "NUCLEX" will appear along with three buttons on the screen: **Abstract**, **Start**, and **Exit**. The functions of these buttons are the following:

- **Abstract** – The panel appears on the screen containing a brief abstract of the NUCLEX code;
- **Start** – start of the NUCLEX session;
- **Exit** – exit from NUCLEX.

## *Beginning of work*

The **Start** button initiates the NUCLEX session. The main menu bar will appear at the top of the screen, and the Mendeleev Periodical System of Chemical Elements is displayed just below. The Mendeleev table is used further for choosing a target and product of a nuclear reaction. The main menu items include:

- **Projectile** – assign the nuclear reaction projectile as default;
- **Reaction** – choose the nuclear reaction(s) of interest;
- **References** – operation on a list of bibliographic sources containing an experimental data;
- **Output** – output to the screen, file or printer;
- **Isotopes** – reference data on stable and radioactive isotopes;
- **Help** – helper;
- **Exit** – exit from NUCLEX.

## *Choosing excitation functions*

The menu item **Reaction** from the main menu displays a sub-menu containing three items: **Packet**, **Analyse**, and **Targets**.

**Packet** and **Targets** provide two different ways of choosing a set of reactions of interest. **Packet** allows to create an arbitrary packet of excitation functions for further comparative analysis. **Targets** gives a total list of the excitation functions for fixed projectile and target and permits to consider them one by one.

## *Packet*

If one chooses **Packet**, the panel “Create Packet of Reactions” appears on the screen. The tool buttons of the panel allow to create current packet of the excitation functions (see Figure 1).

Choosing of regular excitation function(s) is provided with buttons **Projectile**, **Target**, and **Product**. The **Projectile** button of the panel “Create Packet of Reactions” allows to assign different projectiles for specific reactions. The **Target** and **Product** buttons (together with the element buttons of the Mendeleev table) allow to specify the excitation function.

The chosen reaction will be added to the current packet after pressing the **Next** button. Herewith the reactions number counter on the panel “Create Packet of Reactions” will be increased by the number of reactions added.

Further, the user can continue to form the current packet, i.e. to define and add new reaction(s) to the packet as described above, or **Edit** the current packet. Editing the packet consists of deleting and inserting the reactions (see Figure 2).

Figure 1

**Production of Radionuclides at Intermediate Energies**

Projectile Reaction References Output Isotopes Help Exit

**MENDELEEV PERIODICAL SYSTEM OF CHEMICAL ELEMENTS**

Period	Row	Groups of elements									
		I	II	III	IV	V	VI	VII	VIII	0	
1	1	H 1								He 2	
2	2	Li 3	Be 4	B 5	C 6	N 7	O 8	F 9		Ne 10	
3	3	Na 11	Mg 12	Al 13	Si 14	P 15	S 16	Cl 17		Ar 18	
4	4	K 19	Ca 20	Sc 21	22 Ti	23 V	24 Cr	25 Mn	26 Fe	27 Co	28 Ni
	5	29 Cu	30 Zn	Ga 31	Ge 32	As 33	Se 34	Br 35			Kr 36
5	6	Rb 37	Sr 38	39 Y	40 Zr	41 Nb	42 Mo	43 Tc	44 Ru	45 Rh	46 Pd
	7	47 Ag	48 Cd	In 49	Sn 50	Sb 51	Te 52	I 53			Xe 54
6	8	Cs 55	Ba 56	57 La*	72 Hf	73 Ta	74 W	75 Re	76 Os	77 Ir	78 Pt
	9	79 Au	80 Hg	Tl 81	Pb 82	Bi 83	Po 84	At 85			Rn 86
7	10	Fr 87	Ra 88	89 Ac*	Ku104						

Create Packet of Reactions:

Proton +  12

Projectile Target Product

NewPacket Next More Edit

Restore Save

**LANTHANIDES**

Ce58	Pr59	Nd60	Pm61	Sm62	Eu63	Gd64
Tb65	Dy66	Ho67	Er68	Tm69	Yb70	Lu71

**ACTINIDES**

Th90	Pa91	U 92	Np93	Pu94	Am95	Cm96
Bk97	Cf98	Es99	Fm100	Md101	No102	Lr103

Figure 2

**Production of Radionuclides at Intermediate Energies**

Projectile Reaction References Output Isotopes Help Exit

**MENDELEEV PERIODICAL SYSTEM OF CHEMICAL ELEMENTS**

Packet Editing All Ok

$^1_1\text{H} + ^6_6\text{C} \rightarrow ^7_4\text{Be}$	149
$^1_1\text{H} + ^6_6\text{C} \rightarrow ^{11}_6\text{C}$	188
$^1_1\text{H} + ^{13}_6\text{C} \rightarrow ^{13}_7\text{N}$	129
$^1_1\text{H} + ^7_7\text{N} \rightarrow ^{11}_6\text{C}$	160
$^1_1\text{H} + ^{13}_{13}\text{Al} \rightarrow ^{22}_{11}\text{Na}$	227
$^1_1\text{H} + ^{13}_{13}\text{Al} \rightarrow ^{24}_{11}\text{Na}$	208
$^1_1\text{H} + ^{23}_{23}\text{V} \rightarrow ^{51}_{24}\text{Cr}$	198
$^1_1\text{H} + ^{65}_{29}\text{Cu} \rightarrow ^{66}_{30}\text{Zn}$	297

Period	Row	Groups of elements								
		V	VI	VII	VIII	0				
										He 2
		N 7	O 8	F 9	60 144.24 Nd NEODIMIUM					Ne 10
		P 15	S 16	Cl 17						Ar 18
		23 V	24 Cr	25 Mn	26 Fe	27 Co	28 Ni			
2		As 33	Se 34	Br 35						Kr 36
		41 Nb	42 Mo	43 Tc	44 Ru	45 Rh	46 Pd			
3		Sb 51	Te 52	I 53						Xe 54
		73 Ta	74 W	75 Re	76 Os	77 Ir	78 Pt			
4		Bi 83	Po 84	At 85						Rn 86

Create Packet of Reactions:

Proton  12

Projectile Target Product

Delete Insert Done

Restore Save

**LANTHANIDES**

Ce58	Pr59	Nd60	Pm61	Sm62	Eu63	Gd64
Tb65	Dy66	Ho67	Er68	Tm69	Yb70	Lu71

**ACTINIDES**

Th90	Pa91	U 92	Np93	Pu94	Am95	Cm96
Bk97	Cf98	Es99	Fm100	Md101	No102	Lr103

All selecting and scrolling frames have scroll bar and six control buttons such as **Home**, **Up**, **PgUp**, **End**, **Down**, **PgDn** of keypad. To scroll, press the left mouse button and move it inside the frame. To select, click the left mouse button on the left side of the frame or the right mouse button on the selected item.

### *Targets*

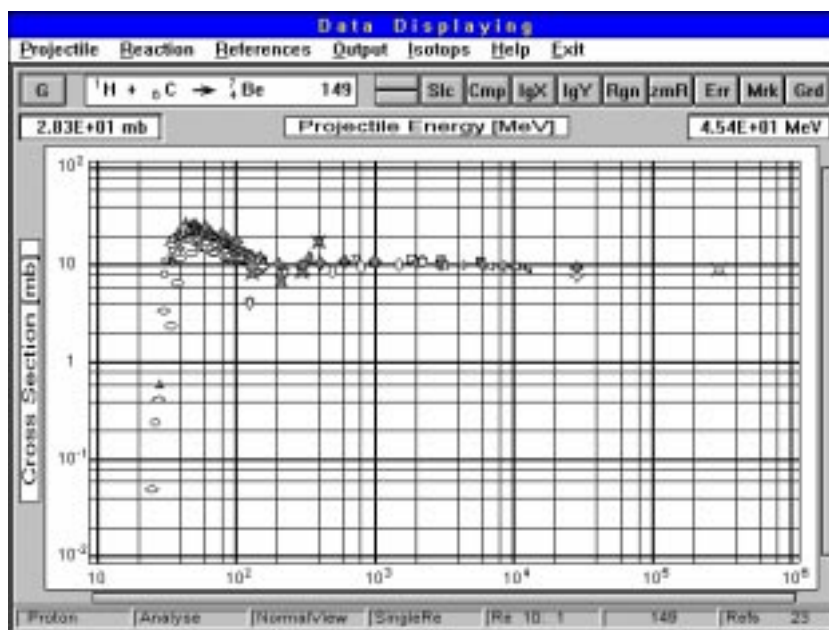
Contrary to the **Packet** item, **Targets** instantaneously gives all available excitation functions for given projectile and target elements. After the **Targets** command is done one should assign the projectile (using the **Projectile** command from the main menu) and press the button of the desirable target-element in the Mendeleev table. The graphical representation of the first excitation function appears on the screen. The user can then work with the set of excitation functions one by one.

### *Analysing excitation functions*

If the item **Targets** was selected, all element buttons will represent all targets for a given projectile. After selecting the target element or **Analyse** items one can see graphical representation of the first function from the list (see Figure 3). The graphical mode has a number of possibilities. It allows to examine an individual excitation function, to compare several functions, zoom, scale and so on. A description of the screen view during graphical mode follows.

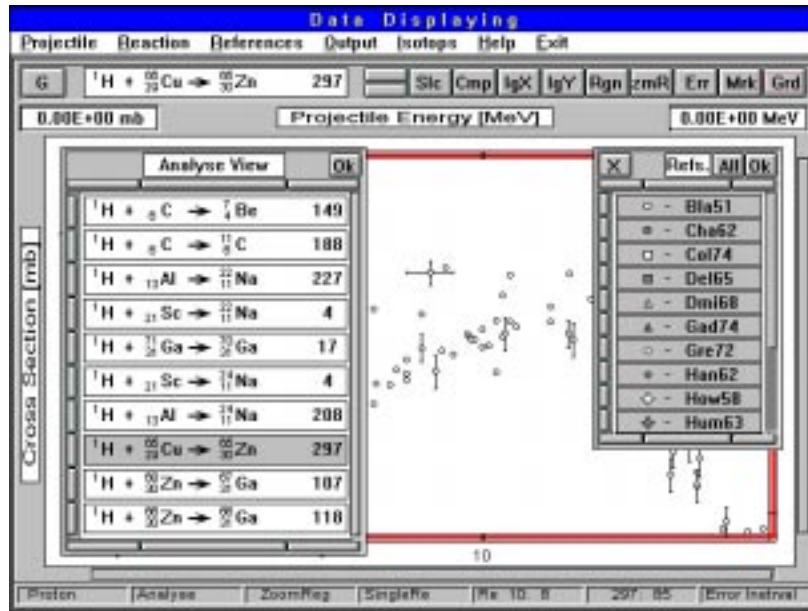
Below the main menu bar there is a toolbar with an indicator window, and at the bottom of the screen is a status line. Along the abscissa axis of the graphic “Projectile Energy, MeV” is displayed and along the ordinate axis “Cross-Section, mb”. If the mouse cursor is in the graphical field the co-ordinates of the cursor (MeV,mb) are indicated in two windows above the graphic frame. This allows to know immediately the co-ordinates of any experimental point.

**Figure 3**



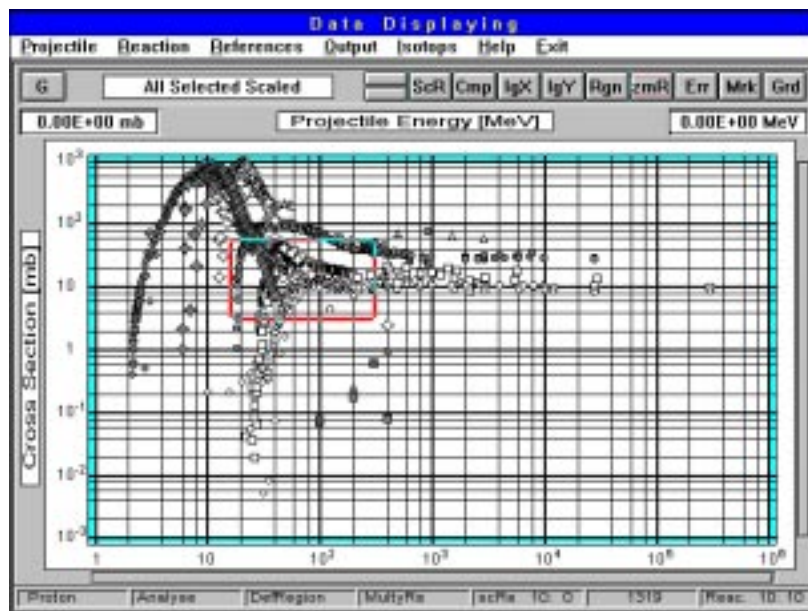
Each point marker codes reference source. One can also work with point markers after pressing the **Mrk** button. The user can select any function from the list by using the **Slc** button or the bifeed button (previous/next). At any moment the user can replace a marker by error interval if it is presented in the source by means of the **Err** button. One can hide/display the scale grid by using the **Grd** button (see Figure 4).

Figure 4



After selecting the **Analyse** item button **Cmp** lets see simultaneously on the screen any group of functions of the packet (up to all of them) scaled on all functions or on any selected one. Each function has its own marker (see Figure 5).

Figure 5



To zoom any area of the graphic one must define region after pressing **Rgn** (see Figure 5) and zoom out/in by button **zmR**. (See Figure 6).

**lgX/liX** and **lgY/liY** buttons let change between logarithmic and linear scaling in both axes. Switching between graphic and table representation can be done by means of the **G/T** button if a single function is in consideration (see Figure 7).

Figure 6

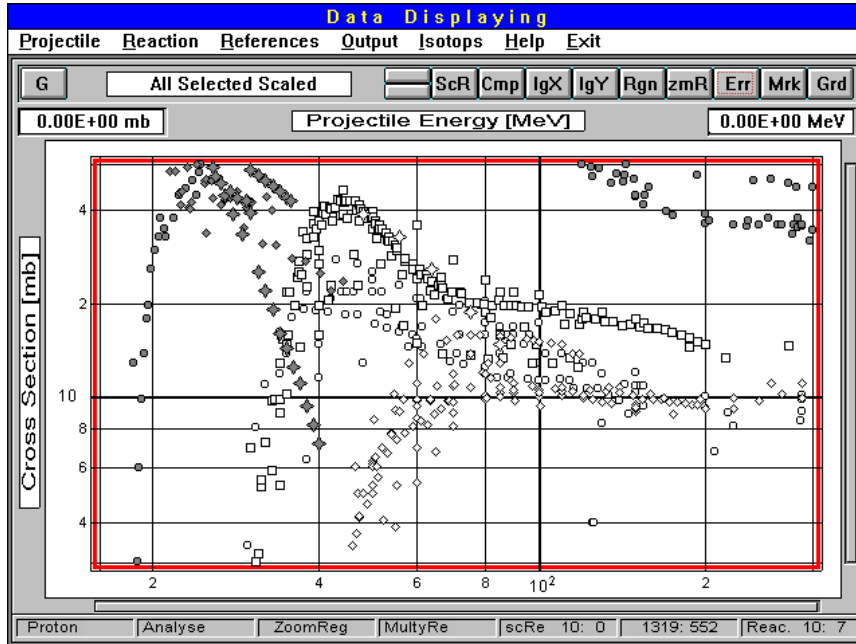


Figure 7

	Prj.Enrg.[MeV]	Ers.[MeV]	Cr.Sect.[mb]	Ers.[mb]	Reference
1.	24.50		0.500E-1		Wil67 *
2.	26.50	1.40	0.240	0.40E-1	Ale90 *
3.	27.40		0.420		Wil67 *
4.	28.00		0.600		Bod91
5.	29.80		3.400		Wil67 *
6.	30.80	1.20	8.100	1.10	Ale90 *
7.	31.90		11.100		Wil67 *
8.	34.00		16.300		Wil67 *
9.	34.00		12.000		Bod91
10.	34.00		2.300	0.20	Dic51
11.	35.00		10.400	1.00	Bru62a*
12.	35.00	0.50	14.000	2.00	Ale90 *
13.	35.80		18.200		Wil67 *
14.	37.50		19.300		Wil67 *
15.	38.00		6.400	0.20	Dic51
16.	38.00		22.000		Bod91
17.	39.50		19.200		Wil67 *
18.	40.00		11.700	0.40	Dic51
19.	40.00		15.000	1.50	Bru62a*
20.	41.50		18.900		Wil67 *

\* digitalized data

### *Operation with the list of bibliographical references*

The **References** command from the main menu allows to work with a list of bibliographical references. This list involves the references to publications containing experimental data included in the NUCLEX database.

The user can deal with total list of references or with the list related to excitation function(s) under consideration. Accordingly one should select either the **All** or the **Related** command from the main menu item **References**.

After that the panel appears on the screen containing buttons-abbreviation (see Figure 8). They can be arranged in alphabetical order or by date with the **Auth./Date** button. The reference list can be shown on the screen (see Figure 9) or saved in a file, as a whole or only partly. In the last case one should press **Slc** and the buttons/abbreviations of interest. The right mouse button allows select/unselect abbreviations between two pressing.

Figure 8

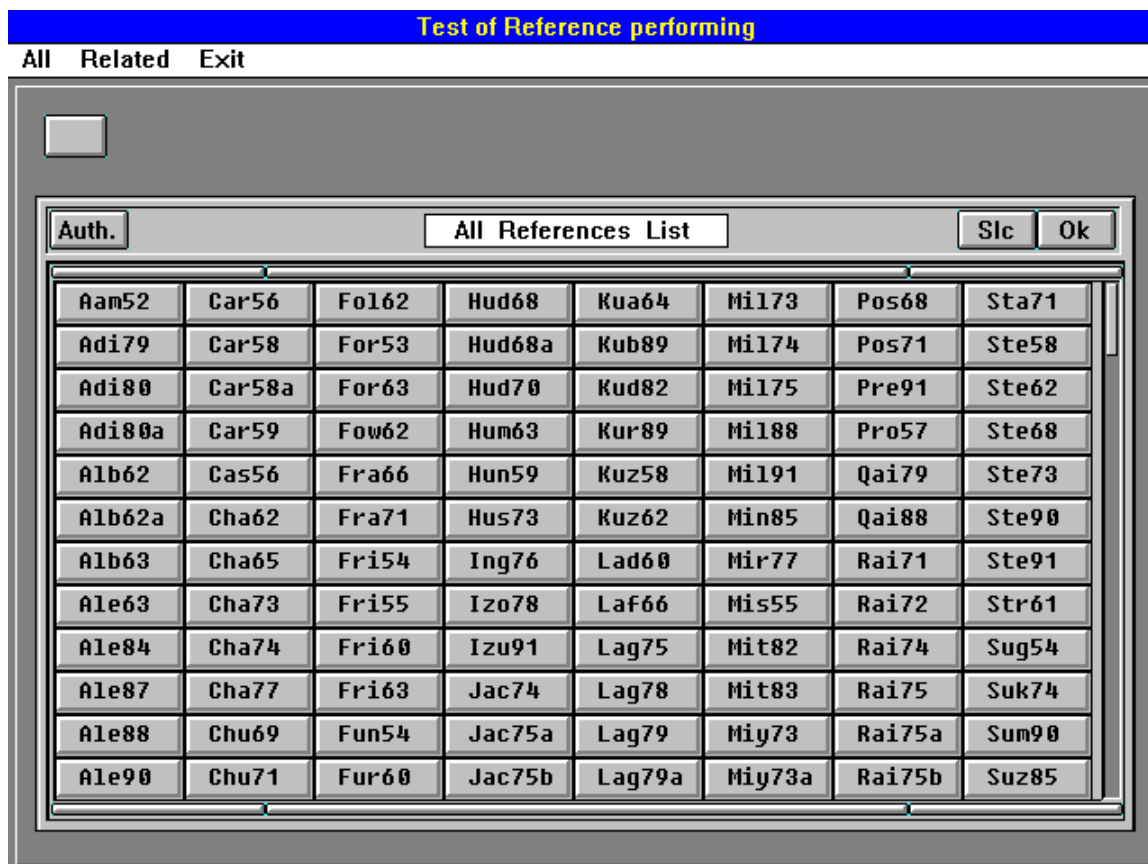
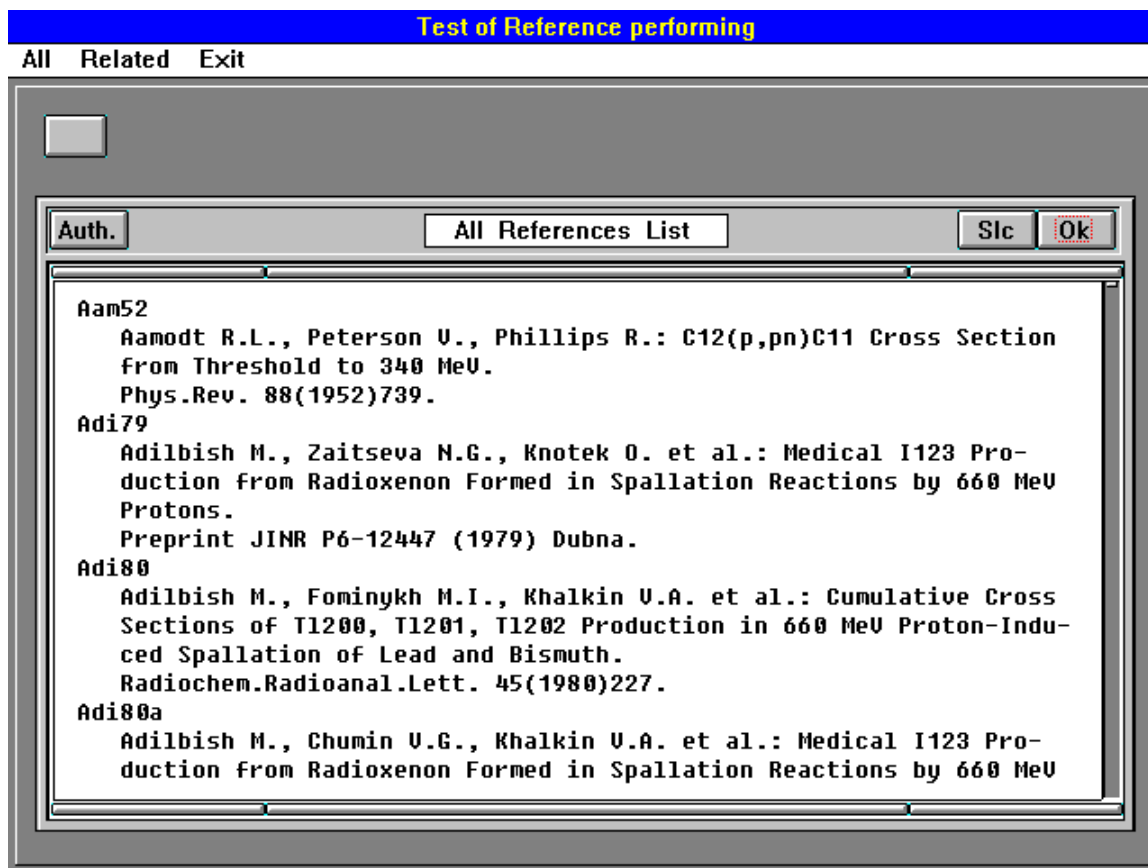


Figure 9



### *Output*

Using the **Output** command from the main menu one can output the desirable information (in the needed format: bitmap, metafile, text) in a file or directly on printer.

### *Reference on isotopes*

The **Isotopes** command from the main menu allows to get an inquiry on any isotope known presently. The stable isotope abundance and radioactive isotope half-decay periods are presented.

After the **Isotopes** command is done the Mendeleev table appears on the screen for selecting the chemical element. One should press the necessary element button. The data on isotopes of selected element appear on panels **Stable** and **Radioactive** (see Figure 10).

Figure 10

Production of Radionuclides at Intermediate Energies											
Projectile Reaction References Output Isotopes Help Exit											
MENDELEEV PERIODICAL SYSTEM OF CHEMICAL ELEMENTS											
Period	Row	Groups of elements									
		I	II	III	IV	V	VI	VII	VIII	0	
1	1	H 1							He 2		
2	2	Li 3	Be 4	B 5	C 6	N 7	O 8	F 9	Ne 10		
3	3	Na 11	Mg 12	Al 13	Si 14	P 15	S 16	Cl 17	Ar 18		
4	4	K 19	Ca 20	Sc 21	Ti 22	V 23	Cr 24	Mn 25	Fe 26	Co 27	Ni 28
	5	Cu 29	Zn 30	Ga 31	Ge 32	As 33	Se 34	Br 35			Kr 36
5	6	Rb 37	Sr 38	Y 39	Zr 40	Nb 41	Mo 42	Tc 43	Ru 44	Rh 45	Pd 46
	7	Ag 47	Cd 48	In 49	Sn 50	Sb 51	Te 52	I 53			Xe 54
6	8	Cs 55	Ba 56	La* 57	Hf 72	Ta 73	W 74	Re 75	Os 76	Ir 77	Pt 78
	9	Au 79	Hg 80	Tl 81	Pb 82	Bi 83	Po 84	At 85			Rn 86
7	10	Fr 87	Ra 88	Ac* 89	Ku104						

Stable (8)		Radioactive (31)		LANTHANIDES						
Sn	%	Sn	t	Ce58	Pr59	Nd60	Pm61	Sm62	Eu63	Gd64
<sup>112</sup> <sub>50</sub> Sn	0.97	<sup>103</sup> <sub>50</sub> Sn	7.0s	Tb65	Dy66	Ho67	Er68	Tm69	Yb70	Lu71
<sup>114</sup> <sub>50</sub> Sn	0.65	<sup>105</sup> <sub>50</sub> Sn	31.0s	ACTINIDES						
<sup>115</sup> <sub>50</sub> Sn	0.36	<sup>106</sup> <sub>50</sub> Sn	2.1m	Th90	Pa91	U 92	Np93	Pu94	Am95	Cm96
				Bk97	Cf98	Es99	Fm100	Md101	No102	Lr103

REFERENCE

- [1] "Production of Radionuclides at Intermediate Energies", ed. H. Schopper. Springer Verlag, Landolt-Bernstein, New Series, Vol. I/13a (1991), I/13b (1992), I/13c (1993), I/13d (1994), I/13e (1994), I/13f (1995), I/13g (1996), I/13h (1996). Berlin, Heidelberg, New York, London, Paris, Tokyo, Hong Kong, Barcelona, Budapest.

# *Dose Conversion Coefficient and Anthropomorphic Phantom*



## **CONVERSION COEFFICIENTS FOR HIGH-ENERGY RADIATION**

**Maurizio Pelliccioni**

Istituto Nazionale di Fisica Nucleare, Italy

### **Abstract**

During the last two years, fluence-to-effective dose conversion coefficients have been evaluated by Monte Carlo simulations with the FLUKA code for various kinds of radiation (photons, electrons, positrons, protons, neutrons, muons). Calculations have been performed for four geometrical conditions of irradiation (AP, PA, LAT, ISO) of an anthropomorphic phantom, placed in a vacuum. The energy range investigated was extended up to 100 GeV for photons, electrons and positrons and up to 10 TeV for protons, neutrons and muons. The calculated results can be used for purposes of radiation protection around high energy accelerators and of dose assessment affecting the aircrew on the long distance flights. The work is still in progress and it is planned to consider further types of particles. A summary of the available results is presented.

## Introduction

For the sake of radiation protection in workplaces around high energy accelerators, a systematic estimate of the conversion coefficients fluence-to-effective dose for various kinds of radiation is in progress. The calculated results can be useful also for other purposes, as for example the assessment of the exposure to cosmic rays of aircraft crews during long distance flights. The energy range of interest in these applications is often beyond the region usually considered in the publications of international bodies (ICRU and ICRP).

## Calculations

Calculations have been carried out by means of the most recent version of the FLUKA code [1], which simulates the development of showers initiated by high energy particles having an energy up to several tens of TeV. Details about the ability of the FLUKA code to simulate electron-photon and hadron transport are discussed elsewhere [2-5].

An hermaphrodite phantom derived from ADAM, the male phantom developed at GSF [6], has been used [7,8]. The female organs were added to the FLUKA version of ADAM, and some other modifications relevant for the evaluation of effective dose have been included (i.e. the specific representation of bone surfaces and red bone marrow) [8]. Internal organs have been considered to be homogenous in composition and density. The composition used for the lungs, bone, red bone marrow, soft tissues and skin were limited to the 14 elements H, C, N, O, Na, Mg, P, S, Cl, K, Ca, Fe, Zr, Pb. The density assumed was  $0.296 \text{ g}\cdot\text{cm}^{-3}$  for the lungs,  $1.486 \text{ g}\cdot\text{cm}^{-3}$  for the bone,  $1.028 \text{ g}\cdot\text{cm}^{-3}$  for red bone marrow,  $0.987 \text{ g}\cdot\text{cm}^{-3}$  for soft tissues,  $1.105 \text{ g}\cdot\text{cm}^{-3}$  for skin. The volumes of the organs were estimated stochastically by FLUKA itself by track-length estimators.

Calculations were performed for whole-body irradiation of the anthropomorphic phantom placed in a vacuum with broad parallel beams and fully isotropic radiation incidence. The directions of incidence of the parallel beams were anterior-posterior (AP), posterior-anterior (PA) and right lateral (LAT). The isotropic irradiation (ISO) was obtained by the use of an inward-directed, biased cosine source on a spherical surface. Monoenergetic particle beams have been considered.

The energy per primary particle deposited in the 68 regions of the hermaphrodite phantom, representing the various organs and tissues of the human body, has been determined by simulations. The organ doses have been calculated as arithmetic mean of the doses received by the single constituent regions, although this simple rule would require some clarification, as claimed in previous papers [8-11].

The effective dose has been evaluated according to the definition given in ICRP Publication 60, as modified in ICRP Publication 69 [13]. The remainder dose has been obtained as arithmetic mean of the single organ doses, although also this rule still requires some clarification [14]. The values of the radiation weighting factors recommended in ICRP Publication 60 [12] have been used. They are shown in Table 1. Notice that all values in Table 1 relate to the radiation incident on the body.

The statistical uncertainties were estimated by making calculations in several batches and computing the standard deviation of the mean. The total number of histories was large enough to keep the standard deviation on the effective doses below few per cent.

**Table 1. Radiation weighting factors recommended in ICRP Publication 60**

Type and energy range	$w_R$
Photons, electrons and muons, all energies	1
Neutrons, energy < 10 keV	5
10 keV to 100 keV	10
> 100 keV to 2 MeV	20
> 2 MeV to 20 MeV	10
> 20 MeV	5
Protons, other than recoil protons, energy > 2 MeV	5
Alpha particles, fission fragments, heavy nuclei	20

Papers showing the results of the calculations partly have been published [8,9,15] and partly are in press [10,11] or in preparation (for muons). This paper is restricted to a graphical presentation of the available results.

Figure 1 shows the conversion coefficients for photons in the energy range 50 keV-100 GeV. The conversion coefficients for ambient dose equivalent and maximum dose equivalent, according to previous calculations [16,17], are also displayed. The recommended operational quantity ambient dose equivalent appears to provide a conservative estimate of the effective dose only up to about 3 MeV.

**Figure 1. Fluence-to-effective dose conversion coefficients ( $\text{Sv}\cdot\text{cm}^2$ ) as a function of photon energy for various geometrical conditions of irradiation. For a comparison, the ambient dose equivalent and the maximum dose equivalent in a ICRU sphere are also shown.**

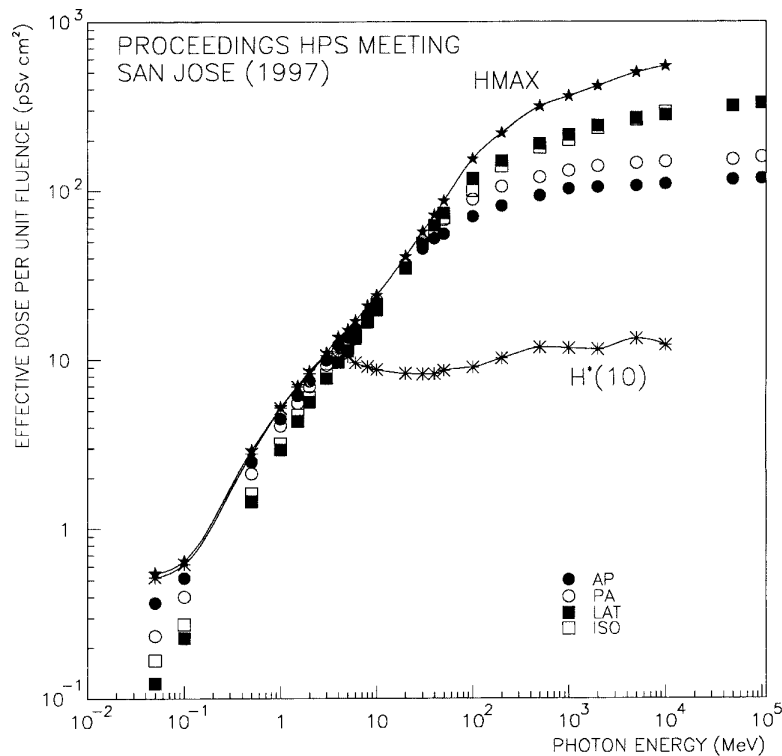


Figure 2 shows the conversion coefficients for electrons in the energy range 5 MeV-100 GeV. For photons, the conversion coefficients for ambient dose equivalent and maximum dose equivalent, according to previous calculations [16,17], are also displayed. The ambient dose equivalent appears to provide a conservative estimate of the effective dose only up to about 30 MeV.

**Figure 2. Fluence-to-effective dose conversion coefficients ( $\text{Sv}\cdot\text{cm}^2$ ) as a function of electron energy for various geometrical conditions of irradiation. For a comparison, the ambient dose equivalent and the maximum dose equivalent in a ICRU sphere are also shown.**

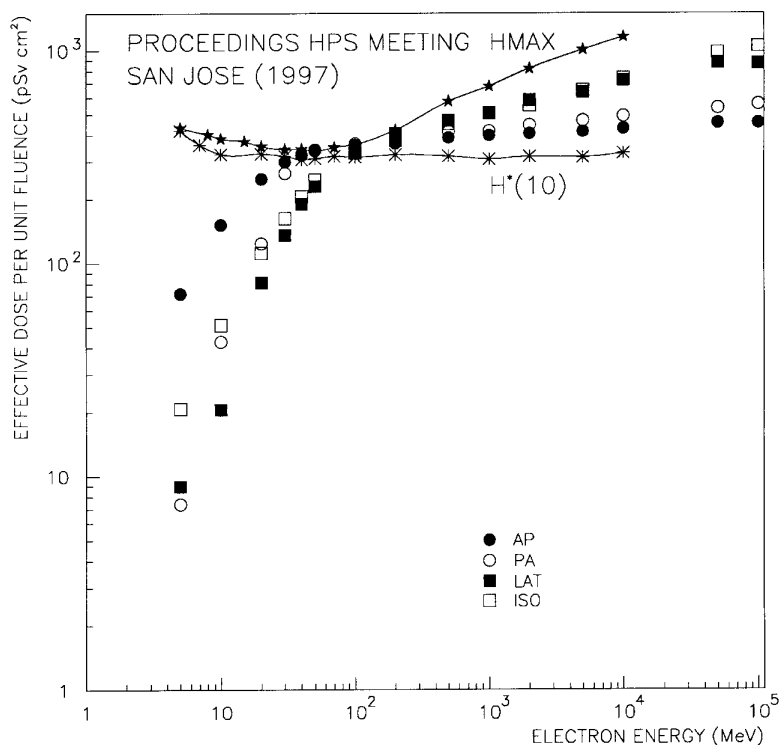


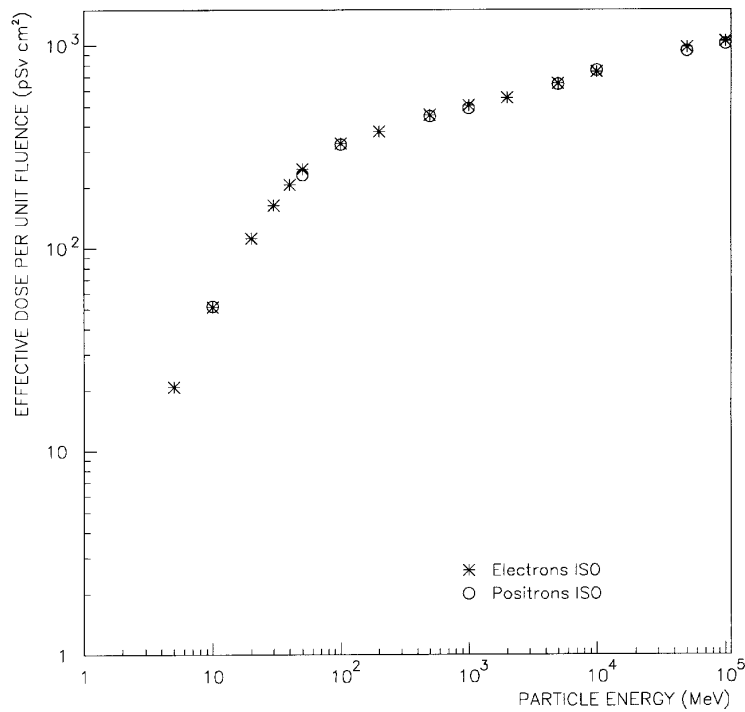
Figure 3 shows a comparison between the conversion coefficients for electrons and positrons in the energy range 5 MeV-100 GeV, for the isotropic irradiation. It is clear from this figure that the same coefficients as those for electrons can be applied in practice for positrons.

Figure 4 shows the conversion coefficients for protons in the energy range 5 MeV-10 TeV [10]. No comparison with operational quantities has been made, because no data on the matter was found in literature. Since no other set of conversion coefficients between a basic field quantity and proton effective dose is known at present, the results here presented close an important data gap.

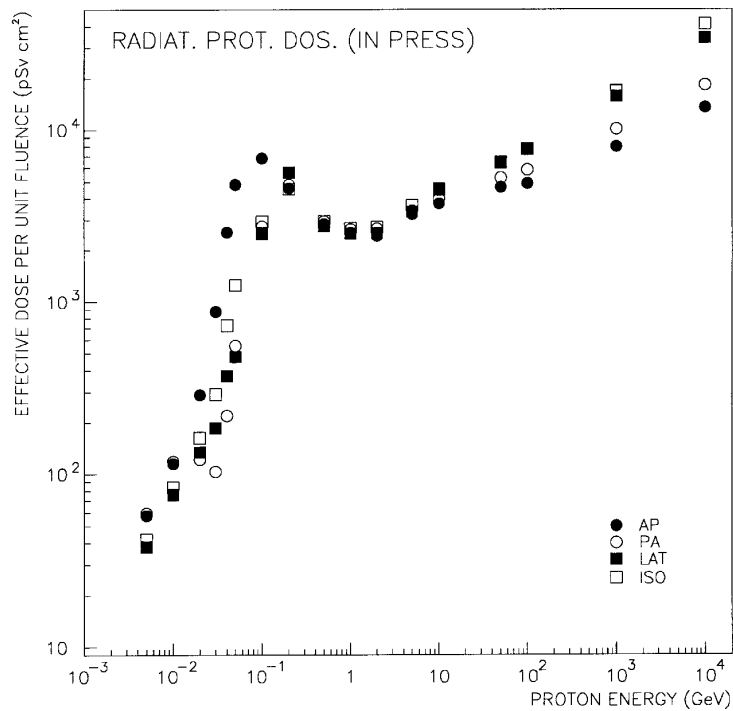
Figure 5 shows the conversion coefficients for neutrons in the energy range 5 MeV-10 TeV [11]. They have been compared with the results of other calculations, when available. In spite of some differences, the agreement was generally satisfactory.

Figure 6 shows a comparison between the present results for neutron effective dose and ambient dose equivalent, according to the calculations of other authors [18,19]. It is evident from Figure 6 that the ambient dose equivalent can not be used as a conservative estimate of the effective dose for neutron radiation over the whole energy range, in contrast to the intention of its introduction.

**Figure 3. Fluence-to-effective dose conversion coefficients ( $\text{Sv}\cdot\text{cm}^2$ ) as a function of electron and positron energy for isotropic irradiation**



**Figure 4. Fluence-to-effective dose conversion coefficients ( $\text{Sv}\cdot\text{cm}^2$ ) as a function of proton energy for various geometrical conditions of irradiation**



**Figure 5. Fluence-to-effective dose conversion coefficients ( $\text{Sv}\cdot\text{cm}^2$ ) as a function of neutron energy for various geometrical conditions of irradiation**

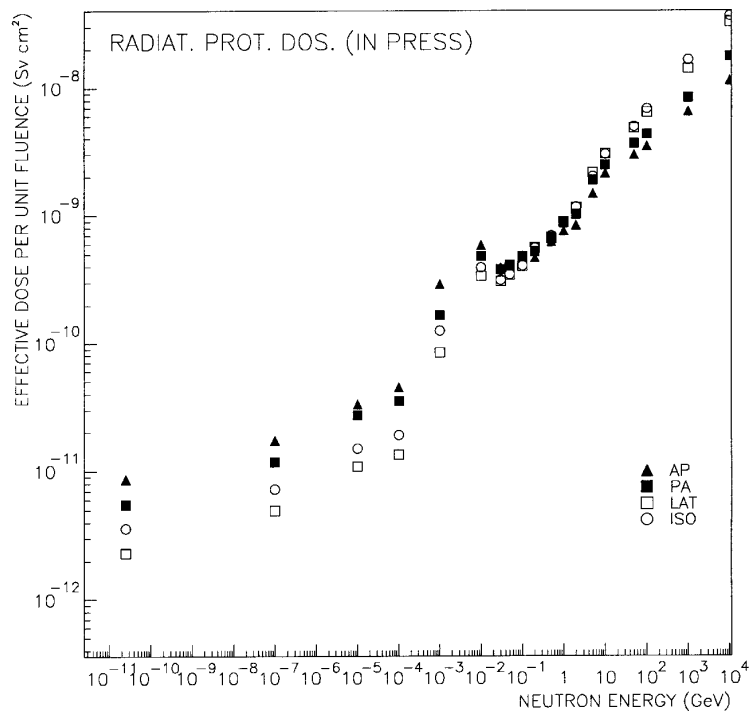


**Figure 6. A comparison between effective dose and ambient dose equivalent for neutrons**

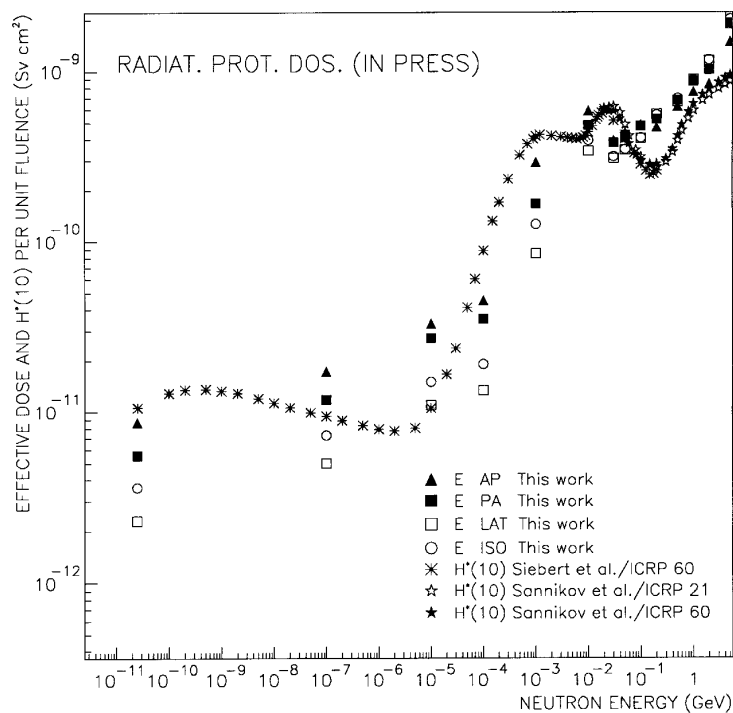
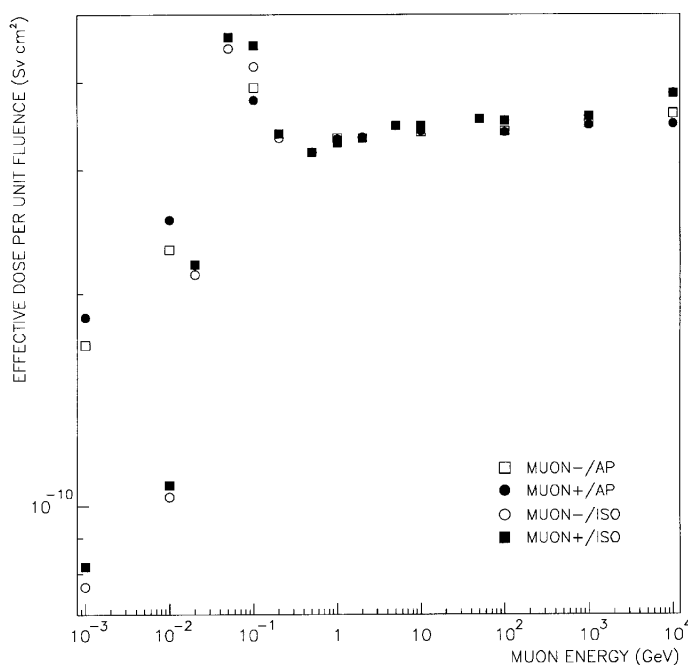


Figure 7, for AP and ISO irradiation, and Figure 8, for PA and LAT irradiation, show the conversion coefficients for positive and negative muons in the energy range 1 MeV-10 TeV. No comparison with operational quantities has been made, since no data on the matter was found in literature. Differences between the values for negative and positive muons can be observed at energies lower than about 100 MeV. The largest effective doses for muons positively charged are due to the largest values of the energy deposited by electron-photon cascade induced by positrons which arise from positive muon decay, with respect to the electron-photon cascade induced by electrons coming from negative muon decay. The contribution of the neutrons produced by muons negatively charged is practically insignificant in terms of organ doses. For energies greater than 100 MeV, the effective doses have resulted practically comparable for all the geometrical conditions of irradiation considered here.

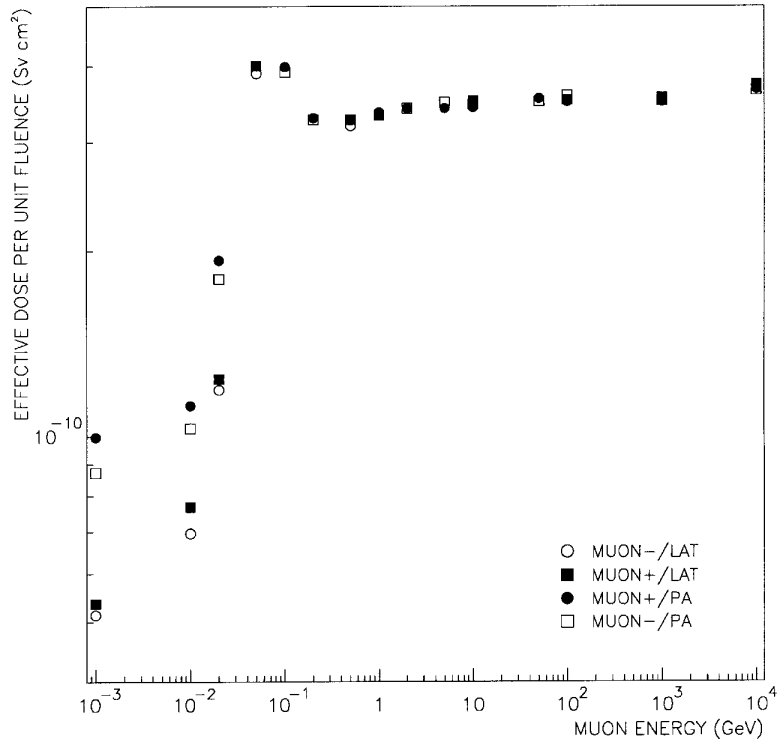
## Conclusions

The objective of this paper is to provide information to the accelerator specialists on the conversion coefficients from particle fluence to effective dose for use in high energy external dosimetry. The data presented here for photons, electrons, positrons, protons, neutrons and muons, in a very extended energy range and for four different irradiation geometries, cover most of practical applications. For all kinds of radiation considered, generally the AP incidence has the maximum effective dose at lowest energies, the upper edge depending on the type of concerned radiation, while lateral and isotropic incidence lead to the highest values of the effective dose at very high energies. A detailed discussion of this aspect can be found in the papers dedicated to the matter [8-11]. Data for pions are still lacking. Calculations for these particles are just now in progress and the results will be made available as soon as possible.

**Figure 7. Fluence-to-effective dose conversion coefficients ( $\text{Sv}\cdot\text{cm}^2$ ) as a function of muon energy for AP and ISO irradiation**



**Figure 8. Fluence-to-effective dose conversion coefficients ( $\text{Sv}\cdot\text{cm}^2$ ) as a function of muon energy for PA and LAT irradiation**



## REFERENCES

- [1] A. Fassò, A. Ferrari, J. Ranft and P.R. Sala, "An Update about FLUKA", Proceedings of the Second Workshop on Simulating Accelerator Radiation Environments, CERN 8-11 Oct. 1995, pp. 158-170 (1997).
- [2] A. Ferrari, P.R. Sala, G. Guaraldi and F. Padoani, "An Improved Multiple Scattering Model for Charged Particle Transport", *Nucl. Instr. Meth.*, B71 (1992) 412.
- [3] A. Fassò, A. Ferrari, J. Ranft and P.R. Sala, "FLUKA: Present Status and Future Developments", In: Proc. IV Intl. Conf. on Calorimetry in High-Energy Physics, La Biodola, 21-26 September 1993 (Word Scientific, ed.) p. 493 (1994).
- [4] P.A. Aarnio, A. Fassò, A. Ferrari, J.H. Möhring, J. Ranft, P.R. Sala, G.R. Stevenson and J.M. Zazula, "Electron-Photon Transport: Always so Good as We Think? Experience with FLUKA", In: Proc. MC93 Intl. Conf. on Monte Carlo Simulation in High-Energy and Nuclear Physics, Tallahassee, 22-26 September 1993 (Word Scientific, ed.) p. 100 (1994).
- [5] A. Fassò, A. Ferrari, J. Ranft and P.R. Sala, "FLUKA, Performances and Applications in the Intermediate Energy Range", Proceedings of the Specialists Meeting on Shielding Aspects of Accelerators, Targets and Irradiation Facilities, Arlington, 28-29 April 1994, published by OECD/NEA, p. 287 (1995).
- [6] R. Kramer, M. Zankl, G. Williams and G. Drexler, "The Calculation of Dose from External Photon Exposures Using Reference Human Phantoms and Monte Carlo Methods. Part I: The Male (Adam) and Female (Eva) Adult Mathematical Phantoms", Neuherberg: GSF-Forschungszentrum für Umwelt und Gesundheit, GSF-Bericht S-885, (1982).
- [7] M. Pelliccioni and M. Pillon, "Comparison between Anthropomorphic Mathematical Phantoms Using MCNP and FLUKA Codes", *Radiat. Prot. Dos.*, 67 pp. 253-256 (1996).
- [8] A. Ferrari, M. Pelliccioni and M. Pillon, "Fluence to Effective Dose and Effective Dose Equivalent Conversion Coefficients for Photons from 50 keV to 10 GeV", *Radiat. Prot. Dos.*, 67, pp. 245-251 (1996).
- [9] A. Ferrari, M. Pelliccioni and M. Pillon, "Fluence to Effective Dose and Effective Dose Equivalent Conversion Coefficients for Electrons from 5 MeV to 10 GeV", *Radiat. Prot. Dos.*, 62 (9), pp. 97-104 (1997).
- [10] A. Ferrari, M. Pelliccioni and M. Pillon, "Fluence to Effective Dose and Effective Dose Equivalent Conversion Coefficients for Protons from 5 MeV to 10 TeV", *Radiat. Prot. Dos.* (in press).

- [11] A. Ferrari, M. Pelliccioni and M. Pillon, “Fluence to Effective Dose Conversion Coefficients for Neutrons up to 10 TeV”, *Radiat. Prot. Dos.* (in press).
- [12] International Commission on Radiological Protection, 1990 Recommendations of the International Commission on Radiological Protection, ICRP Publication 60, *Annals of ICRP*, 21 (1-3) (1991).
- [13] International Commission on Radiological Protection, Age-Dependent Doses to Members of the Public from Intake of Radionuclides: Part 3 Ingestion Dose Coefficients, ICRP Publication 69, *Annals of ICRP*, 25 (1) (1995).
- [14] M. Zankl and G. Drexler, “An Analysis of the Equivalent Dose Calculation for the Remainder Tissues”, *Health Physics*, 69, pp. 346-355 (1995).
- [15] A. Ferrari, M. Pelliccioni and M. Pillon, “High-Energy Electron and Photon Dosimetry”, *Health Physics of Radiation Generating Machines, Proceedings of the 30th Midyear Topical Meeting of the Health Physics Society, 5-8 January 1997, S. Jose, California (USA)*, pp. 151-181 (1997).
- [16] A. Ferrari and M. Pelliccioni, “On the Conversion Coefficients from Fluence to Ambient Dose Equivalent”, *Radiat. Prot. Dosim.*, 51 (4), pp. 331-335 (1994).
- [17] A. Ferrari and M. Pelliccioni, “Fluence-to-Dose Equivalent Conversion Coefficients for Electrons and Photons of Energy up to 10 GeV”, In: *Proceedings 8th International Conference on Radiation Shielding, Arlington, 24-28 April 1994*, 2, pp. 893-899 (1994).
- [18] B.R.L. Siebert and H. Schuhmaker, “Quality Factors, Ambient and Personal Dose Equivalent for Neutrons, Based on the New ICRU Stopping Power Data for Protons and Alpha Particles”, *Radiat. Prot. Dos.*, 58, pp. 177-183 (1995).
- [19] A.V. Sannikov and E.N. Savitskaya, “Ambient Dose Equivalent Conversion Factors for High Energy Neutrons Based on the New ICRP Recommendations”, *IHEP 95-98, Protvino* (1995).

**OVERVIEW OF FLUENCE TO DOSE EQUIVALENT CONVERSION COEFFICIENTS  
FOR HIGH-ENERGY RADIATIONS – CALCULATIONAL METHODS AND RESULTS OF  
EFFECTIVE DOSE EQUIVALENT AND EFFECTIVE DOSE PER UNIT PARTICLE FLUENCE**

**Satoshi Iwai, Takashi Uehara**  
Mitsubishi Heavy Industries, Japan

**Osamu Sato, Nobuaki Yoshizawa, Shiori Furihata, Shunji Takagi**  
Mitsubishi Research Institute, Japan

**Shun-ichi Tanaka**  
Japan Atomic Research Institute  
Office of Planning, Japan

**Yukio Sakamoto**  
Japan Atomic Research Institute  
Applied Radiation Lab. Dept. of Reactor Engineering, Japan

**Abstract**

In and around high energy accelerator facilities, high energy radiation dose estimation is important for the radiation protection of workers. The contribution of high energy protons and neutrons to the radiation exposure of astronauts can also not be disregarded inside a spacecraft. This report provides an overview of calculational methodologies and estimated results of effective doses and effective dose equivalents for high energy radiations such as photons, neutrons, protons, and electrons in several groups. These data will be helpful to establish an authoritative dose equivalent conversion coefficients for high energy radiations.

## Introduction

Due to the increase of high energy accelerator facilities and space missions, high energy radiation has come to be an important issue. Effective dose or effective dose equivalents are adequate radiological protection quantities to evaluate radiation risk of individuals, exposed to radiations not only of low and intermediate energy but also of high energy.

This work summarises the comparisons of calculational methodologies and results of dose conversion coefficients of effective dose and effective dose equivalents for high energy neutrons, photons, protons, and electrons up to maximum 10 GeV.

## Definitions of effective dose and effective dose equivalent

The ICRP26 [1] introduced the averaged organ dose equivalent  $\hat{H}_T$  expanded from the dose equivalent at a point in organ or tissue T. By use of  $\hat{H}_T$  this publication defined the effective dose equivalent  $H_E$  which is the weighted sum of the dose equivalents of six specified organs and a remainder consisting of five organs at most:

$$H_E = \sum_T W_{T,26} \hat{H}_T \quad (1)$$

where  $W_{T,26}$  is the tissue weighting factor specified in the ICRP26.

In 1990, the ICRP60 [2] recommended new quantities used for radiological protection: equivalent dose  $H_T$  is defined as the average organ-absorbed-dose multiplied by a radiation weighting factor  $W_R$ ; the ICRP recommended weighting factors in place of effective quality factor Q because of the uncertainties in the radio-biological information for the high LET part of the Q-L relationship specified in the ICRP60. Although the radiation weighting factors are presented in the ICRP60, the theoretical background on the derivation of the factors is not explained in this publication.

The effective dose E is defined as the weighted sum of the equivalent dose of twelve specified organs and a remainder consisting of ten organs additionally specified in the ICRP60 (the equivalent dose to the colon  $H_{\text{colon}}$  is given as:  $H_{\text{colon}}=0.57H_{\text{ULI}}+0.47H_{\text{LLI}}$ , where  $H_{\text{ULI}}$  and  $H_{\text{LLI}}$  are the equivalent doses to the ULI (upper large intestine) and the LLI (lower large intestine), according to the ICRP67 [3]).

$$E = \sum_T W_{T,60} H_T \quad (2)$$

where  $W_{T,60}$  is the appropriate tissue weighting factor shown in the ICRP60.

In 1993, the ICRU51 [4] redefined the effective dose equivalent  $H_E$  by use of Eq. (3) according to the consistency to the ICRP26, ICRP60, and ICRP67 [3].

$$H_E = \sum_T W_{T,60} D_T Q_T = \sum_T W_{T,60} \hat{H}_T \quad (3)$$

where  $D_T$  and  $Q_T$  are the mean absorbed dose and the mean quality factor in a specified tissue (or organ) T, respectively. In Eq. (3)  $Q_T$  is defined as follows:

$$Q_T = \frac{1}{m_T D_T} \int \int_{m_T L} Q(L) \bullet D(L) dL dm \quad (4)$$

where  $Q_T$  is the mass of the tissue or organ T,  $D(L)$  denotes an absorbed dose distribution in the tissue (or organ) T as a function of L, and  $Q(L)$  denotes the Q-L relationship of ICRP60.  $\hat{H}_T$  is the averaged dose equivalent in the tissue (or organ) T. This paper employs the definition of Eq. (3) as the term of “effective dose equivalent,  $H_E$ ”. “Effective dose equivalent,  $H_E$ ” of Eq. (1) defined in the ICRP26 is denoted by  $H_{E,26}$  in this paper.

### **Calculational methodologies and conditions for effective dose and effective dose equivalent**

This section provides methodologies and conditions calculating conversion coefficients from unit fluence to effective dose, E, and effective dose equivalent,  $H_E$ . Table 1 summarises the radiological protection quantities, emitted particles, energy ranges,  $Q(L)$  data, physical databases, application of kerma factors, anthropomorphic phantoms, and irradiation geometries used for the calculation of these dose conversion coefficients in each group of authors. The purpose of this report is an overview of conversion coefficients of fluence to effective dose and effective dose equivalent base on the most recent concept and data in the ICRP60,67 and the ICRU51. Therefore in this table, data corresponding to effective dose, E, and effective dose equivalent,  $H_E$  (based on the ICRP60, not on the ICRP26) are presented except the reference data such as  $H_{E,26}$  of Ferrari *et al.* [28,29] and ambient dose equivalent of Sanikov *et al.* [31]. Conversion coefficients of ambient dose equivalent,  $H_{E,26}$ , and ICRU sphere depth dose calculated in each group are eliminated in principle, because these data are out of scope in this report.

### **Comparison of estimates of effective dose and effective dose equivalent per unit fluence calculated in each group**

#### ***Conversion coefficients for neutrons***

Figure 1 shows the comparison of estimates of E calculated by three groups, for AP geometry with the reference of  $h^*(10)$  calculated by Sanikov *et al.* [31]. Estimates E values are fairly in good agreement in spite of several kinds of differences in computer codes, physical databases, and anthropomorphic phantom geometries. The quantity of  $h^*(10)$  dose not show conservative values above 50 MeV.

Figure 2 provides the comparisons of estimates of  $H_E$  calculated by the three groups. The values of  $h^*(10)$  are shown for reference. There is good agreement between the data of Nabelssi *et al.* [5,6] and our data [17]. Our data are shown in the tables and figures in Appendix A. The estimates of Mares *et al.* [9] show 20% larger values than the former two kinds of data [5,6,17], especially at 100 MeV. For a detailed analysis of the difference, comparison of organ doses will be required in the three groups. The  $h^*(10)$  of Sannikov *et al.* shows a fairly good agreement with the  $H_E$  for PA geometry of [17] above 50 MeV. But the  $h^*(10)$  is also a little lower than the estimates of  $H_E$  within the difference of 5%. The  $h^*(10)$  shows maximum two times smaller values than E above the energy of 50 MeV.

### ***Conversion coefficients for photons***

The comparison of estimates of E calculated by two groups are shown for AP geometry in Figure 3, for PA geometry in Figure 4, for LAT geometry in Figure 5, and for ISO geometry in Figure 6. These data are in good agreement except some data within maximum 20% difference. The analysis of these differences are discussed in [28].

### ***Conversion coefficients for protons***

High energy protons inside space shuttles are estimated up to about 80% of astronauts' whole body dose equivalent. Nevertheless proton dose conversion coefficient of fluence to E and  $H_E$  are not shown in any document. The ICRP51 [31] provides the maximum dose equivalent and 10 mm depth dose equivalent in 30 cm thick semi-infinite slab phantom for proton incidence up to 10 GeV.

The dose conversion coefficients from proton fluence to E and  $H_E$  were calculated from the energy range of 20 MeV to 10 GeV, by use of the same computer code system and the same databases to those of high energy neutrons employed in [16]. These data are shown in Appendix B.

Figure 7 represents the comparisons of E for AP and PA irradiation geometries and the maximum dose equivalent and 10 mm depth dose equivalent shown in the ICRP51. The estimates E of the present work shows larger values than the maximum dose equivalent of the ICRP51 in the energy range from 20 MeV to 5 GeV.

Figure 8 shows the comparisons of  $H_E$  for AP and PA irradiation and the maximum dose equivalent and 10 mm depth dose equivalent in the ICRP51. The estimates of  $H_E$  of the present work shows fairly good agreement with the 10 mm depth dose above 200 MeV.

### **Summary**

- Comprehensive comparisons were performed for methodologies and conditions adopted in the four different groups calculating dose conversion coefficients from fluence to effective dose, E, and effective dose equivalent,  $H_E$  of high energy neutrons, photons, protons and electrons.
- Comparisons of high energy neutron conversion coefficients of E and  $H_E$  were performed in the three groups. The estimates of E in the three group show fairly good agreement. The estimates of  $H_E$  agree within the difference of 20% without some exceptions.
- Ambient dose equivalent  $h^*(10)$  of high energy neutron shows maximum two times lower values than E above 50 MeV. The quantity of  $h^*(10)$  agrees well with  $H_E$  within the difference of 5%, especially for PA irradiation geometry above the energy range of 50 MeV.
- Comparisons were performed for the dose conversion coefficients of high energy photons calculated in the two groups. These data agree well within the maximum of 20% for the irradiation geometries of AP, PA, LAT, and ISO conditions.
- Conversion coefficients of E and  $H_E$  for high energy protons were calculated from 20 MeV to 10 GeV. These data were compared with the maximum dose equivalent and 10 mm depth dose equivalent in the ICRP51.

## REFERENCES

- [1] ICRP Publication 26, "Recommendations of the ICRP", Annals of the ICRP1 (3) (1977), Reprinted (with additions) in 1987, Superseded by ICRP Publication 60.
- [2] ICRP Publication 60, "Recommendations of the International Commission on Radiological Protection", Annals of the ICRP21 (1-3) (1991).
- [3] ICRP Publication 67, "Age-Dependent Doses to Members of the Public from Intake of Radionuclides: Part 2, Ingestion Dose Coefficients", Annals of the ICRP23 (3/4) (1993).
- [4] ICRU Publication 51, "Quantities and Units in Radiation Protection Dosimetry", International Commission on Radiation Units and Measurements (1993).
- [5] B.K. Nabelssi and N.E. Hertel, "Ambient Dose Equivalents, Effective Dose Equivalents, and Effective Doses for Neutrons from 10 to 20 MeV", *Radiat. Prot. Dosim.*, 48 (1993) 153.
- [6] B.K. Nabelssi and N.E. Hertel, "Effective Dose Equivalents and Effective Doses for Neutrons from 30 to 180 MeV", *Radiat. Prot. Dosim.*, 48 (1993) 227.
- [7] R.E. Prael and H. Lichtenstein, "User Guide to LCS: The LAHET Code System. Radiation Transport Group", LA-UR-89-3014 (Los Alamos National Laboratory) (1989).
- [8] R.D. Stewart, J.E. Tanner and J.A. Lenowich, "An Extended Tabulation of Effective Dose Equivalent from Neutrons Incident on a Male Anthropomorphic Phantom", accepted for publication in *Health Phys.* (1993).
- [9] V. Mares, G. Leuthold and H. Schraube, "Organ Doses and Dose Equivalents for Neutrons Above 20 MeV", *Radiat. Prot. Dosim.*, 70 (1997) 391
- [10] J.F. Briesmeister, ed., MCNP - A General Monte Carlo N-Particle Transport Code, Version 4A, LA-12625-M (Los Alamos).
- [11] P.G. Young, *et al.* "Transport Data Libraries for Incident Proton and Neutron Energies to 100 MeV", LANL Report LA 11753-MS (Los Alamos) (1990).
- [12] J.S. Hendricks, S.C. Frankle, and J.D. Court, "ENDF/B-VI Data for MCNP", LANL Report LA-12891 (Los Alamos) (1994).
- [13] J.H. Hubbell, W.J. Veigele, E.A. Briggs, R.T. Brown, D.T. Cramer, and R.J. Howerton, "Atomic Form Factor Incoherent Scattering Functions and Photon Scattering Cross Sections", *J. Phys. Chem.*, Ref. Data 4 (1975) 471

- [14] R. Kramer, M. Zankl, G. Williams, and G. Drexler, "The Calculation of Dose from External Photon Exposures Using Reference Human Phantoms and Monte Carlo Methods, Part 1: The Male (Adam) and Female (Eva) Adult Mathematical Phantoms", GSF-Bericht S-885 (1982).
- [15] M. Zankl, N. Petoussi, and G. Drexler, "Effective Dose and Effective Dose Equivalent - The Impact of the New ICRP Definition for External Photon Irradiation", *Health Phys.*, 62 (1992) 395.
- [16] S. Iwai, T. Uehara, O. Sata, N. Yoshizawa, S. Furihata, S. Takagi, S. Tanaka, and Y. Sakamoto, "Evaluation Fluence to Dose Equivalent Conversion Coefficients for Energy Neutrons - Calculation of Effective Dose Equivalents and Effective Dose", In: Proc. 2nd Specialists Meeting on Shielding Aspects of Accelerators, Targets and Irradiation Facilities (SATIF2), CERN, Geneva 12-13 October 1995.
- [17] S. Iwai *et al.* (Appendixes A and B of this report) (SATIF3), Sendai, 12-13 May 1997.
- [18] O. Sata, S. Iwai, S. Tanaka, T. Uehara, Y. Sakamoto, N. Yoshizawa, and S. Furihata, "Calculations of Equivalent Dose and Effective Dose Conversion Coefficients for Photons from 1 MeV to 10 GeV", *Radiat. Prot. Dosim.*, 62 (1997) 119.
- [19] N. Yoshizawa, K. Ishibashi, and H. Takada, *J. Nucl. Sci. and Technol.*, 32 (1995) 601.
- [20] P. Cloth, D. Filges, R.D. Neef, G. Sterzenbach, Ch. Ruel, T.W. Armstrong, B.L. Colbom, B. Anders, and H. Bruckman, "HERMES: A Monte Carlo Program for Beam-Materials Interaction Studies", KFA-IRE-EAN 12/88 (1988).
- [21] K. Shibata, T. Nakagawa, T. Asami, T. Fukahori, T. Narita, S. Chiba, M. Mizumoto, A. Hasegawa, Y. Kikuchi, Y. Nakajima and S. Igarashi, "Japanese Evaluated Nuclear Data Library, Version-3, JENDL-3", JAERI 1319 (1990).
- [22] W.R. Nelson, H. Hirayama and D.W.O. Rogers: "The EGS4 Code System", Stanford Linear Accelerator Center Report SLAC-265 (Stanford Calif.) (1985).
- [23] D.K. Trubey, M.J. Berger and J.H. Hubbell: "Photon Cross-Section for ENDF/B-VI", Advanced in Nuclear Computation and Radiation Shielding, American Nuclear Society Topical Meeting (1989).
- [24] ICRU: "Stopping Powers for Electrons and Positrons", Report 37, Bethesda MD (1984).
- [25] M. Cristy and K.F. Eckerman: Specific Absorbed Fractions of Energy at Various Ages from Internal Photon Sources", ORNAL-TM-8381/V1-V7 (1987).
- [26] Y. Yamaguchi, "DEEP Code to Calculated Dose Equivalents in Human Phantom for External Photon Exposure by Monte Carlo", JAERI-M 90-235 (1990).
- [27] C.A. Lewis and R.E. Ellis, "Additions to the Snyder Mathematical Phantom", *Phys. Med. Biol.*, 24 (1979) 1019.

- [28] A. Ferrari, M. Pelliccioni, and M. Pillon, "Fluence to Effective Dose and Effective Dose Equivalent Conversion Coefficients for Photons from 50 keV to 10 GeV", *Radiat. Prot. Dosim.*, 67 (1996) 245.
- [29] A. Ferrari, M. Pelliccioni, and M. Pillon, "Fluence to Effective Dose and Effective Dose Equivalent Conversion Coefficients for Electrons from 5 MeV to 10 GeV", *Radiat. Prot. Dosim.*, 69 (1997) 97.
- [30] A. Fassò, A. Ferrari, J. Ranft, and P.R. Sala, "An Update about FLUKA. In: Proc. Second Workshop on Simulating Accelerator Radiation Environments", CERN, 8-11 October 1995.
- [31] A.V. Sanikov and E.N. Savitskaya, "Ambient Dose Equivalent Conversion Factor for High Energy Neutrons Based on the ICRP60 Recommendations", *Radiat. Prot. Dosim.*, 70 (1997) 386.
- [32] V.T. Golovachik, V.N. Kustarjov, E.N. Savitskaya and A.V. Sannikov, "Absorbed Dose and Dose Equivalent Depth Distributions for Protons with Energies from 2 to 600 MeV", *Radiat. Prot. Dosim.*, 28 (1989) 189.
- [33] E.N. Savitskaya and A.V. Sannikov, "High Energy Neutron and Proton Kerma Factors for Different Elements", *Radiat. Prot. Dosim.*, 60 (1995) 135.
- [34] ICRP Publication 51, "Data for Use in Protection Against External Radiation", Annals of the ICRP17 (2/3) (1987).

**Table 1. Summary of calculational methodologies and conditions of conversion coefficients**

Group	Contributors	Particles (energy range)	Calculated dose equivalent
The University of Texas at Austin	B.K. Nabelssi N.E. Hertel	Neutron [5,6] (10 MeV-180 MeV)	(1) Effective dose (E) (2) Effective dose equivalent ( $H_E$ ) ( $Q(L)$ , $W_T$ :ICRP60)
GSF	V. Mares G. Leuthold H. Schraube	Neutron [9] (20 MeV-100 MeV)	(1) Effective dose (E) (2) Effective dose equivalent ( $H_E$ ) ( $Q(L)$ , $W_T$ :ICRP60)
Mitsubishi and JAERI	S. Iwai, T. Uehara O. Sato, N. Yoshizawa S. Furihata, S. Takagi S. Tanaka, Y. Sakamoto	Neutron[16,17], Proton [17] (20 MeV - 10 GeV) Photon [18] (1 MeV - 10 GeV)	(1) Effective dose (E) (2) Effective dose equivalent ( $H_E$ ) ( $Q(L)$ , $W_T$ :ICRP60)
INFN and EURATOM-ENEA	A. Ferrari M. Pelliccioni M. Pillon	Photon [28] (50 keV - 10 GeV) Electron [29] (5 MeV - 10 GeV)	(1) Effective dose (E) (2) Effective dose equivalent ( $H_{E,26}$ ) <sup>†</sup> ( $Q(L)$ , $W_T$ :ICRP60)
IHEP	A.V. Sanikov E.N. Savitskaya V.T. Golovachik V.N. Kustarjov	Neutron [31] (20 MeV-5 GeV)	Ambient Dose Equivalent ( $h^*(10)$ ) <sup>†</sup> ( $Q(L)$ :ICRP60)

<sup>†</sup> Reference data

**Table 2. Summary of calculational methodologies and conditions of conversion coefficients**

Group	Application of $Q(L)$ for calculating	Application of Kerma factor
The University of Texas at Austin	p, d, t, $^3\text{He}$ , $\alpha$ - $Q(L)$ of ICRP60 recoil nuclei ( $A>4$ )- $Q(L)=20$	Below 20 MeV (neutron)
GSF	$q^*(10)$ is used as <u>neutron quality factor</u> ( $q^*(10)=H^*(10)/D^*(10)$ at 10 mm depth in ICRU sphere)	Below 100 MeV (neutron) (all energy range)
Mitsubishi & JAERI	$Q(L)$ of ICRP60 for all charged particles	Below 15 MeV (proton)
INFN & EURATOM-ENEA	$Q(L) = 1$ $W_R = 1$ } for photon, electron and positron	
IHEP	$Q(L)$ of ICRP60 for all charged particles	

**Table 3. Summary of calculational methodologies and conditions of conversion coefficients**

Group	Computer code and data library			Phantom	Irradiation geometries
The University of Texas at Austin	Above 20 MeV neutron LAHET [7]	HMCNP [7] ( ENDF/B-V - n DLC-7E - $\gamma$ )		Modified PNL phantom (male, female) [8]	AP, PA R-LAT (L-LAT) ROT
GSF	MCNP [10] ( LA100 [11] ENDF/B-VI [12] extrapolation } <sup>n</sup> Hubbell's data [13] ————— $\gamma$ )			ADAM phantom (male) [14,15]	AP, Different angle of incidence (15°, 30°, 45°, 60, 75°)
Mitsubishi & JAERI	Above 15 MeV neutron Modified HERMES (HETC-3STEP [19])	Below 15 MeV neutron MORSE-CG/KFA [20] (JENDL-3.1 [21]) (PHOTX [23])	photon EGS4 [32] (PHOTX, ICRU37[24])	Modified Christy adult Phantom (hermaphrodite)	AP, PA ( R - LAT L - LAT ISO )
INFN & EURATOM-ENEA	FLUKA [30]			Modified ADAM phantom (hermaphrodite) [14,15]	AP, PA R-LAT ISO
IHEP	HADRON [32,33]			ICRU sphere	Parallel incidence

**Figure 1. Comparison of effective dose E for AP and PA irradiation neutron beam (the error bars are within circles)**

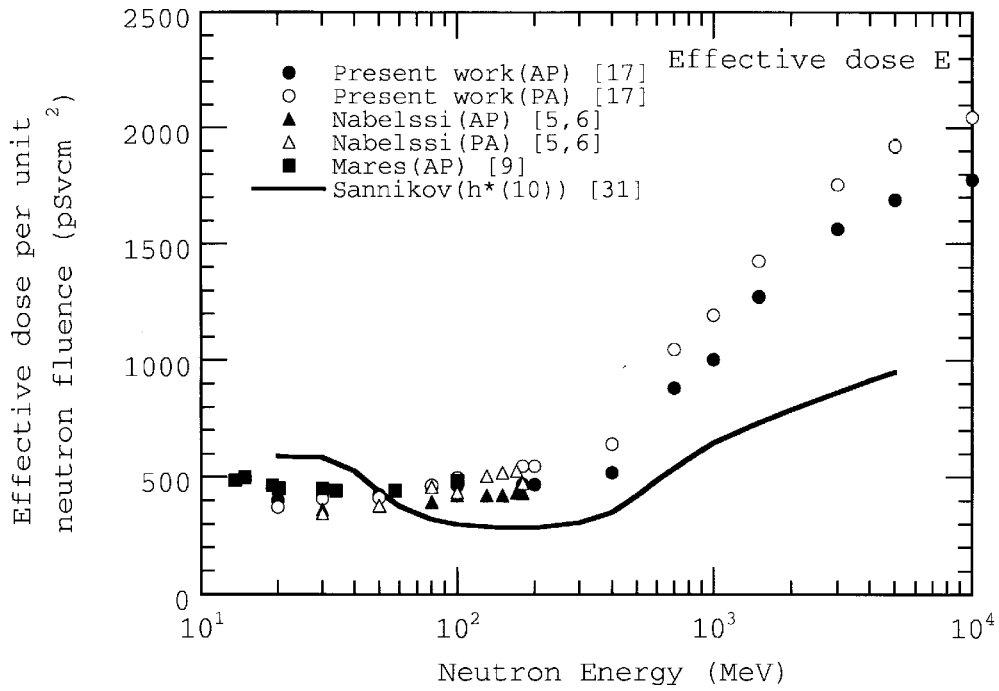


**Figure 2. Comparison of effective dose equivalent H<sub>E</sub> for AP and PA irradiation neutron beam (the error bars are within circles)**

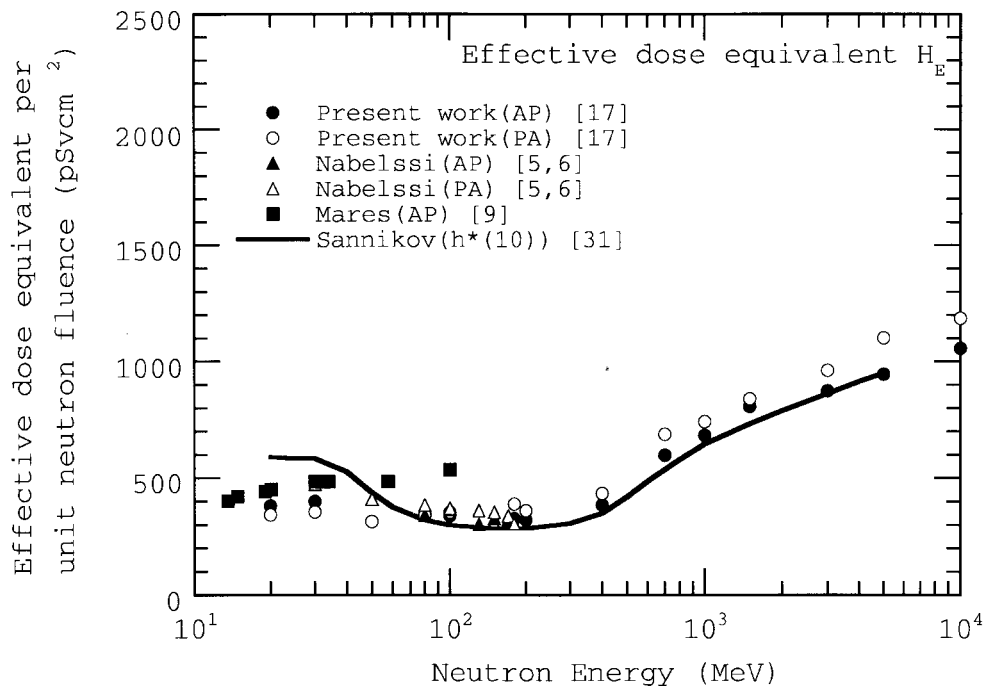


**Figure 3. Comparison of effective dose E for AP irradiation photon beam (the error bars represent Monte Carlo calculation error)**

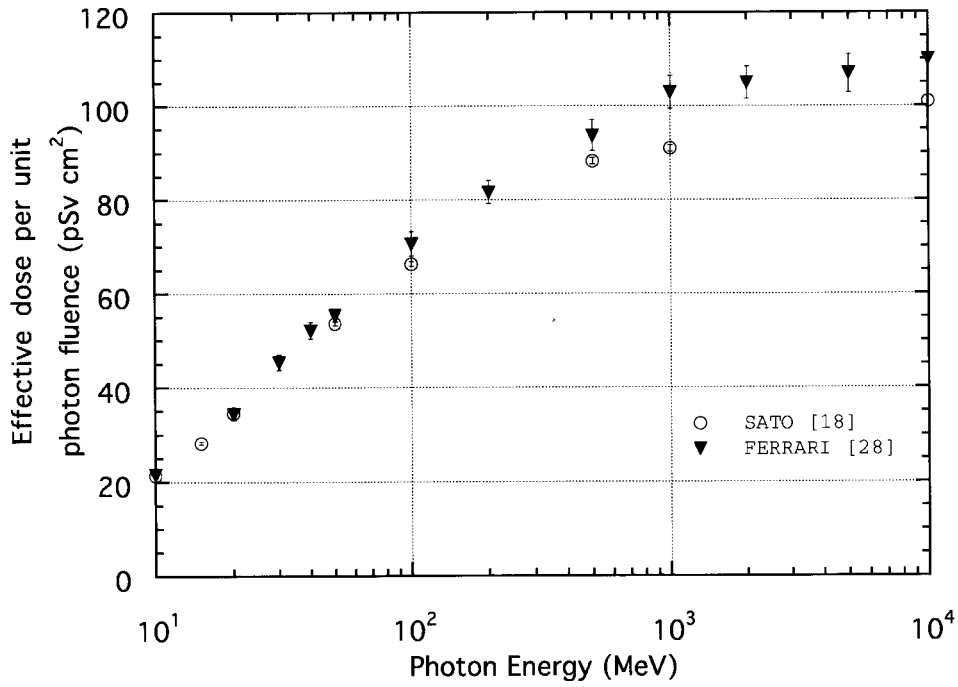


**Figure 4. Comparison of effective dose E for PA irradiation photon beam (the error bars represent Monte Carlo calculation error)**

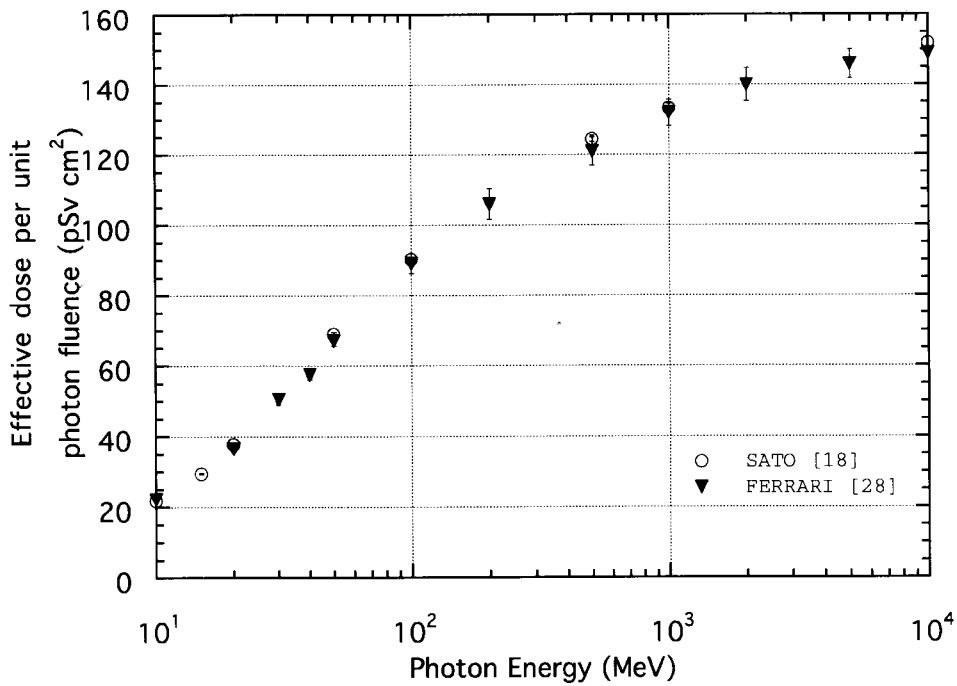


**Figure 5. Comparison of effective dose E for LAT irradiation photon beam (the error bars represent Monte Carlo calculation error)**

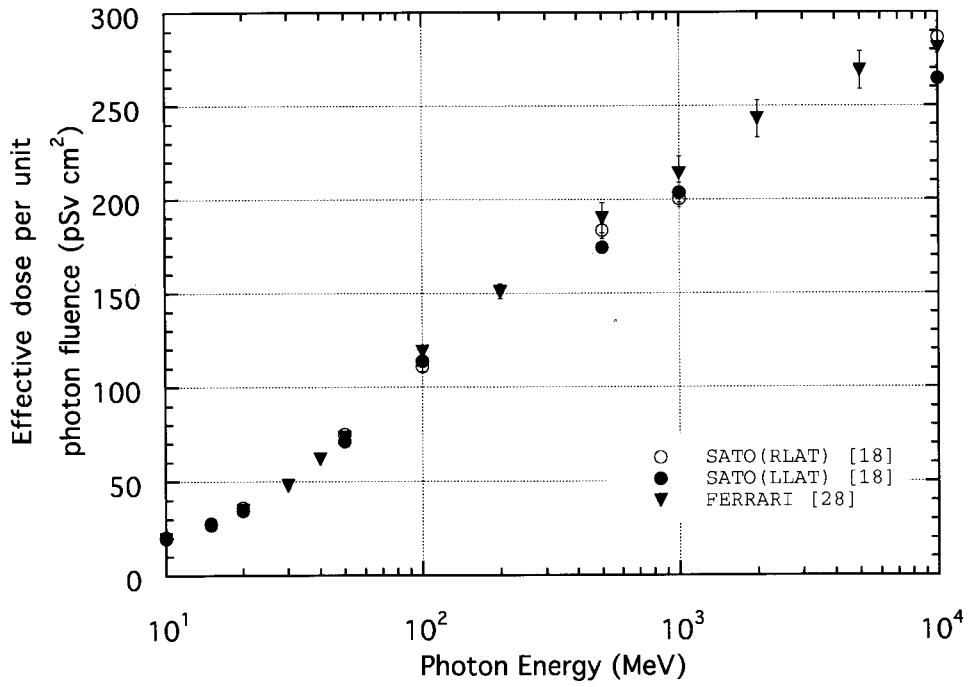


**Figure 6. Comparison of effective dose E for ISO irradiation photon beam (the error bars represent Monte Carlo calculation error)**

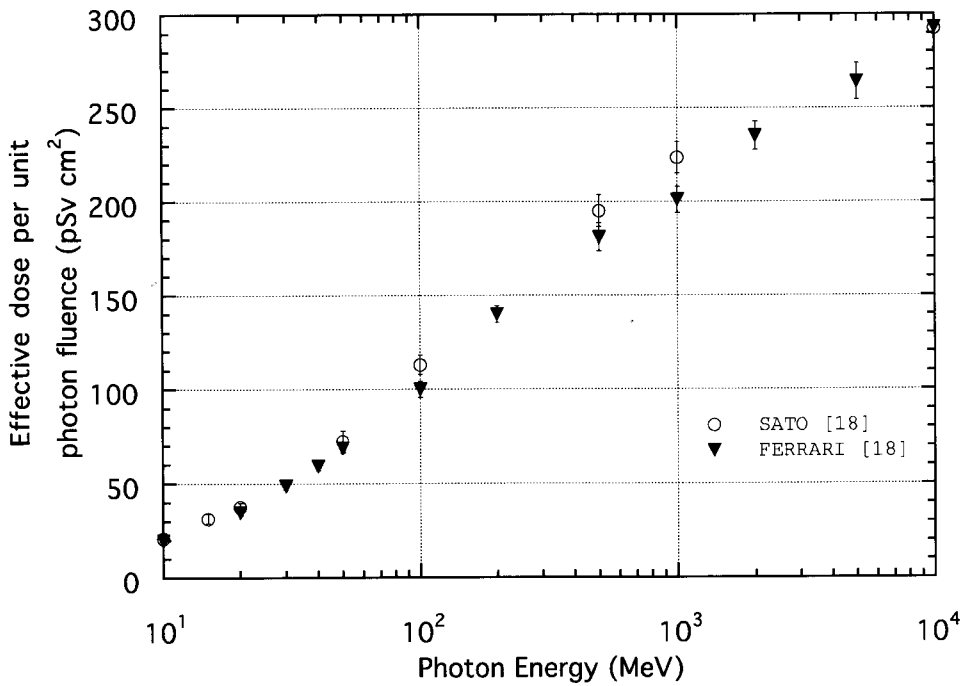


**Figure 7. Comparison of effective dose E for AP and PA irradiation proton beam (the error bars with Monte Carlo calculation are smaller than symbols)**

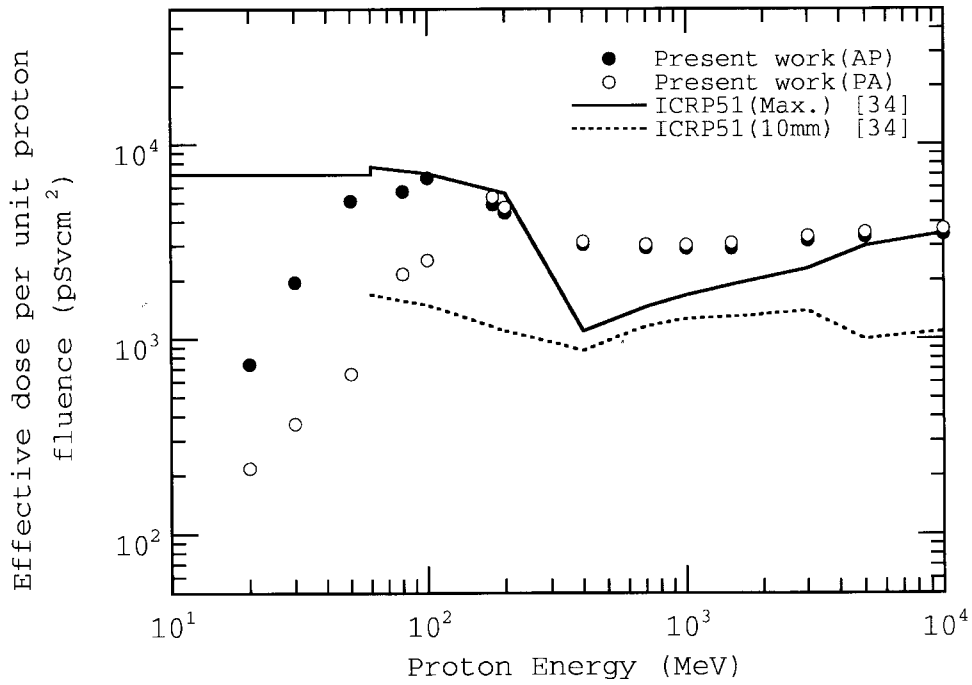
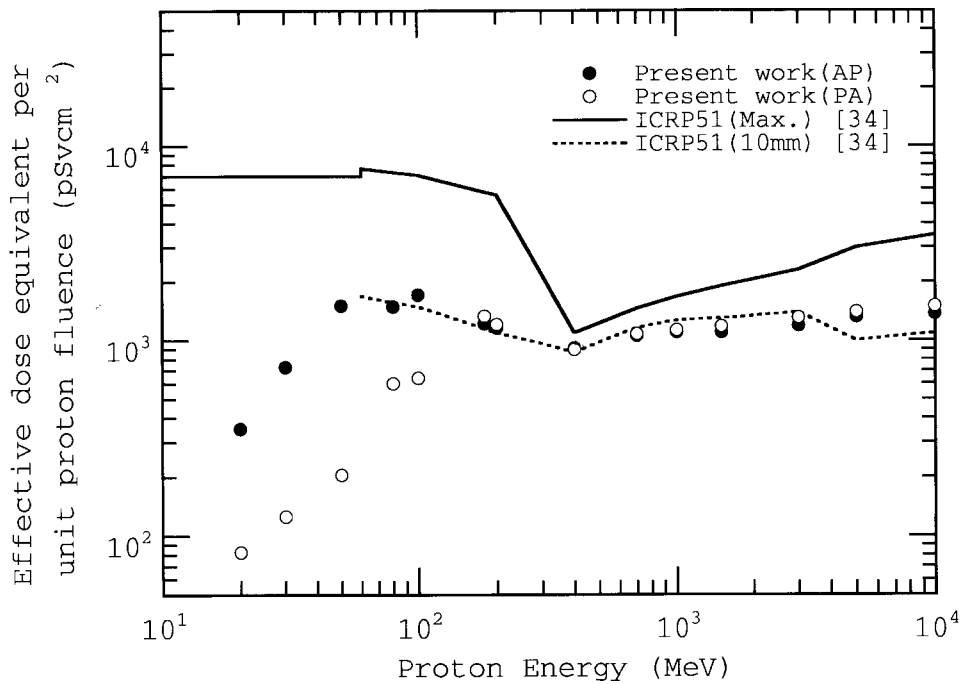


**Figure 8. Comparison of effective dose equivalent H<sub>E</sub> for AP and PA irradiation proton beam (the error bars with Monte Carlo calculation are smaller than symbols)**



## Appendix A

*Dose conversion coefficients from neutron fluence to  $E$ ,  $H_E$  equivalent dose, averaged tissue dose equivalent, averaged tissue absorbed dose from the energy range of 20 MeV to 10 GeV*

**Table A-1. Absorbed dose, effective dose and effective dose equivalent for neutron calculated by HERMES code system**

Neutron energy (MeV)	Absorbed dose				Effective dose				Effective dose equivalent				Mean quality factor	
	AP		PA		AP		PA		Based on the New Q-L (ICRP Pub. 60)		AP		PA	
	(pGycm <sup>2</sup> )	error	(pGycm <sup>2</sup> )	error	(pScm <sup>2</sup> )	error	(pScm <sup>2</sup> )	error	(pScm <sup>2</sup> )	error	(pScm <sup>2</sup> )	error	AP	PA
20	59.41	2.50%	55.21	2.50%	401.61	2.50%	373.22	2.50%	382.50	3.40%	343.90	3.10%	6.44	6.23
30	72.37	2.40%	67.92	1.50%	437.11	2.40%	410.24	1.50%	401.50	4.10%	357.60	2.10%	5.55	5.27
50	77.16	1.50%	75.37	1.40%	424.07	1.50%	414.23	1.40%	315.70	1.90%	314.20	3.60%	4.09	4.17
80	88.38	2.60%	88.96	2.40%	462.40	2.60%	465.44	2.40%	345.60	4.00%	341.90	2.10%	3.91	3.84
100	90.46	2.30%	96.81	2.50%	466.59	2.30%	499.35	2.50%	341.20	3.70%	354.40	3.90%	3.77	3.66
180	93.29	2.30%	108.70	1.40%	471.39	2.30%	549.26	1.40%	327.20	3.30%	390.40	5.30%	3.51	3.59
200	93.30	2.40%	108.90	1.40%	470.51	2.40%	549.18	1.40%	322.90	3.60%	361.60	2.30%	3.46	3.32
400	103.90	2.20%	128.40	1.40%	520.54	2.20%	643.28	1.40%	388.20	3.90%	435.70	2.40%	3.74	3.39
700	176.10	1.80%	209.40	1.00%	881.03	1.80%	1047.63	1.00%	599.00	3.30%	690.00	1.90%	3.40	3.30
1000	200.90	1.60%	239.00	1.00%	1004.70	1.60%	1195.24	1.00%	684.10	2.10%	744.20	1.70%	3.41	3.11
1500	254.80	2.20%	285.40	1.00%	1274.00	2.20%	1427.00	1.00%	808.20	3.50%	840.00	1.70%	3.17	2.94
3000	313.10	1.50%	351.10	1.30%	1565.50	1.50%	1755.50	1.30%	874.40	2.60%	963.10	2.80%	2.79	2.74
5000	338.30	1.30%	384.70	1.60%	1691.50	1.30%	1923.50	1.60%	947.30	1.80%	1104.00	3.20%	2.80	2.87
10000	355.50	1.10%	409.70	1.00%	1777.50	1.10%	2048.50	1.00%	1058.00	2.00%	1187.00	2.00%	2.98	2.90

**Table A-2(1). Absorbed dose, effective dose and effective dose equivalent for 20 MeV neutron calculated by HERMES code system**

Neutron energy=20 MeV

Organ	Absorbed dose				Effective dose ( $w_R=6.760$ )				Dose equivalent Based on the New Q-L (ICRP Pub. 60)				Mean quality factor	
	AP ( $\mu\text{Gycm}^2$ )		PA ( $\mu\text{Gycm}^2$ )		AP ( $\mu\text{Scm}^2$ )		PA ( $\mu\text{Scm}^2$ )		AP ( $\mu\text{Scm}^2$ )		PA ( $\mu\text{Scm}^2$ )		AP	PA
		error		error		error		error		error		error		
Testes	57.46	5.5%	50.48	7.0%	388.43	5.5%	341.24	7.0%	321.10	6.9%	304.40	8.4%	5.6	6.0
Ovaries	63.51	11.3%	62.90	10.6%	429.33	11.3%	425.20	10.6%	440.00	14.2%	394.10	12.6%	6.9	6.3
Red marrow	41.21	0.7%	46.39	0.7%	278.58	0.7%	313.60	0.7%	271.60	0.9%	300.00	0.8%	6.6	6.5
Colon	60.07	0.9%	54.27	1.0%	406.07	0.9%	366.87	1.0%	383.50	1.1%	344.80	1.2%	6.4	6.4
Lungs	60.57	1.1%	61.98	1.1%	409.45	1.1%	418.98	1.1%	354.20	1.4%	360.00	1.3%	5.8	5.8
ST	64.01	3.9%	53.29	4.2%	432.71	3.9%	360.24	4.2%	444.90	4.8%	351.10	5.2%	7.0	6.6
Urinary bladder	63.42	4.2%	46.58	4.7%	428.72	4.2%	314.88	4.7%	404.60	5.3%	310.20	5.6%	6.4	6.7
Breasts	66.18	2.5%	52.57	3.3%	447.38	2.5%	355.37	3.3%	373.50	3.4%	330.40	4.4%	5.6	6.3
Liver	61.33	1.1%	55.46	1.2%	414.59	1.1%	374.91	1.2%	378.80	1.4%	346.30	1.6%	6.2	6.2
Oesophagus	56.20	4.8%	56.65	5.1%	379.91	4.8%	382.95	5.1%	360.10	5.9%	331.70	6.4%	6.4	5.9
Thyroid	68.82	7.1%	46.46	8.6%	465.22	7.1%	314.07	8.6%	413.60	8.7%	257.40	11.4%	6.0	5.5
Skin	47.14	0.6%	46.61	0.6%	318.67	0.6%	315.08	0.6%	299.20	0.7%	300.10	0.7%	6.3	6.4
Bone surface	42.87	0.4%	45.09	0.4%	289.80	0.4%	304.81	0.4%	278.80	0.6%	292.50	0.5%	6.5	6.5
Adrenals**	48.91	10.3%	66.55	8.0%	330.63	10.3%	449.88	8.0%	288.90	11.9%	389.90	10.1%	5.9	5.9
Brain**	52.80	1.4%	54.52	1.3%	356.93	1.4%	368.56	1.3%	316.60	1.7%	323.00	1.7%	6.0	5.9
SI**	61.07	1.4%	56.14	1.5%	412.83	1.4%	379.51	1.5%	387.70	1.8%	361.20	1.9%	6.3	6.4
Kidneys**	49.47	2.7%	64.57	2.0%	334.42	2.7%	436.49	2.0%	325.20	3.5%	397.30	2.7%	6.6	6.2
Muscle**	58.34	0.2%	58.38	0.2%	394.38	0.2%	394.65	0.2%	353.20	0.3%	353.10	0.3%	6.1	6.0
Pancreas**	50.54	3.5%	61.42	2.8%	341.65	3.5%	415.20	2.8%	316.00	4.3%	350.10	3.7%	6.3	5.7
Spleen**	58.86	4.5%	59.91	4.9%	397.89	4.5%	404.99	4.9%	387.40	5.7%	392.70	5.7%	6.6	6.6
Thymus**	69.00	6.8%	34.62	9.2%	466.44	6.8%	234.03	9.2%	360.30	8.2%	248.10	11.2%	5.2	7.2
Uterus**	55.00	5.1%	53.54	5.1%	371.80	5.1%	361.93	5.1%	352.50	6.2%	338.10	6.5%	6.4	6.3
ULI	60.42	2.3%	52.81	2.7%	408.44	2.3%	357.00	2.7%	382.50	2.9%	334.10	3.3%	6.3	6.3
LLI	59.60	2.7%	56.20	2.8%	402.90	2.7%	379.91	2.8%	384.70	3.2%	359.00	3.5%	6.5	6.4
Remainder	58.18	0.2%	58.27	0.2%	393.30	0.2%	393.91	0.2%	352.70	0.3%	352.80	0.3%	6.1	6.1
Total body	59.41	2.5%	55.21	2.5%	401.61	2.5%	373.22	2.5%	382.50	3.4%	343.90	3.1%	6.4	6.2

\*1 effective dose

\*2 effective dose equivalent

\*\* organ or tissue included in Remainder

**Table A-2(2). Absorbed dose, effective dose and effective dose equivalent for 30 MeV neutron calculated by HERMES code system**

Neutron energy=30 MeV

Organ	Absorbed dose				Effective dose ( $w_R=6.040$ )				Dose equivalent Based on the New Q-L (ICRP Pub. 60)				Mean quality factor	
	AP ( $\mu\text{Gycm}^2$ )		PA ( $\mu\text{Gycm}^2$ )		AP ( $\mu\text{Scm}^2$ )		PA ( $\mu\text{Scm}^2$ )		AP ( $\mu\text{Scm}^2$ )		PA ( $\mu\text{Scm}^2$ )		AP	PA
		error		error		error		error		error		error		
Testes	74.99	5.6%	67.61	6.2%	452.94	5.6%	408.36	6.2%	341.60	7.9%	361.90	9.0%	4.6	5.4
Ovaries	75.55	10.9%	62.21	11.7%	456.32	10.9%	375.75	11.7%	520.50	15.1%	328.30	14.7%	6.9	5.3
Red marrow	53.83	0.7%	58.72	0.6%	325.13	0.7%	354.67	0.6%	305.20	0.9%	322.80	0.9%	5.7	5.5
Colon	75.32	0.9%	67.94	0.9%	454.93	0.9%	410.36	0.9%	412.40	1.3%	363.20	1.3%	5.5	5.3
Lungs	74.54	1.1%	77.08	1.1%	450.22	1.1%	465.56	1.1%	362.00	1.6%	370.90	1.6%	4.9	4.8
ST	78.68	3.7%	68.72	4.0%	475.23	3.7%	415.07	4.0%	419.40	5.5%	374.30	6.1%	5.3	5.4
Urinary bladder	80.46	4.3%	70.85	4.6%	485.98	4.3%	427.93	4.6%	412.90	6.0%	375.40	6.7%	5.1	5.3
Breasts	74.03	2.9%	66.67	3.1%	447.14	2.9%	402.69	3.1%	344.90	4.2%	345.30	4.4%	4.7	5.2
Liver	75.47	1.0%	69.92	1.0%	455.84	1.0%	422.32	1.0%	394.00	1.4%	367.80	1.5%	5.2	5.3
Oesophagus	63.73	5.0%	75.30	4.7%	384.93	5.0%	454.81	4.7%	340.50	6.6%	387.30	6.8%	5.3	5.1
Thyroid	79.91	7.7%	57.10	8.6%	482.66	7.7%	344.88	8.6%	359.90	10.4%	293.20	11.4%	4.5	5.1
Skin	53.59	0.6%	53.00	0.6%	323.68	0.6%	320.12	0.6%	310.30	1.0%	309.50	1.0%	5.8	5.8
Bone surface	55.51	0.4%	57.17	0.4%	335.28	0.4%	345.31	0.4%	309.60	0.6%	315.10	0.6%	5.6	5.5
Adrenals**	63.40	8.9%	69.69	8.3%	382.94	8.9%	420.93	8.3%	437.90	13.4%	374.20	11.9%	6.9	5.4
Brain**	68.59	1.1%	67.25	1.1%	414.28	1.1%	406.19	1.1%	359.50	1.7%	345.70	1.7%	5.2	5.1
SI**	73.98	1.3%	70.60	1.3%	446.84	1.3%	426.42	1.3%	395.50	1.8%	383.70	1.9%	5.3	5.4
Kidneys**	62.28	2.5%	80.43	2.0%	376.17	2.5%	485.80	2.0%	335.60	3.5%	409.80	3.0%	5.4	5.1
Muscle**	72.21	0.2%	72.34	0.2%	436.15	0.2%	436.93	0.2%	375.10	0.3%	375.20	0.3%	5.2	5.2
Pancreas**	70.75	2.9%	78.14	2.8%	427.33	2.9%	471.97	2.8%	378.90	4.1%	402.60	4.1%	5.4	5.2
Spleen**	72.87	4.4%	74.74	4.3%	440.13	4.4%	451.43	4.3%	409.30	6.4%	430.80	6.5%	5.6	5.8
Thymus**	82.80	7.0%	58.68	9.5%	500.11	7.0%	354.43	9.5%	396.40	10.5%	322.70	12.0%	4.8	5.5
Uterus**	80.82	4.7%	80.13	4.6%	488.15	4.7%	483.99	4.6%	411.30	6.6%	429.40	6.9%	5.1	5.4
ULI	76.06	2.2%	65.03	2.5%	459.40	2.2%	392.78	2.5%	419.30	3.4%	355.90	3.5%	5.5	5.5
LLI	74.35	2.7%	71.78	2.7%	449.07	2.7%	433.55	2.7%	403.20	3.7%	372.90	4.0%	5.4	5.2
Remainder	72.11	0.2%	72.24	0.2%	435.54	0.2%	436.33	0.2%	375.00	0.3%	375.00	0.3%	5.2	5.2
Total body	72.37	2.4%	67.92	1.5%	437.11	2.4%	410.24	1.5%	401.50	4.1%	357.60	2.1%	5.5	5.3

\*1 effective dose

\*2 effective dose equivalent

\*\* organ or tissue included in Remainder

**Table A-2(3). Absorbed dose, effective dose and effective dose equivalent for 50 MeV neutron calculated by HERMES code system**

Neutron energy=50 MeV

Organ	Absorbed dose				Effective dose ( $w_R=5.496$ )				Dose equivalent Based on the New Q-L (ICRP Pub. 60)				Mean quality factor	
	AP (pGycm <sup>2</sup> )		PA (pGycm <sup>2</sup> )		AP (pScm <sup>2</sup> )		PA (pScm <sup>2</sup> )		AP (pScm <sup>2</sup> )		PA (pScm <sup>2</sup> )		AP	PA
		error		error		error		error		error		error		
Testes	79.18	6.4%	72.01	6.4%	435.17	6.4%	395.77	6.4%	321.90	7.9%	292.10	7.8%	4.1	4.1
Ovaries	68.21	11.6%	66.34	11.9%	374.88	11.6%	364.60	11.9%	260.10	16.3%	311.00	17.3%	3.8	4.7
Red marrow	64.75	0.7%	68.53	0.7%	355.87	0.7%	376.64	0.7%	282.80	0.9%	297.60	0.9%	4.4	4.3
Colon	83.41	0.9%	77.45	1.0%	458.42	0.9%	425.67	1.0%	346.60	1.3%	318.00	1.3%	4.2	4.1
Lungs	81.76	1.2%	84.20	1.2%	449.35	1.2%	462.76	1.2%	309.30	1.5%	313.00	1.6%	3.8	3.7
ST	79.31	3.9%	74.06	3.9%	435.89	3.9%	407.03	3.9%	324.40	5.6%	332.80	5.7%	4.1	4.5
Urinary bladder	78.40	4.2%	75.14	4.5%	430.89	4.2%	412.97	4.5%	310.00	6.3%	326.20	6.6%	4.0	4.3
Breasts	62.39	3.5%	75.41	3.4%	342.90	3.5%	414.45	3.4%	271.10	4.5%	290.90	4.1%	4.3	3.9
Liver	83.34	1.1%	79.09	1.1%	458.04	1.1%	434.68	1.1%	338.00	1.4%	328.10	1.4%	4.1	4.1
Oesophagus	72.37	5.2%	77.24	4.9%	397.75	5.2%	424.51	4.9%	288.30	7.2%	303.20	6.7%	4.0	3.9
Thyroid	85.56	7.8%	79.85	7.9%	470.24	7.8%	438.86	7.9%	355.90	10.5%	336.20	11.4%	4.2	4.2
Skin	53.51	0.6%	53.16	0.6%	294.09	0.6%	292.17	0.6%	256.60	1.0%	254.30	1.0%	4.8	4.8
Bone surface	65.92	0.4%	66.88	0.4%	362.30	0.4%	367.57	0.4%	285.80	0.6%	287.20	0.6%	4.3	4.3
Adrenals**	83.58	8.6%	95.94	8.5%	459.36	8.6%	525.64	8.5%	373.50	11.2%	345.20	11.4%	4.5	3.6
Brain**	78.24	1.2%	77.68	1.2%	430.01	1.2%	426.93	1.2%	319.50	1.7%	306.00	1.6%	4.1	3.9
SI**	81.18	1.3%	82.05	1.4%	446.17	1.3%	450.95	1.4%	338.40	1.8%	340.30	1.9%	4.2	4.1
Kidneys**	74.85	2.4%	88.65	2.3%	411.38	2.4%	487.22	2.3%	324.20	3.4%	349.70	3.0%	4.3	3.9
Muscle**	78.38	0.2%	78.30	0.2%	430.78	0.2%	430.34	0.2%	321.70	0.3%	320.60	0.3%	4.1	4.1
Pancreas**	79.25	3.2%	82.07	3.1%	435.56	3.2%	451.06	3.1%	342.80	4.1%	307.90	4.0%	4.3	3.8
Spleen**	82.41	4.5%	80.90	4.7%	452.93	4.5%	444.63	4.7%	377.70	6.6%	354.30	6.8%	4.6	4.4
Thymus**	77.07	8.2%	75.90	8.5%	423.58	8.2%	417.15	8.5%	336.70	11.0%	326.30	11.9%	4.4	4.3
Uterus**	80.40	5.1%	80.30	5.1%	441.88	5.1%	441.33	5.1%	343.90	6.4%	348.30	6.6%	4.3	4.3
ULI	81.34	2.4%	76.36	2.5%	447.04	2.4%	419.67	2.5%	341.00	3.3%	314.60	3.5%	4.2	4.1
LLI	86.16	2.7%	78.89	2.7%	473.54	2.7%	433.58	2.7%	354.10	3.9%	322.50	3.8%	4.1	4.1
Remainder	78.42	0.2%	78.43	0.2%	431.00	0.2%	431.05	0.2%	322.10	0.3%	320.80	0.3%	4.1	4.1
Total body	77.16	1.5%	75.37	1.4%	424.07	1.5%	414.23	1.4%	315.70	1.9%	314.20	3.6%	4.1	4.2

\*1 effective dose

\*2 effective dose equivalent

\*\* organ or tissue included in Remainder

**Table A-2(4). Absorbed dose, effective dose and effective dose equivalent for 80 MeV neutron calculated by HERMES code system**

Neutron energy=80 MeV

Organ	Absorbed dose				Effective dose ( $w_R=5.232$ )				Dose equivalent Based on the New Q-L (ICRP Pub. 60)				Mean quality factor	
	AP (pGycm <sup>2</sup> )		PA (pGycm <sup>2</sup> )		AP (pScm <sup>2</sup> )		PA (pScm <sup>2</sup> )		AP (pScm <sup>2</sup> )		PA (pScm <sup>2</sup> )		AP	PA
		error		error		error		error		error		error		
Testes	58.15	7.6%	95.23	6.2%	304.24	7.6%	498.24	6.2%	293.20	9.8%	378.50	8.3%	5.0	4.0
Ovaries	113.30	9.8%	99.34	10.3%	592.79	9.8%	519.75	10.3%	419.50	15.6%	341.60	13.6%	3.7	3.4
Red marrow	76.25	0.7%	75.76	0.7%	398.94	0.7%	396.38	0.7%	311.70	0.9%	312.00	0.9%	4.1	4.1
Colon	89.73	0.9%	87.73	1.0%	469.47	0.9%	459.00	1.0%	348.40	1.4%	345.00	1.4%	3.9	3.9
Lungs	90.13	1.3%	88.57	1.3%	471.56	1.3%	463.40	1.3%	329.50	1.7%	318.20	1.7%	3.7	3.6
ST	78.94	4.0%	92.55	4.0%	413.01	4.0%	484.22	4.0%	322.40	6.5%	350.50	5.7%	4.1	3.8
Urinary bladder	86.92	4.3%	94.16	4.2%	454.77	4.3%	492.65	4.2%	324.80	7.7%	366.90	6.8%	3.7	3.9
Breasts	54.34	4.2%	86.93	3.1%	284.31	4.2%	454.82	3.1%	280.80	5.2%	304.20	4.3%	5.2	3.5
Liver	89.22	1.2%	89.01	1.1%	466.80	1.2%	465.70	1.1%	350.40	1.4%	344.20	1.5%	3.9	3.9
Oesophagus	92.37	4.4%	88.01	4.9%	483.28	4.4%	460.47	4.9%	358.50	6.4%	361.20	7.0%	3.9	4.1
Thyroid	77.90	8.4%	87.50	7.9%	407.57	8.4%	457.80	7.9%	321.30	12.4%	316.00	11.0%	4.1	3.6
Skin	55.76	0.6%	55.98	0.6%	291.74	0.6%	292.89	0.6%	275.10	1.1%	274.50	1.0%	4.9	4.9
Bone surface	76.76	0.5%	75.98	0.5%	401.61	0.5%	397.53	0.5%	312.70	0.6%	311.00	0.6%	4.1	4.1
Adrenals**	86.27	8.6%	86.93	8.1%	451.36	8.6%	454.82	8.1%	351.00	12.0%	298.70	11.6%	4.1	3.4
Brain**	87.02	1.4%	85.29	1.4%	455.29	1.4%	446.24	1.4%	327.40	1.7%	329.70	1.7%	3.8	3.9
SI**	92.32	1.4%	92.42	1.5%	483.02	1.4%	483.54	1.5%	359.70	1.8%	366.70	1.9%	3.9	4.0
Kidneys**	84.83	2.4%	86.29	2.4%	443.83	2.4%	451.47	2.4%	321.20	3.5%	338.70	3.4%	3.8	3.9
Muscle**	82.57	0.2%	82.39	0.2%	432.01	0.2%	431.06	0.2%	331.60	0.3%	331.10	0.3%	4.0	4.0
Pancreas**	95.80	3.2%	93.58	3.2%	501.23	3.2%	489.61	3.2%	377.40	4.2%	346.20	4.2%	3.9	3.7
Spleen**	90.59	4.7%	90.59	4.6%	473.97	4.7%	473.97	4.6%	354.80	6.9%	407.00	6.6%	3.9	4.5
Thymus**	82.28	8.8%	85.21	7.9%	430.49	8.8%	445.82	7.9%	344.50	12.9%	274.60	11.5%	4.2	3.2
Uterus**	96.48	5.2%	95.96	5.3%	504.78	5.2%	502.06	5.3%	357.30	6.3%	370.60	6.4%	3.7	3.9
ULI	89.91	2.4%	88.17	2.5%	470.41	2.4%	461.31	2.5%	348.40	3.5%	358.40	3.6%	3.9	4.1
LLI	89.49	2.7%	87.14	3.0%	468.21	2.7%	455.92	3.0%	348.30	4.1%	327.20	4.2%	3.9	3.8
Remainder	82.96	0.2%	82.75	0.2%	434.05	0.2%	432.95	0.2%	332.30	0.3%	332.00	0.3%	4.0	4.0
Total body	88.38	2.6%	88.96	2.4%	462.40	2.6%	465.44	2.4%	345.60	4.0%	341.90	2.1%	3.9	3.8

\*1 effective dose

\*2 effective dose equivalent

\*\* organ or tissue included in Remainder

**Table A-2(5). Absorbed dose, effective dose and effective dose equivalent for 100 MeV neutron calculated by HERMES code system**

Neutron energy=100 MeV

Organ	Absorbed dose				Effective dose ( $w_R=5.158$ )				Dose equivalent Based on the New Q-L (ICRP Pub. 60)				Mean quality factor	
	AP (pGycm <sup>2</sup> )		PA (pGycm <sup>2</sup> )		AP (pScm <sup>2</sup> )		PA (pScm <sup>2</sup> )		AP (pScm <sup>2</sup> )		PA (pScm <sup>2</sup> )		AP	PA
		error		error		error		error		error		error		
Testes	58.11	7.6%	97.76	6.5%	299.73	7.6%	504.25	6.5%	265.30	10.0%	338.70	8.7%	4.6	3.5
Ovaries	100.90	9.7%	114.60	10.2%	520.44	9.7%	591.11	10.2%	339.10	17.7%	390.50	16.8%	3.4	3.4
Red marrow	83.71	0.7%	78.62	0.7%	431.78	0.7%	405.52	0.7%	324.20	1.0%	314.70	1.0%	3.9	4.0
Colon	98.62	0.9%	97.43	0.9%	508.68	0.9%	502.54	0.9%	351.90	1.4%	355.50	1.5%	3.6	3.6
Lungs	93.80	1.3%	88.93	1.3%	483.82	1.3%	458.70	1.3%	352.50	1.7%	334.20	1.8%	3.8	3.8
ST	90.82	3.8%	102.10	3.7%	468.45	3.8%	526.63	3.7%	368.70	6.1%	384.20	6.3%	4.1	3.8
Urinary bladder	90.93	4.4%	96.36	3.8%	469.02	4.4%	497.02	3.8%	350.50	7.9%	348.50	7.1%	3.9	3.6
Breasts	53.80	4.2%	98.63	3.0%	277.50	4.2%	508.73	3.0%	298.50	5.4%	314.70	4.6%	5.5	3.2
Liver	92.12	1.2%	95.24	1.2%	475.15	1.2%	491.25	1.2%	351.10	1.4%	353.70	1.5%	3.8	3.7
Oesophagus	99.45	4.5%	95.78	4.6%	512.96	4.5%	494.03	4.6%	343.90	6.7%	355.10	7.5%	3.5	3.7
Thyroid	74.86	8.4%	97.23	7.5%	386.13	8.4%	501.51	7.5%	315.90	11.8%	366.00	11.8%	4.2	3.8
Skin	57.77	0.6%	58.36	0.6%	297.98	0.6%	301.02	0.6%	271.20	1.1%	272.40	1.2%	4.7	4.7
Bone surface	81.88	0.5%	80.52	0.5%	422.34	0.5%	415.32	0.5%	318.20	0.6%	318.10	0.6%	3.9	4.0
Adrenals**	103.00	8.2%	93.06	8.3%	531.27	8.2%	480.00	8.3%	427.00	14.5%	346.40	12.5%	4.1	3.7
Brain**	91.79	1.4%	89.07	1.5%	473.45	1.4%	459.42	1.5%	336.50	1.8%	328.00	1.7%	3.7	3.7
SI**	99.30	1.5%	101.40	1.4%	512.19	1.5%	523.02	1.4%	366.40	1.9%	379.30	1.7%	3.7	3.7
Kidneys**	96.61	2.5%	78.19	2.5%	498.31	2.5%	403.30	2.5%	372.30	3.4%	334.90	3.6%	3.9	4.3
Muscle**	85.24	0.2%	85.72	0.2%	439.67	0.2%	442.14	0.2%	334.90	0.3%	336.20	0.3%	3.9	3.9
Pancreas**	107.50	3.0%	89.94	3.3%	554.49	3.0%	463.91	3.3%	402.00	4.0%	337.70	4.3%	3.7	3.8
Spleen**	102.60	4.6%	96.74	4.2%	529.21	4.6%	498.98	4.2%	386.60	6.8%	322.30	6.8%	3.8	3.3
Thymus**	58.93	9.0%	94.39	8.1%	303.96	9.0%	486.86	8.1%	206.00	14.2%	376.00	13.9%	3.5	4.0
Uterus**	96.57	5.8%	94.05	5.5%	498.11	5.8%	485.11	5.5%	368.10	6.8%	392.50	7.4%	3.8	4.2
ULI	92.97	2.4%	92.85	2.5%	479.54	2.4%	478.92	2.5%	340.00	3.8%	349.40	3.9%	3.7	3.8
LLI	106.10	2.6%	103.50	2.5%	547.26	2.6%	533.85	2.5%	367.60	4.2%	363.60	4.0%	3.5	3.5
Remainder	85.85	0.2%	86.12	0.2%	442.81	0.2%	444.21	0.2%	336.10	0.3%	336.90	0.3%	3.9	3.9
Total body	90.46	2.3%	96.81	2.5%	466.59	2.3%	499.35	2.5%	341.20	3.7%	354.40	3.9%	3.8	3.7

\*1 effective dose

\*2 effective dose equivalent

\*\* organ or tissue included in Remainder

**Table A-2(6). Absorbed dose, effective dose and effective dose equivalent for 180 MeV neutron calculated by HERMES code system**

Neutron energy=180 MeV

Organ	Absorbed dose				Effective dose ( $w_R=5.053$ )				Dose equivalent Based on the New Q-L (ICRP Pub. 60)				Mean quality factor	
	AP (pGycm <sup>2</sup> )		PA (pGycm <sup>2</sup> )		AP (pScm <sup>2</sup> )		PA (pScm <sup>2</sup> )		AP (pScm <sup>2</sup> )		PA (pScm <sup>2</sup> )		AP	PA
		error		error		error		error		error		error		
Testes	53.22	8.2%	126.90	5.2%	268.92	8.2%	641.23	5.2%	266.30	11.9%	404.50	8.6%	5.0	3.2
Ovaries	115.40	9.0%	125.30	9.3%	583.12	9.0%	633.14	9.3%	337.90	14.8%	515.90	19.6%	2.9	4.1
Red marrow	99.20	0.7%	81.42	0.7%	501.26	0.7%	411.42	0.7%	339.40	0.9%	314.80	1.0%	3.4	3.9
Colon	94.87	0.9%	114.00	0.8%	479.38	0.9%	576.04	0.8%	328.80	1.5%	374.80	1.4%	3.5	3.3
Lungs	88.90	1.3%	84.91	1.3%	449.21	1.3%	429.05	1.3%	327.90	2.0%	329.80	2.0%	3.7	3.9
ST	94.19	4.1%	124.70	3.5%	475.94	4.1%	630.11	3.5%	374.10	6.8%	372.10	6.0%	4.0	3.0
Urinary bladder	83.29	4.3%	122.00	3.6%	420.86	4.3%	616.47	3.6%	334.00	8.6%	385.10	7.3%	4.0	3.2
Breasts	41.91	5.0%	115.90	2.9%	211.77	5.0%	585.64	2.9%	275.60	6.5%	369.40	4.7%	6.6	3.2
Liver	88.58	1.3%	106.40	1.2%	447.59	1.3%	537.64	1.2%	327.80	1.6%	361.70	1.5%	3.7	3.4
Oesophagus	105.60	4.2%	103.90	4.4%	533.60	4.2%	525.01	4.4%	316.00	7.4%	348.20	8.0%	3.0	3.4
Thyroid	59.77	9.2%	127.30	6.8%	302.02	9.2%	643.25	6.8%	201.30	13.1%	491.50	12.7%	3.4	3.9
Skin	63.22	0.6%	64.12	0.6%	319.45	0.6%	324.00	0.6%	272.80	1.2%	278.30	1.2%	4.3	4.3
Bone surface	88.59	0.5%	81.13	0.5%	447.65	0.5%	409.95	0.5%	321.50	0.6%	311.20	0.6%	3.6	3.8
Adrenals**	119.30	6.3%	78.06	9.5%	602.82	6.3%	394.44	9.5%	370.30	10.3%	349.80	16.1%	3.1	4.5
Brain**	93.11	1.5%	90.82	1.6%	470.48	1.5%	458.91	1.6%	323.00	1.8%	310.10	1.8%	3.5	3.4
SI**	102.50	1.5%	117.50	1.4%	517.93	1.5%	593.73	1.4%	367.50	2.0%	390.40	1.8%	3.6	3.3
Kidneys**	135.60	2.0%	74.97	2.8%	685.19	2.0%	378.82	2.8%	416.90	3.3%	346.50	3.8%	3.1	4.6
Muscle**	88.84	0.3%	89.20	0.3%	448.91	0.3%	450.73	0.3%	330.00	0.3%	330.00	0.3%	3.7	3.7
Pancreas**	112.90	2.9%	84.30	3.5%	570.48	2.9%	425.97	3.5%	360.60	4.4%	323.80	5.1%	3.2	3.8
Spleen**	107.20	4.1%	103.20	4.5%	541.68	4.1%	521.47	4.5%	331.60	6.9%	338.10	7.6%	3.1	3.3
Thymus**	61.73	9.5%	124.30	6.5%	311.92	9.5%	628.09	6.5%	308.80	14.7%	373.10	11.7%	5.0	3.0
Uterus**	100.60	5.4%	123.50	4.9%	508.33	5.4%	624.05	4.9%	371.90	7.5%	404.00	6.8%	3.7	3.3
ULI	91.23	2.4%	115.00	2.1%	460.99	2.4%	581.10	2.1%	316.20	3.9%	361.60	3.6%	3.5	3.1
LLI	99.70	2.5%	112.70	2.4%	503.78	2.5%	569.47	2.4%	345.40	4.5%	392.20	4.3%	3.5	3.5
Remainder	89.59	0.3%	89.77	0.3%	452.70	0.3%	453.61	0.3%	331.20	0.3%	330.90	0.3%	3.7	3.7
Total body	93.29	2.3%	108.70	1.4%	471.39	2.3%	549.26	1.4%	327.20	3.3%	390.40	5.3%	3.5	3.6

\*1 effective dose

\*2 effective dose equivalent

\*\* organ or tissue included in Remainder

**Table A-2(7). Absorbed dose, effective dose and effective dose equivalent for 200 MeV neutron calculated by HERMES code system**

Neutron energy=200 MeV

Organ	Absorbed dose				Effective dose ( $w_R=5.043$ )				Dose equivalent Based on the New Q-L (ICRP Pub. 60)				Mean quality factor	
	AP (pGycm <sup>2</sup> )		PA (pGycm <sup>2</sup> )		AP (pScm <sup>2</sup> )		PA (pScm <sup>2</sup> )		AP (pScm <sup>2</sup> )		PA (pScm <sup>2</sup> )		AP	PA
		error		error		error		error		error		error		
Testes	47.03	9.1%	126.60	5.2%	237.17	9.1%	638.44	5.2%	251.30	13.2%	370.20	9.2%	5.3	2.9
Ovaries	118.90	9.0%	118.50	9.0%	599.61	9.0%	597.60	9.0%	337.30	15.6%	337.00	14.4%	2.8	2.8
Red marrow	100.60	0.7%	82.23	0.7%	507.33	0.7%	414.69	0.7%	343.60	1.0%	318.20	1.0%	3.4	3.9
Colon	94.62	0.9%	112.50	0.9%	477.17	0.9%	567.34	0.9%	338.20	1.5%	380.10	1.5%	3.6	3.4
Lungs	88.27	1.3%	83.84	1.3%	445.15	1.3%	422.81	1.3%	327.30	1.9%	318.00	2.0%	3.7	3.8
ST	87.99	4.1%	128.80	3.2%	443.73	4.1%	649.54	3.2%	321.60	7.3%	409.90	6.0%	3.7	3.2
Urinary bladder	79.86	4.3%	120.90	3.7%	402.73	4.3%	609.70	3.7%	305.70	8.6%	377.10	7.4%	3.8	3.1
Breasts	39.32	4.9%	118.00	2.8%	198.29	4.9%	595.07	2.8%	237.50	6.6%	388.50	4.8%	6.0	3.3
Liver	88.58	1.3%	105.90	1.1%	446.71	1.3%	534.05	1.1%	330.20	1.6%	360.50	1.5%	3.7	3.4
Oesophagus	99.95	4.3%	99.18	4.4%	504.05	4.3%	500.16	4.4%	293.90	8.6%	311.20	7.9%	2.9	3.1
Thyroid	70.70	9.7%	131.00	6.8%	356.54	9.7%	660.63	6.8%	296.40	13.7%	441.30	12.2%	4.2	3.4
Skin	64.33	0.6%	64.49	0.6%	324.42	0.6%	325.22	0.6%	280.40	1.3%	281.60	1.2%	4.4	4.4
Bone surface	89.47	0.5%	81.67	0.5%	451.20	0.5%	411.86	0.5%	323.10	0.6%	316.10	0.6%	3.6	3.9
Adrenals**	129.00	6.4%	75.18	9.3%	650.55	6.4%	379.13	9.3%	390.00	11.5%	298.30	15.6%	3.0	4.0
Brain**	92.60	1.6%	89.68	1.6%	466.98	1.6%	452.26	1.6%	327.70	1.9%	314.40	1.9%	3.5	3.5
SI**	102.30	1.4%	114.40	1.4%	515.90	1.4%	576.92	1.4%	369.30	1.9%	368.10	1.9%	3.6	3.2
Kidneys**	126.60	2.1%	69.86	3.0%	638.44	2.1%	352.30	3.0%	379.80	3.3%	324.50	4.2%	3.0	4.6
Muscle**	88.94	0.3%	89.26	0.3%	448.52	0.3%	450.14	0.3%	328.80	0.3%	330.50	0.3%	3.7	3.7
Pancreas**	108.80	3.0%	81.78	3.6%	548.68	3.0%	412.42	3.6%	344.00	4.5%	317.90	4.6%	3.2	3.9
Spleen**	108.20	4.2%	108.80	4.6%	545.65	4.2%	548.68	4.6%	415.20	7.7%	369.50	7.4%	3.8	3.4
Thymus**	62.80	9.4%	133.40	6.1%	316.70	9.4%	672.74	6.1%	350.50	14.1%	390.80	12.3%	5.6	2.9
Uterus**	98.11	5.2%	113.20	4.9%	494.77	5.2%	570.87	4.9%	386.50	7.2%	348.70	6.7%	3.9	3.1
ULI	89.13	2.4%	113.70	2.2%	449.48	2.4%	573.39	2.2%	325.40	4.0%	380.60	3.8%	3.7	3.3
LLI	101.90	2.6%	111.00	2.5%	513.88	2.6%	559.77	2.5%	355.20	4.6%	379.40	4.5%	3.5	3.4
Remainder	89.61	0.3%	89.71	0.3%	451.90	0.3%	452.41	0.3%	330.10	0.3%	330.80	0.3%	3.7	3.7
Total body	93.30	2.4%	108.90	1.4%	470.51	2.4%	549.18	1.4%	322.90	3.6%	361.60	2.3%	3.5	3.3

\*1 effective dose

\*2 effective dose equivalent

\*\* organ or tissue included in Remainder

**Table A-2(8). Absorbed dose, effective dose and effective dose equivalent for 400 MeV neutron calculated by HERMES code system**

Neutron energy=400 MeV

Organ	Absorbed dose				Effective dose ( $w_R=5.010$ )				Dose equivalent Based on the New Q-L (ICRP Pub. 60)				Mean quality factor	
	AP (pGycm <sup>2</sup> )		PA (pGycm <sup>2</sup> )		AP (pScm <sup>2</sup> )		PA (pScm <sup>2</sup> )		AP (pScm <sup>2</sup> )		PA (pScm <sup>2</sup> )		AP	PA
		error		error		error		error		error		error		
Testes	54.89	8.4%	169.60	4.6%	275.00	8.4%	849.70	4.6%	295.10	11.8%	545.80	8.3%	5.4	3.2
Ovaries	115.20	9.3%	122.20	8.6%	577.15	9.3%	612.22	8.6%	376.10	18.4%	473.90	17.5%	3.3	3.9
Red marrow	117.30	0.7%	94.34	0.7%	587.67	0.7%	472.64	0.7%	406.70	0.9%	370.70	1.0%	3.5	3.9
Colon	105.70	0.9%	129.20	0.8%	529.56	0.9%	647.29	0.8%	389.40	1.6%	422.40	1.4%	3.7	3.3
Lungs	101.30	1.2%	95.21	1.3%	507.51	1.2%	477.00	1.3%	375.10	1.9%	357.90	2.0%	3.7	3.8
ST	104.10	4.1%	140.60	3.4%	521.54	4.1%	704.41	3.4%	451.60	6.8%	465.20	6.7%	4.3	3.3
Urinary bladder	95.16	4.4%	140.10	3.4%	476.75	4.4%	701.90	3.4%	342.80	8.7%	458.40	7.5%	3.6	3.3
Breasts	49.07	5.2%	132.00	2.7%	245.84	5.2%	661.32	2.7%	286.30	6.3%	407.70	4.8%	5.8	3.1
Liver	102.90	1.3%	122.00	1.2%	515.53	1.3%	611.22	1.2%	377.90	1.6%	420.60	1.5%	3.7	3.4
Oesophagus	116.80	4.5%	120.40	4.2%	585.17	4.5%	603.20	4.2%	418.10	8.2%	412.00	8.2%	3.6	3.4
Thyroid	87.83	8.3%	135.70	6.6%	440.03	8.3%	679.86	6.6%	413.80	13.5%	432.10	13.5%	4.7	3.2
Skin	74.56	0.6%	74.33	0.6%	373.55	0.6%	372.39	0.6%	325.40	1.2%	321.00	1.2%	4.4	4.3
Bone surface	104.00	0.5%	94.16	0.5%	521.04	0.5%	471.74	0.5%	384.20	0.6%	367.80	0.6%	3.7	3.9
Adrenals**	149.90	6.4%	100.70	7.8%	751.00	6.4%	504.51	7.8%	495.50	12.5%	436.10	12.7%	3.3	4.3
Brain**	101.50	1.6%	99.71	1.6%	508.52	1.6%	499.55	1.6%	373.10	1.9%	362.30	1.9%	3.7	3.6
SI**	117.70	1.4%	130.50	1.3%	589.68	1.4%	653.81	1.3%	434.20	2.0%	442.30	1.9%	3.7	3.4
Kidneys**	145.80	2.0%	83.95	2.8%	730.46	2.0%	420.59	2.8%	444.60	3.3%	372.40	3.8%	3.0	4.4
Muscle**	101.80	0.3%	102.20	0.3%	510.02	0.3%	512.02	0.3%	383.30	0.3%	383.00	0.3%	3.8	3.7
Pancreas**	123.80	2.9%	97.81	3.3%	620.24	2.9%	490.03	3.3%	398.30	4.2%	393.80	4.7%	3.2	4.0
Spleen**	122.20	4.0%	119.40	4.0%	612.22	4.0%	598.19	4.0%	414.60	7.1%	420.30	7.2%	3.4	3.5
Thymus**	79.80	9.5%	145.90	6.1%	399.80	9.5%	730.96	6.1%	431.00	14.5%	436.10	11.9%	5.4	3.0
Uterus**	114.80	4.5%	135.90	4.3%	575.15	4.5%	680.86	4.3%	448.40	6.9%	475.10	6.5%	3.9	3.5
ULI	102.00	2.3%	130.40	2.1%	511.02	2.3%	653.30	2.1%	383.00	4.2%	422.00	3.6%	3.8	3.2
LLI	110.50	2.7%	127.60	2.3%	553.61	2.7%	639.28	2.3%	398.00	4.8%	422.90	4.2%	3.6	3.3
Remainder	102.50	0.3%	102.60	0.3%	513.53	0.3%	514.03	0.3%	384.60	0.3%	383.80	0.3%	3.8	3.7
Total body	103.90	2.2%	128.40	1.4%	520.54	2.2%	643.28	1.4%	388.20	3.9%	435.70	2.4%	3.7	3.4

\*1 effective dose

\*2 effective dose equivalent

\*\* organ or tissue included in Remainder

**Table A-2(9). Absorbed dose, effective dose and effective dose equivalent for 700 MeV neutron calculated by HERMES code system**

Neutron energy=700 MeV

Organ	Absorbed dose				Effective dose ( $w_R=5.003$ )				Dose equivalent Based on the New Q-L (ICRP Pub. 60)				Mean quality factor	
	AP (pGycm <sup>2</sup> )		PA (pGycm <sup>2</sup> )		AP (pScm <sup>2</sup> )		PA (pScm <sup>2</sup> )		AP (pScm <sup>2</sup> )		PA (pScm <sup>2</sup> )		AP	PA
		error		error		error		error		error		error		
Testes	102.10	6.5%	249.80	3.7%	510.81	6.5%	1249.75	3.7%	496.00	9.3%	808.40	6.8%	4.9	3.2
Ovaries	189.30	8.1%	222.90	7.5%	947.07	8.1%	1115.17	7.5%	517.70	17.6%	688.00	14.5%	2.7	3.1
Red marrow	194.70	0.5%	162.20	0.6%	974.08	0.5%	811.49	0.6%	648.10	0.8%	611.60	0.8%	3.3	3.8
Colon	185.40	0.7%	217.60	0.7%	927.56	0.7%	1088.65	0.7%	626.30	1.3%	694.00	1.2%	3.4	3.2
Lungs	172.60	1.0%	164.80	1.1%	863.52	1.0%	824.49	1.1%	618.30	1.7%	588.30	1.6%	3.6	3.6
ST	185.30	3.4%	240.50	2.6%	927.06	3.4%	1203.22	2.6%	687.60	6.2%	750.00	5.1%	3.7	3.1
Urinary bladder	178.80	3.3%	234.00	2.6%	894.54	3.3%	1170.70	2.6%	676.20	7.1%	716.30	6.3%	3.8	3.1
Breasts	96.58	4.1%	204.60	2.3%	483.19	4.1%	1023.61	2.3%	509.20	5.3%	637.50	4.2%	5.3	3.1
Liver	174.80	1.1%	206.20	1.0%	874.52	1.1%	1031.62	1.0%	612.50	1.3%	665.70	1.2%	3.5	3.2
Oesophagus	190.00	3.3%	186.10	3.3%	950.57	3.3%	931.06	3.3%	559.10	6.7%	562.80	6.3%	2.9	3.0
Thyroid	120.00	7.4%	243.10	5.1%	600.36	7.4%	1216.23	5.1%	523.80	12.0%	806.90	9.1%	4.4	3.3
Skin	126.60	0.5%	125.50	0.5%	633.38	0.5%	627.88	0.5%	516.30	1.0%	503.20	1.0%	4.1	4.0
Bone surface	175.60	0.4%	161.70	0.4%	878.53	0.4%	808.99	0.4%	621.70	0.5%	606.80	0.5%	3.5	3.8
Adrenals**	240.30	5.1%	177.90	7.0%	1202.22	5.1%	890.03	7.0%	633.80	10.2%	716.50	13.3%	2.6	4.0
Brain**	171.70	1.3%	166.90	1.4%	859.02	1.3%	835.00	1.4%	592.20	1.6%	578.80	1.6%	3.4	3.5
SI**	201.40	1.2%	221.50	1.0%	1007.60	1.2%	1108.16	1.0%	667.90	1.6%	698.40	1.5%	3.3	3.2
Kidneys**	240.40	1.7%	145.30	2.3%	1202.72	1.7%	726.94	2.3%	701.80	2.8%	593.30	3.2%	2.9	4.1
Muscle**	172.90	0.2%	172.50	0.2%	865.02	0.2%	863.02	0.2%	605.90	0.3%	608.90	0.3%	3.5	3.5
Pancreas**	224.00	2.3%	168.50	2.8%	1120.67	2.3%	843.01	2.8%	712.50	3.4%	593.30	4.3%	3.2	3.5
Spleen**	197.80	3.3%	209.30	3.6%	989.59	3.3%	1047.13	3.6%	644.20	5.9%	678.10	6.0%	3.3	3.2
Thymus**	123.40	7.7%	222.80	5.6%	617.37	7.7%	1114.67	5.6%	480.60	12.6%	666.60	11.1%	3.9	3.0
Uterus**	187.30	4.0%	232.10	3.5%	937.06	4.0%	1161.20	3.5%	663.30	6.4%	766.10	5.2%	3.5	3.3
ULI	184.80	2.0%	219.60	1.7%	924.55	2.0%	1098.66	1.7%	645.00	3.2%	678.50	3.2%	3.5	3.1
LLI	186.30	2.1%	215.10	2.0%	932.06	2.1%	1076.15	2.0%	601.60	3.8%	714.60	3.7%	3.2	3.3
Remainder	174.00	0.2%	173.30	0.2%	870.52	0.2%	867.02	0.2%	607.70	0.2%	610.10	0.2%	3.5	3.5
Total body	176.10	1.8%	209.40	1.0%	* 881.03	1.8%	1047.63	1.0%	*2 599.00	3.3%	*2 690.00	1.9%	3.4	3.3

\*1 effective dose

\*2 effective dose equivalent

\*\* organ or tissue included in Remainder

**Table A-2(10). Absorbed dose, effective dose and effective dose equivalent for 1000 MeV neutron calculated by HERMES code system**

Neutron energy=1000 MeV

Organ	Absorbed dose				Effective dose( $w_R=5.001$ )				Effective dose Based on the New Q-L (ICRP Pub. 60)				Mean quality factor	
	AP		PA		AP		PA		AP		PA		AP	PA
	(pGycm <sup>2</sup> )	error	(pGycm <sup>2</sup> )	error	(pScm <sup>2</sup> )	error	(pScm <sup>2</sup> )	error	(pScm <sup>2</sup> )	error	(pScm <sup>2</sup> )	error		
Testes	150.20	6.1%	261.70	3.7%	751.15	6.1%	1308.76	3.7%	688.50	9.0%	722.60	7.2%	4.6	2.8
Ovaries	202.80	7.1%	230.00	7.8%	1014.20	7.1%	1150.23	7.8%	619.00	15.3%	670.20	18.0%	3.1	2.9
Red marrow	226.30	0.5%	192.30	0.6%	1131.73	0.5%	961.69	0.6%	730.90	0.8%	691.50	0.8%	3.2	3.6
Colon	220.60	0.7%	245.60	0.6%	1103.22	0.7%	1228.25	0.6%	706.50	1.2%	747.10	1.2%	3.2	3.0
Lungs	202.40	1.0%	201.00	1.0%	1012.20	1.0%	1005.20	1.0%	690.10	1.6%	703.10	1.6%	3.4	3.5
ST	195.10	3.5%	277.20	2.7%	975.70	3.5%	1386.28	2.7%	671.80	6.0%	856.00	5.0%	3.4	3.1
Urinary bladder	195.60	4.2%	282.40	2.6%	978.20	4.2%	1412.28	2.6%	686.80	7.4%	889.00	5.9%	3.5	3.1
Breasts	108.30	3.9%	234.70	2.2%	541.61	3.9%	1173.73	2.2%	521.40	5.1%	704.60	3.8%	4.8	3.0
Liver	210.70	1.0%	230.40	0.9%	1053.71	1.0%	1152.23	0.9%	712.90	1.2%	727.80	1.2%	3.4	3.2
Oesophagus	232.70	3.2%	234.80	3.3%	1163.73	3.2%	1174.23	3.3%	803.00	6.3%	737.30	6.7%	3.5	3.1
Thyroid	159.40	7.3%	279.30	5.7%	797.16	7.3%	1396.78	5.7%	543.60	11.8%	801.70	10.1%	3.4	2.9
Skin	147.00	0.5%	147.90	0.5%	735.15	0.5%	739.65	0.5%	570.40	1.0%	564.70	1.0%	3.9	3.8
Bone surface	204.50	0.4%	192.20	0.4%	1022.70	0.4%	961.19	0.4%	701.90	0.5%	692.10	0.5%	3.4	3.6
Adrenals**	308.00	5.1%	184.90	6.7%	1540.31	5.1%	924.68	6.7%	979.50	10.1%	823.70	11.4%	3.2	4.5
Brain**	195.40	1.2%	196.20	1.3%	977.20	1.2%	981.20	1.3%	637.20	1.4%	644.20	1.5%	3.3	3.3
SI**	236.60	1.2%	257.50	1.1%	1183.24	1.2%	1287.76	1.1%	759.20	1.5%	784.20	1.5%	3.2	3.0
Kidneys**	277.00	1.5%	177.80	2.3%	1385.28	1.5%	889.18	2.3%	819.50	2.6%	647.60	3.1%	3.0	3.6
Muscle**	203.30	0.2%	203.30	0.2%	1016.70	0.2%	1016.70	0.2%	686.80	0.2%	686.60	0.2%	3.4	3.4
Pancreas**	259.10	2.2%	192.20	2.8%	1295.76	2.2%	961.19	2.8%	835.60	3.5%	667.70	3.9%	3.2	3.5
Spleen**	229.40	3.3%	234.10	3.3%	1147.23	3.3%	1170.73	3.3%	705.30	5.7%	752.90	5.6%	3.1	3.2
Thymus**	151.10	7.4%	272.60	4.9%	755.65	7.4%	1363.27	4.9%	650.90	12.7%	769.40	8.8%	4.3	2.8
Uterus**	237.10	3.6%	259.00	3.6%	1185.74	3.6%	1295.26	3.6%	772.70	5.7%	779.60	5.6%	3.3	3.0
ULI	212.50	1.9%	242.70	1.7%	1062.71	1.9%	1213.74	1.7%	691.10	3.1%	712.70	2.9%	3.3	2.9
LLI	231.30	2.1%	249.60	1.9%	1156.73	2.1%	1248.25	1.9%	727.00	3.9%	792.80	3.6%	3.1	3.2
Remainder	204.50	0.2%	204.10	0.2%	1022.70	0.2%	1020.70	0.2%	688.30	0.2%	687.40	0.2%	3.4	3.4
Total body	200.90	1.6%	239.00	1.0%	1004.70	1.6%	1195.24	1.0%	684.10	2.1%	744.20	1.7%	3.4	3.1

\*1 effective dose

\*2 effective dose equivalent

\*\* organ or tissue included in Remainder

**Table A-2(11). Absorbed dose, effective dose and effective dose equivalent for 1500 MeV neutron calculated by HERMES code system**

Neutron energy=1500 MeV

Organ	Absorbed dose				Effective dose ( $w_R=5$ )				Dose equivalent Based on the New Q-L (ICRP Pub. 60)				Mean quality factor	
	AP (pGycm <sup>2</sup> )		PA (pGycm <sup>2</sup> )		AP (pScm <sup>2</sup> )		PA (pScm <sup>2</sup> )		AP (pScm <sup>2</sup> )		PA (pScm <sup>2</sup> )		AP	PA
		error		error		error		error		error		error		
Testes	160.80	5.7%	327.30	3.8%	804.00	5.7%	1636.50	3.8%	548.90	8.3%	913.60	6.0%	3.4	2.8
Ovaries	310.80	8.5%	291.60	6.5%	1554.00	8.5%	1458.00	6.5%	963.70	14.1%	833.00	13.7%	3.1	2.9
Red marrow	271.50	0.5%	230.80	0.5%	1357.50	0.5%	1154.00	0.5%	838.80	0.7%	778.40	0.8%	3.1	3.4
Colon	252.10	0.7%	287.60	0.6%	1260.50	0.7%	1438.00	0.6%	750.10	1.3%	822.20	1.1%	3.0	2.9
Lungs	241.20	1.0%	236.40	1.0%	1206.00	1.0%	1182.00	1.0%	755.60	1.5%	760.80	1.6%	3.1	3.2
ST	240.90	3.0%	341.20	2.6%	1204.50	3.0%	1706.00	2.6%	788.30	5.1%	967.20	4.7%	3.3	2.8
Urinary bladder	232.20	3.4%	326.00	2.9%	1161.00	3.4%	1630.00	2.9%	738.80	7.0%	904.40	6.3%	3.2	2.8
Breasts	130.90	4.0%	254.70	2.1%	654.50	4.0%	1273.50	2.1%	566.70	5.5%	716.90	3.7%	4.3	2.8
Liver	251.60	0.9%	277.40	0.9%	1258.00	0.9%	1387.00	0.9%	785.20	1.1%	811.40	1.1%	3.1	2.9
Oesophagus	287.30	3.1%	246.20	3.1%	1436.50	3.1%	1231.00	3.1%	898.20	6.0%	662.50	6.2%	3.1	2.7
Thyroid	212.40	6.6%	342.40	4.9%	1062.00	6.6%	1712.00	4.9%	758.30	10.8%	1026.00	9.9%	3.6	3.0
Skin	174.50	0.5%	173.90	0.5%	872.50	0.5%	869.50	0.5%	623.80	1.0%	618.50	1.0%	3.6	3.6
Bone surface	244.40	0.4%	227.90	0.4%	1222.00	0.4%	1139.50	0.4%	793.90	0.5%	766.40	0.5%	3.2	3.4
Adrenals**	346.70	5.1%	220.00	6.1%	1733.50	5.1%	1100.00	6.1%	945.40	9.1%	769.40	12.2%	2.7	3.5
Brain**	234.20	1.2%	236.10	1.1%	1171.00	1.2%	1180.50	1.1%	725.80	1.4%	739.70	1.4%	3.1	3.1
SI**	280.40	1.1%	308.00	1.1%	1402.00	1.1%	1540.00	1.1%	851.50	1.5%	893.90	1.5%	3.0	2.9
Kidneys**	325.60	1.5%	212.20	2.2%	1628.00	1.5%	1061.00	2.2%	891.40	2.5%	697.00	2.9%	2.7	3.3
Muscle**	240.40	0.2%	240.20	0.2%	1202.00	0.2%	1201.00	0.2%	756.90	0.2%	756.90	0.2%	3.1	3.2
Pancreas**	305.40	2.3%	240.50	2.6%	1527.00	2.3%	1202.50	2.6%	889.80	3.5%	785.90	3.8%	2.9	3.3
Spleen**	284.40	3.3%	310.50	3.2%	1422.00	3.3%	1552.50	3.2%	878.70	5.5%	905.20	5.7%	3.1	2.9
Thymus**	196.00	7.2%	306.00	4.6%	980.00	7.2%	1530.00	4.6%	765.50	11.6%	706.30	8.8%	3.9	2.3
Uterus**	270.70	3.7%	302.60	3.2%	1353.50	3.7%	1513.00	3.2%	831.40	5.6%	876.80	5.4%	3.1	2.9
ULI	244.90	1.9%	285.40	1.6%	1224.50	1.9%	1427.00	1.6%	749.20	3.3%	761.20	2.9%	3.1	2.7
LLI	261.70	1.9%	290.60	1.9%	1308.50	1.9%	1453.00	1.9%	751.30	3.6%	903.00	3.3%	2.9	3.1
Remainder	241.80	0.2%	241.40	0.2%	1209.00	0.2%	1207.00	0.2%	759.40	0.2%	759.20	0.2%	3.1	3.1
Total body	254.80	2.2%	285.40	1.0%	1274.00	2.2%	1427.00	1.0%	808.20	3.5%	840.00	1.7%	3.2	2.9

\*1 effective dose

\*2 effective dose equivalent

\*\* organ or tissue included in Remainder

**Table A-2(12). Absorbed dose, effective dose and effective dose equivalent for 3000 MeV neutron calculated by HERMES code system**

Neutron energy=3000 MeV

Organ	Absorbed dose				Effective dose ( $w_R=5$ )				Dose equivalent Based on the New Q-L (ICRP Pub. 60)				Mean quality factor	
	AP		PA		AP		PA		AP		PA		AP	PA
	(pGycm <sup>2</sup> )	error	(pGycm <sup>2</sup> )	error	(pScm <sup>2</sup> )	error	(pScm <sup>2</sup> )	error	(pScm <sup>2</sup> )	error	(pScm <sup>2</sup> )	error		
Testes	203.30	5.5%	361.10	3.3%	1016.50	5.5%	1805.50	3.3%	681.10	8.3%	851.70	6.5%	3.4	2.4
Ovaries	361.70	6.1%	369.80	5.6%	1808.50	6.1%	1849.00	5.6%	851.90	12.3%	1030.00	12.2%	2.4	2.8
Red marrow	348.00	0.5%	294.30	0.5%	1740.00	0.5%	1471.50	0.5%	983.70	0.7%	896.50	0.7%	2.8	3.0
Colon	330.50	0.6%	376.50	0.6%	1652.50	0.6%	1882.50	0.6%	938.60	1.1%	977.30	1.0%	2.8	2.6
Lungs	299.70	0.9%	287.40	0.9%	1498.50	0.9%	1437.00	0.9%	847.90	1.4%	819.30	1.4%	2.8	2.9
ST	285.20	2.7%	422.50	2.3%	1426.00	2.7%	2112.50	2.3%	830.50	5.4%	1116.00	4.7%	2.9	2.6
Urinary bladder	309.40	3.3%	394.30	2.4%	1547.00	3.3%	1971.50	2.4%	958.70	6.3%	996.50	5.1%	3.1	2.5
Breasts	171.30	3.6%	329.80	2.0%	856.50	3.6%	1649.00	2.0%	672.60	4.8%	909.50	3.6%	3.9	2.8
Liver	306.70	0.9%	349.10	0.9%	1533.50	0.9%	1745.50	0.9%	868.80	1.1%	942.50	1.1%	2.8	2.7
Oesophagus	346.30	2.8%	356.10	2.8%	1731.50	2.8%	1780.50	2.8%	1029.00	6.4%	954.30	6.0%	3.0	2.7
Thyroid	240.30	6.9%	393.90	4.9%	1201.50	6.9%	1969.50	4.9%	728.40	11.4%	1016.00	8.9%	3.0	2.6
Skin	214.90	0.5%	216.90	0.5%	1074.50	0.5%	1084.50	0.5%	675.10	0.9%	689.50	0.9%	3.1	3.2
Bone surface	312.80	0.3%	294.00	0.4%	1564.00	0.3%	1470.00	0.4%	917.70	0.4%	888.10	0.5%	2.9	3.0
Adrenals**	417.10	4.3%	294.00	5.6%	2085.50	4.3%	1470.00	5.6%	1029.00	9.0%	1004.00	10.0%	2.5	3.4
Brain**	300.30	1.1%	303.70	1.2%	1501.50	1.1%	1518.50	1.2%	852.90	1.3%	859.40	1.4%	2.8	2.8
SI**	358.50	1.0%	393.00	1.0%	1792.50	1.0%	1965.00	1.0%	982.00	1.4%	1038.00	1.3%	2.7	2.6
Kidneys**	416.80	1.4%	258.50	2.0%	2084.00	1.4%	1292.50	2.0%	1040.00	2.3%	802.10	2.9%	2.5	3.1
Muscle**	301.60	0.2%	301.90	0.2%	1508.00	0.2%	1509.50	0.2%	858.90	0.2%	859.70	0.2%	2.8	2.8
Pancreas**	379.10	2.1%	307.00	2.4%	1895.50	2.1%	1535.00	2.4%	1015.00	2.9%	903.80	3.5%	2.7	2.9
Spleen**	348.90	3.0%	375.20	3.0%	1744.50	3.0%	1876.00	3.0%	946.10	5.1%	1074.00	5.0%	2.7	2.9
Thymus**	223.30	6.3%	403.20	4.3%	1116.50	6.3%	2016.00	4.3%	626.20	10.5%	999.80	8.2%	2.8	2.5
Uterus**	327.00	3.3%	385.60	3.1%	1635.00	3.3%	1928.00	3.1%	900.80	5.8%	1017.00	4.8%	2.8	2.6
ULI	319.80	1.6%	380.80	1.5%	1599.00	1.6%	1904.00	1.5%	976.40	2.8%	974.60	2.6%	3.1	2.6
LLI	344.80	1.9%	370.90	1.7%	1724.00	1.9%	1854.50	1.7%	888.40	3.3%	980.80	3.0%	2.6	2.6
Remainder	303.70	0.2%	303.80	0.2%	1518.50	0.2%	1519.00	0.2%	862.80	0.2%	863.50	0.2%	2.8	2.8
Total body	313.10	1.5%	351.10	1.3%	1565.50	1.5%	1755.50	1.3%	874.40	2.6%	963.10	2.8%	2.8	2.7

\*1 effective dose

\*2 effective dose equivalent

\*\* organ or tissue included in Remainder

**Table A-2(13). Absorbed dose, effective dose and effective dose equivalent for 5000 MeV neutron calculated by HERMES code system**

Neutron energy=5000 MeV

Organ	Absorbed dose				Effective dose( $w_R=5$ )				Dose equivalent Based on the New Q-L (ICRP Pub. 60)				Mean quality factor	
	AP (pGycm <sup>2</sup> )		PA (pGycm <sup>2</sup> )		AP (pScm <sup>2</sup> )		PA (pScm <sup>2</sup> )		AP (pScm <sup>2</sup> )		PA (pScm <sup>2</sup> )		AP	PA
		error		error		error		error		error		error		
Testes	262.60	6.6%	409.90	3.2%	1313.00	6.6%	2049.50	3.2%	874.50	7.9%	1081.00	6.2%	3.3	2.6
Ovaries	361.40	5.6%	429.40	6.7%	1807.00	5.6%	2147.00	6.7%	777.00	10.9%	1340.00	12.6%	2.1	3.1
Red marrow	389.60	0.5%	325.50	0.5%	1948.00	0.5%	1627.50	0.5%	1112.00	0.7%	997.60	0.7%	2.9	3.1
Colon	355.90	0.6%	403.50	0.6%	1779.50	0.6%	2017.50	0.6%	1029.00	1.1%	1076.00	1.1%	2.9	2.7
Lungs	315.10	0.9%	302.30	0.9%	1575.50	0.9%	1511.50	0.9%	913.50	1.4%	900.00	1.4%	2.9	3.0
ST	333.40	3.3%	447.90	2.2%	1667.00	3.3%	2239.50	2.2%	960.30	5.3%	1199.00	4.1%	2.9	2.7
Urinary bladder	332.20	4.8%	441.50	2.5%	1661.00	4.8%	2207.50	2.5%	962.70	7.0%	1197.00	5.5%	2.9	2.7
Breasts	199.70	3.4%	352.20	2.1%	998.50	3.4%	1761.00	2.1%	693.40	4.6%	978.70	3.6%	3.5	2.8
Liver	342.70	0.9%	382.00	0.9%	1713.50	0.9%	1910.00	0.9%	987.20	1.1%	1042.00	1.0%	2.9	2.7
Oesophagus	376.90	2.8%	381.40	2.9%	1884.50	2.8%	1907.00	2.9%	1018.00	5.4%	1046.00	6.0%	2.7	2.7
Thyroid	273.50	7.2%	428.30	4.9%	1367.50	7.2%	2141.50	4.9%	818.00	12.5%	1120.00	8.9%	3.0	2.6
Skin	244.10	0.5%	243.60	0.5%	1220.50	0.5%	1218.00	0.5%	788.40	0.9%	786.50	0.9%	3.2	3.2
Bone surface	347.70	0.3%	319.70	0.4%	1738.50	0.3%	1598.50	0.4%	1033.00	0.4%	984.80	0.5%	3.0	3.1
Adrenals**	436.20	5.0%	306.70	5.5%	2181.00	5.0%	1533.50	5.5%	1127.00	9.6%	888.70	10.7%	2.6	2.9
Brain**	332.80	1.2%	331.60	1.2%	1664.00	1.2%	1658.00	1.2%	953.50	1.4%	942.40	1.4%	2.9	2.8
SI**	391.90	1.0%	427.10	1.0%	1959.50	1.0%	2135.50	1.0%	1126.00	1.4%	1168.00	1.3%	2.9	2.7
Kidneys**	459.40	1.3%	269.50	1.9%	2297.00	1.3%	1347.50	1.9%	1184.00	2.3%	854.20	2.7%	2.6	3.2
Muscle**	328.80	0.2%	327.40	0.2%	1644.00	0.2%	1637.00	0.2%	963.10	0.2%	956.70	0.2%	2.9	2.9
Pancreas**	399.50	1.9%	311.10	2.5%	1997.50	1.9%	1555.50	2.5%	1126.00	3.1%	964.00	3.5%	2.8	3.1
Spleen**	372.90	2.8%	387.80	3.1%	1864.50	2.8%	1939.00	3.1%	1063.00	5.0%	1112.00	5.3%	2.9	2.9
Thymus**	269.80	6.5%	443.80	4.1%	1349.00	6.5%	2219.00	4.1%	867.70	11.4%	980.30	8.7%	3.2	2.2
Uterus**	363.50	3.1%	408.20	3.4%	1817.50	3.1%	2041.00	3.4%	962.10	5.1%	1131.00	5.4%	2.6	2.8
ULI	345.10	1.6%	414.60	1.4%	1725.50	1.6%	2073.00	1.4%	1006.00	2.8%	1085.00	2.7%	2.9	2.6
LLI	370.30	1.9%	388.80	1.7%	1851.50	1.9%	1944.00	1.7%	1060.00	3.1%	1064.00	3.2%	2.9	2.7
Remainder	331.20	0.2%	329.30	0.2%	1656.00	0.2%	1646.50	0.2%	967.90	0.2%	960.40	0.2%	2.9	2.9
Total body	338.30	1.3%	384.70	1.6%	1691.50	1.3%	1923.50	1.6%	947.30	1.8%	1104.00	3.2%	2.8	2.9

\*1 effective dose

\*2 effective dose equivalent

\*\* organ or tissue included in Remainder

**Table A-2(14). Absorbed dose, effective dose and effective dose equivalent for 10000 MeV neutron calculated by HERMES code system**

Neutron energy=10000 MeV

Organ	Absorbed dose				Effective dose( $w_R=5$ )				Dose equivalent Based on the New Q-L (ICRP Pub. 60)				Mean quality factor	
	AP (pGycm <sup>2</sup> )		PA (pGycm <sup>2</sup> )		AP (pScm <sup>2</sup> )		PA (pScm <sup>2</sup> )		AP (pScm <sup>2</sup> )		PA (pScm <sup>2</sup> )		AP	PA
		error		error		error		error		error		error		
Testes	289.10	4.2%	445.90	4.2%	1445.50	4.2%	2229.50	4.2%	924.00	5.8%	1296.00	7.8%	3.2	2.9
Ovaries	366.70	5.1%	413.70	6.1%	1833.50	5.1%	2068.50	6.1%	954.80	10.2%	1234.00	11.9%	2.6	3.0
Red marrow	414.60	0.4%	353.30	0.6%	2073.00	0.4%	1766.50	0.6%	1232.00	0.5%	1098.00	0.7%	3.0	3.1
Colon	383.40	0.5%	432.10	0.6%	1917.00	0.5%	2160.50	0.6%	1165.00	0.8%	1202.00	1.0%	3.0	2.8
Lungs	331.20	0.7%	317.30	1.2%	1656.00	0.7%	1586.50	1.2%	1032.00	1.1%	991.30	1.9%	3.1	3.1
ST	344.00	2.0%	471.70	2.2%	1720.00	2.0%	2358.50	2.2%	1057.00	3.7%	1321.00	4.2%	3.1	2.8
Urinary bladder	340.00	2.3%	493.50	2.7%	1700.00	2.3%	2467.50	2.7%	1035.00	4.9%	1368.00	6.7%	3.0	2.8
Breasts	228.40	2.3%	359.70	2.2%	1142.00	2.3%	1798.50	2.2%	805.10	3.5%	1030.00	3.6%	3.5	2.9
Liver	365.90	0.7%	415.70	1.0%	1829.50	0.7%	2078.50	1.0%	1101.00	0.9%	1200.00	1.1%	3.0	2.9
Oesophagus	406.40	2.3%	407.50	2.9%	2032.00	2.3%	2037.50	2.9%	1204.00	4.1%	1180.00	6.0%	3.0	2.9
Thyroid	283.70	4.6%	478.60	4.8%	1418.50	4.6%	2393.00	4.8%	962.00	8.5%	1254.00	10.9%	3.4	2.6
Skin	263.40	0.5%	263.80	0.8%	1317.00	0.5%	1319.00	0.8%	874.90	0.7%	866.80	1.0%	3.3	3.3
Bone surface	367.60	0.3%	342.50	0.4%	1838.00	0.3%	1712.50	0.4%	1133.00	0.3%	1073.00	0.5%	3.1	3.1
Adrenals**	458.60	3.0%	340.90	5.6%	2293.00	3.0%	1704.50	5.6%	1410.00	6.4%	1005.00	10.3%	3.1	2.9
Brain**	365.10	0.8%	363.90	1.2%	1825.50	0.8%	1819.50	1.2%	1075.00	1.0%	1054.00	1.4%	2.9	2.9
SI**	412.10	0.8%	462.70	1.0%	2060.50	0.8%	2313.50	1.0%	1197.00	1.0%	1319.00	1.4%	2.9	2.9
Kidneys**	487.10	1.1%	308.50	2.2%	2435.50	1.1%	1542.50	2.2%	1365.00	1.7%	1003.00	2.8%	2.8	3.3
Muscle**	354.00	0.2%	353.60	0.2%	1770.00	0.2%	1768.00	0.2%	1068.00	0.2%	1063.00	0.2%	3.0	3.0
Pancreas**	423.60	1.4%	342.70	2.6%	2118.00	1.4%	1713.50	2.6%	1265.00	2.4%	1003.00	3.7%	3.0	2.9
Spleen**	430.80	2.2%	444.70	3.2%	2154.00	2.2%	2223.50	3.2%	1222.00	3.5%	1328.00	5.5%	2.8	3.0
Thymus**	310.60	4.0%	591.70	15.8%	1553.00	4.0%	2958.50	15.8%	1047.00	7.7%	1442.00	12.4%	3.4	2.4
Uterus**	410.90	2.3%	491.20	3.3%	2054.50	2.3%	2456.00	3.3%	1178.00	3.8%	1421.00	4.9%	2.9	2.9
ULI	373.20	1.2%	442.00	1.4%	1866.00	1.2%	2210.00	1.4%	1160.00	2.0%	1244.00	2.6%	3.1	2.8
LLI	396.90	1.5%	419.10	2.0%	1984.50	1.5%	2095.50	2.0%	1172.00	2.4%	1146.00	3.2%	3.0	2.7
Remainder	356.60	0.2%	356.10	0.2%	1783.00	0.2%	1780.50	0.2%	1073.00	0.2%	1068.00	0.2%	3.0	3.0
Total body	355.50	1.1%	409.70	1.0%	1777.50	1.1%	2048.50	1.0%	1058.00	2.0%	1187.00	2.0%	3.0	2.9

\*1 effective dose

\*2 effective dose equivalent

\*\* organ or tissue included in Remainder

**Figure A-1. Comparison of effective dose E for AP irradiation neutron beam (the error bars are within circles)**

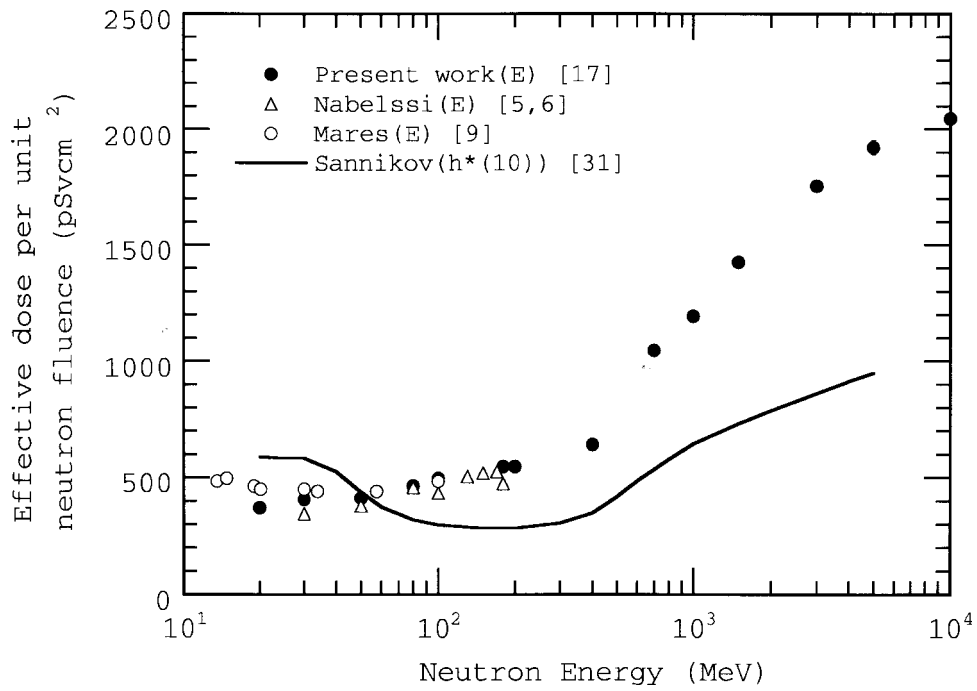


**Figure A-2. Comparison of effective dose E for PA irradiation neutron beam (the error bars are within circles)**

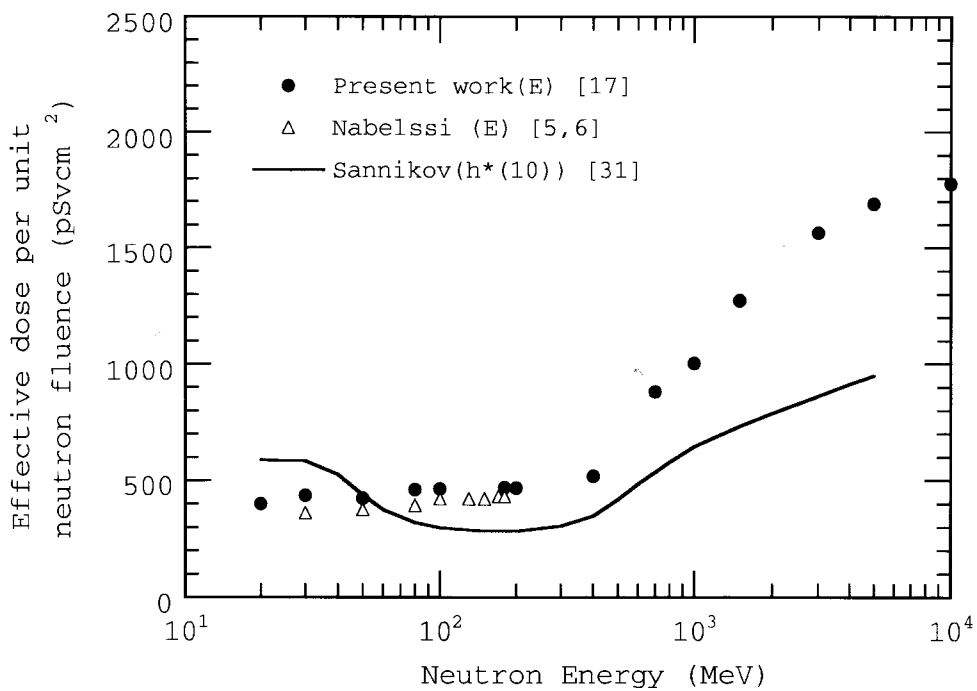


**Figure A-3. Comparison of effective dose equivalent  $H_E$  for AP irradiation neutron beam (the error bars are within circles)**

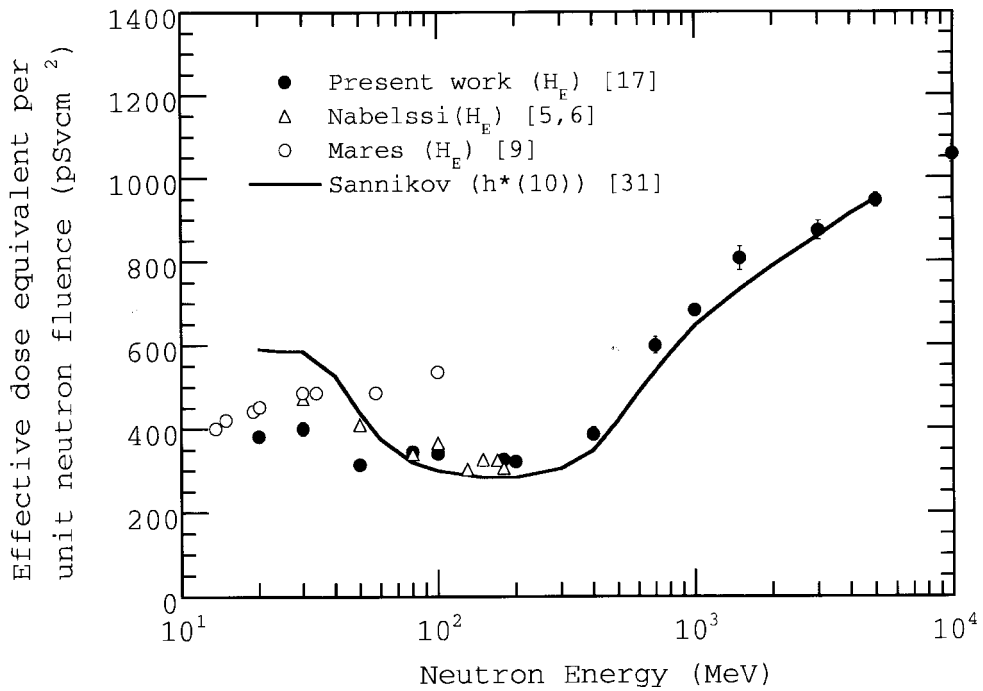
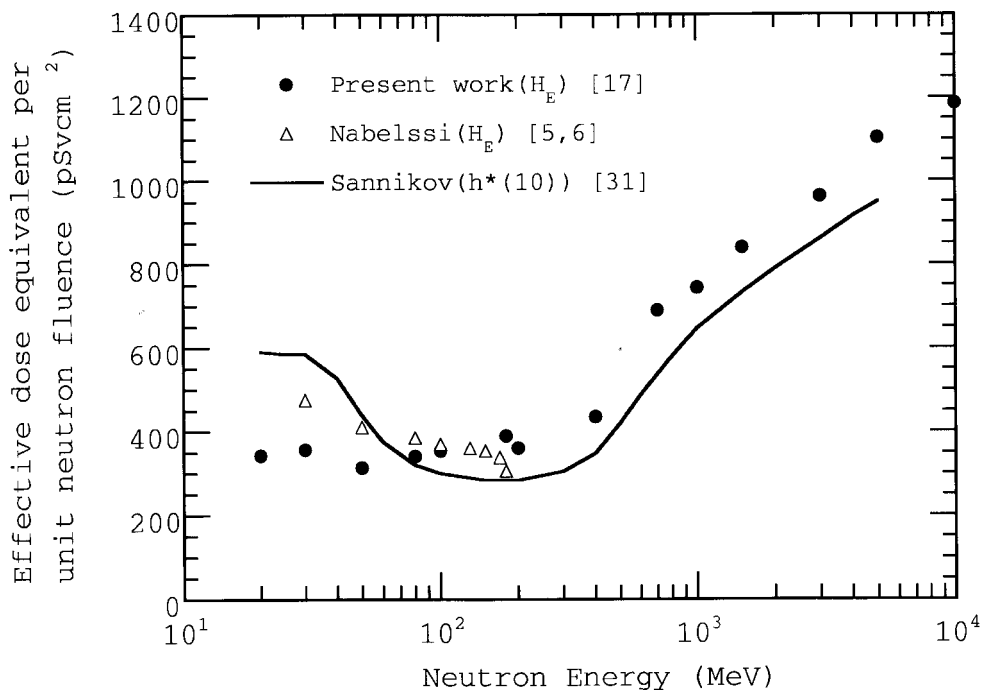


**Figure A-4. Comparison of effective dose equivalent  $H_E$  for PA irradiation neutron beam (the error bars are within circles)**



## Appendix B

*Dose conversion coefficients from proton fluence  
to E and H<sub>E</sub> from the energy range of 20 MeV to 10 Gev*

**Table B-1. Absorbed dose, effective dose and effective  
dose equivalent for neutron calculated by HERMES code system**

Neutron energy (MeV)	Absorbed dose				Effective dose (W <sub>R</sub> =5)				Effective dose equivalent				Mean quality factor	
	AP		PA		AP		PA		Based on the New Q-L (ICRP Pub. 60)		Based on the New Q-L (ICRP Pub. 60)		AP	PA
	(pGycm <sup>2</sup> )	error	(pGycm <sup>2</sup> )	error	(pScm <sup>2</sup> )	error	(pScm <sup>2</sup> )	error	(pScm <sup>2</sup> )	error	(pScm <sup>2</sup> )	error		
20	148.80	0.60%	43.65	0.10%	744.00	0.60%	218.25	0.10%	354.50	0.80%	82.71	0.10%	2.38	1.89
30	390.50	0.80%	73.59	0.10%	1952.50	0.80%	367.95	0.10%	731.60	0.90%	125.70	0.20%	1.87	1.71
50	1027.00	0.80%	132.70	0.20%	5135.00	0.80%	663.50	0.20%	1515.00	0.90%	206.20	0.30%	1.48	1.55
80	1149.00	0.50%	432.00	0.20%	5745.00	0.50%	2160.00	0.20%	1502.00	0.50%	604.50	0.30%	1.31	1.40
100	1348.00	0.30%	508.70	0.20%	6740.00	0.30%	2543.50	0.20%	1721.00	0.50%	642.90	0.30%	1.28	1.26
180	980.10	0.40%	1071.00	0.40%	4900.50	0.40%	5355.00	0.40%	1224.00	1.10%	1338.00	0.70%	1.25	1.25
200	892.10	0.50%	946.20	0.40%	4460.50	0.50%	4731.00	0.40%	1166.00	1.70%	1210.00	0.70%	1.31	1.28
400	610.30	0.60%	631.70	0.40%	3051.50	0.60%	3158.50	0.40%	913.30	2.20%	899.60	1.80%	1.50	1.42
700	586.60	0.70%	610.60	0.40%	2933.00	0.70%	3053.00	0.40%	1058.00	2.50%	1082.00	1.20%	1.80	1.77
1000	584.40	0.70%	607.20	0.50%	2922.00	0.70%	3036.00	0.50%	1105.00	2.50%	1130.00	1.30%	1.89	1.86
1500	585.70	0.80%	624.40	0.50%	2928.50	0.80%	3122.00	0.50%	1106.00	2.80%	1180.00	1.20%	1.89	1.89
3000	641.80	0.70%	678.90	0.60%	3209.00	0.70%	3394.50	0.60%	1191.00	1.90%	1310.00	1.40%	1.86	1.93
5000	670.10	0.90%	709.10	0.50%	3350.50	0.90%	3545.50	0.50%	1324.00	2.40%	1408.00	1.20%	1.98	1.99
10000	690.50	0.50%	735.70	0.60%	3452.50	0.50%	3678.50	0.60%	1376.00	1.00%	1505.00	2.40%	1.99	2.05

**Figure B-1. Comparison of effective dose E for AP irradiation proton beam  
(the error bars with Monte Carlo calculation are smaller than symbols)**

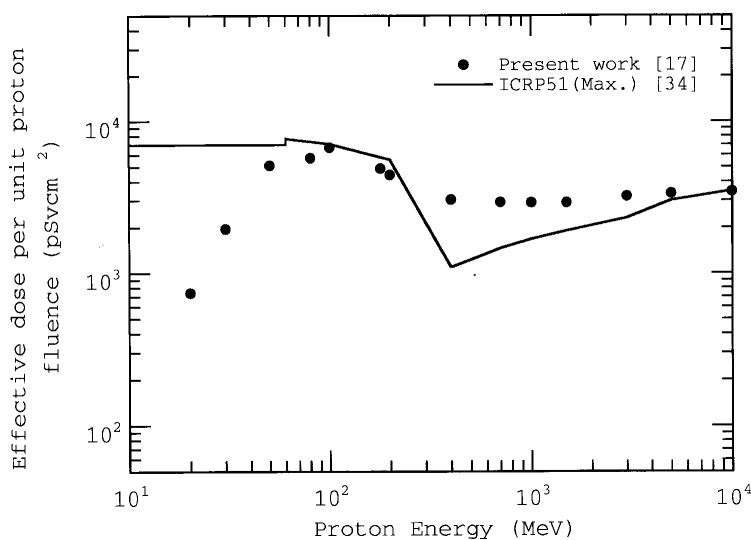


**Figure B-2. Comparison of effective dose E for PA irradiation proton beam (the error bars with Monte Carlo calculation are smaller than symbols)**

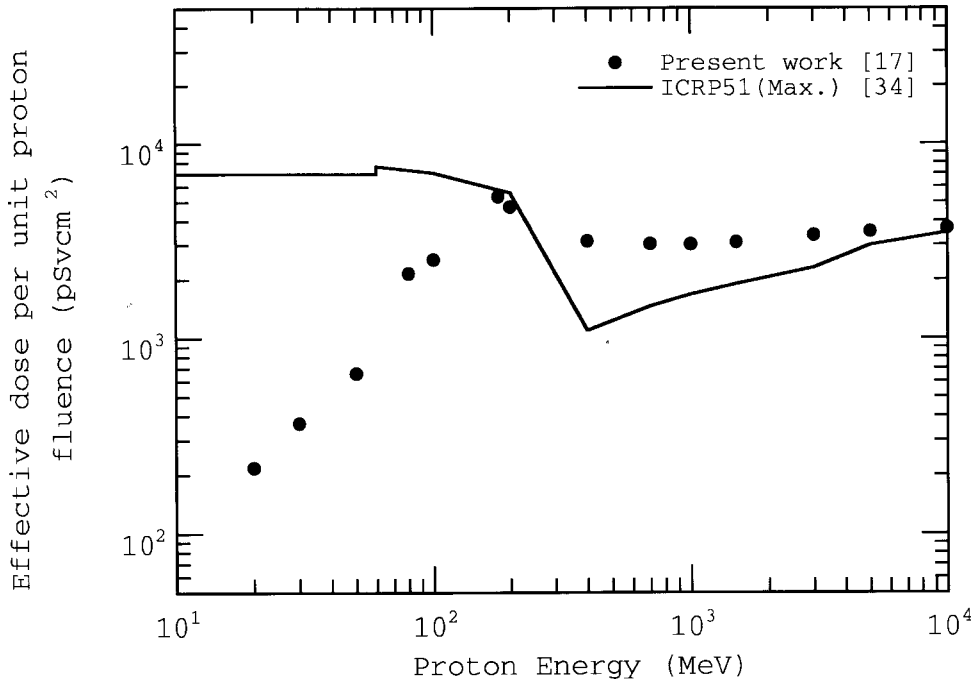


**Figure B-3. Comparison of effective dose equivalent H<sub>E</sub> for AP irradiation proton beam (the error bars with Monte Carlo calculation are smaller than symbols)**

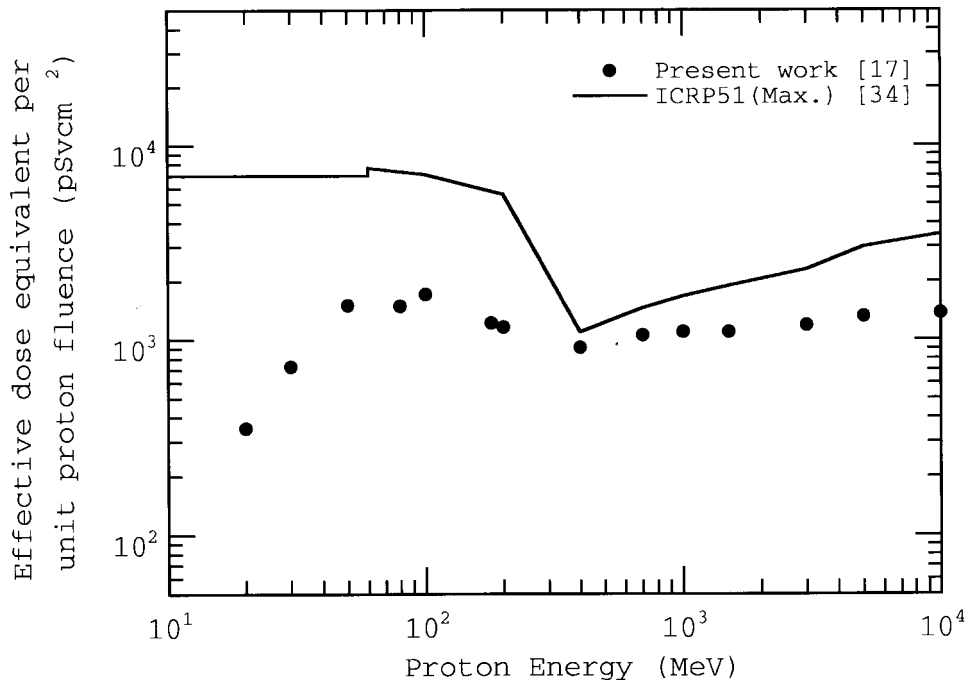
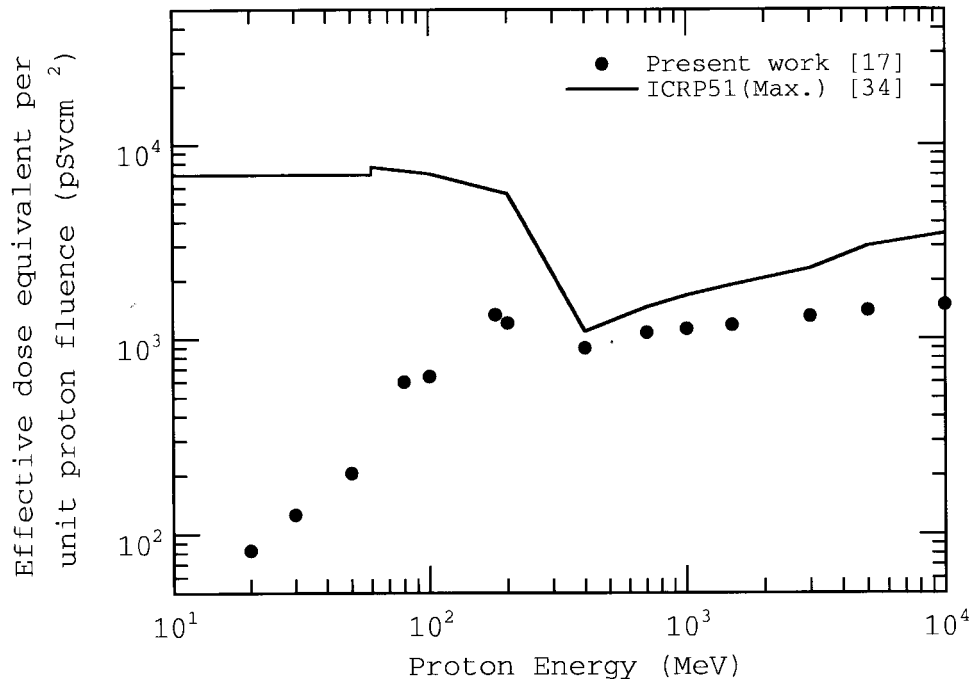


**Figure B-4. Comparison of effective dose equivalent  $H_E$  for PA irradiation proton beam (the error bars with Monte Carlo calculation are smaller than symbols)**





# SESSION V

## **Present Status of Computer Codes and Cross-Section and Shielding Data Libraries**

*Chairs: B. Kirk and P. Vaz*



## **PROGRESS REPORT ON THE COLLECTION OF COMPUTER CODES AND DATA SETS FOR ACCELERATOR SHIELDING ANALYSIS**

**Bernadette L. Kirk**

ORNL/RSICC, Oak Ridge, TN 37831-6362, USA

**Enrico Sartori and Pedro Vaz**

OECD/NEA/DB, 12 Boulevard des Iles, 92130 Issy-les-Moulineaux, France

### **Abstract**

During the Specialists Meeting on Shielding Aspects of Accelerators, Targets and Irradiation Facilities held in Arlington, Texas, on 28-29 April 1994 (SATIF-1) it was felt that the NEA/DB (Data Bank of the Nuclear Energy Agency/Organisation for Economic Co-operation and Development (OECD), in Paris, France) and RSICC (Radiation Safety Information Computational Centre (formerly RSIC, Radiation Shielding Information Centre) at the Oak Ridge National Laboratory (ORNL), in Oak Ridge, Tennessee, USA) can provide beneficial services to the accelerator shielding specialists by packaging and disseminating modern frozen versions of the transport and auxiliary codes and data libraries in common use. At the same time it was recommended that these two centres try to obtain new or updated versions of a number of computer codes, some performing low-energy neutron transport, others modelling hadronic and electromagnetic cascades or implementing intermediate energy nuclear models. Then, at the Second Specialists Meeting on Shielding Aspects of Accelerators, Targets and Irradiation Facilities (SATIF-2) held at CERN (European Laboratory for Particle Physics in Geneva, Switzerland) on 12-13 October 1995, a status report was presented on the collection of computer codes and data libraries useful for the communities of physicists, engineers and technicians working in the fields of shielding modelling. This note summarises the progress made since then in collecting new computer codes and data libraries. An exhaustive survey is also presented in the form of tables displaying the computer codes available from the two centres in the areas previously mentioned. These tables supersede those presented both in the Arlington and CERN Specialists Meetings<sup>\*,†</sup>.

---

\* Proceedings of the Specialists Meeting on Shielding Aspects of Accelerators, Targets and Irradiation Facilities, held in Arlington, Texas (USA) on 28-29 April 1994, published as an OECD document ISBN 92-64-14327-0.

† Proceedings of the Second Specialists Meeting on Shielding Aspects of Accelerators, Targets and Irradiation Facilities (SATIF-2), held at CERN, Geneva (Switzerland) on 12-13 October 1995, published as an OECD document ISBN 92-64-15287-3

## **Introduction**

RSICC and the NEA/DB collect, test and distribute computer programs and data in the field of nuclear applications. This activity is co-ordinated with other similar centres in the United States (ESTSC, NNDC), Japan (RIST) and outside the OECD area through an arrangement with the IAEA.

This information is shared world-wide for the benefit of scientists and engineers working on the safe and economic use of nuclear technology. Among the fields RSICC is specialised, technology for radiation transport holds an eminent place; the NEA/DB covers instead a wider range of topics with less specific expertise. The two centres share to a large extent the same programs through a long standing co-operative arrangement.

Major emphasis has been given in the past to nuclear energy applications. In order to respond to needs expressed by new communities of users, covering other aspects of nuclear technology, special efforts were made to acquire programs and data in their fields of interest. Shielding aspects of accelerators and targets has in fact received attention over the last several years. It is the intention of both centres to devote additional effort so that state-of-the-art technology in this field is shared among the specialists.

## **Radiation Safety Information Computational Centre (RSICC)**

RSICC (formerly RSIC, Radiation Shielding Information Centre) is part of the Radiation Information Analysis Section (RIAS), embedded in the Computational, Physics and Engineering Division of the directorate for Computing, Robotics and Education (CRE) at ORNL. That Division is noted for its role as a leader in the development of radiation transport technology over the years. It is very beneficial for RSICC to be located with such an organisation so that staff members have close proximity to these major developments and the transfer of such technology is enhanced by a climate of close co-operation.

In practice, RSICC is an information analysis centre following the concepts suggested by Alvin Weinberg in 1963 [1]. It is staffed by scientists, engineers, computer specialists and support personnel. While being physically located at ORNL, it is embedded in the national research and development of its sponsors and interacts dynamically with contributors and users.

It was founded in 1962 by the US Atomic Energy Commission to provide support for its reactor research programmes. Over the years the scope of RSICC has broadened to include radiation transport for nuclear weapons, radioisotopes, accelerators, fusion reactors, nuclear waste. It collects, analyses, maintains and distributes computer software and data sets in the areas of radiation transport and safety. Current sponsors include the US Department of Energy (Nuclear Energy, Fusion, Defense Programs, Environmental), and the Defense Nuclear Agency.

## **The NEA Data Bank (NEA/DB)**

The NEA Data Bank is part of the OECD Nuclear Energy Agency, financed by 21 of the 29 OECD countries (Austria, Belgium, Czech Republic, Denmark, Finland, France, Germany, Greece, Italy, Japan, Republic of Korea, Hungary, Mexico, The Netherlands, Norway, Portugal, Spain, Sweden, Switzerland, Turkey, United Kingdom). A co-operative agreement is in force which covers the exchange of computer programs and data among these countries, Canada and the USA. Exchange with other countries is governed by an arrangement with the International Atomic Energy Agency.

The work programme is approved yearly by the Nuclear Science Committee, one of the NEA Committees (others cover Nuclear Safety, Development, Waste Management).

The staff consists of physicists, engineers, computing experts and is international. In order to stay in close contact with the scientific community and engineers in the Member countries, modern communication systems are extensively used.

### **Progress since the second SATIF meeting (October 1995) – Highlights**

Since the second SATIF meeting held in October 1995 at CERN, emphasis has been put in the collection of codes performing computations of the differential or total cross-sections and implementing model predictions for nuclear reactions of neutrons and charged particles in the energy range above 20 MeV (codes CCMRN, HFMOD, OPTMOD and SPEC, among others). Many additional options and physics have been incorporated in “super-codes” such as HETC, leading to the development of multiple versions (e.g. HETC/Bruyere, HETC-FRG, HETC/KFA2, HETC-3STEP) used in benchmarking exercises or Model Intercomparison exercises (see for instance [4]). Other major developments occurred, namely:

- in the area of electron-photon transport, a new code PENELOPE has been released and the Version 3.0 of the NRCC EGS4 distribution for several UNIX platforms has been made available;
- the new system DOORS (discrete ordinates system for deep penetration neutron and gamma transport) has been released;
- new versions of the HERMES system and of the program CALOR has been released;
- the newly released version of the plotting program EPICSHOW allows to display and visualise neutron data, in addition to the electron/positron and photon data;
- a new version of NJOY has been released;
- the new data libraries ENDLIB-94 (coupled electron & photon transport library in ENDL format), HILO86R (update of HILO86, 66 neutron groups up to 400 MeV and 22 gamma groups up to 20 MeV), VITAMIN-B6 (cross-sections, in AMPX master library format, derived from ENDF/B-VI Release 3, 199 neutron groups and 42 gamma groups) and XCOM (photon cross-sections from 1 KeV up to 100 GeV) have been released;
- a new release of the time dependent, coupled neutron-photon-electron Monte Carlo code MCNP4B;
- as a general trend, we have assisted the released of new versions of existing or newly produced codes for different UNIX platforms and systems.
- in the framework of the DOELAP program (please refer to section *Progress report on anthropomorphic computational models* for additional details), the new code MRIPP will soon be available.

Please refer to Tables 1 through 4 for a more detailed description of the programs and data libraries available at present.

## **Progress report on SINBAD, the Shielding Benchmarks Database**

The Shielding Integral Benchmark Archive and Database (SINBAD) is a new electronic database [5] developed to store a variety of radiation shielding benchmark data in a format that will allow them to be easily retrieved and incorporated into user's calculations. A brief description of the selected benchmarks was first given in [6], at the SATIF-2 Meeting. Since then, several actions have been undertaken in order to collect and add relevant benchmark data to the SINBAD database. Indeed, about two dozen benchmark data sets (described in Tables 5 and 6), have been compiled and peer-reviewed. They are being incorporated into SINBAD, and will be available to the user community via RSICC and the NEA/DB. Further progress is underway and additional data sets, concerning fusion and accelerator shielding benchmarks, will be incorporated into SINBAD in 1997.

## **Progress report on anthropomorphic computational models**

The results of an enquiry performed by E. Sartori on anthropomorphic computational models for the SATIF-2 Meeting were published in [7]. Since then:

- Laurie Waters has performed an extensive compilation of bibliography on the anthropomorphic models as well as on other topics related to medical applications. These and other results are available at the LANL Web site, under the XTM Medical Applications Directory (<http://www.xdiv.lanl.gov/XTM/app/med/>).
- Robert Loesch has started to compile a library of input files in the framework of the activities of the Department of Energy's Laboratory Accreditation Program (DOELAP), to evaluate, using MCNP, phantoms used for dosimetric irradiation and calibration of in vivo counting systems. This library will be made available through the DOELAP's Web home page and will include data mainly on:
  - irradiation phantoms;
  - in vivo phantoms.
- The NEA has contacted the developers of anthropomorphic computational models asking them to release the computer specific inputs. This work will be co-ordinated with LANL and DOELAP.

## REFERENCES

- [1] President's Science Advisory Committee (PSAC), "Science, Government, and Information: The Responsibilities of the Technical Community and the Government in the Transfer of Information", (commonly known as the Weinberg Report), US Government Printing Office, 10 January 1963, 55 p.
- [2] "Sharing of Computer Codes and Data for Accelerator Shield Modelling", by R.W. Roussin and E. Sartori, in Proceedings of the Specialists Meeting on Shielding Aspects of Accelerators, Targets and Irradiation Facilities, held in Arlington, Texas (USA) on 28-29 April 1994, published as an OECD document ISBN 92-64-14327-0.
- [3] "Status Report on the Collection of Computer Codes and Data Libraries for Accelerator Shielding Modelling", by R.W. Roussin, E. Sartori and P. Vaz, in Proceedings of the Second Specialists Meeting on Shielding Aspects of Accelerators, Targets and Irradiation Facilities", held at CERN, Geneva (Switzerland) on 12-13 October 1995, published as an OECD document ISBN 92-64-15287-3.
- [4] "International Codes and Model Intercomparison for Intermediate Energy Activation Yields", OECD/NEA Nuclear Science Committee (NSC) publication, January 1997.
- [5] "SINBAD – A Shielding Integral Benchmark Archive and Database for PCs", by H.T. Hunter *et. al.*, in Proceedings of the Eighth International Conference on Radiation Shielding, Arlington, Texas, 24-28 April 1994, p. 795, American Nuclear Society, La Grange Park, Illinois, 1994.
- [6] "SINBAD – Shielding Integral Benchmark Archive and Database", by H.T. Hunter, D.T. Ingersoll, R.W. Roussin, C.O. Slater, I. Kodeli and E. Sartori, in Proceedings of the Second Specialists Meeting on Shielding Aspects of Accelerators, Targets and Irradiation Facilities", held at CERN, Geneva (Switzerland) on 12-13 October 1995, published as an OECD document ISBN 92-64-15287-3.
- [7] "Results of Inquiry on Anthropomorphic Computational Models", by E. Sartori in Proceedings of the Second Specialists Meeting on Shielding Aspects of Accelerators, Targets and Irradiation Facilities", held at CERN, Geneva (Switzerland) on 12-13 October 1995, published as an OECD document ISBN 92-64-15287-3.
- [8] "Experimental Benchmark Compilations Housed at SCINBAD – Shielding Criticality Integral Benchmark Archive and Database", private communication by H.T. Hunter, April 1997.

**Table 1. List of programs and data in alphabetical order**

<b>Name</b>	<b>Identification</b>	<b>Function</b>
ACTIV-87(*)	IAEA1275	Library with fast neutron activation x-sections
AIRSCAT	CCC-0341	Dose rate from gamma air scattering, single scat. approx.
ALBEDO	NEA 1353	Gamma, neutron attenuation in air ducts
ALDOSE(*)	CCC-0577	Calculates of absorbed dose and dose equivalent rates as function of depth in water irradiated by alpha source
ALICE91	PSR-0146	Precompound/compound nuclear decay model
ALPHN(*)	CCC-0612	Calculates the (alpha,n) production rate in a mixture receiving alpha particles from emitting actinides
AMALTHEE	NEA 0675	Emission spectra for n, p, d, h3, he3, alpha reaction
ANISN	CCC-0254	1-D Sn, n, gamma transport in slab, cylinder, sphere
ASOP	CCC-0126	1-D Sn shield calculation
ASTAR(*)	IAEA1282	Calculates stopping power and range for alphas
ASTROS	CCC-0073	Primary/secondary proton dose in sphere/slab tissue
AUJP	IAEA0906	Optical potential parameters search by chi**2 method
BALTORO	NEA 0675	n, gamma transport perturbation from MORSE, ANISN calculation
BASACF(***)	IAEA0953	Integral neutron adjustment and dosimetry
BERMUDA	NEA 0949	1-D,2-D,3-D n. gamma transport for shielding
BETA-2B	CCC-0117	MC time-dependent bremsstrahlung, electron transport
BREESE	PSR-0143	Distribution function for MORSE from albedo data
BREM RAD	CCC-0031	External/internal bremsstrahlung
BRHGAM	CCC-0350	MC absorbed dose from x-rays in phantom
CADE	NEA 1020	Multiple particle emission xsec by Weisskopf-Ewing
CALOR89	CCC-0610	MC system for design, analysis of calorimeter system
CALOR93		Idem
CALOR95(***)		Idem
CAMERA	CCC-0240	Radiation transport and computerised man model
CARP-82	PSR-0131	Currents for BREESE from DOT flux
CASCADE	CCC-0176	High energy electron-photon transport in matter
CASIM	NESC0742	MC high energy cascades in complex shields
CCRMN(***)	IAEA1347	Computation of reactions of a medium-heavy nucleus with six light particles
CEM95(*)	IAEA1247	MC calculation of nuclear. reactions (Cascade Exciton Model)
CENDL(*)	IAEA1256	Chinese Evaluated Nuclear Data Library, namely the Optical Model Parameters for 6 types of projectiles (neutron, proton, deuteron, triton, <sup>3</sup> He and <sup>4</sup> He)
CEPXS/ONELD	CCC-0544	1-D coupled electron photon multigroup transport

Programs marked (\*) or (\*\*) in the following table, represent additions to the corresponding table of [2]

(\*) Programs available

(\*\*) Programs known but not available

(\*\*\*) Additions since the SATIF-2 meeting

---

CCC-,PSR-,DLC- : original packaging by RSICC  
 NESC : original packaging by NESC (now ESTSC)  
 USCD : originated in US/Canada, packaged by NEA/DB  
 NEA, IAEA : original packaging by NEA/DB  
 <blank> : acquisition sought  
 xsec : cross-section  
 lib. : library

**Table 1. List of programs and data in alphabetical order (cont.)**

Name	Identification	Function
CFUP1	IAEA1266	n, charged-particle reaction of fissile nuclei E<33 MeV
CHARGE-2/C	CCC-0070	Electron, p, heavy particle flux/dose behind shield
CHUCK	USCD1021	n, charged particle xsec, coupled channel model
CMUP2	IAEA1265	Reaction xsec for n ,p, d, t, he3, he4, E<50 MeV
COLLI-PTB	NEA 1126	MC n fluence spectra for 3-D collimator system
COMNUC3B	PSR-0302	Compound nucleus interaction in n reactions
COVFILES(*)	DLC-0091	Library of neutron x-sections covariance data, useful to estimate radiation damage or heating
DANTSYS(*)	CCC-0547	1-D, 2-D, 3-D Sn neutron, photon transport
DASH	CCC-0366	Void tracing Sn – MC coupling with fluxes from DOT
DCTDOS	CCC-0520	n, gamma penetration in composite duct system
DDCS(*)	IAEA1290	Calculation of neutron, proton, deuteron, triton, He3, and alpha induced reactions of medium heavy nuclei in the energy range up to 50 MeV
DISDOS	CCC-0170	Dose from external photons in phantom
DOMINO	PSR-0064	Coupling of Sn DOT with MC MORSE
DOORS3.1(***)	CCC-0650	Discrete ordinates system for deep penetration neutron and gamma transport
DORT	CCC-0543	1-D 2-D Sn n, photon transport with deep penetration
DOSDAT-2	DLC-0079	Gamma, electron dose factors data lib. for body organs
DOSEDAT-DOE	DLC-0144	Dose rate factors for external photon, electron exposure
DOT	CCC-0276	2-D Sn n, photon transport with deep penetration
DROSG-87(*)	IAEA1234	Library of Legendre coefficients for neutron reactions
DUST	CCC-0453	Albedo MC simulation of n streaming inducts
DWBA82	NEA 1209	Distorted Wave Born Approximation nuclear model
DWUCK-4	NESC9872	Distorted Wave Born Approximation nuclear model
E-DEP-1	CCC-0275	Heavy ion energy deposition
EADL(*)	USCD1192	Library of atomic subshell and relaxation data
ECIS-95(*)	NEA 0850	Schroedinger/Dirac nuclear model with experimental fit
ECPL-86(*)	DLC-0106	Evaluated charged particle cross-sections
EDMULT	NEA 0969	Electron depth dose in multilayer slab absorbers
EEDL(*)	USCD1193	Electron interaction x-section from 10 eV to 100 GeV
EGS4	CCC-0331	MC electron photon shower simulation
EGS4(***)	CCC-0331	Version 3.0 of the UNIX distribution of EGS4
ELBA	CCC-0119	Bremsstrahlung dose from electron flux on Al shield
ELPHIC-PC	IAEA1223	Statistical model MC simulation of heavy ion reaction
ELPHO	CCC-0301	MC muon, electron, positron generation from pions

Programs marked (\*) or (\*\*) in the following table, represent additions to the corresponding table of [2]

(\*) Programs available

(\*\*) Programs known but not available

(\*\*\*) Additions since the SATIF-2 meeting

---

CCC-,PSR-,DLC- : original packaging by RSICC  
 NESC : original packaging by NESC (now ESTSC)  
 USCD : originated in US/Canada, packaged by NEA/DB  
 NEA, IAEA : original packaging by NEA/DB  
 <blank> : acquisition sought  
 xsec : cross-section  
 lib. : library

**Table 1. List of programs and data in alphabetical order (cont.)**

Name	Identification	Function
ELTRAN	CCC-0155	MC 1-D electron transport
EMPIRE-MSC	IAEA1169	Multistep compound nucleus/pre-equilibrium xsec
ENLOSS	PSR-0047	Energy loss of charged particles
ENDLIB-94(***)	DLC-0179	Coupled electron & photon transport library (in LLL ENDL format)
EPDL-VI/MOD(*)	USCD1187	Photon interaction x-sections library(10 eV to 100 GeV)
EPICSHOW(*)	IAEA1285	Interactive Viewing of the Electron-Photon Interaction Code (EPIC) system databases (10 eV < E < 1 GeV)
EPICSHOW-96.1 (***)		Interactive Viewing of the Electron-Photon Interaction Code (EPIC) system databases and Neutron cross-section data
ERINNI	NEA 0815	Multiple cascades emission spectra by optical model
ESTAR(*)	IAEA1282	Calculates stopping power and range for electrons
ETRAN	CCC-0107	MC electron, gamma transport with secondary radiation
EVA(*)		Codes performing the nuclear evaporation processes (working on the output from ISABEL)
EVALPLOT(*)	IAEA0852	Plots x-sections in ENDF/B format, angular and energy distributions
EVAP_F(**)		Modified version of the Dresner evaporation code (run in HETC@PSI)
EXIFONGAMMA	IAEA1211	n, alpha, proton, gamma emission spectra model
FALSTF	CCC-0351	n, gamma flux detector response outside cylindrical shields
FEM-RZ	NEA 0566	2-D multigroup n transport in r-z geometry
FGR-DOSE(*)	DLC-0167	Library of dose coefficients for intake and exposure to radionuclides
FLEP	DLC-0022	Neutron, proton non-elastic xsec and spectra E<400MeV
FLUKA	CCC-0207	MC high energy extranuclear hadron cascades
FLUNEV-DESY		
FOTELP	CCC-0581	MC photons, electrons and positron transport
FRITIOF(**)		Hadronic cascades in high-energy Heavy Ion Collisions (used to be available from the CERN Program Library)
FSMN	IAEA1264	Fission spectra by compound-nucleus optical model
FSXLIB-J3R2(***)	NEA 1424	JENDL-3 Evaluated Nuclear Data File, fusion neutronics
G33-GP	CCC-0494	Multigroup gamma scattering using gp build-up factor
GAMMONE	NEA 0268	MC gamma penetration from various geometrical sources
GBANISN(***)	CCC-0628	1-D neutron & gamma fluxes with group band fluxes
GEANT-CERN		

Programs marked (\*) or (\*\*) in the following table, represent additions to the corresponding table of [2]

(\*) Programs available

(\*\*) Programs known but not available

(\*\*\*) Additions since the SATIF-2 meeting

---

CCC-,PSR-,DLC- : original packaging by RSICC  
 NESG : original packaging by NESG (now ESTSC)  
 USCD : originated in US/Canada, packaged by NEA/DB  
 NEA, IAEA : original packaging by NEA/DB  
 <blank> : acquisition sought  
 xsec : cross-section  
 lib : library

**Table 1. List of programs and data in alphabetical order (cont.)**

Name	Identification	Function
GGG-GP	CCC-0564	Multigroup gamma-ray scattering – build-up factors
GNASH-FKK(*)	PSR-0125	Multi-step direct and compound and Hauser Feshbach models
GNASH-LANL	PSR-0125	Pre-equilibrium/statistical xsec, emission spectra
GRACE-1	NESC0045	Multigroup gamma attenuation, dose in slab
GRAPE	NEA 1043	Precompound/compound nuclear reaction models
GRPANL(***)	PSR-0321	Germanium gamma and alpha detector spectra unfolding
HELLO	DLC-0058	47 n, 21 gamma group coupled xsec from VITAMIN-C library
HERMES-KFA	NEA 1265	MC high-energy radiation transport
HERMES96b(***)		Idem
HETC NMTC	CCC-0178	MC high energy nucleon meson cascade transport
HETC-KFA	CCC-0496	MC high energy nucleon-meson cascades
HETC95(**)		MC high energy nucleon-meson cascades and transport
HFMOD(***)	IAEA1317	Elastic and Inelastic x-section calculation by Hauser-Feshbach and Moldauer
HFTT	IAEA0954	n xsec by compound-nucleus evaporation model
HIC-1	CCC-0249	MC heavy ion reactions at E>50 MeV/nucleon
HIJET(**)		Hadronic cascades in high-energy Heavy Ion Collisions (used to be available from the CERN Program Library)
HILO86	DLC-0119	66 N, 22 gamma group x-section lib. for ANISN ORNL, DORT, MORSE-CGA
HILO86R(***)	DLC-0187	66 N, 22 gamma group x-section, up to 400 MeV (neutron) and 20 MeV (gamma). Update of HILO86
HOMO(*)	IAEA1253	Program for mixing/converting libraries in ANISN format
HUGO-VI	DLC-0146	Photon interaction evaluated data library ENDF-6 format
IDC	CCC-0384	ICRP dosimetric calculational system
IHEAS-BENCH(*)	NEA 1468	High energy accelerator shielding benchmarks
IMPACTS(*)	ESTS0005	Radiological assessment code
INFLTB(***)	PSR-0313	Dosimetric Mass Energy Transfer and Absorption Coefficients.
ISABEL(*)	NEA 1413	Intranuclear cascade model allowing hydrogen and helium ions and antiprotons as projectiles (run in LAHET)
ISAJET(**)		Hadronic cascades in high-energy Heavy Ion Collisions (used to be available from the CERN Program Library)

Programs marked (\*) or (\*\*) in the following table, represent additions to the corresponding table of [2]

(\*) Programs available

(\*\*) Programs known but not available

(\*\*\*) Additions since the SATIF-2 meeting

---

CCC-,PSR-,DLC- : original packaging by RSICC  
 NESC : original packaging by NESC (now ESTSC)  
 USCD : originated in US/Canada, packaged by NEA/DB  
 NEA, IAEA : original packaging by NEA/DB  
 <blank> : acquisition sought  
 xsec : cross-section  
 lib : library

**Table 1. List of programs and data in alphabetical order (cont.)**

<b>Name</b>	<b>Identification</b>	<b>Function</b>
ISO-PC(*)	CCC-0636	Kernel integration code system for general purpose isotope shielding
ITS-3.0 JENKINS	CCC-0467	MC tiger system of coupled electron photon transport photon, neutron dose in electron accelerator
K009 KAPSIES	CCC-0062	Charged particle penetration – phantom quantum mechanical multi-step direct model
LA100	DLC-0168	Evaluated data library for n, p up to 100 MeV, ENDF-6 format
LAHET		MC nucleon, pion, muons, tritons, He-3, alpha transport
LAHIMAC	DLC-0128	Neutron, gamma xsec – response functions, E<800MeV
LEP	DLC-0001	Results from intra-nuclear cascade and evaporation
LIMES	NEA 1337	Intermediate mass fragments in heavy ion nuclear reactions
LPPC	CCC-0051	Proton penetration, slab
LPSC	CCC-0064	p, n flux, spectra behind slab shield from p irradiation
LRSPC	CCC-0050	Range and stopping power calculator for ions
MAGIK	CCC-0359	MC for computing induced residual activation dose rates
MAGNA	NEA 0163	Dose rates from gamma source in slab or cylindrical shell shields
MARLOWE	PSR-0137	Atomic displacement cascades in solids
MARMER	NEA 1307	Point-kernel shielding, ORIGEN-S nuclide inventories
MATXS10(*)	DLC-0176	Library with 30n-12 gamma energy groups for particle transport codes and high energy calculations
MATXS11(*)	DLC-0177	Library with 80n 24 gamma energy groups for particle transport codes and high energy calculations
MCNP-4A	CCC-0200	MC 3-D time-dependent coupled n, photon, electron transport
MCNP-4B(***)	CCC-0660	MC 3-D time-dependent coupled n, photon, electron transport
MCNPDAT(*)	DLC-0105	X-section data library for the MCNP-4A transport code
MCNPDAT6(*)	DLC-0181	X-section data library from ENDF/B-VI for MCNP-4A
MECC-7	CCC-0156	Medium energy intra-nuclear cascade model
MENSLIB	DLC-0084	Neutron 60 group xsec, E<60MeV
MERCURE-4	NEA 0351	MC 3-D gamma heating/gamma dose rate, fast flux
MEVDP	CCC-0157	radiation transport in computerised anatomical man
MICAP	PSR-0261	MC ionisation chamber responses
MORSE-CGA	CCC-0474	MC n, gamma multigroup transport

Programs marked (\*) or (\*\*) in the following table, represent additions to the corresponding table of [2]

(\*) Programs available

(\*\*) Programs known but not available

(\*\*\*) Additions since the SATIF-2 meeting

---

CCC-,PSR-,DLC- : original packaging by RSICC  
 NESC : original packaging by NESC (now ESTSC)  
 USCD : originated in US/Canada, packaged by NEA/DB  
 NEA, IAEA : original packaging by NEA/DB  
 <blank> : acquisition sought  
 xsec : cross-section  
 lib : library

**Table 1. List of programs and data in alphabetical order (cont.)**

Name	Identification	Function
MUONLM(*)	NEA 1475	Calorimeter Interaction of Muons
MUP-2	IAEA0907	Fast n reaction xsec of medium-heavy nuclei
MUTIL(*)	NEA-1451	Calculates the asymmetry factor of the Mott scattering of electrons and positrons by point nuclei
NDEM(**)		Generates a gamma-ray source from the de-excitation of residual nuclei, assuming all particle decay modes have been exhausted (part of the HERMES system)
NESKA	NEA 1422	Electron, positron scattering from point nuclei
NFCLIST(*)	ESTS0352	Radionuclide decay data tabulations (240 radionuclides)
NJOY-94(*)	PSR-0171	n, p, photon evaluated data processing system
NJOY-94.61(***)		Idem
NMTC/JAERI	NEA 0974	MC high-energy p, n, pion reactions
NMF-90(***)	IAEA1279	Database for neutron spectra unfolding
NUCDECAY(*)	DLC-0172	Nuclear decay data for radiation dosimetry calculations
NUCHART(***)	IAEA1320	Nuclear. properties and decay data chart
NUCLEUS		Nuclear spallation simulation and primary products
OPTMOD(***)	IAEA1316	Elastic & total x-section, polarisation calculations. using the optical model
PACE2(**)		Codes performing the nuclear evaporation processes (working on the output from ISABEL)
PALLAS-2DY	NEA 0702	2-D n ,gamma transport for fixed source
PCROSS	IAEA1220	Pre-equilibrium emission spectra in neutron reaction
PCNUDAT(***)	USCD1205	Nuclear Properties database & retrieval system
PCNULIB(***)	USCD1205	Idem
PEGAS	IAEA1261	Unified model of particle and gamma emission reactions
PELSHIE	IAEA0855	Dose rates from gamma source, point-kernel method
PENELOPE(***)	NEA 1525	Monte Carlo code for electron-photon transport.
PEQAG-2	IAEA1185	Pre-equilibrium model nucleon, gamma spectra, xsec
PEREGRINE(**)		Used to model dose to humans from radiation therapy.
PHOTX	DLC-0136	Photon interaction xsec library for 100 elements
PICA	CCC-0160	MC calculation of nuclear cascade reactions caused by the collision of photons (30<E<400 MeV) with nuclei
PIPE	NEA 0416	1-D gamma transport for slab, spherical shields
PLACID	CCC-0381	MC gamma streaming in cylindrical duct shields
PNESD	IAEA1235	Elastic xsec of 3 MeV to 1000 MeV p on natural isotopes
POTAUS	IAEA1249	H through U ion ranges, stopping power for various materials

Programs marked (\*) or (\*\*) in the following table, represent additions to the corresponding table of [2]

(\*) Programs available

(\*\*) Programs known but not available

(\*\*\*) Additions since the SATIF-2 meeting

---

CCC-,PSR-,DLC- : original packaging by RSICC  
 NESK : original packaging by NESK (now ESTSC)  
 USCD : originated in US/Canada, packaged by NEA/DB  
 NEA, IAEA : original packaging by NEA/DB  
 <blank> : acquisition sought  
 xsec : cross-section  
 lib : library

**Table 1. List of programs and data in alphabetical order (cont.)**

Name	Identification	Function
PREANG	NEA 0809	Nuclear model particle spectra, angular distribution
PRECO-D2	PSR-0226	Pre-equilibrium, direct reaction double differential xsec
PREM	NEA 0888	Nucleon emission pre-equilibrium energy spectra, xsec
PSTAR(*)	IAEA1282	Calculates stopping power and range for protons
PTRAN	CCC-0618	MC proton transport for 50 to 250 MeV
PUTZ	CCC-0595	Point-kernel 3-D gamma shielding
QAD-CGGP-A(***)	CCC-0645	Fast neutron and gamma ray penetration in shields
QMD		Intra-nuclear cascade and classical molecular dynamics
RADCOMPT(*)	PSR-0348	Sample analysis for alpha and beta dual channel detect.
RADDECAY	DLC-0134	Decay data library for radiological assessment
RADHEAT-V3	NEA 0467	Transport, heat, radiation damage xsec in reactor, shield
RAID	CCC-0083	Gamma, n scattering into cylindrical or multibend duct
REAC	CCC-0443	Activation and transmutation
REAC-2	NESC9554	Nuclide activation, transmutation
REAC*3 (***)	CCC-0443	Isotope activation & transmutation in fusion reactors
REBEL-3	IAEA0846	MC radiation dose to human organs
RECOIL/B	DLC-0055	Heavy charged particle recoil spectra lib. for radiation. damage
REMIT(*)	ESTS0579	Radiation. Exposure Monitoring and Inf. Transmittal system
REPC	PSR-0195	Dose from protons in tissue
RESRAD(*)	CCC-0552	Calculation of residual radioactive material guidelines, site specific radiation doses and risks
SAM-CE	CCC-0187	MC time-dependent 3-D n, gamma transport in complex geometry
SAMSY	IAEA0837	n, gamma dose rates, heat source for multilayer shields
SAND-II(*)	PSR-0345	Determines neutron energy spectra by an analysis of multiple experimental activation detector data
SANDYL	CCC-0361	MC 3-D time-dependent gamma electron cascade transport
SCAP-82	CCC-0418	Scattering, albedo, point-kernel anal. in complex geometry
SCINFUL(*)	PSR-0267	MC to compute the response of scintillation neutron detector (incident neutron energies from 0.1 to 75 MeV)
SEECAL(*)	CCC-0620	Computes age-dependent effective energies for 54 and 32 target regions in the human body (825 radionuclides)
SFERXS	NEA 1239	Photon absorption, coherent, incoherent xsec for shielding

Programs marked (\*) or (\*\*) in the following table, represent additions to the corresponding table of [2]

(\*) Programs available

(\*\*) Programs known but not available

(\*\*\*) Additions since the SATIF-2 meeting

---

CCC-,PSR-,DLC- : original packaging by RSICC  
 NESC : original packaging by NESC (now ESTSC)  
 USCD : originated in US/Canada, packaged by NEA/DB  
 NEA, IAEA : original packaging by NEA/DB  
 <blank> : acquisition sought  
 xsec : cross-section  
 lib. : library

**Table 1. List of programs and data in alphabetical order (cont.)**

<b>Name</b>	<b>Identification</b>	<b>Function</b>
SHIELD(**)	IAEA1287	Universal code for exclusive simulation of hadron cascades in complex macroscopic targets. Transport of nucleons, pions, kaons, antinucleons and muons in the energy range up to 100 GeV is taken into account. Electromagnetic cascades are simulated by means of the EGS4 code, intranuclear cascades follow the model CASCAD, hadron-nucleus and nucleus-nucleus intranuclear interactions generated according to the QGSM based quark-gluon string model, Fermi break-up, multi-fragmentations and evaporation/fission according to the extended nuclear de-excitation model DEEX.
SIGMA-A(*)	DLC-0139	Photon interaction and absorption data 1 KeV-100 MeV
SITHA(**)	IAEA1179	Simulation Transport HAdron, used to calculate hadron transport in matter blocks of complex geometry. The nucleon and charged pions transport are carried out for the energy interval 10 MeV to 10 GeV and neutron transport for energies less than 20 MeV.
SKYPORT	DLC-0093	Importance of n, photon skyshine dose from accelerators
SNLRML(*)	DLC-0178	Dosimetry library compendium
SNL/SAND-II(*)	PSR-0345	Enhanced version of SAND-II
SOURCE(**)		Description of the proton transmission and generation of n source. Based on the Moving Source Model formalism and Bethe stopping theory with relativistic corrections for protons, allows the estimation of the proton range and the changes of the proton current and the neutron production versus the depth.
SPACETRAN	CCC-0120	Radiation leakage from cylinder with ANISN flux
SPAR	CCC-0228	Stopping power and ranges from muons, pions, protons ions
SPARES	CCC-0148	Space radiation environment and shielding evaluation
SPEC(***)	IAEA1332	Computation of neutron and charged particle reactions using the optical and evaporation models
SPCHAIN(**)		Calculates accumulation and decay of nuclides by taking the half-life and the decay chain of each nuclide into account.
SPECTER-ANL	PSR-0263	n damage for material irradiation
STAC-8		Transmitted, absorbed power/spectrum – synchrotron radiation
STAPRE-H	IAEA0971	Evaporation, pre-equilibrium model reaction xsec

Programs marked (\*) or (\*\*) in the following table, represent additions to the corresponding table of [2]

(\*) Programs available

(\*\*) Programs known but not available

(\*\*\*) Additions since the SATIF-2 meeting

---

CCC-,PSR-,DLC- : original packaging by RSICC  
 NESC : original packaging by NESC (now ESTSC)  
 USCD : originated in US/Canada, packaged by NEA/DB  
 NEA, IAEA : original packaging by NEA/DB  
 <blank> : acquisition sought  
 xsec : cross-section  
 lib. : library

**Table 1. List of programs and data in alphabetical order (cont.)**

<b>Name</b>	<b>Identification</b>	<b>Function</b>
STARCODES	PSR-0330	Stopping power, ranges for electrons, protons, alpha
STOPOW	IAEA0970	Stopping power of fast ions in matter
STR92(***)	ESTS1041	Energy deposition in accelerator ring components
STRAGL	CCC-0201	Energy loss straggling of heavy charged particles
SWIMS(*)	ESTS0682	Calculates the angular dispersion of ion beams that undergo small-angle incoherent multiple scattering by gaseous or solid media
TART95(*)		3D MC transport program for neutrons and photons
TART96(***)		Idem
TEST(*)	IAEA1252	Program for sorting/listing/deleting ANISN libraries
TNG1	PSR-0298	N multi-step statistical model
TORT	CCC-0543	3-D Sn n, photon transport with deep penetration
TPASGAM(*)	DLC-0088	Library with gamma-ray decay data for 1438 radionuclides
TRANSX(*)	PSR-0317	Code system to produce neutron, photon transport tables for discrete ordinates and diffusion codes
TRAPP	CCC-0205	Proton and alpha transport, reaction products neglected
TRIPOLI-2	NEA 0874	MC time-dependent 3-D N, gamma transport
TRIPOS	CCC-0537	MC ion transport
TWODANT-SYS	CCC-0547	1-D,2-D multigroup Sn n, photon transport
UNGER	DLC-0164	Effective dose equivalent data for selected isotopes
UNIFY	IAEA1177	Fast n xsec, spectrum calculation for structural materials
UNSPEC(***)	ESTS0827	X-ray spectrum unfolding using an iterative technique
VEGAS(**)		Intranuclear cascade code (from which ISABEL is derived)
VIRGIN(*)	IAEA0932	Calculates uncollided neutron flux and neutron reactions due to transmission of a neutron beam through any thickness of material
VITAMIN-E(*)	DLC-0113	X-section data library with 174n-38 gamma energy groups
VITAMIN-B6(***)	DLC-0184	X-section data library with 199n-42 gamma energy groups derived from ENDF/B-VI Release 3
XCOM(***)	DLC-0174	Photon cross-sections from 1 KeV to 100 GeV

Programs marked (\*) or (\*\*) in the following table, represent additions to the corresponding table of [2]

(\*) Programs available

(\*\*) Programs known but not available

(\*\*\*) Additions since the SATIF-2 meeting

---

CCC-,PSR-,DLC- : original packaging by RSICC  
 NESC : original packaging by NESC (now ESTSC)  
 USCD : originated in US/Canada, packaged by NEA/DB  
 NEA, IAEA : original packaging by NEA/DB  
 <blank> : acquisition sought  
 xsec : cross-section  
 lib : library

**Table 2. Evaluated and processed data  
(cross-sections, dose conversion, ranges, stopping powers)**

Name	Identification	Function
ACTIV-87(*)	IAEA1275	Library with fast neutron activation x-sections
CENDL(*)	IAEA1256	Chinese Evaluated Nuclear Data Library, namely the Optical Model Parameters for 6 types of projectiles (neutron, proton, deuteron, triton, <sup>3</sup> He and <sup>4</sup> He)
COVFILES(*)	DLC-0091	Library of neutron x-sections covariance data, useful to estimate radiation damage or heating
DROSG-87(*)	IAEA1234	Library of Legendre coefficients for neutron reactions
DOSDAT-2	DLC-0079	Gamma, electron dose factors data lib. for body organs
DOSEDAT-DOE	DLC-0144	Dose rate factors for external photon, electron exposure
EADL(*)	USCD1192	Library of atomic subshell and relaxation data
ECPL-86(*)	DLC-0106	evaluated charged particle cross-sections
EEDL(*)	USCD1193	Electron interaction x-section from 10 eV to 100 GeV
ENDLIB-94(***)	DLC-0179	Coupled electron & photon transport library (in LLL ENDL format)
EPDL-VI/MOD(*)	USCD1187	Photon interaction x-sections library(10 eV to 100 GeV)
FGR-DOSE(*)	DLC-0167	Library of dose coefficients for intake and exposure to radionuclides
FLEP	DLC-0022	Neutron, proton nonelastic xsec and spectra E<400MeV
FSXLIB-J3R2(***)	NEA 1424	JENDL-3 Evaluated Nuclear Data File, fusion neutronics
HILO86	DLC-0119	66 N, 22 gamma group XSEC lib. for ANISN-ORNL, DORT, MORSE-CGA
HILO86R(***)	DLC-0187	66 N, 22 gamma group x-section, up to 400 MeV (neutron) and 20 MeV (gamma). Update of HILO86
HELLO	DLC-0058	47 n, 21 gamma group coupled xsec from VITAMIN-C library
HUGO-VI	DLC-0146	Photon interaction evaluated data library ENDF-6 format
IDC	CCC-0384	ICRP dosimetric calculational system
IHEAS-BENCH(*)	NEA 1468	High energy accelerator shielding benchmarks
LA100	DLC-0168	Evaluated data library for n, p up to 100 MeV, ENDF-6 format
LAHIMACK	DLC-0128	Multigroup neutron and gamma x-sections up to 800 MeV
LEP	DLC-0001	Results from intra-nuclear cascade and evaporation

Programs marked (\*) or (\*\*) in the following table, represent additions to the corresponding table of [2]

- (\*) Programs available
- (\*\*) Programs known but not available
- (\*\*\*) Additions since the SATIF-2 meeting

---

CCC-,PSR-,DLC- : original packaging by RSICC  
 NESC : original packaging by NESC (now ESTSC)  
 USCD : originated in US/Canada, packaged by NEA/DB  
 NEA, IAEA : original packaging by NEA/DB  
 <blank> : acquisition sought  
 xsec : cross-section  
 lib. : library

**Table 2. Evaluated and processed data (cont.)**  
(cross-sections, dose conversion, ranges, stopping powers)

Name	Identification	Function
LRSPC	CCC-0050	Range and stopping power calculator
MATXS10(*)	DLC-0176	Library with 30 n-12 gamma energy groups for particle transport codes and high energy calculations
MATXS11(*)	DLC-0177	Idem
MCNPDAT(*)	DLC-0105	X-section data library for the MCNP-4A transport code
MCNPDAT6(*)	DLC-0181	X-section data library from ENDF/B-VI for MCNP-4A
MENSLIB	DLC-0084	Neutron 60 group xsec, E<60MeV
NFCLIST(*)	ESTS0352	Radionuclide decay data tabulations (240 radionuclides)
NMF-90(***)	IAEA1279	Database for neutron spectra unfolding
NUCDECAY(*)	DLC-0172	Nuclear decay data for radiation dosimetry calculations
NUCHART(***)	IAEA1320	Nuclear properties and decay data chart
PCNUDAT(***)	USCD1205	Nuclear properties database & retrieval system
PCNULIB(***)	USCD1205	Idem
PHOTX	DLC-0136	Photon interaction xsec library for 100 elements
PNESD	IAEA1235	Elastic xsec of 3 MeV to 1000 MeV p on natural isotopes
RADDECAY	DLC-0134	Decay data library for radiological assessment
RECOIL/B	DLC-0055	Heavy charged particle recoil spectra lib. for radiation damage
SFERXS	NEA 1239	Photon absorption, coherent, incoherent xsec for shielding
SIGMA-A(*)	DLC-0139	Photon interaction and absorption data 1 KeV-100 MeV
SKYPORT	DLC-0093	Importance of n, photon skyshine dose from accelerators
SNLRML(*)	DLC-0178	Dosimetry library compendium
SPAR	CCC-0228	Stopping power and ranges from muons, pions, protons, ions
STAC-8		Transmitted, absorbed power/spectrum – synchrotron radiation
STARCODES	PSR-0330	Stopping power, ranges for electrons, protons, alpha
STOPOW	IAEA0970	Stopping power of fast ions in matter
TPASGAM(*)	DLC-0088	Library with gamma-ray decay data for 1438 radionuclides
UNGER	DLC-0164	Effective dose equivalent data for selected isotopes
VITAMIN-E(*)	DLC-0113	X-section data library with 174 n-38 gamma energy groups
VITAMIN-B6(***)	DLC-0184	X-section data library with 199 n-42 gamma energy groups derived from ENDF/B-VI Release 3
XCOM(***)	DLC-0174	Photon cross-sections from 1 KeV to 100 GeV

Programs marked (\*) or (\*\*) in the following table, represent additions to the corresponding table of [2]

- (\*) Programs available
- (\*\*) Programs known but not available
- (\*\*\*) Additions since the SATIF-2 meeting

---

CCC-,PSR-,DLC- : original packaging by RSICC  
 NESD : original packaging by NESD (now ESTSC)  
 USCD : originated in US/Canada, packaged by NEA/DB  
 NEA, IAEA : original packaging by NEA/DB  
 <blank> : acquisition sought  
 xsec : cross-section  
 lib. : library

**Table 3. Cross-sections – spectra from nuclear models (for E>20 MeV)**

Name	Identification	Function
ALICE91	PSR-0146	Precompound/compound nuclear decay model
AMALTHEE	NEA 0675	Emission spectra for n, p, d, h3, he3, alpha reaction
ASOP	CCC-0126	1-D Sn shield calculation
AUJP	IAEA0906	Optical potential parameters search by chi**2 method
CADE	NEA 1020	Multiple particle emission xsec by Weisskopf-Ewing
CCRMN(***)	IAEA1347	Computation of reactions of a medium-heavy nucleus with six light particles
CEM95(*)	IAEA1247	MC calculation of nuclear. reactions (Cascade Exciton Model)
CFUP1	IAEA1266	n, charged-particle reaction of fissile nuclei E<33 MeV
CHUCK	USCD1021	n, charged particle xsec, coupled channel model
CMUP2	IAEA1265	Reaction xsec for n ,p, d, t, he3, he4, E<50 MeV
COMNUC3B	PSR-0302	Compound nucleus interaction in n reactions
DWBA82	NEA 1209	Distorted Wave Born Approximation nuclear model
DWUCK-4	NESC9872	Distorted Wave Born Approximation nuclear model
ECIS-95(*)	NEA 0850	Schroedinger/Dirac nuclear model with experimental fit
ELPHIC-PC	IAEA1223	Statistical model MC simulation of heavy ion reaction
EMPIRE-MSC	IAEA1169	Multistep compound nucleus/pre-equilibrium xsec
ERINNI	NEA 0815	Multiple cascades emission spectra by optical model
EVA(*)		Codes performing the nuclear evaporation processes (working on the output from ISABEL)
EVAP_F(**)		Modified version of the Dresdner evaporation code (run in HETC@PSI)
EXIFONGAMMA	IAEA1211	n, alpha, proton, gamma emission spectra model
FRITIOF(**)		MC high-energy heavy ion collisions
GNASH-FKK(*)	PSR-0125	Multi-step direct and compound and Hauser Feshbach models
GNASH-LANL	PSR-0125	Pre-equilibrium/statistical xsec, emission spectra
GRAPE	NEA 1043	Precompound/compound nuclear reaction models
HETC NMTC	CCC-0178	MC high energy nucleon meson cascade transport
HETC-KFA	CCC-0496	MC high energy nucleon-meson cascades
HETC95(**)		MC high energy nucleon-meson cascades and transport
HFMOD(***)	IAEA1317	Elastic and Inelastic x-section calculation by Hauser-Feshbach and Moldauer
HFTT	IAEA0954	n xsec by compound-nucleus evaporation model
HIJET(**)		MC high-energy heavy ion collisions
ISABEL(*)	NEA 1413	Intranuclear cascade model allowing hydrogen and helium ions and antiprotons as projectiles (run in LAHET)

Programs marked (\*) or (\*\*) in the following table, represent additions to the corresponding table of [2]

- (\*) Programs available
- (\*\*) Programs known but not available
- (\*\*\*) Additions since the SATIF-2 meeting

---

CCC-,PSR-,DLC- : original packaging by RSICC  
 NESC : original packaging by NESC (now ESTSC)  
 USCD : originated in US/Canada, packaged by NEA/DB  
 NEA, IAEA : original packaging by NEA/DB  
 <blank> : acquisition sought  
 xsec : cross-section  
 lib. : library

**Table 3. Cross-sections – spectra from nuclear models (for E>20 MeV) (cont.)**

Name	Identification	Function
ISAJET(**)		MC high-energy heavy ion collisions
KAPSIES		Quantum mechanical multi-step direct model
LIMES	NEA 1337	Intermediate mass fragments in heavy ion nuclear reactions
MARLOWE	PSR-0137	Atomic displacement cascades in solids
MECC-7	CCC-0156	Medium energy intra-nuclear cascade model
MUP-2	IAEA0907	Fast n reaction xsec of medium-heavy nuclei
MUTIL(*)	NEA 1451	Calculates the asymmetry factor of the Mott scattering of electrons and positrons by point nuclei
NDEM(**)		Generates a gamma-ray source from the de-excitation of residual nuclei, assuming all particle decay modes have been exhausted (part of the HERMES system)
NJOY-94(*)	PSR-0171	n, p, photon evaluated data processing system
NJOY-94.61(***)		Idem
NMTC/JAERI	NEA 0974	MC high-energy p, n, pion reactions
NUCLEUS		Nuclear spallation simulation and primary products
OPTMOD(***)	IAEA1316	Elastic & total x-section, polarisation calculations. using the optical model
PACE2(**)		Codes performing the nuclear evaporation processes (working on the output from ISABEL)
PCROSS	IAEA1220	Pre-equilibrium emission spectra in neutron reaction
PEGAS	IAEA1261	Unified model of particle and gamma emission reactions
PELSHIE	IAEA0855	Dose rates from gamma source, point-kernel method
PEQAG-2	IAEA1185	Pre-equilibrium model nucleon, gamma spectra, xsec
PREANG	NEA 0809	Nuclear model particle spectra, angular distribution
PRECO-D2	PSR-0226	Pre-equilibrium, direct reaction double differential xsec
PREM	NEA 0888	Nucleon emission pre-equilibrium energy spectra, xsec
QMD		Intra-nuclear cascade and classical molecular dynamics
REAC	CCC-0443	Activation and transmutation
REAC-2	NESC9554	Nuclide activation, transmutation
REAC*3 (***)	CCC-0443	Isotope activation & transmutation in fusion reactors
SPEC(***)	IAEA1332	Computation of neutron and charged particle reactions using the optical and evaporation models
STAPRE-H	IAEA0971	Evaporation, pre-equilibrium model reaction xsec
TNG1	PSR-0298	N multi-step statistical model
UNIFY	IAEA1177	Fast n xsec, spectrum calculation for structural materials
VEGAS(**)		Intranuclear cascade code (from which ISABEL is derived)

Programs marked (\*) or (\*\*) in the following table, represent additions to the corresponding table of [2]

- (\*) Programs available
- (\*\*) Programs known but not available
- (\*\*\*) Additions since the SATIF-2 meeting

---

CCC-,PSR-,DLC- : original packaging by RSICC  
 NESC : original packaging by NESC (now ESTSC)  
 USCD : originated in US/Canada, packaged by NEA/DB  
 NEA, IAEA : original packaging by NEA/DB  
 <blank> : acquisition sought  
 xsec : cross-section  
 lib. : library

**Table 4. Monte Carlo (MC) and deterministic radiation transport**

Name	Identification	Function
Neutron/photon		
ALBEDO	NEA 1353	Gamma, neutron attenuation in air ducts
ANISN	CCC-0254	1-D Sn, n, gamma transport in slab, cylinder, sphere
ASOP	CCC-0126	1-D Sn shield calculation
BALTORO	NEA 0675	n, gamma transport perturbation from MORSE, ANISN calculation
BASACF(***)	IAEA0953	Integral neutron adjustment and dosimetry
BERMUDA	NEA 0949	1-D, 2-D, 3-D n, gamma transport for shielding
BREESE	PSR-0143	Distribution function for MORSE from albedo data
CARP-82	PSR-0131	Currents for BREESE from DOT flux
COLLI-PTB	NEA 1126	MC n fluence spectra for 3-D collimator system
DANTSYS(*)	CCC-0547	1-D, 2-D, 3-D, Sn neutron, photon transport
DASH	CCC-0366	Void tracing Sn – MC COUPLING with fluxes from DOT
DCTDOS	CCC-0520	n, gamma penetration in composite duct system
DOORS3.1(***)	CCC-0650	Discrete ordinates system for deep penetration neutron and gamma transport
DORT	CCC-0543	1-D, 2-D, Sn, n, photon transport with deep penetration
DOMINO	PSR-0064	Coupling of Sn DOT with MC MORSE
DOT	CCC-0276	2-D, Sn, n, photon transport with deep penetration
DUST	CCC-0453	Albedo MC simulation of n streaming inducts
FALSTF	CCC-0351	n, gamma flux detector response outside cylindrical shields
FEM-RZ	NEA 0566	FEM 2-D multigroup n transport in r-z geometry
GBANISN(***)	CCC-0628	1-D neutron & gamma fluxes with group band fluxes
GEANT-CERN		MC hadron shower simulation
MAGIK	CCC-0359	MC induced residual activation dose rates
MCNP-4A	CCC-0200	MC 3-D time-dependent coupled n, photon, electron transport
MCNP-4B(***)	CCC-0660	MC 3-D time-dependent coupled n, photon, electron transport
MICAP(*)	PSR-0261	MC to determine the response of gas filled cavity ionisation chamber, plastic scintillator or calorimeter in a mixed neutron and photon environment
MORSE-CGA	CCC-0474	MC, n, gamma multigroup transport
PALLAS-2DY	NEA 0702	2-D, n ,gamma transport for fixed source
RADHEAT-V3	NEA 0467	Transport, heat, radiation damage xsec in reactor, shield
QAD-CGGP-A(***)	CCC-0645	Fast neutron and gamma ray penetration in shields
RAID	CCC-0083	Gamma, n scattering into cylindrical or multibend duct
SAMSY	IAEA0837	n, gamma dose rates, heat source for multilayer shields

Programs marked (\*) or (\*\*) in the following table, represent additions to the corresponding table of [2]

(\*) Programs available

(\*\*) Programs known but not available

(\*\*\*) Additions since the SATIF-2 meeting

---

CCC-,PSR-, DLC- : original packaging by RSICC  
 NESC : original packaging by NESC (now ESTSC)  
 USCD : originated in US/Canada, packaged by NEA/DB  
 NEA, IAEA : original packaging by NEA/DB  
 <blank> : acquisition sought  
 xsec : cross-section  
 lib. : library

**Table 4. Monte Carlo (MC) and deterministic radiation transport (cont.)**

Name	Identification	Function
SAM-CE	CCC-0187	MC time-dependent 3-d n, gamma transport in complex geometry
SAND-II(*)	PSR-0345	Determines neutron energy spectra by an analysis of multiple experimental activation detector data
SCINFUL(*)	PSR-0267	MC to compute the response of scintillation neutron detector (incident neutron energies from 0.1 to 75 MeV)
SCAP-82	CCC-0418	Scattering, albedo, point-kernel anal. in complex geometry
SNL/SAND-II(*)	PSR-0345	Enhanced version of SAND-II
SPACETRAN	CCC-0120	Radiation leakage from cylinder with ANISN flux
SPECTER-ANL	PSR-0263	n damage for material irradiation
TART95(*)		3-D MC transport program for neutrons and photons
TART96(***)		Idem
TORT	CCC-0543	3-D, Sn, n, photon transport with deep penetration
TRANSX(*)	PSR-0317	Code system to produce neutron, photon transport tables for discrete ordinates and diffusion codes
TRIPOLI-2	NEA 0874	MC time-dependent 3-D, n, gamma transport
TWODANT-SYS	CCC-0547	1-D, 2-D multigroup Sn, n, photon transport
VIRGIN(*)	IAEA0932	Calculates uncollided neutron flux and neutron reactions due to transmission of a neutron beam through any thickness of material
Photon		
AIRSCAT	CCC-0341	Dose rate from gamma air scattering, single scat. approx.
GAMMONE	NEA 0268	MC gamma penetration from various geometrical sources
MERCURE-4	NEA 0351	MC 3-D gamma heating/gamma dose rate, fast flux
PLACID	CCC-0381	MC gamma streaming in cylindrical duct shields
BRHGAM	CCC-0350	MC absorbed dose from x-rays in phantom
BREMRAD	CCC-0031	External/internal bremsstrahlung
GRPANL(***)	PSR-0321	Germanium gamma and alpha detector spectra unfolding
G33-GP	CCC-0494	Multigroup gamma scattering using gp build-up factor
ISO-PC(*)	CCC-0636	Kernel integration code system for general purpose isotope shielding
MAGNA	NEA 0163	Dose rates from gamma source in slab or cylindrical shell shields
MARMER	NEA 1307	Point-kernel shielding, ORIGEN-S nuclide inventories
PELSHIE	IAEA0855	Dose rates from gamma source, point-kernel method
PIPE	NEA 0416	1-D gamma transport for slab, spherical shields
PUTZ	CCC-0595	Point-kernel 3-D gamma shielding

Programs marked (\*) or (\*\*) in the following table, represent additions to the corresponding table of [2]

- (\*) Programs available
- (\*\*) Programs known but not available
- (\*\*\*) Additions since the SATIF-2 meeting

---

CCC-,PSR-,DLC- : original packaging by RSICC  
 NESC : original packaging by NESC (now ESTSC)  
 USCD : originated in US/Canada, packaged by NEA/DB  
 NEA, IAEA : original packaging by NEA/DB  
 <blank> : acquisition sought  
 xsec : cross-section  
 lib. : library

**Table 4. Monte Carlo (MC) and deterministic radiation transport (cont.)**

Name	Identification	Function
STAC-8		Transmitted, absorbed power/spectrum – synchrotron radiation
UNSPEC(***)	ESTS0827	X-ray spectrum unfolding using an iterative technique
Electron/photon		
BETA-2B	CCC-0117	MC time-dependent bremsstrahlung, electron transport
CASCADE	CCC-0176	High energy electron-photon transport in matter
CEPXS ONELD	CCC-0544	1-D coupled electron photon multigroup transport
DOSDAT-2	DLC-0079	Gamma, electron dose factors data lib. for body organs
EDMULT	NEA 0969	Electron depth dose in multilayer slab absorbers
EGS4	CCC-0331	MC electron photon shower simulation
EGS4(***)	CCC-0331	Version 3.0 of the UNIX distribution of EGS4
ELBA	CCC-0119	Bremsstrahlung dose from electron flux on Al shield
EPICSHOW(*)	IAEA1285	Interactive Viewing of the Electron-Photon Interaction Code (EPIC) system databases (10 eV < E < 1 GeV)
EPICSHOW-96.1 (***)		Interactive Viewing of the Electron-Photon Interaction Code (EPIC) system databases and Neutron cross-section data
ESTAR(*)	IAEA1282	Calculates stopping power and range for electrons
ETRAN	CCC-0107	MC electron, gamma transport with secondary radiation
ELTRAN	CCC-0155	MC 1-D electron transport
FOTELP	CCC-0581	MC photons, electrons and positron transport
INFLTB(***)	PSR-0313	Dosimetric Mass Energy Transfer and Absorption Coefficients.
ITS-3.0	CCC-0467	MC tiger system of coupled electron photon transport
MCNP-4A	CCC-0200	MC 3-D time-dependent coupled n, photon, electron transport
MCNP-4B(***)	CCC-0660	MC 3-D time-dependent coupled n, photon, electron transport
PENELOPE(***)	NEA 1525	Monte Carlo for electron-photon transport
SANDYL	CCC-0361	MC 3-D time-dependent gamma electron cascade transport
Protons		
ASTROS	CCC-0073	Primary/secondary proton dose in sphere/slab tissue
LPPC	CCC-0051	Proton penetration, slab
PSTAR(*)	IAEA1282	Calculates stopping power and range for protons
PTRAN	CCC-0618	MC proton transport for 50 to 250 MeV

Programs marked (\*) or (\*\*) in the following table, represent additions to the corresponding table of [2]

(\*) Programs available

(\*\*) Programs known but not available

(\*\*\*) Additions since the SATIF-2 meeting

---

CCC-,PSR-,DLC- : original packaging by RSICC  
 NESC : original packaging by NESC (now ESTSC)  
 USCD : originated in US/Canada, packaged by NEA/DB  
 NEA, IAEA : original packaging by NEA/DB  
 <blank> : acquisition sought  
 xsec : cross-section  
 lib. : library

**Table 4. Monte Carlo (MC) and deterministic radiation transport (cont.)**

Name	Identification	Function
SOURCE(**)		Description of the proton transmission and generation of n source. Based on the Moving Source Model formalism and Bethe stopping theory with relativistic corrections for protons, allows the estimation of the proton range and the changes of the proton current and the neutron production versus the depth.
TRAPP	CCC-0205	Proton and alpha transport, reaction products neglected
Alphas		
ALDOSE(*)	CCC-0577	Calculates of absorbed dose and dose equivalent rates as function of depth in water irradiated by alpha source
ALPHN(*)	CCC-0612	Calculates the (alpha,n) production rate in a mixture receiving alpha particles from emitting actinides
ASTAR(*)	IAEA1282	Calculates stopping power and range for alphas
GRPANL(***)	PSR-0321	Germanium gamma and alpha detector spectra unfolding
RADCOMPT(*)	PSR-0348	Sample analysis for alpha and beta dual channel detectors
Nucleons/hadrons/cascades		
CALOR89	CCC-0610	MC system for design, analysis of calorimeter system
CALOR93		Idem
CALOR95(***)		Idem
CASIM	NESC0742	MC high energy cascades in complex shields
FLUKA	CCC-0207	MC high energy extranuclear hadron cascades
GEANT-CERN		MC hadron shower simulation
HERMES-KFA	NEA 1265	MC high-energy radiation transport
HERMES96b(***)		Idem
HETC NMTC	CCC-0178	MC high energy nucleon-meson cascade transport
HETC-KFA	CCC-0496	MC high energy nucleon-meson cascade transport
LAHET		MC nucleon, pion, muons, tritons, <sup>3</sup> He, alpha transport
LPSC	CCC-0064	p, n flux, spectra behind slab shield from p irradiation
NMTC/JAERI	NEA 0974	MC high-energy p, n, pion reactions
SITHA(**)	IAEA1179	Simulation Transport HAdron, used to calculate hadron transport in matter blocks of complex geometry. The nucleon and charged pions transport are carried out for the energy interval 10 MeV to 10 GeV and neutron transport for energies less than 20 MeV.

Programs marked (\*) or (\*\*) in the following table, represent additions to the corresponding table of [2]

(\*) Programs available

(\*\*) Programs known but not available

(\*\*\*) Additions since the SATIF-2 meeting

---

CCC-,PSR-,DLC- : original packaging by RSICC  
 NESC : original packaging by NESC (now ESTSC)  
 USCD : originated in US/Canada, packaged by NEA/DB  
 NEA, IAEA : original packaging by NEA/DB  
 <blank> : acquisition sought  
 xsec : cross-section  
 lib. : library

**Table 4. Monte Carlo (MC) and deterministic radiation transport (cont.)**

Name	Identification	Function
SHIELD(**)	IAEA1287	Universal code for exclusive simulation of hadron cascades in complex macroscopic targets. Transport of nucleons, pions, kaons, antinucleons and muons in the energy range up to 100 GeV is taken into account. Electromagnetic cascades are simulated by means of the EGS4 code, intranuclear cascades follow the model CASCAD, hadron-nucleus & nucleus-nucleus intranuclear interactions generated according to the QGSM based quark-gluon string model, Fermi break-up, multi-fragmentations and evaporation/fission according to the extended nuclear de-excitation model DEEX.
Heavy-ions		
E-DEP-1	CCC-0275	Heavy ion energy deposition
ELPHIC-PC	IAEA1223	Statistical model MC simulation of heavy ion reaction
HIC-1	CCC-0249	MC heavy ion reactions at E>50 MeV/nucleon
STRAGL	CCC-0201	Energy loss straggling of heavy charged particles
SWIMS(*)	ESTS0682	Calculates the angular dispersion of ion beams that undergo small-angle incoherent multiple scattering by gaseous or solid media
TRIPOS	CCC-0537	MC ion transport
Muons		
MUONLM(*)	NEA 1475	Calorimeter Interaction of Muons
Others/cascades		
CHARGE-2/C	CCC-0070	Electron, p, heavy particle flux/dose behind shield
DDCS(*)	IAEA1290	Calculation of neutron, proton, deuteron, triton, <sup>3</sup> He, and alpha induced reactions of medium heavy nuclei in the energy range up to 50 MeV
ELPHO	CCC-0301	MC muon, electron, positron generation from pions
IMPACTS-BRC(*)	ESTS0005	Radiological assessment code
JENKINS		Photon, neutron dose in electron accelerator
PICA	CCC-0160	MC calculation of nuclear cascade reactions caused by the collision of photons (30 < E < 400 MeV) with nuclei
SPARES	CCC-0148	Space radiation environment and shielding evaluation
Anthropomorphic phantom modelling		
BRHGAM	CCC-0350	MC absorbed dose from x-rays in phantom
CAMERA	CCC-0240	Radiation transport and computerised man model
DISDOS	CCC-0170	Dose from external photons in phantom
K009	CCC-0062	Charged particle penetration – phantom
MEVDP	CCC-0157	Radiation transport in computerised anatomical man
PEREGRINE(**)		Used to model dose to humans from radiation therapy.
REBEL-3	IAEA0846	MC radiation dose to human organs
REPC	PSR-0195	Dose from protons in tissue
SEECAL(*)	CCC-0620	Computes age-dependent effective energies for 54 and 32 target regions in the human body (825 radionuclides)

Programs marked (\*) or (\*\*) in the following table, represent additions to the corresponding table of [2]

(\*) Programs available

(\*\*) Programs known but not available

(\*\*\*) Additions since the SATIF-2 meeting

---

CCC-,PSR-,DLC- : original packaging by RSICC  
 NESC : original packaging by NESC (now ESTSC)  
 USCD : originated in US/Canada, packaged by NEA/DB  
 NEA, IAEA : original packaging by NEA/DB  
 <blank> : acquisition sought  
 xsec : cross-section  
 lib. : library

**Table 5. Benchmark data sets already added or in the process of being added in the SINBAD database at the NEA/DB**

<b>Name</b>	<b>Description</b>
ASPIS-FE(*)	Winfrith Iron Benchmark Experiment (ASPIS)
ASPIS-FE88(*)	Winfrith Iron 88 Benchmark Experiment (ASPIS)
ASPIS-GRAPHITE(*)	Winfrith Graphite Benchmark Experiment (ASPIS)
EURACOS-FE(*)	Ispra Iron Benchmark Experiment (EURACOS)
EURACOS-NA(*)	Ispra Sodium Benchmark Experiment (EURACOS)
KFK-FE(*)	Karlsruhe Iron Sphere Benchmark Experiment
NESDIP-2(*)	Winfrith NESDIP2 Radial Shield and Cavity Experiment
OKTAVIAN-FE(*)	Osaka Iron Benchmark Experiment (OKTAVIAN)
PCA-REPLICA(*)	Winfrith Water/Iron Benchmark Experiment (PCA-Replica)
PROTEUS-FE(*)	Wuerenlingen Iron Benchmark Experiment (PROTEUS)
WINFRITH-H2O(*)	Winfrith Water Benchmark Experiment (ASPIS)
HARMONIE-NA(*)	Cadarache Sodium Benchmark Experiment (HARMONIE)
OKTAVIAN-NI(**)	Osaka Nickel Benchmark Experiment (OKTAVIAN)
NESDIP-1 PV + cavity(**)	Winfrith NESDIP1 Radial Shield and Cavity Experiment
NESDIP-3 PV + cavity(**)	Winfrith NESDIP3 Radial Shield and Cavity Experiment
VENUS-1 PV + cavity (2D)(**)	Mol PWR Benchmark Experiment
VENUS-3 PV + cavity (3D)(**)	Mol PWR Benchmark Experiment
YAYOI fast reactor vessel(**)	University of Tokyo's Iron and Sodium Fast Reactor Shielding Benchmark Experiments

(\*) Benchmarks available

(\*\*) Benchmarks available during 1997

**Table 6. Benchmark data sets added to the SINBAD database, at ORNL/RSICC [8]**

<b>Name</b>	<b>Description</b>
STD1	Iron Broomstick Benchmark Experiment (TSF-ORNL)
STD2	Oxygen Broomstick Benchmark Experiment (TSF-ORNL)
STD3	Nitrogen Broomstick Benchmark Experiment (TSF-ORNL)
STD4	Sodium Broomstick Benchmark Experiment (TSF-ORNL)
STD5	Stainless Steel Broomstick Benchmark Experiment (TSF-ORNL)
SB5	Fusion Reactor Shielding Experiment (ORNL)
SB6	Fusion Reactor Shielding Experiments II: Duct Streaming Experiments and Analysis (ORNL)
FNS Beryllium	Beryllium Slabs Irradiated w/ Deuterium-Tritium Fusion Neutrons (JAERI)
FNS Lithium Oxyde	(Li <sub>2</sub> O) Slabs Irradiated w/ Deuterium-Tritium Fusion Neutrons (JAERI)
FNS Graphite	Graphite Slabs Irradiated w/ Deuterium-Tritium Fusion Neutrons (JAERI)
Jasper	Jasper Radial Shielding Experiment – Shielding Effectiveness of stainless steel, graphite and boron carbide for advanced LMR designs (ORNL)
FNG/ENEA	SS Bulk Shield Benchmark Experiment (Frascati)
“Accelerators”	Penetration of Secondary Neutrons and Photons through a Graphite Assembly Exposed to 52- MeV Protons (Univ. of Tokyo)

## LIST OF PARTICIPANTS

### FRANCE

CLAPIER, Francois  
Ingenieur de Radioprotection  
CNRS-IN2P3  
Institut Physique Nucleaire  
SPR  
91406 ORSAY

Tel: +33 (1) 6941 7170  
Fax: +33 (1) 6941 6470  
Net: clapier@ipncls.in2p3.fr

### GERMANY

DINTER, Herbert  
Deutsches Elektronen - Synchrotron DESY  
Notkestr. 85  
D-22603 HAMBURG

Tel: +49 (40) 89 98 3446  
Fax: +49 (40) 89 98 3282  
Net: dinter@mail.desy.de

FILGES, Detlef  
Institut fuer Kernphysik  
Forschungszentrum Juelich GmbH  
D-52425 JUELICH

Tel: +49 (2461) 61 5232  
Fax: +49 (2461) 61 3930  
Net: D.Filges@kfa-juelich.de

MARES, Vladimir  
Universitaet Muenchen  
Strahlenbiologisches Institut  
Schillerstrasse 42g  
D-80336 MUENCHEN

Tel: +49 (89) 5996 838 or 3187 2652  
Fax: +49 (89) 5996 840 or 3187 3323  
Net: mares@gsf.de

### ITALY

FERRARI, Alfredo  
I.N.F.N., Dipartimento di  
Fisica dell'Universita e INFN  
Via Celoria 16  
I-20133 MILANO

Tel: +39 (2) 2392 310  
Fax: +39 (2) 2392 624  
Net: Alfredo.Ferrari@mi.infn.it

\* MENAPACE, Enzo  
E.N.E.A.  
Applied Physics Division  
Via Don G. Fiammelli 2  
I-40128 BOLOGNA

Tel: +39 (51) 60 98 239  
Fax: +39 (51) 60 98 359  
Net: menapace@risc990.bologna.enea.it

PELLICCIONI, Maurizio  
INFN  
Laboratori Nazionali di Frascati  
Casella Postale 13  
I-00044 Frascati

Tel: +39 (6) 940 32246  
Fax: +39 (6) 940 32364  
Net: pelliccm@lnf.infn.it

RANFT, Johannes  
Lab. Naz. del Gran Sasso  
S.S. 17/bis km 18+910  
I-67010 ASSERGI (AQ)  
TABARELLI DE FATIS, Paola  
Fondazione TERA  
Istituto Europeo di Oncologia  
via Ripamonti 435  
I-20140 MILANO

Tel: +39 (862) 437535  
Fax: +39 (862) 437570  
Net: Johannes.Ranft@cern.ch  
Tel:  
Fax: +39 (2) 574 89208  
Net: ptabarelli@vaxmi.mi.infn.it

## JAPAN

BAN, Syuichi  
KEK, High Energy Accelerator  
Research Organisation  
1-1 Oho  
Tsukuba-shi, Ibaraki-ken 305

Tel: +81 (298) 64 5494  
Fax: +81 (298) 64 1993  
Net: s.ban@kek.jp

FUKAHORI, Tokio  
Nuclear Data Center  
Dept. of Reactor Engineering  
JAERI  
Tokai-Mura, Naka-Gun  
IBARAKI-KEN 319-11

Tel: +81 (292) 82 5907  
Fax: +81 (292) 82 6122  
Net: fukahori@cracker.tokai.jaeri.go.jp

HAYASHI, Katsumi  
Hitachi Engineering Company  
3-2-1 Saiwai-cho  
Hitachi-shi  
Ibaraki-ken 317

Tel: +81 (294) 24 1111  
Fax: +81 (294) 23 6748  
Net: hayashik@po.infosphere.or.jp

HIRAYAMA, Hideo  
KEK, High Energy Accelerator  
Research Organisation  
1-1 Oho  
Tsukuba-shi, Ibaraki-ken 305

Tel: +81 (298) 64 5493  
Fax: +81 (298) 64 1993  
Net: Hideo.Hirayama@kek.jp

IKEDA, Yujiro  
Fusion Neutronics Laboratory  
Dept. of Reactor Engineering  
JAERI  
Tokai-Mura, Naka-gun  
IBARAKI-KEN 319-11

Tel: +81 (292) 82 6074  
Fax: +81 (292) 82 5709  
Net: ikeda@fnshp.tokai.jaeri.go.jp

IKEDA, Hironobu  
Neutron Science Laboratory(KENS)  
KEK, High Energy Accelerator  
Research Organisation  
1-1 Oho  
Tsukuba-shi, Ibaraki-ken 305

Tel:  
Fax: +81 (298) 64 3202  
Net: hironobu.ikeda@kek.jp

IWAI, Satoshi Nuclear Application Techn. G. Mitsubishi Heavy Industries 1-297 Kitabukuro-cho Omiya-shi Saitama-ken 330	Tel: +81 (48) 642 4404 Fax: +81 (48) 645 0189  Net: Q18586@minds.atom.hq.mhi.co.jp
KIYANAGI, Yoshiaki Hokkaido University Sapporo, 060	Tel: +81 (11) 706 6650 Fax: +81 (11) 706 7896  Net: kiyanagi@toybox.hune.hokudai.ac.jp
MATSUURA, Shojiro Vice-President Japan Atomic Energy Institute Fukoku Seimei Bldg. 2-2-2, Uchisaiwai-cho Chiyoda-ku, Tokyo, 100	Tel: +81 (3) 3592 2156 Fax: +81 (3) 3592 2159 or 3580 6107  Net: matsu@hems.jaeri.go.jp
NAKAMURA, Takashi Cyclotron and Radioisotope Centre Tohoku University Aramaki, Aoba, Aoba-ku SENDAI 980-77	Tel: +81 (22) 217 7805 Fax: +81 (22) 217 7809  Net: nakamura@risun1.cyric.tohoku.ac.jp
NAKANE, Yoshihiro Applied Radiation Laboratory Dept. Reactor Engineering JAERI Tokai-mura, Naka-gun IBARAKI-KEN 319-11	Tel: +81 (29) 282 5336 Fax: +81 (29) 282 5663  Net: Nakane@shield2.tokai.jaeri.go.jp
NAKAO, Noriaki KEK, High Energy Accelerator Research Organisation 1-1 Oho Tsukuba-shi, Ibaraki-ken 305	Tel: Fax:  Net: noriaki.nakao@kek.jp
NAKASHIMA, Hiroshi Applied Radiation Laboratory JAERI Tokai Research Establishment Tokai-Mura Ibaraki-Ken 319-11	Tel: +81 (29) 282 5336 Fax: +81 (29) 282 5663  Net: nakasima@shield2.tokai.jaeri.go.jp
SAKAMOTO, Yukio Applied Radiation Laboratory Dept. Reactor Engineering JAERI Tokai-mura, Naka-gun IBARAKI-KEN 319-11	Tel: +81 (29) 282 5355 Fax: +81 (29) 282 5663  Net: Sakamoto@shield2.tokai.jaeri.go.jp

SASAMOTO, Nobuo  
Spring-8 Project Team  
JAERI  
KAMIGORI  
Hyogo 678-12  
SATO, Osamu  
Mitsubishi Research Institute, Inc.  
Time & Life Bldg.  
2-3-6 Otemachi  
Chiyoda-ku, TOKYO 100  
SHIN, Kazuo  
Dept. of Nuclear Engineering  
Kyoto University  
Yoshida  
Sakyo-ku  
Kyoto 606-01  
UWAMINO, Yoshitomo  
Safety Center  
RIKEN  
2-1, Hirosawa  
Wako, Saitama 351-01  
YOSHIZAWA, Nobuaki  
Mitsubishi Research Institute  
3-6, Otemachi 2-chome  
Chiyoda-ku  
TOKYO 100

Tel:  
Fax: +81 (792) 8 1845  
Net: sasamoto@sp8sun.spring8.or.jp  
Tel: +81 (3) 3277 0772  
Fax: +81 (3) 3277 3480  
Net: sato@mri.co.jp  
Tel: +81 (75) 753 5825  
Fax: +81 (75) 753 5845  
Net: Shin@east.nucleng.kyoto-u.ac.jp  
Tel: +81 (48) 467 9292  
Fax: +81 (48) 462 4616  
Net: uwamino@postman.riken.go.jp  
Tel: +81 (3) 3277 0772 X 5253  
Fax: +81 (3) 3277 3480  
Net: yoshizaw@mri.co.jp

#### RUSSIAN FEDERATION

ALEXEEV, Alexandre  
Radiation Research Division  
Inst. for High Energy Physics  
PROTVINO  
Moscow region 14284  
DEGTYAREV, Igor  
Radiation Research Division  
Inst. for High Energy Physics  
PROTVINO  
Moscow region 14284  
GELFAND, Elena  
Moscow Radiotechnical Inst.  
of Russian Academy of Science  
Varshavskoe shosse, 132  
Moscow, 113519  
\* LOKHOVITSKII, Arkady  
Radiation Research Division  
Inst. for High Energy Physics  
PROTVINO  
Pobeda Str. 1  
Moscow region 142284

Tel: +7 (0967) 713 189 or 385  
Fax: +7 (095) 2302 337  
Net: alexeev@mx.ihep.su  
Tel: +7 (0967) 74 49 07  
Fax: +7 (0967) 74 49 07  
Net: yazynin@mx.ihep.su  
Tel: +7 (095) 315 3122  
Fax: +7 (095) 314 1053  
Net: gelfand@mankobv.msk.ru  
Tel: +7 (0967) 74 49 07  
Fax: +7 (0967) 74 49 07  
Net: yazynin@mx.ihep.su

- \* MASLOV, Mikhail  
Radiation Research Division  
Inst. for High Energy Physics  
PROTVINO  
Moscow region 14284  
Tel: +7 (0967) 74 49 07  
Fax: +7 (0967) 74 49 07  
Net: yazynin@mx.ihep.su
- \* PELESHKO, Vladimir  
Radiation Research Division  
Inst. for High Energy Physics  
PROTVINO  
Moscow region 14284  
Tel: +7 (0967) 71 39 65  
Fax:  
Net: peleshko@mx.ihep.su
- SOBOLEVSKY, Nikolay M.  
Instit. for Nuclear Research  
of Russian Academy of Science  
60-th October Anniversary  
Prospect, 7a  
MOSCOW 117312  
Tel: +7 (095) 242 5366  
Fax: +7 (095) 135 2268  
Net: Sobolevsky@al20.inr.troitsk.ru
- SYCHEV, Boris  
Moscow Radiotechnical Inst.  
of Russian Academy of Science  
Varshavskoe shosse, 132  
Moscow, 113519  
Tel: +7 (095) 315 3122  
Fax: +7 (095) 314 1053  
Net: sychev@mankobv.msk.ru

## SWEDEN

- MALMBORG, Petter  
University of Uppsala  
The Svedberg Laboratory (TSL)  
Box 533  
S-752 21 UPPSALA  
Tel: +46 (18) 183837  
Fax: +46 (18) 183833  
Net: petter.malmborg@tsl.uu.se

## UNITED STATES OF AMERICA

- CHARLTON, Lowell A.  
ORNL  
P.O. Box 2008  
Oak Ridge, TN 37831-6363  
Tel: +1 (423) 574 0628  
Fax: +1 (423) 574 9619  
Net: Lac@ornl.gov
- COKINOS, Dimitri  
Brookhaven National Lab.  
Building 197C  
Upton, N.Y. 11973  
Tel: +1 (516) 344 2146  
Fax: +1 (516) 344 7533  
Net: cokinos@bnl.gov
- DEGTYARENKO, Pavel  
Thomas Jefferson National  
Accelerator Facility  
12000, Jefferson Ave.  
Newport News  
VA 23606  
Tel: +1 (757) 269 6274  
Fax: +1 (757) 269 7363  
Net: pavel@cebaf.gov
- DONAHUE, Richard J.  
Lawrence Berkeley Laboratory  
University of California  
1, Cyclotron Rd.  
BERKELEY, CA 94720  
Tel: +1 (510) 486 5597  
Fax: +1 (510) 486 6608  
Net: RJDonahue@lbl.gov

FASSO, Alberto SLAC MS-48 P.O. BOX 4349 Stanford, CA 94309	Tel: +1 (415) 926 4062 Fax: +1 (415) 926 3569  Net: Net: fasso@slac.stanford.edu
FU, C.Y. Building 6010, MS 6364 Oak Ridge National Laboratory P.O. Box 2008 OAK RIDGE, TN 37831-6364	Tel: +1 (423) 574 6116 Fax: +1 (423) 574 9619  Net: Net: cyf@ornl.gov
* GABRIEL, Tony A. Oak Ridge National Laboratory P.O. Box 2008 OAK RIDGE, TN 37831-6364	Tel: +1 (615) 574 6082 Fax: +1 (615) 574 9619  Net: tag@ornl.gov
HUGHES, Grady Los Alamos National Lab. MS B226 LOS ALAMOS 87547-1663	Tel: +1 (505) 667 5957 Fax: +1 (505) 665 5538  Net: hgh@lanl.gov
IPE, Nisy E. SLAC MS-48 P.O. BOX 4349 Stanford, CA 94309	Tel: +1 (415) 926 4324 Fax: +1 (415) 926 3569  Net: ipe@slac.stanford.edu
JOB, Pankakkal Advanced Photon Source Argonne National Laboratory 9700 South Cass Avenue Argonne, Illinois 60439-4803	Tel: +1 (630) 252 6573 Fax: +1 (630) 252 3222  Net: pkj@aps.anl.gov
KIRK, Bernadette L. Radiation Safety Information Computational Center Oak Ridge National Laboratory Post Office Box 2008 OAK RIDGE, TN 37831-6362	Tel: +1 (423) 574 6176 Fax: +1 (423) 574 6182  Net: blk@ornl.gov
MOKHOV, Nikolai FERMILAB MS 345 P.O. Box 500 BATAVIA IL 60510-500	Tel: +1 (708) 840 4409 Fax: +1 (708) 840 4552  Net: mokhov@fnal.gov
WALKER, Lawrence S. MS H815 Los Alamos National Laboratory LOS ALAMOS, NM 87545	Tel: Fax: +1 (505) 665 5387  Net: walker_lawrence_s@lanl.gov
WATERS, Laurie S. MS H813 Los Alamos National Laboratory LOS ALAMOS, NM 87545	Tel: +1 (505) 665 4127 Fax: +1 (505) 667 4344  Net: Net: lsw@lanl.gov

## INTERNATIONAL ORGANISATIONS

### CERN

SILARI, Marco  
CERN  
TIS-RP  
CH-1211 GENEVE 23  
SWITZERLAND

Tel: +41 (22) 767 3937  
Fax: +41 (22) 767 5700

Net: Marco.Silari@cern.ch

ZAZULA, Jan M.  
Div SL/BT (TA)  
CERN  
CH-1211 Geneve 23  
SWITZERLAND

Tel: +41 (22) 767 5372  
Fax: +41 (22) 767 8480

Net: zazula@mail.cern.ch

### OECD/NEA

\* SARTORI, Enrico  
OECD/NEA Data Bank  
Le Seine-Saint Germain  
12 boulevard des Iles  
F-92130 ISSY-LES-MOULINEAUX  
FRANCE

Tel: +33 (0)1 45 24 10 72  
Fax: +33 (0)1 45 24 11 10

Net: sartori@nea.fr

VAZ, Pedro  
OECD/NEA Data Bank  
Le Seine-Saint Germain  
12 boulevard des Iles  
F-92130 ISSY-LES-MOULINEAUX  
FRANCE

Tel: +33 (0)1 45 24 10 74  
Fax: +33 (0)1 45 24 11 10

Net: vaz@nea.fr

\* *Regrets not being able to attend.*



OECD PUBLICATIONS, 2, rue André-Pascal, 75775 PARIS CEDEX 16  
PRINTED IN FRANCE  
(68 98 07 1 P) ISBN 92-64-16071-X – No. 50085 1998